In-plane compression of preconditioned carbon/epoxy panels

PLEASE CITE THE PUBLISHED VERSION

PUBLISHER

© Luis A. Rivera

PUBLISHER STATEMENT

REPOSITORY RECORD

Rivera, Luis A.. 2016. "In-plane Compression of Preconditioned Carbon/epoxy Panels". figshare. https://hdl.handle.net/2134/20136.

In-plane compression of preconditioned carbon/epoxy panels

by
Luis A. Rivera

Doctoral Thesis

Submitted in partial fulfilment of the requirements
for the award of
Doctor of Philosophy of Loughborough University

November 2004

To God,
my family,
my Selmis,
with love

Acknowledgements

Abstract

This thesis investigates the effects of damage characteristics on residual compressive strength (RCS) of 4-mm thick preconditioned carbon/epoxy quasi-isotropic panels through the study of their compressive behaviour. Results of 2-mm thick preconditioned panels mostly from a previous study are also analysed. The preconditions of varying sizes include impact damage, quasi-static damage, single and multiple artificial delaminations of circular and elliptical shapes embedded at different through-the-thickness (TTT) locations, hemispherical-shaped domes of different curvature and depth and open holes. The mechanisms of impact damage and the characteristics of energy absorption were dependent on panel thickness and incident kinetic energy (IKE). A damage threshold for compressive strength (CS) reduction was found at 455-mm^2 and 1257 mm^2 for 2- and 4-mm thick panels, respectively. Panels affected by the presence of internal delaminations followed a sequence of prebuckling, local and global buckling (mode I) and postbuckling (mode II) in both the longitudinal and transverse directions. Their compressive failure was related to mode I to II transition. Possibility of delamination propagation was examined using response characteristics on the basis of the sequences. Evidence of delamination propagation was found only in panels with large damages and was not sensitive to RCS. For low and intermediate IKEs the effect of impact damage could be simulated with a single delamination (2-mm thick panels) and 3 delaminations of medium size (4-mm thick panels). For high IKEs, the additional effect of local curvature change was significant. The combined effect of delamination number, size and curvature change determines the RCSs. It was demonstrated that the present method of embedding artificial delaminations proves to be very useful for studying RCS of impact-damaged panels via the establishment of response characteristics and their links to the effects of the preconditions on them. This thesis also presents two analytical models, one for deflection of transversely loaded panels and the other one for the prediction of compressive strength retention factor (CSRF) based on the correlation between the ratio of maximum transverse force to initial threshold force and the CSRF, observed experimentally in thick panels.

Keywords: composite panels, impact damage, delamination, topology change, open hole, buckling, compression-after-impact, damage tolerance, compression-after-impact prediction.

Contents

1 Introduction

Composite laminates are widely used in the aerospace industry and other sectors. They have an outstanding specific modulus, specific strength and the capability of being tailored for a specific application, offering substantial advantages over traditional metallic materials. Composite structures could encounter impact loads during component manufacture, normal operation or maintenance. Such impact loads could occur at relative low velocities, in the events of tool dropping on the structure or runway debris during take-off or landing. They could also occur at high impact velocities when hailstones hit the structures during flight. The situation could become critical when invisible internal damage further propagates during subsequent loadings. Impact damage is generally manifested in the form of matrix cracking, fibre fracture and delamination. The presence of damage can degrade the structural response of the components, in terms of strength and stiffness. In particular the in-plane compression strength is susceptible to impact damage. An important requirement in the design of composite structures is the ability to tolerate impact damage, thus the damage tolerance assessment is a key process in design and applications of composite structures. Therefore, a thorough understanding of the compressive behaviour of impact-damaged composite structures is essential.

In the past two decades, a significant amount of work has been done on impact damage and the determination of residual compressive strength (RCS) of composite structures. The present chapter reviews relevant work in recent years, focusing on studies done from the 90's onwards. Early studies are reviewed in [1-3]. A summary of the literature reviewed in this chapter is presented in Tables 1.1.1 to 1.1.3. At the end of this chapter the main aims and objectives of the project are listed, taking in account the research issues identified along the literature review.

1.1 Overview of in-plane compression-after-impact research

The determination of RCS involves two phases, the phase for damage introduction and the phase for in-plane compression. RCS results are highly dependent upon factors such as specimen geometry, lay-up, indenter geometry, indenter weight, impact force,

incident kinetic energy (IKE) and boundary conditions for a given composite material with a constant fibre volume fraction. Thus, they are specific to the geometric and physical conditions involved. Numerous combinations of impactor mass and velocity can be obtained for the same level of IKE. If the resin system is strain-rate sensitive then the damage mechanisms induced by impact are dependent on impact velocity. This study is restricted to low velocity impact only, with low impact energy level so that composite panels will not endure perforation, instead suffer mainly from internal delamination with moderate surface damage at the upper end of impact energy range.

The in-plane compressive strength of composite panels is particularly dependent on the particular aspect ratio [4-6]. Thus most research on RCS, including this one, is based on panels as the compressive properties derived from small coupons do not represent the behaviour of the larger panels. The RCS of preconditioned panels has been intensively studied in recent years. Preconditions include impact damage, damage induced by quasi-static transverse loading, artificial delaminations and open holes. However, there is no unified international standard for the determination of RCS. Instead, there are a few major methods, which have been developed as the result of research by various organizations, as shown in [7, 8]. Five major testing methods have been reported in literature and they are NASA, Boeing-SACMA (Suppliers of Advance Composites Materials Association), QMW (Queen Mary and Westfield College) [8], CRAG (Composites Research Advisory Group) and IC/LU (Imperial College and Loughborough University). A substantial amount of studies have used the specimen configuration of Boeing/SACMA method. As shown in Table 1.1.4, in this method the same panel size is used for both impact and in-plane compressive phase with a specific level of impact energy. On the contrary the IC/LU method uses a larger impact testing area so that a slightly wider range of IKE could be delivered.

The advantage of NASA and Boeing/SACMA methods is that the rectangular specimen geometry represents a more realistic scenario for practical structures. Nevertheless, in the impact phase, impact at the centre of the specimen is an event that the panel tends to deform concentrically. If the rectangular panels are used as in the NASA and Boeing/SACMA methods, then deformation reflection from different straight boundaries may affect the impact event differently, particularly if induced damage areas

2

are relatively large. This could be avoided by keeping the damage far away from boundaries and/or by choosing a circular testing area, as in the QMW, CRAG and IC/LU methods.

Table 1.1.4 Compression-after-impact testing methods

	Parameter	Unit	NASA	Boeing/ SACMA	QMW college	CRAG	IC/LU
Impact phase	Specimen geometry		Square	Rectangle	Rectangle	Circle	Circle
	Specimen size [a]	mm	254×177.8× 6.35	150×100× 4.6-5.6	89×55×2	140×3	500-100×10-25
	Impact test area		127×127	127×76.2	Dia. 40	Dia. 100	Dia. 100-500
	Boundary conditions [b]		C	C at four points	C	C	C
	Impactor mass	kg	4.5	4.6-6.8	3.96	As required	As required
	Impact energy	J	28	As required	As required	As required	As required
Compression phase	Specimen size [a]	mm	254×127× 6.35	150×100× 4.6-5.6	89×55×2	180×50×3	350×250× 10-25 or 150×100× 1-6.4
	Loading [b]		End loading, C	End loading, C	End loading, C	End tabs, shear loading, C	Epoxy potted ends, end loading, C
	Side edges [b]		SS	SS	SS	SS	SS
	Loading rate	mm/ min	1.27	0.5	0.3	To cause failure within 30-90 s	1

[a] The specimen size is given by length, width and thickness (L×W×t) for rectangular specimens and diameter and thickness (Dia×t) for circular specimens

[b] C and SS stand for clamped and simple supported boundary conditions, respectively

1.2 Damage characteristics

Damage tolerance assessment requires a detailed description of a state of damage in terms of damage mechanisms, damage size and through-the-thickness (TTT) distribution of size. Damage mechanisms induced by low velocity impact can be divided in two categories, material damages and associated localised geometric change.

Material damages include internal delaminations, matrix cracks and fibres fracture. Local change of geometry around the impact site is due to the impact-induced indentation. The determination of damage size is usually given by delamination area, either the projected area or the cumulative contribution of individual delaminations distributed in the TTT direction of the laminate.

The damage generation process is determined by the interaction between the impactor and the target laminates. On the one hand, laminates with low flexural rigidity develop large bending strains when they are loaded transversely, causing tension failure on the back-face and compression failure on the front. Additionally large deflections could induce membrane stresses [9]. The damage starts locally around the impactor, continuing in the TTT direction as a 'shear cone' that contains matrix cracks and delaminations in a 3-D spiral pattern [10]. On the other hand, the transverse response of stiffer laminates has much higher transverse forces, giving rise to high internal shear stresses [11, 12]. Thus, the damage is dominated by the interlaminar shear stress (ILSS) [13]. A large delamination tends to appear near the mid-plane in addition to a significantly smaller shear cone, as shown in Figure 3.2.4(c). The shear cone develops locally starting on the upper surface and stopping at the ILSS-induced delamination.

The conical pattern of TTT damage distribution has been studied using cross sectioning [1, 14-17] and thermal deply [10, 18] for relatively flexible targets. In [18] a 32-ply quasi-isotropic (QI), CFRP laminate plate was impacted at 25.2 J. The delamination areas were smallest near the upper surface (2 cm^2 per interface) and were the maximum near the bottom surface (10 cm^2). Intra-ply matrix cracks were generated near the impact centre, running parallel to the ply orientations and propagated until they reached interfaces between plies with different orientation and then continued as delamination. Similarly it was observed [10, 11, 18-20] that delamination initiated and grew only between adjacent plies of different orientations and its shape depends on the relative angle between those plies [21] as shown in Figure 1.2.1. It was clear that the projected area of delaminations tended to a circular shape.

The relationship between surface topology change and delamination area has not shown conclusive results. While some studies showed that there was no correlation between

the two by using thin CFRP [22, 23] and thick QI CFRP [23, 24], other studies showed that indent depths correlated to the degree of internal damage in 16-ply QI CFRP panels [25] and GFRP woven roving plates [26].

1.3 Factors affecting damage characteristics

1.3.1 Laminate thickness

The effect of laminate thickness on damage initiation and propagation depends on the flexural stiffness of laminates. As mentioned earlier, the damage induced in relatively flexible panels was dominated by tensile stress and characterised by the presence of a shear cone. On the contrary, damage induced in relatively stiff panels was dominated by ILSS and characterised by a large delamination near the mid-plane. Thicker and stiffer QI CFRP panels had significant larger delamination areas than thinner and flexible panels [9]. At an IKE of 0.5 J/ply the delamination area of 32- and 16-ply panels were 15% and 49% of the correspondent 48-ply panels with the in-plane dimensions and impact conditions remaining constant. Similarly [11] increasing the thickness from 2 to 4 mm (16 to 32 plies) of 127×75 mm CFRP QI panels resulted in a delamination area nearly 3.5 times higher, at the similar IKE of 0.4 J/ply. When the total cumulative area was used instead of the projected delamination area [27] similar results were obtained. An increase in panel thickness from 9 to 21 plies resulted in a delamination area 7.5 times larger for an IKE of 2.1 J/ply and using a lay-up of $[0_3/90_3/0_3]_n$. However, an inverse relationship between delamination rate and thickness was observed in [11] when the variation of thickness was not large enough to produce a significant change in the panel stiffness (i.e. damage governing mechanism). In this case, increasing the thickness from 1 to 2 mm of 127×75 mm CFRP QI panels was reflected in a decrease of 20% of projected delamination area, at 0.38 J/ply.

The effect of panel thickness on the peak load was studied in [28, 29], rectangular laminate plates made of GFRP were impacted at various IKE levels, ranging from 6.64 to 360 J using a 12.5-mm diameter hemispherical impactor. In that study, three sizes of square panels were used, 125, 84 and 12-mm and two thickness values, 6.69 (51-ply) and 2.24 (18-ply). The peak loads were related linearly to low levels of IKEs, varying

from 0 to 16.2 kN (0 to 106 J) and 0 to 4.2 kN (0 to 30 J), for thick and thin panels respectively. However after the fibre breakage onset, the peak load remained relatively constant for a wide range of IKE, 16.2 to 19 kN (190 to 390 J) and 4.2 kN (35 to 360 J) for thick and thick panels respectively. Despite the bending stiffness of the thick panel being nearly 9 times higher than the thin panel, the maximum peak load was just over 4.5 times higher, suggesting that there were additional factors apart from bending in the panel impact response.

1.3.2 In-plane dimensions

The panel in-plane dimensions affect the damage generation in two ways. On the one hand, together with the thickness they determine the flexural response of the panel and consequently the governing damage mechanism. On the other hand, they are one of the factors in the determination of the contact pressure, alongside with the indenter size and shape. The influence of in-plane dimensions in the determination of the damage dominant process was observed for CFRP QI panels [11]. When the in-plane dimensions were increased with a constant thickness, there was a drop in delamination area that indicated the influence of panel dimensions on the panel stiffness and the governing damage mechanisms. The delamination area of 1-mm thick panels was reduced by 53% at an IKE of 3 J by changing the in-plane dimensions from 127×75 to 200×200 mm, keeping constant the impact conditions. For 4-mm thick panels the reduction was 61% at around an IKE of 20 J. In [30] 2-mm thick cross-ply (CP) GFRP woven plates of 102- and 337-mm diameter were impacted. Sizes of delamination were relatively close and for the large plate the area was only 11% less than that of the small plate at an IKE of 7.2 J. This result suggested that both plates had similar dominant damage mechanisms.

The effect of in-plane dimensions on the panel response measured through the transverse peak force depends on the relative size of the impactor to the panel. On the one hand for a relatively small contact area between the impactor and the panel, the effect of in-plane dimensions is negligible. In [31], 32-ply QI CFRP plates of 50.8 and 76.2 mm diameter were quasi-statically loaded with a hemispherical indenter of 6.35 mm diameter. There was a linear trend between the width of delamination and the

maximum applied load and both panel thickness had a proportionality constant of 24.1 mm/kN. Similarly, 102 and 337 mm diameter [30], and 127×75 and 200×200 mm panels [11] were transversely loaded with a 12.7-mm diameter hemispherical-ended indenter. A change of in-plane panel dimensions (keeping the same thickness) did not affect the relationship between transverse peak force and the delamination area. On the other hand, for relatively large impactors the effect of varying the panel size may become significant. In [32] 40 and 120-mm diameter CFRP (woven) circular plates of 2 mm thickness were quasi-statically loaded to a complete failure with indenters of different size (8 and 20 mm diameter) and shape (hemispherical and flat-ended). The average reduction of peak load due to increasing the in-plane dimensions (from 40 to 120 mm) was 23% and 33%, respectively for the 8-mm and 20-mm indenters.

1.3.3 Impactor size and shape

The respective effects of indenter size and shape on the damage generation are closely linked with the effects of in-plane dimensions. The relative size of the indenter with respect to the panel dimensions determines maximum panel deflection and stress distribution. Additionally, the interaction of the impactor and the laminate determines the distribution of contact stress and the distribution of ILSS inside the laminates, thereby dictating the delamination onset and propagation. The effect of the impactor shape and size on the delamination rate was studied in [33], with 100×150 mm panels of woven CFRP impacted at IKE levels ranging from 5.5 to 10.6 J. Two sizes of hemispherical indenter were used, 21 and 6.3 mm. The absorbed energy varied from 70 to 79% of the total IKE, for the large indenter, whereas the variation was from 87 to 94% for the small indenter. Similarly the area of delamination increased 2.3 times by shifting from large to small impactor diameter, at an IKE of 10.6 J.

The effect of impactor size and shape on the critical load for delamination onset was shown in [32]. Hemispherical and flat indenters of 8 to 20 mm diameter were used to apply quasi-static transverse load to 9-ply woven CFRP panels. A change in indenter size from 8 to 20-mm diameter (hemispherical) increased the threshold force for delamination onset by 25%. Moreover, a change in shape from hemispherical to flat changed the panel response so that the threshold value and the maximum force were

practically coincident in the flat indenter case. In [34] similar results were reported for 25.4-mm diameter QI CFRP laminate plates, quasi-statically loaded. Varying the size of a flat indenter from 3.8 to 18-mm was reflected in a threshold range from 10 to 24 kN. Additionally, the threshold force for delamination onset was determined as 13, 9 and 5 kN for flat, hemispherical and conical indenter shapes, respectively.

The impactor shape and size effect on the transverse peak force was shown in [32]. Changing the indenter nose shape from flat to hemispherical resulted in 47% and 73% decrease in the peak load recorded, for small (8-mm diameter) and large (20-mm diameter) indenters respectively. These results agreed with a previous study [34] in which 6.15-mm thick CFRP laminate circular plates were subjected to quasi-static loading until failure. The peak loads were 23, 15 and 9 kN, for flat, hemispherical and conical indenter nose shapes respectively. The nominal diameter for all the indenters was 7.6 mm.

1.3.4 Composite lay-up

The effect of lay-up on damage depends on the relative angle between adjacent plies and the number of plies of the same orientation. On the one hand, increasing the relative angle between plies [10] from $[(-45_2/90_2/45_2/0_2)_2]_s$ to $[(-45_2/90_2/0_2/45_2)_2]_s$ decreased the total cumulative area by 22.5% at an IKE of 16 J. Similarly in [35, 36] two QI lay-ups were impacted at various IKE levels. At the maximum IKE level, the delamination width values were 60 and 49 mm for $[45(90/-45)_3(0/45)_2/0]_s$ and $[45(0/-45)_3(90/45)_2/90]_s$ respectively. On the other hand, increasing the number of equally-orientated adjacent plies was shown to reduce the cumulative area of delamination, since it only appears between adjacent plies of different orientations. The effect of ply groups on delamination rate was studied in [10, 27, 35, 36]. In [27] two lay-ups were used for 21-ply GFRP laminate panels, $(0_7/90_7/0_7)$ and $(0_3/90_3/0_3)_n$. The correspondent cumulative delamination area of the former was around 85% of the latter, at an IKE of 27 J. However ply grouping facilitates early matrix cracking, since the cracks develop within fibres with the same orientation [10], leading to an increase in the projected area of delamination. This effect is shown in [35, 36] using CFRP laminate panels with two different lay-ups, subjected to impact loading. The two lay-ups were $(45_3/90_3/-45_3/0_3)_s$

8

and (45/90/-45/0)$_{3S}$. At the maximum IKE level of 40.7 J the projected delamination diameters were 81 and 28 mm respectively.

For the effects of matrix toughness and fibre architecture on impact damage, the interested reader should refer to [16, 34, 37-39] for the former and to [40] for the latter.

1.3.5 Impactor mass, impact velocity and IKE

The projected and total delamination areas are related to the main parameters of the transverse loading response, in terms of IKE and load. As a general trend, increasing the IKE level leads to an increase in delamination area. However the linearity of this trend depends on the governing damage mechanism. For low IKEs, delamination is the main mechanism and fibre breakage is the dominant one at higher IKEs. Consequently two constant slopes of IKE-delamination areas may be identified as summarised in Table 1.1.1 [10, 11, 27, 30, 33, 37, 39, 41-43] and were used to identify the change of damage mechanisms from delamination to fibre breakage. The delamination areas were also related to peak load, analogous to IKE level [9, 11, 22, 30, 31, 38, 42, 44]. However, the second linear range with a reduced slope as observed with IKE, was not observed [11, 30, 42].

The impactor mass effect on the damage generation was studied in [45]. CFRP laminate panels of 48 plies were impacted at various energy levels. Four impactor masses of 1.13, 2.27, 4.54, and 9.08 kg were used and each one delivered an IKE range from 13.6 to 33.9 J. The study concluded that for panels impacted at the same IKE level, the damage area increased as the mass of the impactor decreased. However there is insufficient information to either support or contradict these findings.

Low-velocity impact and quasi-static transverse loading induce similar type of damage as proved by numerous studies [16, 20, 24, 38, 41, 46]. This similarity is valid provided that the resin is not strain-rate sensitive. An analysis of the impact response of composite panels was presented in [47] with a two-degree-of-freedom spring-mass model. It was concluded that the low-velocity impact can be considered as a quasi-static response provided that the duration of the impact event is many times longer than the

time for generated stress waves to travel to outer boundary of the plate and return. This is indeed the case of large-mass low velocity impact, where the contact stiffness is several orders of magnitude larger than the structural stiffness.

1.3.6 Boundary conditions and panel shape

The effect of the type of boundary condition (i.e. clamped or simply supported) on damage is related to the panel flexural stiffness and the governing damage mechanism. The additional stiffness introduced by clamping the panel boundary could be large enough to result in a change from damage dominated by tensile stress to ILSS, although this effect depends on the panel dimensions. In [11], 1- and 2-mm thick panels of two different in-plane dimensions were impacted. In the case of 200×200 mm panels, the projected areas were 56% (at 2.5 J for 1-mm thick panels) and 150% higher (at 4.2 J, 2-mm thick panels) in clamped panels than in simply supported panels. On the contrary, 127×75-mm panels (1, 2 and 4-mm thick) and 200×200-mm panels (4-mm thick) did not show any significant difference between clamped and simply supported conditions.

The rigidity of the support also affects the damage extent. In [48], two sets of CFRP laminate panels were impacted at 27.1 J. For the first set, the panels were simply supported using a fixture made of wood and aluminium, providing a relatively flexible substrate. The other set used a fixture made of steel, much more rigid. The damage area values were 516 and 710 mm^2 respectively, suggesting that the absorbed energy of a panel supported on a relatively flexible fixture is lower than the one supported on a rigid fixture.

A change in the boundary conditions affects the transverse force only for relatively large impactor sizes. In [11], a 12.7-mm diameter impactor was used. The proportionality between peak force and delamination area was the same for both clamped and simply supported panels. For panels loaded quasi-statically [32], the results between clamped and simply supported conditions offered no significant difference when a 8-mm diameter indenter was used. However, as the diameter of the indenter increased to 20 mm, the peak load values of the clamped plates were higher than the simply supported.

The effect of panel shape (circular or rectangular) on damage is related to the effect of the relative size of the impactor respect to the panel. Two studies used both circular [38] and rectangular [44] panels. In both, the panels were impacted by a hemispherical-ended impactor of 12.7 mm diameter, and they were made of the same composite system (AS4/3501-6) with a similar lay-up (48 plies, QI). The relationship between transverse peak force and delamination diameter had similar proportionality constants, 13.9mm/kN and 12.5 mm/kN, for circular (102 mm diameter) and rectangular (76.2×76.2 mm) plates, respectively. The threshold value for the damage initiation was higher for the rectangular (12 kN) than for the circular (7 kN) shape, probably as a consequence of the larger relative size of the impactor with respect to the in-plane dimension in the rectangular case.

1.4 Factors affecting damage tolerance

Damage tolerance assessment of preconditioned panels is based on the understanding of the relationship between the damage state and the reduction of compressive strength (CS) in terms of delamination size, IKE and transverse peak load. A relative measure of the reduction in CS is provided by the compressive strength retention factor (CSRF) that compares the intact and the post-impact compressive properties. The effect of the damage presence on the in-plane compressive behaviour is reflected on the reduction of critical values of compressive stresses, such as local delamination buckling, global buckling and delamination propagation stress. This section reviews the effect of the damage state and testing parameters on the compressive behaviour and on RCS. The parameters examined include composite system, specimen dimensions, impact testing conditions and environment effect. The damage state characteristics examined include delamination size, number, shape and orientation, and TTT location, apart from local change of geometry. A summary of the main studies reviewed in this section is presented in Tables 1.1.2 to 1.1.3.

1.4.1 Material effect

Toughened composite systems fail at higher compressive loads because the initial delamination areas for the given IKE were smaller as a consequence of the higher resistance to delamination propagation exhibited by toughened matrix during impact loading [37, 39, 43, 49-52]. This was evidenced by the direct relationship found between the increase in CSRF and G_{IIC} [53-55]. The RCS properties were also improved via enhancing the toughness fibre/resin interface [49, 54].

Different fibre architectures can also improve the delamination resistance and damage tolerance of the material. A woven fibre architecture was found to have better RCS properties than UD-based system, as a consequence of the restriction of delamination initiation and growth between fibres with different orientation [56, 57] for the similar IKE levels. For a given architecture such as knitted textiles [58], increasing the total loop density improved interlaminar fracture toughness, thereby improving CSRF.

Innovative TTT reinforcements have been used recently to tackle the inherent weakness of a laminate material towards ILSS, with a varying degree of success. The main concepts were reviewed in [59] and it included knitting [58, 60], braiding and special woven configurations [61, 62], Z-pins [63-65], stitching [66-69], interleaving [70, 71] and hybrid composites [72].

1.4.2 Lay-up effect

The effect of lay-up on the RCS is dictated by its effects on the impact and compressive phases of CAI testing. On the one hand, one of the lay-up effects on the impact phase is seen when plies of equal orientation are grouped together matrix cracks develop easier, delamination tends to be larger and as a consequence the RCS is lower [35, 50]. In terms of damage tolerant design, it was shown that placing 45° fibres in the surface ply increased delamination energy initiation [73]. Consequently the trend for design should be in favour of a panel with damage tolerant skin, which means small proportion of 0° plies (loading direction), and stiffer stringers with mainly 0° plies inside the composite [74]. On the other hand, fibre orientation affects mainly the compressive stage of CAI

testing as shown in [17]. Three QI lay-ups with different proportions of fibres aligned in the load direction were tested in CAI. Laminates with very low percentage (<25%) of plies in the loading direction had similar failure loads but higher failure strain than laminates with higher (>25%) percentage. Similar results were reported in [75]. Panels with 17% and 67% of fibres in the loading direction had a reduction of 58% and 68% in the residual failure strain respectively, for the larger size of delamination studied.

1.4.3 Overall panel dimensions effect

Panel thickness has a marked effect on the damage generation and impact response, as it was discussed earlier in Section 1.3.1. It also affects the compressive panel behaviour, in particular the determination of the buckling load.

The effect of an increment in thickness on the CAI performance was found to be detrimental in terms of CSRF. As discussed earlier, damage inflicted onto stiff laminates is more extensive than damage in flexible laminates, thus a thin laminate has a relatively better CAI performance than a thick one. In [52], IKE/ply levels of 1.6 and 1.42 J/ply were applied to 26- and 96-ply laminates respectively. Despite the similarity in IKE level, the CSRF was 0.75 and 0.42 respectively. In [76] 40 and 24-ply CFRP panels were impacted within a range of 2 to 3 J/mm and 1.6 to 3.3 J/mm respectively. For thick panels the reduction of CS was between 38% and 46%. The CS reduction of thin panels was significantly lower, between 4% and 27%. Additionally it was observed that the correlation between residual compressive strength and strain was good for the majority of the specimens. Similarly in [77] the CS was reduced by 41% when a thin panel (32-ply, 4 mm thick) was impacted at 2.4 J/mm, but by 64% for the 48-ply or 6-mm thick panel.

However when comparing relatively stiff panels, even thicker panels seem to provide better residual strength retention due most likely to the fact that buckling occurrence is not a concern and damage is governed by ILSS. In [78], thick panels had a better CAI performance than thin panels, especially when the transverse peak load was used as the impact parameter. GRFP woven panels of two different thicknesses, 10 and 25 mm, were tested in CAI. The peak loads were between 45 and 92 kN (400 to 1670 J) for thin

13

panels and 67 and 120 kN (350 to 2600 J) for thick panels. The reduction of CS was between 49% and 72% for the thin panels and between 45 and 60% for the thicker panels, indicating a better CAI performance. Similar results were reported in [79] for 14 and 19 mm thick GFRP woven fabric panels.

In-plane dimensions expressed as the aspect ratio, AR, have two major effects on the CS of intact panels. Firstly, AR and thickness are geometrical parameters involved in the buckling load determination. Secondly, an effect unique to composite materials has been observed as a direct consequence of the AR: the amount of unconstrained fibres (unloaded edges) vs. constrained fibres (by the loading platen) during compressive loading. In [4, 5] the compressive strength was found to be inversely proportional to the AR. However AR was found not to be a source of any stiffness trend. Instead, the specimen height played an important roll in the stiffness determination. Taller panels had a stiffer response compared with shorter ones. These trends were followed irrespective of the laminate lay-up.

The effect of AR on the CAI strength has not been thoroughly studied and more research needs to be done. In [80] the AR effect was studied in composite panels subjected to impact loading during compression. No significant difference was found between the compressive failure strain ratio for panels with AR of 1, 1.5 and 2, after being impacted at similar IKE level. The IKE range was between 0 and 5 J. However the panel was held with the unloaded edges fully clamped, which might have provided support to unconstrained fibres.

1.4.4 Material damage effect

Material impact damage mechanisms consist mainly of fibre breakage, matrix cracks and internal delaminations. Among them, internal delaminations have the strongest influence on the CS reduction. The main parameters of describing internal delaminations are size, number, shape, orientation and TTT distribution. Due to its complexity, the individual study of each parameter is virtually impossible with impact-induced damage. However many authors (see Table 1.1.3) have simulated impact-

induced delaminations with artificial delaminations, embedded during manufacturing process, thus each individual effects can be represented.

Delamination size effect

Increasing the delamination size is reflected in a reduction of RCS, as many studies have shown [1, 2]. This section reviews the effect of delamination size not only on the RCS, but also on delamination buckling, propagation and failure.

The minimum size of delamination that causes a reduction of RCS depends on factors like panel thickness, delamination number and TTT depth. Below the threshold size of delamination, the compressive behaviour and failure of a delaminated panel is similar to an intact one. In [81] this value was between 12.7 and 25.4 mm diameter, for a single circular delamination in a 8-ply CFRP woven panel. In [82] this value was between 6 and 9 mm major axis, for a single elliptical delamination (AR 1.72) in a 8-ply CFRP UD laminate. For multiple delaminations, the threshold size is also present, in [83] 4 identical circular delaminations were embedded within one half section of a 32-ply CFRP panel, the other half section was left untouched. The smallest delamination, 12.7 mm, did not show delamination propagation, suggesting that the threshold size was between 12.7 and 19.1 mm. The effect of the resin toughness on the threshold size of delamination is shown in [84]. Five circular delaminations of the same size were evenly embedded in the TTT direction in a 12-ply CFRP woven panel. Two composite systems were used based on the T400 carbon fibre. The system with conventional resin had a threshold size between 10 and 20 mm diameter. On the other hand the toughened resin system had the threshold size between 20 and 30 mm diameter.

Delamination buckling and the propagation stresses are also affected by the size of delamination. In [85, 86] a single circular delamination was embedded at the 4/5 interface of a 24-ply CFRP composite. Two panels with different delamination size were tested in compression, 12.7 and 25.4 mm diameter. The delamination-buckling load was 352 kN and 220 kN respectively. In [81] single circular delaminations of 12.7, 25.4 and 38.1 mm diameter were embedded at the 2/3 interface of an 8-ply CFRP woven panel. Based on strain gauge readings (in back-to-back configuration) the

15

buckling and propagation stresses were determined. In the case of the panel with 38.1 mm diameter delamination, it was observed that the thin sublaminate buckled first at a load of approximately 30 kN (101 MPa). This was followed by the buckling of the remaining six-ply sublaminate at approximately 64 kN (201 MPa). Subsequently strain reversal was detected at the outer strain gauges, indicating propagation of delamination at 243 MPa. Analogously for 25.4 mm size, the delamination buckling of the thin and thick sublaminates was at 211 MPa and 250 MPa, respectively. The delamination propagation stress was at 268 MPa.

The reduction of RCS and the compressive failure mechanisms are affected by the delamination size. In [81] the failure mechanisms of the panel with the smallest delamination (12.7 mm) differed from the larger ones (25.4 mm and 38.1 mm). For the former, failure was similar to the intact panel in overall specimen crippling without any delamination propagation. For the latter, failure was triggered by delamination propagation. As a consequence, the reduction of RCS was 0%, 33% and 34% for 12.7, 25.4 and 38.1 mm diameter respectively. The RCS values in [83] ranged from 323 to 204 MPa for the four sizes studied, from 12.7 to 41.3 mm diameter. Additionally it was noted that buckling was not necessarily synonymous with failure and initial out-of-plane imperfections triggered ILSS and delamination growth before buckling.

The size effect of multiple delaminations on the buckling and propagation stresses has also been studied using delaminations of constant size distributed through the thickness. In [83] four delaminations of equal size were embedded, with diameters of 12.7, 19.1, 25.4 and 41.3 mm. Three replicates of each size were tested. Using shadow Moire, the propagation loads were determined as 250, 223 and 194 MPa for 19.1, 25.4 and 41.3 mm diameter respectively. The smallest delamination of 12.7 mm did not show delamination propagation. In [84] the out-of-plane displacements of panels with 5 delaminations were measured during compressive loading. It was observed that with an increase of the size, buckling mode shifts from global type to a mixed type, characterised by transverse delamination opening. The buckling load reduction becomes significant when the diameter of delamination exceeds certain value depending on specimen and composite system, in particular resin type.

The delamination buckling of panels with multiple delaminations of varying sizes in the thickness direction is determined by the largest delamination. In [87, 88] GFRP woven panels had 7 delaminations located at regular intervals in the thickness direction. The diameter of the delamination increased from the top surface to the bottom. The compressive behaviour was monitored using LVDT at both sides of the panel. Buckling started locally at the side of the largest delamination. Subsequently the global laminate tended to deform into the same direction. Therefore the size of the largest delamination determined the local buckling load. However the global in-plane stiffness was not affected until the deflection of the side with the largest delamination was significant [87]. Similarly delamination buckling was not directly related to the compressive failure of impacted panels. In [77, 89] buckling appeared well before the final failure load is reached. The buckle of the sublaminate had no effect on the variation of the strain-stress relationship, which was linear as measured at a point outside the damaged area. This means that the buckled sublaminate is such a small portion of the whole laminate that a change in the stiffness of this portion does not affect the overall behaviour of the laminate.

Number effect

The number of delamination has a direct effect on the CS reduction, an increase in the total cumulative area results in a reduction in CS of panels with embedded delaminations. In [90] this effect was investigated with 25.4 mm diameter circular delaminations evenly embedded in a 16-ply CFRP panel. The RCS of panels with 1, 3, 5, and 7 delaminations were 306, 181, 168 and 168 MPa respectively. Another distribution was tested, with all the delaminations shifted towards one side of the panel in an asymmetrical arrangement, for 1, 3 and 5 delaminations the RCS was 358, 229 and 194 MPa respectively. Nevertheless, the effect of delamination number is not linear and increasing a large cumulative area with an additional delamination may have a small marginal effect on the RCS. In this case, the size of the delaminations or even their depths, rather than their number, is more important in the degradation of RCS.

The effect of the total cumulative delamination area on the RCS must consider the distribution of delamination size in the thickness direction. In [88] the out-of-plane

measurement of two panels was compared. One of the panels had 8 identical delamination of 30 mm diameter. The other panel had 7 delaminations evenly distributed, increasing from 22.5 mm on the front surface to 37.5 mm towards the back surface. Despite having similar cumulative delamination areas, the buckling and failure loads were much higher in the case of identical delaminations, 78% and 48% of the intact buckling and failure load respectively, compared with 55% and 33% of the panel with conical distribution. Contrastingly in [90], the total cumulative area provided a reliable measurement of the damage extent independently from the size distribution in the thickness direction. The RCS of two panels with similar cumulative area of delamination but different size distribution was compared. One of the panels had 3 circular delaminations evenly distributed, with a constant diameter of 25.4 mm. The other panel had 7 delaminations evenly spaced in a conical distribution increasing from 6.35 to 25.4 mm diameter. The RCSs were 181 and 184 MPa, respectively.

In contrast, the buckling load was not affected by increasing the number of delaminations as shown in [85, 86]. Circular delaminations of 25.4 mm were embedded in 24-ply CFRP laminate panels. Panels with 1, 2 or 3 delaminations were tested in compression; their corresponding buckling loads were 220, 211 and 227 kN.

Shape and orientation effects

Delamination tends to propagate in the transverse direction [81, 87, 91-94]. Delamination shapes such as ellipse or rectangle have a major axis that can be orientated along the transverse axis in the width direction of the panel. This creates a region with high concentration of ILSS, therefore it is intuitively expected that such panels will tend to fail at lower stress levels as a consequence of the delamination propagation. On the contrary, circular shapes are neutral in this respect. However it was found that only the buckling load is affected by delamination shape and orientation and that the reduction in RCS is independent of these variables [82, 85, 86, 95].

The local buckling load of a sublaminate depends on the delamination shape and orientation. In [85, 86] two shapes were compared using 24-ply CFRP laminate panels with elliptical delamination of 25.4/12.7 mm (major/minor axis), 12.7 and 25.4 mm

diameter circular delamination, all embedded at the 4/5 interface. The ellipse was oriented in the width direction. The buckling load was 462, 352 and 220 kN, respectively. The trend of the results may be justified by the fact that narrow and long sublaminates aligned with the load direction tend to buckle easier than flat and short sublaminates. The effect of orientation in the buckling load was studied in [91] using elliptical delaminations of 38/20 mm of major/minor axis oriented at ±45°, in the width or in the loading directions. The delamination buckling stresses were 209, 215, 203 and 189 MPa, respectively, confirming the previous relationship between sublaminate AR and buckling load. However the RCS values were 269, 295, 285 and 278 MPa respectively, without any apparent relationship. Thus, the orientation of delamination did not have any effect on the RCS of these panels, probably due to the complex shapes in which the sublaminates grow and propagate, that do not keep any relationship with the original delamination shape. In [95] 24-ply CFRP laminate panels had an elliptical delamination of 45/20 mm major/minor axis oriented in the width or in the load directions and embedded at the 3/4 interface. The buckling loads were 19 and 10 kN, respectively, showing a marked effect due to the orientation. Nevertheless, the propagation load was in both cases 53 kN. In [82] a single elliptical delamination of 15.3/8.9 mm major/minor axis was embedded at the midsection of 8-ply CFRP UD laminate panels, oriented to 90° (width), 60°, 30° and 0° (loading) directions. The reduction in the local buckling load was 13%, 10%, 11% and 8%, respectively, showing a slightly decrease in the buckling load as the angle of the major axis with the loading axis increases.

Through-the-thickness (TTT) location effect

Embedding delaminations at different TTT depths intends to study the effect of eccentricity and unbalanced sublaminates on the RCS. As a general rule, the distribution of impact damage in the thickness direction is asymmetrical. When such damage interacts with in-plane compressive loading, the eccentricity is combined with the bending-stretching and bending-twisting couplings of the unbalanced sublaminates, producing non-linear behaviours that can trigger local and global buckling, delamination propagation and failure. In [85, 86] the load of delamination buckling was substantially increased from 462 kN to more than 500 kN by shifting an elliptical

delamination from the 4/5 to the 8/9 interface in a 24-ply CFRP laminate panel. Similarly, in [92] and [93] the buckling and propagation loads were determined in 35-ply CFRP laminate panels with single circular delamination embedded at the 3/4, 5/6 or 7/8 interface. The local load for delamination buckling was affected by the depth of the 60-mm delamination, with values of 9.5, 41 and 70 kN for the 3/4, 5/6 or 7/8 interface cases respectively. However the global buckling load remained at a similar level, 104, 107 and 103 kN respectively. For 55-mm diameter delamination the local buckling was at 17.2, 59.3 and 97.2 kN whereas the global buckling was determined at 106.4, 104 and 111 kN for the 3/4, 5/6 or 7/8 interface cases respectively. Contrastingly for the 8-ply CFRP UD laminates used in [82], it was found that the buckling strengths decreased slightly as the delamination was located farther to the centre of the laminates.

The depth of delamination in the thickness direction influences not only delamination buckling load but also out-of-plane displacements. In [96] stereo imaging was used to measure out-of-plane displacements. Single circular delaminations of 64 mm diameter were embedded in 24-ply CFRP laminate panels. Varying the depth of delamination from the 4/5 to the 5/6 interface resulted in a decrease from 1.25 to 1.05 mm in the out-of-plane measurement at the point of delamination growth. The correspondent propagation loads were 54 and 56 kN, respectively. Decreasing the depth of a given delamination reduces its effect on the RCS because the thicker sublaminate governs the global behaviour. In [90] single and multiple (3 and 5) circular delaminations of 25.4 mm diameter were embedded in a symmetric and asymmetric TTT distributions. By shifting from the symmetric to the asymmetric distribution the RCS varied from 306 to 358 MPa (single delamination), 181 to 229 MPa (3 delaminations) and 168 to 194 MPa (5 delaminations). Rectangular delaminations were studied in [97, 98]. The tests on 8-ply GFRP laminate panels showed that the failure load decreases with the TTT position of the delamination. The reductions in the failure load were 16%, 29% and 31% for single rectangular delaminations (25 mm square) embedded at the 1/2, 3/4 and 4/5 interfaces respectively.

1.4.5 Local curvature change

The effect of local change of curvature induced by the impactor nose on the RCS has not been widely investigated. In [26] the permanent indentation related linearly with the crack length. In turn the crack length related linearly to the CSRF, thereby linking the reduction of CS and the permanent indentation value. However other findings [22] have shown that the dent depth cannot be used as a damage measurement. In [99] the effect on the compressive behaviour of the local change of geometry around the impact damage area was described and later incorporated to an analytical model. Previous experimental investigations had indicated that the impact produced a dent on the impacted surface and a bulge on the non-impacted surface. The entire damage region tended to buckle locally in compression in the direction of the geometrical imperfection. As a result, the fibres located within the damage region bended seriously under compressive loading. The contour of the dent was approximately circular before loading but it changed gradually to a transverse ellipse. As the load increased, the dent depth increased and the major axis of the ellipse expanded transversely.

1.4.6 Environmental effects

Humidity and temperature could have the detrimental effects on the CAI performance. The effect of high temperature (up to 150 C) during testing on the RCS of thermoplastic and thermoset resin based composite systems was investigated in [100, 101]. In the case of the thermoset system, panels impacted at high temperatures performed similarly in the CAI test (compression at room temperature) than panels impacted at room temperature. Compression at high temperature resulted in a further reduction of the RCS for both intact and damaged panels. Nevertheless the CSRF was higher for compression at high temperature than at room temperature, using as a reference intact panels compressed under similar conditions. In the case of the thermoplastic system there was no significant effect on the CSRF of the testing temperature at impact or during compression. The results shown for the thermoplastic system had a large scatter that could have masked any minor effect of the temperature on the CSRF. The temperature effect on the CAI strength was also investigated in [25]. CFRP laminates impacted at IKE levels up to 50 J were subjected to temperatures of 300°F, 350°F and

400°F for up to 17500 hours. The decrease in CAI strength was roughly 10% after 500 hr, remaining constant from 5000 to 17000 hr. Specimens impacted before heating showed a slightly greater degradation than specimens heated before impact, although the differences were within the data scatter. Degradation in CAI strength was independent of temperature for the temperatures studied.

The effect of moisture absorption was studied in [102]. Some of the specimens tested in CAI were saturated at 70 C and 95% humidity before impact. The results revealed that only in the case of very brittle matrix materials did a slight increase in RCS occur due to moisture. The reason for this was attributed to the plasticizing effect of water leading to a higher fracture toughness. The combined effect of humidity and temperature on the RCS combined was explored in [103]. Woven-carbon/epoxy panels were subjected to CAI with three different hygrothermal cycles. This cycles controlled the temperature (range over –30C to 100C) and humidity (range over 40 to 99.5%) over a certain period of time. The hygrothermal effect applied before or after impact testing was reflected on matrix cracking that affected the CAI performance similarly.

1.5 Main aims and objectives of this project

The present project intends to study experimentally the reduction of RCS of carbon/epoxy panels that contain various preconditions at room temperature. A three bounding approach is taken to simulate low-velocity impact damage using well-defined damages of different sizes. The first one uses open holes as a representation of complete material damage and has been one of the damage tolerance criteria in the aerospace industry. The second one of more recent time uses artificial delamination embedded in different configurations, to simulate as many elements of impact damage characteristics as possible. The third one is a new type of precondition that uses hemispherical-shaped domes to represent the local curvature change induced by impact. Eventually in this way, realistic damage can be approximated through a controlled refinement. The particular advantage is that this approach provides a quantified state of damage, which is deemed to be closer to low-, intermediate and high-energy impact damage. The main objective of this project is to develop the introduction of preconditions, (artificial embedment and hemispherical domes) from experimental techniques into a systematic

method to simulate impact damage, establish response characteristics in compression and use such characteristics to evaluate the contribution of preconditions to the reduction of CSRF.

Some of the reviewed studies lacked consistency in the presentation of compression-test results. Often neither buckling response nor failure mechanism of the intact panels was reported. In particular, the longitudinal global buckling or bending of the damaged panels was regarded as being synonymous with delamination propagation without comparison with the intact panels. Moreover, the examination of the possibility of delamination propagation was carried out using either the longitudinal strain responses or out-of-plane displacements. In this thesis, the compressive and buckling behaviours of 2- and 4-mm thick carbon/epoxy preconditioned and intact panels of 150 mm by 100 mm were characterised through compression-after-impact (CAI) tests in terms of surface strains with emphasis being placed on transverse SGs. Study of CAI and damage tolerance on T700/LTM45-EL carbon/epoxy system has not been previously reported.

The parameters selected for studying with artificial delaminations are size (10-, 20-, 40- and 60-mm transverse width), number (single and multiple ×3), shape (circular and elliptical), orientation (loading and width directions), TTT location (mid-plane and quarter location) and TTT distribution (symmetrical and asymmetrical). Similarly, the main parameters of local change of geometry (hemispherical-shaped domes) are dome-depth and dome curvature. For open holes, size is the main parameter studied. Impact damage is generated via drop-weight by using a purpose-built impact rig and a hemispherical-ended impactor. During the test force-history and incident and rebound velocities are recorded. Quasi-static transverse loading tests for damage generation are carried out using a universal testing machine. In this case the surface strains and force-displacement response are monitored during the tests. The introduction of preconditions is presented in Chapter 2, impact and quasi-static damage generation are presented in Chapter 3 and compressive response and failure results are presented and discussed in Chapters 4 and 5.

23

Previous studies have shown the effect of flexural rigidity and indenter-nose shape on damage generation and propagation. This project intends to investigate these relationships by studying the force-displacement response, surface strains, damage mechanisms and projected delamination area of 2- and 4-mm thick panels quasi-statically loaded with either hemispherical- or flat-ended indenters. To add more understanding to the experimental observations, an analytical model is developed to predict the intact panel response under similar conditions of load. The effect of flexural rigidity on the energy absorption characteristics is also investigated, using the force histories and damage characterisation of impacted panels.

Finally, this project intends the development of a model to predict CSRF. The model should be characterised by its simplicity and by including the main geometrical, material and impact loading parameters. The different strategies of previous models to tackle the problem of predicting CSRF are reviewed in Chapter 6.
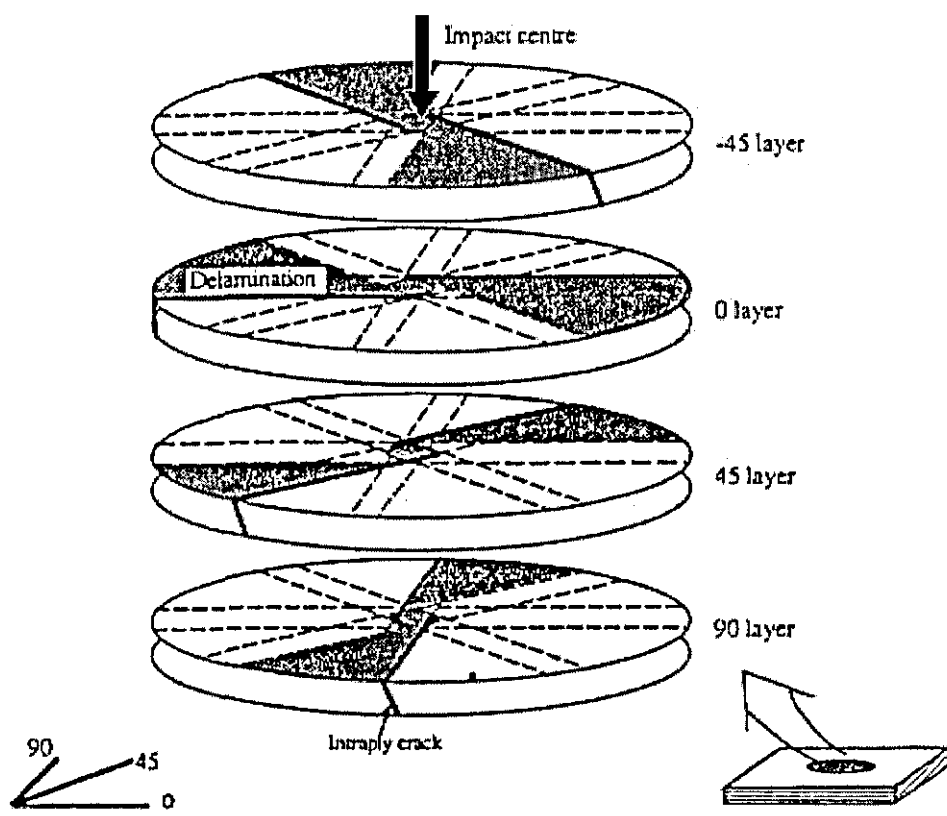
Figure 1.2.1 Schematic diagram showing three-dimensional damage structure in a quasi-isotropic laminate (taken from [10])

TABLE 1.1.1 Literature review for damage induced by transverse loading

Ref.	Author	Panel LxW, mm	Thick. mm	System fibre/resin	Layup	Boundary cond.	Impactor mass/size	IKE, J	IKE/ply, J/ply	AE, J	Velocity m/s	Critical loads, kN	Damage Method mechnsm	Size, mm	Dent, mm	Notes
[20]	Lagace 92	252x89	0.144/ply 0.134/ply	CFRP ud T: IM7G/ X8553-50 B: AS4/ 3501-6	AP 12 ply * QI 16 ply AP 12 ply AP 12 ply AP 12 ply AP 12 ply AP 12 ply AP 12 ply AP 12 ply CP 20 ply AP 12 ply CP 20 ply	2 edges C 2 edges C 2 edges C RF 2 edges C 2 edges C 2 edges C RF RF	1.53/12.7 dia H 1.53/12.7 dia H 1.53/12.7 dia H 1.53/12.7 dia H 1.53/12.7 dia H 1.53/12.7 dia H 1.53/12.7 dia H 1.53/12.7 dia H 1.53/12.7 dia H 1.53/25.4 dia H 1.53/12.7 dia H 1.53/25.4 dia H	0 to 23	-		I: 0 to 5.5 I QS QS I I QS QS QS QS QS QS	M 0.55, 0.93, 1.48 M 0.55, 0.93, 1.48	X-ray X-ray	More Less		* AP: 15, 45, 60,90
[38]	Sun (ref 13 Jackson 92*)	102 dia 127 dia 102 dia 127 dia	7	CFRP ud B: AS4/ 3501-6 T: IM7/ 8551-7	QI 48 ply	C	4.63/12.7 dia H	-	-	-	I QS I QS	M 0-14 ;T 7; P 15 M 0-14 ;T 7 M 0-19; T 10.5; P 20 M 0-19; T 10.5	C scan* MC, D	0-57 dia 0-40 dia	-	* Damage: spiral staircase pattern MC+D Similar results QS and I * Good style for revision
[44]	Srinivasan (ref 9 Jackson)	76.2x76.2	3.43 6.81	CFRP ud B: AS4/ 3501-6	QI 24 ply QI 48 ply	C	2.74/12.7 dia H	-	-	-	I	M 0-10; T 3.8 M 0-20; T 12	C scan D	dia, mm 0-85 0-85	-	
[31]	Kwon (ref 8 Jackson 92*)	50.8 dia 76.2 dia 102 dia 50.8 dia	4.54	CFRP ud B: AS4/ 3501-6	QI 32 ply	SS	6.35 dia H 6.35 dia H 25.4 dia H 25.4 dia H	-	-	-	QS QS QS I*	M 0-8.4; T 3.2 M 0-5.1; T 4.3	C scan D	dia, mm 0-67 0-40	-	Similar results QS and I * Impact with pendulum
[28] [29]	Liu 98 Raju 98	Square * 125x125 84x84 12x12	6.69 6.69 2.24 * R 3	GFRP ud 3M glass/ epoxy	Layup * CP 51 ply CP 51 ply CP 18 ply	C	11.9/ 12.5 dia H	6.64 85.6 176.3 0-106 106-190 190-390 0-30 30-35 35-360 * R 5.4	0.13 1.68 3.46 0-2.08 2.08-3.73 3.73-7.65 0-1.67 1.67-1.94 1.94-20	100% 100% 0% 100% 100% 0%	1.06 3.8 5.46	P 16 M 0-16.2 M 16.2-19 P M 0-4.2 M 4.2-4.2 P * R 4.01	C scan High light intensity I, SC D, MC, FB P	-	-	* Layup thin 2 ply group, thick 3 ply group * Panel dimensions no effect on damage Absorbed energy from force history CAI afterwards * comparing thick. ratio with IKE-force ratios
[159]	Liu Dang 98	100x75	15 ply * 21 ply 15 ply 9 ply 9 ply p ply	CFRP ud AS4/ 3501-6	CP CP AP * CP CP CP	C	12.5 dia H	-	-	0.89 0.84 0.81-0.89 1.04 1.59 25.8-24.8	0.98 0.98 0.97-0.98 0.99 1.59 3.40-4.49	M 3.34 M 4.41 M 3.33-3.50 M 1.78 M T 2.95 M 3.7-3.32; T 2.9	-	-	-	* Ply thickness 0.25 mm * Layup AP 90, 30, 45, 60 Angle did not affect impact response
[27]	Hong Liu 89	152x152	21 ply * 9 ply 21 ply 9 ply	GFRP ud 3M glass/ epoxy	0₇/90₇/0₇ 0₃/90₃/0₃ 0₃/90₃/0₃ 0₃/90₃/0₃	C	12.5 dia F 25 length *	15-29 14-26 27-46 14-27	0.71-1.38 1.56-2.89 1.29-2.19 1.56-3.00	-	20 to 100	-	Cross sec each 5 mm	Cum. Area 20-39 cm2 6-15 cm2 43-75 cm2 6-15 cm2	-	* Ply thickness 0.25 mm Lamination, thickness, angle effects No difference in lamination for same thick. * Impact: gas gun Total delam increases as thick increases

Ref.	Author	Panel LxW, mm	Thick. mm	System fibre/resin	Layup	Boundary cond.	Impactor mass/size	IKE, J	IKE/ply, J/ply	AE, J	Velocity m/s	Critical loads, kN	Damage Method mechnsm	Size, mm	Dent, mm	Notes
[39]	Mahfuz 98	127x76	4.45 4.22 4.45	CFRP w IM7-6K/ Tactix 123 Epon 862 L10	QI 12 layer	SS	5.44/ 16 dia H	13 29 13 29 13 29	1.08 2.42 1.08 2.42 1.08 2.42	6 26 5.9 27 5.5 29	2.4 3.6 2.4 3.6 2.4 3.6	M 7.5; T3.9 M 6.5; T 4.0 M 7.5; T 4.2 M 5.2; T 1.5 (?) M 8; T 3.9 M 8.2; T 1.2	C scan Low IKE D, MC High IKE FB, D, MC	projected cm2 4.6 6 2.3 3.6 4.3 7.2	-	CAI afterwards
[114] [127]	Zhou 96, 98*	100 dia	10 25 14 19	GFRP w E glass/ polyester S glass/ phenolic	-	C	20 dia F	-	-	-	QS	M 45; T 19 M 102; T 60 M 99; T 25 M 123; T 35	C scan*	-	Photo	* Concentric anular shape of delam * Concept of Pmax/Pthresh = CSRF
[78] [127]	Davies 96* Zhou 98	100 dia 500 dia	10 25	GFRP w E glass/ polyester	30% more in the 0 dir	C	8-75/ 20 dia F	25 270 550 - 320 1650 2600	J/mm 2.5 27 55 12.8 66 104		I I I QS I I I	T 18; I 46; M 60 -30% * T 62; I 124; M 145	C scan	0-78.5-78.5 projected cm2 200-1500-1950 mm	-	* Eq. Ultimate threshold force delam growth * QS force -30% of impact force thin panels QS force -22% of impact force thick panels CAI afterwards
[30]	Robinson 92	102 dia 102 dia 337 dia	2 2 2	CFRP w /836S GFRP w /836S	CP 10 ply CP 12 ply	C	variable */ 6.35 dia H 1.15/6.35 dia H 1.70/6.35 dia H	0.4-5.5-10.9 0.5-7.2-8.6 1.5-8.4-11.4	0.04-0.55-1.09 0.04-0.6-0.72 0.13-0.7-0.95	- 0-8.5 0-10.9		M 0.5-2.2-2.2 M 0.45-1.6 M 0.45-1.8	C scan Visual	dia, mm 0-35 0-18-17 0-20-18	0-30 dia 0-14.5 dia 0-14 dia	* Impactor mass 1.15, 1.59, 2.04 fairly good agreement Dent vs delam damage good correlation Good revision style
[11] [42]	Davies 95, 00	125x75 125x75 125x75 200x200 200x200 200x200	1 2 4 1 2 4	CFRP ud HTA/ 6376	QI 8 ply QI 16 ply QI 32 ply QI 8 ply QI 16 ply QI 32 ply	C, SS C, SS C, SS C SS C SS C SS	0.4-2.5 kg/ 12.7 dia H	0.7-2-3 1.6-6.8-9 4-20 0.9-3 1.0-2.5-3.0 4.2-7.0-9.0 4.2-8.2 14-35 14-32	0.09-0.25-0.38 0.1-0.43-0.56 0.13-0.63 0.11-0.38 0.13-0.31-0.38 0.26-0.44-0.56 0.26-0.51 0.44-1.09 0.44-I			T 0.7; M 0.7-1.15; P 1.15 T 1.7; M 1.7-2.4; P 2.4 T 5.5; M 5.5-7.4 T 0.7; M 0.7-1.15; P 1.15 equal to C T 1.7; M 1.7-2.4; P 2.4 equal to C T 5.5; M 5.5-7.4 equal to C	C scan X ray Optical microsc.	mm2 35-120-300 125-262-450 350-1300 25-140 0-90-175 125-260-425 50-210 350-950 400-750	-	Thicker the panel, the larger the delam for the same force Fracture and stress based predictions Circular delam shape Butterfly delam shape
[41]	Delfosse 97 Boeing	76.2x127	4.7 4.65 4.7 4.65	CFRP ud B: IM6 /937 T: T800H /3900-2 B: IM6 /937 T: T800H /3900-2	QI 24 ply	SS	6.14 kg/ 25.4 dia H	3.5-25 25-34 34-50 17.5-22 22-60 34 34 46 Notes * 9 30 58	0.15-1.04 1.04-1.42 1.42-2.08 0.73-0.92 0.92-2.50 1.42 1.42 1.92 0.38 1.25 2.42	1.5-15 15-25 25 4-8.5 8.5-46 30 2 16 43	I I I I I I I QS I I I	M 12 T 11; M 13 T 11; M 13 T 11.5; M 12.5 M 7.5 M 12.5 M 12.5	total mm2 0- -25000 25000-30000 0-1200 1200-5000 C scan: proj* Cross sec: total area * Deplying: FB	total mm2 0- -25000 25000-30000 0-1200 1200-5000 - -	-	Fibre breakage, mm2 - 0-50 50-80 - 0-130 Gi, Gii determined from slope kJ/mm2 total delamination area * Ratio = total area / projected area B: 3.2-4 for 9-46 J; T: 3.4-4.4 for 18-58 J *QS equivalent energy to 46 J AE and damage mech are functions of the IKE therefore Pmax constant It Includes diagram energy distribution

Ref.	Author	Panel LxW, mm	Thick. mm	System fibre/resin	Layup	Boundary cond.	Impactor mass/size	IKE, J	IKE/ply, J/ply	AE, J	Velocity m/s	Critical loads, kN	Damage Method mechnsm	Size, mm	Dent, mm	Notes
[16]	Lesser 94	Boeing 76.2x127	-	CFRP ud AS4/ epoxy: B: A BT: B TB: C T: D	QI 32 - 40 ply	SS	19.1 dia 15.9 dia	-	6.675 J/mm J/mm 3.61 4.32 3.71 2.03		I, QS QS QS I I I I	T 7.6; M 13.3 T 12.5 T 9 kN/m T 1277; M 2452 T 1518; M 2854 T 1214; M 2732 T 1583; M 2662	C scan D, MC	QS=I cm2 28.4 20 15.5 14.8	7 dia *	* ttt photograph, 100-150 e-6 m in depth dent made of radial and central cracks Impact is force controlled EA = hysteresis load displacement curve CAI afterwards
[22]	Wardle 97	102x102 Flat*	0.804 0.804 1.608 1.608 2.412 2.412	CFRP ud AS4/ 3501-6	AP * 6 ply 6 ply 12 ply 12 ply 18 ply 18 ply	-	1.60 kg	0.8 3.2 7.2 12.8 12.8 12.8	0.13 0.53 0.60 1.07 0.80 0.71	-	11.0 12.0 13; QS 14.0 14.0 14.0	M 0.5 M 1.0 M 2.0 M 2.4 M 2.4 M 2.4	X ray	mm * 2.5 7.5 27 28.5 28.5 29	Depth 0.04 0.04 0.17 0.13 0.11 0.085	* Elliptical proj area, size (a+b)/2 *AP ([+45/-45]n/0n)s There is not a relationship between dent depth and delamination extent or thickness Dent depth measured LVDT mounted on a digital milling machine * Also cylindrical shells
[10]	Hull 93	114x76 Boeing	-	CFRP ud T300/ 914C	QI*, 32 ply DP1 DP2	SS	-	10.9 12.8 16.0 18.9 10.6 12.6 15.9 18.8	0.34 0.40 0.50 0.59 0.33 0.39 0.50 0.59	6.0 6.9 10.7 13.1 6.2 7.4 10.9 13.2	-	-	Thermal deply MC, D Micrograph mode II more than mode I	Total cm2 40 55 80 85 47 54 62 72	-	* Layups DP1 [(-45₂/90₂/45₂/0₂)₂]s DP2 [(-45₂/90₂/0₂/45₂)₂]s MC open near impact site = permanent deformation D initiated by MC * Effect of superposing individual delam Distr ttt hat shape: near impact small; back side big No delam between adjacent plies same orient. Include fig 16-17
[12]	Cantwell 89	Beam 25x150 Beam 25x150 120 dia Beam 25x 25-80-150 50-150	0.5 1.0 2.0 4.0 8.0 1.0 2.0 4.0 0.5 1.0 2.0 2.0	CFRP ud XA-5/ BSL 914C	CP* 4 ply 8 ply 16 ply 32 ply 64 ply AP* 8 ply 16 ply 32 ply CP 4 ply 8 ply 16 ply AP 16 ply	SS 3PB SS 3PB C SS 3PB	0.68 kg 6 dia H	T 0.25; P 1.0 T 0.65; P 3.0 T 1.1; P 7.0 T 0.9; P 26 T 0.5 T 1.0 T 1.65 T 0.45 T 0.25; P 0.8 T 0.46, P 3.0 T 1.3; P 8.0 T 0.7-3.4-5.6 P 6.5-10.3 *	T 0.06; P 0.25 T 0.08; P 0.38 T 0.07; P 0.44 T 0.03; P 0.81 T 0.01 T 0.13 T 0.10 T 0.01 T 0.06; P 0.2 T 0.06; P 0.38 T 0.08; P 0.50 T 0.04-0.21-0.35 P 0.41-0.64	-	I	-	C scan X ray Cross sec	mm2 0-260-220* 0-540*	-	*IKE 0-3-9 J *IKE 0-27 J 4,8,16 ply laminates had lower surface damage 32, 64 ply laminates had upper surface damage *CP [(+-45)n]s *AP [(-0₂/+-45)n]s Includes energy distribution diagram *Upper surface-lower surface damage No delam between adjacent plies same orient.
[18]	Guan 02	126x76	3.76	CFRP ud T300/ QY8911	QI 32 ply	C	5.17 kg 12.7 dia H	25.18	0.79	22.5	I	M 7.0	Deply	area cm2 / ttt locat 2 / top 5 / mid sect. 4 / 3/4 10 / bottom		No delam between adjacent plies same orient.

Ref.	Author	Panel LxW, mm	Thick. mm	System fibre/resin	Layup	Impact parameters and response							Damage Method mechnsm	Size, mm	Dent, mm	Notes
						Boundary cond.	Impactor mass/size	IKE, J	IKE/ply, J/ply	AE, J	Velocity m/s	Critical loads, kN				
[23]	Demuts 92	127x127	-	CFRP ud	AP1-AP2 *		25.4 dia H						C scan	mm2	Depth	AP1 =[10/80/10]n - AP2=(40/50/10)n
					AP1 96 ply			140	1.46	104	4.5	M 56.5		7839	0.235	Normalised depth: 1
					AP1 74 ply			140	1.89	124	4.5	M 41.8		5239	0.298	1.65
					AP2 73 ply			140	1.92	135	4.5	M 38.2		4284	0.292	1.63
				IM7/ 5260 BMI	AP1 48 ply			140	2.92	131	4.5	M 30.0		2852	1.353	11.51
					AP2 49 ply			140	2.86	127	4.5	M 30.2		8535	1.226	10.22
					AP1 26 ply			72	2.77	72	4.6	M 10.8		2561	2.356	37.02
					AP2 27 ply			81.3	3.01	82	4.6	M 11.4		2594	2.705	40.94
					AP1 9 ply			17.15	1.91	16.2	3	M 3.1		974	1.162	52.76
					AP2 9 ply	C		15.3	1.70	15.4	2.8	M 4.2		1542	1.441	65.44
				AS4/ 3501-6	AP 96 ply			140	1.46	-	-	-		13548	3.2	Dent depth measured with dial gauge
					74 ply			140	1.89	-	-	-		14839	0.826	Damage area increases with thickness for
					48 ply			140	2.92	-	-	-		12903	0.444	similar IKE
				IM6/ CYCOM 3100	96 ply			140	1.46	-	-	-		17097	0.813	CAI afterwards
					74 ply			140	1.89	-	-	-		15161	0.508	
					48 ply			140	2.92	-	-	-		14194	0.444	
[46]	Belingardi 03	76.2 dia		CFRP ud	AP * 4 ply	C	20 kg 10 dia H	1.4-P 5- 6.3	0.35-P 1.25-1.58	0.6-4.1-6.3	I	T 1.6; M 1.7	-	-	-	*AP layup [0/60/-60]n
					8 ply			4.1-P 13-14.7	0.51-P 1.63-1.84	3-12.1-14.7		T 2.5; M 3				
					16 ply			10.8-P 38-39.2	0.68-P 2.38-2.45	6-38	I	T 5; M 5.8				EA increases with number of layers
					CP 4 ply			5.1-13	1.28-3.25	4.1-13		T 1.7; M 1.8				Force T and M with constant values (this is
					8 ply			5-21	0.63-2.63	3-21	I	T 3.2; M 3.9				wrong for M), justified with AE increase with
					16 ply			10-60	0.63-3.75	5-60		T 5.2; M 6.6				IKE
					AP 4 ply							M 2.1				Factor of damage degree defined in terms of
					8 ply						QS	M 3.2				IKE, AE and RE
					16 ply							T 4.8; M 6.1				
					CP 4 ply							M 2.4				
					8 ply						QS	M 4.1				
					16 ply							T 6.8; M 9.1				
[160]	Qian 90	50x50 100x100 200x200	1.072 2.14 4.29	CFRP ud AS4/ 3501-6	AP * 8 ply 16 ply 32 ply	C	gm / dia H 2.86 / 6.35 22.9 / 12.7 183 / 25.4	0.85 3.83 13.62	0.11 0.24 0.43		24.4 18.3 12.2	-	C scan	mm2 20 130 470	-	* AP layup [(+-72)n/0₂n]s n=1, 2, 4 * Same relative area if velocity^2 is proport. to plate length^-1 Impact with gas gun
[48]	Prandy 91	76x127 Boeing	4.04	CFRP ud IM7/ X5260	QI 32 ply	SS on wood+alum SS on aluminum *	6.2 kg 16 dia H	27.1 27.1	0.85 0.85	3.9 4.5	I I	M 12.9 M 12.9	C scan	516 mm2 710	-	CAI afterwards IKE 6.7 J/mm Wood is more flexible than Aluminum * Aluminum was used instead of steel
[43]	Griffin 87	127x127	6.35	CFRP ud AS4/ T: 2220-1 T: 1806 B: 3502 T: 974 HSC/ T: 1806 AS6/ T: 2220-1	QI 48 ply	C	5.4 kg 10 dia H	P 13.6-54.2-67.8 27.1-81.3 13.6-67.8 27.1-54.2 13.6-81.3 13.6-40.7	P 0.28-1.13-1.41 0.56-1.69 0.28-1.41 0.56-1.13 0.28-1.69 0.28-0.85	-	-	-	C scan	Proj. area mm2 1032-3065-2194 1032-2452 1032-1935 1097-2710 1032-2900 1032-3613	-	CAI afterwards AS6 fibres have 75% dia of AS4 Topology photograph

Ref.	Author	Panel LxW, mm	Thick. mm	System fibre/resin	Layup	Boundary cond.	Impactor mass/size	IKE, J	IKE/ply, J/ply	AE, J	Velocity m/s	Critical loads, kN	Damage Method mechnsm	Size, mm	Dent, mm	Notes
[32]	Zhou 99	40 dia 120 dia	2	CFRP w T300/ LTM45-EL	2x2 twill 9 ply	SS C SS C SS C SS C C C C C	8 dia H 8 dia H 20 dia H 20 dia H 8 dia F 8 dia F 20 dia F 20 dia F 8 dia H 20 dia H 8 dia F 20 dia F	-	-	-	QS	M 1.2 T 12; M 1.5 M 1.3 T 1.5; M 2 M 2.2 M 3 M 5 M 7.3 M 1.2 M 1.25 M 2.2 M 5.2				QS at 5 mm/min
[24]	Nettles 02	Square 152.4 304.8 101.6 50.8 101.6 304.8 152.4	1.02 2.04 2.04 2.04 4.06 6.1 6.1	CFRP * Flex Flex Med Stiff Stiff Med Stiff	QI 8 ply 16 ply 16 ply 16 ply 32 ply 48 ply 48 ply	C SS C SS C, SS C SS C SS C SS C SS	H 2.4 kg 2.4 kg 2.4 kg 2.4 kg 2.4 kg 2.4 kg 2.4 kg 2.4 kg 13.3 kg 13.3 kg 13.3 kg 13.3 kg	7.2 10.5 28.7 35 8.4-11.65 7.8 12.4 16.7 23.3 155.8 155.8 82.8 82.8	0.90 1.31 1.79 2.19 0.53-0.73 0.49 0.78 0.52 0.73 3.25 3.25 1.73 1.73		I, QS I, QS I, QS I, QS I, QS I, QS I, QS I QS I, QS I QS I, QS I QS I, QS	M 1.73-1.93 M 1.86-1.87 M 6.8-7.6 M 4.8-5.8 M 2.9-4.1 M 2.9-3.3 M 2.76-3.36 M 7.5 M 7.5 M 8.7-11 M 23.2-28.2 M 23.2-28.2 M 23.4-29.6 M 22.1-23.5 M 22.1-23.5 M 21-22.7	X ray projected area 	cm2 - - 6.2-8.2 4.2-5.8 1.6-4.9 3.8-6 2.6-3.6 8.8-11.2 10-16 32-42 band 32-42 band 26-32 band 30-60 30-60 32-42	depth* 0.12-0.2 0-0.1 - - - 0.3-1.5 0.3-1.5 0.3-1.5	Crack length, mm 10-90 depth and crack data very scattered 0-32 depth and crack data very scattered * Ratio length square / thickness = Flexible: 150; Medium: 50; Stiff: 25 QS at 0.02 and 0.42 mm/s Transverse load is the main parameter * Dent depth upper surf / crack length bottom Crack length 32-62 32-62 30-63
[47]	Bucinell 91	76.2x127	3.56	CFRP ud IM7/M/ HBRF-554	C	SS	5-25.1 kg 15.9 dia	0-43 43-160	J/mm 0-12.08 12.08-44.94		I low veloc.*	M 0-2200 M 2200 constant it is not f(mass)	Duration ms 6.2-14.2 f(mass)	mm2 0-3000 3000 constant		*AP layup [+-18/90₂/+-18]s *Low velocity impact definition QS=I if m_impactor >> (k₂/k₁)m_target Definition of kbs based on 2 DOF model Impact response f(P,t,mass,IKE,k)
[34]	Delfosse 95	25.4 dia 25.4 dia 25.4 dia 76x127 25.4 dia & 76x127	3.3-8.3 6.15 6.15 6.15 6.15	CFRP ud B: T300/ F593 T: IM7/ 8551-7 T: IM7/ 8551-7 T: IM7/ 8551-7 T: IM7/ 8551-7	QI	SS	7.6 dia F 3.8-18 dia F 7.6 dia F H C * 7.6 dia F H C 6.14 kg 7.6 dia H	- ?	-	-	QS QS QS QS I 0-5	T 5.5-17; M 6-18.2 T 10-24; M 10-52 T 13; M21 T 9; M 18 T5; M18 T 13; M 23 T 9; M 15 T 5; M 9 M 16.5	C scan Thermal deply	-	-	Scaling rules for panel thickness, impactor size in terms of transverse force * Conical impactor with half angle of 18.5

Ref.	Author	Panel LxW, mm	Thick. mm	System fibre/resin	Layup	Boundary cond.	Impactor mass/size	IKE, J	IKE/ply, J/ply	AE, J	Velocity m/s	Critical loads, kN	Damage Method mechnsm	Size, mm	Dent, mm	Notes
[26]	Found 96	100 dia	6.35 6.35 4.75 6.35 6.35 4.75	GFRP r E glass/ polyester A B C A B C	-	C C	12 dia H 0.654-2.473 kg/ 12 dia H	- 6.9	- J/mm 1.09	-	QS I 3	- M 4.3 M 4.25 M 3.0	-	-	Depth 0-3.2 Depth - - -	*A 38%; B-C 34% fibre volume fraction CAI afterwards Crack length 0-85, no difference between A, B, C Dent depth upper surface crack length bottom Crack length 0-9 0-28 0-42
[40]	Winkel 85	127x127	3	AS4/ 3501-6 CFRP ud CFRP w Kevlar 49 /3501-6 KFRP ud KFRP w E glass/ 3501-6 GFRP ud GFRP w	CP 10 ply 10 ply CP 10 ply 10 ply CP 6 ply 10 ply	SS	15.9 kg 12.7 dia H	110.3 105.6 105.1 110.3 103.5 83.6 109.5	11.03 10.56 10.51 11.03 17.26 13.94 10.95	Max * 21.65 15.55 21.76 17.92 46.73 81.77 13.33	3.725 3.645 3.636 3.725 3.609 3.243 3.712	M 3.22 M 2.60 M 3.15 M 2.14 M 7.19 M 10.97 M 1.83	-	-	-	* Max E in the E history diagram corresponding to Perforation E In discussion it is wrong to assume that E at Pmax is the AE
[33]	Siow 98	100x150	?	CFRP w M18-1/ 45% G939	QI	C	0.4/21 dia H 0.6/21 dia H 0.4/6.3 dia H 0.6/6.3 dia H	5.5 7 8.2 10.6 5.5 7 8.2 10.6	-	3.8 6 6.5 8.4 4.8 6.6 6.5 10	-	-	C scan	mm2 20-175 80-400	-	CAI afterwards
[9]	Kelkar 99	127x127	2.06 4.17 6.35	CFRP ud	QI 16 ply 32 ply 48 ply	SS	6.81 kg 25.4 dia H	2.34-11.0 5.71-18.7 17.22-60.8	0.15-0.69 0.18-0.58 0.36-1.27	-	I 0.61-2.82	T 1.41; M 0-3.60 T 3.64; M 0-6.84 T 10.37; M 0-18.57	C scan	cm2 0.52-4.84 0.9-13.23 14.84-70.52	-	
[37]	Cartie 02	150x100	4	CFRP ud HTA/ B: 922 914 924 T: 920 IMS/ B: 922 924 8552	QI 32 ply	SS	16 dia H	4*-20 7-17 8.5-25 10-30 3.4-19 7-20	0.13-0.63 0.22-0.53 0.27-0.78 0.31-0.94 0.11-0.59 0.22-0.63	-	I	T 4.05 T 5.38 T 6.53 T 6.79 T 4.11 T 6.50 T 5.62	C scan	mm2 440-1200 500-900 620-1100 240-780 250-1900 500-1300 -	-	CAI afterwards * First value of energy range is the threshold for damage initiation Fibre HTA similar to T300 Fibre strength IMS > HTA Giic worked out from initial load drop after P thresh
[119]	Gao Kim 01	75 dia	2	CFRP ud AS4/ PEEK* T300/913	QI 16 ply	C	2.42 kg 25.4 dia H	7.3-10-30 10.6-13-30 3.3-10-30	0.46-0.63-1.88 0.66-0.81-1.88 0.2-0.63-1.88	Notes* 2-4.5-15 2-3-10 4-4-11	-	T 5; M 1.5-6-6 T 5.5; M 3.5-5.5-6 T 3.8; M 2-7.5-7.5	-	total mm2 0-1000 0-800 0-1650	-	* AE at 8, 10 and 15 J of IKE respectively * Slow cooling rate * Fast cooling rate Total area vs IKE: SQR CAI afterwards

Ref.	Author	Panel LxW, mm	Thick. mm	System fibre/resin	Layup	Boundary cond.	Impactor mass/size	IKE, J	IKE/ply, J/ply	AE, J	Velocity m/s	Critical loads, kN	Damage Method mechnsm	Size, mm	Dent, mm	Notes
[8]	Prichard, Hogg 90	40 dia	2	CFRP ud T800H/ 924C AS4/ PEEK	QI 16 ply	C	3.96 kg 20 dia H	0-0.86 0.87-7.44-11.18 0-2.02 3.9-14.62	0-0.05 0.05-0.47-0.7 0-0.13 0.24-0.91	-	-	-	-	width, mm 0 14.8-41-43.5 0 13.1-32	Less More	CAI afterwards
[76]	Hosur 98	150x150	3.6 6 6	CFRP ud T300/914	QI 24 ply QI 40 ply QI 40 ply	C	2.57, 5.32 kg 12.7 dia H	6 9 12 12 15 18 8 17 30	0.25 0.38 0.50 0.30 0.38 0.45 0.20 0.43 0.75	-	-	-	Cscan ttt	Proj mm2 - 715 878 1029 1470 1413 92 1447 1743	-	Max individual area, mm2 / Location ttt, mm -/- 658/2.4 789/3.0 964/5.1 1347/5.1 1342/5.1 41/1.2 4250/4.65 1586/4.95 Impact threat to aircraft structure
[45]	Ambur 98	228.6x127		CFRP ud AS4/ 3502	QI 48 ply	SS	12.7 dia H 1.13 kg 2.27 kg 4.54 kg 9.08 kg	10.2-13.6-33.9 13.6-33.9 13.6-33.9 13.6-33.9	0.21-0.28-0.71 0.28-0.71 0.28-0.71 0.28-0.71	-	-	M 6.2-12.45 M 8-16.9 M 13.34-7.12 M 7.12-20.02	C Scan	proj mm2 0-1290 839-2194 161-1935 0-2710	-	For tow weights impacting at specified momentum, the heavier impactor results in a smaller damage area

B Brittle   AP angle ply   C clamped   H Hemispherical   T Threshold   I Impact   M Maximum   MC Matrix cracks

T Tough   CP cross ply   RF rigid foun F Flat   P Perforation   QS Quasist T Threshold   D Delam

w woven   QI quasi isou SS simply sup C Conical   P Perforation   FB Fibre Breakage

ud unidirectional   I Indentation

r roven   SC Surface Cracks

                                                                           P perforation

TABLE 1.1.2 Literature review for panels with impact damage and open hole

Ref.	Author	Panel LxW mm	Thick mm	System fibre/resin	Layup	Factors affecting RCS IKE J	Area mm2	OH	RCS MPa or %	Notes	
[93]	Asp 01	150x150	4.58	CFRP ud	36 ply, CP	30J	Ellipse 60:30	•	-20% RCSI max	Ellipse major axis WD Also embedded delam	No model
[57]	Gottesman 94	254x127	6	CFRP ud	48 ply QI	J 27.1 40.7 54.2 67.8	dia, mm 38.5 55 68 74	•	-61% RCSI -70% RCSI -72% RCSI -71% RCSI	Prepeg tape	•
		254x127	6	CFRP pw	36 ply QI	27.1 40.7 54.2 67.8	35 38.9 49 52		-36% RCSI -52% RCSI -48% RCSI -48% RCSI	Fabric plain weave	
[145]	Xiong 95	152x102	4.54	CFRP ud	24 ply, QI	J 15 30.5 47 51 62	Elliptical 11.2 : 7.3 14 : 9.1 16.2 : 12 19.9 : 15.1 19.1 : 16.1	•	-73.8% RCSI -59.8%RCSI -51.2% RCSI -48% RCSI -40% RCSI	Orientation 57 respect to LD 56.7 respect to LD 35.1 respect to LD 27.5 respect to LD 25 respect to LD	No model
[75]	Nyman 98	254x127	3.12	CFRP ud	24 ply, QI	J 6 to 55	260 310 600 800 1000 1800	•	-48% FS -54% FS -55% FS -55% FS -59% FS -70% FS	25% plies LD	Delam buckling energy release rate Soft inclusion FEA
					QI, 0° dom.		800 1150		-65% FS -68% FS	67% plies LD	
					QI, 90° dom		750 1100		-40% FS -58% FS	17% plies LD	
[89]	Ishikawa 95	254x127	7.3		48 ply QI	J/mm 2 2.8 3.6	1000.9 981 931.7	•	-38% RCSI -43% RCSI -56% RCSI	Nasa	No model
		210x127	6	CFRP ud		3.6	934.5		-63% RCSI	Nasa length effect	
		152x102	4		32 ply QI	3 3.5	510.5 505		-44% RCSI -52% RCSI	SACMA	
[161]	Soutis 00	150x100	4	CFRP ud	32 ply, QI	J 15 22 31 41	dia mm 40 40 50 60	•	-50% RCSI -50% RCSI -57% RCSI -63% RCSI	- - - -	OHC Soutis model approach to CAI with eq. Hole
[51]	Paulisch 01	150x100	4	CFRP ud PEEK/IM7	QI	6 8 18 24 30	0 500 760 1000 1100	•	-13% RCSI -19% RCSI -24% RCSI -32% RCSI -33% RCSI	-	•
				CFRP ud Epoxy/T800		6 8 12 18 30	600 1000 1500 2500 7200		-42% RCSI -44% RCSI -53% RCSI -58% RCSI -67% RCSI		
[103]	Qi 99	117x91	1.1	CFRP woven	12 ply, QI	Width mm 0.4 0.8 1.3 1.75 3 4 4.3 5.6 5.8	3 7 9.3 11 12 14 15 17 19	-	300 RCSI 295 RCSI 260 RCSI 250 RCSI 252 RCSI 218 RCSI 252 RCSI 236 RCSI 195 RCSI	Dry - Imp - CAI	Model stiffness reduction due to impact and due to environmental factors
						0.8 2.2 3.5 3.8 5.2	5 7 8 14 16		236 RCSI 200 RCSI 230 RCSI 200 RCSI 170 RCSI	Wet - Imp - CAI	
						1.5 3 4.5 6	7 13 14 17		200 RCSI 175 RCSI 160 RCSI 150 RCSI	Wet - Imp - SCH - CAI Hygrothermal cycle	
[72]	Park 00	100x100	-	GFRP* glass/ epoxy	-	10.5 23.7 42.1	55433 55433 55433	•	-9% RCSI -13% RCSI -19% RCSI	3 layers * GGG	•
				G/K FRP* glass, aramid /epoxy		10.5 23.7 42.1	352756 398110 483780		-53% RCSI -64% RCSI -69% RCSI	* AAG	
				G/K FRP* glass, aramid /epoxy		10.5 23.7 42.1	388031 382992 443465		-18% RCSI -57% RCSI -65% RCSI	* GAA	
				KFRP* aramid/ epoxy		10.5 23.7 42.1	362835 433386 473701		-51% RCSI -62% RCSI -58% RCSI	* AAA	
[4] [5]	Potter 00 Potter 00	40.5x12.7 19.8x13 10.8x13 7.68x13 19.9x27.1	-	CFRP ud AS4/3502	AP*, 48 ply	•	•	-	181 Suc 182 Suc 202 Suc 217 Suc 208 Suc	* AP: [±45]	AR effect AR proportional to CS^-1 Height proportional to stiffness
		40x13.7 30.8x23.2 17.2x23.5 18.2x13.5 10.4x14 25x13			UD*, 48 ply				886 Suc 808 Suc 917 Suc 791 Suc 878 Suc 1066 Suc	* UD [0], LD=0°	
		AR 0.592-3.17 1.01-3.46 2.23-5.27 0.74-2.91			AP 48 ply (+-45)12s (+-30)12s (+-15)12s 0 48				Intact CS, MPa 217-178 283-243 656-618 878-886	Stiffness, GPa 7.96-7.24 18.2-25.5 56.3-72.7 30.2-65.7	

Ref.	Author	Panel LxW mm	Thick mm	System fibre/resin	Layup	Factors affecting RCS IKE J	Area mm2	OH	RCS MPa or %	Notes	
[77]	Wang 99	150x100	4	CFRP ud	32 ply, QI	J 3.9	·		+10% RCSI	·	Local inhomogeneity local change in material properties due to damage
						4	·		+8% RCSI	·	
						4.9	·		-19% RCSI	·	
						5.5	·		-35% RCSI	·	
						7.1	·		-29% RCSI	·	
						9	·		-52% RCSI	·	
						9.7	·	·	-41% RCSI	·	
			6		48 ply, QI	3.5	·		+5% RCSI	·	
						5	·		0% RCSI	·	
						8.6	·		-49% RCSI	·	
						9.5	·		-61% RCSI	·	
						11.2	·		-56% RCSI	·	
						12.1	·		-58% RCSI	·	
						14	·		-64% RCSI		
[162]	Zhang 99	270x250	4.3	CFRP ud	32 ply, QI	12	550		-26% RCSI	Preload 0 BL	Dynamic response for impact FEA model for post impact response out-of-plane deflection
						12	460		-21% RCSI	1.0 BL	
						12	470	·	-19% RCSI	1.2 BL	
						20	780		-34% RCSI	0 BL	
						20	750		-32% RCSI	1.0 BL	
						21	·		-41% RCSI	1.2 BL	
						32	940		-46% RCSI	0 BL	
						33	1430		-47% RCSI	1.0 BL	
[39]	Mahfuz 98	152x101	4.3	CFRP w Tactix Tactix Epon Epon Aerocy Aerocy	12 ply, QI	J 13	mm2 4.6	·	-36% RCSI	Resin Tactix: BPA Dow	Force time history prediction. Energy based model
						29	6		-48% RCSI	Tactix: BPA Dow	
						13	2.3		-35% RCSI	Epon: BPF Shell	
						29	3.7		-48% RCSI	Epon: BPF Shell	
						13	4.2		-11% RCSI	Aerocy: Dicynate Ciba	
						29	7.1		-31% RCSI	Aerocy: Dicynate Ciba	
[152]	Papanicolaou 98	150x100	4.5	CFRP ud HTA/ SXA	32 ply, QI	J 3	·		0% RCSI		Empirical model based on exponential regression for predicting RCS
						9	·		-33% RCSI		
						12	·		-42% RCSI		
						20	·		-52% RCSI		
						30	·		-57% RCSI		
				IMS-P12/ SXC		3	·		0% RCSI	with fibre surface treatment	
						9	·		-33% RCSI		
						12	·	·	-41% RCSI		
						20	·		-45% RCSI		
						30	·		-57% RCSI		
			2	resin: BASF rigidite 5212	16 ply, CP	2	·		0% RCSI		
						4	·		-30% RCSI		
						8.5	·		-34% RCSI		
						12.5	·		-47% RCSI		
						17	·		-57% RCSI		
[50]	Soutis 96	Lx100	t	CFRP ud	16 ply, QI*	J/m 920	mm 15		190 RCSI	* Layups [(±45,0,90)2]s	Model Soutis compressive kinking failure, crack opening & microbuckling
						920	15		214 RCSI	[(-45,0,45,90)2]s	
						920	22		173 RCSI	[(-45 2,0 2,45 2, 90 2)]s	
						1326	25		167 RCSI	[(±45,0,90)2]s	
						1326	22.5		188 RCSI	[(-45,0,45,90)2]s	
						1326	37.5		164 RCSI	[(-45 2,0 2,45 2, 90 2)]s	
						1326	28		194 RCSI	[(-45,0,45,90)4]s	
						992	25	·	177 RCSI	[(-45,0,45,90)8]s	
		Lx50	2	B: T800H/924C	16 ply, CP*	J 7	mm 9		-61% RCSI	* Layups [(±45,0 2)2]s	
						7	11		-64% RCSI	[(±45)2,0 4]s	
						7	9		-58% RCSI	[(+45,0,-45,0)2]s	
						7	9		-53% RCSI	[(0 2,±45)2]s	
						7	11		-59% RCSI	[0 4(±45)2]s	
						7	9		-53% RCSI	[(0,+45,0,-45)2]s	
		Lx50	2	B: XAS/914 B: T800H/924C T: IM7/977 T: IMS/927	16 ply, QI	7	15		-64% RCSI		
						7	15		-57% RCSI		
						7	8		-53% RCSI		
						7	8		-47% RCSI		
[78]	Davies 96	350x250	10	GFRP w		J / kN 25/18	500		·		
						45/15	2500		·		
						75/22	4500		·		
						120/26	5500		·		
						135/31	5700		·		
						180/42	6500		·		
						225/48	9600		·		
						400 / 45	·		-49% RCSI		
						750 / 60	·		-57% RCSI		
						1150 / 75	·		-67% RCSI		
						1670 / 92	·	·	-72% RCSI	·	·
			25			350 / 67	20000		-45% RCSI		
						700 / 75	40000		-52% RCSI		
						1000 / 80	60000		-58% RCSI		
						1300 / 85	75000		-60% RCSI		
						1650 / 120	100000		-60% RCSI		
						2000 / 130	152000		-65% RCSI		
						2050 / 139	140000		-67% RCSI		
						2300 / 140	160000		-69% RCSI		
						2600 / 145	190000		-70% RCSI		
[79]	Zhou 96	350x250	14	GFRP w	CP	J / kN 330 / 49	8000		-58% RCSI		
						972 / 87	24000		-61% RCSI		
						1306 / 104	60000		-68% RCSI		
						1640 / 114	105000		-82% RCSI		
						2000 / 131	65000		-77% RCSI		
						2030 / 127	80000		-75% RCSI		
						2780 / 146	107000		-80% RCSI		
						3055 / 157	·	·	-78% RCSI	·	·
			19			330 / 54	13950		-47% RCSI		
						670 / 79	23260		-64% RCSI		
						1000 / 95	34880		-68% RCSI		
						1000 / 110	48840		-68% RCSI		
						1330 / 114	60465		-69% RCSI		
						1670 / 123	106980		-74% RCSI		
						2000 / 136	130230		-75% RCSI		
						2580 / 151	151160		-77% RCSI		
						3030 / 163	174420		-78% RCSI		

Ref.	Author	Panel LxW mm	Thick mm	System fibre/resin	Layup	IKE J / Ind mm	Area mm2 / Crack mm	OH	RCS MPa or %	Notes	
[26]	Found 96	100x30	3.65	GFRP roven A*	UD	Ind mm 0.5 1.05 1.4 2.45 2.45	Crack mm 0 46.5 53 71.5 85		-15% RCSI -40% RCSI -46% RCSI -46% RCSI -50% RCSI	Permanent indentation 12 mm dia indentor Hemispherical *A: 38% Fibre vol	
				B*	UD	0.25 0.5 0.7 1.4 1.8	0 15 24 57 73	•	-18% RCSI -27% RCSI -40% RCSI -46% RCSI -60% RCSI	12 mm dia indentor Hemispherical *B: 34% Fibre vol	
			4.75	C*		0 0.4 0.6 1.05 3.2	10 15 27 40 88		-15% RCSI -18% RCSI -31% RCSI -35% RCSI -60% RCSI	*C: 34% Fibre vol	
				A*		• • •	Length mm 0 4 9		-10% RCSI -12% RCSI -14% RCSI	Impact	
				B*		• • •	Length mm 0 10 15		-14% RCSI -22% RCSI -25% RCSI	Impact Material B	
[163]	Ishai 90	70x8	6.4	CFRP ud	48 ply, QI ±45/0/90	IFM Nm/mm 5.1 5.1 5.2 5.6 5.9	• • • • •	•	0% -44% -49% -52% -72%	Damage induced with 3-point bending Simply supported	
						J/mm 0.39 0.44 0.5 0.5 0.53	• • • • •		-0% -28% -20% -46% -42%	Damaged induced with impact Clamped	
						IFM Nm/mm 4.4 4.7 5.1 5.3 5.4 6.2	• • • • • •		0% -10% -15% -63% -83% -88%	Damage induced with 3-point bending Simply supported	
						J/mm 0.36 0.38 0.39 0.4 0.42 0.53	• • • • • •		0% -2% -27% -27% -36% -48%	Damage induced with impact Clamped	
						J/mm 0.23 0.3 0.38 0.39 0.41 0.7	• • • • • •		0% -91% -50% -45% -41% -66%	Damaged induced quasistatic loading Clamped	
[100]	Bibo 95	89x55	2	CFRP ud	16 ply, QI	J 1.2 2.5 6	•	•	-8% -33% -48%	Impact @20C Impact @20C Impact @20C	
						J 1.2 2.5 6			-5% -37% -47%	Impact @80C Impact @80C Impact @80C	
						J 1.2 2.5 6			-13% -42% -55%	Impact @150C Impact @150C Impact @150C	
[37]	Cartie 02	150x100	4	CFRP ud HTA/ B: 922 914 924 T: 920	QI 32 ply	4*-20 7-17 8.5-25 10-30	mm2 440-1200 500-900 620-1100 240-780	•	I -: RCS 225-150 I 440: RCS 260-210 I 400: RCS 260-210 I 425: RCS 350-270	CAI depends only on the matrix	
				IMS/ B: 922 924 8552		3.4-19 7-20	250-1900 500-1300		I -: RCS 225-150 I 450: RCS 260-225		
[33]	Siow 98	Coupon 50x50 (178 grip)	?	CFRP w M18-1/ 45% G939	QI	5.5 7 8.2 10.6	mm2 20-175	•	RCS - RCS 260 RCS 280 RCS 220	Impactor 21 dia H	CAI of both impactors has the same trend (delam area) different trend (with IKE)
						5.5 7 8.2 10.6	80-400		RCS 245 RCS 220 RCS - RCS 145	Impactor 6.3 dia H	Tensile RTS is 50% higher
[43]	Griffin 87	254x127	6.35	CFRP ud AS4/ T: 2220-1 B: 3502	QI 48 ply	27-41	mm2 1419-3065 1774-2645	•	RC microstrain 4800-3600 4000-3300	19 % increment	All systems follow the same trend with delam area
				HSC/ HST-7 974 1806 584 5245C			1050-1500 950-1600 1550-2300 2300-3300 2000-2900		8000-6800 6500-5000 5500-4400 4800-4000 4400-3600		
				AS6/ T: 2220-1			2400-3600		4000-3200		

Ref.	Author	Panel LxW mm	Thick mm	System fibre/resin	Layup	IKE J	Area mm2	OH	RCS MPa or %	Notes	
[48]	Prandy 91	102x152 Boeing	4.04	CFRP ud IM7 /X5260 /X5255-3 /5250-4 /5250-3	QI 32 ply	27.1 27.1	mm2 516 710	•	RCS (MPa) 335 295 335 302 333 292 231 220 211 170	Boundary cond wood + Al Steel (Al) wood + Al Steel (Al) wood + Al Steel (Al) wood + Al Steel (Al) wood + Al Steel (Al)	Dynatup Dynatup Boeing Boeing
[28]	Liu, Raju, Dang, 98	250x125	6.69	GFRP ud 3M glass/ epoxy	CP 51 ply	0-300 0-380 0-180 0-100-380	•	•	Stiffness GPa 1.8-1.6 1.35-1.2 1.4-1.1 BL kN 190-100-100	Impact area, mm 125x125 84x84 12x12 Impact area no effect	Results with crushing end avoided Thus no thin panel results (even with tabs crush end)
[102]	Brandt 86	101x152	?	CFRP ud AS4/APC2* B: HTA/CI1020* T: T400/6376* T: T300/914C* T: IM6/914C T: HTA/CE1008	QI 36 ply	J/mm 3.3 6.6 3.3 6.6 6.6 3.3 6.6 0 3.3 6.6 6.6 0 3.3 6.6 6.6 6.6 6.6	% total area • • • • • • • • 7 14 • • 8 18 • •	•	CSRF / RCS (MPa) 70-80% 60-70% 35-40% 30-35% / 78 / 95 40-50% 50-60% / 386 40-50% / 186 35-40% / 151 / 148 / 396 / 205 / 161 / 169 / 115 / 123	Environmental Dry Moisture saturated before impact Dry Moisture saturated Dry Moisture saturated Dry Moisture saturated	* Thermoplastic PEEK * Untoughened BMI * Toughened * Standard Damage fibre breakage Damage fibre breakage >> BVD: delam BVD: delam
[150]	Long 01	89x55	?	CFRP ud T300/5228	QI 16 ply	0 1-6 6-10	mm2 0 80-800 800-1000	•	RCS, MPa 400 400-160 160-150	•	Model effective damage: open hole stress concentration
[25]	Lin 99	101.6x152.4	•	CFRP ud IM7/K3B	QI	0 11.3 22.6 33.9 50	mm2 • 96.8 354.8 612.9 •	•	RCS, MPa 350 340 A* 320; B* 310 A 320; B 290 300 A 270; B 280 A 260; B 280 265 A 235; B 245 A 230; B 245 230	Aging, hours 0 0 5000 13000 0 5000 13000 0 5000 13000	at 300, 350, 400F temp makes no difference * A before, B after impact
[164]	Amrah, Hogg 01	89x55	•	GFRP non crimp fabric* E glass/ epoxy	QI 16 ply	• 4-12	width, mm 25.7-45.2	Insert* Insert* Insert*	RCS, MPa Intact* 317.3 / 294.6 230.3-149 217-121.3-100.7 216.8-113.5 212.4-134.4	Insert * dia, mm * Nylon 10-30 * Acrylic 10-30-40 * PTFE 10-30 Nearly no difference between inserts, failure depends on stiffness insert. PTFE (ductile) buckled before, Acrylic +/- (brittle)	* ASTM D3410 / QMW rig * OH with inserted material * Non crimpage (undulation of fibre tows caused by weaving)
[165]	Ashton 96	178x279	6.6	CFRP ud IM7/977-3 AS4/3501-6	•	0, 6.8 13.6-27.2-40.7 13.6-27.2-40.7	968-2065-4000 1161-2710-3613	•	RCS, MPa 434 393-310-283 324-248-221	Damage tolerance to design process. Database Bad correlation with dent data	
[80]	Avva 83	88.9x76.2 120.7x76.2 152.4x76.2 88.9x76.2 120.7x76.2 152.4x76.2	4.48 2.24	CFRP ud T300/ 5208	QI 32 ply QI 16 ply	0-5 0-5		•	Strain/CStrainRF 10000-3500 / 1-0.3 7500-2800 / 1-0.3	AR 1 1.5 2 1 1.5 2	Impact during compression Less than 15% specimens failed near the gripping zone
[100] [101]	Bibo, Hogg, Kemp 94, 95	89x55	2	CFRP ud Thermoset T800H/924C Thermoplastic T650-42/ R8350	QI 16 ply	0-1.2-6.5 0-1.2-6.5 0-1.2-6.5 0-1.2-6.5 0-1.2-6.5 0-1.2-6.5	width, mm 16-35* 19-40* 5-22* 5-22*	•	RCS, MPa I* 407, 360, 245 400-400-220* I* 346, 286, 214 380-380-300*	* Intact at 20, 80, 150 * Room temperature * 150 C * I: Any temp; C: RT * Intact at 20, 80, 150 * Room temperature * 150 C * I: Any temp; C: RT	C: @ 80-150 increase in CSRF for thermoset C: @ 80-150 no effect on CSRF thermoplastic, high scatter
[122]	Dost, Finn, Stevens, Lin, Fitch, 92	101.6x152.4	4.57	CFRP ud IM7/8551-7 IM6/3501-6	AP 24 ply	•	Radius, mm 8.3-16.3 66 dia 23.6-38.4 51 dia	•	Applied load, % failure 0-0.5-0.65-1 0-0.6-0.8-1	Buckled damage dia 18-18-52-66 6.5-13-43-51	Measured with moire and micro Moire. No delam growth, instead complex post buckling phenom. Stress cone with Moire
[52]	Demuts Sandhu Daniels 92	177.8x254	9 ply 26 ply 48 ply 74 ply 96 ply 9 ply 26 ply 48 ply 74 ply 96 ply	CFRP ud AS4/ 3501-6 IM6/ Cycom 3100	QI	12.3 43.3 123.8 135.8 135.8 12.4 48.5 124.1 136.2 136.1	mm2 645 1935 10323 11613 11613 627 13297 16962 15102 13525	•	CSRF, % 123 75 31 31 42 108 48 27 27 35	Intact CS, N/ply 1561 3345 6241 6610 5551 1842 4675 7175 7175 6597	Dent depth measured with Moire RCS per ply no difference for different thickness
[17]	Guynn O'Brien 85	101.6x349.2 127x254	16 ply 32 ply 32 ply 32 ply 64 ply	CFRP ud T300/ 5208	QL %0 ply 25% 25% 12.50% 37.50% 25%	J/mm 0.9 1.3 0.9 1.3 0.9 1.3 0.9 1.3 1.9 2.6		•	RC micro strain* 4800 3200 6000 3500 8900 6000 5100 3900 3500 3500	•	* Strain from SG's reading Impacted with small preload 25 lbf Damage: peanut shape, analysis of ttt distr. Also embedded delamination

Ref.	Author	Panel LxW mm	Thick mm	System fibre/resin	Layup	Factors affecting RCS IKE J	Area mm2	OH	RCS MPa or %	Notes	
[119]	Gao, Kim 01	100x100	2	CFRP ud AS4/PEEK thermoplastic	QI 16 ply	7.5-30 9.7-30		·	·	CSRF / RCS MPa 100-51% / 200-102 100-60% / 150-90	RCS better slow cooling CSRF better fast cooling	Rate of cooling Slow Fast
				T300/913		4.6-30			·	100-40% / 110-40	Ductility vs fibre/matrix interface bond = fast vs slow cooling	·
[55]	Henderson, Mylar 01	152.4x101.6 SACMA		CFRP ud M30SC/resin*: 28 49 60 28-1 60-1 49-1	QI 40 ply	6.67 J/mm	mm2 2324 4836 3377 6678 10340 6042	·		Ultimate load, kN 105.8 64.6 116.7 44.9 41.6 57.7	Peak transverse load 16.8 15.8 17.4 14.8 12.18 10.8	* Resin: Dicy (28 49 60) vs DDS (28 49 60-1) Tg of resins 28, 49, 60 = 95, 125, 117 C Transverse loading and unloading paths Influence of Gii, EA and flexural modulus control internal damage size Damage size controls CSRF
[58]	Kohnder 04	115x90	3	GFRP E glass/ resin	Knitted: Milano Rib Plain	1.72-25.28 1.74-24.28 1.73-27.09	mm2 14.48-354.32 28.10-402.53 13.37-286.84	·	CSRF / RCS* MPa 91.1-71% / 154-120 92.6-75.3% / 150-122 94.6-73.7% / 158-123	Intact CS, MPa 169 162 167	Results from loop density 0.86, 0.8, 1.16 mm-3 Antibuckling support covers all panel appart from the damage region
[155]	Kan 98	·	·	·	·	·			·	·	References from: Demuts, 92; Hinrichs, 95; Guy, 92; Jegley, 92.
[8]	Prichard, Hogg 90	89x55	2	CFRP ud T800H/924C (F924C) AS-4/PEEK (APC-2)	QI 16 ply	0-0.86 0.87-7.44 11.18 0-2.02 3.99-14.62	width, mm 0 14.8-41 43.5 0 13.1-32	·	RCS*, MPa 400 318.3-137 155.1 412 364.6-200		* RCS and width linear 6.1 MPa/mm It measures compression, damage generation. It depends on mode I and II fracture. Good statistical approach:, 10% not unusual coefficient of variation When comparing CSRF of 95% prediction intervals small difference between two systems
[76]	Hosur Murthy 98	150x150	3.6 6 6	CFRP ud T300/914	QI 24 ply QI 40 ply QI* 40 ply	6 9 12 12 15 18 8 17 30	mm2 · 715 878 1029 1470 1419 924 1447 1743	·	CSRF % reduction 3.97 19.02 27.44 38.31 43.28 45.52 3.62 47.28 53.2	CStrain RF % red. 13.01 25.73 29.7 37 38.7 44.1 2.1 8.5 52.8	Different IKE levels for aircraft parts Small damage: linear - subl buckling - shear failure Large delam: non linear due to unbalanced sublaminates SGx readings affected by the presence of dent * varying QI layup stacking sequence
[99]	Puhui, Zhen Jun, Yang, 02	200x100 254x125 150x100 150x115 150x115 150x100 150x100 140x100	28 ply 48 ply 48 ply 38 ply 42 ply 40 ply 38 ply 20 ply	CFRP ud T300/5405 T300/QY8911 T300/KH304	QI	12-20 27.1 16.3 21 22.6 22 22 10-20	mm2 397-684 7.97 8.03 1820-2800 1200-2150 2170 2200	·	RCS, MPa 190-210 161.72 166.18 150-171 191-206 160-201 156-181.6 280-230	a / b* 11.2-14.7/1.86-4.75 17/1.8 15/1.6 22.3/1.6 - 27.6-1.9 18.1/1.9 - 24.2/1.6 22.4/6.35 · 6.5-18 / 1.9-6.3	* Dent = 2b; width = 2a Width (not depth) is the key factor governing CAI Results from many references
[143]	Ilcewicz, Dost Coggeshall 89	7x127 102x152	7.52 4.5	CFRP ud AS6/3501-6 IM6/3501-6 IM7/8551-7	QI 40 ply QS 24 ply	I QS I	dia, mm 38.1-76-115 25.4-38.1-76 15-76	·	RCS, MPa 193-138-96 297-193-138 435-83	Intact 501 MPa	Similar response I and QS An. Model: early important paper Brittle vs tough = damage resistance (area, width) Area, width = damage tolerance Both systems similar
[36] [35]	Dost 91 9th DOD., STP 1110	102x152	6.1 4.5	CFRP ud IM7/8551-7	QI* 32 ply 24 ply	16.3-40.7 16.3-40.7 5.4-16.3-40.7 5.4-16.3-40.7 5.4-16.3-40.7 9.5-17.6-40.7 8.1-19-40.7	dia, mm 30-67 41-81.1 0-12.1-27.6 0-27.3-60 0-28.5-49.4 12.4-23-36.3 0-28.5-35.9	·	RCS, MPa 350-230 295-190 410-380-280 345-330-220 345-270-200 420-405-260 380-320-260	Calculated buckl, MPa 638 345 390 370 495 390 395	* Layups (45,/90,/-45,/0,)₂ₛ (45,/90,/-45/0,)ₛ (45/90/-45/0)ₛ (45(90/-45)₂(0/45)₂/0)ₛ (45(0/-45)₂(90/45)₂/90)ₛ (30/60/90/-60/-30/0)₂ₛ (30/60/90/-30/-60/0)ₛ ttt photographs Ply group thickness relates with CAI*
						area/dia, mm 1322/40 2610/58 3700/69 5160/81			Applied stress, MPa 180-295 180-220 180 180	Out of plane displ, mm 0.28-0.81 0.95-1.2 1.5 1.5	Layup affects CAI for high IKE For low IKE, CAI depends on panel stability (upper bond) rahter than damage related
[49]	Manders, Harris 86	101.6x152.4	5.08	CFRP ud T300, T500/ ERL-1962 T700/ERL-1962 T500/MY720 /DDS		J/mm 2.22-22.24 2.22-22.24 2.22-22.24		·	·	379.5-186 379.5-138 262.2-110.4		Fibre surface treatment: T700 has 70% lower surface functionality It has 15% lower CAI It has 50%more delamination area than T300,T500 Matrix toughness effect on CAI Layup and ply thickness no effect on CAI
[53]	Recker 89	100x150	·	CFRP ud Many systems* IM7/5245C IM7/X5255-3 IM7/5208	·	30	· 520 1940		RCS, MPa 130-280 200 315 138	Giic J/m2 320-1020 410 / 615 600 / 910	*Fibres: IM, G40-800, T800, IM7 Resins: expy, BMI, single and multiple phase Giic is proportional to CAI
[54]	Stuart Altstad 89	101.6x152.4	4	CFRP ud T800H/R5245C Same + Y1* Same + Y2*	QI 32 ply	kJ/m 2.22-8.89	400-6400 400-4400 400-3000	·	RCS, MPa 260-125 280-125 300-160	Gi / Giic J/m2 450 / 450 450 / 575 500 / 550	20% improvement in CAI due to higher Giic Standard fibre * Y1: Medium surface treatment * Y2: High surface treatment
[147]	Sjogren 01	180x10 Coupons Inital panel 180x180	2.2 6.4 2.2-6.4	CFRP ud HTA/6376C	QI 16 ply QI 48 ply 16-48 ply	8 30	·	·	RCSStiffness I II III*, GPa 45 / 41 / 36 50 / 49 / 48 50 / - / -	·	* Damage in regions I, II, III: intact, delam, fibre break. RCStiffness controlled by fibre break Delamination had little effect on RCStiffness Analysis ttt (polishing) no effect on RCStiffness
[166]	Zhang 01	100x150	4	CFRP ud T300 /PEK-C /PEK-C mod /PDE mod T300/5428* T700/5428 T800/5428	QI 32 ply	4.45 kJ/m	1200-1500 750-770 750-780 700-850 680-750 1100-1500	·	RCS, MPa 165 218 209 230 260 238	·	Matrix toughening through cross linking and 2 phase resin * Resin 5428 is BMI
[56]	Ying, Chang, Xian, Ning, Xu 01	150x50 Coupon*	2.1 2 2.06	CFRP T300/985 Plain woven ud pw + ud*	(0)10 AP 16 ply AP 16 ply	1-6 1-6 1-6	0-200 0-320 0-800		CSRF 0-0.57 0-0.43 0-0.56	TensileSRF 0-0.34 0-0.50 0-0.68	* Real area of specimen: 50x50 * -45 plain woven, the rest is ud
[45]	Ambur 98	228.6x127	·	CFRP ud AS4/3502	QI 48 ply	10.2-33.9 13.6-33.9 13.6-33.9 13.6-33.9	0-1290 839-2194 1161-1935 0-2710	·	RCS, MPa 283-242 255-204 248-186 269-224	Mass impactor, kg 1.13 2.27 4.54 9.08	Lighter impactor, lower CAI strength Scaling in weight no advicesable

Ref.	Author	Panel LxW mm	Thick mm	System fibre/resin	Layup	Factors affecting RCS IKE J	Area mm2	OH	RCS MPa or %	Notes	
[90]	Lamen 92	76 x 50.8	-	CFRP ud	QI 16 ply			a/W 6.3/50.8 12.7/50.8 19/50.8 25.4/50.8	292 RCSH 230 RCSH 195 RCSH 155 RCSH		Also embedded delamination
		152 x 102				kJ/m 3.5 4.5 5.5 6.5	mm2 440 700 900 1100		292 RCSI 270 RCSI 250 RCSI 242 RCSI		
[167]	Shuart 84	254x127	6.4	CFRP ud	48 ply AP MD MD MD MD AP MD MD MD MD	- - - - - - - - - - J 6 17 35 6 17 35 6 17 35 6 17 35 6 17 35	- - - - - - - - - - Major axis mm 23.6 36.3 59.9 23.6 36.3 70.9 25.4 32.8 61.7 27.2 41.7 96.3 21.8 43.4 79.8	a/W 25.4/127 50.8/127 25.4/127 50.8/127 25.4/127 50.8/127 25.4/127 50.8/127 25.4/127 50.8/127	-25% RCSH -44% RCSH -33% RCSH -51% RCSH -30% RCSH -50% RCSH -33% RCSH -53% RCSH -37% RCSH -57% RCSH -6% RCSH -21% RCSH -39% RCSH +7% RCSH -41% RCSH -57% RCSH 0% RCSH -33% RCSH -53% RCSH -3% RCSH -48% RCSH -67% RCSH -11% RCSH -47% RCSH -63% RCSH	Plies in the width direction 0% plies WD 8% plies WD 17% plies WD 25% plies WD 33% plies WD 0% plies WD 8% plies WD 17% plies WD 25% plies WD 33% plies WD	.
[168]	Baker 94	254x127	-	CFRP AS4/PEEK ud w, film stacked w, corringled ud w, film stacked w, corringled	48 ply QI QI QI QI QI QI	- - - J 27 27 27	- - - mm2 1787 1626 2026	a/W 25.4/127 25.4/127 25.4/127 . . .	265 RCSH 254 RCSH 267 RCSH 212 RCSI 263 RCSI 223 RCSI		.
[169]	Dow 89	254x76.2 254x127		CFRP w	48 ply QI	. . . . J 113 0 113 169 0 113 169 0 113 169		a/W 6.3/76.2 12.7/76.2 6.3/76.2 12.7/76.2 6.3/76.2 12.7/76.2 6.3/76.2 12.7/76.2	52 RCSH 44 RCSH 56 RCSH 44.5 RCSH 52 RCSH 46 RCSH 51 RCSH 44 RCSH -67% RCSI -24% RCSI -31% RCSI -33% RCSI -14% RCSI -36% RCSI -48% RCSI -21% RCSI -38% RCSI -38% RCSI	Reinforcement tit Unstitched Unstitched Kevlar stitched Kevlar stitched Carbon stitched Carbon stitched Glass stitched Glass stitched Unstitched Kevlar stitched Kevlar stitched Kevlar stitched Carbon stitched Carbon stitched Carbon stitched Glass stitched Glass stitched Glass stitched	.
[74]	Krober 92	250x110 250x110 250x110 250x110 250x110 250x110	5.25 1.75 2.6 3.5 5.25 5.25	CFRP ud Ciba 6376/ HTA	42 ply QI 14 ply QI 21 ply QI 28 ply QI 42 ply QI 42 ply QI	. . . . J 23 32 32 48 32 48 42 48 32 48 32 48 32 48 32 48		a/W 4/110 8/110 12/110 24/110 4/110 8/110 12/110 24/110	-18% RCSH -28% RCSH -35% RCSH -48% RCSH -60% RCSH -66% RCSH -72% RCSH -78% RCSH 183 RCSI 130 RCSI 165 RCSI 133 RCSI 218 RCSI 173 RCSI 210 RCSI 178 RCSI -34% RCSI -53% RCSI -31% RCSI -45% RCSI -70% RCSI -74% RCSI -68% RCSI -70% RCSI	10% plies LD 10% plies LD 10% plies LD 10% plies LD 70% plies LD 70% plies LD 70% plies LD 70% plies LD . . . . 10% plies LD, air gun 10% plies LD, drop w 10% plies LD, air gun 10% plies LD, drop w 70% plies LD, air gun 70% plies LD, drop w 70% plies LD, air gun 70% plies LD, drop w	.

Ref.	Author	Panel LxW mm	Thick mm	System fibre/resin	Layup	Factors affecting RCS IKE J	Area mm2	OH	RCS MPa or %	Notes	
[170]	Ishikawa 01	118x38.1 (*)	4		32 pli QI	•	•	a/W 6..3/38.1	-43% RCSH		(*) Rectangular window 25.4x16.5
						•	•	9.5/38.1	-52% RCSH		
						•	•	12.7/38.1	-60% RCSH		
						•	•	15.9/38.1	-63% RCSH		
						J/mm					
		254x127	6		48 ply QI	1	0	•	-3% RCSI		NASA
						1.4	1350	•	-22% RCSI		
						2	1750	•	-40% RCSI		
				CFRP ud		2.5	2000	•	-48% RCSI	•	
						3	3500	•	-50% RCSI		
						3.7	2800	•	-58% RCSI		
		152x102	4		32 ply QI	1	0	•	+5% RCSI		SACMA
						1.4	500	•	-39% RCSI		
						2	650	•	-52% RCSI		
						2.5	1100	•	-61% RCSI		
						3	2400	•	-55% RCSI		
						4	3700	•	-64% RCSI		
		102x76	4		32 ply QI	1.4	600	•	-48% RCSI		Half SACMA
						2	750	•	-53% RCSI		
						2.5	1750	•	-56% RCSI		
						3	2800	•	-59% RCSI		
						4	3900	•	-63% RCSI		
						6	3800	•	-67% RCSI		

RCSE Residual compressive strength for embedded delamination
PS Failure strain
Suc Ultimate stress
RCSI Residual compressive strength for impacted panel
RCSH Residual compressive strength for open hole
BL Buckling load
BS Buckling stress
PL Propagation load
PS Propagation strain
SS, FE Simply supported, free end
LD, WD Loading direction, width direction
QI Quasi-isotropic
CP Cross ply (0.90)
AP Angle ply (±45)
MD Multidirectional (±45, 0) 0 is LD
MD' Multidirectional (±45, 90) 90 is WD
IFM Initial flexural moment

TABLE 1.1.3 Literature review of panels with embedded delamination

Ref	Author	Panel LxWxt	Shape	Size	No.	Depth	Orient.	RCS [MPa]	Notes
[87]	Suemasu 00	150x100x3.3 16 plies QI GFRP woven	Circular	22.5-37.5	7		.	-13% RCSE	22.5, 25, 27.5, 30, 32.5, 35, 37.5 — Buckl load
			Circular	22.5-47.5	7	Even	.	-26% RCSE	22.5, 25, 27.5, 30, 32.5, 35, 47.5 — low due to
			Circular	37.5-52.5	7	every 2 ply	.	-34% RCSE	37.5, 40, 42.5, 45, 47.5, 50, 52.5 — large delam
			woven	37.5-62.5	7		.	-26% RCSE	37.5, 40, 42.5, 45, 47.5, 50, 62.5 — near the
[84]	Suemasu 96	150x100x2.5 12 plies QI CFRP woven	Circular	10	5		.	-0% RCSE	Toughened matrix: 30K
			Circular	20	5		.	-0% RCSE	Toughened matrix: 30K
			Circular	30	5	Even	.	-12% RCSE	Toughened matrix: 30K — 0.2911
			Circular	10	5	every 2 ply	.	-0% RCSE	Conventional matrix 06M
			Circular	20	5		.	-8% RCSE	Conventional matrix 06M
			Circular	30	5		.	-29% RCSE	Conventional matrix 06M
[88]	Suemasu 01	150x100x3.3 16 plies QI GFRP woven	Circular	12.5-27.5	7		.	+7% RCSE; +7%BL	12.5, 15, 17.5, 20, 22.5, 25, 27.5
			Circular	12.5-37.5	7		.	-6% RCSE; -12%BL	12.5, 15, 17.5, 20, 22.5, 25, 37.5
			Circular	17.5-32.5	7		.	-	17.5, 20, 22.5, 25, 27.5, 30, 32.5
			Circular	17.5-42.5	7		.	-	17.5, 20, 22.5, 25, 27.5, 30, 42.5 — Constant distribution
			Circular	22.5-37.5	7	Even	.	-45% RCSE; -66%BL	22.5, 25, 27.5, 30, 32.5, 35, 37.5 — ttt greater reduction
			Circular	22.5-47.5	7	every 2 ply	.	-70% BL	22.5, 25, 27.5, 30, 32.5, 35, 47.5 — RCSE than conical:
			Circular	32.5-47.5	7		.	-	32.5, 35, 37.5, 40, 42.5, 45, 47.5 — see cummulated area
			Circular	32.5-57.5	7		.	-85% BL	32.5, 35, 37.5, 40, 42.5, 45, 57.5
			Circular	37.5-52.5	7		.	-37% RCSE; -87% BL	37.5, 40, 42.5, 45, 47.5, 50, 52.5 — Energy release rate
			Circular	37.5-62.5	7		.	-31% RCSE; -87% BL	37.5, 40, 42.5, 45, 47.5, 50, 62.5 — FEA prediction
			Circular	30	8		.	-22% RCSE; -52% BL	30x8
[91]	Davidson 90	244x140x3.3 28 plies QI and CP CFRP	Ellip ar 1.9	38:20	1	4/5	LD	285 RCSE; 189 BS	QI
			Ellip ar 1.9	38:20	1	4/5	+45	269 RCSE; 209 BS	QI
			Ellip ar 1.9	38:20	1	4/5	WD	278 RCSE; 203 BS	QI
			Ellip ar 1.9	38:20	1	4/5	-45	295 RCSE; 215 BS	QI
			Ellip ar 1.16	58:50	1	6/7	WD	267 RCSE; 198 BS	QI: 267 RCSE; 198 BS
			Ellip ar 1.16	58:50	1	4/5	LD	211 RCSE; 184 BS	CP: 211 RCSE; 184 BS
			Ellip ar 1.16	58:50	1	4/5	WD	220 RCSE; 190 BS	CP: 220 RCSE; 190 BS
			Ellip ar 1.9; 1.37 & 1.32	Notes	4	2/3-6/7 10/11-13/14	-45, +45 LD, WD	170 RCSE, 143.4 BS	QI 57:30, 57:30, 41:30, 25:19
[85] [86]	Davidson 89, 91	254x127 24 plies, QI CFRP	Circular	12.7	1	4/5	.	352 kN BL	- — Buckling analysis
			Circular	25.4	1	4/5	.	220 kN BL	- — for QI intact panels
			Ellip ar 2	12.7:25.4	1	4/5	WD	462 kN BL	- — Blister model
			Ellip ar 2	12.7:25.4	1	8/9	WD	>500 kN BL	-
			Circular	25.4	2	4/5-20/21	.	211 kN BL	-
			Circular	25.4	3	4/5-12/13-20/21	.	227 kN BL	-
		244x140 28 plies, QI CFRP	Ellip ar 1.89	38.3:20.3	1	4/5	LD	188.7 BS	-
			Ellip ar 1.89	38.3:20.3	1	4/5	-45	209.1 BS	-
			Ellip ar 1.89	38.3:20.3	1	4/5	WD	202.7 BS	-
			Ellip ar 1.89	38.3:20.3	1	4/5	+45	215.3 BS	-
[90]	Laman 92	76 x 51 16 plies, QI CFRP	Circular	25.4	1	2/3	.	358 RCSE	- — 786 MPa Undamaged ?!
			Circular	25.4	1	8/9	.	306 RCSE	-
			Circular	12.7	3	2/3-4/5-6/7	.	275 RCSE	-
			Circular	25.4	3	2/3-4/5-6/7	.	229 RCSE	-
			Circular	25.4	3	Even	.	181 RCSE	-
			Circular	25.4	5	Notes	.	194 RCSE	Depth: 2/3-4/5-6/7-8/9-10/11
			Circular	25.4	5	Even	.	168 RCSE	-
			Circular	6.35	7	Even	.	325 RCSE	-
			Circular	12.7	7	Even	.	237 RCSE	-
			Circular	25.4	7	Even	.	168 RCSE	-
			Circular	6.35-25.4	7	Even	.	184 RCSE	Size: 6.35, 9.52, 12.7, 15.9, 19, 22.2, 25.4
[83]	Cairns 94	152x102 32 plies, QI CFRP	Circular	12.7	4	Notes	.	PS, FS, MPa -, 323	3/4, 7/8, 11/12, 15/16 — FEA modeling
			Circular	19.1	4	Notes	.	250, 279	3/4, 7/8, 11/12, 15/16
			Circular	25.4	4	Notes	.	223, 257	3/4, 7/8, 11/12, 15/16
			Circular	41.3	4	Notes	.	194, 204	3/4, 7/8, 11/12, 15/16
[81]	Tratt 91	102x84x2.9 8 plies, CP CFRP woven	-	0	.	-	.	BDS, PS, FS, MPa 360, -, 428	- — FEA modeling
			Circular	12.7	1	2/3	.	383, 383, 436	-
			Circular	25.4	1	2/3	.	211, 250, 287	-
			Circular	38.1	1	2/3	.	101, 201, 283	-
[82]	Yeh 94	60x40x0.96 8 plies UD CFRP	Ellip ar 1.72	3	1	3/4	LD	-2% BL	Aspect ratio of the ellipse = 1.72 — FEA modeling
			Ellip ar 1.72	6	1	3/4	LD	0% BL	-
			Ellip ar 1.72	9	1	3/4	LD	-3% BL	-
			Ellip ar 1.72	12	1	3/4	LD	-5% BL	-
			Ellip ar 1.72	15.3	1	3/4	LD	-8% BL	-
			Ellip ar 1.72	15.3	1	3/4	30°	-11% BL	Angle measured respect to LD
			Ellip ar 1.72	15.3	1	3/4	60°	-10% BL	Angle measured respect to LD
			Ellip ar 1.72	15.3	1	3/4	WD	-13% BL	-
			Ellip ar 1.72	18.3	1	3/4	LD	-11% BL	Layup: UD
			Ellip ar 1.72	18.3	1	3/4	LD	-	-70% BL; layup: AP (-45,+45)
			Ellip ar 1.72	18.3	1	3/4	LD	-	-89% BL; layup: UD 90
			Ellip ar 1.72	21.5	1	3/4	LD	-20% BL	-
			Ellip ar 1.72	21.5	1	1/2	LD	-15% BL	-
			Ellip ar 1.72	21.5	1	2/3	LD	-20% BL	-
			Ellip ar 1.72	21.5	1	4/5	LD	-25% BL	-
[171]	Reddy 84	304.8x254x2 16 ply, QI CFRP	Rectang	101.6x76.2	1	MP	WD	-2.3% BL	Side edges: free edge — Control panel wide column 4627
			Rectang	152.4x50.8	1	MP	WD	+0.2% BL	Side edges: free edge
			Rectang	101.6x76.2	1	MP	LD	+1.3% BL	Side edges: free edge — Control panel single bay, ss 11292
			Rectang	101.6x76.2	1	MP	WD	-1.2% BL	Side edges: simply supported
			Rectang	152.4x50.8	1	MP	WD	+5.7% BL	Side edges: simply supported
			Rectang	101.6x76.2	1	MP	LD	+12.2% BL	Side edges: simply supported
[95]	Guedra 92	100x100 24 plies, QI CFRP	Circular	30	1	3/4	.	15 kN BL; 55 kN PL	- — FEA modeling
			Ellip ar 2.25	45:20	1	3/4	LD	10 kN BL; 53 kN PL	-
			Ellip ar 2.25	45:20	1	3/4	WD	19 kN BL; 53 kN PL	-
[92]	Nilsson 01	150x150x4.58 35 plies, CP CFRP			0	-	.	DBL, BL, PL, kN -, 112, -	Delta delam size postlouding, mm — Load and size average values
			Circular	55	1	3/4	.	113, 113, 113	6.2 — Stepped loading for C-scanning. Data corresponds
			Circular	55	1	3/4	.	17.2, 106.4, 106.4	6 — to the 1st delam growth
			Circular	55	1	5/6	.	59.3, 104, 104	20.2 to failure — Delam material 55/60 Polyimide
			Circular	55	1	7/8	.	97.2, 111, 110	5.75 to failure — 7.5 micron/Teflon 25 microm
[93]	Asp* 01				0	-	.	-, 115, -	- — Drilled hole
			Circular	60	1	3/4	.	26.2, 104, 104	6.25 — 1.2 mm dia for pressure
			Circular	60	1	3/4	.	9.5, 104, 104	7 — * in both ref
			Circular	60	1	5/6	.	41, 107, 107	20&38 — * in both ref
			Circular	60	1	7/8	.	70, 103, 103	12.3 — * in both ref

Ref	Author	Panel LxWxt	Methods of Damage Generation Art. Embedded Delam.					RCS [MPa]	Notes	
			Shape	Size	No.	Depth	Orient.			
[98]	Short 01	100x50x2.4 8 plies, MD GFRP	Square	10x10	1	1/2	-	-9% RCSE	-	FEA modeling
			Square	15x15	1	3/4	-	-15% RCSE	-	Isotropic modeling
			Square	15x15	1	1/2	-	-10% RCSE	-	
			Square	25x25	1	4/5	-	-31% RCSE	-	
			Square	25x25	1	3/4	-	-29% RCSE	-	
			Square	25x25	1	1/2	-	-16% RCSE	-	
[97]	Short 99	200x50x2.4 8 plies, MD GFRP	Square	10x10	1	1/2	-	-9% RCSE	-	
			Square	15x15	1	1/2	-	-10% RCSE	-	
			Square	25x25	1	4/5	-	-24% RCSE	-	
			Square	25x25	1	3/4	-	-31% RCSE	-	
			Square	25x25	1	1/2	-	-16% RCSE	-	
[75]	Nyman 98	250x127x5.2 40 plies, QI CFRP	Circular	20	1	4/5	-	2000 µe PS, 6000 FS	Drilled hole and prebuckled, SL	FEA modeling
			Circular	30	1	4/5	-	3225 µe PS, 5200 FS	Successive loading (SL)	Energy release rate
			Circular	40	1	4/5	-	2650 µe PS, 5900 FS	Successive loading (SL)	
			Circular	30	1	6/7	-	3700 µe PS, 8800 FS	Drilled hole and prebuckled, SL	
[96]	Reeder et al 2002	114x229x 24 ply, QI+AP CFRP ud AS4/3501-6	Circular	64	1	4/5	-	DBL, PL, kN 48, 54	Out of plane displ, mm 1.25	Stereo imaging for out of plane displ
			Circular	64	1	5/6	-	50, 56	1.05	Also cylindrical panels
									At delamination growth	Flat results shown

RCSE	Residual compressive strength for embedded delamination
FS	Failure strain
RCSI	Residual compressive strength for impacted panel
RCSH	Residual compressive strength for open hole
DBL	Delamination buckling load
BL	Buckling load
BS	Buckling stress
PL	Propagation load
PS	Propagation strain
SS, FE	Simply supported, free end
LD, WD	Loading direction, width direction
QI	Quasi-isotropic
CP	Cross ply (0.90)
AP	Angle ply (±45)
MD	Multidirectional (±45, 0) 0 is LD
MD'	Multidirectional' (±45, 90) 90 is WD

2 Manufacturing of Preconditioned Composite Panels

In this chapter, the fabrication process of composite laminate plates is described. Specimens were made for two tests configurations, namely, in-plane compression and transverse loading. The latter includes quasi-static and impact loading. The major steps needed for manufacturing and preparing composite panels include cutting of individual plies, laying-up, curing, machining of cured panels, end potting and strain gauging. The preconditions introduced during the manufacturing process were embedded artificial delamination and local change of geometry. Additionally, open holes were drilled from intact panels. The panel dimensions for impact and quasi-static loading were 150×150 mm with a testing area of 100 mm diameter. For compression-after-impact (CAI) tests the damaged panels were trimmed down to 150×100 mm.

2.1 Basic material properties

A typical laminate composite material is made of two basic constituents, fibres and resin. The fibres provide strength and stiffness, whereas the matrix provides a continuous medium that binds the fibres. The damage tolerance of any given composite system is dependent on material aspects such as fibre architecture, surface treatment, matrix type, lay-up and fibre volume fraction as described in Chapter 1. The specimens investigated on this study were fabricated from T700 carbon fibres in low viscosity LTM-45EL epoxy resin, supplied in the form of unidirectional (UD) prepreg. The ply thickness was determined as 0.128 mm and the nominal volume fraction was about 60% as there was very little bled resin. The UD mechanical properties of this composite system were determined in [104] and are summarised in Table 2.1.1.

Table 2.1.1 Basic mechanical properties for T700/LTM-45EL

Property	Unit	Value	Property	Unit	Value
E_{11}	GPa	127	G_{12}	GPa	5.6
E_{22}	GPa	9.1	τ_{12}	MPa	66.3
σ_{11}	MPa	1032	$G_{13/23}$	GPa	5.3
σ_{22}	MPa	130	G_{IC}	J/m^2	265.9
ν_{12}	-	0.31	G_{IIC}	J/m^2	940

2.2 Lay-up and cure

Quasi-isotropic laminate panels of 16 and 32 plies were manufactured from T700/LTM45-EL UD prepreg. Lay-ups were $(-45°/0°/+45°/90°)_{2S}$ for 16-ply laminates and $(-45°/0°/+45°/90°)_{4S}$ for 32-ply laminates. The latter was the focus of this study. In the case of 150×100 mm panels intended for axial compression, the 90° plies were oriented to the loading direction as shown in Figure 2.2.1.

Individual plies were cut from the UD prepreg tape of 300 mm wide following the cutting plan shown in Figures 2.2.2(a-b) for 150×100 mm and for 300×300 mm panels (the latter was subsequently cut into four panels of 150×150 mm each), respectively. A frozen prepreg drum was removed from a freezer and hanged onto a roller at the end of a lay-up table, as shown in Figure 2.2.3. To cut individual plies, the prepreg tape was fed through a guillotine (Figure 2.2.3) and cut by either sliding the guillotine through the tape or using a sharp blade. Special care was required to get the correct ply orientation, in the case of 0 and 90 plies the guide of the guillotine was aligned perpendicular to the prepreg edge. In the case of ±45 plies, the cut path was first indicated with a marker on the prepreg and then it was aligned and secured to the guillotine using the marked line. When prepreg was left at room temperature for a while, it became tacky affecting the precision of cutting, in particular along the ±45 direction. Therefore, cutting was performed with the prepreg tapes in a frozen state just taken out of the freezer (where they were normally kept). All the cut plies were put back in the freezer and taken out one by one according to the stacking sequence. The plies were laid up on a lay-up table in Figure 2.2.3. The table surface was mounted by a glass, which provided a smooth and clean surface to lay the plies on. In a corner it had a mounted steel square angle, as a reference for alignment of plies. To start the process, the first ply was located with two edges aligned with the square angle, with the top protective paper peeled off, exposing resin and fibres. Then the second ply with its bottom protective paper peeled off was placed on top with the respective orientation. The same process was repeated for the rest of the plies until the whole laminate was laid up. If the specimen was intended to contain artificial delamination(s) as precondition, these delaminations were inserted during this lay-up process, with details given in Section 2.3.

43

The laminate stack was then placed into the autoclave, in between layers of porous Teflon, bleeder, bagging film and breathe fabric, respectively. Figure 2.2.4 shows the usual autoclave set-up for laminate curing. The closest layer to the laminate is the porous Teflon peel ply. During the laminate consolidation it allows a controlled amount of resin to flow out of the specimen. The second layer is the fabric bleeder that absorbs the bleeding resin and could be either Nylon or glass fabric. The resin absorption is uniform in both sides throughout the specimen area, giving a constant uniform thickness. The third layer is the bagging film and its function is to keep the resin away from the caul plate and from the autoclave structure. The caul plate is placed between the third and the forth layers to distribute the applied pressure uniformly. The fourth layer is the breathe fabric, which allows air to flow out of the laminate and smoothes any sharp edge from the laminate curing fixture, avoiding piercing of the vacuum chamber. All these materials are wrapped with a sheet of a bagging film, which is held in between silicon seals to ensure a vacuum environment. All the panels were cured in an autoclave with the manufacturer's recommended curing cycle of 18 hours at 60°C at 80 psi, at an initial ramp rate of 2°C/min. The curing cycle is shown in Figure 2.2.5. The average thickness of these panels after curing was 2.048 mm for 16-ply laminates or 4.096 mm for 32-ply laminates (0.128 per ply).

2.3 Introduction of artificial delamination

As identified in Chapter 3, the main damage mechanisms are matrix cracks, internal delaminations and fibre breakage in addition to local change of geometry in the impact area. Due to the complexity of impact damage, the study of individual parameters was done using preconditioned panels with artificial delaminations [104]. In the present study additional panels are prepared with artificial delaminations, local change of curvature and open holes.

Internal delaminations are considered as the main factor in the degradation of compressive properties (Chapter 1, 4-6). The main characteristics of impact-induced delamination are size, shape, orientation, number and through-the-thickness (TTT) distribution. This was implemented as illustrated in Table 2.3.1 and Figure 2.3.1. The

delamination shape was either circular or elliptical, with size ranging from 10% to 60% of panel width. The ellipse orientation was either in the loading or in the transverse direction, keeping an aspect ratio of 3:1 for all the sizes tested. Two TTT locations were considered, middle-section and quarter-section as illustrated in Figure 2.3.1. They were embedded at 5th-6th, 8th-9th and 11th-12th ply interfaces in 16-ply laminates and at 10th-11th, 16th-17th and 22nd-23rd ply interfaces in 32-ply laminates for a symmetric arrangement. For an asymmetric arrangement they were embedded at 4th-5th, 10th-11th and 16th-17th ply interfaces in 32-ply laminates. Thus all the sub-laminates in the delaminated section in either arrangement were asymmetric.

Table 2.3.1 List of specimens with artificial delamination

Panel thickness	Delamination number	Location TTT		Circular delamination	Elliptical delamination	
		Description	Plies		Horizontal	Vertical
2 mm (16 plies)[a]	1	Symmetric	8/9	*CR10, CR20, CR40, CR60*	*EH10, EH20, EH40, EH60*	*EV10, EV20, EV40, EV60*
	3	Symmetric	5/6, 8/9, 11/12	*CR20x3S*	*EH40x3S*	-
4 mm (32 plies)	1	Middle Section	16/17	*C20MS, C40MS, C60MS*	*4EH10, 4EH20, 4EH40, 4EH60*	-
		Quarter Location	8/9	*C20QS, C40QS, C60QS*	-	-
	3	Symmetric	10/11, 16/17, 22/23	*C20x3S, C40x3S, C60x3S*	-	-
		Asymmetric	4/5, 10/11, 16/17	*C20x3AS, C40x3AS, C60x3AS*	-	-

[a] Results from 2-mm thick panels were taken from [104], except CR20x3S and EH40x3S

The delamination characteristics were simulated by embedding 0.051-mm thick thermoplastic fluonnate ethylene propylene (FEP) films. The aims of using these delaminations were to simulate internal delaminations without involving fibre and matrix fractures. To embed an artificial delamination into the laminated, firstly a steel template was placed on a large piece of a FEP film. The inclusions of selected size and shape were cut by pressing the steel templates into the FEP film sheet. Once the right quantity of insertions was cut out of the film, they were inserted in the designated TTT locations during the lay-up process. The relative in-plane locations of these artificial delaminations within the panel were estimated with respect to the reference corner on

the lay-up table. After laying up all the plies and insertions, the resulting laminate had the internal delaminations properly centred and oriented and the panel was ready for curing. Once the panels were cured, they were C-Scanned. The trimming of the panels' edges was carried out with respect to the centres revealed by the C-Scanning, as described in Section 2.5.1.

2.4 Introduction of local curvature

In Chapter 3 it is well established that the panels subjected to transverse loading experienced local indentation in the impacted area along with other damage mechanisms. As an attempt to simulate this geometrical change caused by impact separately from the material damages, curved bumps were introduced into flat panels. The bump shape was assumed to be hemispherical dome for simplicity.

2.4.1 Mould design and fabrication

The description of local hemispherical bumps requires two parameters, surface curvature and dent depth. Thus, two different ways can be used to achieve different bump sizes. One is that dent depths were altered while a constant radius of curvature was maintained. The other varied curvatures while the dent depth was kept as a constant. As a result, two sets of moulds were made for fabricating the corresponding panels. For the moulds with the constant dent depths three different curvatures were used; on the other hand for the constant curvatures three different dent depths were used as shown in Table 2.4.1. Figure 2.4.1 shows the technical drawings of the five pairs of female and male moulds with the correspondent panel identification. A finished set of moulds (male and female) corresponding to the panel CD60CC, are shown in Figure 2.4.2. This mould could be closed during cure with the guidance of a pair of alignment pins located at the top of each panel end. These pins allowed only vertical movement so that the mould closing and laminate shaping were guaranteed. Nevertheless, the introduction of the hemispherical domes implied that some of the fibres within the plies could be shortened in length. Constant fibre length is absolutely crucial for in-plane compression, since all the plies should undergo the same applied load. Therefore the moulds were built with 4 mm excess in length (154×100 mm) so that the length of each

46

individual ply had to be increased from 150 to 154 mm. Consequently the final length of about 150 mm was ensured in all the panels with the bumps. The addition of 4 mm in length to each ply was made without any major alteration of the cutting plan shown in Figure 2.2.2(a).

Table 2.4.1 Dome dimensions (referenced to the mid-plane TTT)

Mould [a]	Panel identification [b]	Dome diameter mm	Dome dent depth mm	Dome radius of curvature mm	Type of approach Constant/
1 [a]	CD20	20.32	0.80	64.90	Curvature-Depth
2	CD40CC	40.62	3.26	64.90	Curvature
3	CD60CC	61.02	7.62	64.90	Curvature
4	CD40CD	40.16	0.80	252.40	Depth
5	CD40CD	60.11	0.80	564.90	Depth

[a] Reference panel
[b] CC and CD at the end of the panel identification stand for constant curvature and constant depth respectively

The moulds were manufactured using a numerically controlled lathe. For this purpose, rectangular steel plates of 9.5 mm and 12 mm (in the case of CD60CC) thickness were held by the chuck jaws of the lathe with the rotation axis perpendicular to the plate and coinciding with the bump centre. Once the bumps were machined, the rectangular plates were cut down to the required in-plane dimensions leaving a small additional area to allocate the alignment pins, as shown in Figure 2.4.1.

2.4.2 Cure cycle adjustment

The presence of steel moulds of 10 mm thick within the autoclave could affect the curing cycle. The curing cycle was thus modified slightly according to the time taken by the mould to reach 60°C. This time was estimated in two different ways, analytically and experimentally.

The analytical heat transfer modelling of the autoclave was based on the assumption of the transient or unsteady state applied to an infinite wall [105], which as illustrated in Figure 2.4.3. The large thermal resistance of the autoclave structure justifies this approach.

The determination of the thermal resistance is based on the simplification of the autoclave structure as indicated in Figure 2.4.4. Heat conduction in steady state between any point 1 and 2 is defined by

$$q = \frac{kA}{L}(T_1 - T_2)$$

(2.3.3)

where q is the heat transfer rate, k is the thermal conductivity, A is the area perpendicular to the heat flux vector, L is the distance between locations 1 and 2 and T_1 and T_2 are temperatures at locations 1 and 2 respectively. The thermal resistance can be defined as the inverse of the thermal conductivity by

$$\frac{1}{R_{1,2}} = \frac{kA}{L}$$

(2.3.4)

The overall thermal resistance for the autoclave can be worked out by adding up the resistance of each individual component, as shown in Figure 2.4.4. For the entire autoclave it yields

$$\sum R = \frac{1}{A}\left(\frac{L_{\text{mould 1}}}{k_{\text{steel}}} + \frac{L_{\text{panel}}}{k_{\text{composite}}} + \frac{L_{\text{mould 2}}}{k_{\text{steel}}} + \frac{L_{\text{breathe fabric}}}{k_{\text{breathe fabric}}} + \frac{L_{\text{air gap}}}{k_{\text{air gap}}} + \frac{L_{\text{alumiminium}}}{k_{\text{alumiminium}}} \right)$$

(2.3.5a)

Substituting the correspondent values of thermal conductivity k and length L in the above gives

$$\sum R = \frac{1}{A}\left(\frac{0.0095}{60.5} + \frac{0.004}{0.87} + \frac{0.0095}{60.5} + \frac{0.002}{0.033} + \frac{0.017}{0.028} + \frac{0.04}{237} \right) \text{ W/K}$$

(2.3.5b)

$$\sum R = \frac{1}{A} 0.67283 \text{ W/K}$$

(2.3.5c)

This thermal resistance is equivalent to a steel wall of 40.697 m thickness, as shown by replacing Eq. (2.3.5c) into Eq. (2.3.4) and solving for the length L

$$L = \frac{k_{steel} \times A}{A} 0.67283 = 60.5 \times 0.67283 = 40.697 \quad \text{m} \tag{2.3.6}$$

Therefore, the infinite wall assumption of the transient analysis is justified, since the autoclave has the thermal resistance of a very large wall made of steel. Steel was the selected material because it is the material of the mould in contact with the laminate.

The first step in the infinite wall analysis was to define the boundary conditions. The temperature distribution T is a function of the time t and the position x, which refers to the spatial coordinate. If the base is assumed to have x-coordinate $x = 0$ and the upper surface of the mould is located at $x = 9.5$ mm, then the initial conditions at $t = 0$ are described by:

$$\begin{aligned}
T(base,t) &= T(0,0) = T_s = 60^\circ C = 333.15K \\
T(mould,t) &= T(9.5mm,0) = T_i = 20^\circ C = 293.15K
\end{aligned} \tag{2.3.1}$$

Infinite wall transient analysis [105] has established

$$\frac{T(x,t) - T_s}{T_i - T_s} = erf\left(\frac{x}{2\sqrt{\alpha \times t}}\right) \tag{2.3.2}$$

where $T(x,t)$ is the temperature of the mould, T_s it the temperature on the heating surface (60 C), T_i is the initial temperature of the mould, x is the location of the mould within the autoclave (9.5mm), α is the thermal diffusivity of the steel (17.7×10^{-6} m²/s) and t is the unknown time that takes the mould to get to the temperature $T(x,t)$. Values for the Gaussian error function erf can be found tabulated in many text books. In Figure 2.4.5 the mould temperature is plotted against time, using the Eq. (2.3.6). It can be seen that the additional time needed for the bump shaping mould to reach 60±1°C is 3000 seconds, i.e. 50 minutes.

On the other hand, an experiment was carried out to measure the time taken for the mould to reach 60°C with a J-type thermocouple. A steel mould at room temperature

(23°C) was placed on top of the platen of a hot press, which was already heated up to 60°C. The time needed for the mould to reach 60±1°C was 1000 seconds, i.e. 16 minutes. The correspondent results are plotted in Figure 2.4.5. Clearly the experimental result is only one-third of the analytical estimation. In order to be on the safe side, the longer period of 50 minutes was selected and was added to the heating-up period in the curing cycle. As a result, the ramp rate was reduced from 2°C/min to 0.57°C/min. Figure 2.4.6 shows both previous and new curing processes diagrams.

2.5 Panel preparation and strain gauging

After cure, panels were prepared for testing. In the case of panels intended for transverse loading, preparation included trimming, measurement and strain gauging. The preparation of in-plane compression panels included C-Scan, trimming, end-potting, machining, measuring and strain gauging.

2.5.1 Inspection of preconditions and trimming

For in-plane compression panels with embedded artificial delamination, the centre of its embedded delamination must be located in order to allow subsequent trimming to be carried out properly. Such inspection was carried out by using ultrasonic C-scan. Panels with either impact damage or quasi-static damage, C-scan was carried out as a routine. A subsequent trimming down to 150×100 mm was guided by the marked centre of the embedded delamination revealed by the scanning. Figure 2.5.1 shows a typical C-scanning image of a panel with circular delamination, used for the determination of the centre of delamination. The panels were trimmed down using a diamond coated wheel trimmer as shown in Figure 2.5.2. The trimming table had a couple of adjustable steel guides to position the panel respect to the cutting wheel, ensuring in this way the precision of the cut in terms of edge straightness and perpendicularity between adjacent sides of the panel. The first guide determined the parallel distance from the cutting wheel to the panel edge. The second guide was in permanent square angle with the first guide and was able to slide up and down, pushing the panel against the cutting wheel. The steel wheel was water cooled to avoid any thermal damage to the specimens.

2.5.2 End potting and machining

The aim of machining the panel ends was to enable a uniform longitudinal compressive loading to be applied to the panels. Both far and loading ends of each panel were first potted in a mixture of epoxy and aluminium slate powder, following the formulation shown in Table 2.5.1. The mass formulation indicated is based on a total of 175 g which is around 3 times the amount required for one mould, thus the correspondent quantities were worked out for one single mould. The ingredients were mixed in a disposable container and then poured into a wooden mould as shown in Figure 2.5.3. The mould was previously sprayed with release agent. Each panel was introduced into the liquid resin and clamped to restrain any possible movement during the resin curing. Resin was cured in 36 hours at room temperature and the process was repeated for the other end of the panel. Once both ends were potted with epoxy resin, the ends were machined flat and parallel to each other.

Table 2.5.1 Epoxy formulation for potting ends

Ingredient	Density	Mass formulation	Volume formulation	Mass 1 mould	Volume 1 mould
	g/cm^3	g	cm^3	g	cm^3
Araldite CY 219	1.175	100	85.11	32.19	27.40
Hardener HY 219	1.150	50	43.48	16.10	14.00
Accelerator DY 219	1.250	5	4.00	1.61	1.29
Slate powder (toughener)	2.800	20	7.14	6.44	2.30
TOTAL	1.252	175	139.73	56.33	44.98

2.5.3 Open holes

Drilling a hole at the centre of panels intended to introduce only material damage by a complete material removal. The panels with open holes were expected to provide a low bound of compressive strength when compared to panels with other preconditions. For each panel, a central hole was ground using diamond-coated core drills of respective hole diameters. Each panel was clamped and fully supported on the opposite side with a wooden block, to avoid transverse deflection and surface damage at the exit of the drill. The hole diameters drilled in 4 mm thick panels were 20, 40 and 60 mm. These hole sizes were selected in order to compare their effects with other preconditions of similar

size. An additional feature was studied with the open hole specimens, the effect of system change on the RCS of damaged panels. Thus, in addition to the usual T700/LTM45-EL system, panels made of T300/LTM45-EL were also tested. The T300 fibres have a lower axial strength and stiffness than T700 fibres.

2.5.4 Strain gauging

The strain readings provided a useful insight into the mechanical behaviour, in particular if they are monitored in the back-to-back configuration. The most common way of strain monitoring was to use strain resistance gauges connected in a Wheatstone bridge circuit. Once the panel has been prepared, the three main dimensions, length, width and thickness were systematically measured every 25 mm along the four edges, using a digital calliper. The results from these measurements are listed in Appendix A. These measurements allowed a precise position marking of the strain gauges on both front and back faces of each panel. The selected locations for strain monitoring are shown in Figure 2.5.4-2.5.7, for both transverse load and in-plane compression of preconditioned panels respectively. In the case of transverse loading, in Figure 2.5.4, a strain gauge was bonded on the bottom centre of the panel to monitor the maximum tensile strain. Similarly one additional gauge was bonded on the top side to monitor compressive strain. Due to the presence of the indenter, it was located 20 mm away from the panel centre. Both gauges were oriented along the fibres of the surface plies.

For in-plane compression of preconditioned panels (except for panels with open hole), five pairs of strain gauges were located as shown in Figure 2.5.5. The locations were identified by letters A, B, C, D, and E. The strain gauge pair at location A was bonded on a far-field location (front/back) at 25 mm away from the far-end, to monitor the global panel response to compressive loading. Those at D/E and B/C (longitudinal/transverse) locations on the mid-section were intended to monitor local behaviour associated with embedded delamination(s), at the centre and at the defect edge respectively. For panels with impact damage and transverse quasi-static load damage, central locations D/E were skipped when the dent left by the impactor interfered with strain gauging. Also the edge-of-defect locations B/C were skipped when the internal delamination border reached the lateral edge of the panel.

In the case of panels with open holes the far-field strain was monitored at location A. Additional to this, strains at the hole wall were recorded using two gauges bonded in the TTT direction on the open hole wall. One gauge was on the longitudinal axisymmetric line, whereas the other one was on the mid-section transverse line, both in the TTT direction, as shown in Figure 2.5.6. This exercise was intended to pick up the effect of strain concentration in the transverse direction due to the presence of the open hole.

In the case of in-plane compression of intact panels the lack of preconditions made them appealing for monitoring additional effects, mainly panel stability and Poisson's ratio effect. Consequently different strain gauge locations were used, as shown in Figure 2.5.7.

Prior to bonding strain gauges, the panel surface at the marked locations was prepared to allow a good quality adhesion between strain gauges and the laminate skins. Firstly, the surface was slightly smoothed using a wet-and-dry paper, without affecting any fibre. Then any contaminant was removed by using a paper towel impregnated with acetone. Secondly, the top side of a strain gauge was stuck to a piece of Sellotape, to facilitate handling. Then, the strain gauge was placed at the respective location aligning the four arrow-shape indicators with the previously drawn marks on the panel. These indicators are shown in Figure 2.5.8. To avoid any contact between the terminals and the laminate, a piece of non-sticky paper (supplied with the strain gauge) was placed under the electrical wires. Thirdly after the strain gauge was positioned, a drop of CN glue was applied onto its back surface. After this, gentle pressure was applied while the glue was curing to remove any air trapped between the strain gauge and the panel. However, an excessive amount of pressure could induce unwanted residual strain in the gauge; therefore it was important to press on the Sellotape gently. Finally, after 5 minutes the Sellotape and the non-sticky paper were removed, leaving the gauge ready to be connected.

The strain gauge connection to wiring was ideally arranged via terminals. A copper terminal was bonded right underneath the strain gauge, as shown in Figure 2.5.8. Then, the electric wires of about 1 m long and the strain gauge leads were both soldered to the

terminals, as indicated in Figure 2.5.8. Subsequently, the electrical resistance of the strain gauges was checked to be around 120Ω. A significantly different reading could indicate a faulty connection. After checking the connections, each pair of wires was labelled with the strain gauge location and the intended channel number in the data logger, as shown in Table 2.5.2.

Table 2.5.2 Strain gauge terminals labelling and numbering for in-plane compression of preconditioned panels

Gauge	Location	Orientation	Side	Terminals numbering		SG type
A	Far field	Longitudinal	Front	1	2	Single
A	Far field	Longitudinal	Rear	3	4	Single
B	Delam. side	Longitudinal	Front	5	6	Rosette
B	Delam. side	Longitudinal	Rear	7	8	Rosette
C	Delam. side	Transverse	Front	9	10	Rosette
C	Delam. side	Transverse	Rear	11	12	Rosette
D	Centre	Longitudinal	Front	13	14	Rosette
D	Centre	Longitudinal	Rear	15	16	Rosette
E	Centre	Transverse	Front	21	22	Rosette
E	Centre	Transverse	Rear	23	24	Rosette
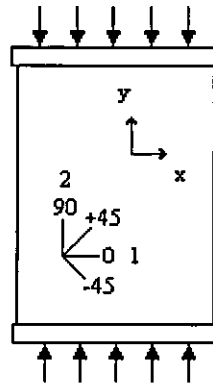
Figure 2.2.1 Load and material co-ordinate systems
with respect to panel geometry

(a)

55

90

0

300

300

300

1200

300

300

300

1061

+45

-45

1273

(b)
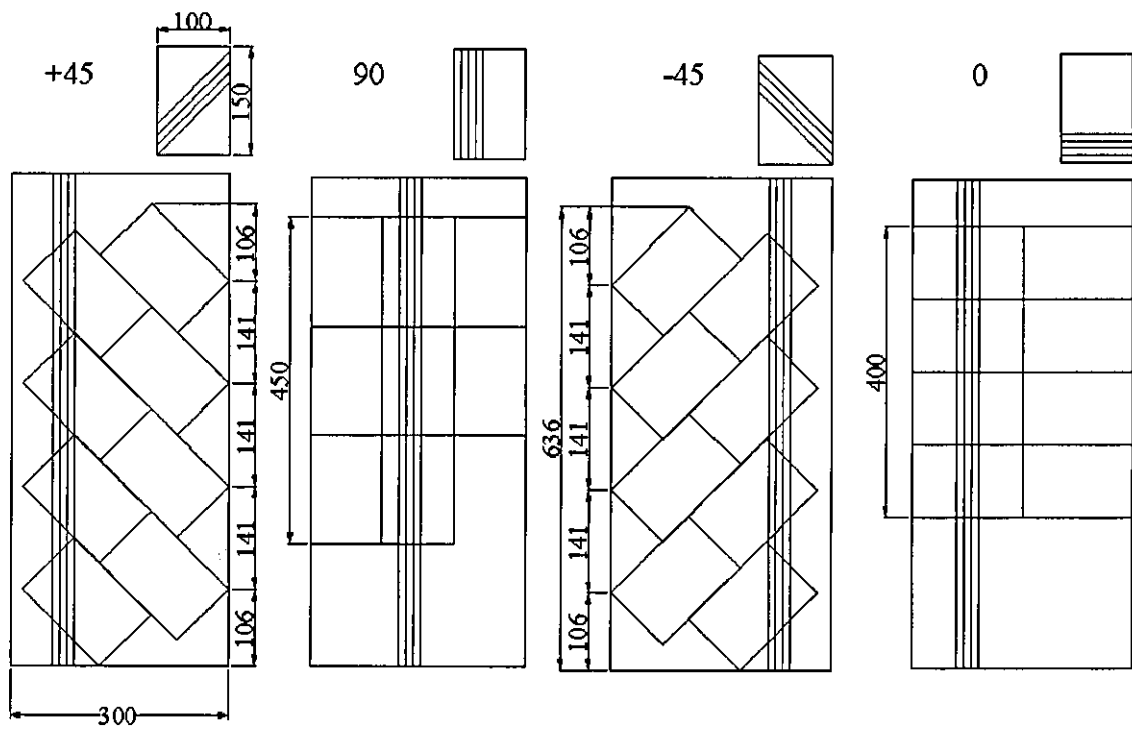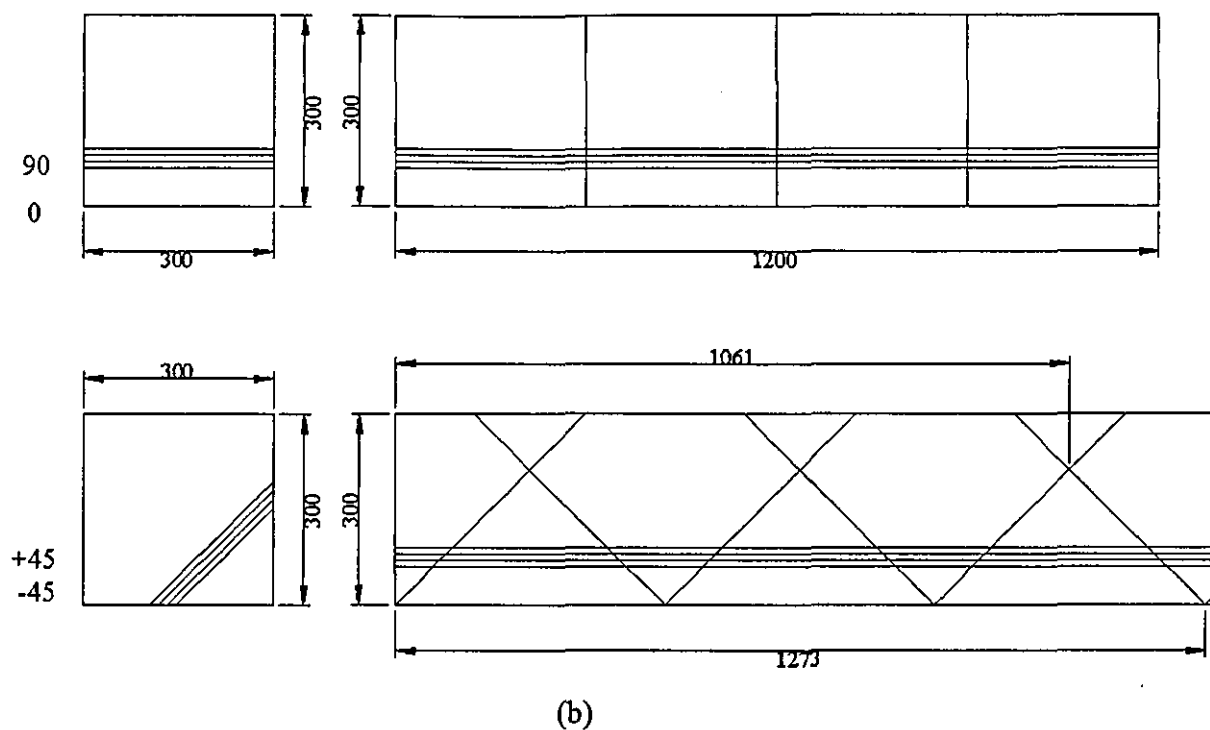
Figure 2.2.2 Cutting plan of (a) 150 by 100-mm and (b) 300 by 300-mm panels, (all the dimensions are in mm). Fibre orientation in the prepreg and in the plies is shown with four straight lines
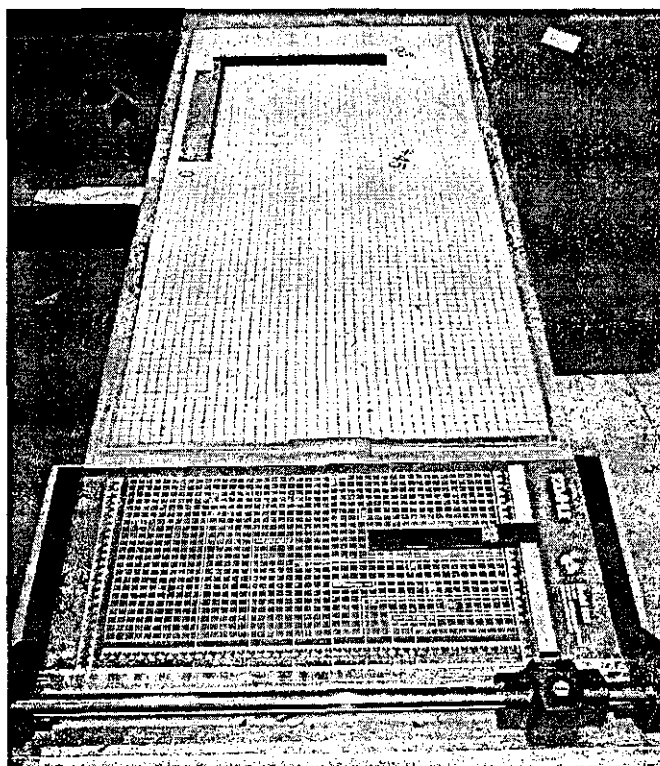
Figure 2.2.3 Lay-up table (upper part) and guillotine (bottom part)
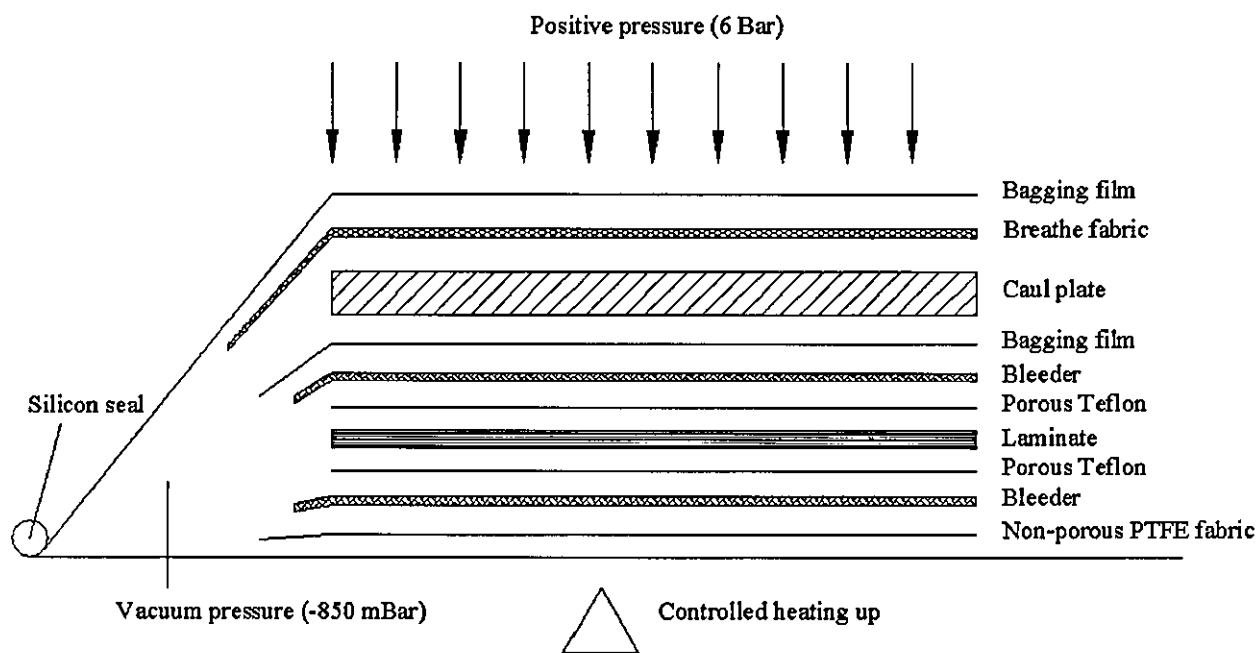
Figure 2.2.4 Autoclave curing set-up
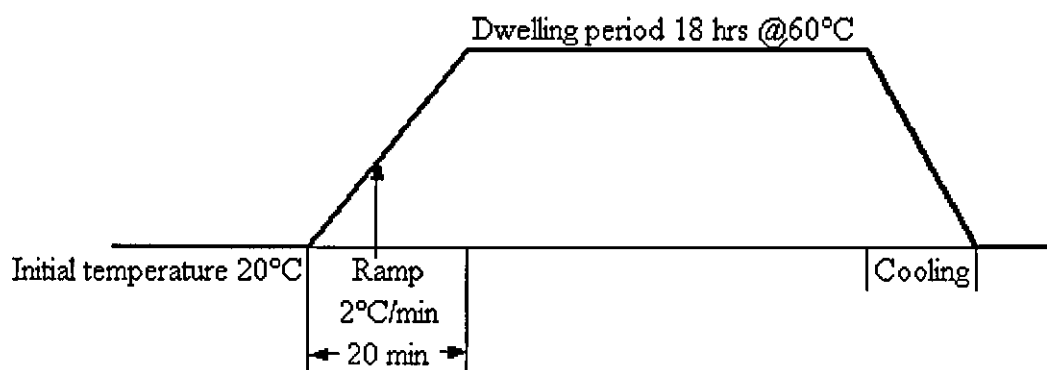
Figure 2.2.5 Autoclave curing cycle

Ply number	Ply orientation	Delamination distribution				Ply number	Ply orientation	Distribution	
		Asymmetrical		Symmetrical				Symmetrical	
		Single	Mulitple	Single	Multiple			Single	Multiple
1	-45	*FRONT SIDE*							
2	0								
3	+45								
4	90	←							
5	-45								
6	0								
7	+45								
8	90	←							
9	-45						1	-45		
10	0		←		←		2	0		
11	+45						3	+45		
12	90						4	90		
13	-45						5	-45		←
14	0						6	0		
15	+45						7	+45		
16	90	←	←	←			8	90	←	←
17	90						9	90		
18	+45						10	+45		
19	0						11	0		←
20	-45						12	-45		
21	90						13	90		
22	+45				←		14	+45		
23	0						15	0		
24	-45						16	-45		
25	90									
26	+45									
27	0									
28	-45									
29	90									
30	+45									
31	0									
32	-45	*BACK SIDE*							

Figure 2.3.1 Through-the-thickness locations of single and multiple delaminations

Figure 2.4.1 Technical drawings of the five sets of moulds for bump introduction (next 5 pages)

R62.9

9.5

8.7

0.8

R66.9

9.5

0.85

8.65

154

Ø21.27

Ø20

100

Female mould

Male mould

Alignment holes

28.7

14.35

Ø6.35

MOULD 1		
Mould	female [mm]	male [mm]
Row Plate thickness:	9.5	9.5
Curvature radius:	66.90	62.90
Indentator depth:	0.85	0.8
Defect Diameter:	21.27	20.00

R62.9

R66.9

9.5

6.24

3.26

3.47

6.03

9.5

154

Ø42.54

Ø40

100

Alignment holes

28.7

14.35

Ø6.35
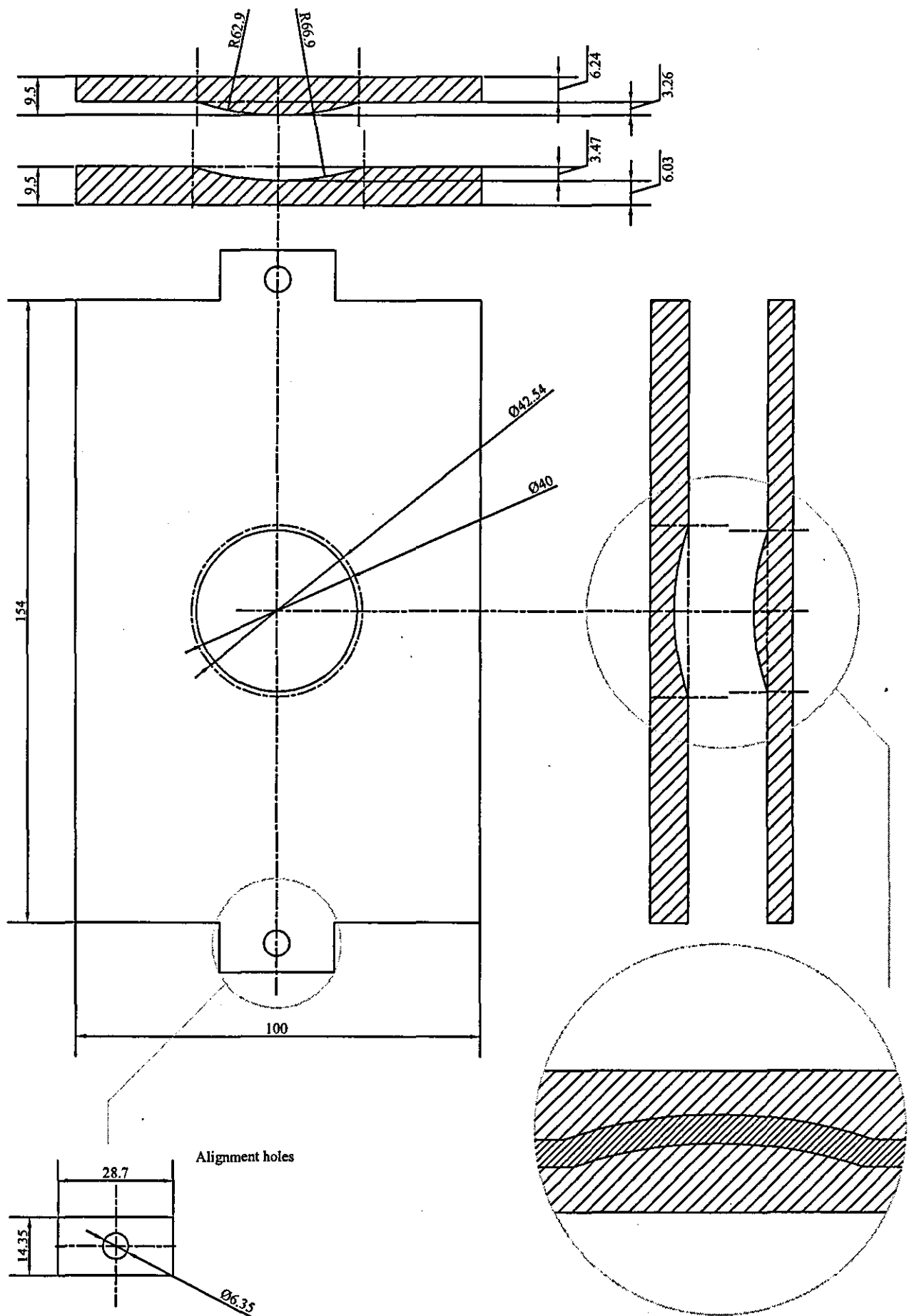
MOULD 2		
Mould	female [mm]	male [mm]
Row Plate thickness:	9.5	9.5
Curvature radius:	66.90	62.90
Indentator depth:	3.47	3.26
Defect Diameter:	42.54	40.00

Alignment holes

Ø6.35

Female mould
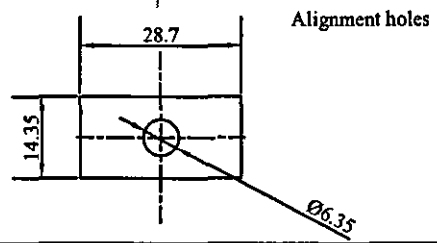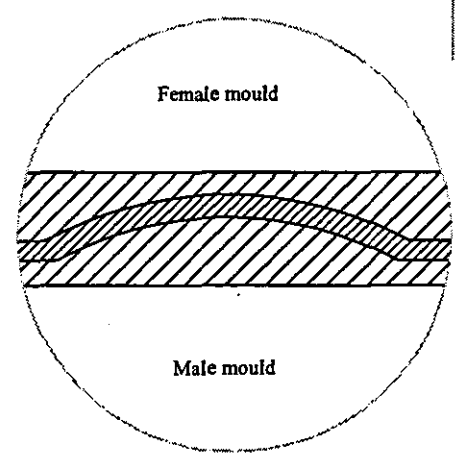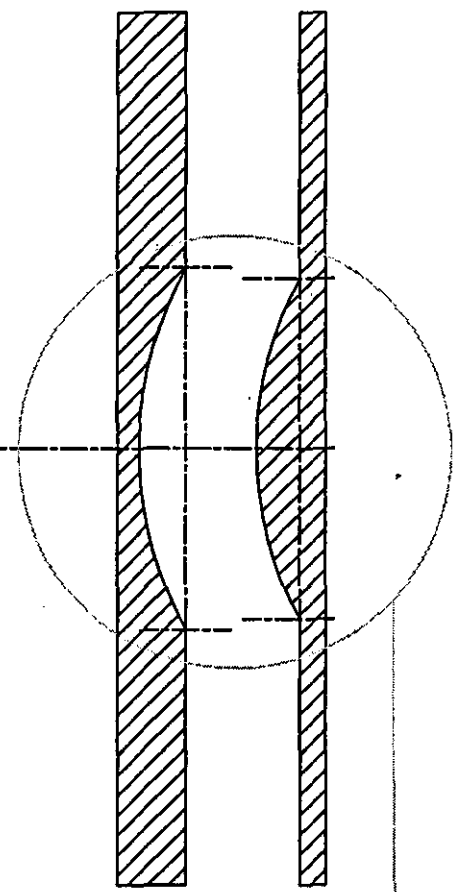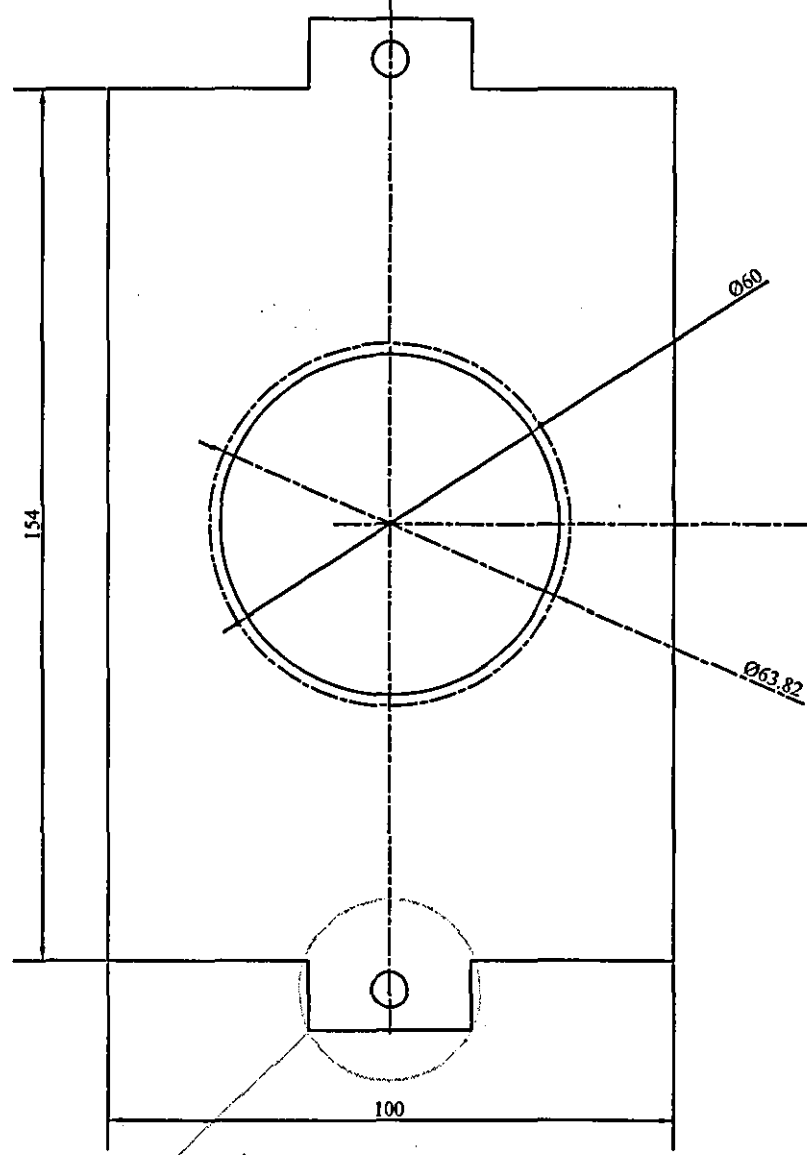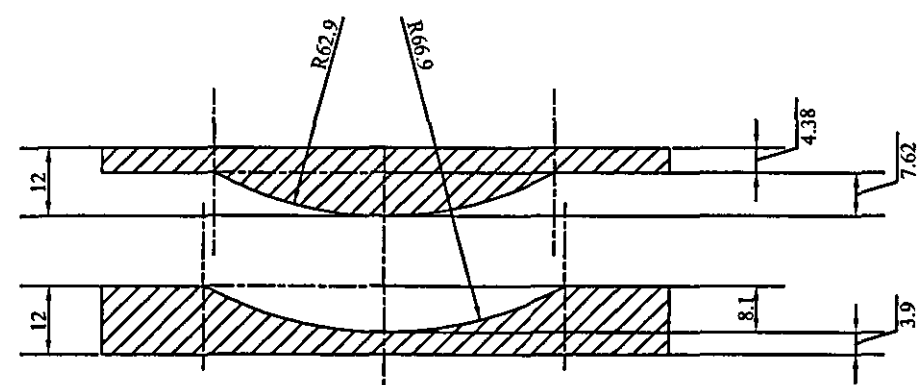
Male mould

JUGHBOROUGH
NIVERSITY
A.E Department

DRAWN BY: L. A. Rivera
Research Student
Materials and Structures

Dimensions in mm

MOULD 3		
Mould	female [mm]	male [mm]
Row Plate thickness:	12	12
Curvature radius:	66.90	62.90
Indentator depth:	8.1	7.62
Defect Diameter:	63.82	60.00

R250.4
R254.4

9.5
8.7
0.8

9.5
0.81
8.69

154
100

Ø40
Ø40.64

Alignment holes

28.7
14.35
Ø6.35

Female mould

Male mould

MOULD 4		
Mould	female [mm]	male [mm]
Row Plate thickness:	9.5	9.5
Curvature radius:	254.4	250.4
Indentator depth:	0.81	0.8
Defect Diameter:	40.64	40.00

R562.9

R566.9

9.5

8.7

0.8

9.5

0.81

8.69

Ø60

Ø60.43

154

100

Female mould

Male mould

Alignment holes

28.7

14.35

Ø6.35

MOULD 5		
Mould	female [mm]	male [mm]
Row Plate thickness:	9.5	9.5
Curvature radius:	566.9	562.9
Indentator depth:	0.81	0.8
Defect Diameter:	60.43	60.00
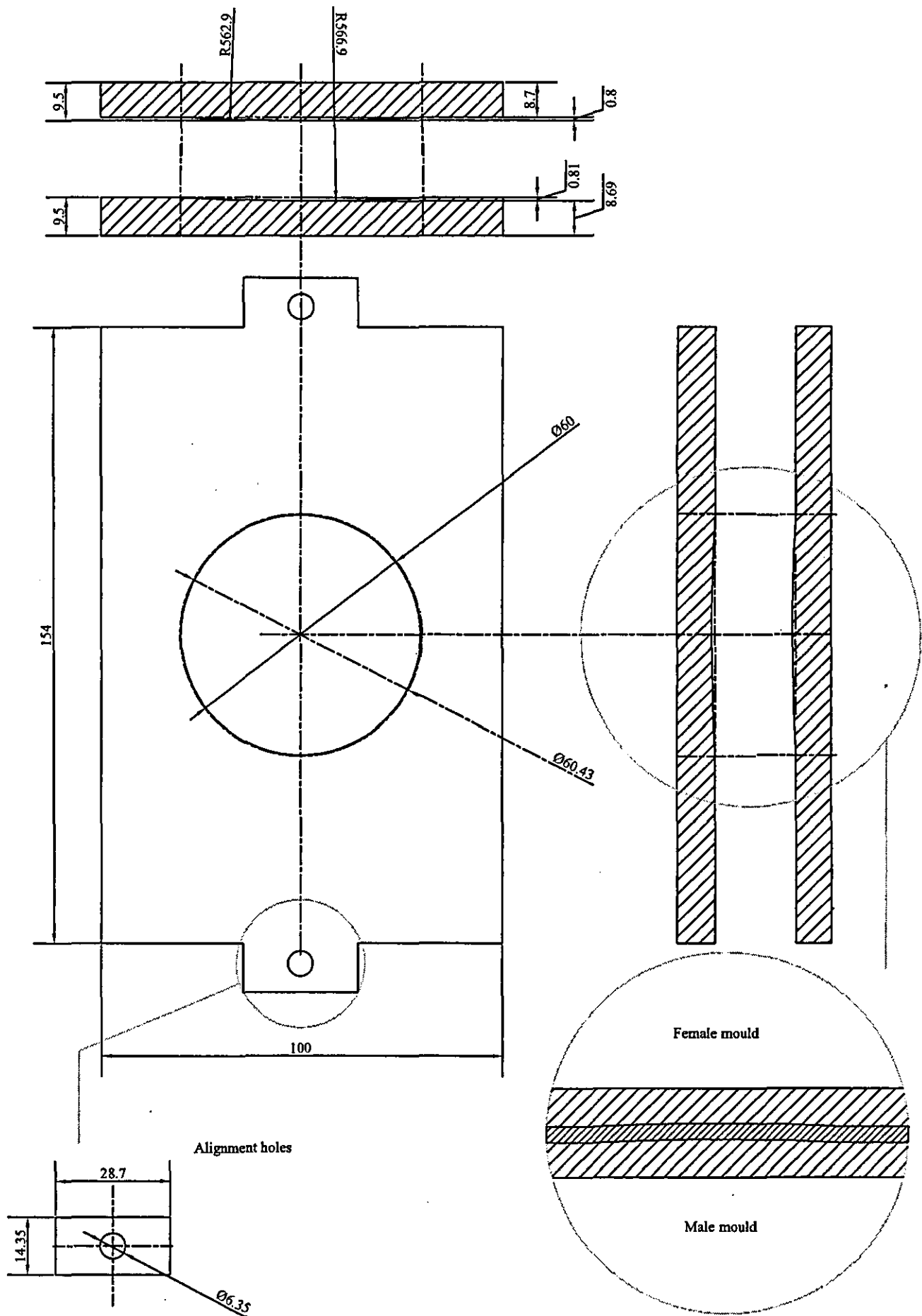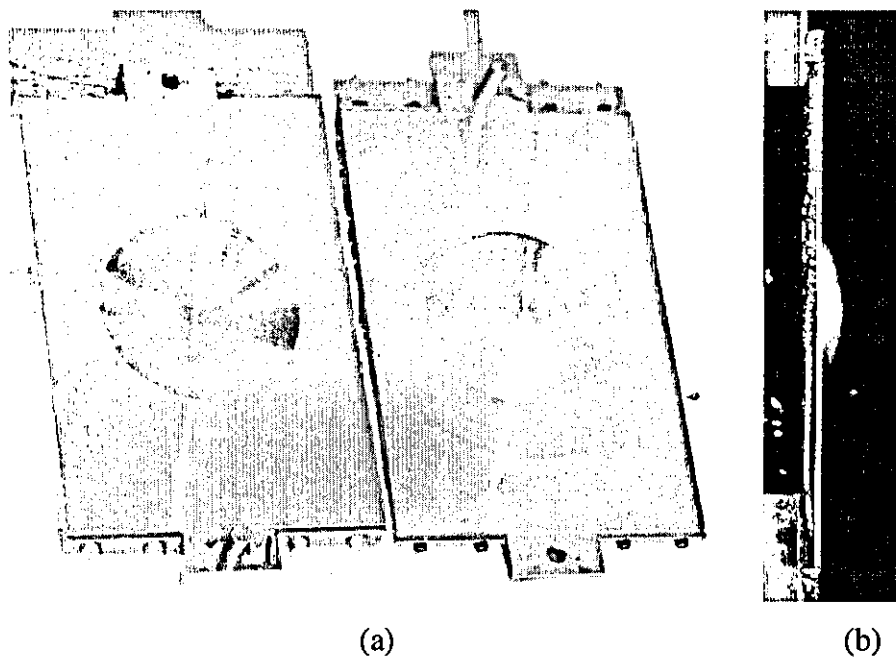
Figure 2.4.2 Photograph of a finished set of moulds, in (a) top view and (b) side view (male mould only), correspondent to the panel CD60CC
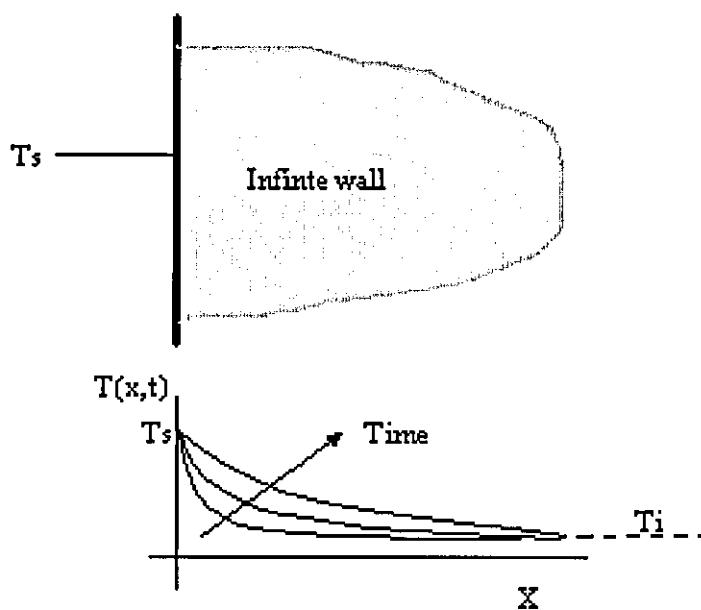
Figure 2.4.3 Temperature field on the infinite wall model for the heat transient analysis of the autoclave
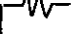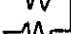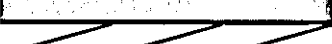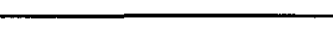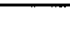
Description	Autoclave Diagram	Resistance approach	Material	Thermal conductivity W/(m-K)	Length L mm
Aluminum cover			Al	237	40
Air Gap			Air	2.80E-02	17
Breathe fabric			PET	0.033	2
Mould			Steel	60.5	9.5
Composite			C/E	0.87	4
Mould Base			Steel	60.5	9.5

Figure 2.4.4 Diagram of the theoretical approach inside autoclave
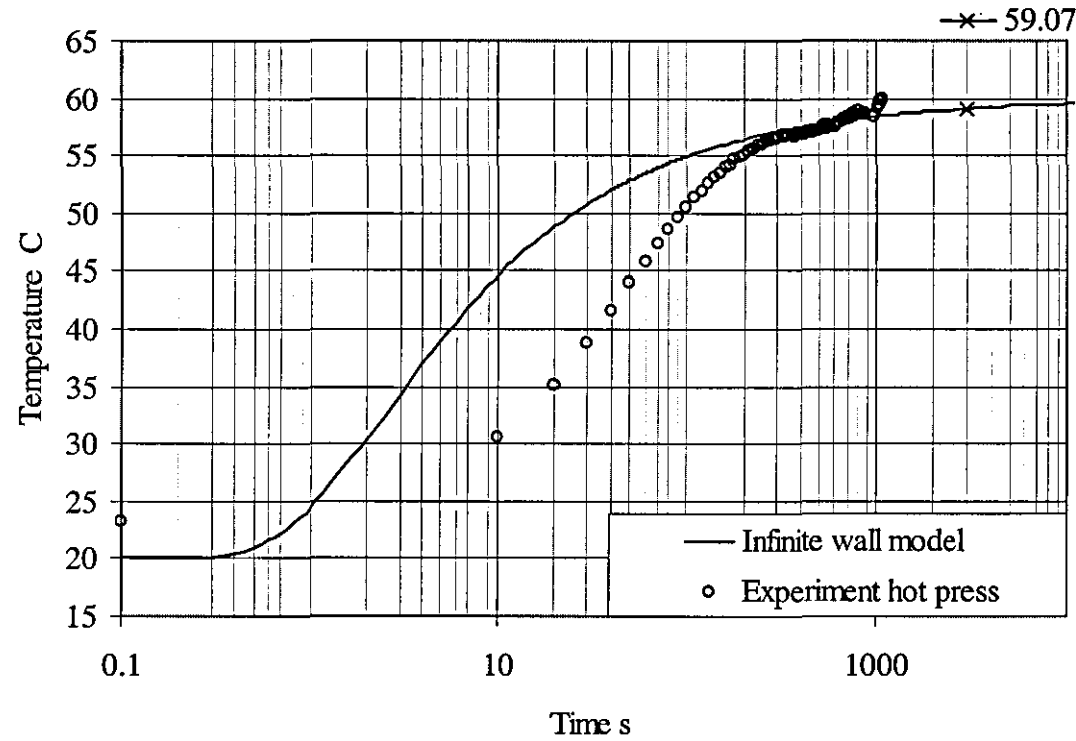
Figure 2.4.5 Transient heat transfer analysis for autoclave

Dwelling period 18 hrs @60°C

Initial temperature 20°C | Modified ramp | Usual ramp rate

0.57°C/min | 2°C/min

|← 50 min →|← 20 min →|

|← 70 min →|

Cooling
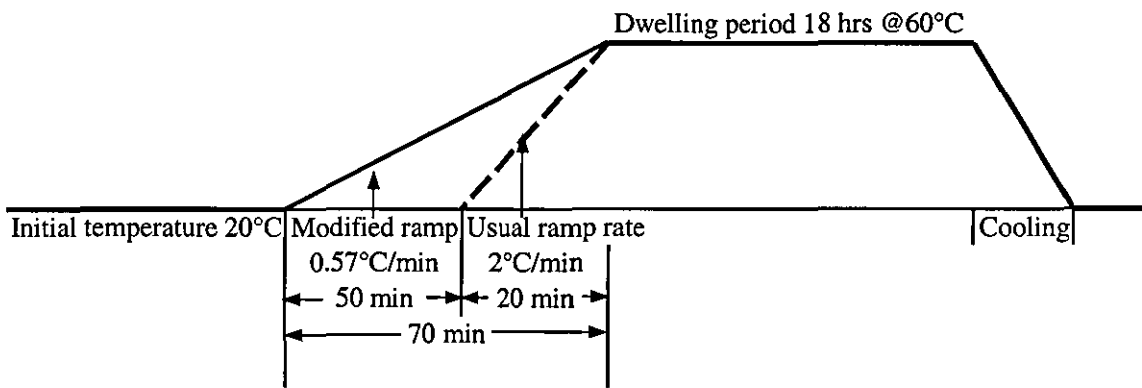
Figure 2.4.6 Curing process alteration due to the presence of steel moulds in the autoclave

0   20   40 mm
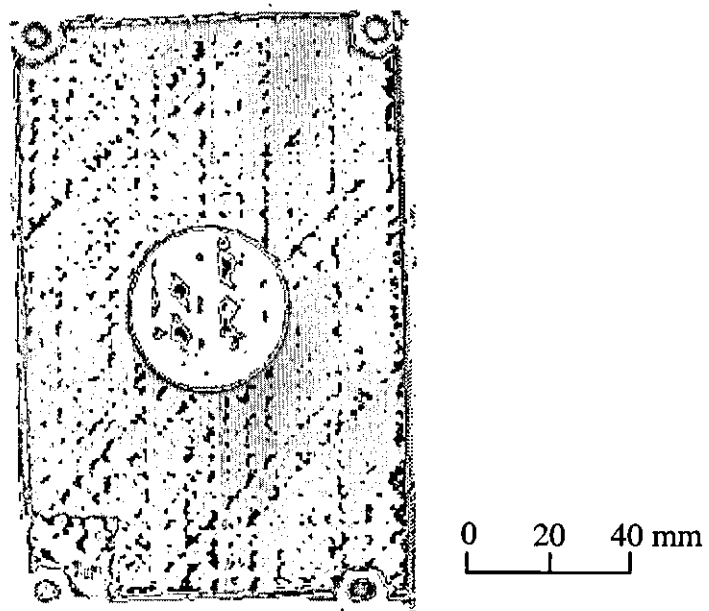
Figure 2.5.1 Typical C-scan image of a panel with artificial embedded delamination

66
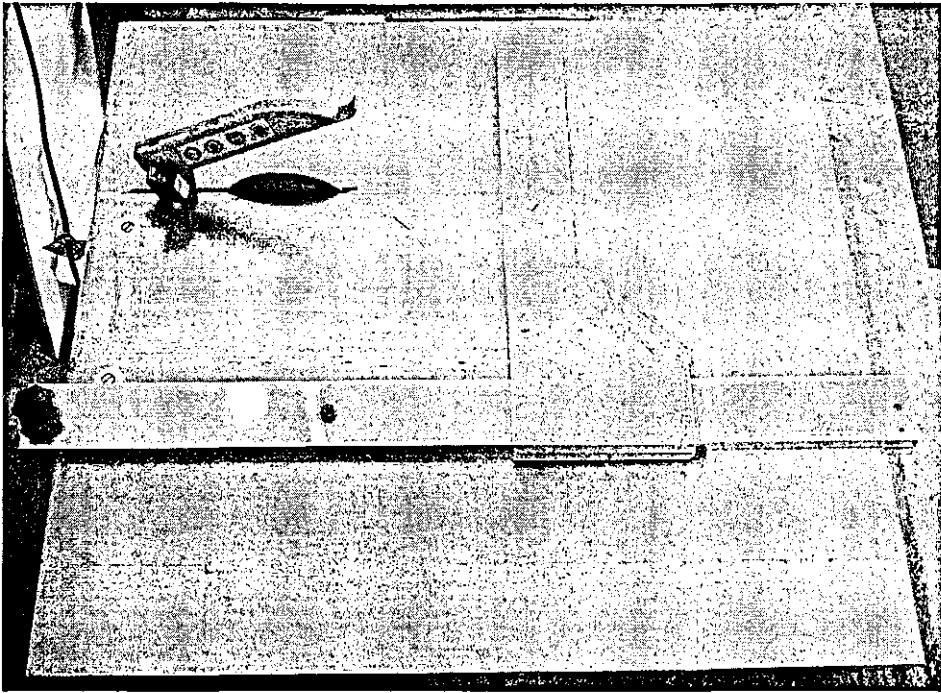
Figure 2.5.2 Diamond coated wheel trimmer and trimming table
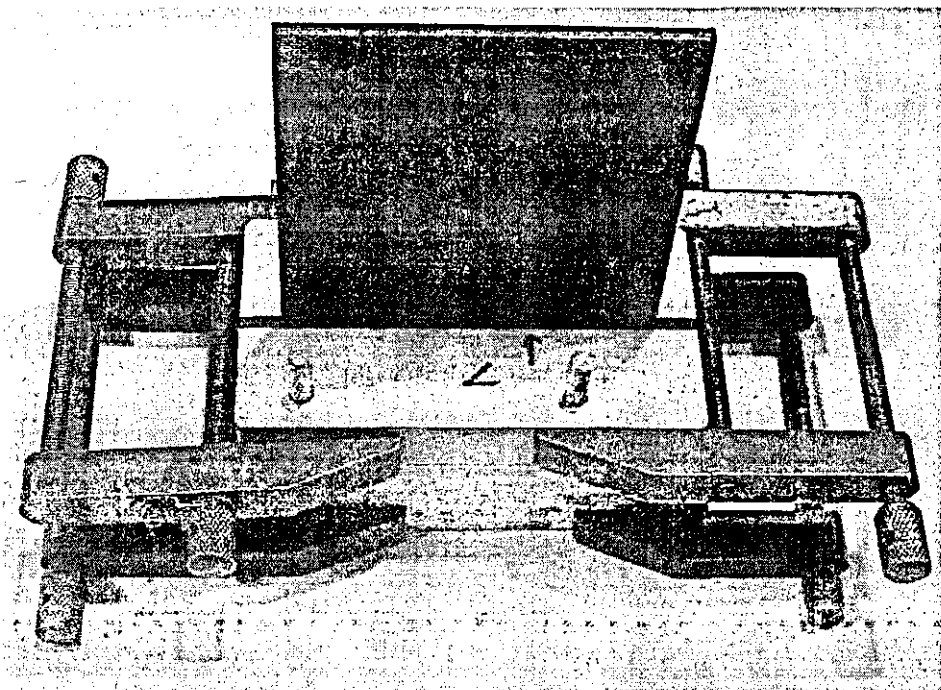
Figure 2.5.3 Photograph of a wooden mould for end potting
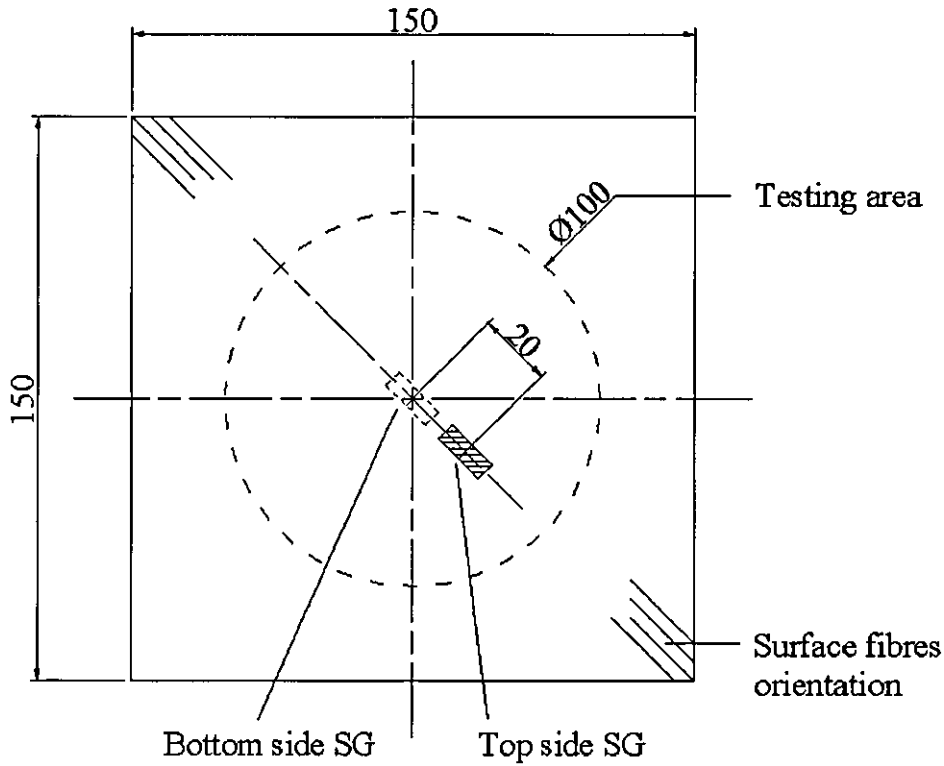
Figure 2.5.4 Specimen dimensions and strain gauge (SG) locations for transverse load. All dimensions are in mm
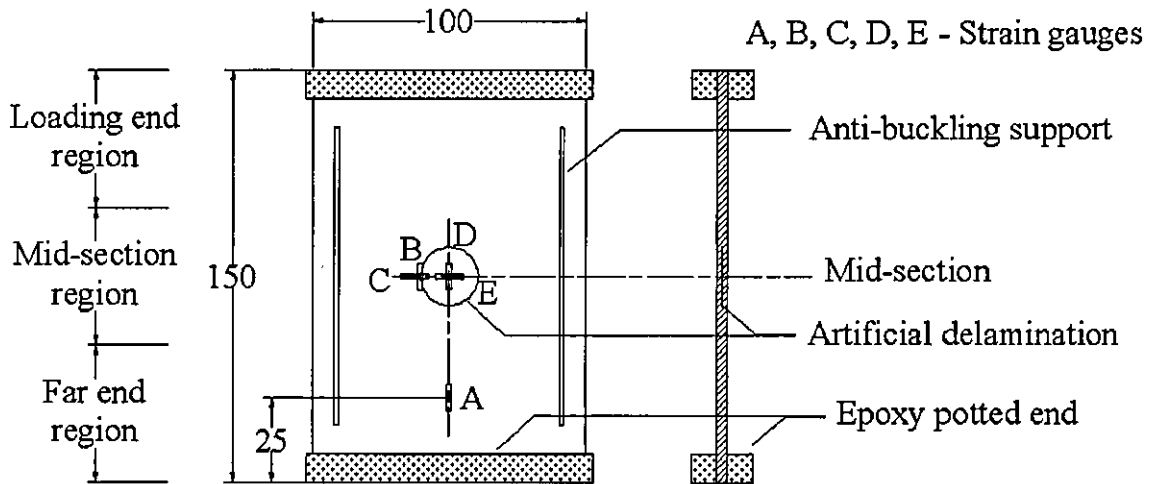
Figure 2.5.5 Preconditioned specimen dimensions and strain gauge locations for in-plane compression load. All dimensions are in mm
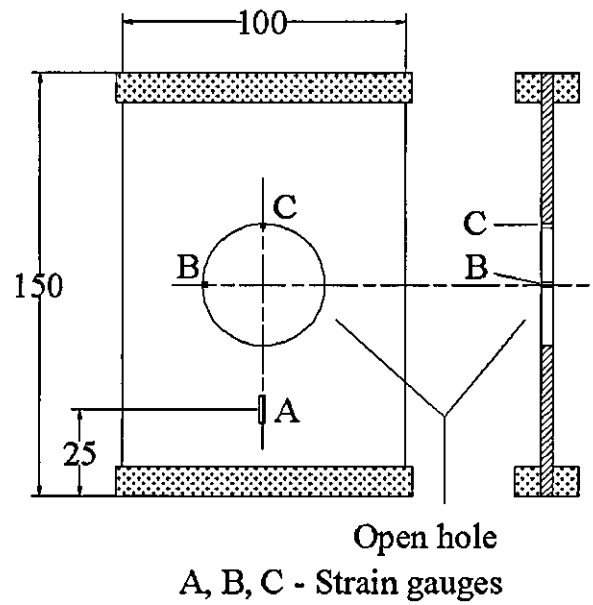
Figure 2.5.6 Strain gauge locations for in-plane compression specimens with open hole. All dimensions are in mm
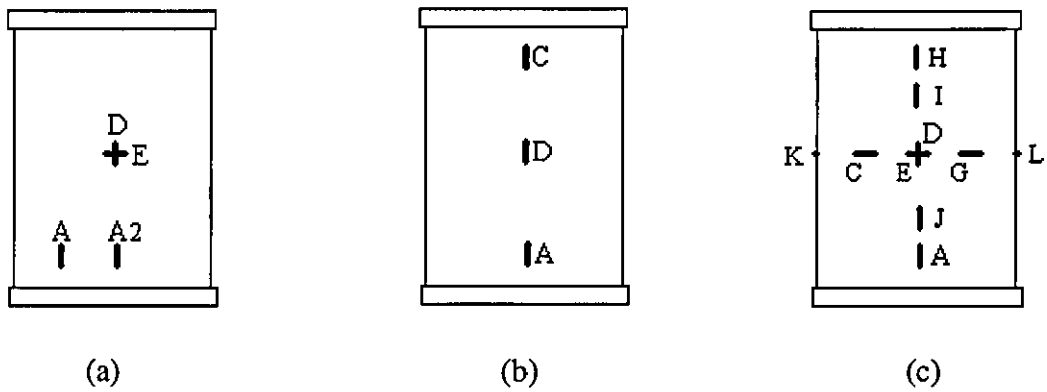
Figure 2.5.7 Schematic distribution of strain gauges on (a-b) 2-mm and (c) 4-mm thick intact panels

69

Strain gauge   Indicator arrow   Strain gauge   Connection   Extension wire
wires   terminal

Soldering
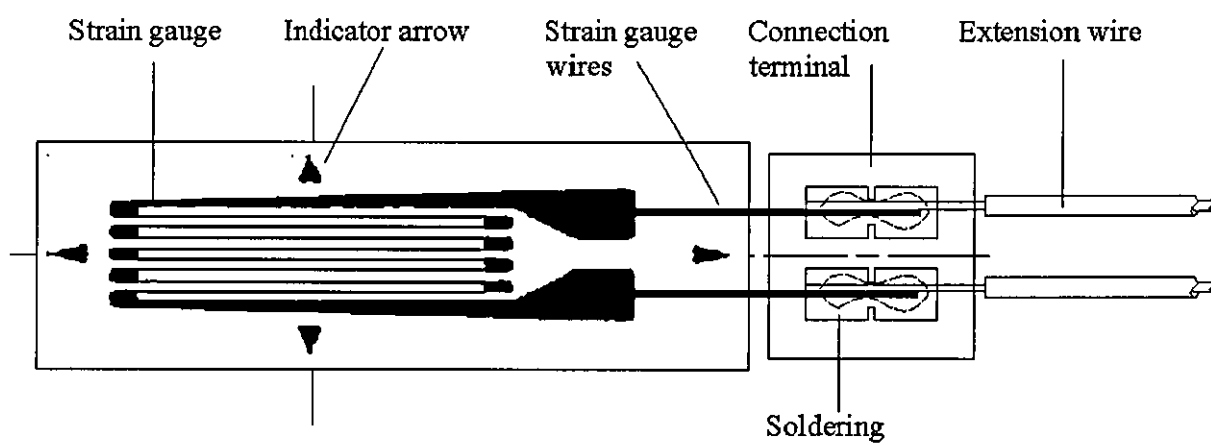
Figure 2.5.8 Typical strain gauge connection

3 Damage introduction and characterisation

This chapter presents the test results of impact and quasi-static transverse loading in terms of panel response (force and displacement data), damage mechanisms and damage size. It discusses the relationships between incident kinetic energy (IKE), absorbed energy (AE), transverse load, specimen dimensions and impactor-nose shape.

3.1 Transverse loading of composite plates

Two types of transverse loading were applied to the present panels. The first type was impact loading at various levels of IKE and at low impact velocities. The second type was quasi-static transverse loading. As the current resin system of LTM45-EL is not strain-rate sensitive [104], a similar nature of damage was expected with both types of loads.

3.1.1 Low-velocity impact loading

Experimental set-up

Impact tests were conducted using an instrumented, tailor-made falling-weight rig as shown in Figure 3.1.1. Two different impactor masses were used, initially 1.69 kg and later 1.49 kg after a modification, as shown in Figure 3.1.5. With the maximum drop height of 6 m, the IKE levels could be regulated from 1 to 100 J for the former impactor mass and from 1 to 90 J for the latter. Two photodiodes located on the rail-guide measured the incident and rebound elapsed times when a steel-foil flag bolted onto the impactor made a return journey. As the photodiodes had the fixed distance of 50.1 mm, incident (primary timer) and rebound (secondary timer) velocities were obtained by dividing the respective elapsed times with the distance. The impactor was captured after rebound to prevent a second impact in each test. A simple illustration of the main components of the impact rig is shown in Figure 3.1.2.

Each specimen was clamped using a two steel plate fixture with a central circular opening of 100-mm diameter, giving a testing area of 7854 mm^2 as shown in Figures

3.1.2 and 3.1.3. The whole fixture was fastened onto the impactor tower base, with a solid support. Once the target specimen was located with its centre aligned with the impactor, the instrumented impactor was raised to a desired height, corresponding to a selected IKE. The impactor was then dropped and the load cell data was recorded, providing a force-time history. The entire data acquisition system is shown in Figure 3.1.4.

The impactor consisted of three main parts, an impactor nose, a strain-gauged load cell and a guide. While the third part was bolted on the second or central part, the first two parts were made in one piece as shown in Figure 3.1.5. The steel impactor nose had a hemispherical-ended shape of 20-mm diameter. The force measurement took place in the second part by means of four strain gauges mounted on a load cell cylinder. The Wheatstone bridge was set up and the output signal was later amplified. The third part made of aluminium had a set of guides with nylon pads and a narrow middle section for additional masses. The guides were intended to keep a precise vertical alignment of the central axial line of the impactor profile with the impact action line during free fall. The impactor so designed was intended to keep the centre of gravity as close to the nose as possible. The impactor was calibrated as shown in Figure 3.1.6, so that the calibration constant was 7.79 mV/kN.

The experimental data corresponding to impact force history was recorded by a *Microlink 4000* data acquisition unit with a sampling rate of 50 μs. The Microlink 4000 had 5 different modules, which were controlled by a computer. These modules were the *Power Unit* (PU), the *Control Unit* (CU), the *Time Base Unit* (TB), the *Comparator Unit* (CMP) and the *Input Channel Unit* (AD12). The TB controls the frequency of sample acquisition; the CMP controls the triggering (i.e. input signal level at which the acquisition is triggered) with an optional setting to manually trigger the data acquisition by using the computer's keyboard. The AD12 records the data through a differential voltage input port, with the option of connecting a single signal by grounding the free input port so that noise can not creep into the signal. There were two additional AD12 input channels, which were not used. Figure 3.1.4 shows the experimental layout for sensors and connections. The Microlink 4000 is controlled with the software *Windspeed WaveCap*. In the sub-menus of the program, variables were set to the following values:

```
Menu <Settings>
Submenu <Comparator>
        <Range> = 0 to 500 mV
        <Coupling> = DC
        <Trigger level> = 15,0 mV (not necessary)
        Submenu <Time Base>
                <Clock rate> = 50 μs. (This will give a testing time of 1.638 s)
        Submenu <AD0703>

                <Range> = -250 to 250 mV
                <Coupling> = DC
Menu <Trigger>
        Submenu <Options>
                <Arm options> = Arm using mouse or key press
                <Trigger options> = Trigger using mouse or key press
Menu <Display>
        <Status> = Displayed
        <Summary> = Displayed
```

Impact test results

The IKE and AE of each impact test were calculated from the incident and rebound velocities, as shown in Table 3.1.1 and 3.1.2 for 2-mm and 4-mm thick panels respectively.

Table 3.1.1 Previous impact test results with a 1.7-kg impactor for 2-mm thick panels [104]

Description	Units	Specimen							
		2I 0.125m	2I 0.25m	2I 0.375m	2I 0.5m	2I 0.625m	2I 0.75m	2I 1m	2I 1.25m
Thickness	mm	2.17	2.20	2.14	2.16	2.14	2.19	2.18	2.18
Impactor mass	kg	1.689	1.689	1.689	1.689	1.689	1.689	1.689	1.689
Distance sensors	mm	50.1	50.1	50.1	50.1	50.1	50.1	50.1	50.1
Height	m	0.13	0.25	0.38	0.50	0.63	0.75	1.00	1.25
Potential energy	J	2.07	4.14	6.21	8.28	10.36	12.43	16.57	20.71
Primary timer	μs	40883	25591	20062	16966	14967	13629	11750	10501
Secondary timer	μs	46703.8	29158.4	22564.6	19380.4	18045.8	17452.4	20801.2	19251.5
Incident velocity	m/s	1.43	2.08	2.60	3.04	3.42	3.74	4.32	4.82
Rebound velocity	m/s	1.30	1.86	2.33	2.68	2.86	2.96	2.51	2.70
IKE	J	1.72	3.67	5.69	7.78	9.88	11.83	15.77	19.64
Rebound energy	J	1.43	2.93	4.59	6.07	6.93	7.38	5.32	6.14
AE	J	0.29	0.74	1.10	1.72	2.95	4.45	10.45	13.50

Impact force histories of 4-mm thick panels at the IKE of 6.9, 13.7 and 21.1 J are shown in Figure 3.1.7 and they seem to indicate that all the tests were impacted beyond their damage resistance threshold. After the initial threshold force, delamination developed

with a clear load drop. The responses differed from the ideal intact panel, which is half sine wave [13].

Table 3.1.2 Impact test results with a 1.5-kg impactor

Description	Units	Specimens					
		4I 0.5m [a]	4I 1.0m [a]	4I 1.5m [a]	4I1.68m	4I2.52m	2I0.5m II [a]
Thickness	mm	4.07	4.05	4.04	4.25	4.21	1.95
Impactor mass	Kg	1.4895	1.4895	1.4895	1.689	1.689	1.4895
Distance sensors	mm	50.1	50.1	50.1	50.1	50.1	50.1
Height	M	0.50	1.00	1.50	1.68	2.52	0.57
Potential energy	J	7.31	14.61	21.92	27.84	41.75	8.34
Primary timer	μs	16939	11834	9501	8884	-	15763
Secondary timer	μs	28644.9	17633.7	14054.6	13491.2	-	18619.9
Incident velocity	m/s	3.04	4.29	5.32	5.68	-	3.26
Rebound velocity	m/s	1.89	2.93	3.63	3.78	-	2.78
IKE	J	6.89	13.72	21.08	27.27	-	7.89
Rebound energy	J	2.66	6.38	9.83	12.06	-	5.76
AE	J	4.23	7.33	11.24	15.21	-	2.13
Critical loads							
Initial threshold	kN	3.73	3.83	4.07	-	3.88	1.53
Peak load	kN	4.27	7.35	8.57	-	13.41	4.73

[a] These panels were tested with a redesigned version of the impactor

The acceleration, velocity and displacement histories of the impacted panels were determined after further treatment of the force history data, as shown in Figure 3.1.8 for 4-mm thick panels impacted at IKE levels of 6.9, 13.7 and 21.1 J. The acceleration history was determined by dividing the force history data by the mass of the impactor. The velocity and kinetic energy histories (Figure 3.1.8(b-c)) were obtained after an integration of the acceleration over the time. The second integration resulted in the displacement history of the impactor. It can be seen that the impactor velocity reduced from the moment it contacted the laminate, reaching zero value when it was fully stopped. At this point the kinetic energy was practically zero. This period of time (around 1500 μs) corresponds to the conversion of kinetic energy to elastic and absorbed (i.e. damage and plastic deformation) energies. From this point onwards the conversion back from stored elastic to rebound energy (kinetic energy) took place, with some energy permanently absorbed by the panel as damage.

Figure 3.1.8(d) shows the displacement-history curves, starting with an initial zero value corresponding to the position at which the impactor made contact with the laminates. The maximum displacement was proportional to the incident velocity.

74

Comparing the incident velocities for the high (5.32 m/s) and low (3.04 m/s) IKE levels, the former is 1.75 times higher than the latter. On the other hand the maximum displacement is 1.76 times higher (4.95 mm vs. 2.81 mm). This means that the maximum displacement is proportional to the square root of the IKE, as seen when comparing the square roots of 21.7 J and 6.9 J (the value of the ratio is 1.75).

The AE-history curves in Figure 3.1.10 were determined from the force and displacement data. Firstly, using the data from Figures 3.1.7 and 3.1.8(d) the force-displacement curve was plotted in Figure 3.1.9 for 4-mm thick panels impacted at IKE levels of 6.9, 13.7 and 21.1 J. The loading and unloading paths created a hysteresis-area loop which provided a measurement of the energy absorbed as damage. Secondly, the area was measured and plotted against to time, as shown in Figure 3.1.10. Using the final values of the AE-history curves is another way to determine the amount of IKE that was absorbed as damage by the panel as shown in [28, 33, 39-41, 48, 78, 106, 107]. The AE values determined in this way were 4.3, 7.4 and 11.2 J for the 4-mm thick panels impacted at IKE levels of 6.9, 13.7 and 21.1 J respectively

3.1.2 Quasi-static transverse load

Damage induced by transverse quasi-static loading could be similar to impact-induced damage if rate sensitivity does not contribute to damage resistance and propagation. Quasi-static loading offers the additional advantages due to easy control and data gathering. Thus, it is appealing for developing a preliminary understanding of damage characteristics due to transverse loading. It also allows the study of the interaction between local indentation and global plate deflection and its effect on the onset and growth of damage. Additionally, the greater adaptability of indenter noseshapes on the universal testing machine facilitates the study of the nose-shape effect on panel responses and damage generation.

Experimental set-up

Plates of two different thickness, 2-mm and 4-mm, were manufactured following the process is described in Chapter 2. Each plate was clamped using the same clamping

75

device as the impact tests, shown in Figure 3.1.3, providing a circular testing area of 100-mm diameter. The strain on the panel surface was monitored using strain gauges bonded on the bottom skin at the panel centre and on the top skin 20-mm away from the centre, as described in Chapter 2. Transverse load was applied quasi-statically at the centre of each clamped specimen at a cross-head speed of 5 mm/min, with either flat- or hemispherical-ended indenter of 20-mm diameter on a Mand universal testing machine.

Two different types of tests were conducted depending on load levels and the damage resistance of the panel. In the first one, load was applied until the panel failed transversely after the peak load. In the second type of loading, load was suspended right after the onset of delamination at the initial threshold force level. Load, strain and crosshead displacement in all the tests were recorded through an Orion delta 353D acquisition system at a sampling rate of 0.5 Hz. A total of eight specimens were tested in quasi-static transverse loading, as shown in Table 3.1.3. From the eight plates tested, five of them were subsequently prepared for a compressive test, to determine their residual strength as described in Chapter 2. One of the remaining plates was used for cross sectioning analysis of internal damage and its damage characterisation is shown in the second part of this chapter.

Quasi-static transverse load results

Table 3.1.3 summarises the main experimental results for quasi-static transverse loading tests. It was observed that panel thickness affected the transverse responses before the onset of damage, due to different flexural rigidities. The linear flexural response governed the initial range for relatively small deflections as shown in Figure 3.1.11 and 3.1.12(a) for thin and thick panels respectively. From these figures it is observed that at the given deflection of 1 mm, the transverse force was about 8 times higher in the thick panel than in the thin panel, 0.48 and 3.65 kN respectively.

Typical quasi-static strain-force curves are presented in Figures 3.1.13 and 3.1.14(a-b) for 2-mm and 4-mm thick plates respectively. The strain gauges were located on the top side 20-mm away from the centre and on the bottom side at the centre. Some of the diagrams also show details with an insert of close-up.

Table 3.1.3 Quasi-static loading results in terms of force and displacement

Specimen [a]	Thickness [b]	Indenter Nose	Force		Indenter displacement at		Intended use [c]
	mm		Initial threshold kN	Maximum KN	Initial threshold mm	Maximum mm	
2QSI H	1.99	H	1.06	8.24	1.79	6.44	QSI
2QSI H HW	1.97	H	1.09	1.09	2.04	2.04	C
4QSI H	4.18	H	3.65	17.21	1.16	7.45	C
4QSI H II	4.21	H	3.63	16.48	1.06	6.53	QSI
4QSI H HW	4.16	H	3.66	3.66	1.08	1.08	C
4QSI F	4.22	H	10.23	27.92	1.75	6.42	C
4QSI F HW	4.20	F	10.84	10.84	2.13	2.13	C
4QSI F HW II	4.22	F	12.66	12.66	2.37	2.37	CS

[a] QSI, H, F, HW and II stand for quasi-static loading, hemispherical end-nose shape, flat end-nose shape, half-way loaded (i.e. partially loaded) and second specimen respectively

[b] Panel thickness was later re-measured after panel trimming, for the compressive test

[c] QSI, C and CS stand for quasi-static loading, compressive test and cross sectioning respectively

3.1.3 Determination of contact stiffness

Transverse loading of a plate involves two main types of deformation. Firstly, there is a global bending elastic deformation with both the flexural and membrane contributions. Secondly, there is a local indentation due to local contact pressure developed between the indenter and the plate. This local indentation α can be significant when compared with the deflection of the plate. For a given load P, it is governed by the indentation law defined as

$$P = k_i \alpha^n \tag{3.1.1}$$

in which k_i and n are indentation constants, which are material specific. Thus they must be experimentally determined. Thirty-two-ply carbon/epoxy samples used [108] were the same material as in this project. Figure 3.1.15 shows the specimen under quasi-static indentation with the bottom side fully supported. As the support condition did not allow flexural deformation, the displacement δ of the indenter was equal to the local indentation α. Photographs of tested specimens are shown in Figure 3.1.16. A total of five tests were carried out with a hemispherical-ended indenter of 20-mm diameter. The average values of these constants are k_i of 47.2 GPa.mm$^{1/n}$ and n of 1.83.

3.1.4 Analytical model of laminate quasi-static loading response

The quasi-static load-displacement response of a clamped circular panel can be divided into two stages, separated by the onset of delamination. Models developed in this section predict the deflections up to the onset of delamination of circular composite panels. Three models are presented, the first one is a simple model based on the small deflection analysis that considers a linear relationship between load and deflection and is applicable to deflection of plates with the deflection/thickness ratio w_0/h of less than 0.4. This model includes the effect of indenter size on deflection. The second one is a more sophisticated model for large deflections of greater than $0.4h$, which takes into account the effects of membrane stretching. The third model is extended on the basis of the second model with the addition of local indentation.

The quasi-static transverse response has been analytically predicted by many authors [109-116] with fairly good results. However, the model developed below includes the size effect of indenter, which is a helpful tool for analysis in the subsequent sections of this thesis. It provides an opportunity for future improvement by taking into account the indenter shape effect on the deflection through a distributed contact pressure. The derivation of the expression for deflection also includes the composite material considerations.

Small deflection analysis

This section summarises the main results of the derivation in Appendix B for the deflection of a clamped plate under a uniformly distributed load on a concentric circular area, as shown in Figure 3.1.17. Timoshenko and Woinowsky-Krieger [109] devised a solution method for similar loading conditions and the edges of the plate simply supported. Following their method, the expression for the central deflection $w(0)$ of a clamped plate of radius a under a load P uniformly distributed on a concentric circular area of radius c was determined as follow, with details given in Appendix B in Eq. (B.1.10), is

$$w(0) = \frac{Pa^2}{16\pi D'}\left\{1 + \left[(c/a)^2\left(\log(c/a) - \frac{3}{4}\right)\right]\right\} \qquad (3.1.2)$$

The flexural stiffness D' for anisotropic laminates is given by [109, 117]

$$D' = \frac{1}{8}[3D_{11} + 2(D_{12} + 2D_{66}) + 2D_{22}] \qquad (3.1.3)$$

When c in Eq. (3.1.2) approaches zero, a similar expression for deflection of a plate loaded with concentrated force could be introduced as

$$w(0) = \frac{Pa^2}{16\pi D'} \qquad (3.1.4)$$

With this equation, a *Loading Area Factor* (LAF) is introduced to take into account the effect of an indenter size as

$$LAF = \left\{1 + \left[(c/a)^2\left(\log(c/a) - \frac{3}{4}\right)\right]\right\} \qquad (3.1.5)$$

Table 3.1.4 shows values for various *LAF*s associated with different size/plate radius ratios for centrally concentrated load. From this table it is clear that an increase of the area of load distribution results in a lower value of central deflection for a constant load.

Table 3.1.4 Variation of Loading Area Factor (LAF) with c/a ratio

Scenario	c/a ratio	Loading Area Factor, *LAF*
Concentrated load	0	1
•	0.1	0.9695
•	0.2	0.9056
•	0.3	0.8241
•	0.4	0.7333
•	0.5	0.6392
Fully distributed load	1	0.25

For comparison purposes, the central deflection of a uniformly loaded plate is obtained by setting $c = a$ in Eq. (3.1.2) as [109]

$$w(0) = \frac{Pa^2}{64\pi D'}$$

(3.1.6)

Large deflection analysis

In cases where deflections are no longer small in comparison with the plate thickness, the deflection analysis has to be extended to include the effect of membrane stretching. The deflection equation can be defined using the principle of virtual displacements, in terms of strain energy due to bending V and strain energy due to membrane stretching V_I as [109]

$$\frac{d(V + V_1)}{dw_0} \delta w_0 = 2\pi \int_0^a q \delta w r dr$$

(3.1.7)

As shown in Appendix B, Eq. (3.1.7) is a third order polynomial expression in the form of

$$T_1 w_0 + T_2 w_0^3 = T_3 P$$

(3.1.8)

The polynomial coefficients T_1, T_2 and T_3 are analogous to bending and membrane stiffness as given by

$$k_b w_0 + k_m w_0^3 = P$$

(3.1.9a)

If the effect of transverse shear is considered for the thick plates, then Eq. (3.1.9a) becomes

$$k_{bs} w_0 + k_m w_0^3 = P$$

(3.1.9b)

80

The term T_1 of Eq. (3.1.8) can be considered similar to the small deflection analysis in Eq. (3.1.2) as

$$T_1 = \frac{16\pi D'}{LAF} \tag{3.1.10}$$

The approximate expression for T_2 as derived in Appendix B is

$$T_2 = \pi A_{11} \frac{1}{LAF^4}\left\{0.217 - 0.465\left(\frac{c}{a}\right)^2\right\} \tag{3.1.11}$$

The term T_3 is equal to the square of plate radius a^2, as indicated in Appendix B. Therefore, with all the expression for T_1, T_2 and T_3, Eq. (3.1.8) finally becomes

$$\frac{16\pi D'}{a^2}\frac{1}{LAF}w_0 + \frac{\pi A_{11}}{a^2}\frac{1}{LAF^4}\left\{0.217 - 0.465\left(\frac{c}{a}\right)^2\right\}w_0^3 = P \tag{3.1.12}$$

where the bending and membrane stiffness in Eq. (3.1.9a) are given by

$$k_b = \frac{16\pi D'}{a^2}\frac{1}{LAF}$$

$$\tag{3.1.13a, b}$$

$$k_m = \frac{\pi A_{11}}{a^2}\frac{1}{LAF^4}\left\{0.217 - 0.465\left(\frac{c}{a}\right)^2\right\}$$

Transverse shear effect k_s

Transverse shear effect becomes substantial in thick panels, being on the same order of magnitude of deflection due to pure bending. As a consequence, combined bending and shear response is needed. Transverse shear effect is introduced by adding the shear stiffness to the bending stiffness as expressed in Eq. (3.1.13a). This interpretation follows [110]

81

$$\frac{1}{k_{bs}} = \frac{1}{k_b} + \frac{1}{k_s} \qquad\qquad (3.1.14)$$

in which

$$k_s = \frac{4\pi G_{zr}h}{3}\left(\frac{E_r}{E_r - 4v_{rz}G_{zr}}\right)\left(\frac{1}{4/3 + \log(a/c_i)}\right) \qquad\qquad (3.1.15)$$

The value for G_{zr} is equivalent to $G_{13/23}$ of 5.3±0.3 GPa for the current composite system [104]. Poisson's ratio value v_{rz} is 0.31. The radial flexural modulus E_r is evaluated using the relationship for the laminate equivalent engineering elastic constant in bending mode

$$E_r = \frac{12}{d_{11} \times h^3} \qquad\qquad (3.1.16)$$

Where d_{11} is the first term of the inverse of matrix $[D]$. The ratio between plate radius and indentation radius a/c_i is a function of the indenter shape and the applied force. For a flat-ended indenter, the indentation radius c_i and the indenter diameter c are the same as shown in Figure 3.1.18(a). As a result, Eq. (3.1.15) becomes

$$k_s = \frac{4\pi G_{zr}h}{3}\left(\frac{E_r}{E_r - 4v_{rz}G_{zr}}\right)\left(\frac{1}{4/3 + \log(a/c)}\right) \qquad\qquad (3.1.17a)$$

On the other hand, for a hemispherical ended indenter, the radius of indentation depends on the applied force, laminate and nose material properties. It was estimated as half of the laminate thickness, $c_i = h/2$ as shown in Figure 3.1.18(b). The experimental contact stiffness value, obtained in the previous section, is in agreement with this assumption within the initial elastic range. Thus Eq. (3.1.15) becomes

$$k_s = \frac{4\pi G_{zr} h}{3} \left(\frac{E_r}{E_r - 4\nu_{rz} G_{zr}} \right) \left(\frac{1}{4/3 + \log(2a/h)} \right) \qquad (3.1.17b)$$

Indentation effect on deflection analysis

A force-based analytical model was proposed in [114]. The model combines indentation law with both plate flexural and membrane stretching responses. Figure 3.1.19 shows a total displacement δ of a clamped plate with a hemispherical-ended indenter. The total displacement is the sum of the plate deflection and indentation as

$$\delta = \alpha + w_0 \qquad (3.1.18)$$

Combining Eqs. (3.1.9b) and (3.1.1) with Eq. (3.1.18) yields

$$\frac{k_m}{k_i^{3/n}} P^{3/n} - 3\delta \frac{k_m}{k_i^{2/n}} P^{2/n} + \left(k_{bs} + 3\delta^2 k_m\right)\frac{P^{1/n}}{k_i^{1/n}} - \left(k_{bs} + \delta^2 k_m\right)\delta + P = 0 \qquad (3.1.19)$$

A solution of this equation in terms of P can only be numerically found for the given total or indenter displacement. To this end a Newton-Raphson algorithm was written in Matlab® as shown in Appendix C. Inputs of this model are shown in Table 3.1.5.

Analytical prediction results for central deflection

Figure 3.1.20 and 3.1.21 show predictions of this model along with experimental results. The predictions shown correspond to the small deflection model in Eq. (3.1.2), the large deflection model in Eq. (3.1.9b) and the large deflection model with local indentation effects in Eq. (3.1.19), which are referred to as *model 1*, *model 2* and *model 3*, respectively, from now onwards.

In the case of 2-mm thick panels loaded with a hemispherical indenter in Figure 3.1.20, all three models underestimate the experimental displacement for a given load. This suggests that the flexural rigidity may have been overestimated. In addition, it also

suggests that in reality it is not possible to achieve a 100% clamped boundary condition, which is reflected with the larger deflections for a given load. In particular the experimental membrane effect is low when compared to the analytical prediction.

Table 3.1.5 Input values for analytical model prediction

Property	Units	Equation	16 plies	32 plies
D_{11}	GPa.mm^3	-	44.44	336.96
D_{12}	GPa.mm^3	-	13.61	101.58
D_{22}	GPa.mm^3	-	30.50	277.21
D_{16}	GPa.mm^3	-	-4.48	-16.93
D_{26}	GPa.mm^3	-	-4.48	-16.93
D_{66}	GPa.mm^3	-	15.59	117.38
D'	GPa.mm^3	3.1.3	39.30	314.40
A_{11}	GPa.mm	-	112.44	224.88
Plate radius, a	mm	-	50	50.00
Indenter radius, c	mm	-	10	10.00
Indenter nose shape	-	-	H	H F
c/a	-	-	0.2	0.20
LAF	-	3.1.5	0.9056	0.91
Bending stiffness, k_b	GPa.mm	3.1.13a	0.8725	6.98
Membrane stiffness, k_m	Gpa/mm	B.1.27a	0.0417	0.08
Membrane stiffness approx. k_m	Gpa/mm	3.1.13b	0.0417	0.08
Compliance term, d_{11}	(GPa.mm^3)$^{-1}$	-	0.0263	0.00
Plate thickness	mm	-	2.048	4.10
Engng. Flexural modulus, E_r	GPa	3.1.16	53.12	52.92
$G_{13/23}$	GPa	-	5.3	5.30
Radial Poisson's ratio, v_{rz}	-	-	0.31	0.31
Shear stiffness, k_s	GPa.mm	3.1.17(a-b)	9.94	22.93 35.28
Bending-shear stiffness, k_{bs}	GPa.mm	3.1.14	0.8021	5.3511 5.8273
Contact stiffness, k_i	GPa/mm^n	3.1.1	47.2	47.20
Exponential constant, n	-	3.1.1	1.83	1.83

Figure 3.1.21(a) shows the displacement responses of 4-mm thick panels quasi-statically loaded with a hemispherical indenter. Predictions are much closer to the experimental results, probably as a consequence of the increase in bending response with respect to the membrane stretching. Among three models in Figure 3.1.21(a), the prediction of Model 3 is the closest to the experimental results. The local indentation effect seems to be more substantial for thick panels. Figure 3.1.21(b) shows the displacement responses of 4-mm thick panels quasi-statically loaded with a flat-ended indenter along with predictions. Similarly to the hemispherical case, predictions of Model 3 are in good agreement with the experimental results, although predictions of

the other two models are also in reasonably good agreement with the experimental results. The reason could be that flat-ended indenter may have distributed load better than the hemispherical-ended case. Also it seems that the effect of local indentation is more substantial than the membrane effect for the initial pre-damage stage. Apparently the deflections within this range are not large enough to induce significant membrane stretching. However if a post-damage analysis of thick panels is intended, it is necessary to include the membrane effects by using a reduced stiffness as proposed in [114, 116].

3.2 Examination of damage mechanisms

On a macroscopic scale, the effects of impact loading can be divided into material damages and local change of curvature. Material damages include delamination, matrix cracking, fibre fracture and ply shear-out as shown in Figure 3.2.1. On the other hand local curvature change is related to changes on the surface topology around the indentation site. In the present study, damaged and artificially delaminated panels were examined using C-scan and micrographs of cross sectioning.

3.2.1 Cross sectioning results

Cross-sectioning micrographs intend to provide physical evidence of damage, especially through-the-thickness (TTT) distribution of delaminations, which cannot be shown by the current C-scanning. Two specimens selected for sectioning were impact-damaged at 28.7 J with a hemispherical nose and quasi-statically damaged with a flat-ended indenter. For the latter the test was stopped beyond the onset of damage.

The specimens were sectioned diametrically. The samples of about 12-mm deep from the cut surface were further sectioned off. The diametric surfaces of the sample intended for inspection were pushed to the bottom of a rubber disk mount. Epoxy as prepared in Section 2.5.2 was poured into the mount. Once epoxy cured, the disk was fixed to the spinning head of a lapping polisher machine for grinding and polishing. The spinning head-epoxy disk fixture was then positioned with the disk surface pressed against the rotating base. Grinding was divided into two stages. In the first one the rotating base was SiC wet-and-dry paper, at a radial velocity of 300 rpm for 2.5 min using water as

lubricant agent. A finer grinding followed, the SiC paper was changed to a special rotating base (MD-Largo), at 150 rpm for 6 min using 6-μm aluminium oxide spray (DP-Spray) as grinding media and special lubricant (DP-Blue). Subsequently the sample was polished in two stages. A first polishing was done at 150 rpm for 4 min using a rotating base with a satin fabric, DP-Spray 6-μm as media and DP-Blue as lubricant. Then a finer polishing was done at 150 rpm for 3 min using another satin base (to avoid cross contamination), DP-Spray 1-μm as media and DP-Blue as lubricant. Between each stage the disk was thoroughly rinsed and cleaned to avoid media contamination. Finally the samples were placed under a camera-mounted microscope to inspect the polished surface.

Three micrographs from impacted specimen are shown in Figure 3.2.2(a), with a corresponding schematic drawing of the damage in Figure 3.2.2(b). The main damage mechanisms present in the impacted panel of Figure 3.2.2(a) were matrix cracks, delamination and fibre breakage in addition to local change of geometry. The location of matrix cracks in the panel of Figure 3.2.2(a-b) was mainly under the contact point of the impactor, with higher crack concentration close to the top surface. Delaminations initiated at the tip of these matrix cracks and propagated in the radial direction. A typical shear cone pattern was observed, formed by the combination of matrix cracks and TTT delamination. Three large delamination were detected in Figure 3.2.2(a), one running close to the top surface, a second one close to the mid-plane and another one close to the bottom surface. A small amount of fibre breakage was noticeable only on the 90° plies with fibres parallel to the polished surface and was marked with bold lines on the drawing of Figure 3.2.2(b). A permanent plastic deformation with an associated local change of surface geometry created during the transverse loading was visible in Figure 3.2.2(a). Figure 3.2.2(c) show this local change in panel surface geometry for an impact energy level of 28.7 J. The dent dimensions were 0.138 mm depth and 2.452 mm in-plane radius, so that a curvature radius of 21.85 mm could be implied if a hemispherical-shaped dent is assumed. Dents were also found in the remaining panels with impact damage, but it was not possible to measure them accurately without a cross-section.

A micrograph of the quasi-statically damaged specimen is shown in Figure 3.2.3. The panel was loaded until the damage onset level, around 3.6 kN. The micrograph shows a large delamination near the mid-plane, probably caused by the high ILSS. It also shows fibre breakage and matrix cracks caused by the contact stress under the edge of the flat indenter. The signature left by the indenter on the top ply indicated high contact stresses, even at low levels of applied load.

Based on these micrographs, it was observed that damage induced by transverse loading in 4-mm thick panels was governed mainly by ILSS. The governing damage mechanism mainly depends on the flexural rigidity of the laminate. On the one hand, damage from transverse loading in flexible laminates is governed by a localised shear cone, delaminations and fibre breakage [12], as shown in Figure 3.2.4(a). The shear cone contains matrix cracks and localised delaminations distributed in the thickness direction. On the other hand, damage in stiffer laminates is governed by ILSS and it consists of a small shear cone with a massive single delamination near the mid-plane, as shown in Figure 3.2.4(b). The cross section photograph of the panel impacted at 28.7 J (Figure 3.2.2) shows a major delamination near the mid-plane due to high ILSS concentration. However there was widespread TTT delamination as a consequence of the high IKE level. The quasi-static loaded panel contained less amount of delamination (Figure 3.2.3), but it had a massive delamination near the mid-plane. A photograph in Figure 3.2.4(c) seems to further support this observation with a cross-sectional view of a impact damaged glass/epoxy laminate [unpublished work from Zhou, G., 2004]. Damage was characterised by a small shear cone in the vicinity of the impact together with a large delamination near the mid-plane.

3.2.2 Process of damage propagation in transversely-loaded panels

Depending on the energy absorption characteristics during impact, four deformation stages were identified in Figure 3.1.10. Firstly, the IKE was absorbed by the panel as elastic energy, up to the initial threshold force value that corresponds to the onset of damage. The period that took the panel to reach the damage threshold was 700, 500 and 450 μs, for IKE levels of 6.9, 13.7 and 21.1 J, respectively. The initial threshold for

delamination onset could be identified from the force history plots in Figure 3.1.7. This value was on average 3.88 ±0.14 kN, corresponding to 6.14 J.

Secondly, after the delamination onset, the energy was not only elastically stored in the panel deformation but also absorbed as internal damage. From previous studies [10, 41] it is known that during this stage a shear cone develops with matrix cracks generated by shear or tensile flexural stresses around the indentation area. Matrix cracks are followed by interface delaminations, growing from the crack tips. Delaminations usually occurred between plies of different orientation, having a peanut shape elongated along the fibre direction of the lower ply at that interface. The presence of a shear cone was probably initiated by the contact stress distribution in the in-plane and TTT directions around the contact point. Figure 3.2.5 shows two schematic predictions of TTT distribution of stress in a circular plate during transverse loading, taking the approaches of thin and thick plates [118]. The contribution of contact stresses is significant in the case of small deflections (Model 1 for thick plates), inducing large compressive and shear stress near the top surface. This implies that damage initiates as a shear cone. As the plate deflects, the distribution resembles more the prediction from Model 1 for thin plates. Finally, for large deflections, it resembles Model 3 of large membrane stresses. In the case of thick panels, high ILSS developed could induce a large delamination near the mid-plane. The micrograph in Figure 3.2.3 shows such damage.

Thirdly, a stage before perforation was observed in relatively flexible (thin) panels, with a shift of the governing damage mechanism from shear cone to fibre fracture. As fibre fracture became more dominant, the proportion of energy absorption increased dramatically, as explained later in Figure 3.3.7. Previous studies [30, 39, 119] have shown the similar behaviour for panels close to the perforation limit. In these studies the relationship between peak load and IKE was dramatically modified at relatively high IKEs.

Finally, no further energy was absorbed neither elastically nor as damage after the AE had reached its maximum in the AE history. The energy transfer was reversed from the panel to the impactor and the impactor gained the stored elastic energy of the panel as kinetic rebound energy, RE, until the impactor bounced off. The AE history of the three

panels studied did not reach the final asymptotic value, probably due to the inherent noise of the load cell signal that added few micro-volts (i.e. kN) at the end of the force-history, as seen in Figure 3.1.7.

Similar energy absorption characteristics were observed in [41] as shown in Figure 3.2.6. The figure shows the load and energy histories of a 24-ply quasi-isotropic carbon/epoxy rectangular (76.2 by 127 mm) panel impacted at 46 J. Three critical load levels were identified, the critical threshold for damage initiation, the onset of fibre breakage and the maximum (i.e. peak) transverse load. Figure 3.2.6 also shows the breakdown of the energy history in the different mechanisms. Initially the main damage mechanisms were matrix cracks and delamination. Fibre breakage was developed at a later stage as also suggested by [39], increasing the initial proportion of IKE that was absorbed by the panel. The extent of fibre breakage of individual specimens at various IKE levels was accurately measured using the thermal deplying technique.

Strain responses can also be used to confirm the damage development stages mentioned above. Typical strain gauge readings are shown in Figure 3.1.13 from a 2-mm thick panel transversely loaded with a hemispherical indenter. Figure 3.1.13 indicates a first stage up to the onset of delamination at 1.06 kN. Within this stage, the top gauge reached its peak in compression at 0.3 kN (-65 $\mu\varepsilon$) while the bottom gauge linearly increased in tension, reaching around 7000 $\mu\varepsilon$. Taking the approach of Model 1, the value of top and bottom strains should be equal in magnitude and opposite in sign for the same radial location. The difference in the bending strain magnitude between the bottom gauge at the centre and the top gauge 20 mm away indicates a highly localised bending response within the first load range. For loads higher than 0.3 kN the top gauge started decreasing while the bottom gauge continued the linear increase in the tensile region. The increase in the tensile component of the top-gauge strains indicated a growing predominance of membrane deformations over bending deformations, i.e. the panel was entering the range of large deflections. At 1.06 kN the top gauge changed from compression to tension and the bottom gauge experienced a significant drop in load, corresponding to the onset of delamination. A second stage initiated after the onset of damage. The strain readings of the bottom gauge increased with reduced stiffness due to the presence of damage. Additionally the compression-to-tension switch of the top

gauge indicated an increased contribution of membrane effect to a global response. The increase in membrane effect was also evident with the switch in the bottom-gauge strain response from linear to a third-order type. The reason for that was the division of the original laminate into thinner sublaminates with much lower flexural rigidity. After 5 kN a third stage was identified from the reduction in slope of the top-gauge response, probably due to the initiation of major fibre breakage.

3.3 Determination of damage size using C-Scanning

The projected damage areas of all the damaged panels were obtained by C-Scanning. In principle, ultrasonic signal emitted by a probe travels transversely through the thickness of the material and then is detected, either by a different probe at the rear of the specimen (through-transmission) or by the same probe (pulse-echo detection). By a proper selection of signal frequency of the probe, the attenuation resulting from the presence of damage can be maximized. Since there is a large impedance mismatch between air and solid material, the specimen and the transducer are coupled via a liquid or a solid medium. Size and defect location are estimated by measuring the signal amplitude and/or the time of flight of the ultrasonic signal. Using the same basic equipment, results can be displayed in different ways, via A, B or C scans. The A-scan gives information about a single point in the material. The B-scan is a linear collection of A-scans, therefore it gives a cross-section image of the specimen. The C-scan combines many B-scan lines at a selected perpendicular interval and is the most useful type of ultrasonic technique. To provide planar size and location of damage, scanned delamination areas are presented in Table 3.3.1, for panels containing damage from both impact and quasi-static loading. Figure 3.3.1 shows C-scan graphs for 2-mm thick impact damaged panels [104]. Figure 3.3.2 shows C-scan graphs of 4-mm thick impact damaged panels. Similarly, C-scan graphs of quasi-statically damaged panels are shown in Figure 3.3.3.

Table 3.3.1 Energy and force parameters of panels transversely loaded either in impact or quasi-statically

Specimen[a]	Thickness	Indenter shape	IKE	AE	Impact duration	Peak force	Initial threshold force	Delamination area [b]
	mm		J	J	μs	kN	kN	mm2
2I 0.125 *	2.19	H	1.72	0.3	-	-	-	77.00
2I 0.25 *	2.22	H	3.66	0.7	-	-	-	177.00
2I 0.375 *	2.17	H	5.69	1.1	-	-	-	264.50
2I 0.5 *	2.18	H	7.78	1.7	-	-	-	427.80
2I 0.625 *	2.17	H	9.88	2.9	-	-	-	453.50
2I 0.75 *	2.22	H	11.83	4.4	-	-	-	523.30
2I 1.0 *	2.20	H	15.77	10.4	-	-	-	676.00
2I 0.5 ii	1.96	H	7.89	2.1	3400	4.73	1.53	-
2QSI H HW	1.97	H	-	-	-	1.09	1.09	33.00
2QSI H	1.99	H	-	-	-	8.24	1.06	Perforated
4I 0.5m	4.09	H	6.9	4.2	2700	4.27	3.73	913.75 *
4I 1.0m	4.08	H	13.7	7.3	2750	7.35	3.83	1697.75 *
4I 1.5m	4.08	H	21.1	11.2	2900	8.57	4.07	5468.25 *
4I 1.7m	4.25	H	27.3	15.2	-	-	-	7854.00
4I 2.52m	4.22	H	41.7	-	3300	13.41	3.88	7854.00
4QSI H HW	4.20	H	-	-	-	3.66	3.66	206.50
4QSI H	4.25	H	-	-	-	17.21	3.63	8302.75
4QSI F HW	4.22	F	-	-	-	10.84	10.84	4734.25
4QSI F	4.30	F	-	-	-	27.92	10.23	8582.00

[a] Data correspondent to 2-mm thick panels marked with a star (*) sign are taken from [104]
[b] C-scanning results from these panels were obtained differently by analysing the echo signal of individual locations using a grid (0.5 mm spacing) on the panel due to technical problems

3.3.1 Panel thickness effect

Thickness directly affects the flexural rigidity of the transversely loaded panel. Before the onset of delamination this was reflected on the panel response as observed from Figure 3.3.4. After the onset of delamination, the reduced rigidity also affects the damage governing mechanism and the energy absorption characteristics. The force-history of a 2-mm thick panel impacted at 7.9 J has different characteristics than a 4-mm thick panel impacted at 6.89 J, as illustrated in Figure 3.3.4. Firstly, the impact duration was longer for 2-mm thick panels. Similar results were reported in [28] for panels impacted below the critical IKE for major fibre breakage onset. Secondly, the behaviour after the initial threshold force (onset of delamination) was different. The force-time trend in 2-mm thick panels resembles more a smooth half sine wave after the initial threshold at 1.53 kN. On the contrary, other hand 4-mm thick panels experienced a sharper load drop after the initial threshold at 3.73 kN. Finally, the peak force of the two panels were relatively close; contrasting with the fact that the thin panel absorbed only 2.13 J and the thick panel absorbed 4.23 J. These features arise due to the

difference in delamination onset and growth between flexible and stiff panels, as discussed in Section 3.2.

The thickness effect from the damage onset onwards until failure is also significant as shown by experimental data in Tables 3.1.2 and 3.1.3. An increase in panel flexural rigidity was reflected in an increase in the initial threshold load for the delamination onset. Using the same indenter shape and size, the initial threshold loads were on average 1.06 and 3.6 kN for 2-mm and 4-mm thick panels, respectively. The associated indenter displacements were 1.85 and 1.02 mm, respectively. The failure peak loads of thick panels were twice large as the thin panels, 8.24 and 16.84 kN (average values for hemispherical indenter) for 2-mm and 4-mm thick panels, respectively, with associated indenter displacements of 6.44 and 6.99 mm, respectively.

On the basis of C-scan results, it was observed that the delamination area increases linearly with the IKE, both for 2-mm and 4-mm thick panels. In the case of 2-mm thick panels, the proportionality constant was 45.24 mm^2/J, without any apparent initial energy threshold for damage onset as shown in Figure 3.3.5(a). On the other hand, 4-mm thick panels had a proportionality constant value of 358.74 mm^2/J, up to the energy level where delamination area reaches the panel boundaries as shown in Figure 3.3.5(b). The initial threshold energy value is defined as the minimum IKE value at which damage starts and it corresponds with the damage onset. This value was 6.14 J as determined by a linear regression of delamination area versus IKE. However more specimens may be required to obtain a precise value for the initial energy threshold [13].

The propagation of delamination was also affected by panel thickness. On the one hand, 2-mm thick panels had a circular shape of damage up to 7.78 J (height 0.5m). For higher IKE levels, fibre breakage started to develop along with delamination, as can be seen in Figure 3.3.1(e-h). From this IKE onwards, the delamination growth shifted from a localised concentric area to delamination growing along the split broken fibres in the ±45° direction. On the other hand, 4-mm thick panels presented much more widespread concentric delamination with circular shape as shown in Figure 3.3.2. For these panels, a physical limitation was imposed to the delamination growth by the size of the testing

area. Therefore panels in Figure 3.3.2(d-e) had similar delamination areas. Delamination reached the plate boundaries for panels with IKE equal or higher than 27.3 J.

Panel thickness also affected the energy absorption characteristics during impact. Panels of 4-mm thick absorbed more IKE as internal damage as shown in Figure 3.3.6 and were not able to undergo large deflections without suffering considerable delamination. In contrast, the thinner 2-mm panels absorbed only about 21% of IKE within an initial linear region. They were able to store comparable higher elastic energy and to undergo larger deflections. Figure 3.3.7 summarises the dependence of the IKE-delamination area and IKE-AE on the panel thickness and thereby on the governing damage mechanism. This figure presents a breakdown of IKE of 2-mm thick panels into energy dissipated as delamination, broken fibres and rebound energy, RE. Initially up to 3.57 J/mm (7.78 J) the proportion of the total IKE absorbed by the panel was 21% for this initial linear region. Coincidently the delamination area had also a linear relationship with the IKE, suggesting that the main damage mechanism during this initial linear stage were internal delamination and matrix cracks in a shear cone arrangement. Beyond 3.57 J/mm (7.78 J) the AE-IKE relationship followed an exponential trend. Also from this energy level onwards, fibre breakage developed so that the increment in AE proportion was probably due to the broken fibres. At the largest IKE tested, the IKE was approximately dissipated into 20% delamination, 60% fibre breakage and 20% RE. In the case of 4-mm thick panels, the AE-IKE relationship was linear for all the IKE levels tested. In average 55% of the IKE was absorbed by the panel. The generated damage (AE) was predominantly in the way of matrix cracks and internal delamination, with nearly inexistent fibre breakage (see Figure 3.2.4).

3.3.2 Indenter nose shape effect

The effect of changing the indenter nose shape on the force-deflection response is shown in Figures 3.1.12(a-b) earlier. The force response for loading with flat-ended indenters was consistently higher than the hemispherical case. The initial threshold force was on average 3 times higher, and the transverse peak force was 1.7 times higher, for flat-ended and hemispherical indenters respectively. The relative drop in load after

the onset of damage (after the initial threshold force) was higher for flat-ended indenter, around 43%, compared with a relative drop of 22% in the hemispherical case as extracted from the detail in Figure 3.1.12(a-b). This seems to suggest that the onset of damage was more catastrophic in the flat-ended case, inflicting more damage within a very short period of time. Additionally, the failure load was significantly higher (62% higher) for the flat-ended case (Table 3.3.1), despite having similar damage areas as shown in Figures 3.3.3(b and d).

The apparent more catastrophic onset of damage in flat-ended indenters can be explained through its contact stress distribution. Figure 3.3.8 shows the contact pressure distributions of both the hemispherical-ended and the flat-ended indenters. In the case of hemispherical-ended indenter, the contact pressure distribution is [120]

$$q = \frac{3P}{2\pi c^2}\sqrt{1-\left(\frac{r}{c}\right)^2} \quad , 0 \leq r \leq c \tag{3.2.1}$$

Where q is the shear force distribution, P the applied transverse load, c the indenter radius and r the radius coordinate. In the case of flat-ended indenter nose shape, the contact pressure distribution is [120]

$$q = \frac{P}{2\pi c\sqrt{c^2 - r^2}} \quad , 0 \leq r \leq c \tag{3.2.2}$$

From Figures 3.2.2 and 3.2.3 it is clear that in the case of hemispherical-ended, damage would tend to initiate right under the axisymmetric line. On the other hand, for a flat-ended indenter, damage would tend to initiate around the indenter on concentric ring area, with much higher local stresses (it tends to infinite).

The effect of indenter shape on the local indentation process was observed in the panel strain readings in Figures 3.1.14(a-b). On the one hand, the strain of the panel loaded with hemispherical-ended indenter presented a gradual development of local indentation. Once the top fibres were affected by the indentation (after 8 kN) the increase in tensile strain dropped gradually to zero, as observed in Figure 3.1.14(a). On

94

the other hand, the development of local indentation for flat-ended indenter and the correspondent surface fibre breakage was more abrupt. A larger number of fibres were affected within a short period. The strain response of a panel loaded with a flat-ended indenter is shown in Figure 3.1.14(b). Likewise the hemispherical-ended case, the top and bottom gauges picked up a first load drop (around 11 kN) related with the initial threshold force for delamination onset. Contrastingly, the bottom gauge showed a dramatic strain reversal at 14.75 kN probably due to breakage of top-ply fibres as a consequence of the initiation of perforation.

3.3.3 Loading rate effect

Figure 3.3.9 shows the delamination area in terms of peak force for 4-mm thick panels with damage induced either by impact or quasi-static loading. As expected, the relationship between transverse peak force and delamination area was similar for both impacted and quasi-statically loaded panels, using a hemispherical-ended indenter. The trend is indicated with a dashed line in Figure 3.3.9. The initial threshold forces for delamination onset were not affected by the loading rate, as shown in Figure 3.3.10. The difference between the two is almost indistinguishable.

The load-displacement response of impact and quasi-static load tests followed a similar pattern as shown in Figure 3.3.11. The quasi-static response curve acted as an upper boundary to the impact response, exhibiting similar slope and threshold for delamination onset. There was a small initial offset between impact and the quasi-static responses which was not expected. In the case of impact, this offset corresponded to an initial displacement of 0.5 mm. Findings in [20] suggested that the dynamic effects might slightly affect the panel response. However, it is more likely that the offset is the result of the presence of noise in the impact data. After approximately 0.5 mm (i.e. 100 μs), the load of all the impact tests started to increase with a similar slope than the quasi-static loading response.

95

3.4 Concluding remarks

The impact response of all the panels tested showed some degree of damage generation, since the maximum force was higher than the initial threshold force. The amount of damage generated can be related with the proportion in which the force threshold has been exceeded, as shown in Figure 3.3.12. Quasi-static loaded panels also showed an initial threshold force; beyond this force level the bending stiffness was significantly reduced. The value of the threshold depended on panel thickness and on the indenter-nose shape. Damage propagation was more catastrophic for flat-ended than for hemispherical-ended indenters. The main types of damage identified after C-scan and cross section were dependent on the internal stress distribution resulting from the applied contact pressure at the indenter/laminate area. These main damage mechanisms were internal delamination, matrix cracks, fibre breakage and local change of geometry.

The relationship between AE and delamination area is linear up to the level of fibre breakage onset. Then the fibre breakage process absorbs a significant amount of the IKE, having an exponential increasing trend with the IKE. However the energy necessary for delamination area generation increases linearly with the IKE, irrespectively of the existence of fibre breakage.

Panel thickness determined the flexural rigidity of the panel that in turn dictated the governing damage mechanism (either membrane or ILSS governed), the size of delamination, the energy absorption characteristics and the damage generation sequence. Panel thickness also determined the significance of local indentation process on the overall panel deformation. The damage generation was not strain-rate dependent. Quasi-static loading and impact loading showed similar features in the force-displacement response of the panel such as slope and initial threshold force for delamination onset.

96
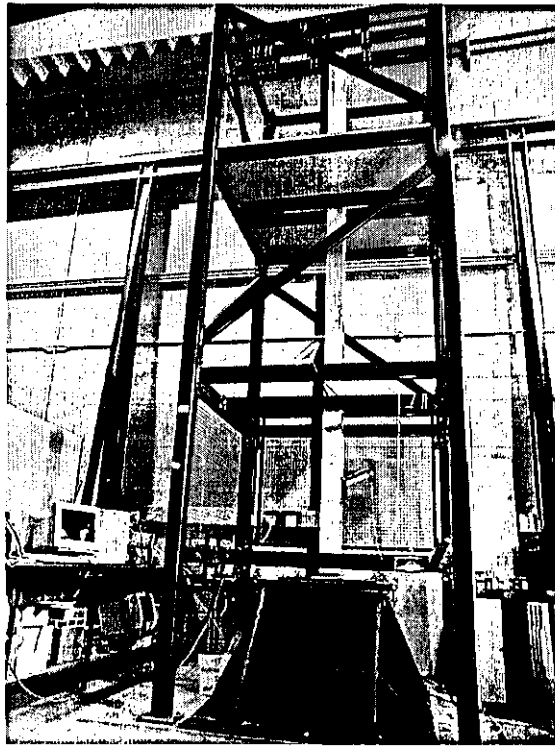
Figure 3.1.1 Photograph of the drop-weight impact rig
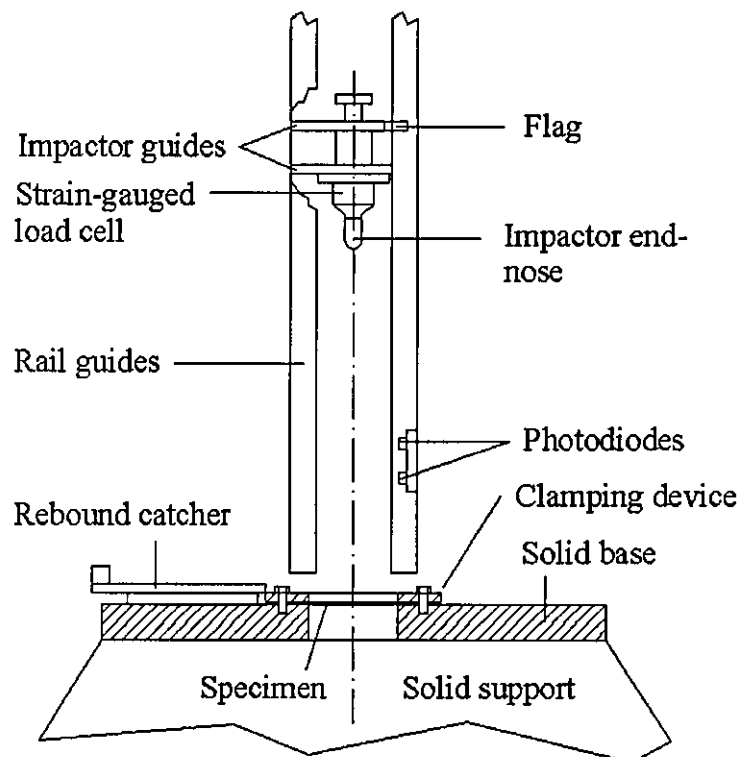
Figure 3.1.2 Drop-weight impact test rig set-up

97
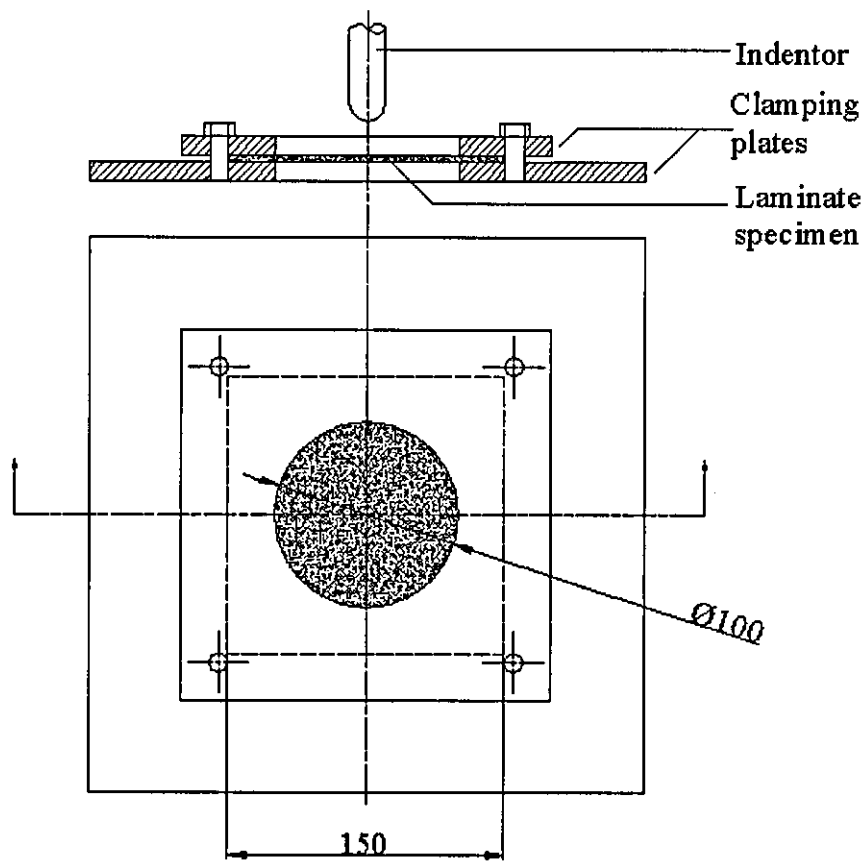
Figure 3.1.3   Specimen clamping arrangement for impact and quasi-static tests
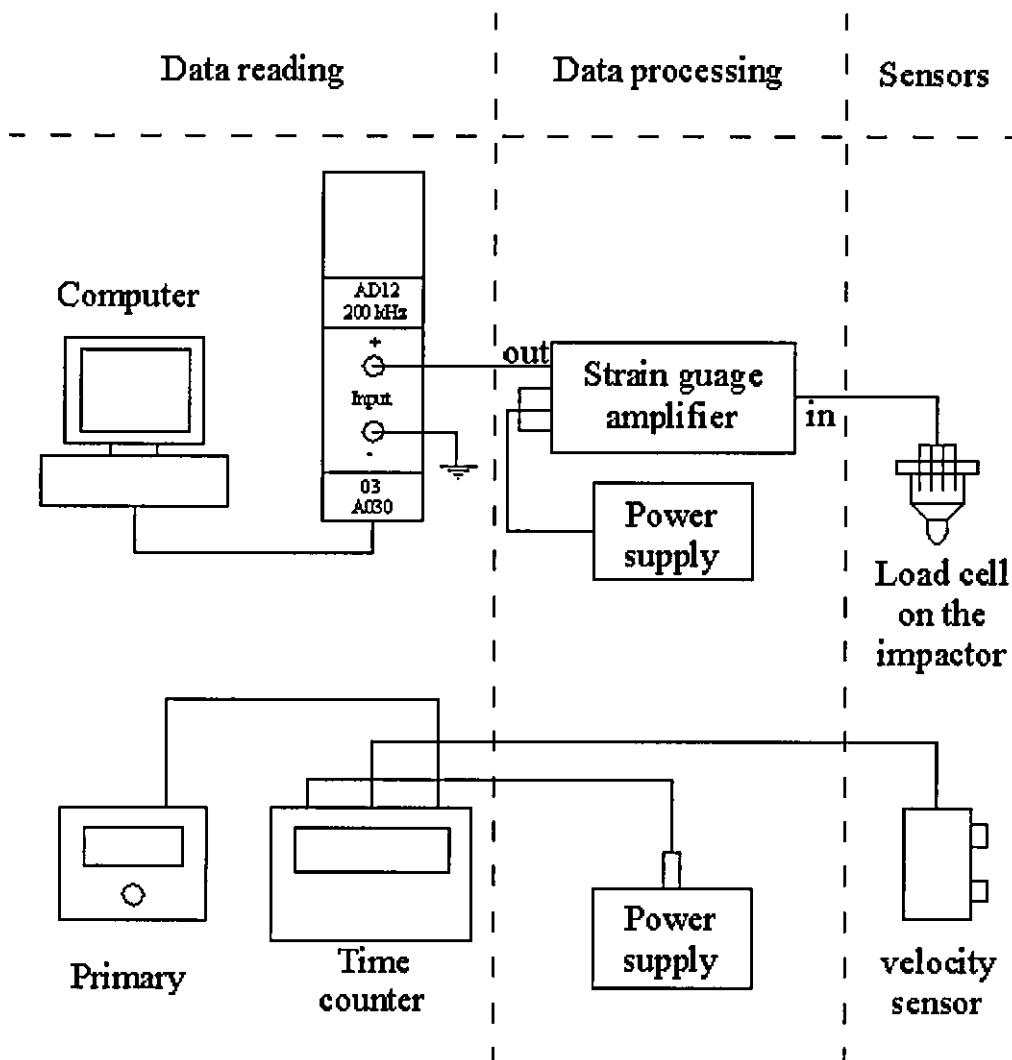
Figure 3.1.4 Impact test connection layout

All the dimensions in mm
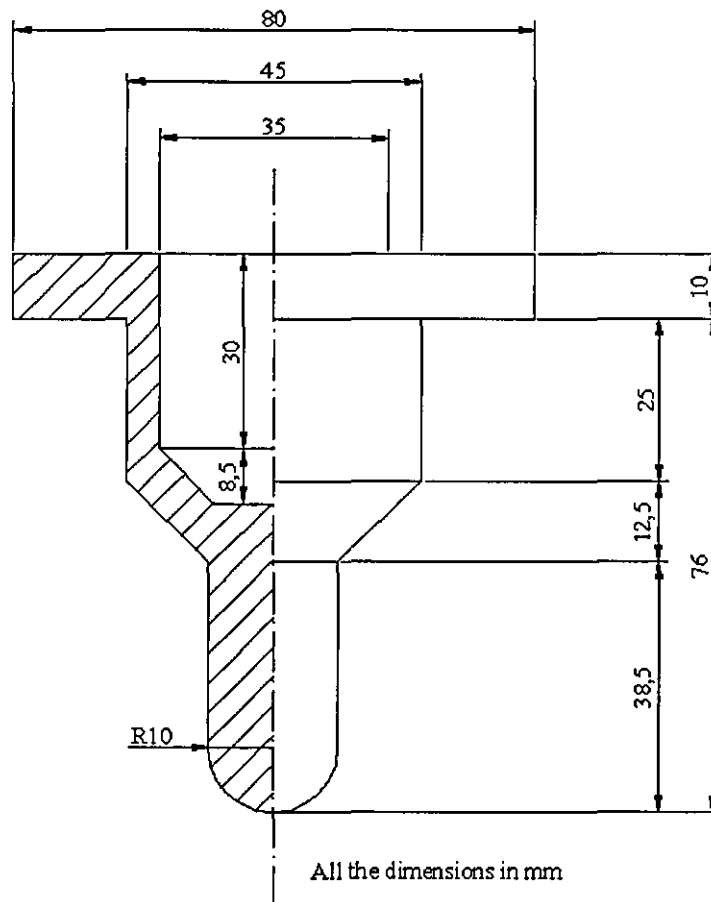
Figure 3.1.5 Impactor end-nose section and strain gauged load cell section dimensions, after modification

y=0.128x + 0.19
1kN = 7.79mV
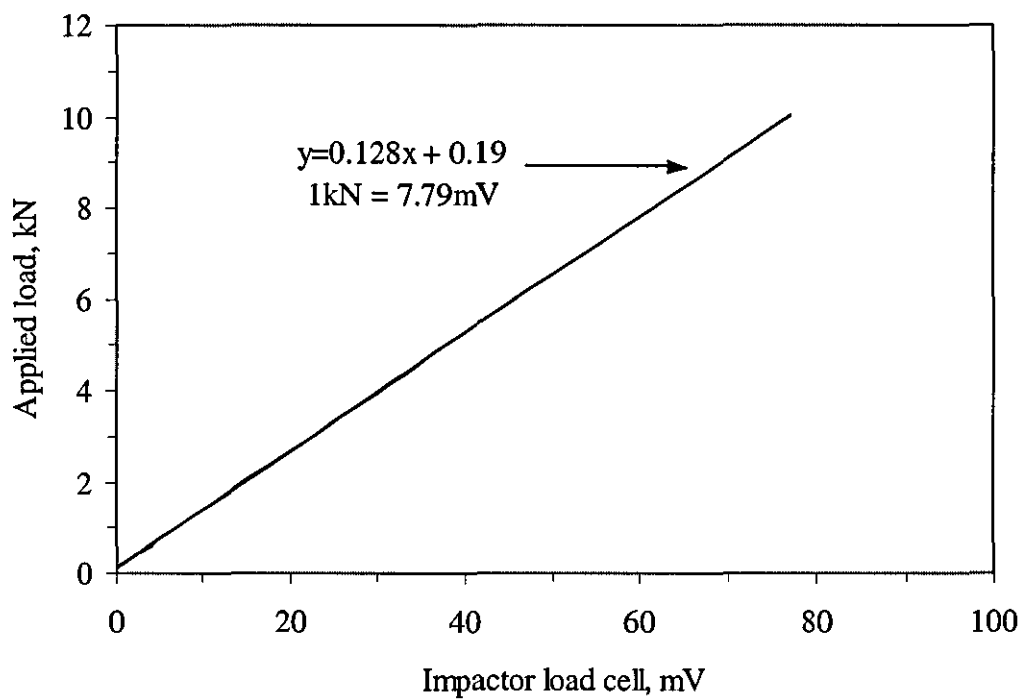
Figure 3.1.6 Impact load cell calibration curve
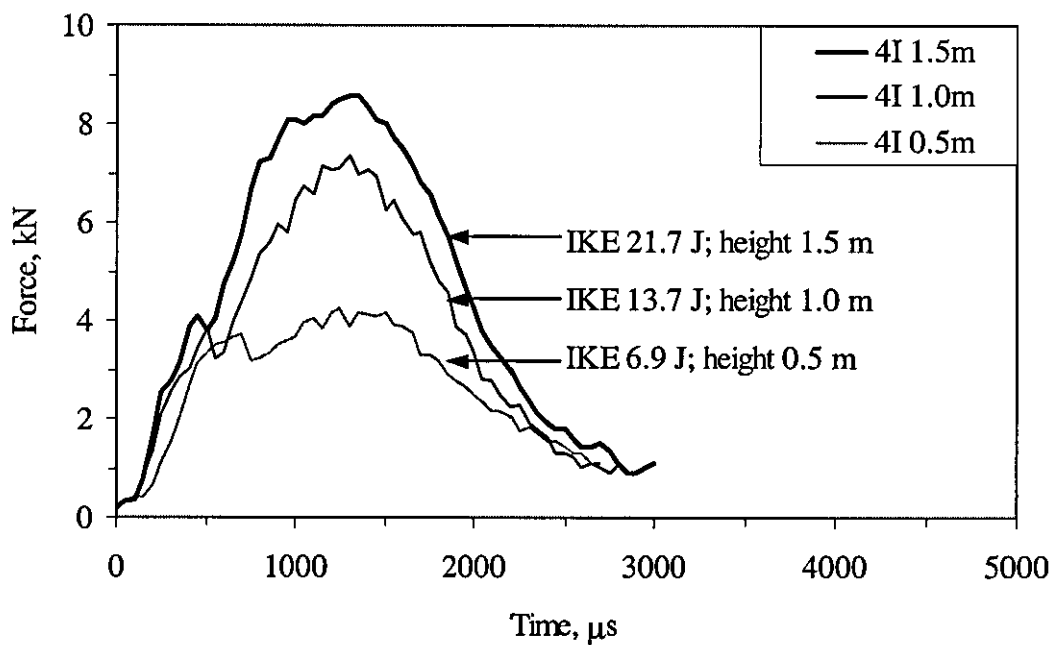
Figure 3.1.7 Force history curves for 4-mm thick panels impacted at 6.9, 13.7 and 21.1J

(a)

(b)

(c)

102
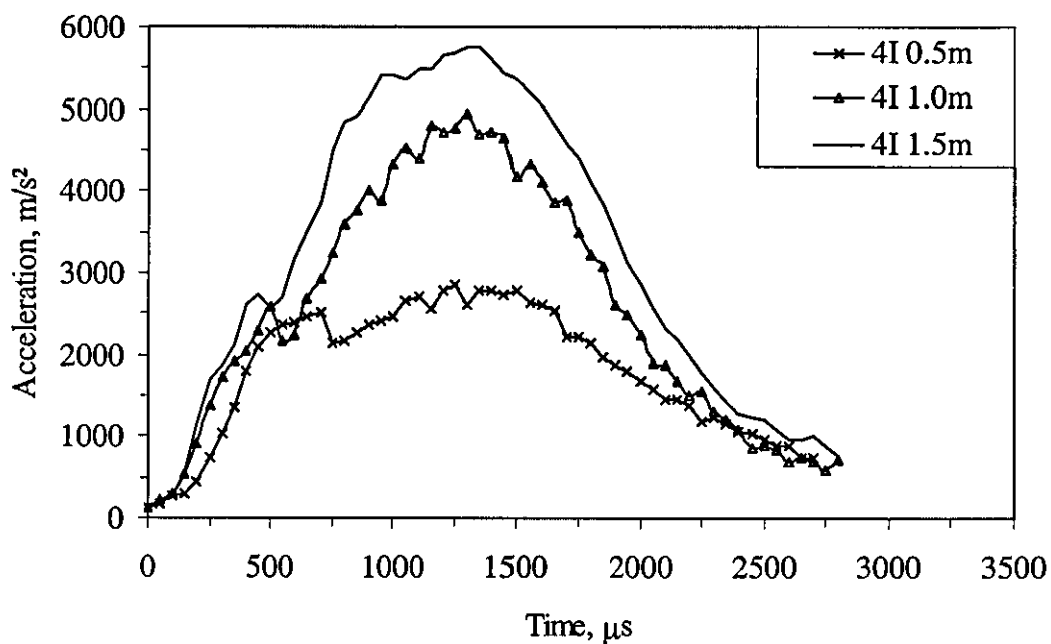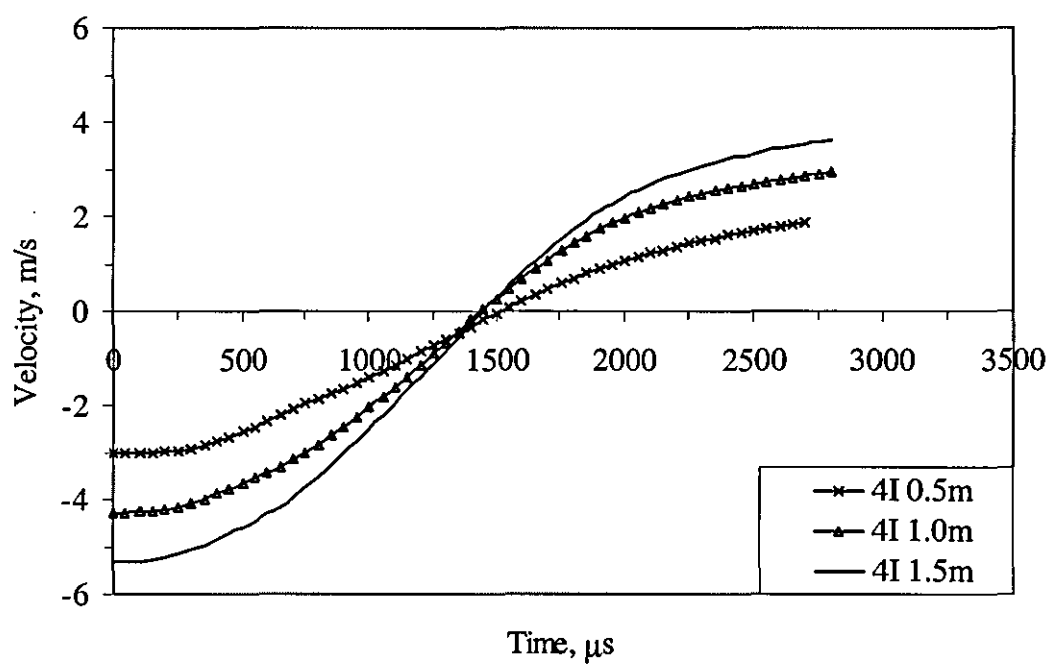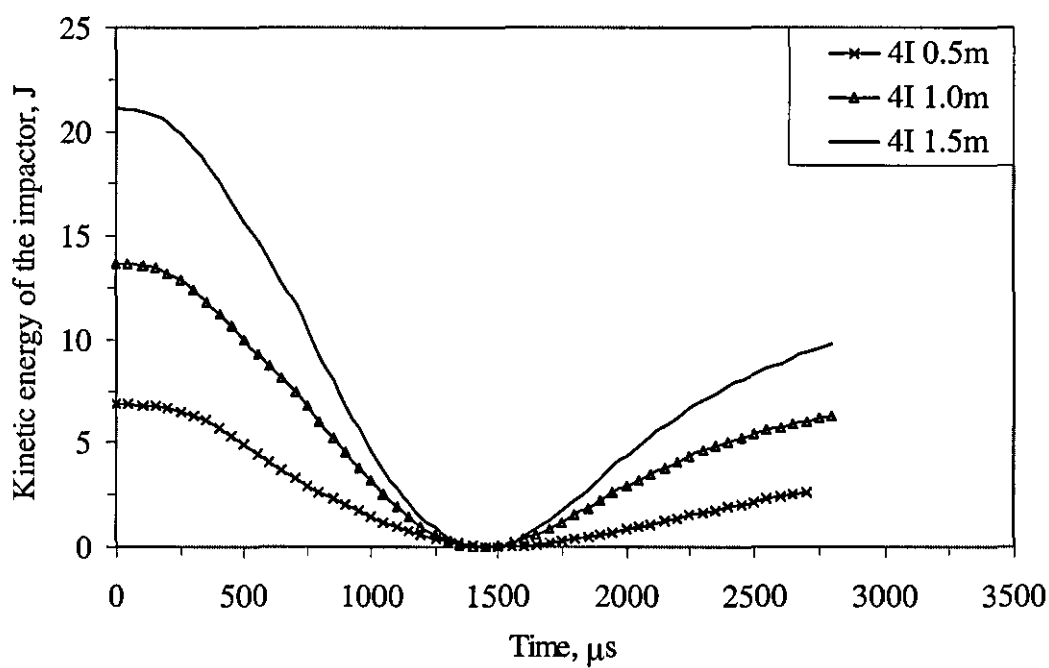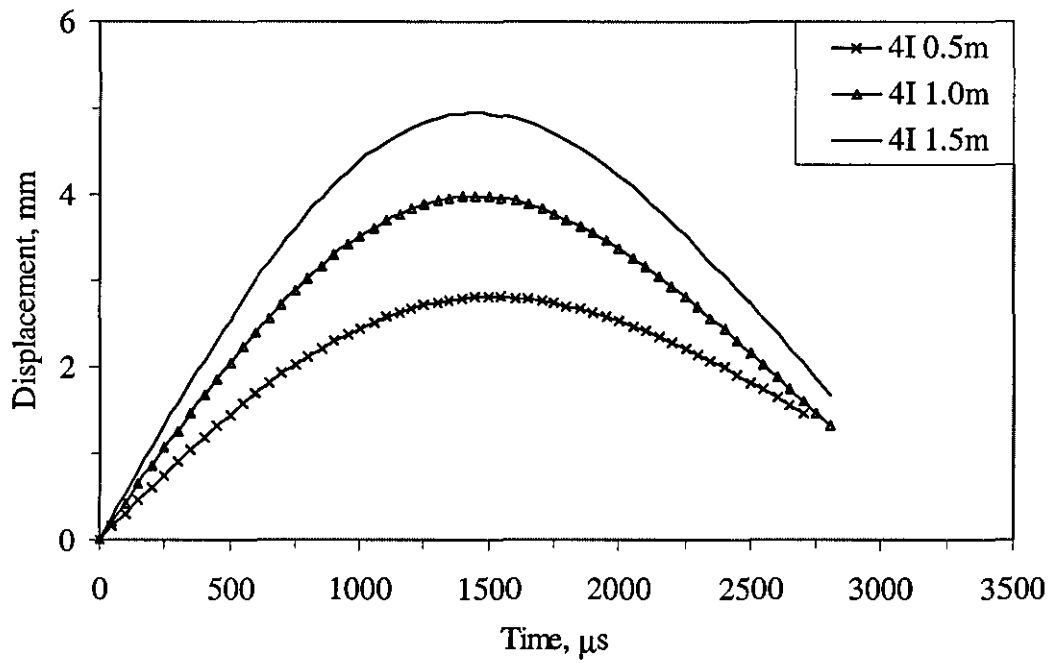
(d)

Figure 3.1.8 (a) Acceleration, (b) velocity, (c) impactor kinetic energy and (d) displacement history curves of 4-mm thick panels impacted at 6.9 J (4I 0.5m), 13.7 J (4I 1.0m) and 21.1 J (4I 1.5m)
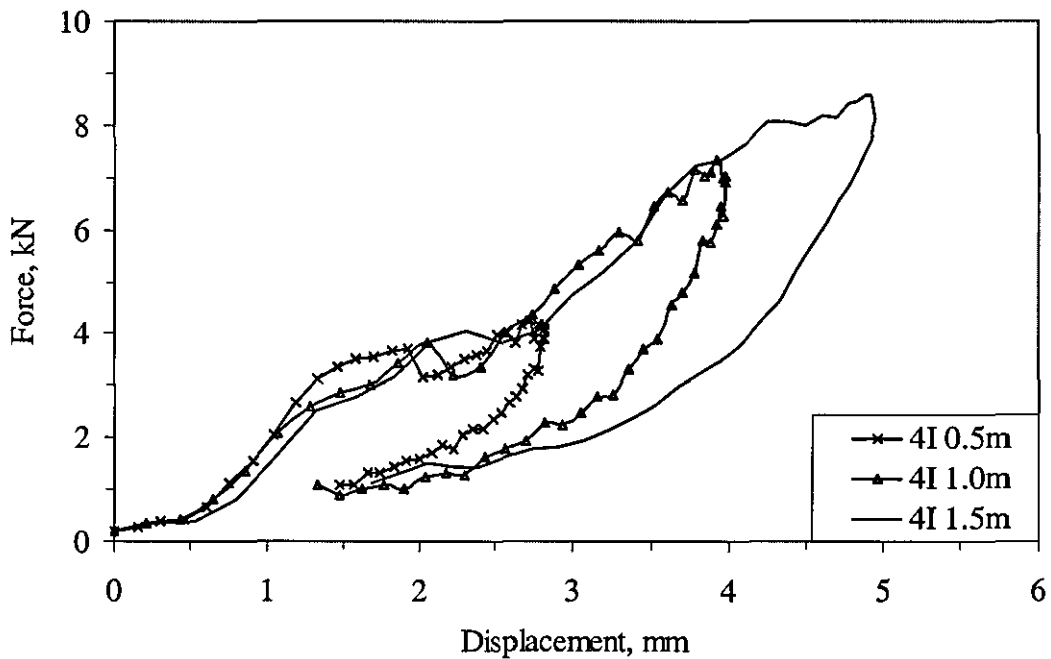
Figure 3.1.9 Load-displacement curve of 4-mm thick panels impacted at 6.9 J (4I 0.5m), 13.7 J (4I 1.0m) and 21.1 J (4I 1.5m)

103

(a)

(b)

104
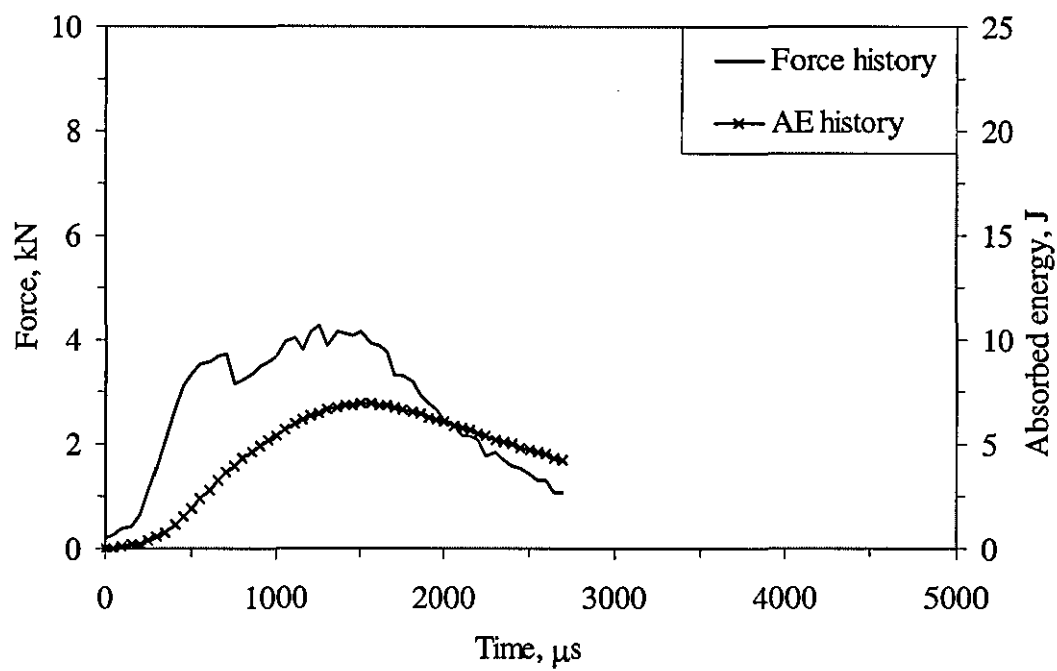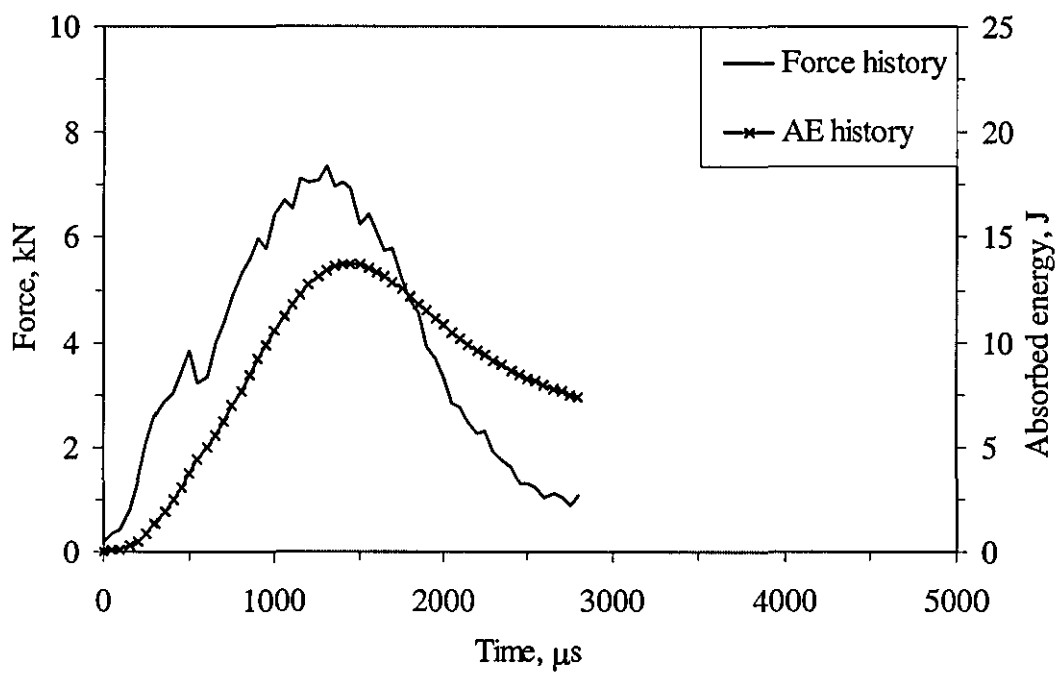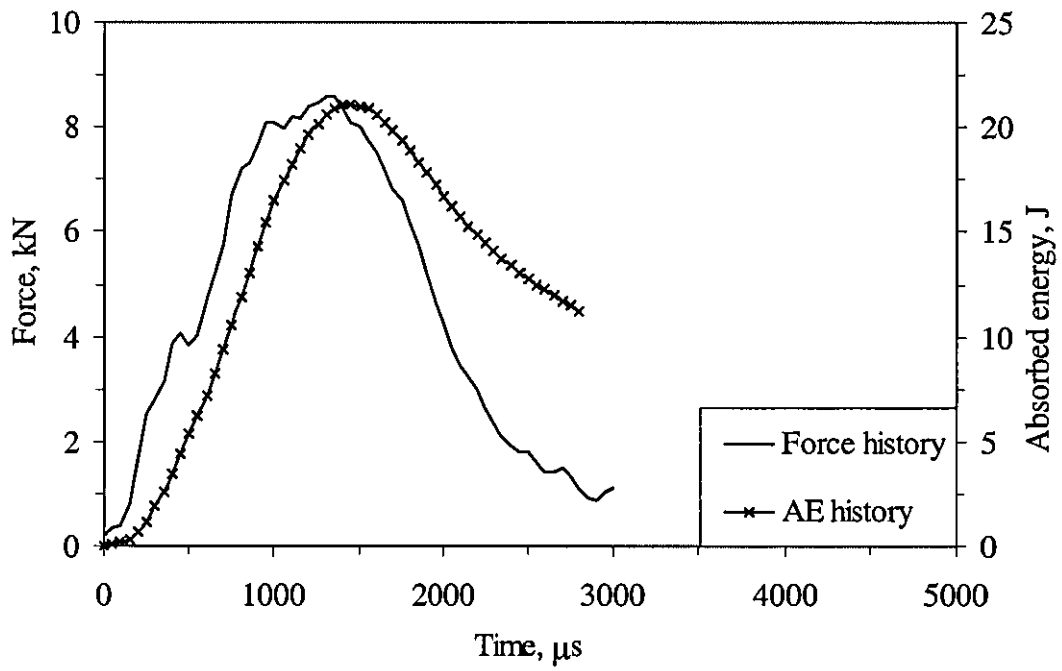
(c)

Figure 3.1.10 Absorbed energy (AE) and force histories of 4-mm thick panels impacted
at (a) 6.9 J (4I 0.5m) (b) 13.7 J (4I 1.0m) and (c) 21.1 J (4I 1.5m)
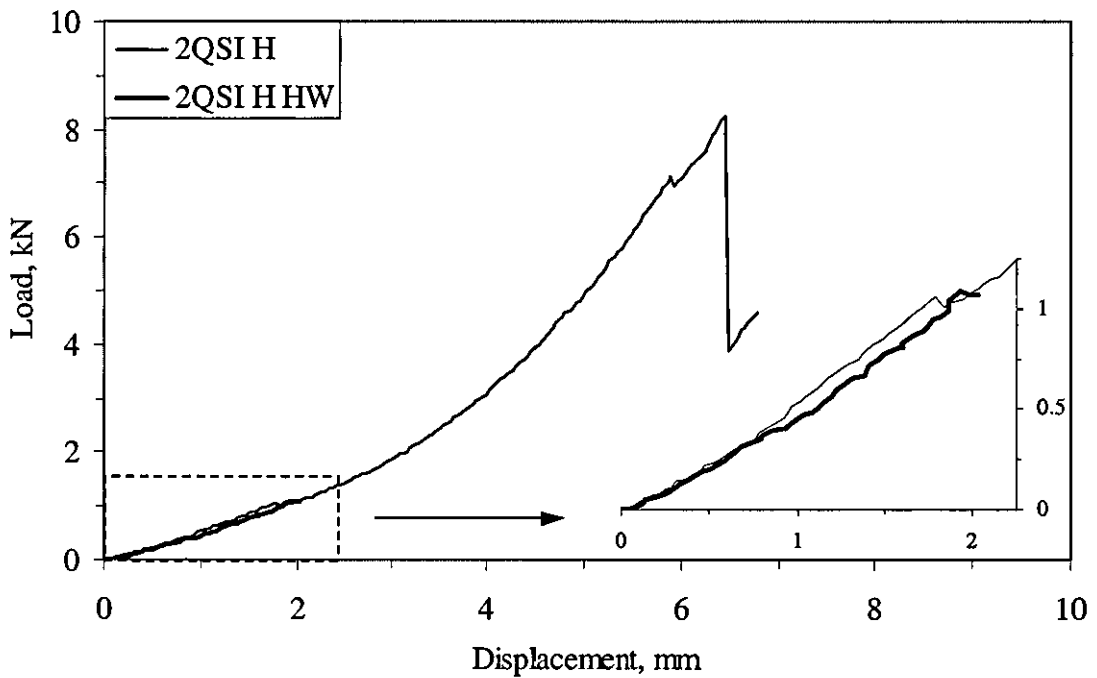
Figure 3.1.11 Force-displacement curve for 2-mm thick panels quasi-statically loaded
with a hemispherical-ended indenter
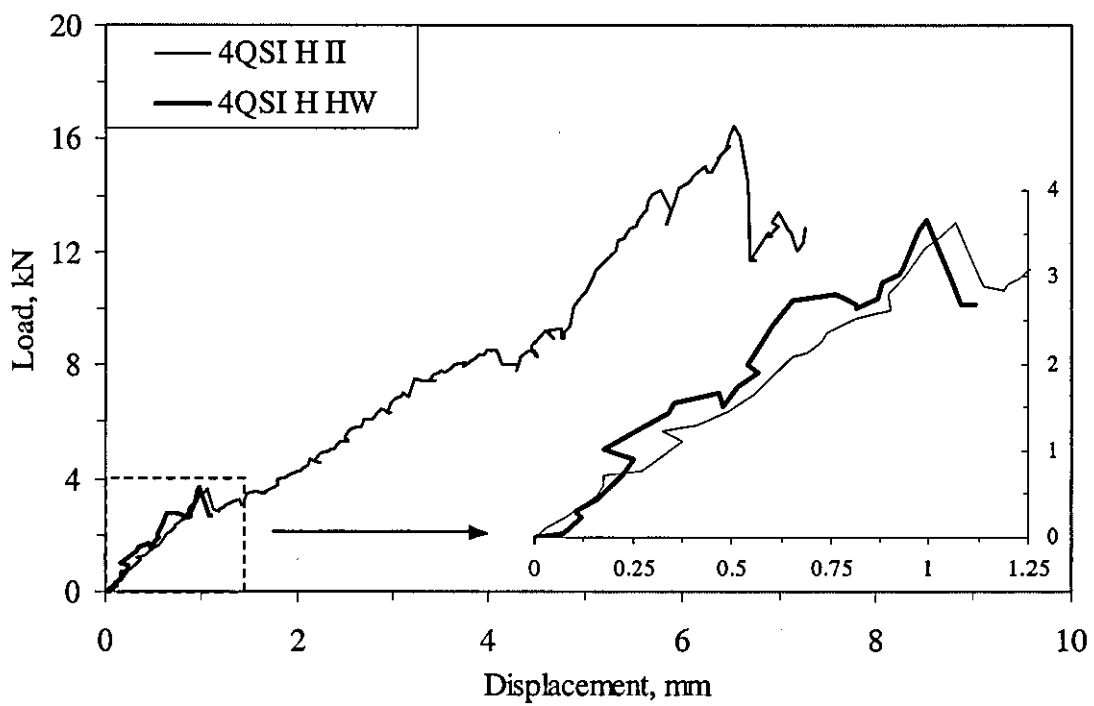
(a)
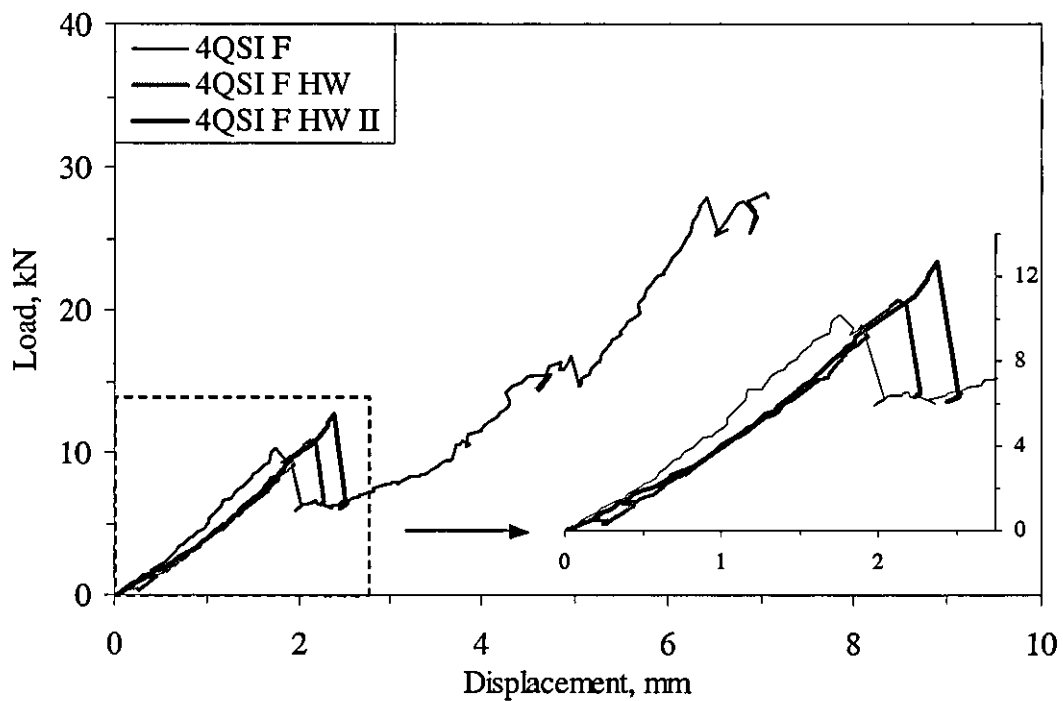
(b)

Figure 3.1.12 Force-displacement curve for 4-mm thick panels quasi-statically loaded
with a (a) hemispherical-ended and (b) flat-ended indenter

106
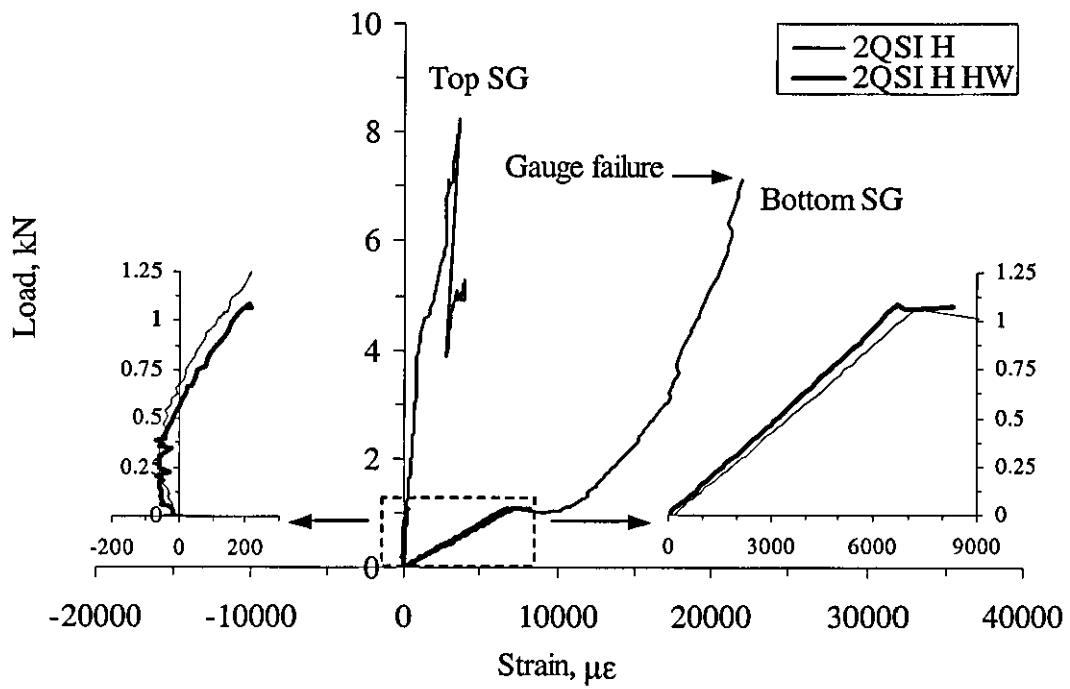
Figure 3.1.13 Force-strain response from 2-mm thick panels quasi-statically loaded
with a hemispherical-ended indenter
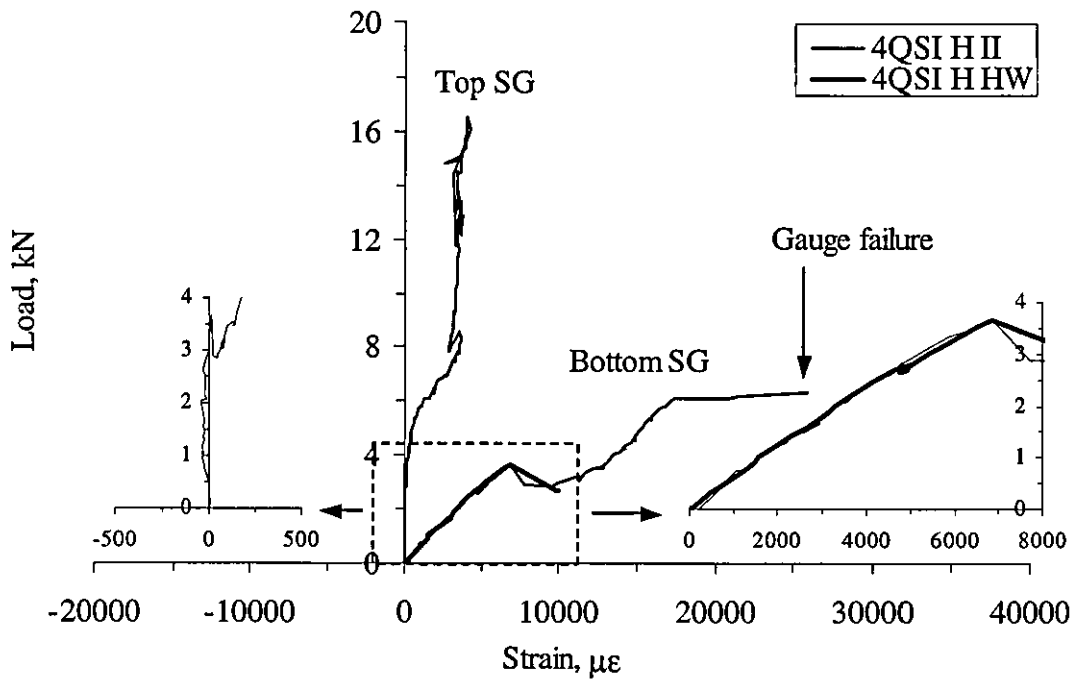
(a)
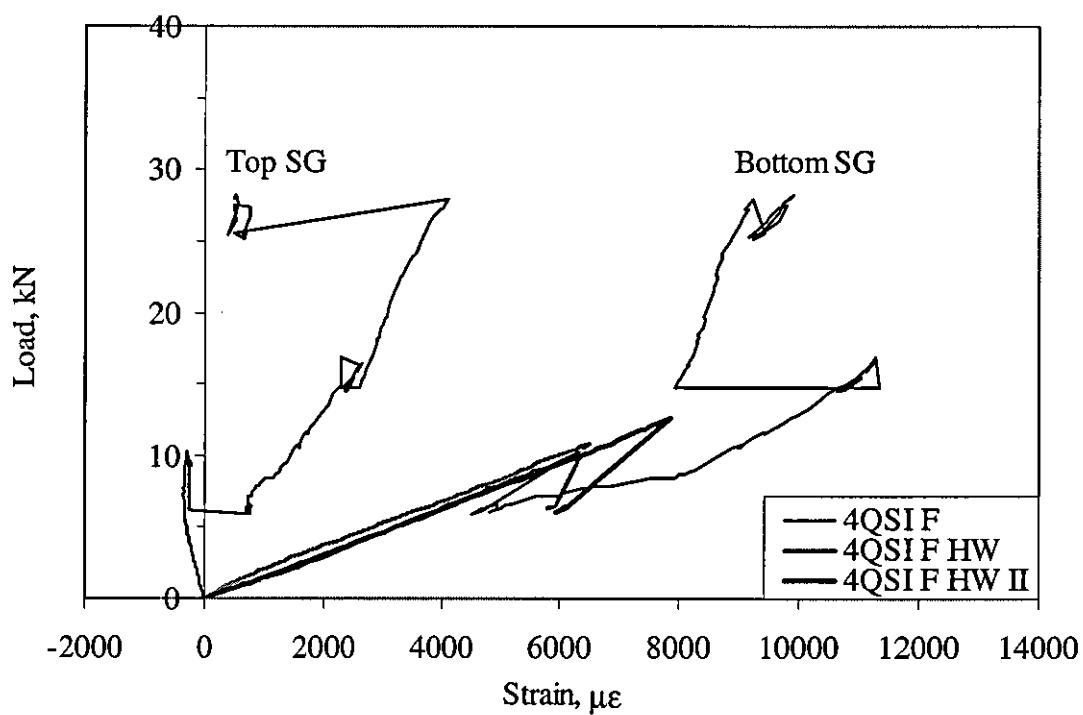
(b)

Figure 3.1.14 Force-strain response curves from 4-mm thick panels quasi-statically loaded with a (a) hemispherical-ended and (b) flat-ended indenter
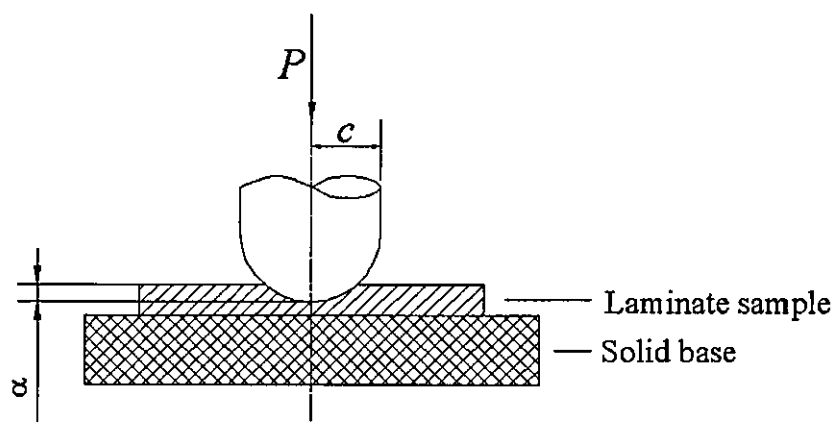
Figure 3.1.15 Quasi-static indentation test for contact stiffness determination
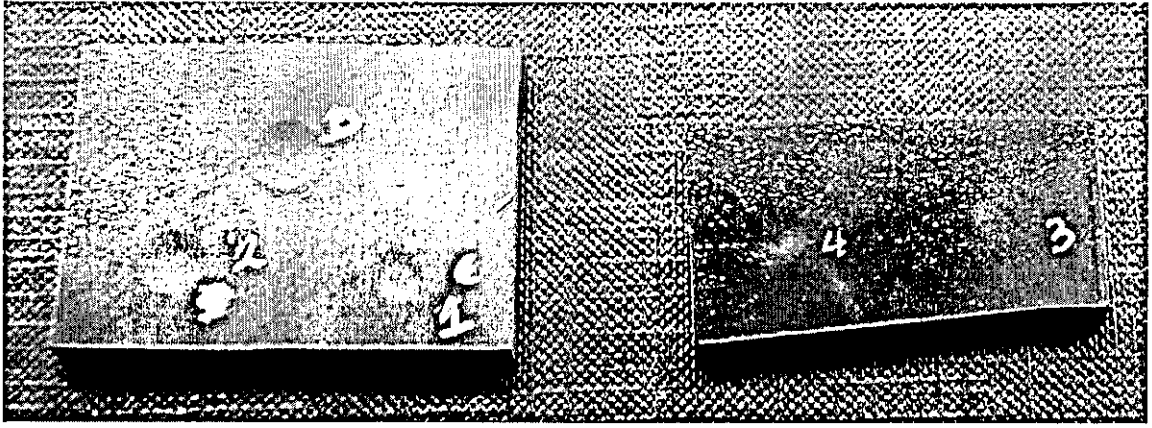
Figure 3.1.16 Photographs of quasi-static indentation test specimens
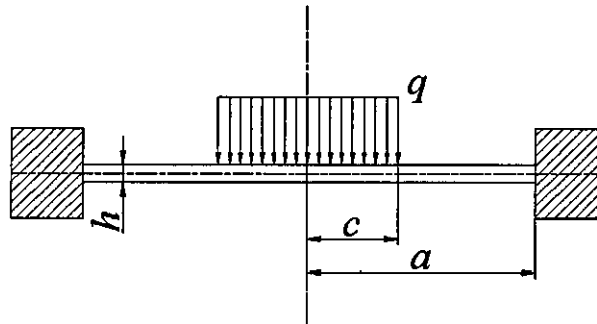
Figure 3.1.17 Circular plate uniformly loaded over a concentric area

| (a) | (b) |
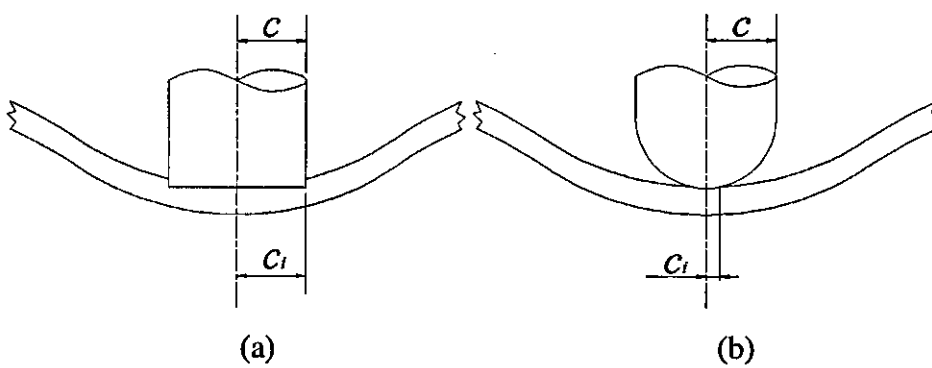
Figure 3.1.18 Indentation radius for (a) flat and (b) hemispherical indenter
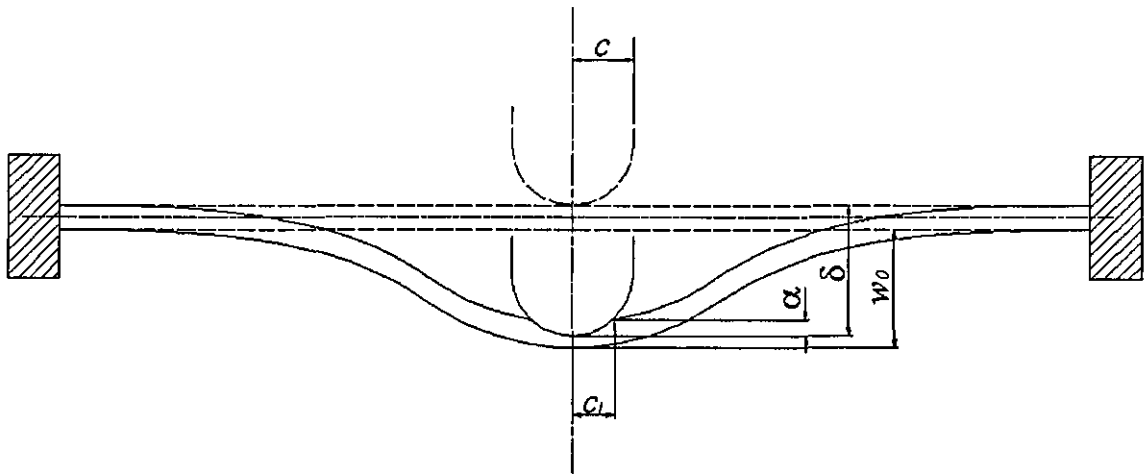
Figure 3.1.19 Local indentation process for hemispherical indenter
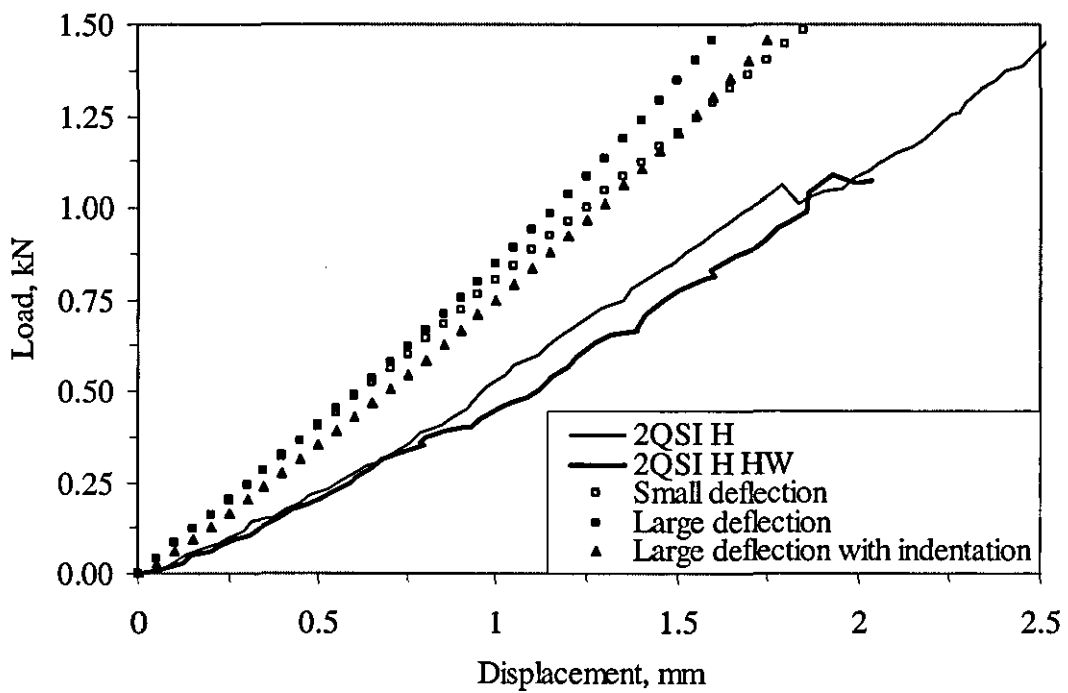
Figure 3.1.20 Force-displacement predictions for central deflection of a 2-mm thick, 100-mm diameter panel loaded with a hemispherical indenter using small deflection, large deflection and large deflection with indentation models
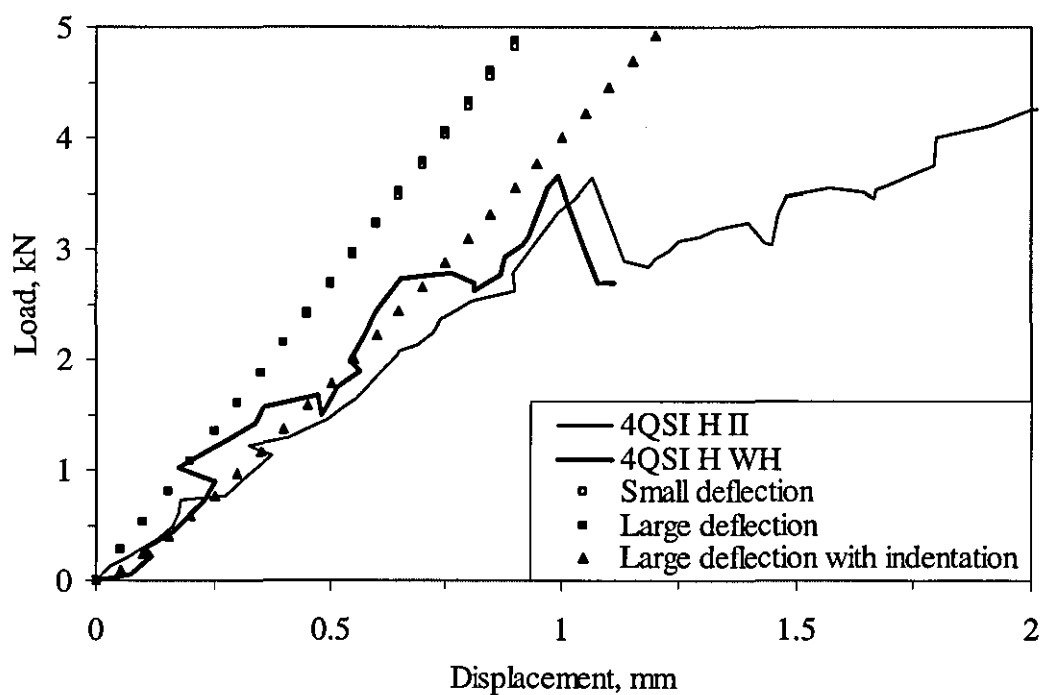
(a)
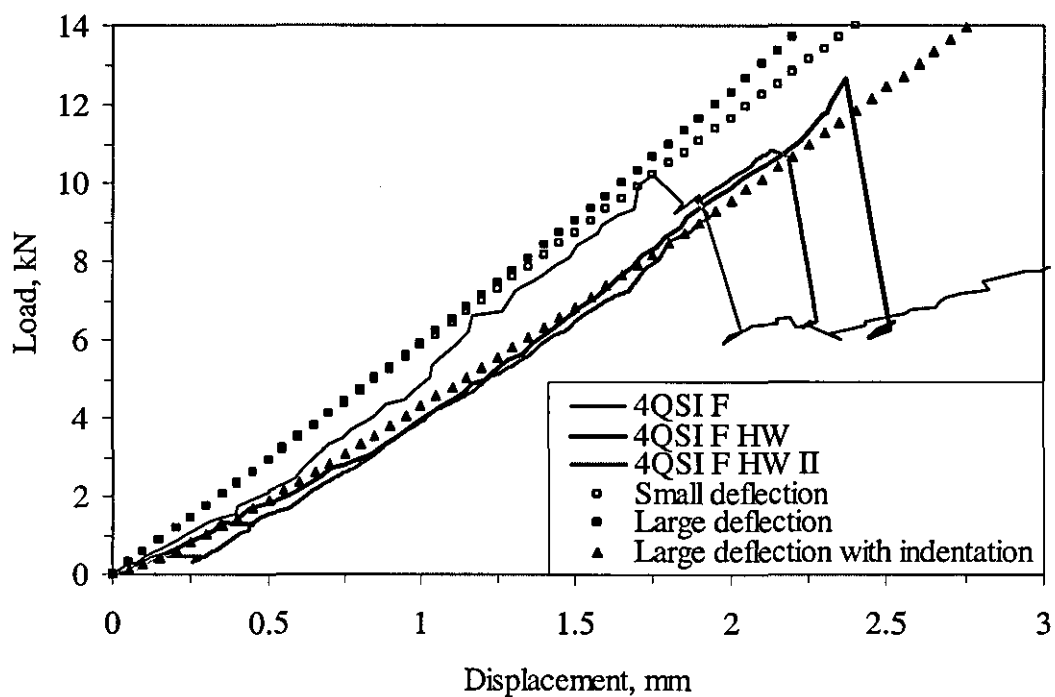
(b)

Figure 3.1.21 Force-displacement predictions for central deflection of a 4-mm thick,
100-mm diameter panel loaded with a (a) hemispherical and (b) flat indenters, using
small deflection, large deflection and large deflection with indentation models

111
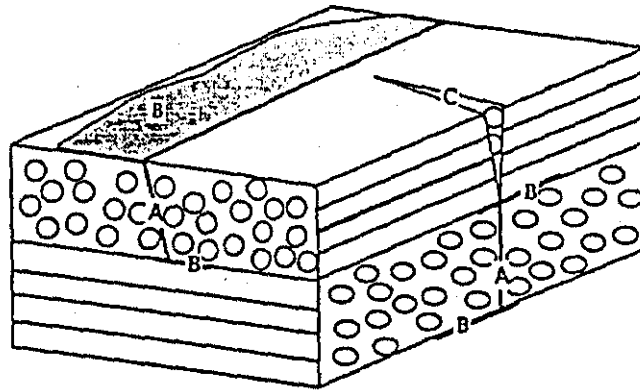
Figure 3.2.1 Three basic damage modes of composite laminates:
A, matrix cracking; B, delamination; C, fibre breakage
(Taken from [10])

Impact location

0   2   4 mm

Major delaminations
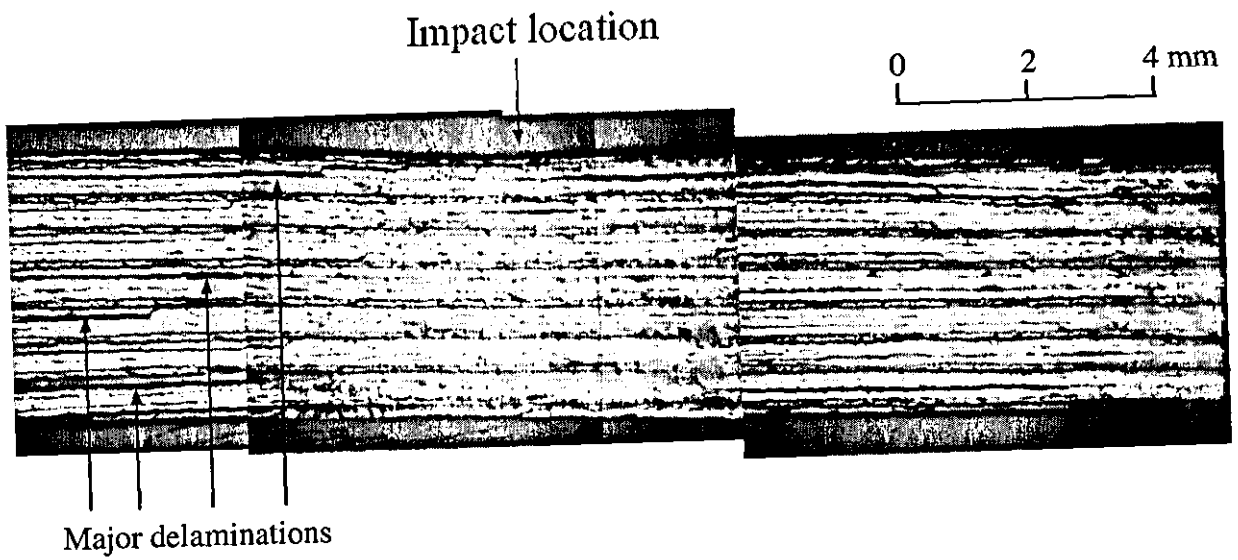
(a)
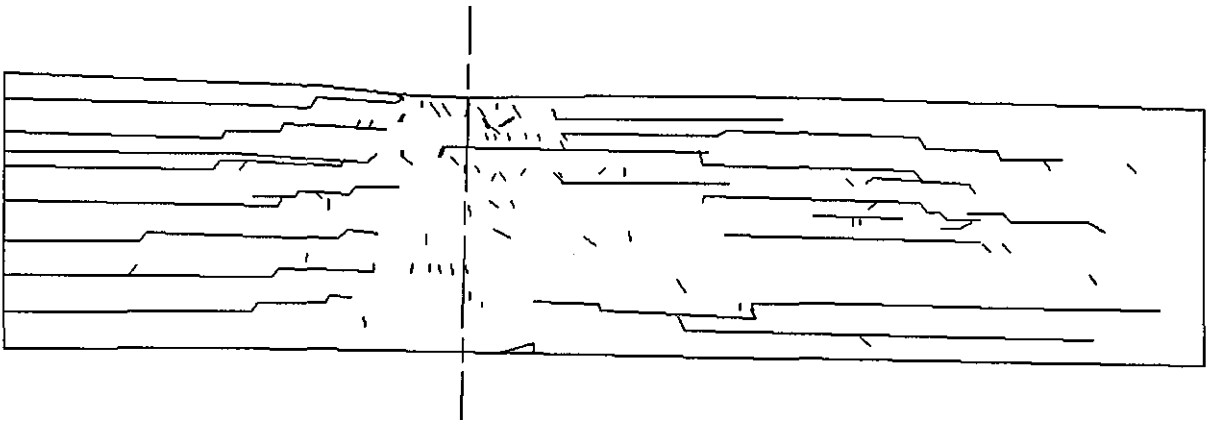
(b)
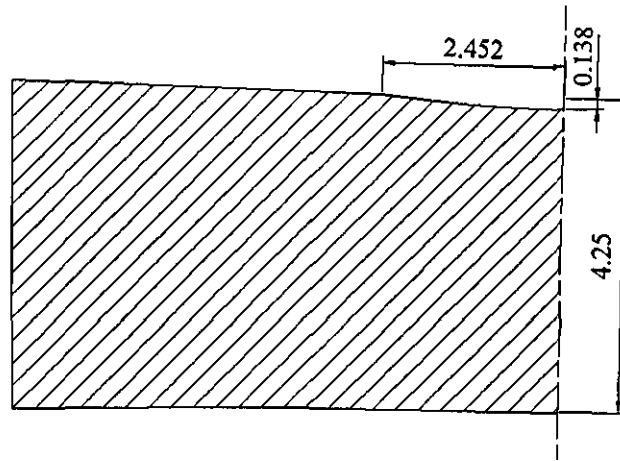
(c)

Figure 3.2.2 Microscopic analysis of a 4-mm thick panel impacted at 28J
(a) micrograph, (b) sketch indicating delaminations and (c) dimensions of local
curvature change

Delamination   (a)

(b)
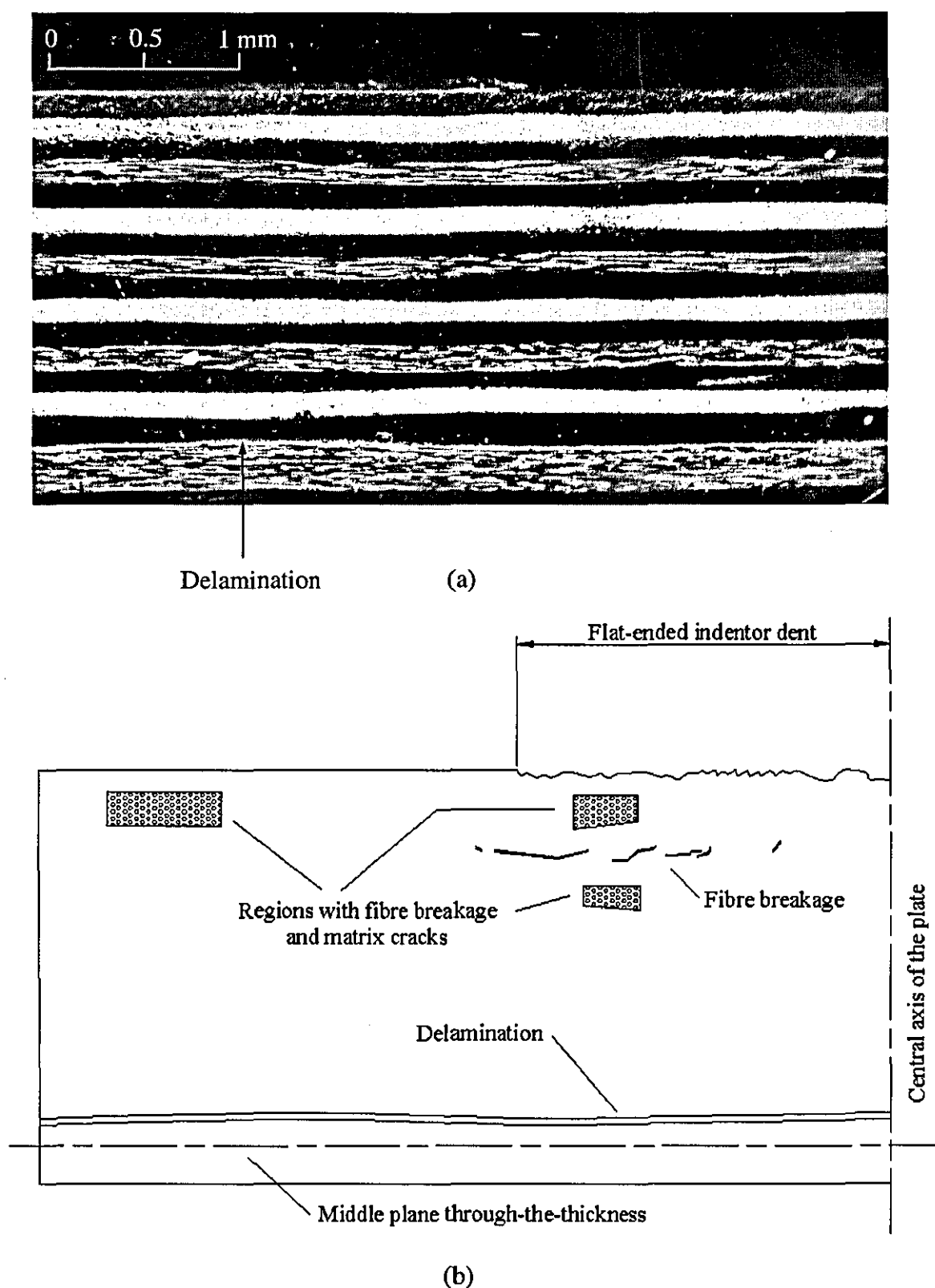
Figure 3.2.3 Micrograph cross section from 4-mm thick panel quasi-statically loaded halfway with flat-ended indenter, (a) micrograph and (b) sketch for analysis

114

(a)   (b)

(c)
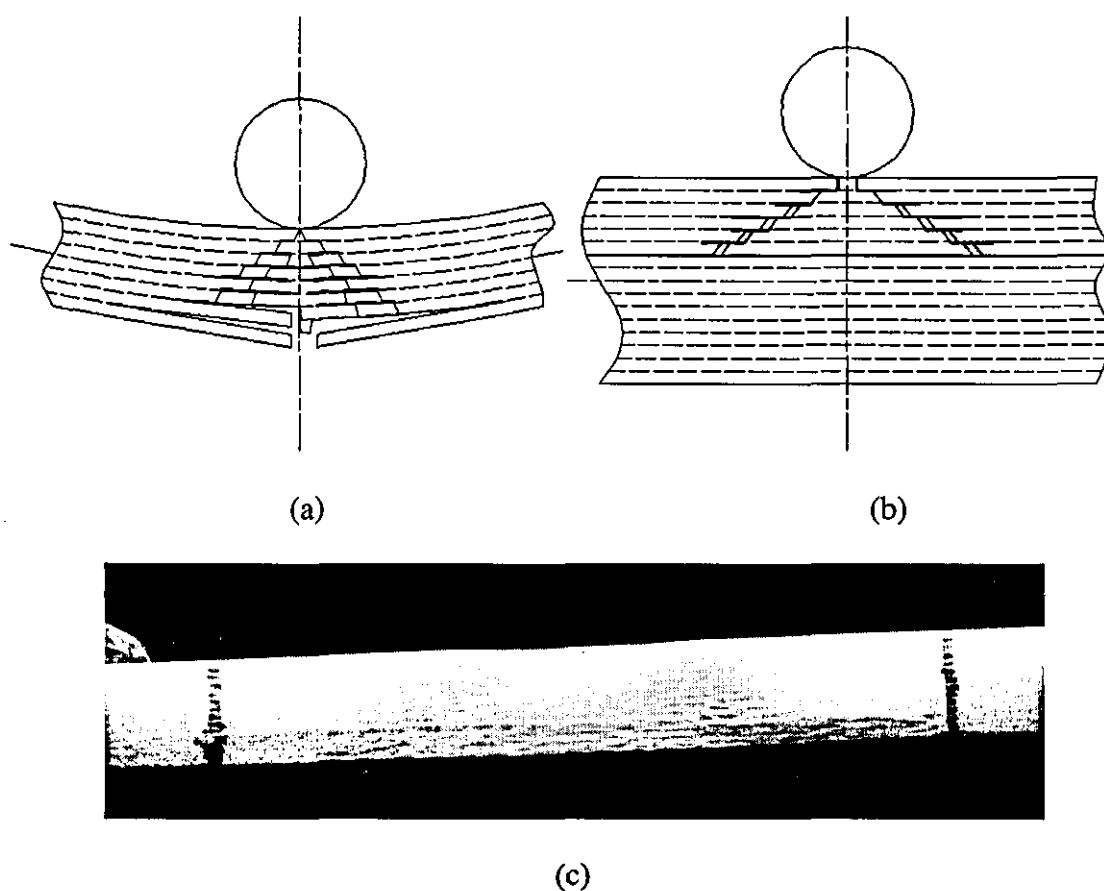
Figure 3.2.4 Damage development in (a) flexible target, (b) rigid target and (c)
photograph of damage in rigid target (unpublished work from Zhou, G., 2004)

— — — — — Classical theory
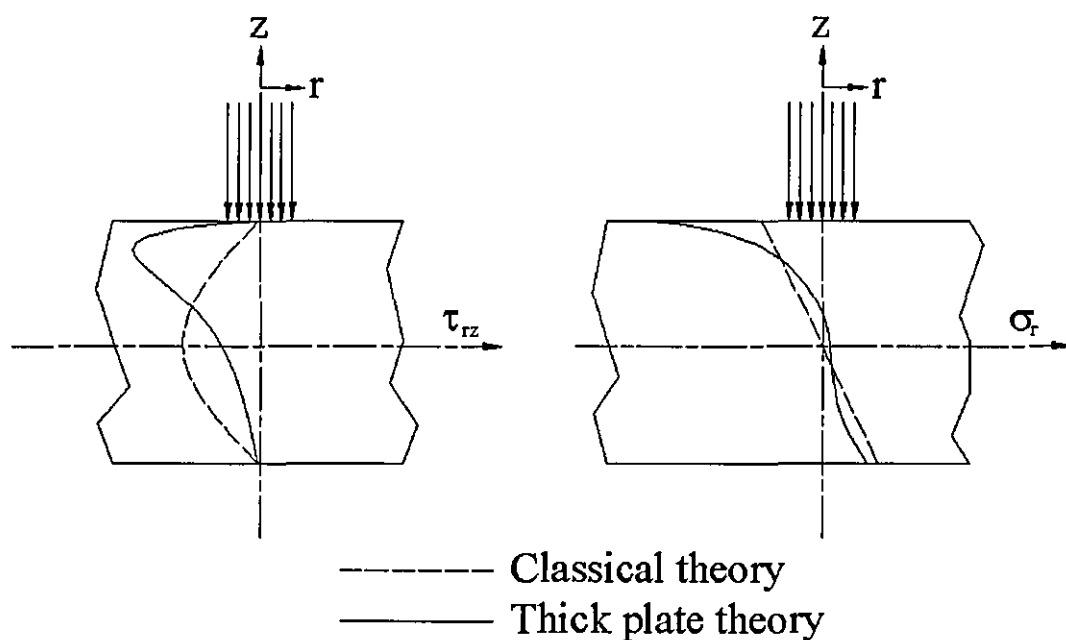
——————— Thick plate theory

Figure 3.2.5 Shear and normal stress distribution for classical plate theory
and thick plate theory with transverse shear and stress concentration effects

115
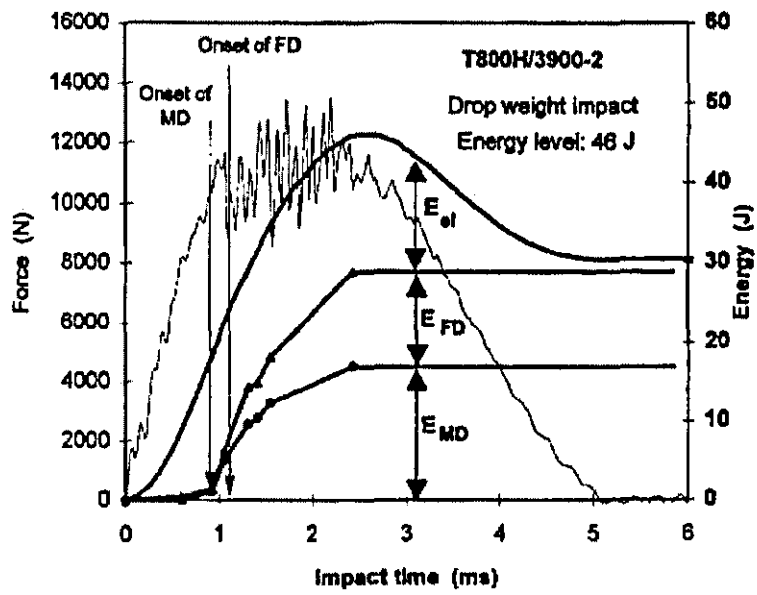
Figure 3.2.6 Breakdown of energy absorption or storage by each mechanism as a function of time for an impact test at 46 J on a tough laminate (taken from [41])

(a)2I 0.125m   (b)2I 0.250m   (c)2I 0.375m

(d)2I 0.5m   (e)2I 0.625m   (f)2I 0.75m

(g)2I 1.0m   (h)2I 1.125m
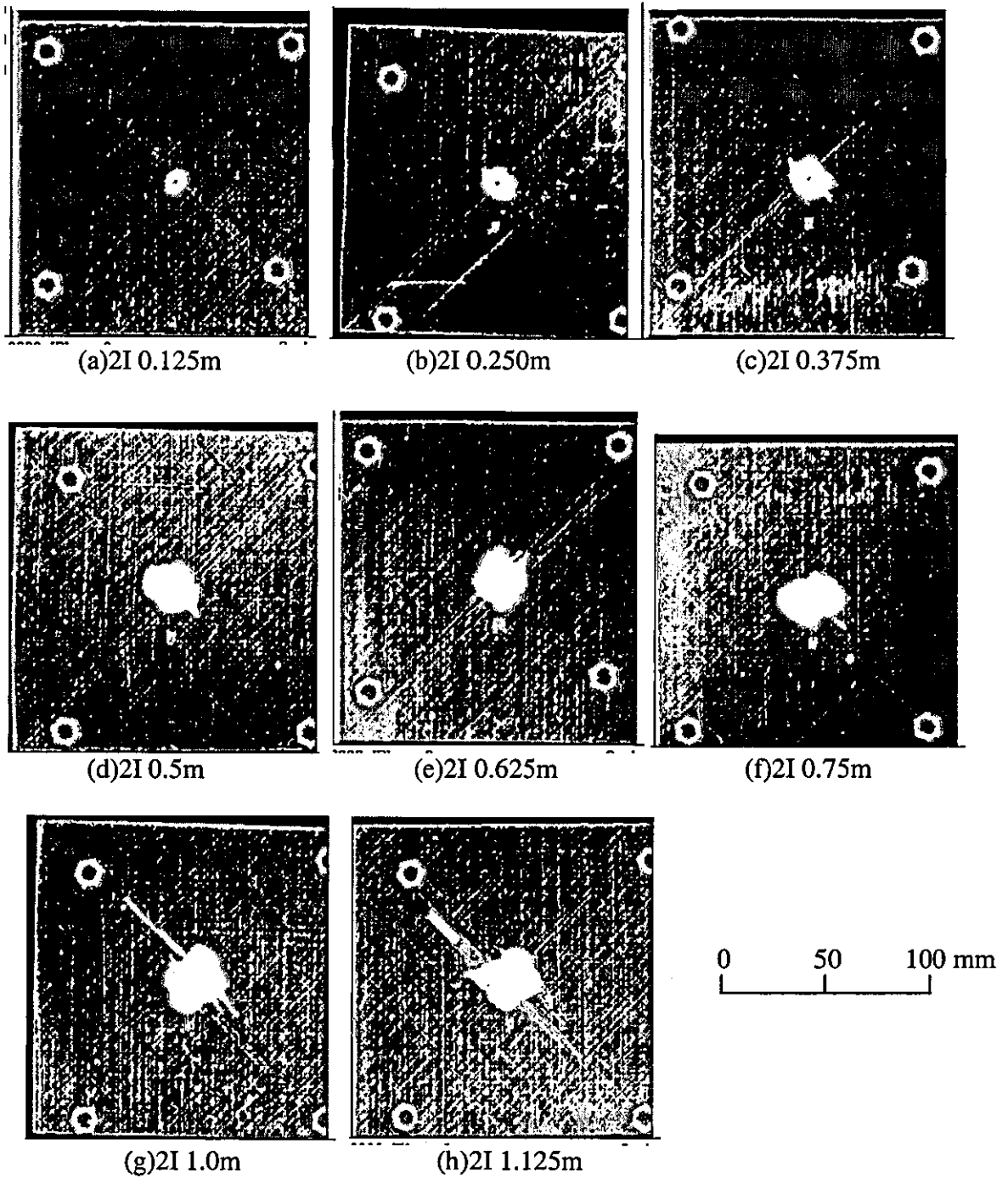
0   50   100 mm

Figure 3.3.1 C-scan graphs for 2-mm thick panels with impact-induced damage for (a) 1.7 J, (b) 3.7 J, (c) 5.7 J, (d) 7.8 J, (e) 9.9 J, (f) 11.8 J, (g) 15.8 J and (h) 19.6 J IKE levels [104]

117
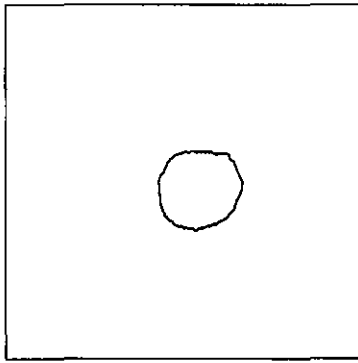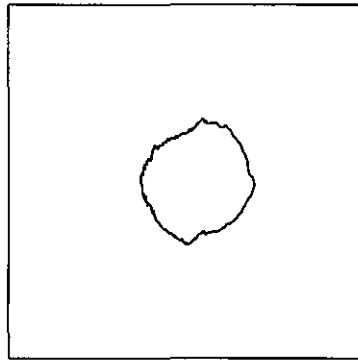
(a)4I 0.5m   (b) 4I 1.0m   (c) 4I 1.5m
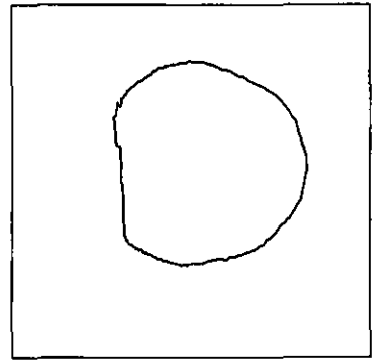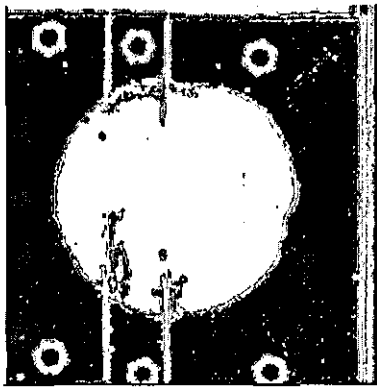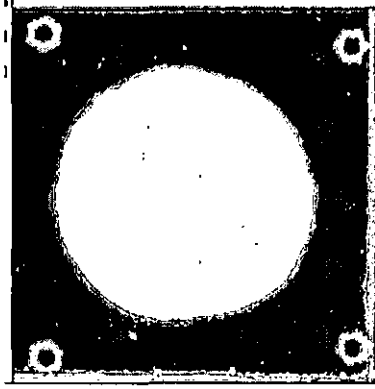
0   50   100 mm

(d) 4I 1.68m   (e) 4I 2.52m

Figure 3.3.2 C-scan graphs for 4-mm thick panels with impact-induced damage for
(a) 6.9 J, (b) 13.7 J, (c) 21.1 J, (d) 27.3 and (e) 41.7 J IKE levels

(a) QSIH HW

(b) QSIF

(c) QSIF HW

(d) QSIF

0   50   100 mm
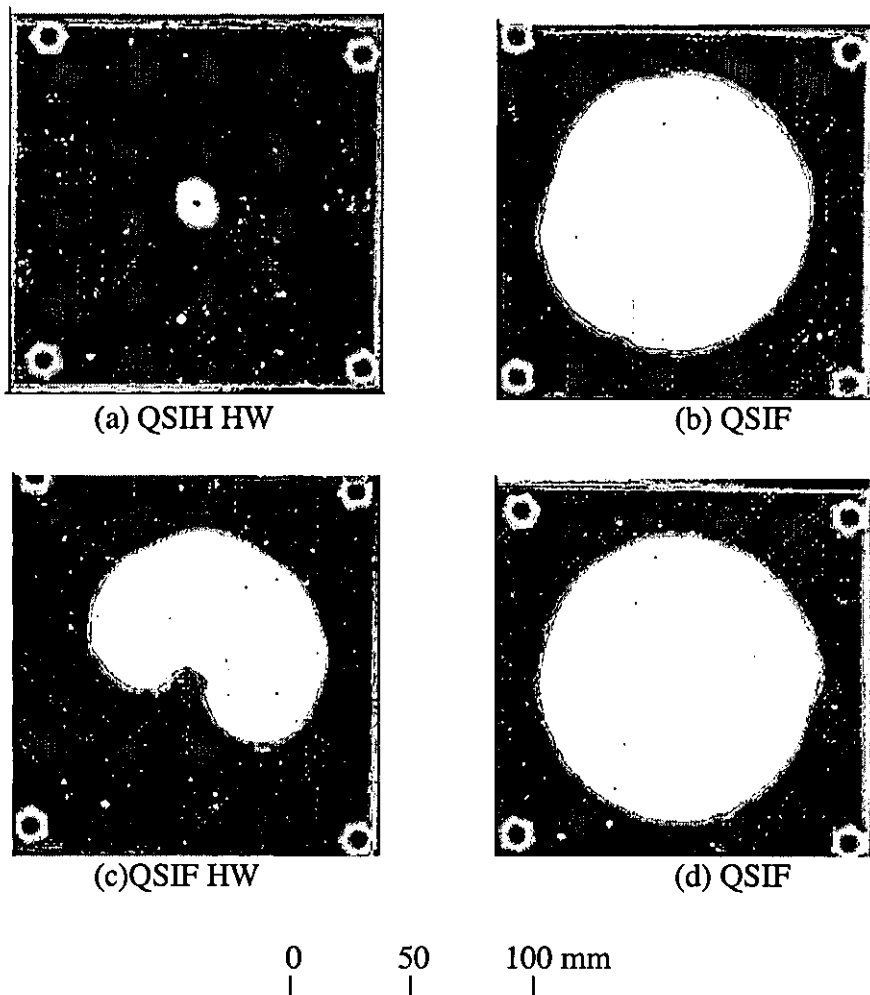
Figure 3.3.3 C-scan graphs for 4-mm thick panels with quasi-static loading induced damage for (a) hemispherical-ended partially loaded, (b) hemispherical-ended fully loaded, (c) flat-ended partially loaded and (d) flat-ended fully loaded

119
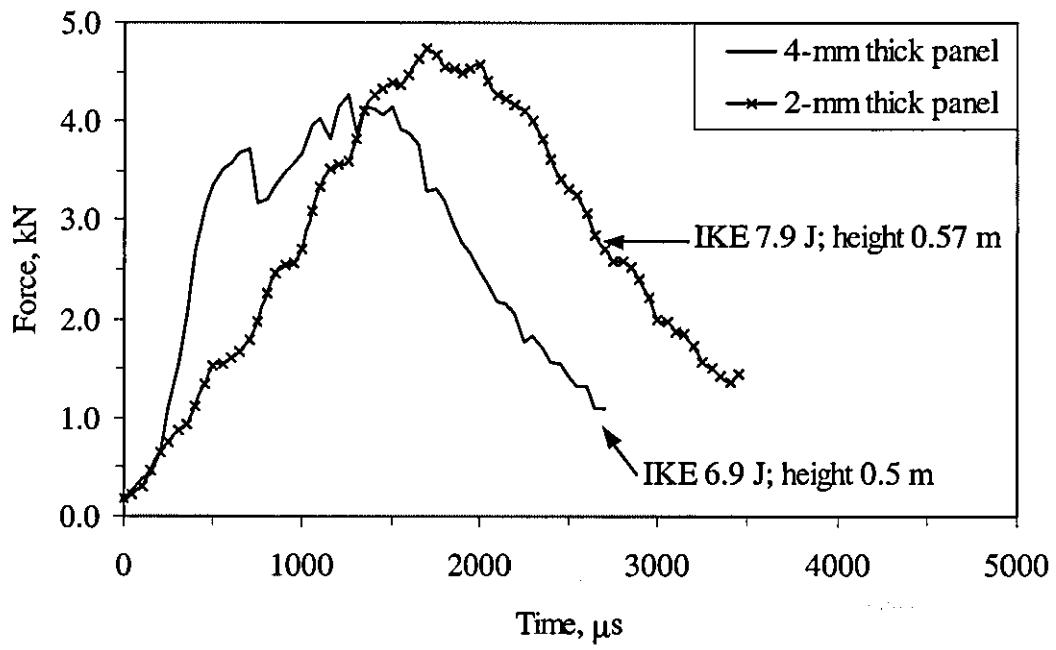
Figure 3.3.4 Force history for 2-mm and 4-mm thick panels impacted at 6.9 J and 7.9 J respectively
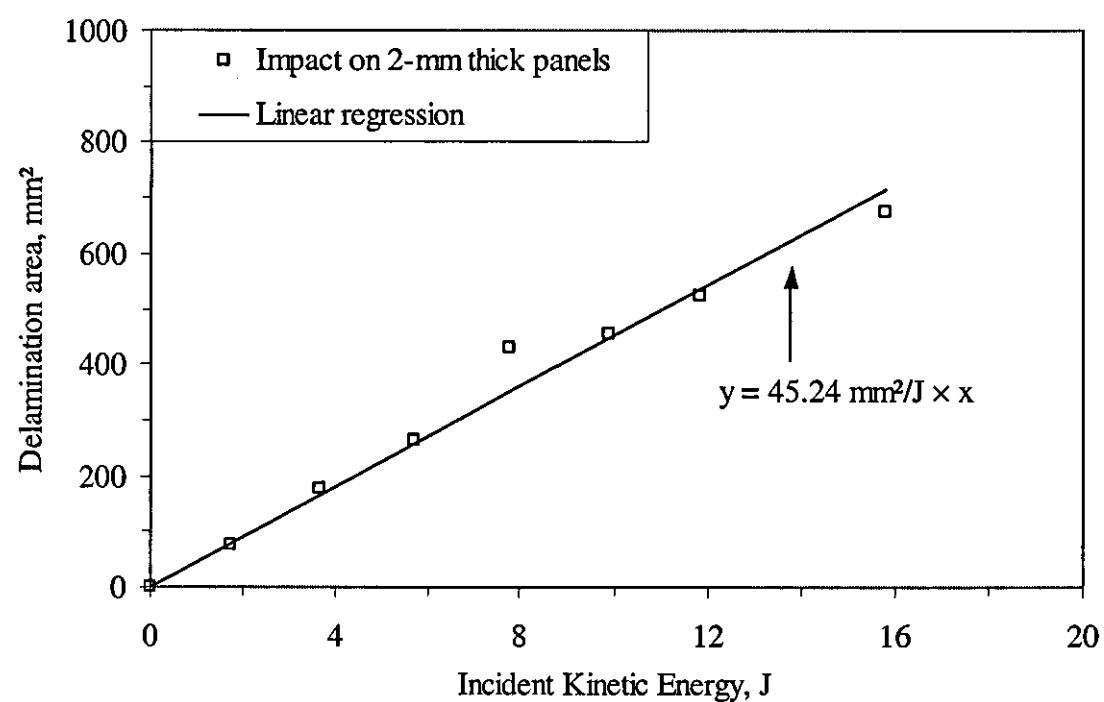
(a)
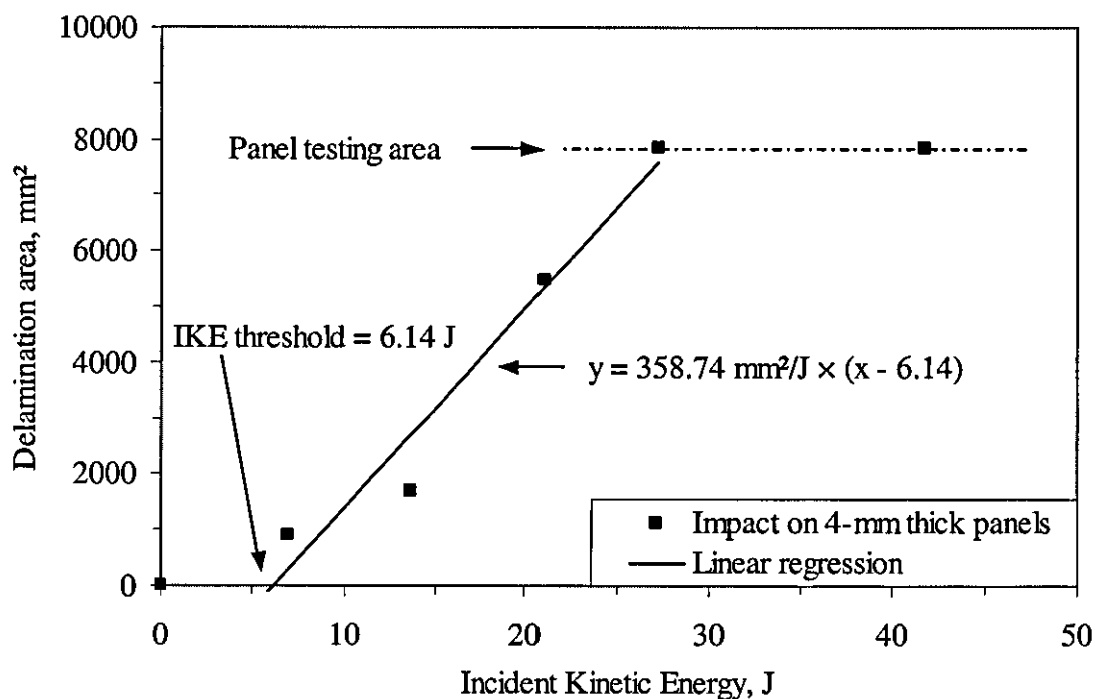
(b)

Figure 3.3.5 Delamination area variation with IKE for (a) 2-mm thick panels and (b) 4-mm thick panels after impact loading
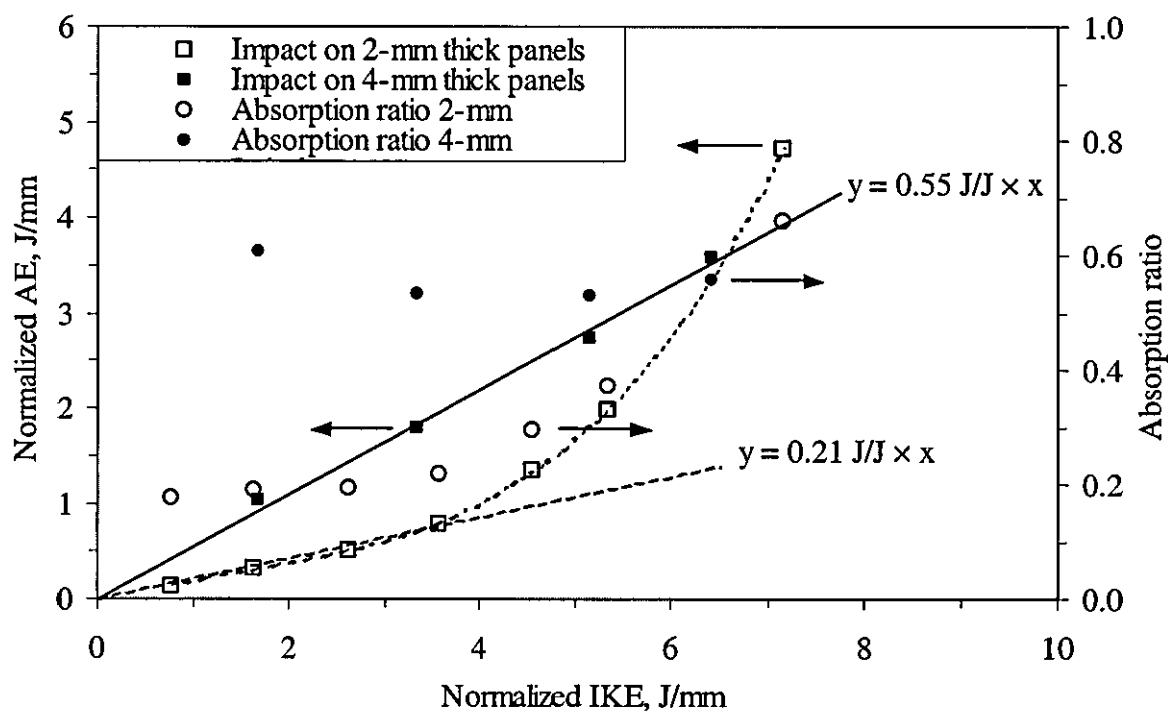
Figure 3.3.6 Variation of Absorbed Energy (AE) and absorption energy ratio with Incident Kinetic Energy (IKE) for 2-mm and 4-mm thick panels

121
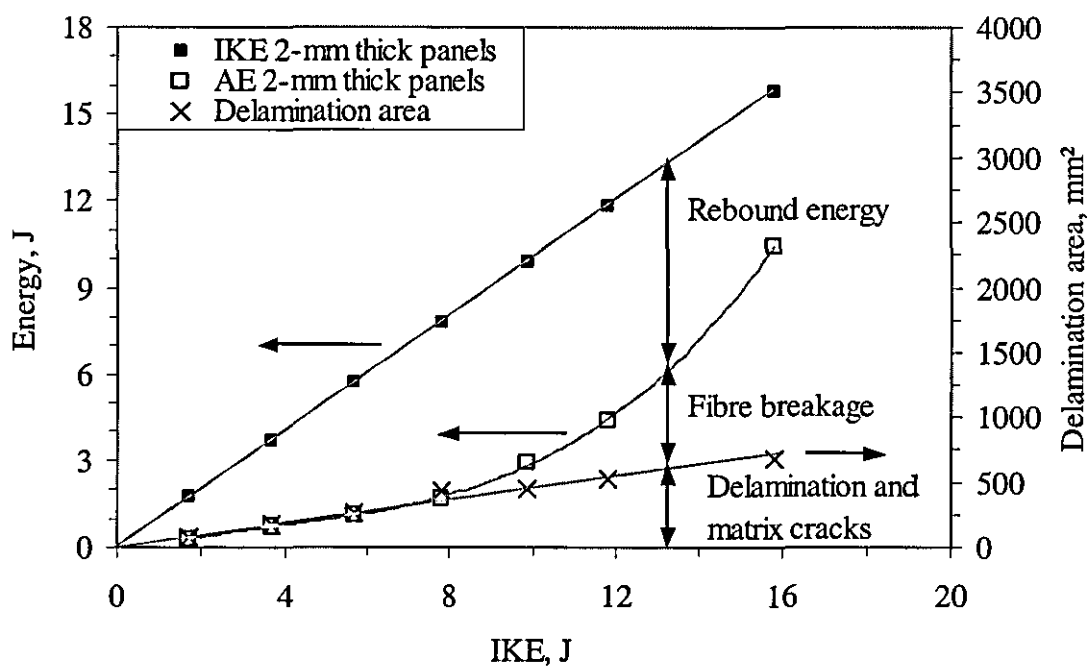
Figure 3.3.7 Absorbed Energy (AE) and delamination area variation with Incident Kinetic Energy (IKE) for 2-mm thick panels
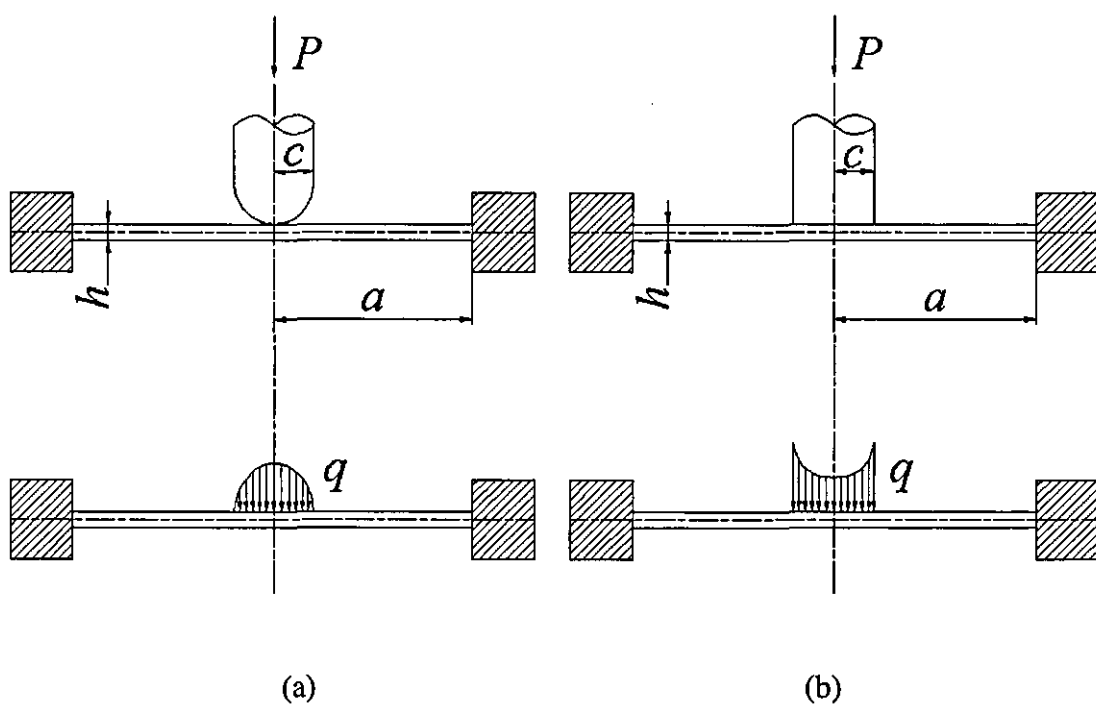
Figure 3.3.8 Effect of indenter nose shape on stress distribution (a) hemispherical ended and (b) flat ended indenter

122
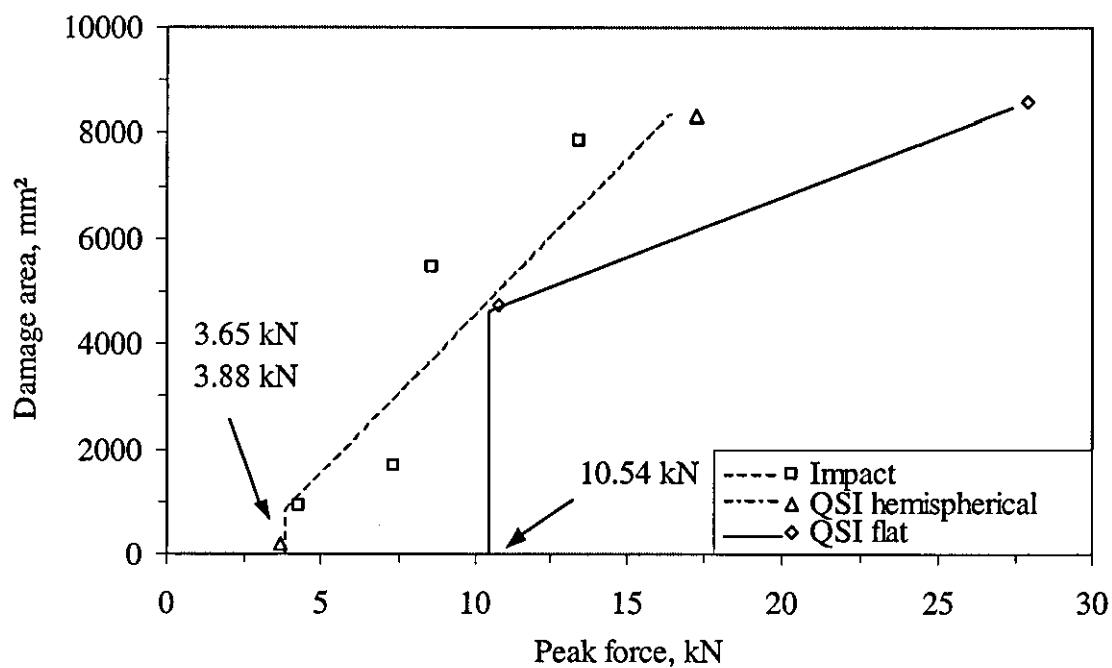
Figures 3.3.9 Damage area variation with transverse peak force for 4-mm thick panels
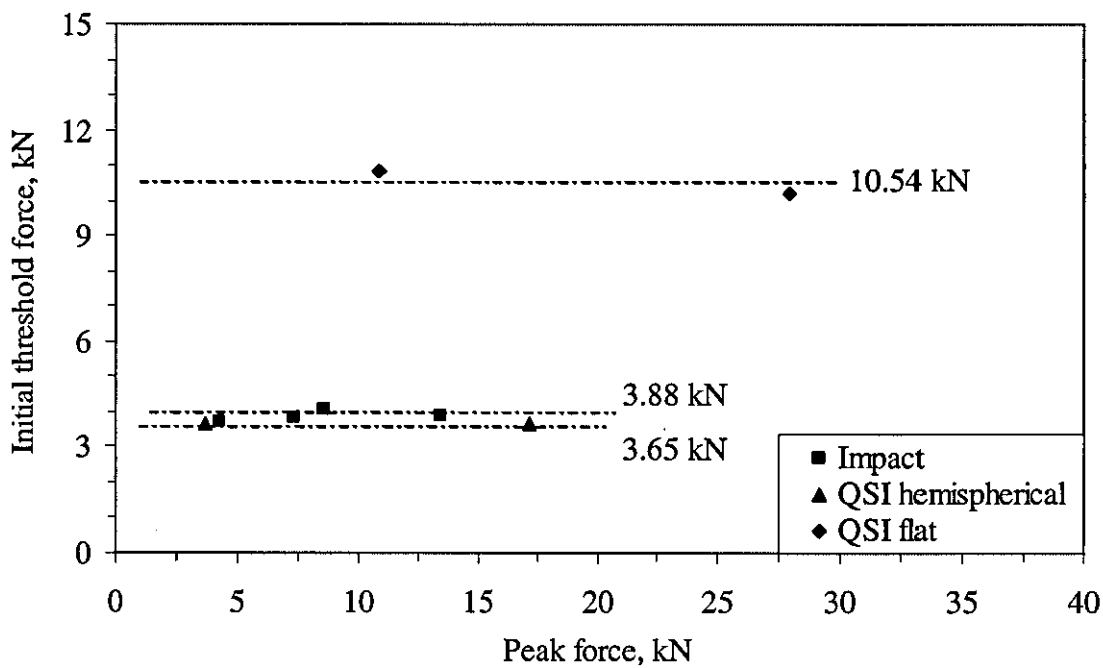
Figure 3.3.10 Initial threshold force for delamination onset variation with transverse peak force for 4-mm thick panels

123
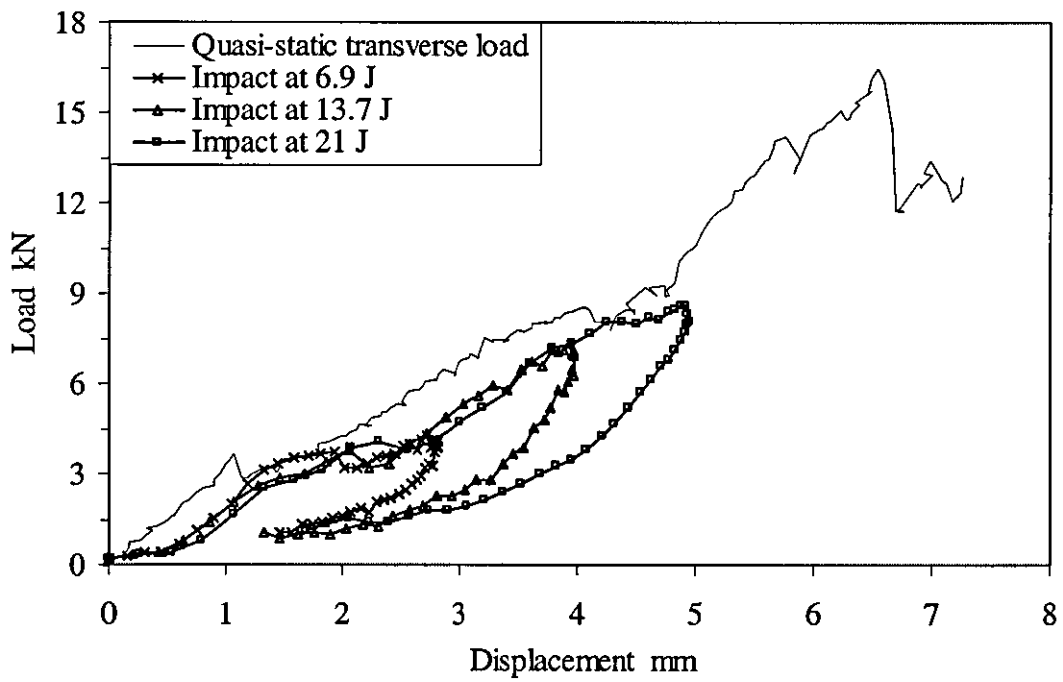
Figure 3.3.11 Displacement-force diagram for impact loading and quasi-static
transverse loading (hemispherical indenter) in 4-mm thick panels
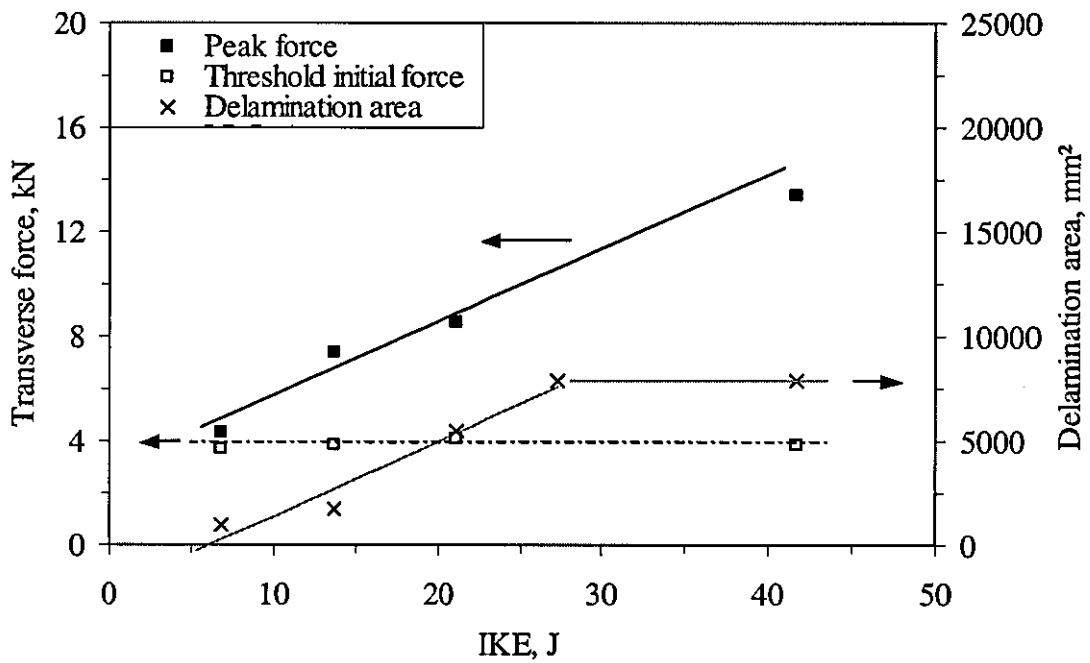
Figure 3.3.12 Initial threshold force, maximum force and delamination area for 4-mm
thick panels with impact induced damage

124

4 In-plane compressive behaviour of intact and preconditioned panels

The aim of this chapter is to study the effect of a given damage state on the residual compressive behaviour. The methodology chosen was to divide the effects of impact loading into two aspects, the first one was concerning material damage and the other one was local change in geometry. To simulate the effect of material damage on the compressive behaviour, a set of preconditioned panels were prepared with artificial embedded delaminations of different sizes, shapes, numbers and through-the-thickness (TTT) distributions. Also panels with open holes were prepared to represent the ultimate material failure. To simulate the local change of geometry, a set of panels was prepared for testing with a local hemispherical dome at the centre, emphasizing the study of the main geometrical parameters, dome depth and curvature. Finally, results from panels with the mentioned preconditions were compared with either impact or quasi-static loaded panels.

4.1 Experimental procedures

In a compression test, each panel was placed in a purpose-built support jig, as illustrated in Figure 4.1.1. The jig consists of two pairs of cylindrical-edged support plates that are intended to prevent global buckling of the panel at the initial stage of loading. The supports were positioned squarely to the panel surfaces 10 mm away from epoxy pots and were only finger-tightened through adjustable bolts. They represented simple support condition on the unloaded edges, which were free to move in the width direction during loading. A quasi-static load was then applied to the panel at the machined ends via a Denison universal testing machine. Although the loaded ends were not physically clamped, the contact end areas increased by the epoxy pots prevented hinge-like rotation at the initial stage of the loading. Thus the loaded ends were effectively close to clamped condition but without clamping surface pressure. Nevertheless, substantial end rotation never took place in any tests, otherwise epoxy pots with limited bonding strength to the panel surfaces could easily break off. Load, strain and cross-head displacement in all the tests were recorded through a data acquisition system at a sampling rate of 0.5 Hz.

4.2 Fundamental characteristics of panel in-plane compression

The panel compressive strain behaviour is established schematically in Figures 4.2.1, on the basis of central mid-section and far-field strain responses. In the figure, mean and bending strains are defined as

$$\varepsilon^0 = \frac{\varepsilon^{front} + \varepsilon^{back}}{2}$$

$$\varepsilon^{bending} = \varepsilon^{front} - \varepsilon^{back}$$

(4.2.1a,b)

There are four critical loads, namely local buckling (mode-I), local-to-global buckling (mode-I), global buckling (mode I to II) and failure. Correspondingly, there are four deformation stages, namely in-plane compression (or prebuckling), local buckling (mode-I), global buckling (mode-I) and postbuckling (mode-II). Figure 4.2.1(a) shows the prebuckling stage characterised for a generalised linear load-strain relationship and exclusive in-plane deformation. As there is no out-of-plane deformation, the bending strain is zero for both mid-plane and far-field strains. The second deformation stage is characterised by local buckling (mode-I), occurring when the mid-section region starts to buckle locally, while the far-field strains indicating no bending. However, some bending exists only at the mid-section location as illustrated by Figure 4.2.1(b). The third deformation stage starts with the local-to-global buckling transition (mode-I), with the panel in a half-sine-wave shape. The presence of bending strain is reflected in both mid-section and far-field gauge readings, as shown in Figure 4.2.1(c). The maximum curvature and bending strain occur at the mid-section, with far-field bending strain comparatively lower. Since the panel is deforming not only in-plane but also in bending, the overall panel stiffness is lower than during prebuckling. Therefore the far-field mean strain shows the 'knee' effect.

The critical global buckling (mode I to II) load marks the division between the global buckling (mode-I) and postbuckling (mode-II) stages, as shown in Figure 4.2.1(d). The panel shape changes from a single half-wave to two half-waves, with two maximum curvature locations at the top and bottom far-field location and an inflection point at the mid-section. Curvature at the mid-section location goes gradually back to zero, reaching

an unstable equilibrium, as a consequence the bending strain reverses and approaches a zero value. In contrast, the bending strain at the quarter-section location increases showing a strain reversal. Mean strain at the mid-section location starts to increase towards the tensile side as a consequence of the stretching effect at the inflection point. The far-field deformation is mainly out-of-plane, since the curvature takes a maximum value at this position. Therefore the mean strain value remains relatively constant, with an increase of the bending strain only, as shown in Figure 4.2.1(d).

Two-mm thick intact panels were prepared and tested in [104]. Since these panels are more prone to buckle than 4-mm thick ones, their examination for response characteristics serves as a precursor of the thicker panels. Figure 4.2.2(a) shows the load-strain response curves of both far-field and central strain gauges from an intact panel (Control B) [104]. On the basis of the central SGs, the four panel deformation stages can clearly be identified as described in the paragraph above. At the prebuckling stage, compressive load was relatively small and the panel was shortened stably with no lateral deflection shown in Figure 4.2.2(b-c). As the axial compressive stress distribution across the width was uniform, thus the panel responded linearly. The critical local buckling (mode-I) load was reached at about 10 kN when the central SGs started exhibiting the strain divergence in Figure 4.2.2(a) or bending strain as shown in Figure 4.2.2(c), whereas the far-field SGs did not. Beyond this load, local buckling steadily developed into global buckling at about 16 kN with the strain divergence or bending strains reaching the far-field SGs. Both the occurrence of local buckling and this local-to-global buckling transition are stable with one longitudinal half-wave. As loading increased, the strain reversals occurred gradually in both the loading and the width directions. The compressive response became significantly non-linear. At about 34 kN, the second strain reversals occurred and then the buckled panel switched to (mode-II) postbuckling with two longitudinal half-waves as indicated schematically in Figure 4.2.10(b-c). This global mode I-to-mode II transition seemed unstable and the crescent of one longitudinal half-wave became a nodal line of two half-waves. Strain measurements from other intact panels with additional SGs indicated that the two longitudinal half-waves were slightly unequal. The final catastrophic failure at 52 kN is about 50% greater than the global buckling (mode I to II) load. The failure location of this panel, as photographs in Figure 4.2.3 show, is close to its mid-section where shear

forces at this postbuckling stage would be highest whereas bending moment could be close to zero. On viewing the sides of the panel, the fracture plane through the panel thickness is rugged with extensive delaminations and fibres fracture and in particular is noticeably oblique to its mid-section. It is interesting to observe that there seems no correlation between strain divergence, strain reversal and global buckling load. Two other intact panels showed very similar behaviour with nearly the identical failure load as seen in Table 4.2.1. This typical four-stage compressive behaviour therefore has provided the basis of subsequent interpretation of strain response characteristics in the preconditioned panels.

Table 4.2.1   Compression test results of 2-mm and 4-mm thick composite intact panels

Specimen identity	Thickness	Length	Failure load	Failure axial strain	Failure comp. Strength	Failure location [a]
	mm	mm	kN	%/$\mu\varepsilon$	MPa	
Control A	2.08	148.03	52.16	1.046 %	256.6	MS
Control B	2.09	148.56	52.34	1.126 %	256.4	MS-FE
Control C	2.06	149.69	52.13	1.100 %	257.3	MS
Control 0	4.07	146.76	135.70	5,720.5 $\mu\varepsilon$	333.9	FE
Control 1	4.10	149.46	147.21	4,786.2 $\mu\varepsilon$	361.9	LE
Control 2	4.44	149.13	169.23	-	382.4	FE
Control 3 [b]	3.89	148.90	125.80	-	322.6	FE

[a] MS, FE and LE denote the mid-section, far end and loading end positions along a panel, respectively.
[b] Data for this test between 114 kN and 125.80kN were lost

4.2.1   4-mm thick intact panels

The majority of 4-mm intact panels failed prematurely with crushing at one loaded end, although failure of the intact panels occurred consistently at the average compressive stress of 359±24 MPa or 151±17 kN and coefficients of variation of 6.7% and 11.25%, for compressive strength and failure load respectively. Figures 4.2.4(a-b) show the individual strain response curves of intact panel Control 0, on which all the strain gauges were bonded on the symmetric axis in the loading direction. Although there is a little non-linear behaviour at both loaded ends right at the beginning of the loading (pair C), which may be associated with poor initial contact, major part of the panel behaviour is linear right up to ultimate end-crushing failure at the bottom end (closest to pair A). The final failure with the failed specimen shown in a photograph in Figure 4.2.5 may

have initiated way back at the load of about 52 kN as indicated in Figure 4.2.4(a). This is primarily because the end crushing was very much localised so that the other two pairs of strain gauges far away from the bottom end could not pick it up. Figures 4.2.6 shows the longitudinal strain-load graphs for the intact panel Control 3. This panel failed in end crushing, similar to Control 0. It had a localised failure picked up only by the gauge located at the far-field bottom end (location A). The final failure may have initiated at 80 kN near the bottom end similarly to the one shown in Figure 4.2.5. The final failure of the panel happened prematurely at 125.8 kN.

Based on the failure location (Table 4.3.1), it can be concluded that the load range for all the 4-mm intact panels was within the prebuckling stage without signs of buckling. Consequently, failure mechanisms did not seem to link to shear stress unlike the 2-mm thick panels. The occurrence of failure near the loading/far edge may be attributed to some localised phenomenon such as poor contact or uneven ply loading. For panels with their failure load below the global buckling (mode-I) load, sign of any local buckling is very limited.

To confirm the established deformation characteristics in the width and thickness directions, a further examination of the results is necessary as the example from intact panel Control 3 shows. Figure 4.2.7(a) shows the bending strains in the width direction, for three different locations along the transverse mid-section. As the bending strain from gauge E suggests, in-plane compressive behaviour was fully achieved only near the centre of the panel. When moving towards the free edges, the panel buckled slightly with opposite curvature. It seems that during in-plane loading, some geometric imperfections and localised effects could have generated a coupling between stretching and twisting. The magnitude of this coupling was low compared with the global in-plane action. As a result of the twisting in the transverse direction, the free edges deformed with a consequent interlaminar TTT elongation at the edge, as seen in Figure 4.2.7(b). This may have affected the Poisson's ratio when derived from the displacement readings, as shown in Figure 4.2.8. Both longitudinal and horizontal transverse deformations were measured using a pair of LVDT's. However the reading from the transverse LVDT was measuring not only the transverse stretching due to the Poisson's effect, but also the ILS deformation at the edge as illustrated by Figure 4.2.9.

In Figure 4.2.8 it was observed that the Poisson's ratio at the centre of the panel was unaffected by the transverse twisting. It can be seen that around 35 kN both readings coincided, but then Poisson's ratio derived from the displacement increased around 40% with respect to the centre of the panel, presumably due to the shear deformation at the edge.

4.2.2 Prediction of intact panel behaviour

This section shows an attempt to develop an analytical model for predicting the intact panel behaviour in compression up to the critical global buckling (mode-I) load. During the initial loading stage of prebuckling, the load-strain relationship is dictated by the classical laminate theory (CLT). The laminate extensional and flexural stiffness are calculated in Appendix D and are summarised in Table 4.2.2.

Table 4.2.2 Material properties

Description	Material properties	16 plies	32 plies	Units
Ply thickness	–	0.128	0.128	mm
UD Stiffness	E_{11}	127.00	127.00	GPa
UD Poisson's ratio	v_{12}	0.31	0.31	-
Extensional stiffness matrix	A_{11}	112.44	224.88	GPa-mm
Extensional stiffness matrix	A_{12}	33.71	67.42	GPa-mm
Extensional stiffness matrix	A_{22}	112.44	224.88	GPa-mm
Bending stiffness matrix	D_{11}	44.44	336.96	GPa.mm^3
Bending stiffness matrix	D_{12}	13.61	101.58	GPa.mm^3
Bending stiffness matrix	D_{22}	30.50	277.21	GPa.mm^3
Bending stiffness matrix	D_{66}	15.59	117.38	GPa.mm^3
Panel length	a	150	150	mm
Panel width	b	100	100	mm
Panel thickness	h	2.048	4.096	mm

Prebuckling behaviour

For the prebuckling analysis of a plate, the loading ends are under uniformly distributed load as shown in Figure 4.2.10(a). The panel coordinate system is shown in Figure 2.2.1. As there is no bending curvature, the load-strain relationship can be described by

$$\begin{Bmatrix} N_x \\ N_y \\ N_{xy} \end{Bmatrix} = \begin{Bmatrix} 0 \\ P/b \\ 0 \end{Bmatrix} = \begin{bmatrix} A_{11} & A_{12} & A_{16} \\ A_{12} & A_{22} & A_{26} \\ A_{16} & A_{26} & A_{66} \end{bmatrix} \begin{Bmatrix} \varepsilon_x^0 \\ \varepsilon_y^0 \\ \gamma_{xy}^0 \end{Bmatrix} \qquad (4.2.1)$$

The distributed force in the width x-direction is zero as

$$N_x = A_{11}\varepsilon_x^0 + A_{12}\varepsilon_y^0 = 0 \qquad (4.2.2)$$

From Eq.(4.2.2), the ratio between transverse and longitudinal mean strain (i.e. Poisson's ratio for the laminate) is observed to have a constant value

$$\frac{\varepsilon_x^0}{\varepsilon_y^0} = -\frac{A_{12}}{A_{11}} \qquad (4.2.3)$$

For loading in the y-direction one can obtain from Eq. (4.2.1),

$$N_y = \frac{P}{b} = A_{12}\varepsilon_x^0 + A_{22}\varepsilon_y^0 \qquad (4.2.4)$$

Substituting Eq. (4.2.3) into Eq. (4.2.4) yields a linear relationship between applied load and mean strain for both transverse and longitudinal directions

$$P = b\varepsilon_x^0 \left(A_{12} - \frac{A_{22}A_{11}}{A_{12}} \right) = b\varepsilon_x^0 \left(A_{12} - \frac{A_{11}^2}{A_{12}} \right) \qquad (4.2.5a)$$

$$P = b\varepsilon_y^0 \left(A_{22} - \frac{A_{12}^2}{A_{11}} \right) = b\varepsilon_y^0 \left(A_{11} - \frac{A_{12}^2}{A_{11}} \right) \qquad (4.2.5b)$$

The predictions of mean strains from Eq. (4.2.5a-b) are plotted alongside experimental mean strain results in Figures 4.2.11 and 4.2.12 for 2-mm and 4-mm thick panels respectively. It is clear that CLT predicts accurately the panel behaviour during the first linear loading stage.

131

In-plane compressive failure prediction

The in-plane compressive failure load is predicted by using the maximum (principal) stress and the Tsai-Hill criteria. The results of such predictions are meaningful only if they fail in the prebuckling stage of loading. To apply these criterions it is necessary to obtain the lamina stresses on the respective principal coordinates for each ply by using the CLT as

$$\left\{ \begin{array}{c} \varepsilon_x^0 \\ \varepsilon_y^0 \\ \gamma_{xy}^0 \end{array} \right\} = \left[A_{ij} \right]^{-1} \left\{ \begin{array}{c} 0 \\ Ny \\ 0 \end{array} \right\} \qquad (4.2.6)$$

$$\left\{ \begin{array}{c} \sigma_x \\ \sigma_y \\ \tau_{xy} \end{array} \right\}_k = \left[\overline{Q} \right]_k \left\{ \begin{array}{c} \varepsilon_x^0 \\ \varepsilon_y^0 \\ \gamma_{xy}^0 \end{array} \right\} \qquad (4.2.7)$$

$$\left\{ \begin{array}{c} \sigma_1 \\ \sigma_2 \\ \tau_{12} \end{array} \right\} = \left[\begin{array}{ccc} \cos^2 \theta & \sin^2 \theta & 2\sin\theta\cos\theta \\ \sin^2 \theta & \cos^2 \theta & -2\sin\theta\cos\theta \\ -\sin\theta\cos\theta & \sin\theta\cos\theta & \cos^2 \theta - \sin^2 \theta \end{array} \right] \left\{ \begin{array}{c} \sigma_x \\ \sigma_y \\ \tau_{xy} \end{array} \right\} \qquad (4.2.8)$$

The respective values for these matrices are shown in Appendix D. Figures 4.2.13(a-c) show the normal and shear principal stresses for 16 and 32-ply panels of 100 mm width. These results were calculated using a Matlab® script shown in Appendix C. The maximum (principal) strengths are marked on Figures 4.2.13(a-c) using a dotted line. The intersection between the dotted line and the load-strain curves determines the maximum (principal) stress criterion failure value. Failure for ±45° plies is under shear stress and for 90° plies is under normal stress at 187 and 167 kN, respectively, for the 32-ply panel and at 93.5 and 83.5 kN, respectively, for the 16-ply panel. Using Tsai-Hill criterion as in Eq. (4.2.9a)

$$\frac{\sigma_1^2}{\sigma_{1C}^2} - \frac{\sigma_1\sigma_2}{\sigma_{1C}^2} + \frac{\sigma_2^2}{\sigma_{2C}^2} + \frac{\tau_{12}^2}{\tau_{12S}^2} < 1 \tag{4.2.9a}$$

with the normal and shear strengths data from [104] yields

$$\frac{\sigma_1^2}{1032^2} - \frac{\sigma_1\sigma_2}{1032^2} + \frac{\sigma_2^2}{130^2} + \frac{\tau_{12}^2}{66.3^2} < 1 \tag{4.2.9b}$$

The variation of the Tsai-Hill factor is shown in Figure 4.2.14 in terms of the applied load. The failure loads predicted for ±45° and 90° plies are 168 and 166 kN, respectively, for the 32-ply panel and at 84 and 83 kN, respectively, for the 16-ply panel.

Global buckling (mode-I) load prediction

The stage of global buckling (mode-I) starts from the local-to-global buckling (mode-I) transition. Figure 4.2.1(c) represents the respective strain-load behaviour and panel deformation at this stage and Figure 4.2.10(b) illustrates the panel deformation. The onset of global buckling (mode-I) can be predicted using Von Karman large deflection expression as the governing equation, with geometric (or forced) boundary conditions given by the simply-supported plate case, with $w = 0$ at $x = 0,a$ and $w = 0$ at $y = 0,b$. The global buckling (mode-I) of a rectangular quasi-isotropic plate, loaded in compression with a distributed load N_y and out-of-plane deflections w, is given by

$$D_{11}w_{,xxxx} + 4D_{16}w_{,xxxy} + 2(D_{12} + 2D_{66})w_{,xxyy} + 4D_{26}w_{,xyyy} + D_{22}w_{,yyyy} = N_y w_{,yy} \tag{4.2.11}$$

The expression in Eq. (4.2.11) can be reformulated on the basis of the special-orthotropic plate solution with D_{16} and D_{26} being zero

$$D_{11}w_{,xxxx} + 2(D_{12} + 2D_{66})w_{,xxyy} + D_{22}w_{,yyyy} = \frac{P}{b}w_{,yy} \tag{4.2.12}$$

Governing equation (4.2.12) corresponds to a special orthotropic laminate, despite the real laminate being quasi-isotropic. This is a mathematic simplification that allows the use of double sine series (DSS) as a solution for the deflection w. Nevertheless, there is an error involved in using DSS for a quasi-isotropic laminate because the boundary conditions are not entirely fulfilled, however the magnitude of the error is negligible for quasi-isotropic laminates [121]. The DSS expression for w is

$$w = A \times \sin\left(\frac{m\pi y}{a}\right) \sin\left(\frac{n\pi x}{b}\right) \tag{4.2.13}$$

Substituting Eq. (4.2.13) into Eq. (4.2.12) the critical buckling load is obtained

$$P_0 = \frac{b}{(m\pi/a)^2}\left[D_{11}\left(\frac{n\pi}{b}\right)^4 + 2(D_{12} + 2D_{66})\left(\frac{m\pi}{a}\right)^2\left(\frac{n\pi}{b}\right)^2 + D_{22}\left(\frac{m\pi}{a}\right)^4 \right] \tag{4.2.14}$$

Based on Table 4.2.2, the global buckling (mode-I) load is calculated for 2-mm and 4-mm thick panels, with $m = 1$ and $n = 1$, using Eq. (4.2.14). The results are 20.05 kN and 153.38 kN for 2-mm and 4-mm thick panels respectively. The global buckling (mode-I) loads are marked on Figures 4.2.11 and 4.2.12 for 2-mm and 4-mm thick panels respectively. The predicted values agree well with the experimental results, although the local buckling (at 10 kN for 2-mm thick panels) was not accounted for. For 2-mm thick panels the initial prebuckling stage covers a loading range around 20% of the failure load, thus further analysis is necessary to predict the panel behaviour over the full load range. However, 4-mm thick panels did not undergo buckling, thus they could have failed as in the prebuckling stage. The experimental failure load of 151±17 kN was relatively close to the predicted buckling load value of 153.38 kN. It seems that the current CLT analysis might be able to predict the compressive behaviour of 4-mm thick intact panels.

4.3 Panels with embedded artificial delamination

The most critical type of damage resulting from impact is in the form of delamination accompanied by matrix cracks. In particular the projected area of delamination has a

Table 4.3.1   Compression test results of 2-mm thick composite panels containing artificial delamination(s) [104]

Specimen identity [a]	Defect size	Defect area	Thickness	Length	Failure load	Failure axial strain	Failure comp. strength	Failure location [b]
	mm	mm²	mm	mm	kN	%	MPa	
EH10	10	26.2	2.09	148.95	52.80	1.100	256.6	MS
EH20	20	104.7	2.07	148.71	51.20	0.999	251.9	MS-FE
EH40	40	418.9	2.10	148.78	44.10	0.814	212.5	MS
EH60	60	942.5	2.08	149.37	38.20	0.685	185.5	MS
EH40x3S [c]	40	418.9	1.91	149.47	30.93	0.783	161.3	MS
EV10	10	26.2	1.94	148.12	44.70	1.072	231.1	LE-MS
EV20	20	104.7	1.96	148.18	46.30	1.072	240.8	LE-MS
EV40	40	418.9	1.96	148.19	46.10	1.008	235.8	MS
EV60	60	942.5	1.94	148.22	34.40	1.085	179.6	MS
CR10	10	78.5	1.98	149.30	42.74	1.061	219.0	MS
CR20	20	314.2	1.97	149.29	48.20	1.143	247.8	MS
CR40	40	1256.6	1.98	148.91	35.38	0.938	181.3	MS
CR60	60	2827.4	1.99	148.87	33.35	0.820	169.6	MS
CR20x3S [c]	20	314.2	1.87	149.54	30.90	0.754	165.6	MS

[a] E and C denote elliptical and circular shapes, respectively. H and V denote horizontal and vertical orientation of the ellipse, respectively.

[b] MS, LE and FE denote mid-section, loading-end and far-end positions along a panel, respectively.

[c] These panels were tested in this project. Other specimens were tested in [104].

Table 4.3.2   Compression test results of 4-mm thick composite panels containing artificial delaminations

Specimen Identity [a,b]	Defect size	Defect number	Defect area	Location [c]	Thickness	Length	Failure load	Failure far field mean strain	Failure comp. strength	Failure location [c]
	mm		mm²		Mm	mm	KN	με	MPa	
4EH10	10	1	26.2	MP	4.13	149.06	147.46	6,541.0	357.3	LE
4EH20	20	1	104.7	MP	4.11	148.93	143.76	5,924.5	350.9	FE
4EH40	40	1	418.9	MP	4.15	149.23	146.52	4,266.0	354.5	FE
4EH60	60	1	942.5	MP	4.13	148.97	150.58	4,354.0	361.1	FE
C20MS1	20	1	314.2	MP	3.82	145.17	150.37	7,836.0	417.5	LE
C20MS2	20	1	314.2	MP	3.94	149.72	168.24	7,775.0	429.3	FE
C40MS	40	1	1256.6	MP	4.11	147.56	151.00	6,663.5	372.3	FE
C60MS	60	1	2827.4	MP	4.11	147.58	132.37	5,345.5	324.3	LE-MS
C20QS	20	1	314.2	QL	4.14	147.63	170.21	7,436.5	414.6	FE
C40QS	40	1	1256.6	QL	4.21	149.14	132.33	5,744.0	316.7	LE
C60QS	60	3	2827.4	QL	4.17	147.43	128.92	4,831.0	310.5	LE
C20x3S	20	3	314.2	Sym	3.93	148.97	114.00	-	294.16	LE
C20x3Sii	20	3	314.2	Sym	3.96	149.72	113.96	4,853.0	286.8	LE
C40x3S	40	3	1256.6	Sym	3.93	148.75	99.72	3,083.0	251.9	MS
C60x3S	60	3	2827.4	Sym	3.93	148.58	86.34	1,338.5	219.2	MS
C20x3AS	20	3	314.2	Asym	3.84	148.20	113.87	3,669.5	295.6	LE
C40x3AS	40	3	1256.6	Asym	3.92	148.86	106.61	3,159.5	272.2	MS
C60x3AS	60	3	2827.4	Asym	3.83	147.66	92.86	2,547.5	242.2	MS

[a] E and C denote elliptical and circular shapes, respectively. H and V denote horizontal and vertical orientation of the ellipse, respectively.

[b] MS and QS in the first column denote the mid-plane and a quarter TTT location of a panel, respectively.

[c] MS, LE and FE in the last column denote mid-section, loading-end and far-end positions along a panel, respectively.

direct relationship with the compressive strength reduction, as discussed earlier. Internal delaminations may appear in different shapes, orientations and TTT locations. The effect of each of these parameters can be studied with preconditioned panels that simulate certain delamination configuration. Tables 4.3.1 and 4.3.2 show panel characteristics and compressive test results for panels with artificially-embedded delamination.

4.3.1 2-mm thick panels with artificially-embedded delamination

The presence of a single delamination with a substantial size creates two sublaminates and during loading could induce strain concentration in the delaminated or locally weakened area. Moreover, two asymmetric sublaminates, albeit balanced, could induce extension-bending and bending-twisting coupling. A combination of the two should therefore contribute to variations of the characteristic compressive behaviour and thereby reduction of RCS. Nevertheless, if the delamination is not large enough to induce strain concentration and weaken the local area, the characteristics of the panel behaviour may not be affected. One such case from panel EH20 with a 20-mm (major axis) horizontal elliptical delamination is shown in Figures 4.3.1(a-d). Consequently, the four deformation stages could still be clearly identified in the strain response curves in both longitudinal and transverse directions in Figures 4.3.1(a-b). The local buckling (mode-I) load of about 11 kN is almost the same as that of intact panel B. Moreover, the global buckling (mode I to II) load of 32 kN and the failure load of 51 kN are again similar to respective values of the intact. The bending strain responses in Figure 4.3.1(d) clearly confirm that the panel developed into local buckling from the load of 11 kN up to 32 kN as there was little bending from the far-field SGs during this loading period. Immediately after the global buckling (mode I to II) load, both longitudinal and transverse mean strains from the mid-section in Figure 4.3.1(c) started decreasing linearly to accommodate the mode shift. With these trends, both central and side transverse SGs show more or less the same level of tensile strains. This seems to suggest that induced interlaminar shear (ILS) stress gradients may not be high enough to trigger delamination propagation. Instead, as the central longitudinal bending strain reversed to the convex side whereas the far-field bending strain (the lower left part)

swung to the concave side, panel twisting in the postbuckling (mode-II) stage was evident. This understanding is consistent with the actual fracture plane shown by the back side of the panel in a photograph in Figure 4.3.2. Clearly, buckling should not be synonymous with delamination propagation as also found out in [77, 83, 89, 122].

When the size of delamination increased to 60 mm for horizontal delamination (EH60) and 40 mm for circular delamination (CR40), the characteristics of the panel behaviour changed substantially as shown in Figures 4.3.3(a-c) and 4.3.4(a-c). For panel EH60, both the global buckling (mode I to II) load of 27 kN and the failure load of 38 kN in Figure 4.3.3 were reduced by 18% and 27%, respectively, whereas the local buckling (mode-I) load of 10 kN remained unaffected, compared with the intact panel values. The second respective strain reversals are much less obvious than that of the other cases and they seem to be much closer to the strain divergence. Especially, the transverse bending strains C and E in Figures 4.3.3(b-c) indicate the development of two half-waves across the panel width. This suggests that the unstable transition of global buckling (mode-I) to postbuckling (mode-II) triggered the catastrophic failure of this panel. This observation can be reinforced by results of panel CR40 in Figure 4.3.4. From there, the much more abrupt first strain reversals at about 21 kN correlate well with the strain divergence thereby indicating an unstable transition of local to global buckling (mode-I). This dramatic transition confirms that the present delamination was large enough to have weakened local resistance to the compressive loading. The ultimate failure at 36 kN occurred shortly after the second respective strain reversals or global buckling-to-postbuckling (mode I to II) transition at 30 kN. This time, the dramatic divergence of the transverse mean strains C and E in Figure 4.3.4(c) provided a strong indication of delamination propagation. Photographs of the failed panel are shown in Figure 4.3.5. Strain responses of panel CR60 are very similar to that of this panel. These characteristics confirm that sufficiently large delaminations with induced strain concentration could indeed precipitate the premature ultimate failure. Characteristics of strain responses from two panels (EH40x3S and CR20x3S) with three delaminations are similar to that of those two panels.

4.3.2 4-mm thick panels with artificially-embedded single delamination

Similar to the 4-mm thick intact panel (see Figure 4.2.5), all the preconditioned panels containing a single horizontal elliptical delamination at the mid-plane also failed prematurely in crushing near one loaded end. The strain response curves of one such panel (4EH40) are shown in Figures 4.3.6(a-b). The 'stiffening' non-linearity from 56 kN in Figure 4.3.6(a) was picked up only by far-field strain gauges and thereby may have been attributed to the initiation of end crushing. This is very similar to that of the intact panel as discussed earlier. Very limited local buckling started in both directions at about 90 kN with bifurcation. Judging the transverse strain responses in Figures 4.3.6(a-b) with a Poisson's ratio mismatch, there is no sign whatsoever for delamination propagation, although the extension-bending and bending-twisting couplings existed in the delaminated section. For the panels containing a single circular mid-plane delamination of less than 40 mm in diameter, crushing failure occurred at one loaded end consistently. Another example of such typical behaviour from the panel (C40MS) with a circular delamination is given in Figures 4.3.7(a-b) with no sign for global buckling (mode I to II), although local buckling developed at about 40 kN in the loading direction. Again, strain reversals at about 48 kN may well be attributed to the initiation of end crushing.

Unsurprisingly, only when the size of delamination reached 60 mm in diameter, the well-defined development of buckling (mode-I) from the mid-section with local bifurcation to the loaded ends could again be observed in Figures 4.3.8(a-b) (C60MS). Bifurcation was observed from the central (longitudinal) strain gauge pair at 45 kN, reaching the far-field pair at 128 kN, following a sequence similar to 2-mm thick panels. Nevertheless, the failure load of the panel seems to coincide almost with the global buckling (mode I to II) load, since both strain gauges in the width direction in Figure 4.3.8(a) seem to show small strain reversals. The failure occurred between the loading end and the mid-section, with a clear skew angle as shown in Figure 4.3.9. The failure may well be attributed to the mode shifting influenced by the coupling between stretching and twisting of the unbalanced sublaminate.

Moving the TTT position of a delamination from the mid-plane to the quarter location (see Chapter 2) did not seem to affect the panel behaviour for relatively small delaminations. This is shown in Figure 4.3.10 from panel C40QS where strain responses from its mid-section were almost linear right up to ultimate failure. It was necessary a further increase of single delamination size (e.g. C60QS) to alter slightly the compressive behaviour. Figure 4.3.11 shows strain gauge readings from panel C60QS, only the gauge at central location on the front side of the panel (D front) picked up a strain reversal, around 115 kN. The rest of the gauges followed the linear trend showed by the previous specimens with smaller delaminations. This panel did not undergo global buckling (mode I to II) transition as it is evidenced by the failure location, towards the loading end. Consequently the strain reversal was attributed to a very specific phenomenon, the local weakening of the thinnest sublaminate at the delamination centre. This can be described as *frontal bulging*. Compared to the in-plane characteristic failure, the photograph of panel C60QS in Figure 4.3.12 shows that there was an incipient location shift from the loading end towards the mid-plane, probably due to the starting of local buckling (mode-I) development.

4.3.3   4-mm thick panels with artificially-embedded multiple delaminations

When three delaminations of the same size were embedded in 4-mm thick panels (see Chapter 2), the intensity of delamination increased three times but the projected damage size was the same. In addition, all four sublaminates in the symmetric arrangement were unbalanced. However, in the asymmetric arrangement, two inner ones were unbalanced whereas two outer ones were balanced. Moreover, all the sublaminates in either arrangement were asymmetric so that stiffness couplings existed in the delaminated section. The existence of the couplings could in theory weaken buckling (mode-I) and global buckling (mode I to II) stresses. Surprisingly, three 20-mm delaminations in either arrangement were still insufficient to reduce the RCS of the corresponding panels (C20x3S and C20x3AS). To verify this, an additional panel with three symmetric 20-mm delaminations was tested. All three panels failed at one loaded end in the same manner as that of the intact panel. Consequently, the effect of small multiple delaminations on the compressive behaviour seemed negligible in addition to the effect of all the couplings in the delaminated section. The effect of preconditions became

139

significant only when the delamination size reached 40 mm as one such panel (C40x3S) with three 40-mm symmetric delaminations shows in Figures 4.3.13(a-b). It is worth noting from these curves, especially from Figure 4.3.13(b), that strain reversals around 82 kN during global buckling (mode I to II) were very dramatic and profound, although local buckling (mode-I) started around 29 kN. Beyond that, the panel offered little resistance without the second strain reversals, similar to 2-mm thick impact-damaged panels in Figures 4.5.3 and 4.5.4. Photographs of the failed specimen in Figure 4.3.14 show the familiar fracture characteristics similar to that of 2-mm thick panels.

When three large delaminations of the same size were embedded in an asymmetric manner as illustrated in Chapter 2, two of the three were located on one side of the mid-plane with the outmost delamination being only four-ply away from the front face. In addition, the Poisson's ratios of these sub-laminates may not be balanced. When deformation increases, these imbalances could create high local internal stresses, which may in turn promote the tendency for delamination propagation. Figure 4.3.15 shows individual strain gauge readings from a panel containing three delaminations of 20-mm diameter in an asymmetrical TTT arrangement (C20x3AS). The panel behaved globally with the linear trend of the in-plane compressive stage. However it buckled (mode-I) locally at central location on the front side of the panel around 103 kN as suggested by the SG D front. This behaviour is similar to the one exhibited by the panel the largest single delamination in asymmetric arrangement (C60QS). Panel C20x3AS failed in end-crushing, suggesting that the local buckling did not affect the overall linear behaviour. When the delamination size increased to 40 mm (C40x3AS) the characteristics of the panel behaviour changed substantially as shown in Figure 4.3.16. SG's at the central location (D, E) showed local buckling around 45 kN. However around 60 kN there was a localised strain reversal only on the front side, picked up by the gauges located near the delamination. Apparently, the weakening of the upper thin sublaminate affected the local panel response on this side, thus this can described as frontal bulging, similar to panel C60QS. The gauges from both far-field and all locations on the back-side did not pick up any change until 95 kN when there was a global strain reversal and the panel went into the postbuckling (mode-II) stage, affected by the presence of three delamination in a similar way to the symmetrical case. Such 'progressive' failure with local buckling (mode-I) followed by frontal bulging and then

by postbuckling (mode-II) was only found in panels with asymmetrical delamination arrangement. However this difference in panel behaviour between symmetric and asymmetric TTT distribution of delaminations was not reflected on the RCS. Photographs of the failed specimen in Figure 4.3.17 show the familiar fracture characteristics similar to that of 2-mm thick panels and 4-mm symmetrical arrangement.

Panel with 60-mm delaminations (C60x3AS) showed additional features of the compressive behaviour of panels with asymmetrical delamination distribution, as observed from Figure 4.3.18. The response curves of strain gauges in the width direction seemed to show local buckling right from the beginning, especially with much greater strain magnitudes from the front strain gauges. On the contrary, there was no sign of longitudinal buckling until a very dramatic strain reversal occurred on the front side at about 42 kN. With local strains on both surfaces reaching about 1%, the delamination must have propagated sideways. Nevertheless, this delamination propagation did not seem to trigger ultimate failure of this panel (C60x3AS) as the latter failed at 93 kN in the mid-section region. As a few strain gauges on both faces showed visibly the second strain reversals shortly before the ultimate failure, it is likely that the shift of buckling mode I to II triggered ultimate failure instead.

4.4 Panels with change in surface curvature

A local curvature change in the shape of semi-spherical dome was introduced at the centre of a panel during the curing process as explained in Chapter 2. Table 4.4.1 shows the compressive test results for panels with local change of geometry.

4.4.1 Compression test results of panels with local curvature change

The first parameter, depth, introduced certain amount of built-in eccentricity. Under the in-plane load, it created a bending moment near the centre of the panel. The second factor, curvature, introduced an angle between the flat fibres on the panel and the curved fibres on the dome. When the panel was axially loaded, shear stresses were induced along the boundary between the flat panel and the dome. Figure 4.4.1(a-b) shows these two geometrical parameters.

141

Table 4.4.1 Compression test results of 4-mm thick composite panels containing local change of geometry

Specimen Identity [a]	Defect dimensions [b]			Panel			Failure		
	In-plane size	Depth	Curvature	Thickness	Length	Load	Far-field mean strain	Compressive strength	Location [c]
	mm	mm	mm	mm	mm	KN	$\mu\varepsilon$	MPa	
CD20	20.32	0.80	64.9	3.99	149.08	117.8	4,812.00	295.61	FE
CD40CC	40.62	3.26	64.9	3.92	149.07	97.2	2,577.50	249.42	FE
CD60CC	61.02	7.62	64.9	3.66	149.22	61.4	926.00	167.49	MS
CD40CD	40.16	0.80	252.4	3.88	149.21	100.5	-	259.50	FE
CD40CDii	40.16	0.80	252.4	3.86	149.10	89.1	2,858.50	230.24	FE
CD60CD	60.11	0.80	564.9	3.87	150.05	115.1	3,577.50	297.22	FE

[a] CC and CD on the end of the identity label denote constant curvature and constant depth of the geometric defect respectively.
[b] Defect dimensions are measured respect to the mid-plane TTT.
[c] MS and FE in the last column denote mid-section and far-end positions along a panel, respectively.

Figure 4.4.2 shows the compressive test result for the baseline panel CD20. The local strain response at the centre of the panel (gauge D) showed the superimposed effects of in-plane compression and bending. The in-plane compressive stress was either reduced on the front (convex) side or increased on the back (concave) side due to the bending moment effect. This can be easily identified when comparing in-plane strains from the inner region of the dome (Figure 4.4.2(a)) with the outer region (Figure 4.4.2(b) and (c)). However the panel failed at the far end in end crushing, with a failure probably initiated around 97 kN, as indicated by the far-field gauge in Figure 4.4.2(c). This suggests that although the bending effect introduced by the circular dome was noticeable, it was insufficient to trigger a global failure. Therefore the panel globally remained in the in-plane compressive stage until the ultimate load.

Increasing the TTT dome depth, maintaining the same curvature, led to an increase in the load eccentricity as well as in the magnitude of the bending moment at the centre of the dome as shown by panels CD40CC and CD60CC. This is reflected in the apparent stiffness reduction at the centre of the panel, shown in Figure 4.4.3(a). Nevertheless this local behaviour did not prevail on the whole panel, as seen in Figure 4.4.3(b), far-field strain gauge readings kept the same trend despite the increase of dome depth and size. On the other hand, increasing the dome curvature, keeping the same depth, did not affect the stiffness at the centre as Figure 4.4.4(a) suggests, even the far-field behaviour was similar as shown in Figure 4.4.4(b). The expected reduction of shear stress when

increasing the radius of curvature (i.e. the flatness of the panel) was not visible from the strain gauge readings, but it was reflected on the final failure trend as explained in Chapter 5. Figure 4.4.5 shows photographs of failed specimens CD20 and CD60CC with the failure location at the far-end and at the mid-section respectively.

4.4.2 Compressive behaviour prediction

The panel can be considered to have two separate regions with different in-plane stiffness, one is the region with a dome and the other is the surrounding flat region. When these two regions are axially loaded in compression, it becomes a redundant system, with similar overall displacement, but with an internal redistribution of axial force. This redistribution is also present in panels with open holes, although to a greater extent. As many authors have found in the case of open hole, the internal redistribution of stress is not linear [123]. However for the sake of simplicity, the model developed in the following only deals with linear redistribution of stresses.

A simplification of the real case is presented in Figure 4.4.6, taking in account only the main parameters: eccentricity (given by the dome depth) and damage size (given by the curvature). For the eccentricity, the average value of the dome is estimated using the definition for centroid, so the force acting on the whole dome region is replaced by an equivalent one applied on the geometrical centroid of the dome. The centroid location is given by

$$\overline{z} = \frac{\sum_i A_i z_i}{\sum_i A_i} = \frac{\int z dA}{\int dA} \qquad (4.4.1a)$$

Using dome geometry as shown in Figure 4.4.1(c), the centroid can be evaluated from the addition of infinitesimal concentric rings of radius $R\sin\theta$ and z-location $R\cos\theta$, so that Eq. (4.4.1a) yields

$$\overline{z} = \frac{\int_0^\alpha (R\cos\theta)(2\pi R\sin\theta)Rd\theta}{\int_0^\alpha (2\pi R\sin\theta)Rd\theta} = \frac{R}{2}\left(\frac{\sin^2\alpha}{1-\cos\alpha}\right) \qquad (4.4.1b)$$

Where R is the radius of curvature of the dome. The angle α can be derived from Figure 4.4.1(c) as

$$\alpha = \arcsin\left(\frac{c}{2R}\right) \quad \text{or} \quad \alpha = \arccos\left(\frac{R-e}{R}\right) \qquad (4.4.2)$$

Where e is the dome depth or maximum eccentricity and c is the dome diameter. Then, the final expression of the centroid is given by

$$z = \frac{c^2}{8R} \qquad (4.4.3)$$

Finally, the average eccentricity used in the panel analysis becomes

$$e_{avg} = \frac{c^2}{8R} - (R-e) \qquad (4.4.4)$$

It is expected that the initial bending curvature will affect the panel strain response, however this was neglected for simplicity. The central strain was derived on the basis of the CLT, approximating the semi-spherical dome by a curved beam. Based on the applied force and moment, the mean strains and curvatures are given by

$$\begin{Bmatrix} \varepsilon_x^0 \\ \varepsilon_y^0 \\ \gamma_{xy}^0 \end{Bmatrix} = \begin{bmatrix} A_{11}' & A_{12}' & 0 \\ A_{12}' & A_{22}' & 0 \\ 0 & 0 & A_{66}' \end{bmatrix} \begin{Bmatrix} 0 \\ N_y \\ 0 \end{Bmatrix} \qquad (4.4.5a)$$

$$\begin{Bmatrix} \kappa_x \\ \kappa_y \\ \kappa_{xy} \end{Bmatrix} = \begin{bmatrix} D_{11}' & D_{12}' & D_{16}' \\ D_{12}' & D_{22}' & D_{26}' \\ D_{16}' & D_{26}' & D_{66}' \end{bmatrix} \begin{Bmatrix} 0 \\ M_y \\ 0 \end{Bmatrix} \qquad (4.4.5b)$$

Where the matrices [A'] and [D'] are the inverse of the extensional and bending stiffness matrices, respectively. The panel is considered as a statically indeterminate structure, with two semi-panels compressed simultaneously, one flat designated as region 1 and the other with a local change of geometry designated as region 2. This partition is shown in Figure 4.4.6. To solve it, the displacements due both to external and redundant loads are expressed in terms of the loads and are made to be equal. If the loading head is removed, the longitudinal strain of the flat region 1 due to the external load P is

$$\varepsilon_{y1}^0 = A'_{22} \times \frac{-P_1}{b-c} \qquad (4.4.6)$$

Where b is the panel width and c is the width of the region 1 (local change of geometry). The curvature is null, since the panel is flat. On the other hand, in the region 2, the maximum compressive strain is reached on the back side of the panel and it is evaluated on the basis of the Kirchhoff hypothesis, with the bending moment and load taken as illustrated on Figure 4.4.1, thus we have

$$\varepsilon_{y2} = \varepsilon_{y2}^0 - \frac{t}{2} \kappa_{y2} \qquad (4.4.7)$$

Replacing the mean strain and the curvature in Eq. (4.4.7) by the corresponding values of applied load and bending moment in Eqs. (4.4.5a-b), it yields

$$\varepsilon_{y2} = \left(A'_{22} \frac{-P_2}{c} \right) - \left(\frac{t}{2} D'_{22} \frac{P_2 e_{avg}}{c} \right) \qquad (4.4.8)$$

Since the actual compressive strain of the two regions is supposed to be the same, Eqs. (4.4.6) and (4.4.8) should be equal and this leads to

$$A'_{22} \frac{-P_1}{b-c} = \left(A'_{22} \frac{-P_2}{c} \right) - \left(\frac{t}{2} D'_{22} \frac{P_2 e_{avg}}{c} \right) \qquad (4.4.9)$$

Knowing that $P_{total} = P_1 + P_2$, the following relationships are obtained for each loads in terms of the applied external load P_{total}

$$P_2 = P_{total} \frac{1}{1 + \dfrac{b-c}{c}\left(1 + \dfrac{te_{avg}}{2}\dfrac{D'_{22}}{A'_{22}}\right)} \qquad (4.4.10a)$$

$$P_1 = P_{total} - \frac{P_{total}}{1 + \dfrac{b-c}{c}\left(1 + \dfrac{te_{avg}}{2}\dfrac{D'_{22}}{A'_{22}}\right)} \qquad (4.4.10b)$$

Substituting Eq.(4.4.10a) into (4.4.8) leads to

$$\varepsilon_{y2} = \left(\frac{-A'_{22}}{c} \mp \frac{te_{avg}D'_{22}}{2c}\right) \times P_{total} \frac{1}{1 + \dfrac{b-c}{c}\left(1 + \dfrac{te_{avg}}{2}\dfrac{D'_{22}}{A'_{22}}\right)} \qquad (4.4.11)$$

Figure 4.4.7 shows prediction of Eq. (4.4.11) for central longitudinal strain compared with the experimental results from gauge D. The approximation follows the experimental trend found when the depth was increased, cases (a), (b) and (c). However the prediction for the case (c), i.e. panel CD60CC, is not very precise, since the non-linearity of the stress redistribution is more noticeable for large dome diameters (when the eccentricity value is large as well). On the other hand the model accurately picked up the effect of increasing the radius of curvature, maintaining the same depth, on the central longitudinal strain, as the cases (a), (d) and (e) show.

4.5 Panels with damage from impact or quasi-static testing

Previous sections have separately provided information on the concepts of material damages such as internal delamination, matrix cracking and fibre breakage and geometrical damages represented in a local change of geometry. Both types of damage are present in impact-induced damage. The interactions between the damage state and

146

axial compressive loading determine the compressive behaviour of the panel. This section studies the post-impact compressive behaviour of composite panels.

Table 4.5.1 Compression test results of impact-damaged and quasi-statically-damaged carbon/epoxy 2-mm thick panels

Specimen Identity[a]	Thickness	IKE	Absorbed energy	Max force	Damage area	Length	Failure load	Failure axial strain	Failure comp. strength	Failure location[b]
	mm	J	J	kN	mm²	mm	kN	%	MPa	
2I0.125	2.19	1.7	0.3	-	77.0	147.39	59.36	0.989	270.7	LE-MS
2I0.250	2.22	3.7	0.7	-	177.0	147.16	48.57	0.785	218.9	MS
2I0.375	2.17	5.7	1.1	-	264.5	147.19	43.47	0.679	200.7	MS
2I0.500	2.18	7.8	1.7	-	427.8	147.14	38.50	0.613	176.8	MS
2I0.625	2.17	9.9	2.9	-	453.5	147.45	36.94	0.576	170.8	MS
2I0.750	2.22	11.8	4.4	-	523.3	147.56	37.16	0.521	168.0	MS
2I1.000	2.20	15.8	10.4	-	676.0	147.59	18.65	0.609	175.7	MS
2I0.500ii	1.96	7.9	2.1	4.73	-	147.10	40.53	0.713	207.6	MS

[a] Data corresponding to the first seven panels are taken from [104]. All panels tested with hemispherical indentor nose shape.
[b] MS, LE and FE denote mid-section, loading-end and far-end positions along a panel, respectively.

Table 4.5.2 Compression test results of impact-damaged and quasi-statically-damaged carbon/epoxy 4-mm thick panels

Specimen Identity	Thick.	IKE	AE	Max force	Nose shape[a]	Damage area	Length	Failure load	Failure far field mean strain	Failure comp. strength	Failure location[b]
	mm	J	J	kN		mm²	mm	kN	με	MPa	
4I0.5	4.09	6.9	4.2	4.27	H	913.8	149.32	88.9	2,461.0	216.8	MS
4I1.0	4.08	13.7	7.3	7.35	H	1697.8	146.21	70.9	1,623.0	172.8	MS
4I1.5	4.08	21.1	11.2	8.57	H	5468.3	147.91	70.9	980.0	173.3	MS
4I2.520	4.22	41.7	-	13.41	H	7854	149.26	57.34	1,335.0	136.0	FE
4QSIFHW	4.22	-	-	10.84	F	4734.2	149.20	100.21	4,165.0	235.3	FE
4QSIF	4.20	-	-	27.92	F	8582	148.19	81.16	2,214.0	187.9	MS
4QSIHHW	4.30	-	-	3.66	H	206.5	147.45	137.90	4,614.5	325.7	LE
4QSIH	4.25	-	-	17.21	H	8302.7	148.68	64.20	851.5	150.4	MS

[a] H and F denote hemispherical and flat indentor nose shape, respectively.
[b] MS, LE and FE denote mid-section, loading-end and far-end positions along a panel, respectively.

Table 4.5.1 and 4.5.2 show the compressive test results for 2-mm and 4-mm thick panels respectively, previously damaged via impact or quasi-static indentation, as described in Chapter 3. Data corresponding to 2-mm thick panels with impact damage were taken from [104].

4.5.1 2-mm thick panels with impact or quasi-statically-induced damage

For the impact-damaged panels 2I0.250 and 2I0.500 (impacted respectively at 3.7 and 7.8 J), the four deformation stages could still be identified by the mid-section strain responses in Figures 4.5.1 and 4.5.2. Panel 2I0.250 was damaged at the relatively low impact energy of 3.7 J and has the projected damage area of only 177 mm^2 with little surface damage. Its strain response characteristics in Figures 4.5.1 are similar to that of panel EH20 with artificial delamination, as expected. As can be seen, the strain divergence and the first strain reversal do not correlate with each other, the local-to-global buckling (mode-I) transition is stable and there is little reduction in its RCS. At the relatively high impact energy of 7.8 J, panel 2I0.500 has noticeable local surface curvature associated with impact damage and the projected damage area of 428 mm^2 shown in Figure 3.3.1(d) with a scan graph. Also this projected damage area is nearly circular. Strain response characteristics shown in Figures 4.5.2 are similar to that of panel EH60. This panel seemed to have failed at the global buckling-to-postbuckling (mode I to mode II) transition as very little sign of postbuckling could be observed. Interestingly, all the panels impacted at the energy of greater than 7.8 J failed catastrophically at the loads that are only fractionally higher than respective global buckling (mode I to II) loads, similar to panel 2I0.500.

The panels that were damaged by impact energies of 7.8 J and greater also have noticeable local surface curvature (see Figure 4.5.3) in addition to interior delaminations and extensive matrix cracks. This aspect may have contributed to the catastrophic compression-after-impact (CAI) failure and thus to a 29% reduction of CSRF along with other aspects of the damage characteristics. Additionally, sublaminates of the impact-damaged panels are likely to be both balanced and unbalanced but most certainly asymmetric. Thus the associated in-plane and out-of-plane couplings could degrade bending stiffness and in theory create a Poisson's ratio mismatch of the sublaminates, thereby contributing to degradation of such panels, as also discussed in [86].

4.5.2 4-mm thick panels with impact damage

Panels of 4-mm thick were subjected to impact loading at various IKE levels. Their damage characterisation in terms of delamination size and internal damage mechanisms is shown in Chapter 3. The area of delamination increased proportionally with IKE and AE. The damage was governed mainly by ILSS, thereby the damage was characterised by dominating large delamination alongside with a small shear cone. This contrasts with 2-mm thick panels, which damage was governed by tensile stress and characterised by a dominant shear cone. Therefore 4-mm thick panels had larger projected delamination areas than the corresponding 2-mm thick panels impacted at similar IKE, as explained in Chapter 3.

The compressive behaviour of panels with impact damage contained characteristics of the both, panels with delaminations and panels with local change of geometry. The similarity with one or the other depended on the degree of damage. For large IKEs, the compressive panel behaviour tended to the panels with artificial change of geometry. On the other hand, for low IKEs the panel behaved similarly to the panels with artificial delamination, in particular to circular multiple delaminations in asymmetric TTT arrangement. Figure 4.5.4 shows the compressive strain response of a panel impacted at low energy (IKE 6.9J, 0.5m height). It is clear from the linear strain behaviour at the far-field location (Figure 4.5.4(a)), that the global trend of the panel was typical of the prebuckling stage, being the effect of damage rather localised. While the strains on the front gauges located at the centre of the delamination (Figure 4.5.4(b)) followed a linear trend, the gauges on the back side revealed weakening of the thinner sublaminate (delamination bulging) starting around 60 kN. The difference between front and back gauges lays probably on the asymmetric distribution of delamination in the thickness direction. The gauge C back, in Figure 4.5.4(a), picked up an apparent local buckling around 20 kN, although it was not noticeable in the other strain gauge readings. Shortly before failure, there was a second strain reversal at 87.3 kN, that could be linked with mode shifting from buckling mode I to II. The panel failed in the postbuckling (mode-II) stage with a shear failure located at the mid-section, as shown in Figure 4.5.5.

149

The effect of increasing the impact energy is shown in Figure 4.5.6, by the compressive strain response from a panel impacted at 13.7 J (1.0-m height). The increase of impact energy did not seem to affect the global in-plane compressive behaviour of the panel as reflected in the far-field location response, in Figure 4.5.6(a). However, the local effect of the damage was more extended than the previous panel. Buckling developed locally at 22 kN as can be seen in the central location (Figure 4.5.6(b)) both transverse and longitudinal. Apparently, increasing the impact energy had an effect of extending the area where the panel underwent local buckling, since it was picked up not only by one gauge (gauge C in the case of the panel 4I0.5m) but also by all the gauges surrounding the damage. At 57.3 kN there was a strain reversal, visible in the central gauges D and E, which marked the shifting from global buckling mode I to mode II in this region of the panel. Gauges D and C on the back side also showed a much larger response than the counterparts on the front side, suggesting delamination bulging, starting also at 57.3 kN. The failure was reached at 70.9 kN, at the mid-section as shown in Figure 4.5.7.

The compressive response of panels 4I1.5m and 4I2.52m were affected by the large material and geometrical damage induced by the high IKEs, as shown in Figures 4.5.8 and 4.5.10. On the one hand, panel 4I1.5m (21.1 J) buckled from the start of the test and shifted from buckling mode I to mode II at 58.9 kN, as the readings from the central gauges D and E suggest. At 64 kN there was another strain reversal much more sudden and large in magnitude, only picked up by the gauges located at the delamination side, B and C. This reflected likely delamination propagation in the transverse direction. However the propagation had probably initiated at 45 kN for reasons explained in Section 4.7. This panel failed at 70.9 kN with the failure located at the mid-section as shown in Figure 4.5.9. The line of failure had some degree of skewing due to the couplings between stretching, bending and twisting, of the asymmetric sublaminates. The effect of these couplings became more noticeable due to the large size of delamination. On the other hand, panel 4I2.52m (41.7 J) also buckled from the beginning, but it did not shift to mode II. It failed at 57.34 kN with the failure located at the far end. Probably the particularly extensive damage present on this panel triggered failure before the mode shifting as a consequence of stress concentration, as shown in Figure 4.5.11. It seems that in both panels the geometric change due to impact was significant enough to trigger out-of-plane deformations at the centre of the panel. This

was reflected on the fact that these panels tended to buckle right from the beginning of the compressive loading, similarly to panels with local change of curvature.

Two additional features were observed from panels 4I1.5m and 4I2.52m. One was the apparent stiffening of the panel, in particular at the location B as seen in Figures 4.5.8(b) and 4.5.10(b). Probably, the opening of delamination stretched the panel at this location, affecting the strain response of the panel. The other feature was a probable transition from buckling mode I to mode II with a slight weakening of the back side (similar to delamination bulging) around 40 kN and 29 kN for IKEs 21.1 and 41.7 J, respectively, suggested by the observation of the longitudinal gauges at the centre and side of the damage on the back side of the panel.

4.5.3 4-mm thick panels with quasi-statically-induced damage

Quasi-static tests with both hemispherical-nosed and flat-ended indentors were carried out by transversely loading the plates either to the onset of delamination (QSIF-HW and QSIH-HW) or to ultimate failure (QSIF and QSIH). For the former, smaller delamination areas were contained within respective panels as shown in Chapter 3, for the latter, delamination areas spread to the edges of respective panels. In addition, severe local damage around the contact region with the indenter made bonding strain gauges impossible. The two panels loaded until the onset of delamination failed in compression with end crushing similar to the intact panel or panels with a small single delamination. Figures 4.5.12(a-b) show the strain response curves of panel QSIF-HW with no sign of buckling, similar to that of the panels containing a small single delamination. Although local buckling developed initially from the beginning up to about 5 kN in Figure 4.5.12(b), it reversed to compression beyond 22 kN and this was found to be associated with local curvature change that resulted from the transverse quasi-static loading. On the other hand the two panels fully loaded failed in the mid-section region, as expected. Table 4.5.2 shows the compressive test results for panels with damage induced by quasi-static transverse loading.

4.6 Panels with open holes

The compressive behaviour of panels with open holes should present a low bound of CSRF when compared to other types of preconditions. Material removal caused by drilling a hole through the laminate strongly affects compressive properties. Previous open-hole compressive testing [124] has revealed that main failure mechanisms are governed by stress concentration and are fibre microbuckling and matrix cracking followed by induced delamination caused by the interaction of the first two mechanisms. Table 4.6.1 shows the compressive test results for panels containing open hole. An additional feature studied was the effect on compressive behaviour of changing the composite system from the usual T700 fibres to a less stiff one based on T300 fibres.

Table 4.6.1   Summary of compression test results of 4-mm thick composite panels containing open hole

Specimen Identity	Hole size mm	System [a]	Thickness mm	Length mm	Ultimate load kN	Ultimate far field mean strain μE	Ultimate comp. strength MPa	Failure location [b]
Hole20	20	T700	3.89	149.79	95.86	2,755.50	248.00	MS
Hole40	40	T700	3.96	149.36	84.77	1,009.50	212.70	MS
Hole60	60	T700	3.92	149.46	53.39	-377.50	135.68	MS
Control OH1	-	T300	3.99	149.64	105.86	3,787.00	269.13	LE
Control OH2	-	T300	3.98	151.81	95.92	-	244.17	LE
Hole5	5	T300	3.99	150.50	88.63	4,299.50	224.19	LE
Hole10	10	T300	3.97	150.80	85.67	4,369.50	218.75	LE
Hole20	20	T300	4.00	150.00	77.52	3,750.00	195.76	MS
Hole40	40	T300	4.00	150.00	76.54	2,900.00	193.28	MS
Hole60	60	T300	4.00	150.00	57.06	2,300.00	144.09	MS

[a] T300 and T700 denote for T300/LTM-45EL and T700/LTM-45EL systems respectively. System T700 is the system normally used in the other specimens of this study.
[b] MS and LE denote mid-section and loading-end positions along a panel, respectively.

Open hole reduces the overall stiffness of the panel and lowers the ultimate failure load. Figure 4.6.1 illustrates this for the composite system based on T700. It also includes the load-displacement curve of a 4-mm thick intact panel (Control 2) as a reference. In the case of the largest hole size (Hole 60, 60% of panel width) the reduction of in-plane stiffness was 40% respect to the smallest hole (Hole 20, 20% of panel width). Comparing the compressive strength of the same pair of panels the reduction was 45%.

152

The effect of the hole on the internal stress and strain distribution is dramatic, since it can increase several times the far-field value, close to the hole edge, as shown by [123]. However, the strain redistribution not only happened in the width direction, but also in the longitudinal direction. In [123] the far-field strain value was reached at approximately one diameter distance from the hole edge, in the width direction. Longitudinally, this happened as well as shown for the far-field strain in Figure 4.6.2. All three panels (system T700) were strain-gauged at distance of 25 mm from the bottom edge, for far-field strain monitoring. The reading for the far-field location for the panel Hole 20 can be considered as the real far-field value, since it is 40 mm (2 hole diameters) distanced from the edge of the hole. If the size of the hole increases to 40 mm, then the far-field location is only 45 mm away, or half hole diameter. At this distance there was stress and strain redistribution, with lower compressive stress below the hole, and higher stress along the remaining material. The corresponding strain readings showed lower compressive values than the previous panel. For the panel Hole 60, the far-field gauge was only 10 mm away from the bottom edge of the hole (1/6 of the diameter away). The compressive strain vanished completely under the hole and the strain gauge only picked up the Poisson's ratio effect from the two parallel strips loaded at either side of the hole, that in this case were compressing the central region laterally. The strain gauge readings of the panel Hole 60 showed stretching (tensile) generated by this lateral compression, with a negligible contribution from the compressive loading. The distribution of stress and strain in the load direction is schematically shown in Figure 4.6.3. Figure 4.6.4 shows photographs of the failed panel Hole 60, with the far-field location marked.

Through-the-thickness strains were measured at two points on the free edge of the hole, using strain gauges orientated parallel to the hole axis as explained in Chapter 2. The two locations chosen were labelled as 'top' for the one on the loading axis and 'side' for the one in the mid-section axis. Data measured by these gauges are shown in Figure 4.6.5. On the one hand, Gauge B at the side of the hole indicated a tensile strain for the three panels, decreasing their slope when the size of hole increases. In other words the interlaminar shear strain and stress were affected by the size of hole, the larger the hole the larger the ILSS was for the same axial load level. Close to failure, the readings from gauge at location B in panels Hole 20 and Hole 40 had a small disturbance, as the detail

in Figure 4.6.5 shows. This probably reflects the combined effect of high in-plane compressive strain and high ILSS near the hole, causing local delamination to occur and propagate across the specimen as the applied load increases [123, 124]. On the other hand, SG at C was under compression, due to the complex deformation pattern around the edge of the hole and interactions with the Poisson's stretching effects. Similar results were found by [123].

4.7 Mechanisms of delamination propagation

The general consensus in the investigation of RSC is that the existing delaminations propagate sideways or transversely in the width direction during compressive loading if their size is large enough [81, 87, 91-94]. Having established the strain response characteristics for the panels without and with the preconditions, a subsequent significant issue is whether or not such propagation triggers or precipitates catastrophic failure. And if it does, whether the global buckling (mode I to II) load correlates with RSC or not. Since it is extremely difficult, if still possible, to experimentally measure interior ILS stresses, local ILS stresses or internal stress gradients within the panels can only be deduced on the basis of strain response characteristics. Interrogation of transverse strain responses in addition to longitudinal ones could be particularly helpful to establishing physical mechanisms of delamination propagation.

For small delaminations, the occurrence of local buckling (mode-I) and local-to-global buckling (mode-I) transition were found to be stable earlier with the strain divergences, strain reversals and global buckling loads all appearing at the different load levels. Therefore, the likelihood of inducing significant local transverse ILS stresses was small and there was slim possibility for the delamination to propagate or reach the critical state in those stages of loading. However, unstable global buckling-to-postbuckling transition (mode I to mode II) could induce substantial variations of local ILS stresses when the mid-section crescent of one half-wave becomes the nodal line in the longitudinal direction. Contrastingly in the majority of cases, the transverse readings exhibited some degree of bending caused by the couplings induced by two or more asymmetric sublaminates. Since two balanced sublaminates in the delaminated section are asymmetric, the extension-bending and bending-twisting couplings existed. That is,

in-plane compressive force results in bending and twisting curvatures in addition to the in-plane deformations leading to mid-plane strains. This was reflected on a to a skewed fracture plane, consistent with the fracture plane of panel EH20 among many others, as shown in a photograph in Figure 4.3.2. A similar finding by using holographic interferometry was also reported in [125].

The lack of delamination propagation was found to be common among 2-mm thick panels with either a single vertical elliptical delamination of any size or single circular and horizontal elliptical delaminations of less than 40 mm wide. Similarly, panels with impact-induced damage did not seem to show any indication of sideways propagation of delaminations, as seen in panels 2I0.250 and 2I0.500 in Section 4.5.2. For relatively large delamination sizes of 40 mm and beyond, the unstable global buckling-to-postbuckling (mode I to mode II) transition triggered delamination propagation. In some panels (CR40 and CR60), even the local-to-global buckling (mode I) transition led to delamination propagation. For instance panel (EH60) with a 60-mm horizontal elliptical delamination showed a clear split of mean strains in both directions (Figure 4.3.3(b)) particularly marked on the side of delamination (strain gauge B), which confirms that such delamination may have propagated sideways in the postbuckling stage so as to precipitate the catastrophic failure of the current panel at the load of about 38 kN. This also suggests that the presence of the larger delaminations did cause some stress redistribution around the delaminated areas. On the contrary, the impact-damaged panels yielded very little clear sign to allow the similar deduction to be made due partially to the limited number of SGs used.

In the case of 4-mm thick panels, the apparent lack of delamination propagation was common even with the largest single artificial delamination (60-mm diameter). It was not until multiple (C40x3S/AS) 40-mm diameter delamination were embedded, that the strain reversals at the global buckling-to-postbuckling transition (mode I to mode II) became unstable and indicated a likely delamination propagation, as shown for example in panel C40x3S in Figure 4.3.13. In the case of panels with impact-induced damage, the mode shifting was clearly unstable for IKE's equal or greater than 21.1 J with a projected delamination area of 5468 mm^2.

4.7.1 Analysis of panel in-plane compressive deformation

On the basis of all these established characteristics from the present panels, two cases of the compressive and buckling behaviour can symbolically be depicted sequentially in Figure 4.7.1 for the loading direction and in Figure 4.7.2 for the width direction. Clearly, the longitudinal sequence of I→II→III→IV→V in Figure 4.7.1 in conjunction with the transverse sequence of i→ii or i→ii→iiia in Figure 4.7.2 represent the strain response characteristics of 2-mm thick panels with no damage, small artificial delamination, or little impact damage. Panel EH20 in Figure 4.3.1(b) is an example of such behaviour. The key feature of the transverse sequences is that the delamination is not large enough to be involved in the two transverse half-waves, irrespective of the transverse mode shapes. Thus, local ILS stresses at the transverse fronts of the delamination are likely to be small as if the mid-section region of the panels behaved as long 'beams'. On the contrary, the longitudinal sequence of I→II→III→V along with the transverse sequence of i→ii→iiib represent the strain response characteristics of both 2-mm and 4-mm thick panels with large artificial delamination(s) or substantial impact damage. The transverse fronts involving the two transverse half-waves are very likely to promote delamination propagation as it was observed in panel CR40 in Figure 4.3.4(c).

In panels with artificial delamination it was observed that the extensional-twisting coupling induced a skewed deformation. This was observed in the transverse direction as illustrated in Figures 4.7.2(iiia-iiib). Depending on the size of delamination, the delamination propagation may be influenced by the ILSS concentration at the edge of delamination due to the transverse deformation in conjunction with the longitudinal buckled shape. A preconditioned 2-mm thick panel (CR40) containing a 40-mm circular delamination seems to demonstrate the mixed effect of bifurcation and high ILS stress concentration. Figure 4.3.4(c) shows the transverse strain gauge readings at the centre (E) and side locations (C). It shows two probable delamination propagations, one after 20 kN and the other with increased magnitude at 30 kN. Then strain bifurcation and ILS shear concentration might have triggered delamination opening.

156

For 4-mm thick panels, intact panels and panels with delamination area lower than 1257 mm^2 only underwent a longitudinal sequence given by I→II along a transverse deformation i or in some cases i→iiia, like in the intact panel Control 3 (Figure 4.2.7). However, panels with higher cumulative areas of artificial delamination such as panel C40x3S followed the longitudinal sequence I→II→III→V with the transverse sequence i→ii→iiib. This sequence was slightly altered in panels with asymmetrical distribution of delamination, such as panel C40x3AS. The longitudinal sequence in this case was I→II→III→IIIb→V, so that frontal bulging of the thinner sublaminate was included. To summarise, the transverse deformation sequences derived from the transverse SGs readings are i→ii for panels C60QS, C20x3AS, 4I0.5m; i→ii→iiia for panels C40x3AS, C60x3AS; and i→ii→iiib for panels C40x3S, C60x3S, 4I1.0m, 4I1.5m and 4I2.52m.

The in-plane deformation step in the longitudinal sequence was not present when the dent left by the impact in 4-mm thick panels was significant, inducing local change of geometry. Panels with such characteristics were 4I1.5 and 4I2.52, impacted at 21.1 and 41.7 J respectively. These panels had buckling (mode-I) from the start of compressive loading, as reported in Section 4.5. They also had bulging of the thinner sublaminate, since their damage distribution was asymmetrically distributed through the thickness. The longitudinal deformation sequence for these panels was III→IIIb→V.

4.7.2 Poisson's effect

Clearly the global buckling and postbuckling in both loading and width directions interacted to each other and to the existing delamination as well. This interaction seemed most significant at the unstable global buckling-to-postbuckling transition. As monitoring the Poisson's effect of the mid-section of the panels during loading presents a collected response of four SGs, thus it would logically be more instructive to the mechanisms of delamination propagation than interrogating individual SG pairs. This is demonstrated in Figures 4.7.3(a-e) for five representative 2-mm thick panels. Once proper contact was established at the beginning of prebuckling, respective Poisson's ratios from the two mid-section SG pairs rapidly approached about 0.25, which is

reasonably close to v_{yx} of 0.3 predicted by the classical lamination theory. While slowly increasing for intact panel B and panel EH20 with small delamination, they more or less remained constant during local and global buckling (mode-I) for the two panels EH60 and CR40 with large delaminations. Beyond the global buckling (mode I to II) loads, the Poisson's ratio of panels with small or no damage rapidly decreased with the same rate shown in Figures 4.7.3(a-b). In panels with medium damage it increased as shown in Figure 4.7.3(c) (2I0.500ii).

For panels with significant damage, the Poisson's ratio exhibited a dramatic divergence as shown in Figures 4.7.3(d-e). As discussed earlier, there was little evidence found for delamination propagation in the former. In the latter, this distinctive divergence could promote a critical state of local ILS stress at the delamination fronts in the width direction and thus the existing delamination could have propagated. This suggests that the unstable transition of buckling modes at the global buckling loads precipitated the propagation of the existing delamination of a substantial size. Among all the tested 2-mm panels, only four panels (EH60, CR40, CR60 and 2I1.000) have large respective delamination areas of 942 mm^2, 1256 mm^2, 2827 mm^2 and 676 mm^2. They are much greater than the transitive area of 455 mm^2, which was observed in Section 4.3 earlier.

For the same token as Figure 4.7.3(a-e) for 2-mm thick panels, the Poisson's ratios of 4-mm thick panels can also be examined in Figure 4.7.4(a-e). It is clear that the panels (C20QS, 4EH20 and QSIH-HW) with little damage show the dominant and well-defined Poisson's effect in Figure 4.7.4(a-c) with little sign of local or global buckling (mode-I) and no sign at all for postbuckling (mode-II), thereby giving no evidence for delamination propagation. When the size and intensity of delaminations grew, the existing delaminations in Figure 4.7.4(d) for panel C40x3S propagated in a dramatic manner, similar to 2-mm thick panel in Figure 4.7.3(d). This simply confirms that the progressive transition of the buckling modes at global buckling (mode I to II) load triggers propagation of the large existing delamination.

In the case of impact damage, a close examination of strain gauge readings of the panel 4I1.5m in Figure 4.5.8 suggests delamination propagation beyond 45 kN. The Poisson's ratio plot in Figure 4.7.4(e) shows an initial decreasing trend for both central and side

locations from 40 to 45 kN, followed by an opposite trend with the central location increasing and the side location decreasing. This load level coincides with the detection of delamination bulging by the longitudinal gauges, biased towards the back side of the panel. Thus, the transition from local to global buckling (mode-I) with delamination bulging is in this case what triggered delamination propagation. In this case it was not the mode shifting that triggered the propagation, since the global buckling (mode I to II) load was reached in a later stage at 58.9 kN, as shown in Figure 4.5.8.

4.8 Concluding remarks

The compressive load range of 4-mm thick intact panels was within the denominated in-plane compressive stage, characterised by linear strain response from the panel. On the other hand all the 2-mm thick panels failed in the post-buckling (mode-II) stage, characterised by a failure location at the mid-plane, and triggered by a high ILSS concentration.

A damage threshold was found for 2-mm and 4-mm thick panels. On the one hand, for 2-mm thick panels the damage threshold was found at the 25% panel width or 455-mm^2 damage area, irrespective of shape, orientation or nature of damages. The panels failed soon after the unstable global buckling-to-postbuckling (mode-I to mode-II) transition and lost most postbuckling resistance. Some evidence was found for the sideways propagation of the delaminations. On the other hand for 4-mm thick panels, there was also a damage threshold that separate two types of compressive failure, in-plane failure and shear failure due to panel buckling. This threshold was 1257 mm^2, which includes all elliptical delaminations and single circular delaminations up to 40-mm diameter.

The degree of RCS's reduction of panels with a semi-spherical dome was up to 55% of the intact panel CS. The failure was related with ILSS concentration around the dome and flexural bending at the centre.

Post-impact compressive strength and compressive behaviour depends on the severity of the damage induced by impact loading. For low IKE (panels 4I0.5, 4I1.0) the damage inflicted onto the panel consists mainly of internal delaminations. Therefore the

behaviour is similar to the panels with multiple artificial embedded delaminations, with local buckling on the damage area and bulging of the thinner sublaminate. When the IKE increases, the effect of the local change of geometry become significant (panels 4I1.5 and 4I2.52). The compressive behaviour of impact-damaged panels can be considered as a combined action of local change of geometry and internal delaminations.

The effect of open hole on the RCS of a panel is dramatic. The effect of removing material is not only to lower the CS but also to determine the strain distribution around the hole up to one diameter distance in all directions.

The key issue in the determination of delamination propagation and its relationship with compressive behaviour and failure is whether the ILSS concentration at the transverse edge of delamination is large enough or not to trigger propagation. The ILSS state at the edge of delamination is determined by the size of delamination and by the degree of skewing (in one or two half-sine waves) of the panel caused by the stretching-twisting and stretching-bending couplings of the sublaminates in the damaged region.
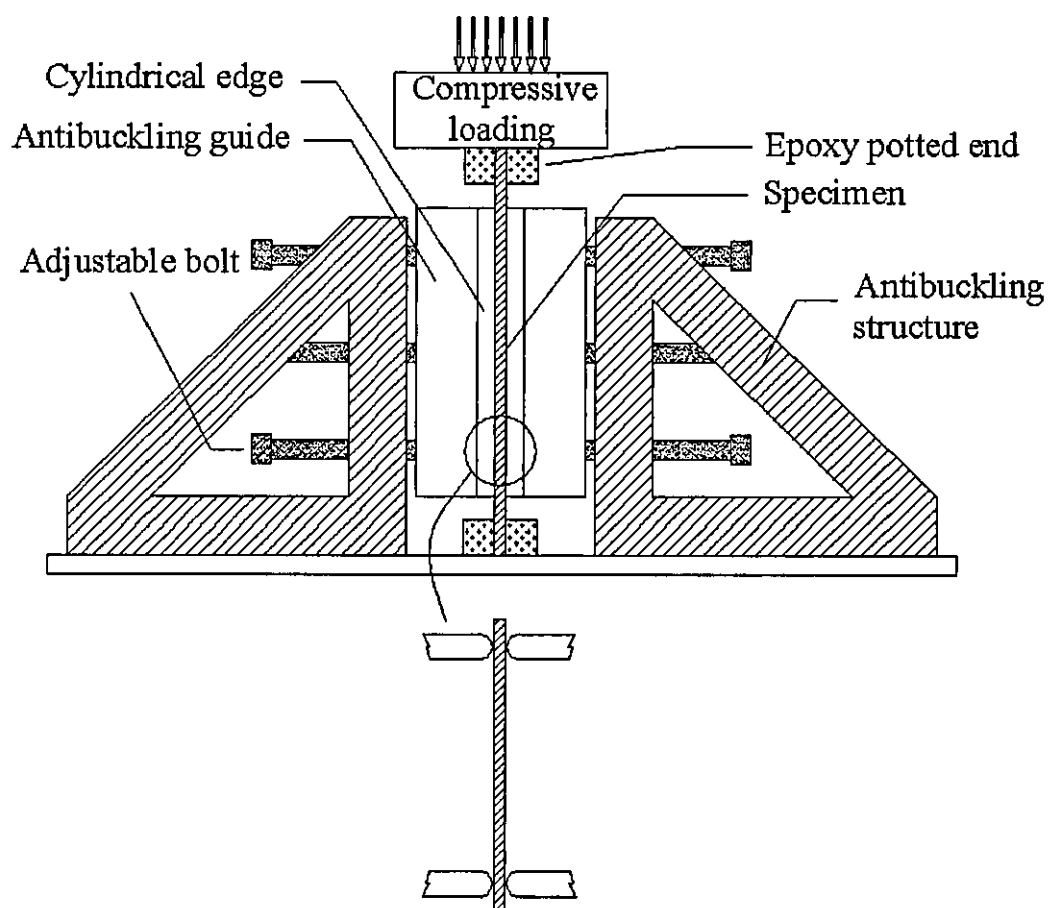
Figure 4.1.1   Experimental set-up of panel in compression with anti-buckling support rig

Figure 4.2.1 Schematic characterisation of the compressive behaviour of an intact panel at the mid-plane and far-field locations for the three stages in compression (a) in-plane (pre-buckling) compressive loading (b) local buckling mode I, (c) buckling mode I and (d) postbuckling mode II

(a)

(b)

163
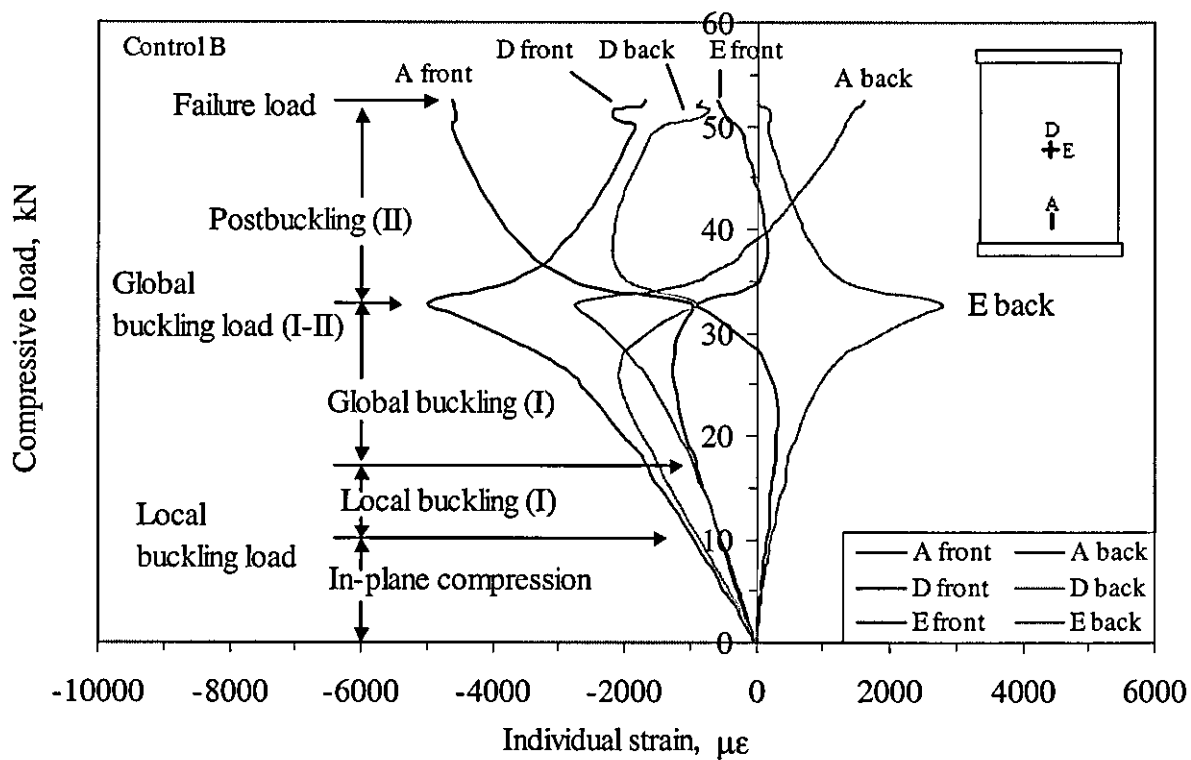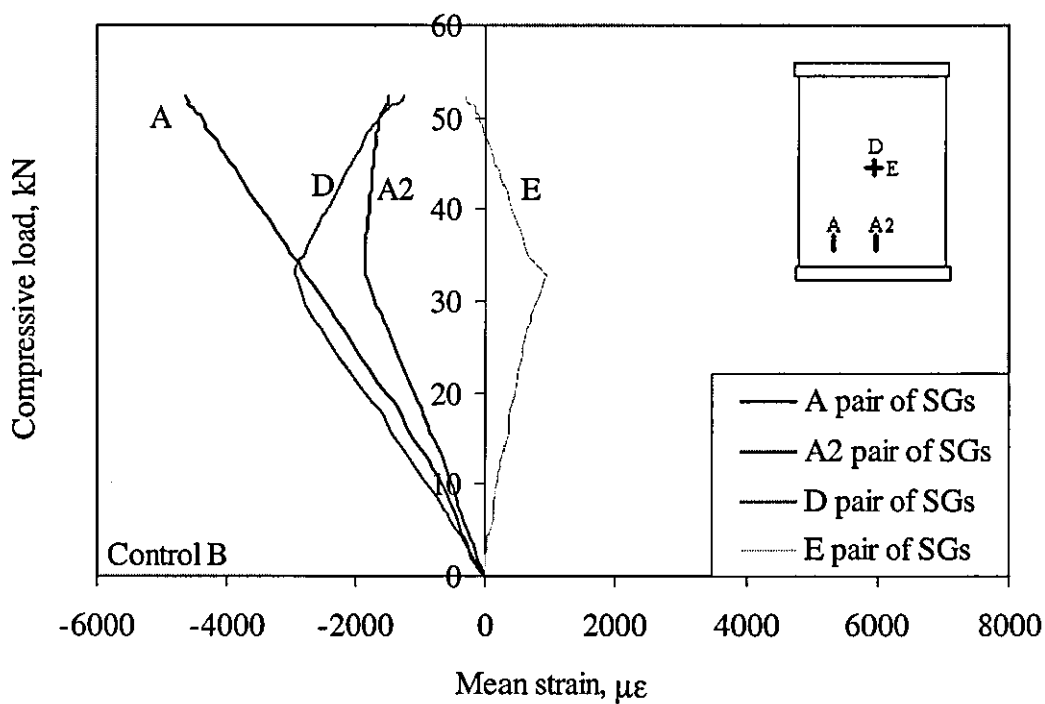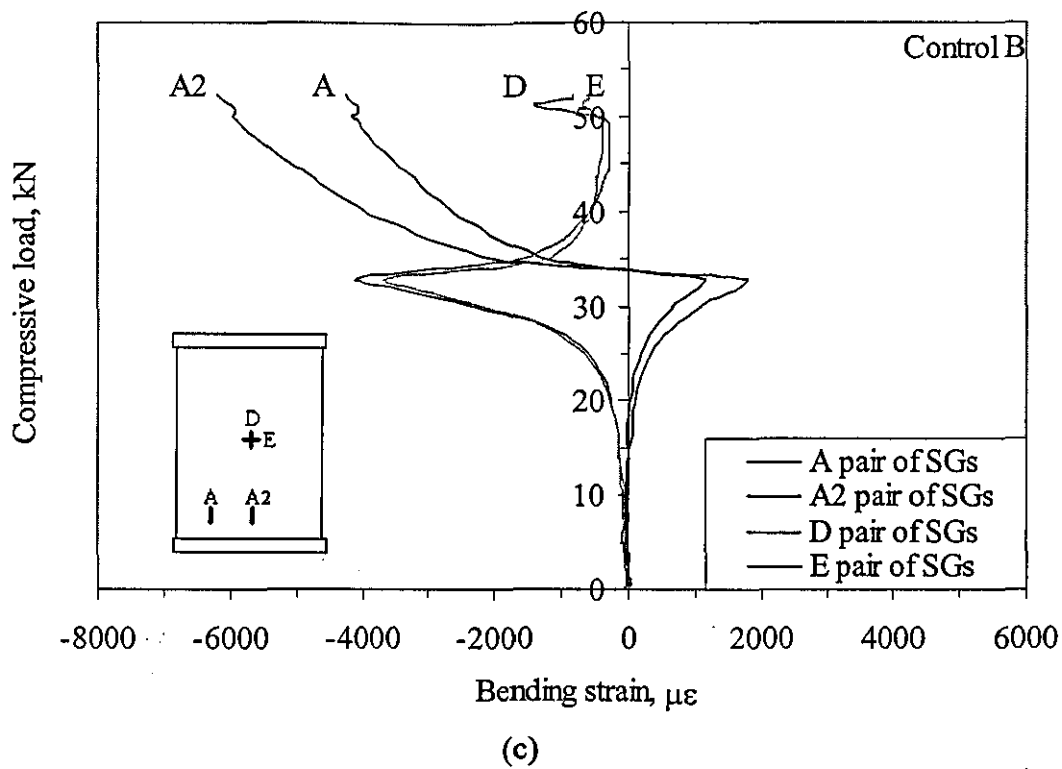
Figure 4.2.2 (a) Load-individual, (b) load-mean and (b) load-bending strain response curves of far-field, longitudinal central and transverse central locations from a 2-mm thick intact panel [104]
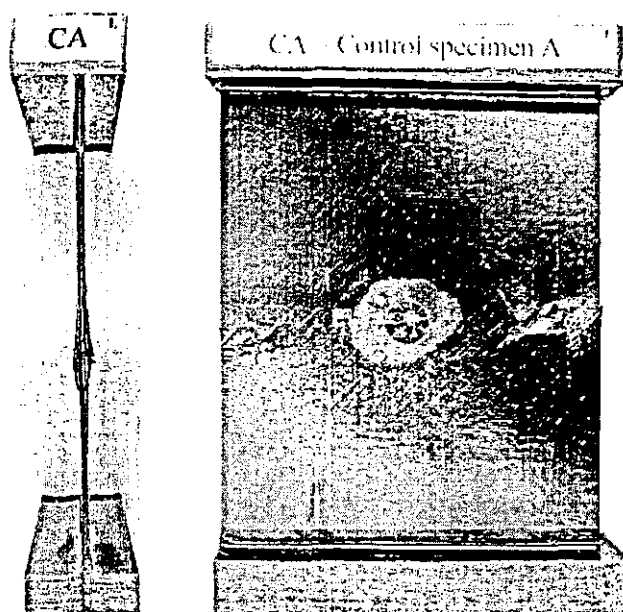
Figure 4.2.3 Photographs of a failed 2-mm thick intact panel [104]
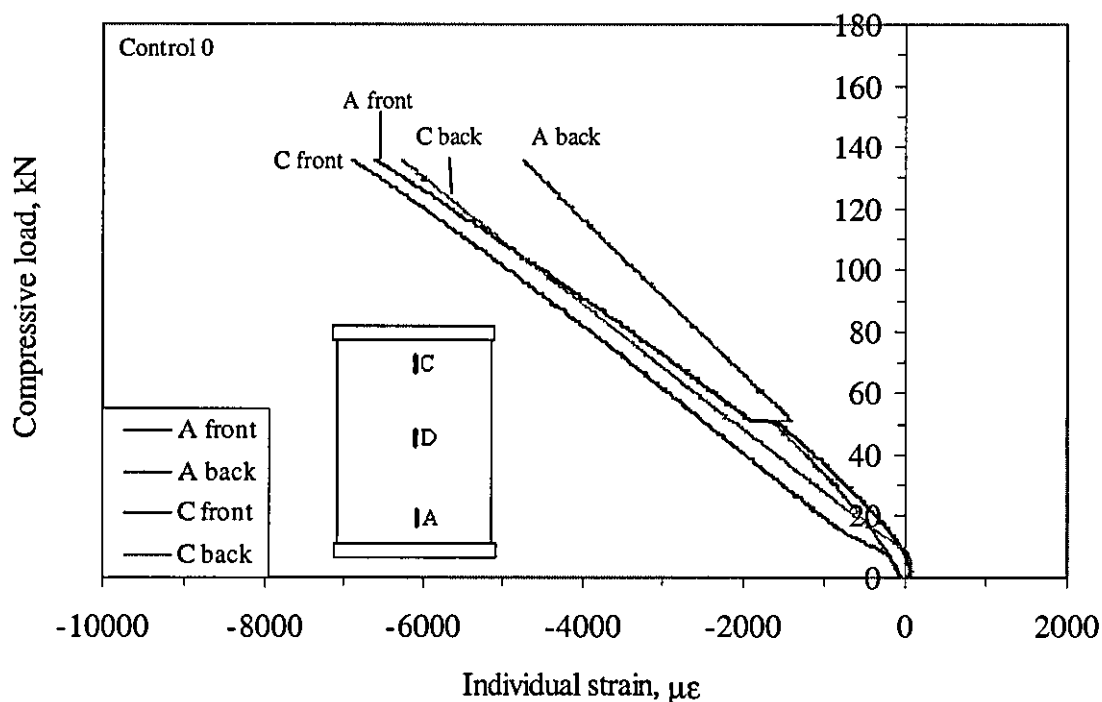
(a)
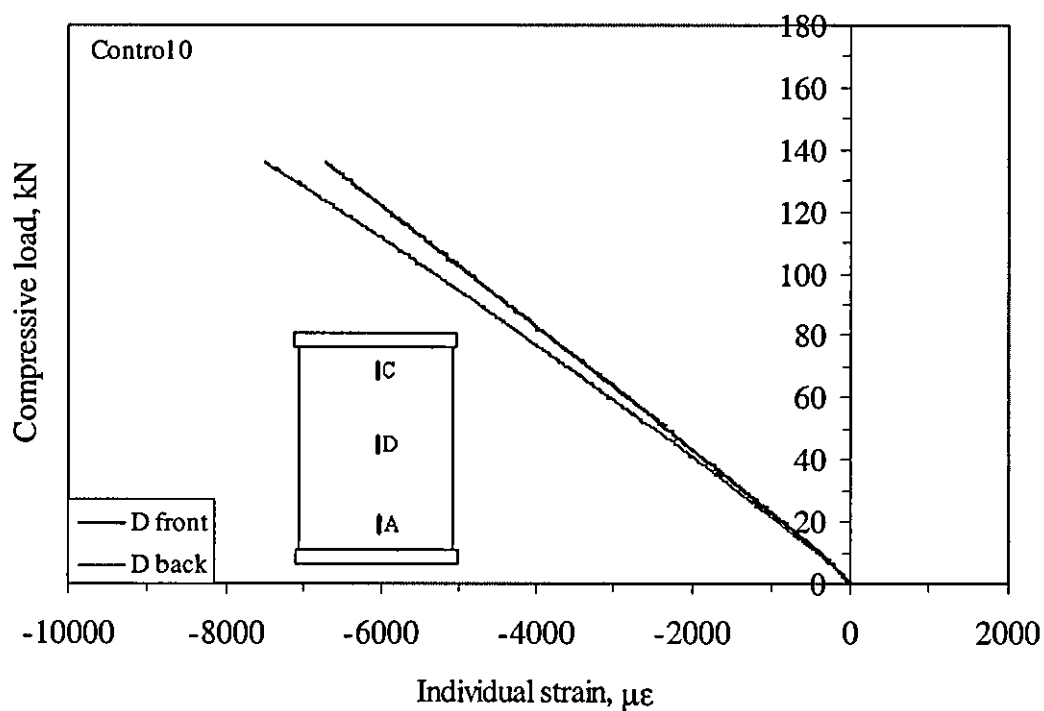
(b)

Figure 4.2.4 Individual strain response curves from (a) far-field and (b) mid-section
locations of a 4-mm thick intact panel (Control 0)

165

(a)   (b)
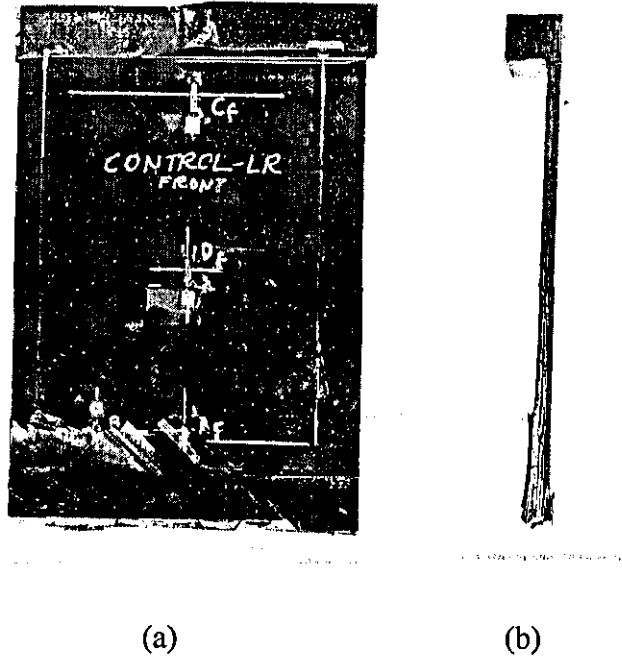
Figure 4.2.5 Photographs of a failed 4-mm thick intact panel (Control 0) (a) front view
and (b) side view
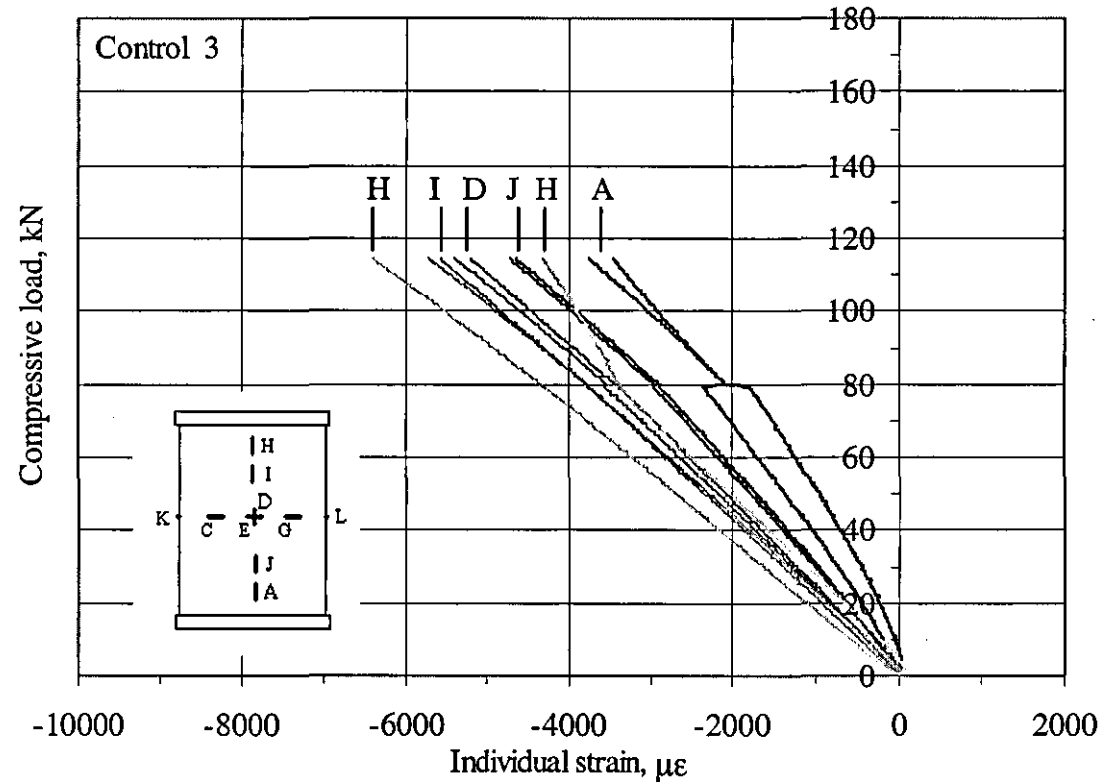
Figure 4.2.6 Individual strain response curves from longitudinal strain gauge locations
of a 4-mm thick intact panel Control 3 (Data between 114 and 125.8 kN were lost)
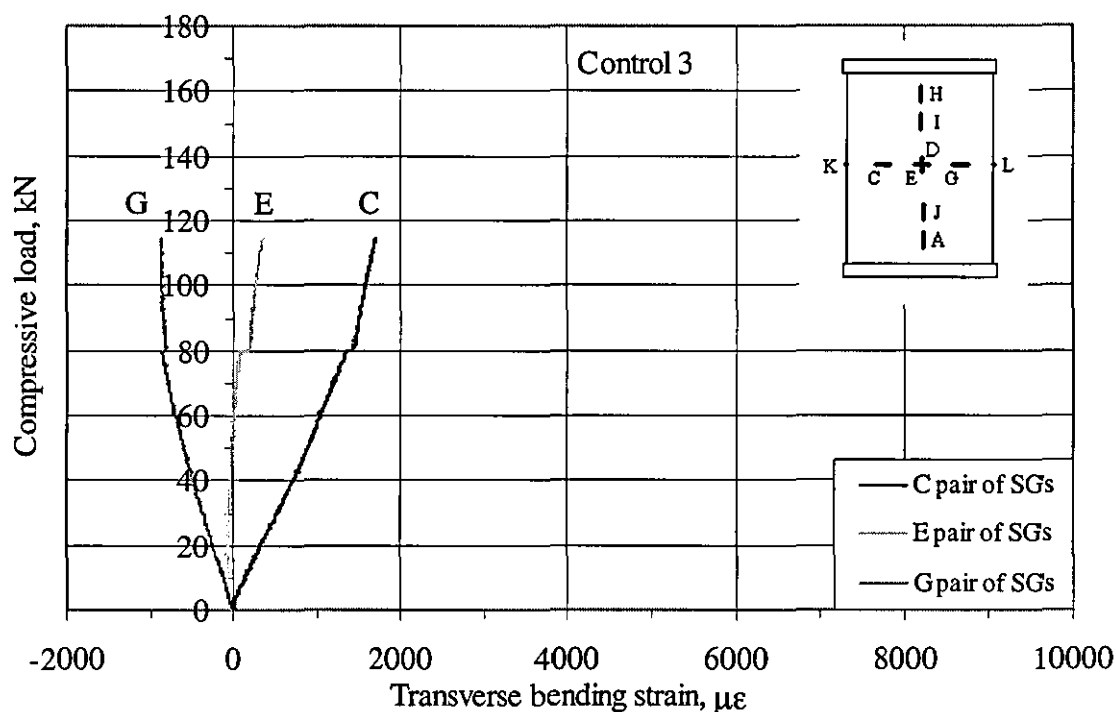
(a)
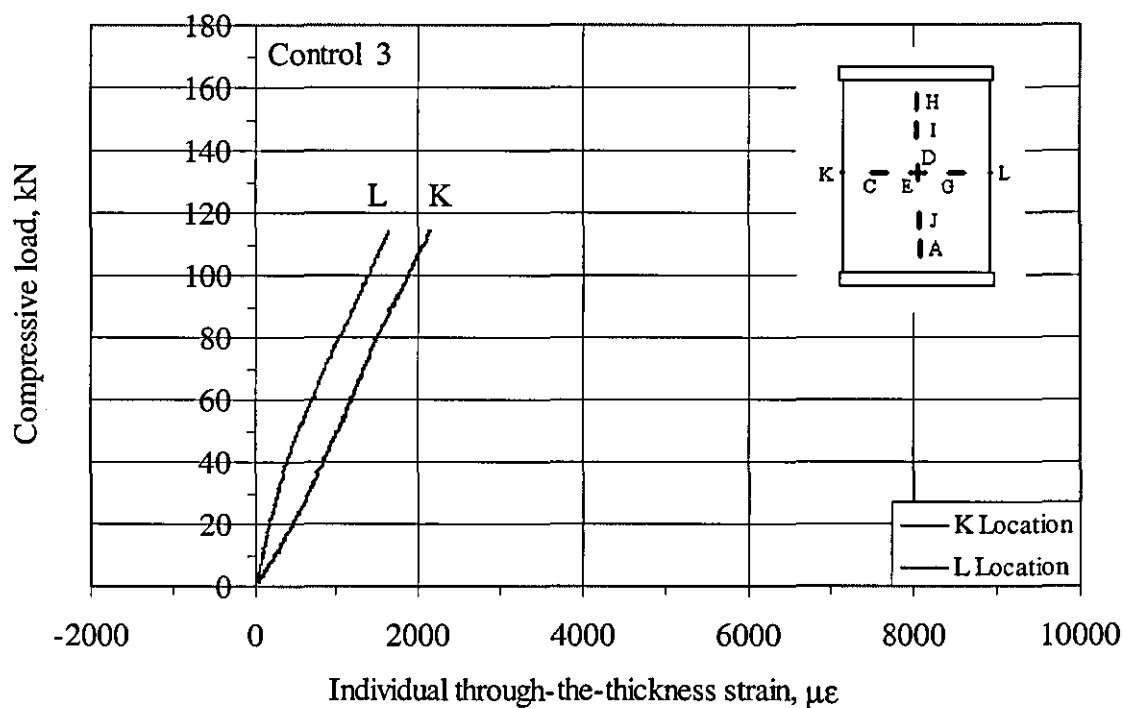
(b)

Figure 4.2.7 Load-strain response curves from (a) bending strain in the width direction and (b) individual strain through-the-thickness of a 4-mm thick intact panel Control 3 (Data between 114 and 125.8 kN were lost)
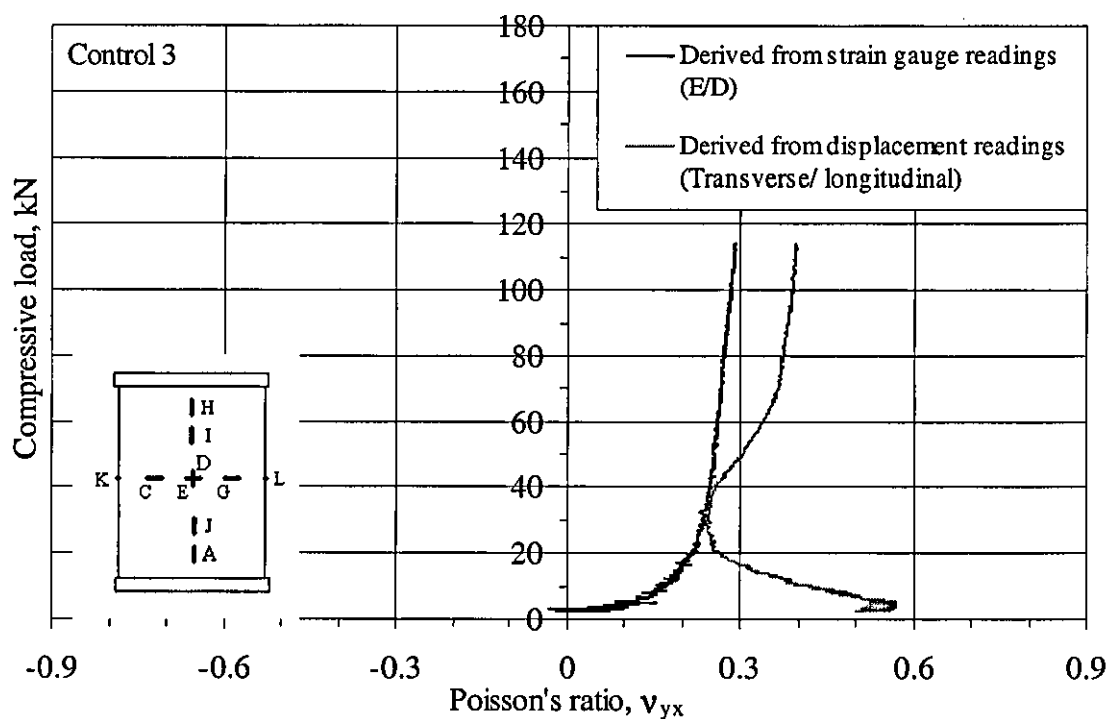
Figure 4.2.8 Poisson's ratio – load curves of an intact 4-mm thick panel Control 3
(Data between 114 and 125.8 kN were lost)
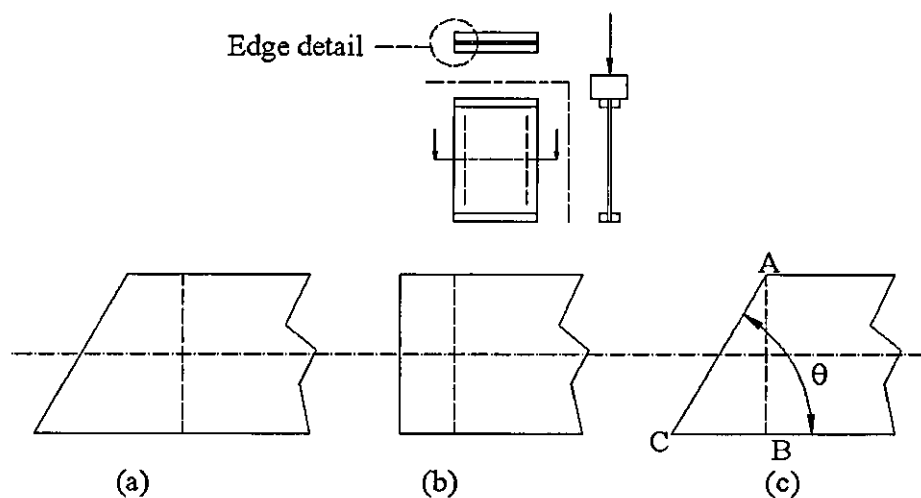
Figure 4.2.9 Edge deformation during in-plane loading (a) full deformation, (b)
Poisson's effect contribution and (c) ILSS deformation contribution

168
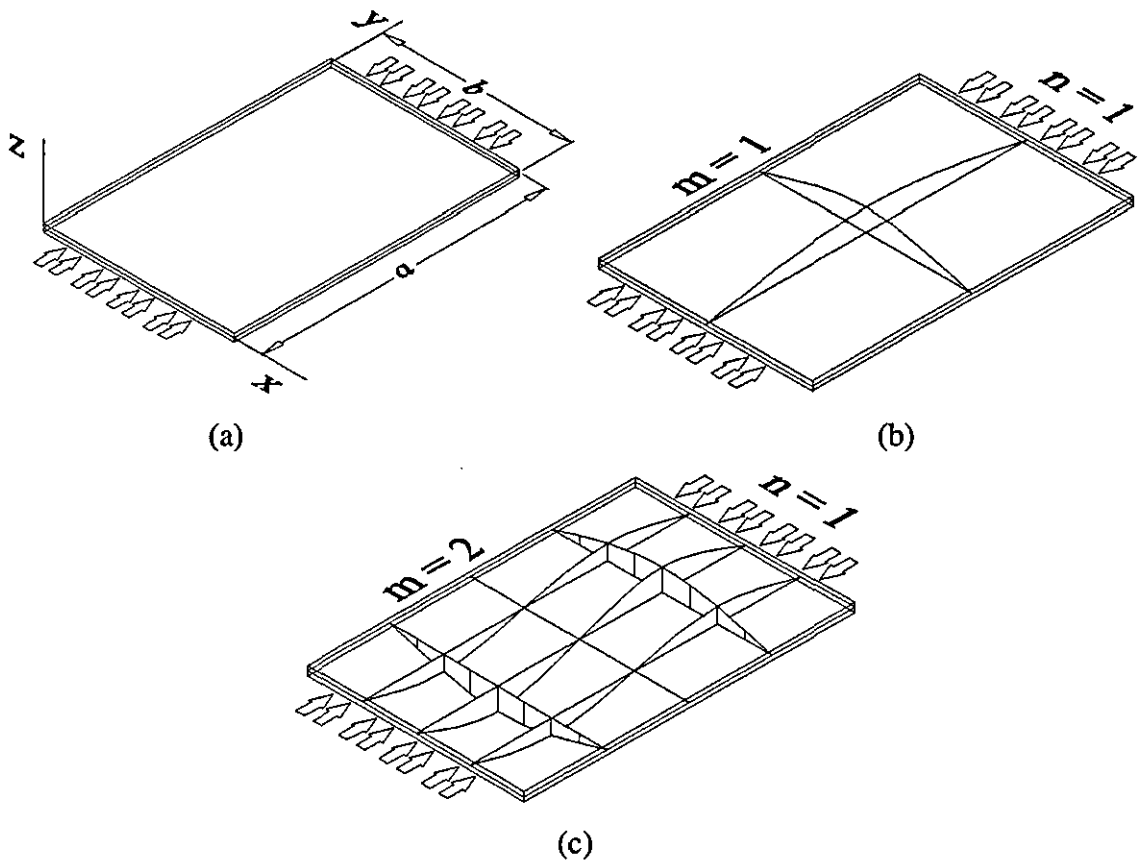
Figure 4.2.10 Panel deformation during loading stages (a) in-plane compression, (b) buckling mode I and (c) buckling mode II
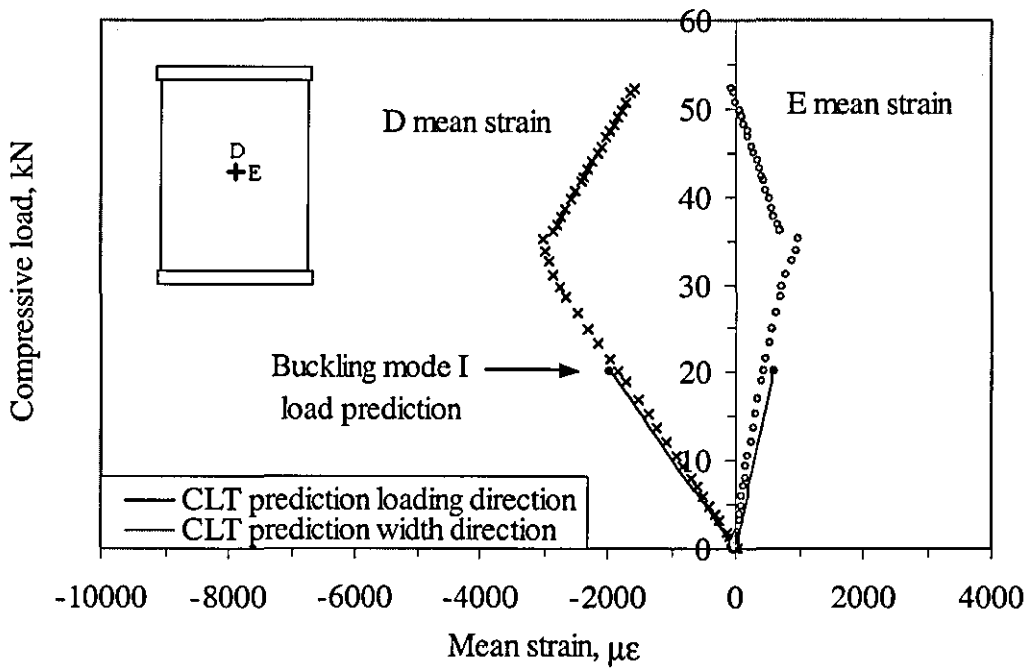
Figure 4.2.11 Classical laminate theory prediction during the in-plane compressive stage for 2-mm thick panel, compared with experimental results from Control A
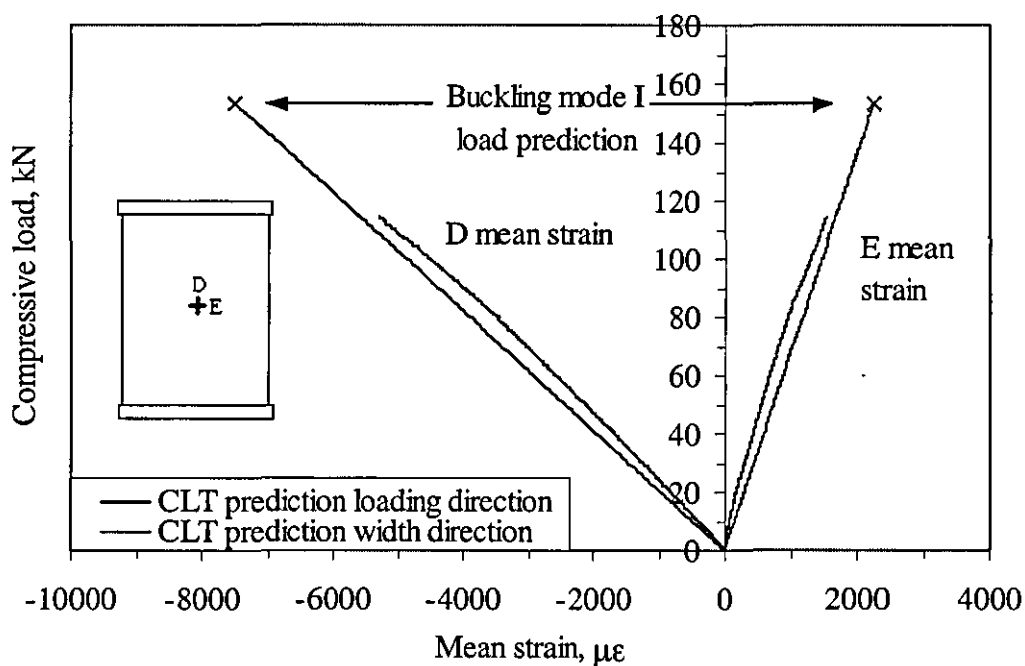
Figure 4.2.12 Classical laminate theory prediction during the in-plane compressive stage for 4-mm thick panel, compared with experimental results from Control 3

(a)
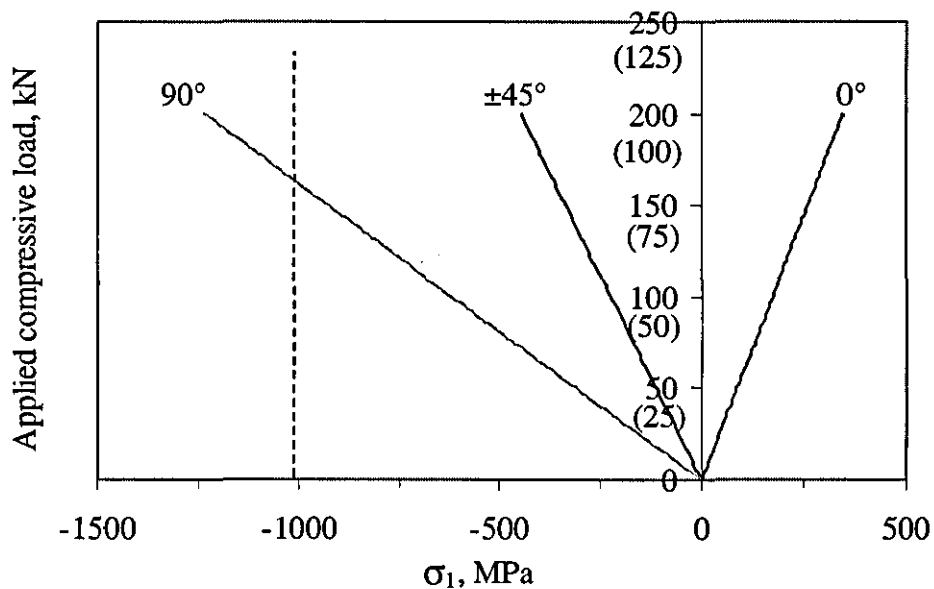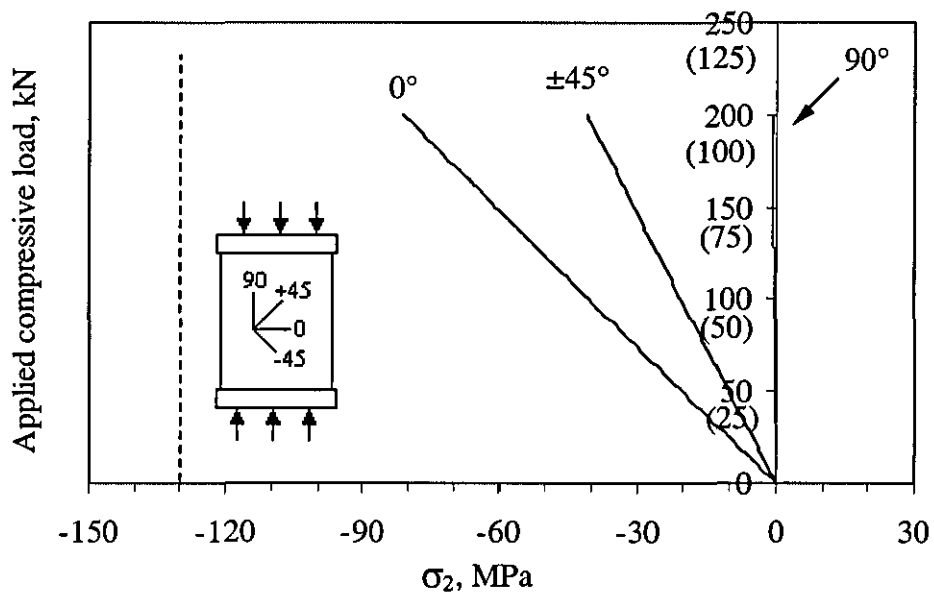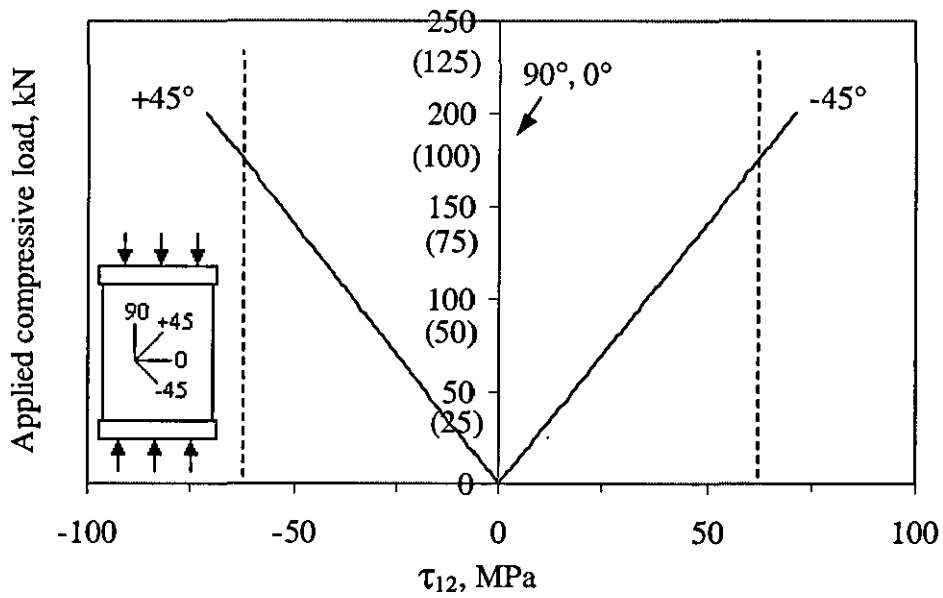
Figure 4.2.13 (a-b) Normal and (c) shear stresses in principal ply coordinates for 16 and 32-ply panels (values for 16-ply panel are in brackets)

171
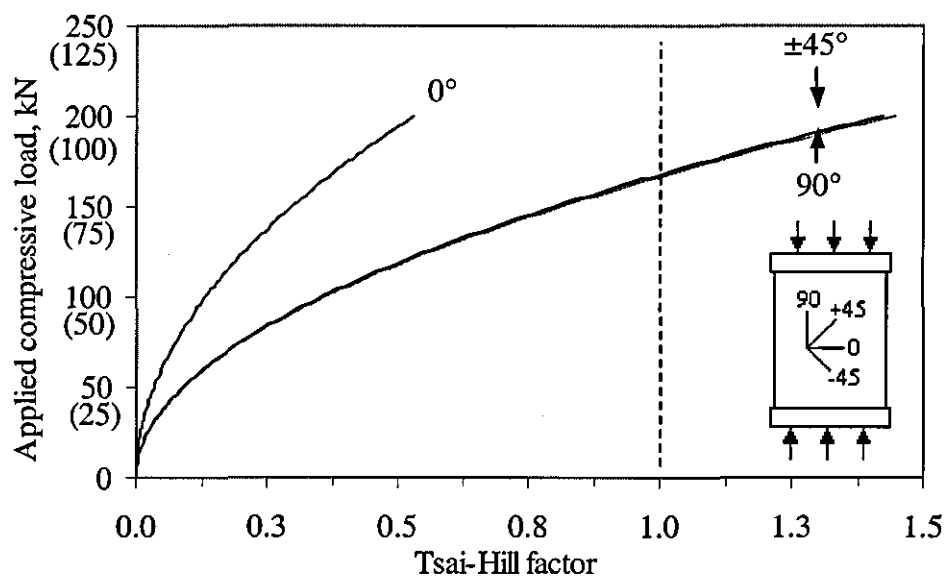
Figure 4.2.14 Variation of Tsai-Hill criterion factor with in-plane compressive load for
16 and 32-ply panels (values for 16-ply panel are in brackets)

(a)

172

(b)

(c)

173
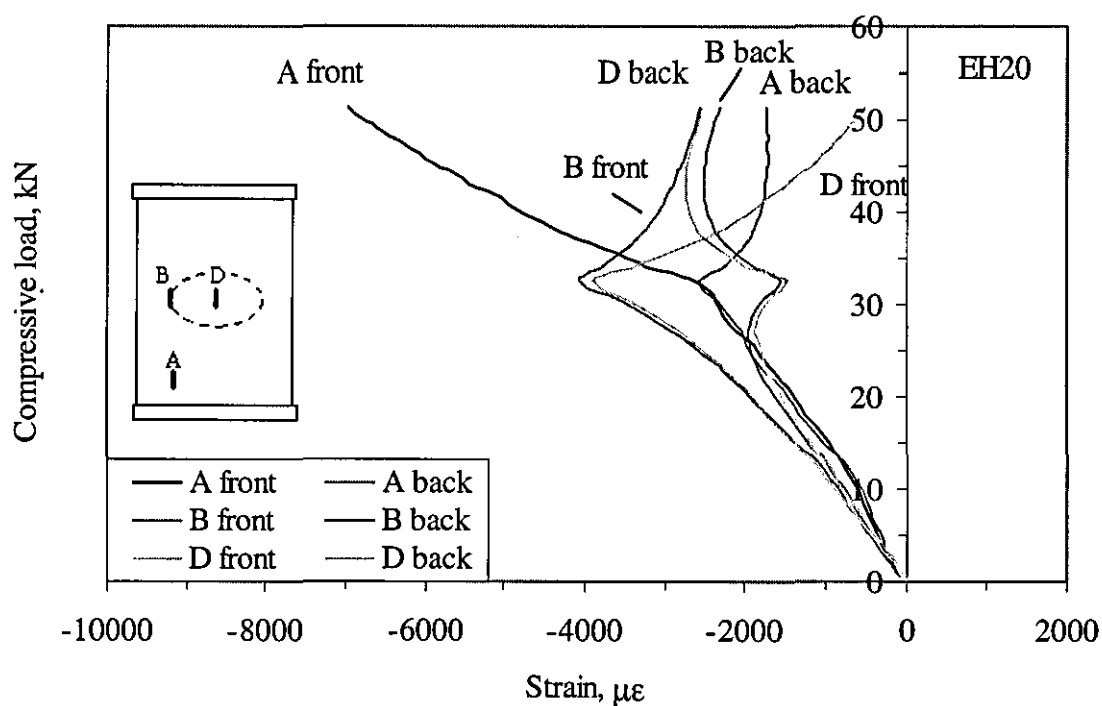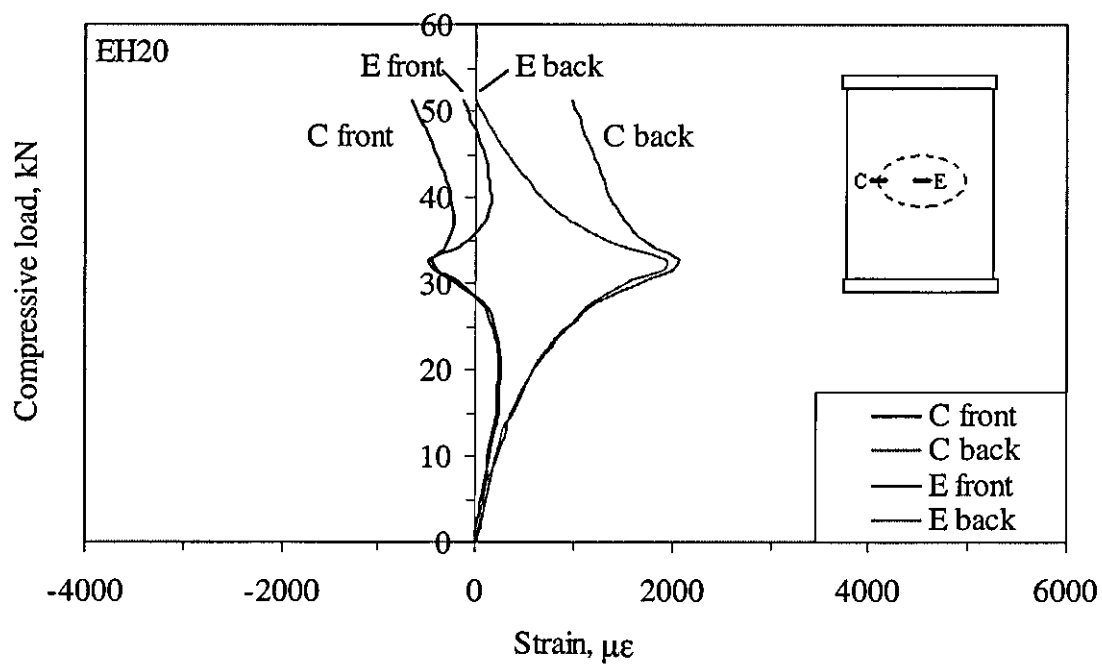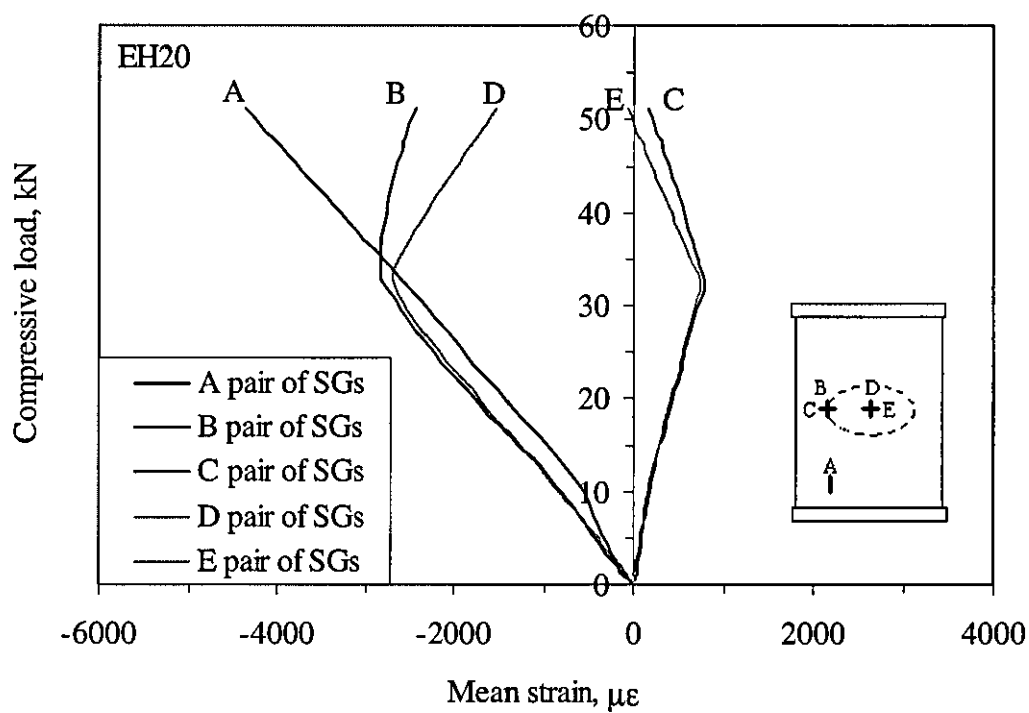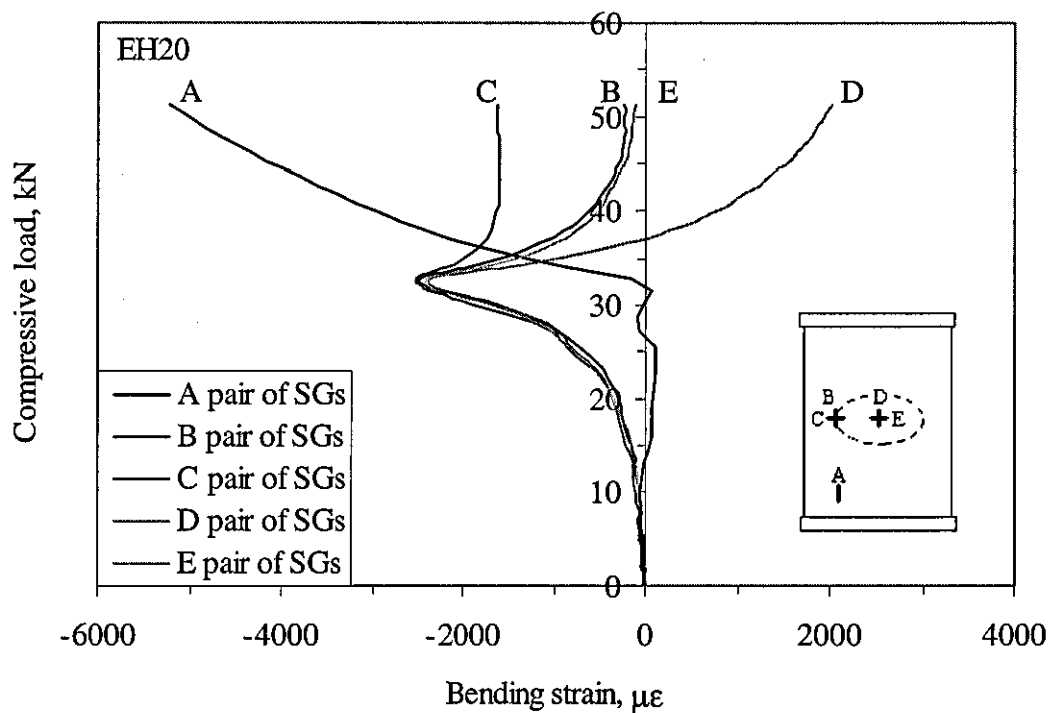
(d)

Figure 4.3.1 (a) Load-longitudinal strain, (b) load-transverse strain, (c) load-mean strain and (d) load-bending strain response of a 2-mm thick panel with a 20-mm horizontal elliptical delamination (EH20)
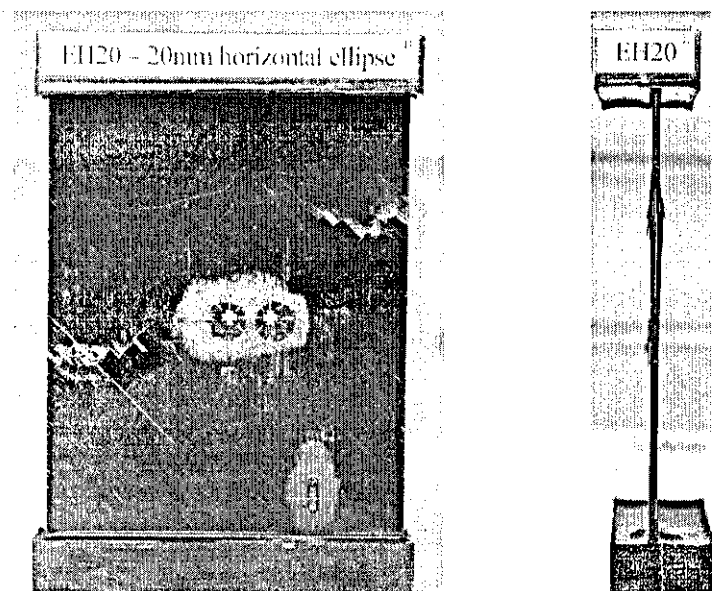
Figure 4.3.2 Photographs of a failed 2-mm thick panel with a 20-mm horizontal elliptical delamination (EH20)

(a)

(b)

175
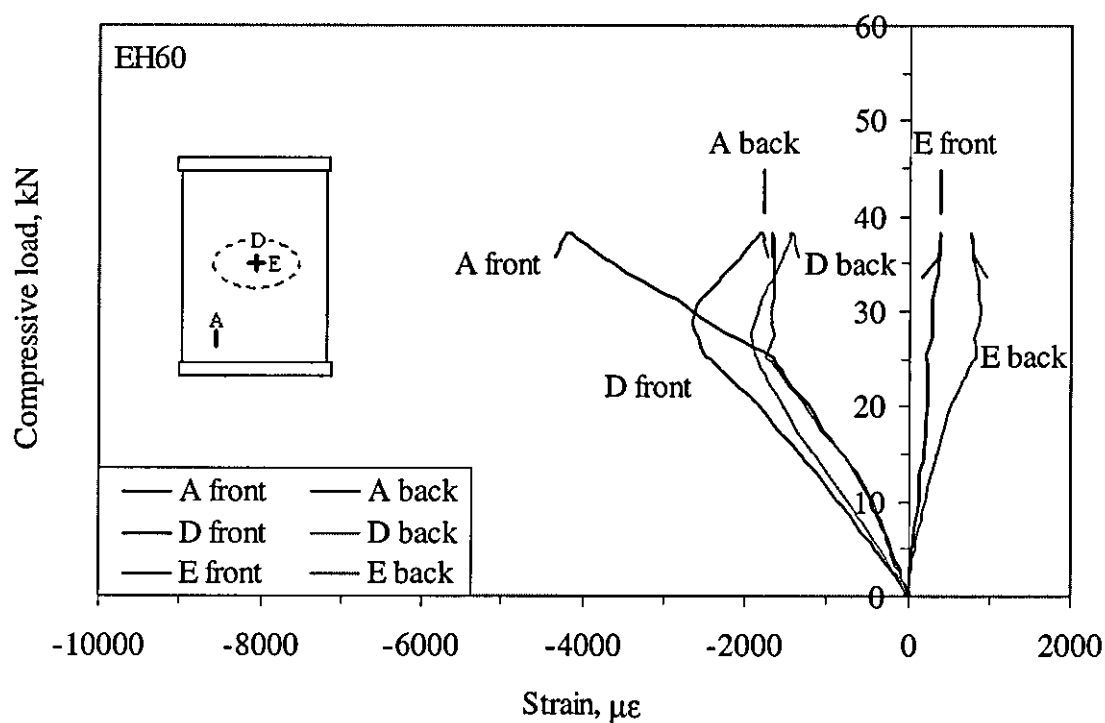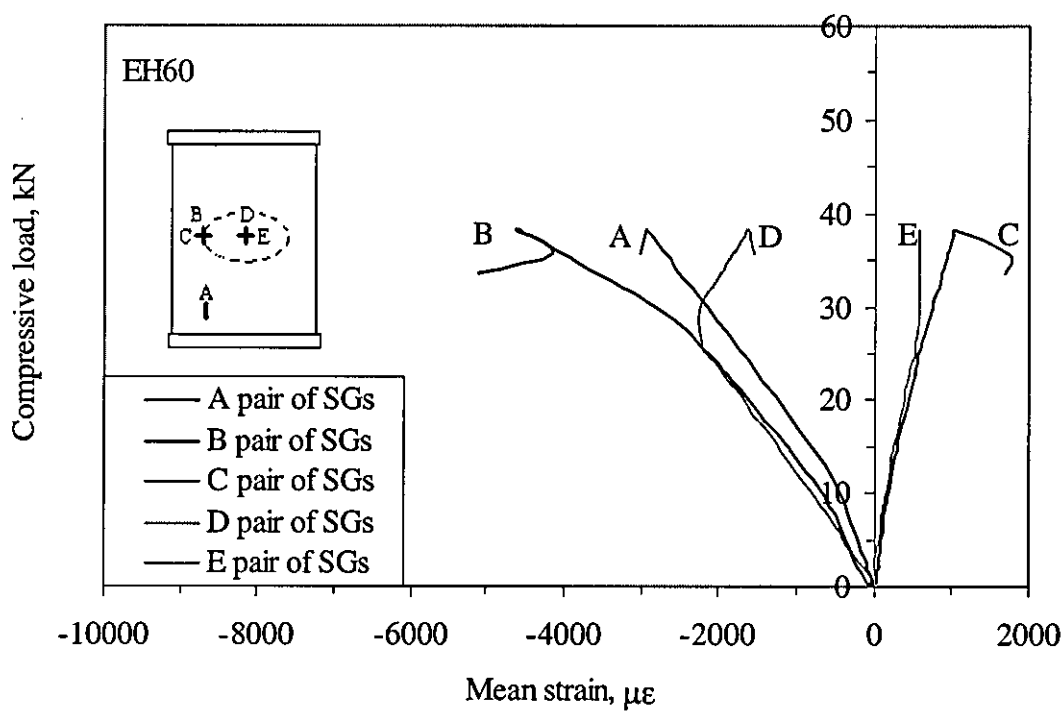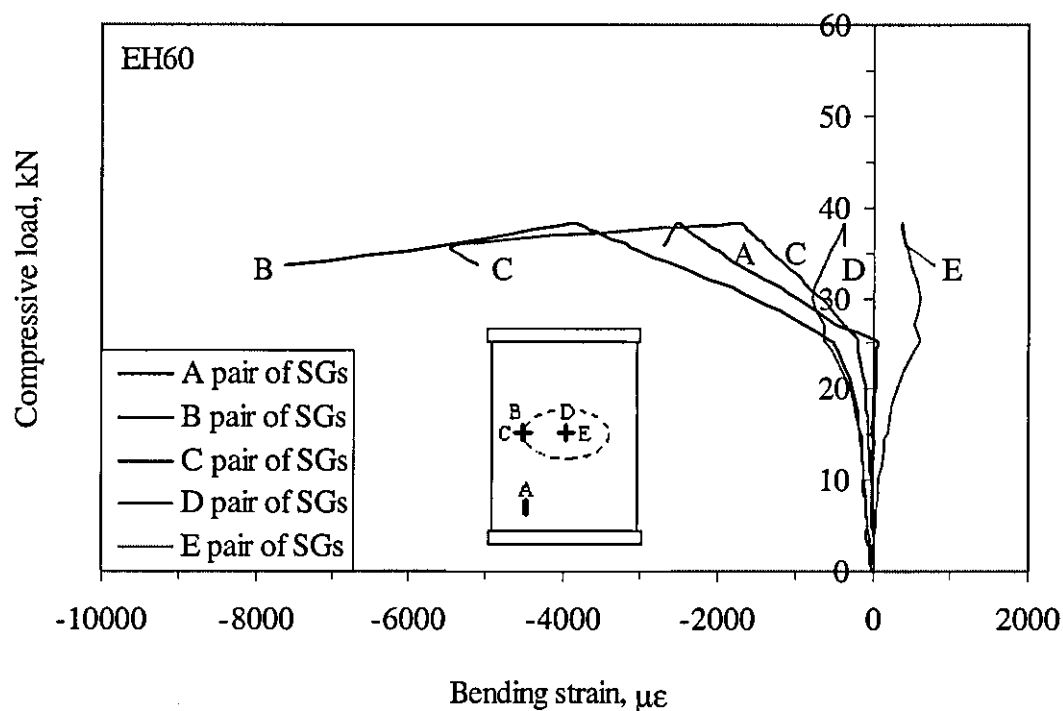
Figure 4.3.3 (a) Load-strain, (b) load-bending and (c) load-mean strain response of a 2-mm thick panel with a 60-mm horizontal elliptical delamination (EH60)
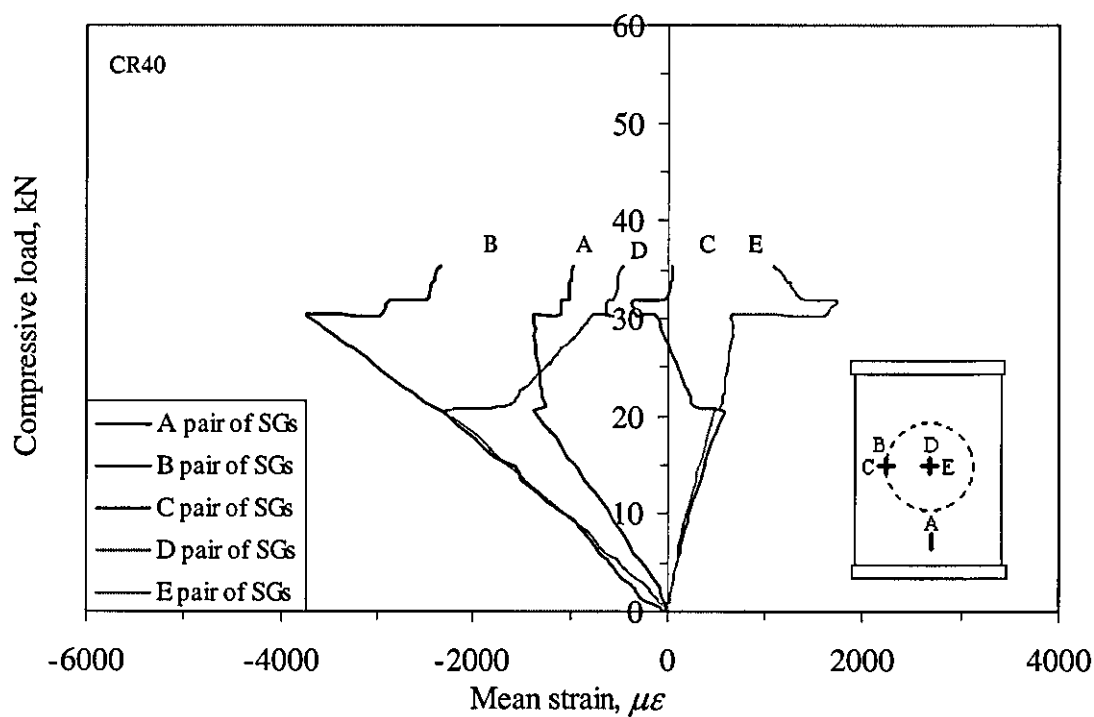
(a)
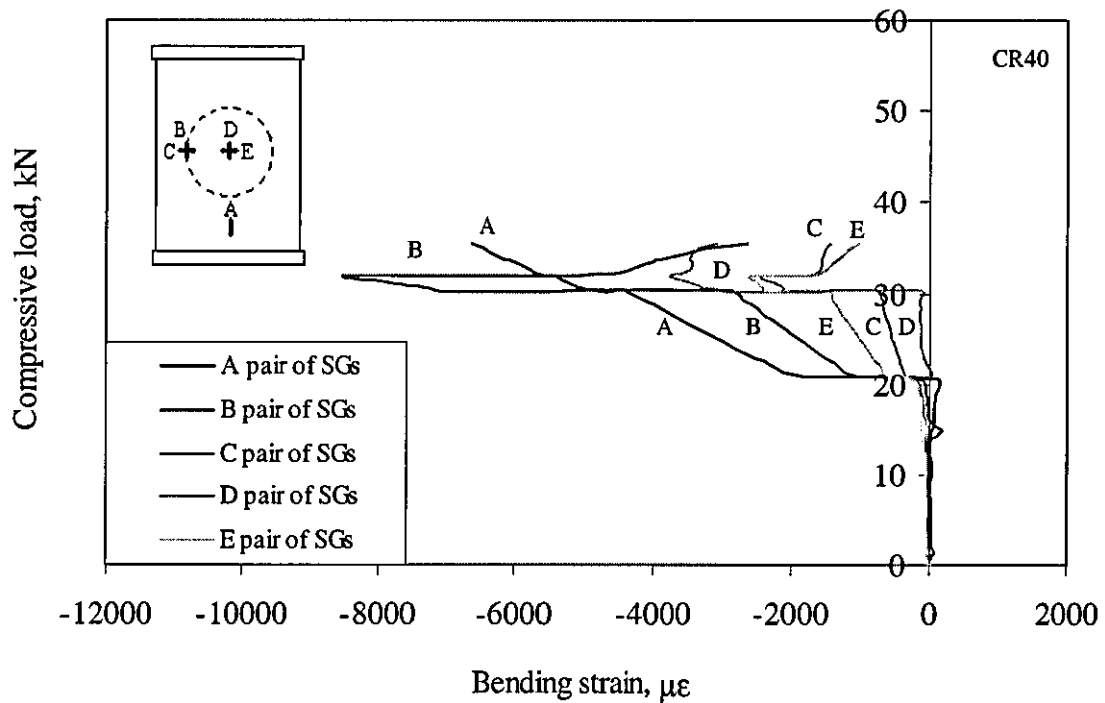
(b)
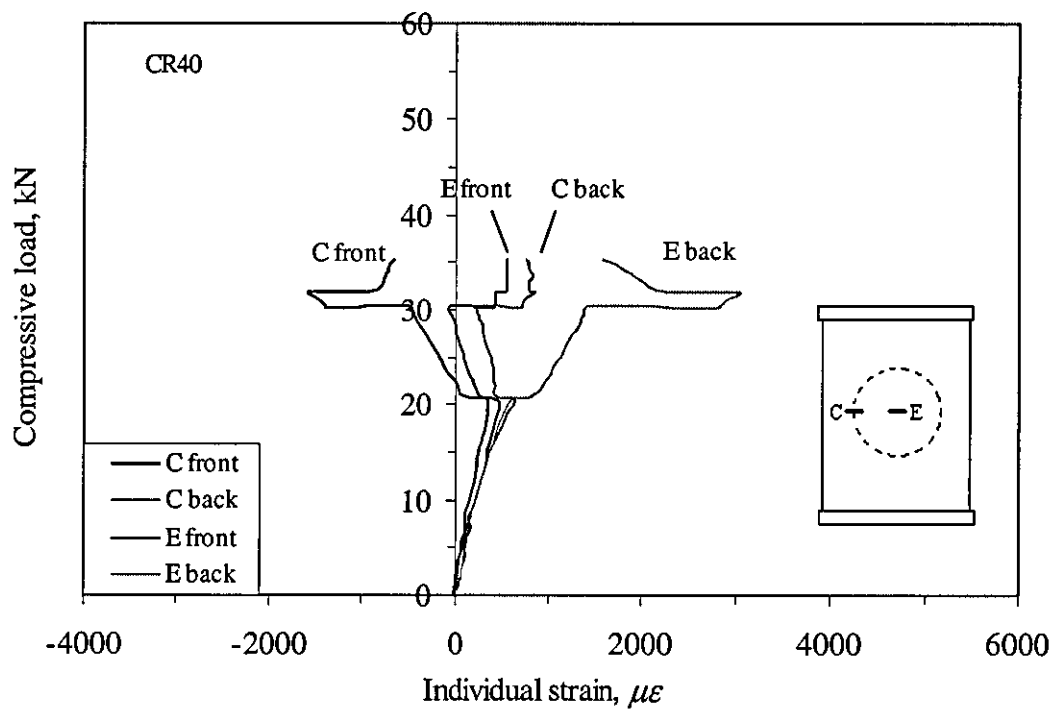
(c)

Figure 4.3.4 (a) Load-mean strain, (b) load-bending strain and (c) load-longitudinal strain response curves from a 2-mm thick panel containing a 40-mm circular delamination

177
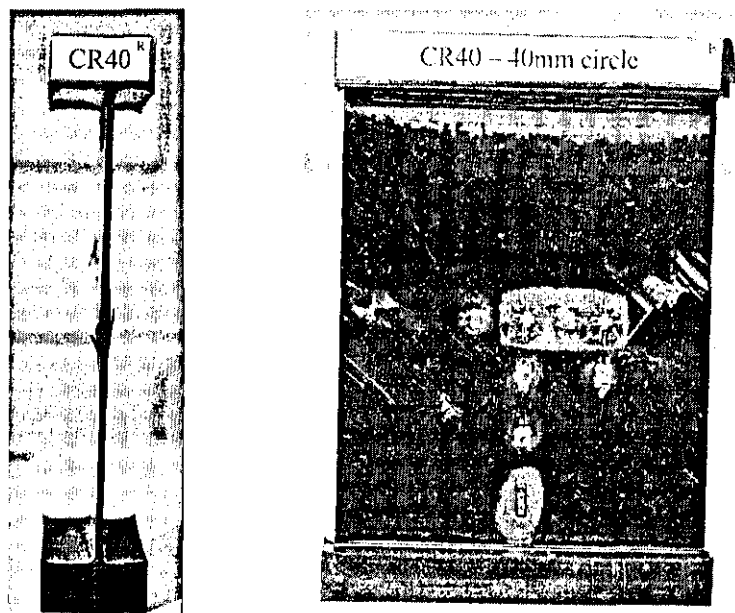
Figure 4.3.5 Photographs of a failed 2-mm thick panel containing a 40-mm circular
delamination
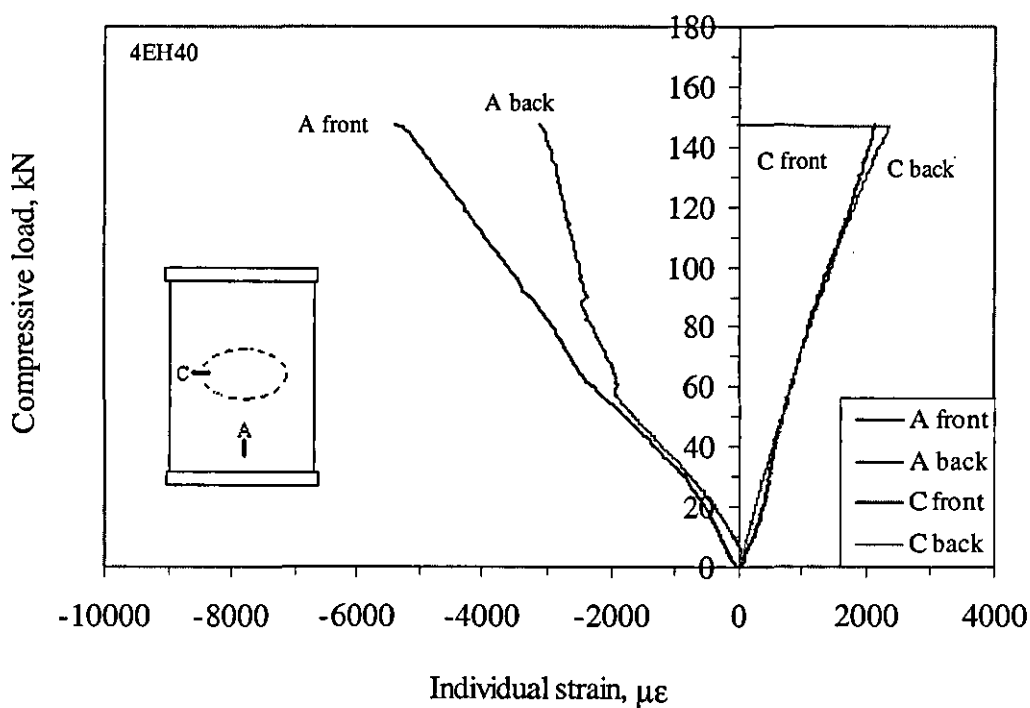
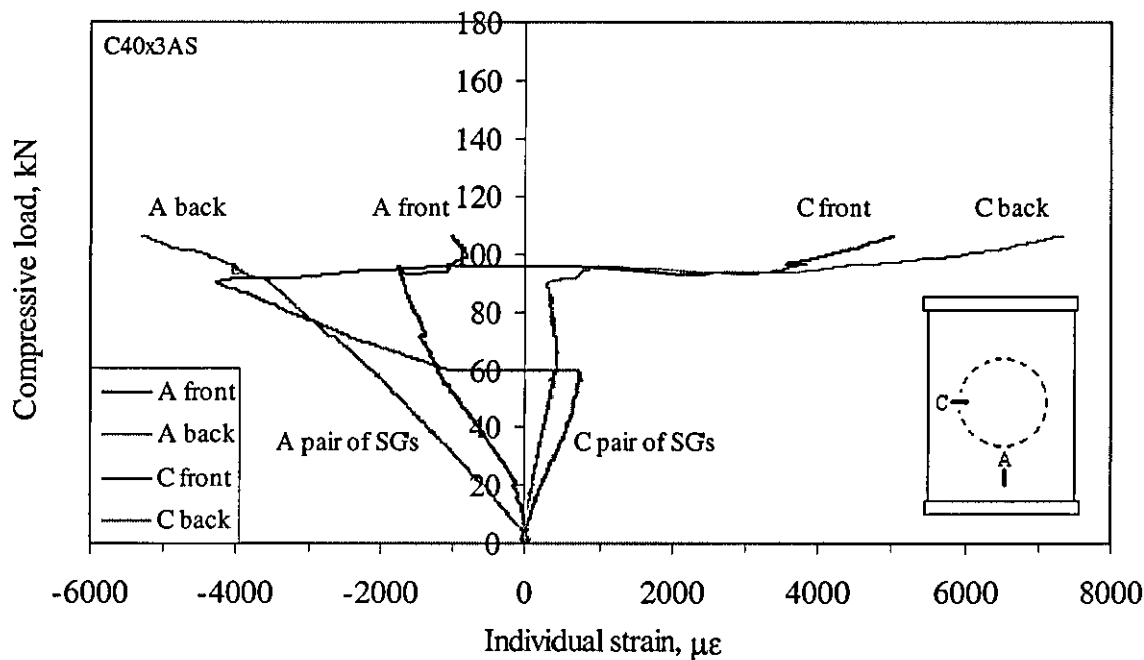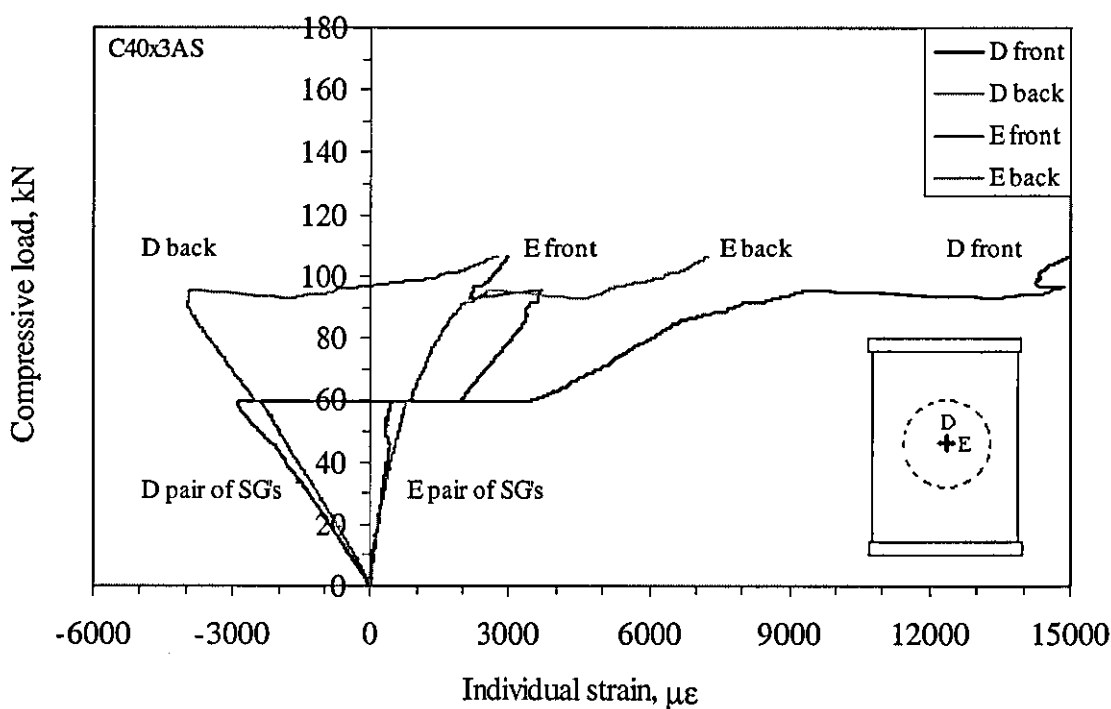(a)
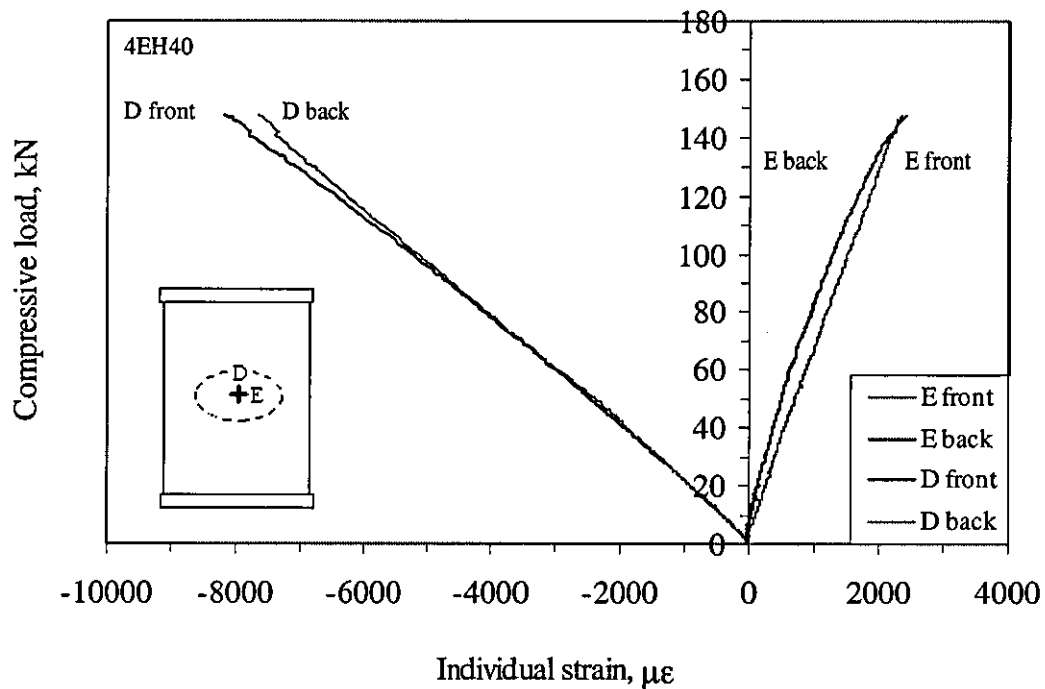
(b)

Figure 4.3.6 Individual strain response curves of (a) far-field and transverse side and (b) longitudinal and transverse central strain gauges from a 4-mm thick panel with a single 40-mm horizontal elliptical delamination at the mid-plane

(a)

179
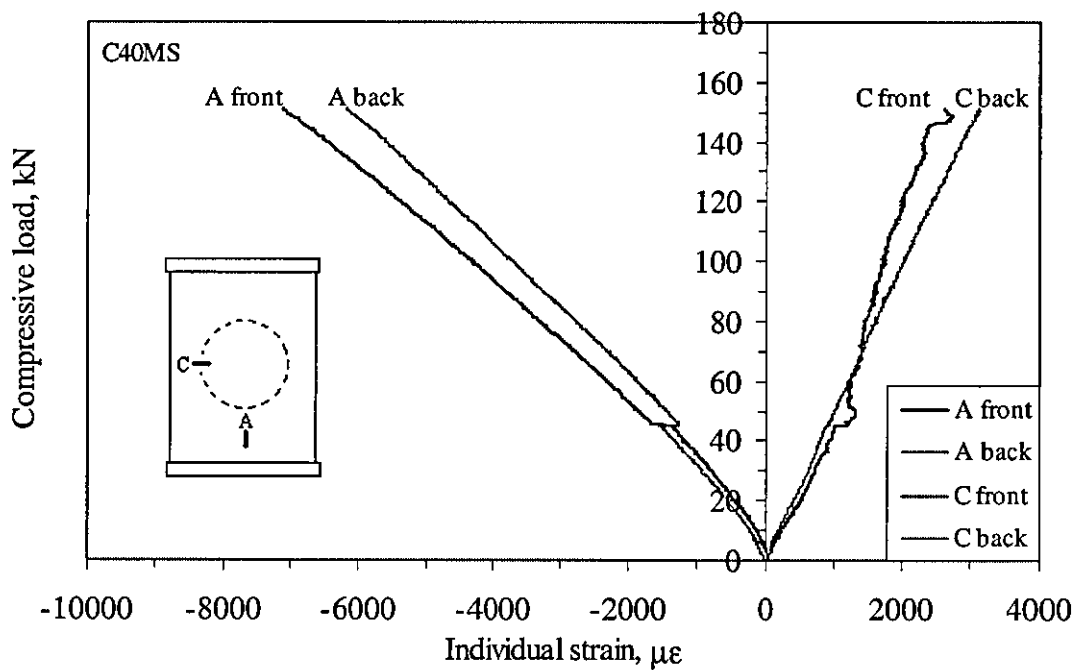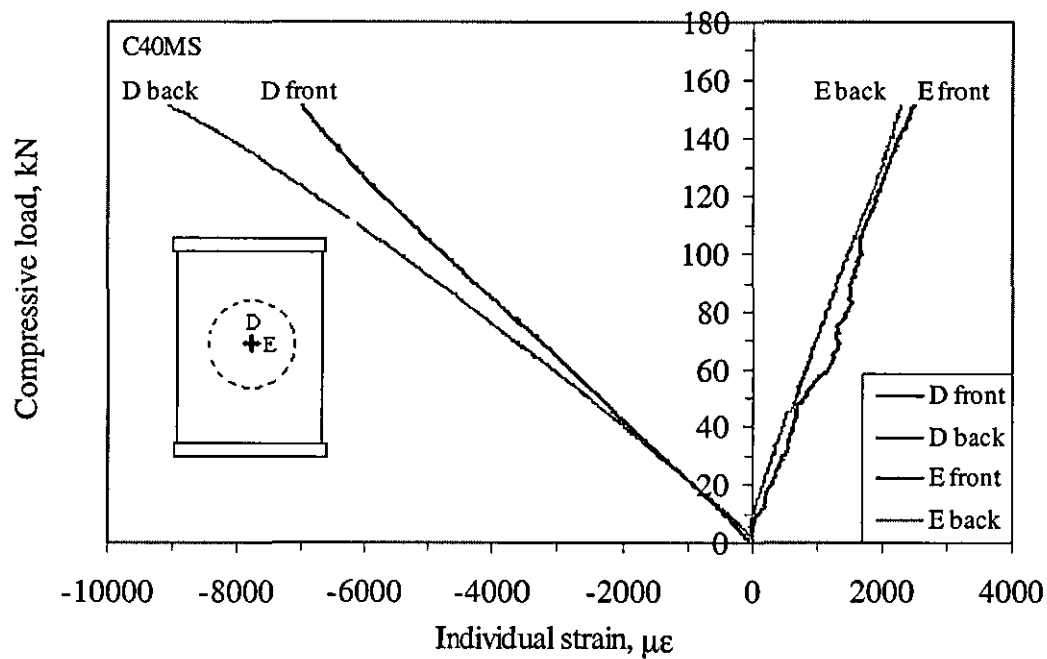
(b)

Figure 4.3.7 Individual strain response curves of (a) far-field and transverse side and (b) longitudinal and transverse central strain gauges from a 4-mm thick panel with a single 40-mm circular delamination at the mid-plane
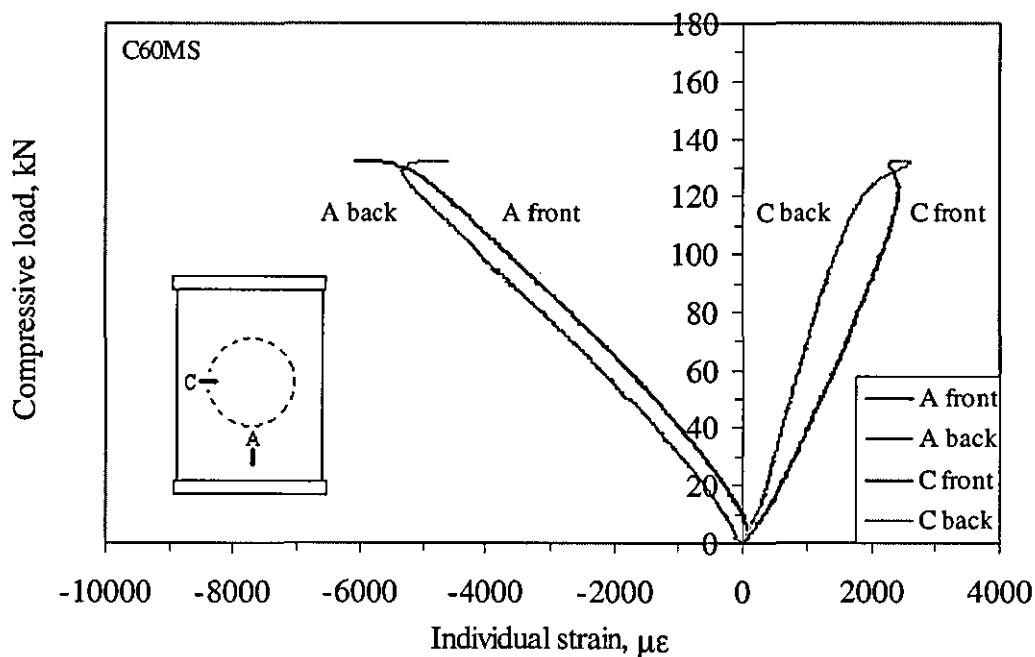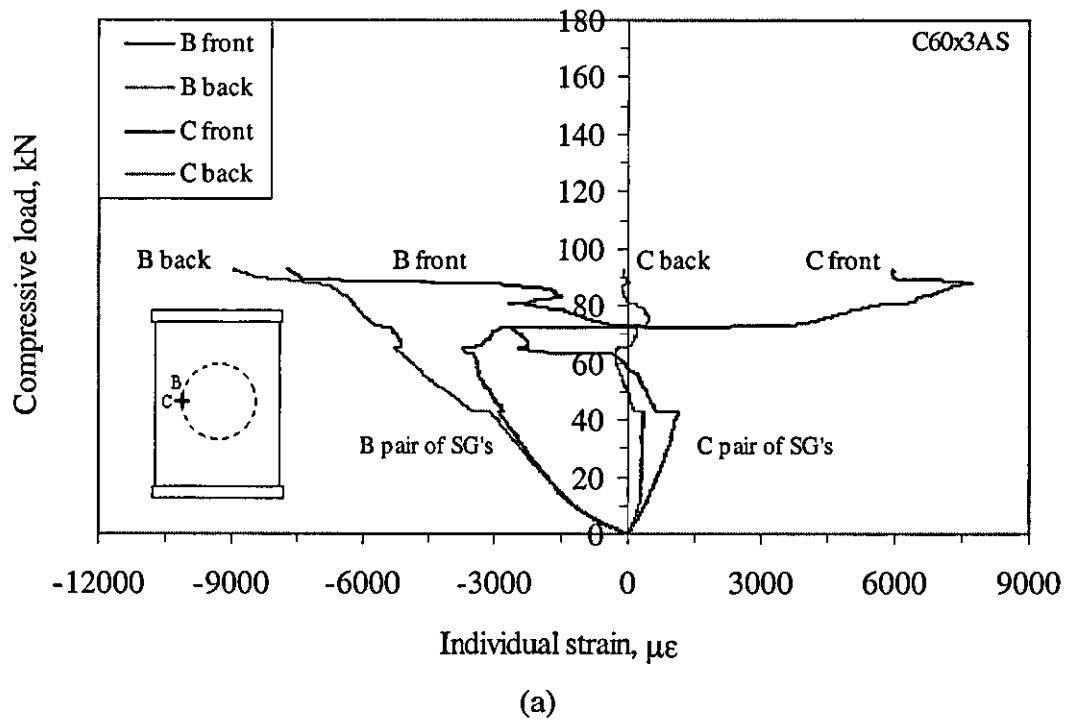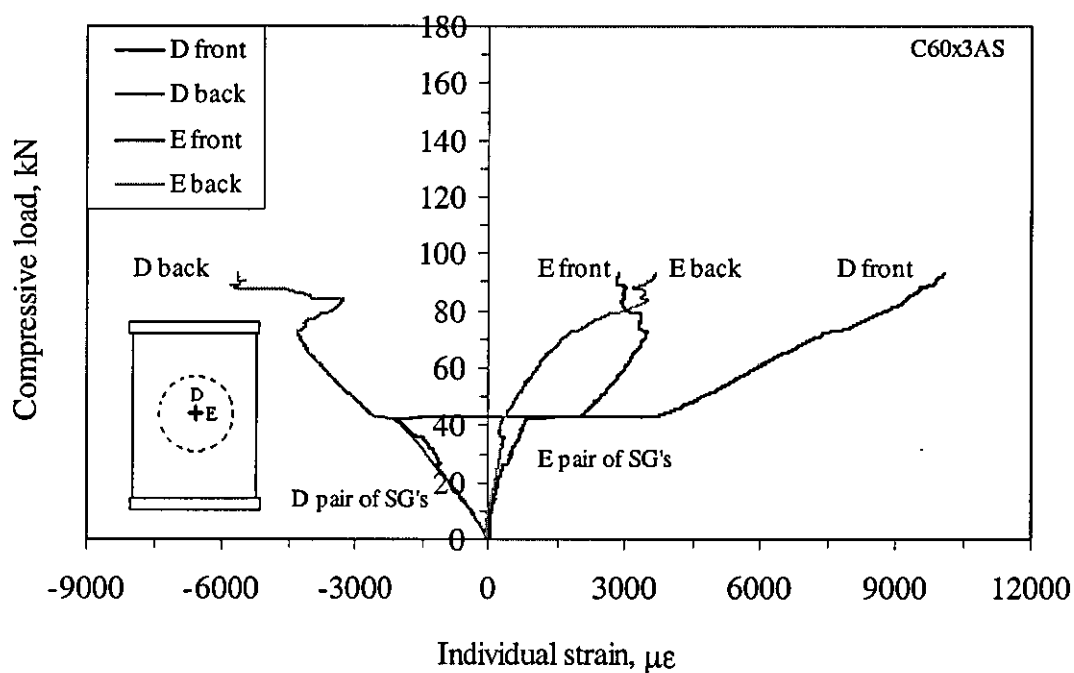

(a)
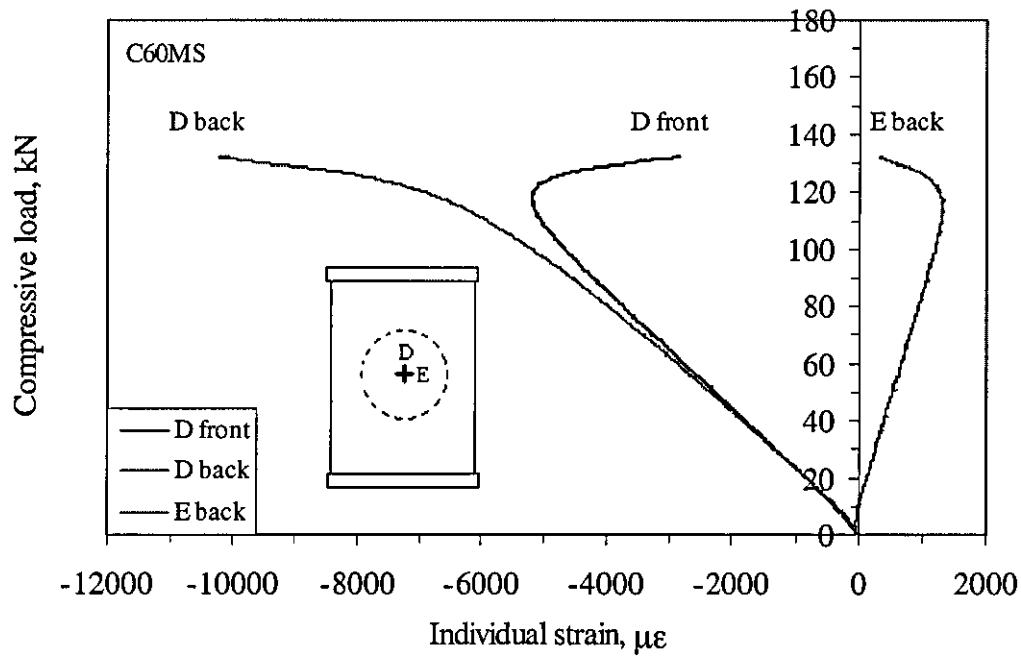
(b)

Figure 4.3.8 Individual strain response curves of (a) far-field and transverse side and (b) longitudinal and transverse central strain gauges from a 4-mm thick panel with a single 60-mm circular delamination at the mid-plane
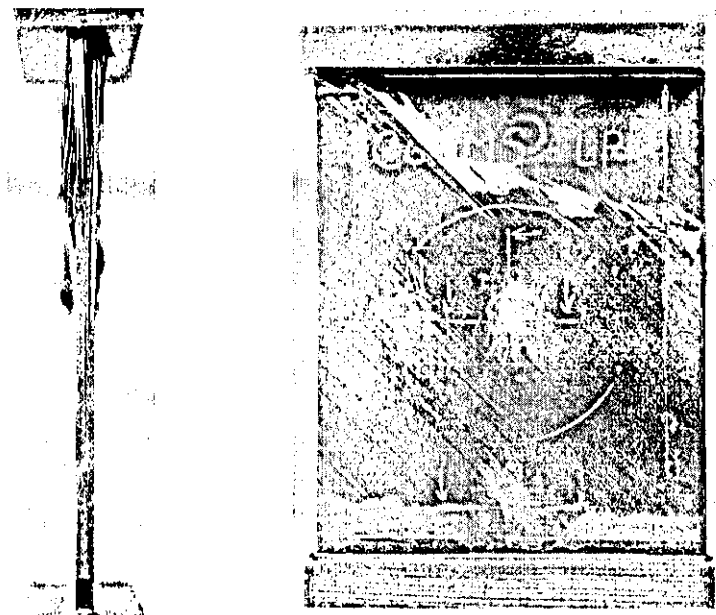
Figure 4.3.9 Photographs of a failed 4-mm thick panel containing a 60-mm circular delamination at the mid-section through-the-thickness (C60MS)
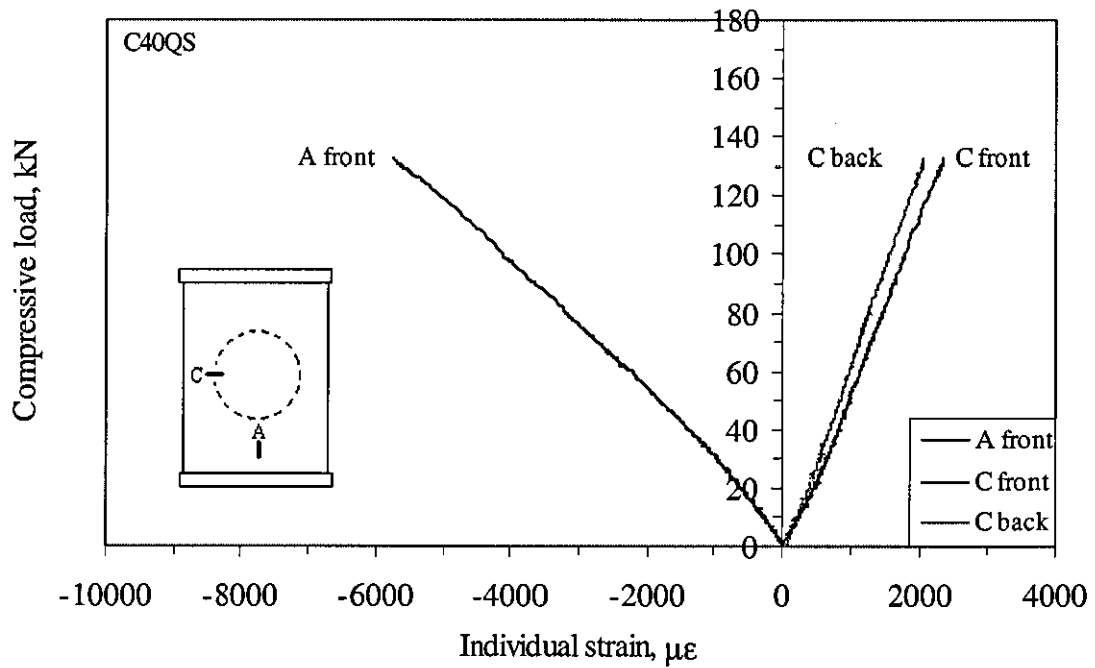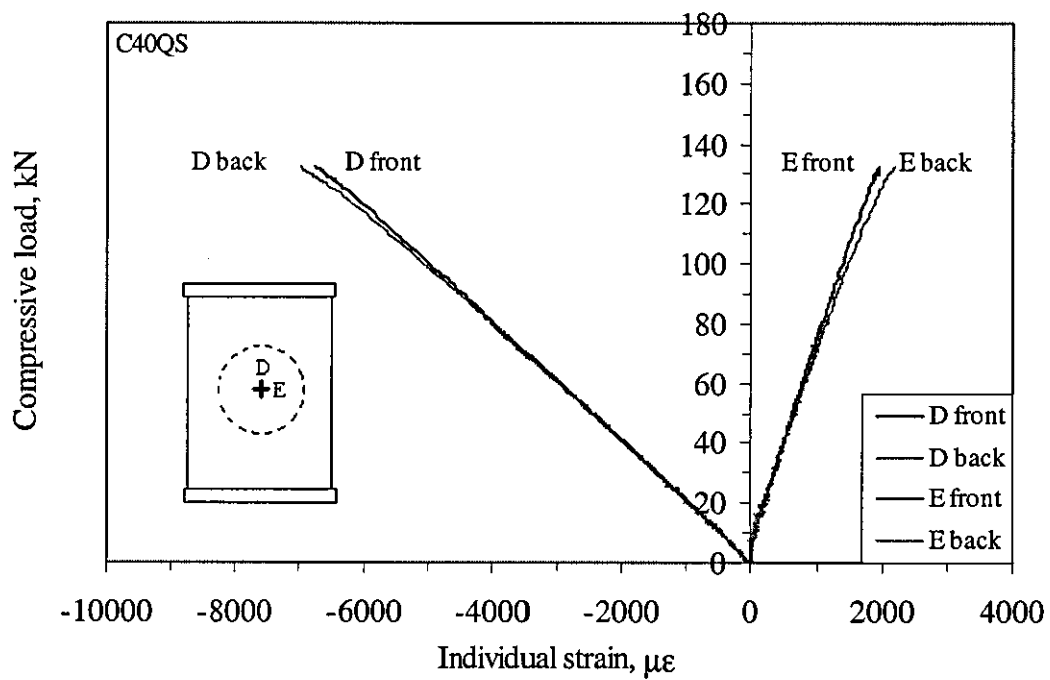
Figure 4.3.10 Individual strain response curves of (a) far-field and transverse side and (b) longitudinal and transverse central strain gauges from a 4-mm thick panel with a single 40-mm circular delamination at one quarter position

182
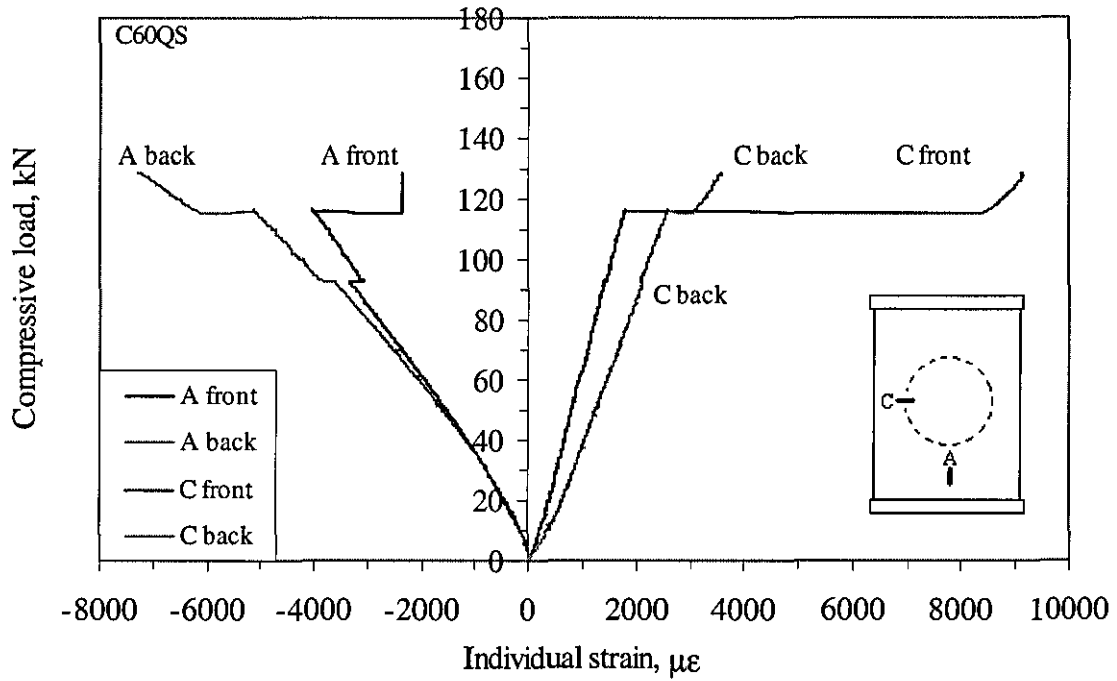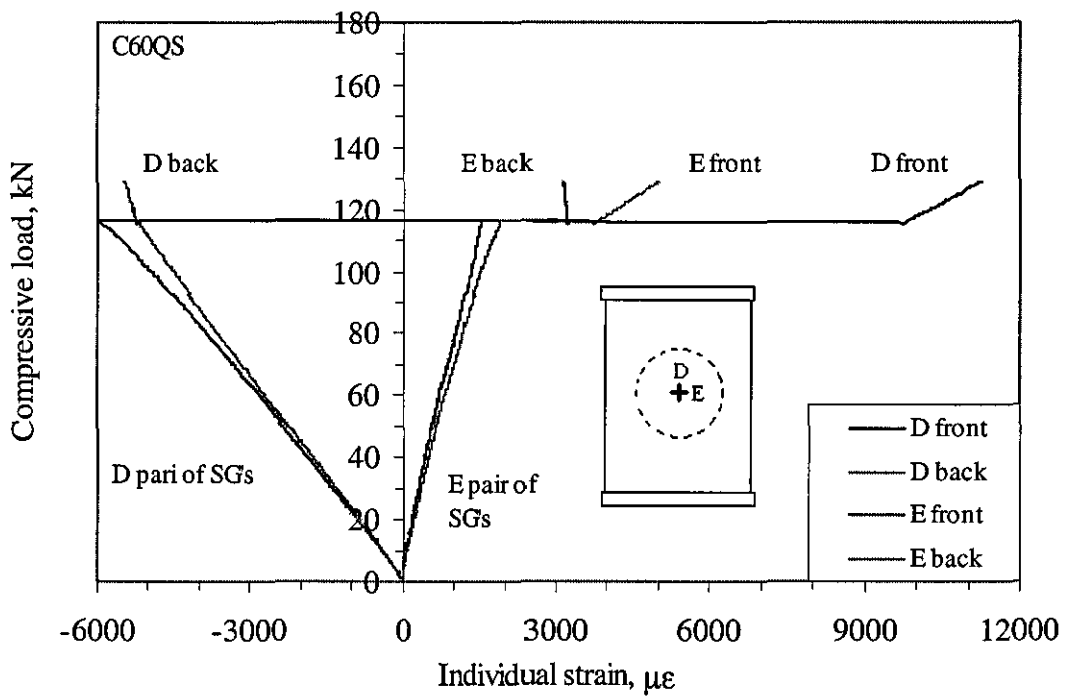
Figure 4.3.11 Individual strain response curves of (a) far-field and transverse side and (b) longitudinal and transverse central strain gauges from a 4-mm thick panel with a 60-mm circular delamination at one quarter position (C60QS)
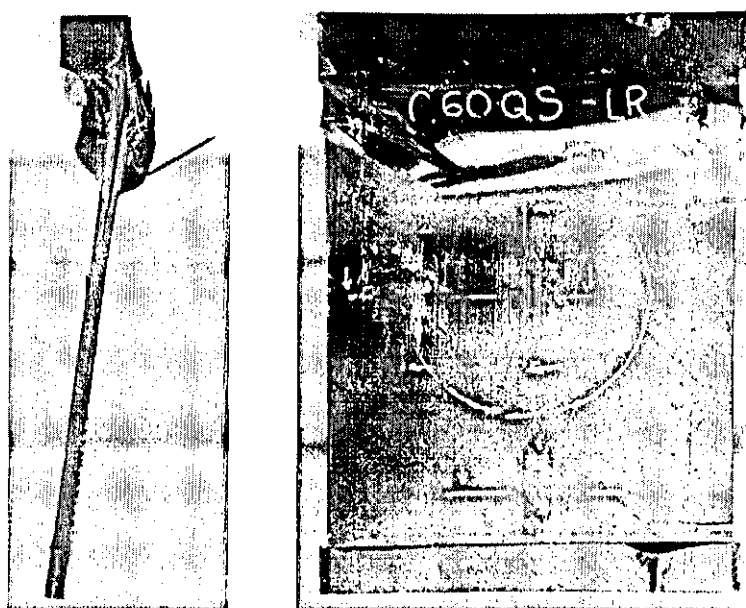
(a)   (b)

Figure 4.3.12 Photographs of a failed 4-mm thick panel containing a 60-mm circular
delamination at one quarter location (C60QS) (a) side view and (b) front view
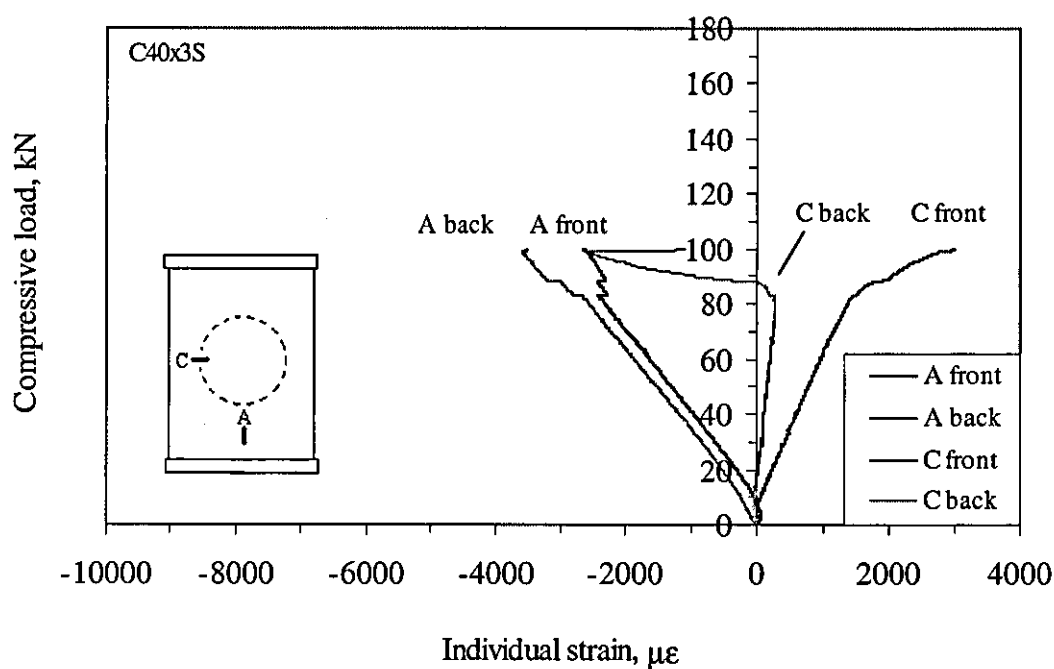
(a)
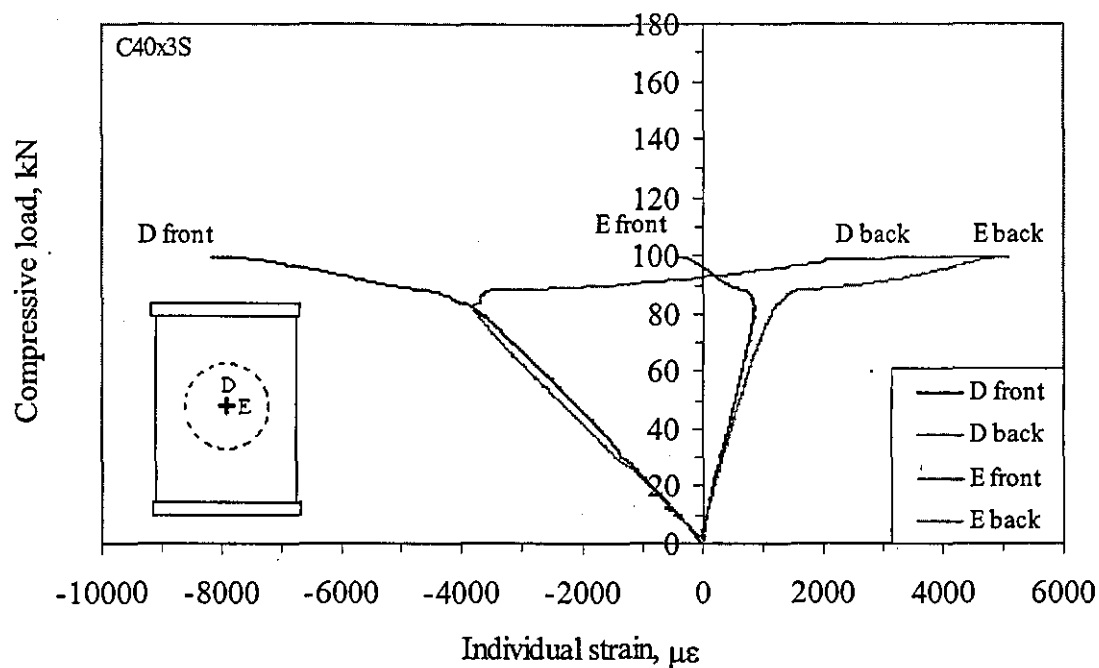
(b)

Figure 4.3.13 Individual strain response curves of (a) far-field and transverse side and (b) longitudinal and transverse central strain gauges from a 4-mm thick panel with three 40-mm circular delaminations in a symmetric arrangement (C40x3S)
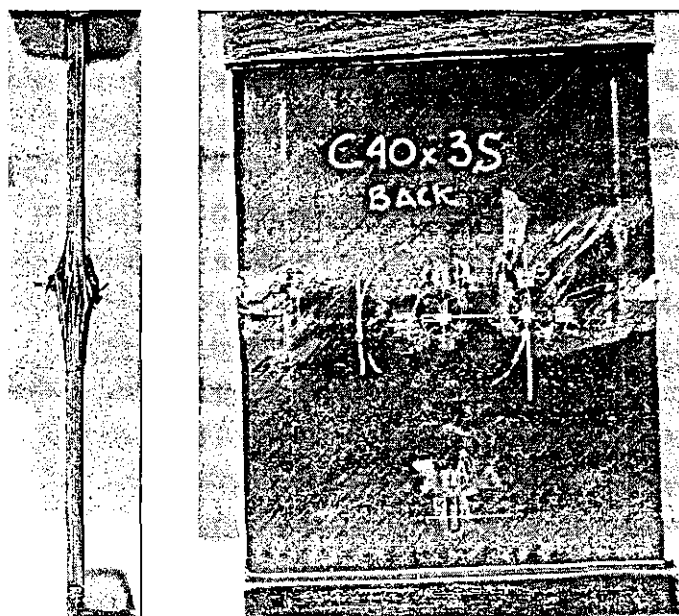

Figure 4.3.14 Photographs of a failed 4-mm thick panel containing three 40-mm circular delaminations in symmetrical arrangement through-the-thickness (C40x3S)
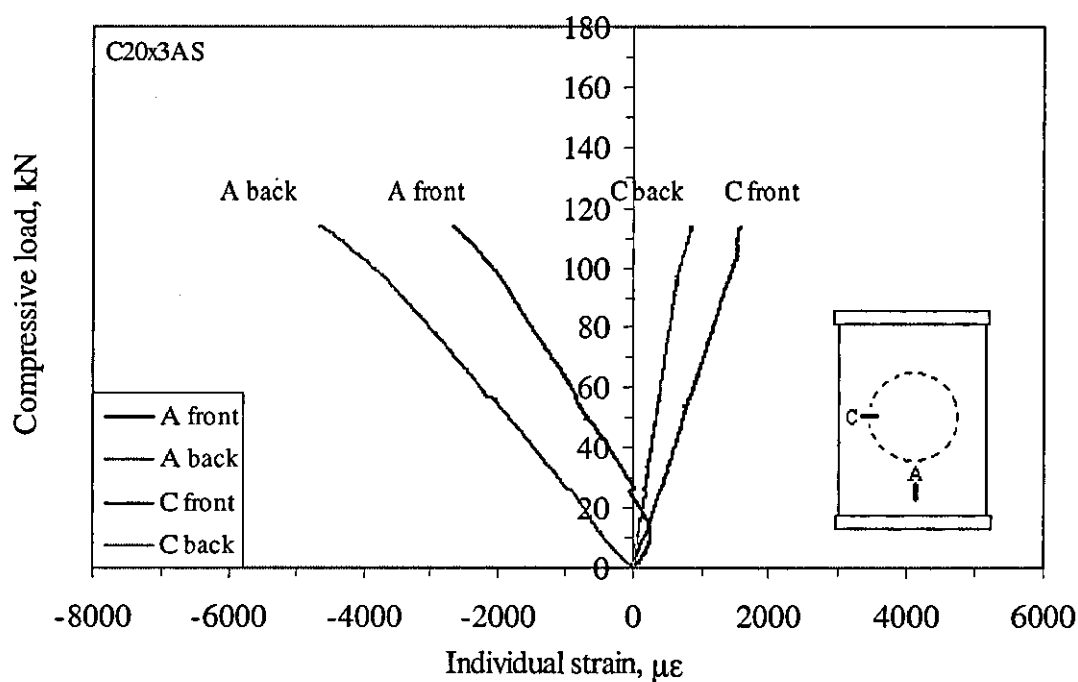
(a)
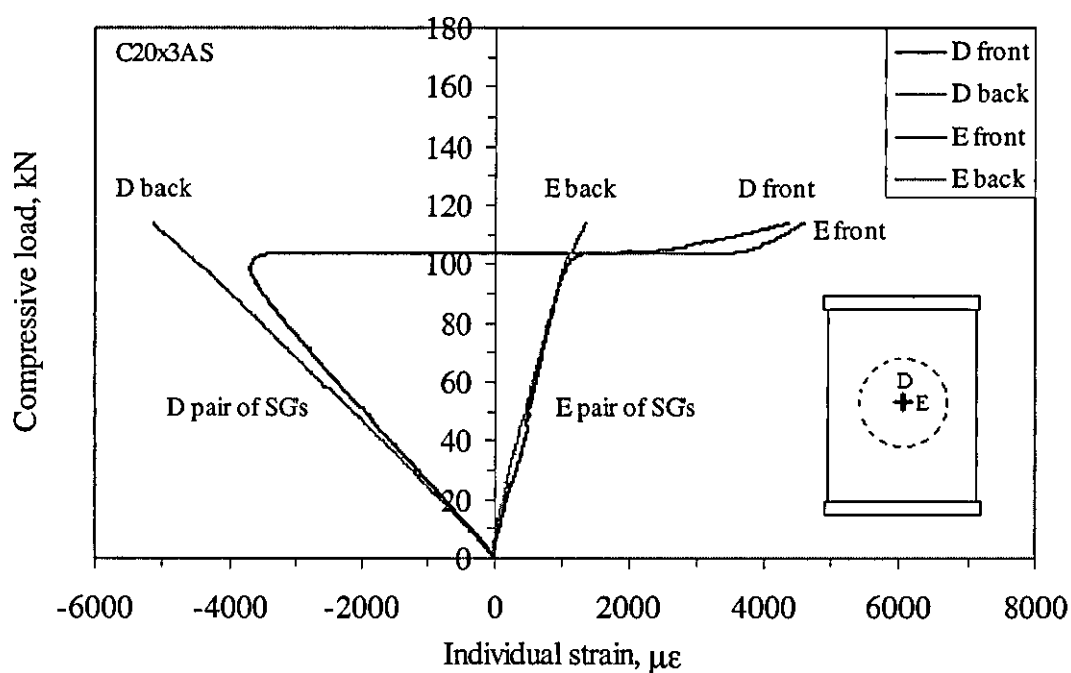
(b)

Figure 4.3.15 Individual strain response curves of (a) far-field and transverse side and
(b) longitudinal and transverse central strain gauges from a 4-mm thick panel with three
20-mm circular delaminations in a asymmetric arrangement (C20x3AS)

Figure 4.3.16 Individual strain response curves of (a) far-field and transverse side and (b) longitudinal and transverse central strain gauges from a 4-mm thick panel with three 40-mm circular delaminations in a asymmetric arrangement (C40x3AS)

Figure 4.3.17 Photographs of a failed 4-mm thick panel containing three 40-mm circular delaminations in asymmetrical arrangement through-the-thickness (C40x3AS)


(a)

(b)

Figure 4.3.18 Individual strain response curves of (a) longitudinal and transverse central and (b) longitudinal and transverse side strain gauges from a 4-mm thick panel with three 60-mm circular delaminations in an unsymmetric arrangement
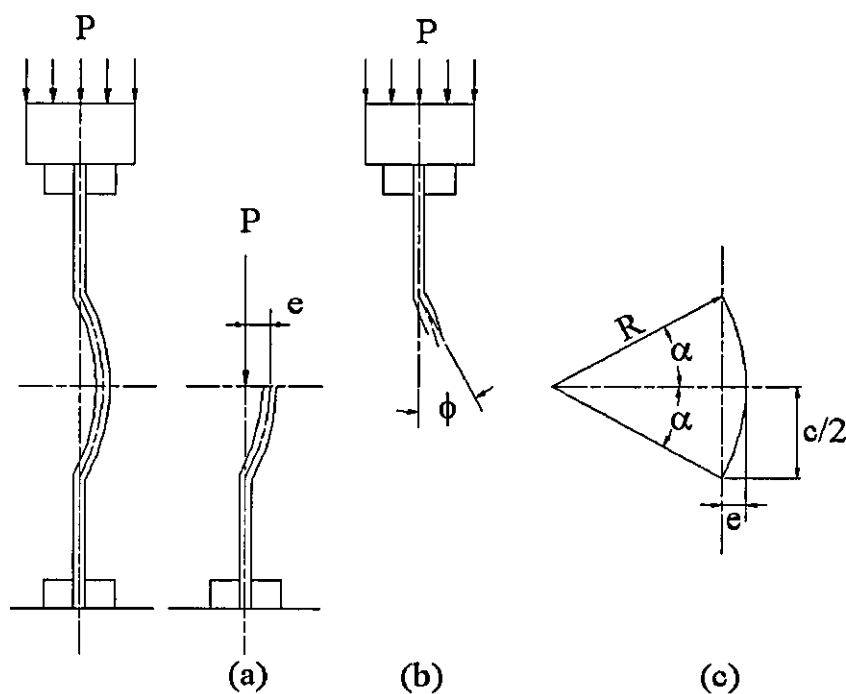
Figure 4.4.1 Geometric variables of semi-hemispherical dome related with (a) bending moment, (b) shear and (c) curvature

189

(a)

(b)

190
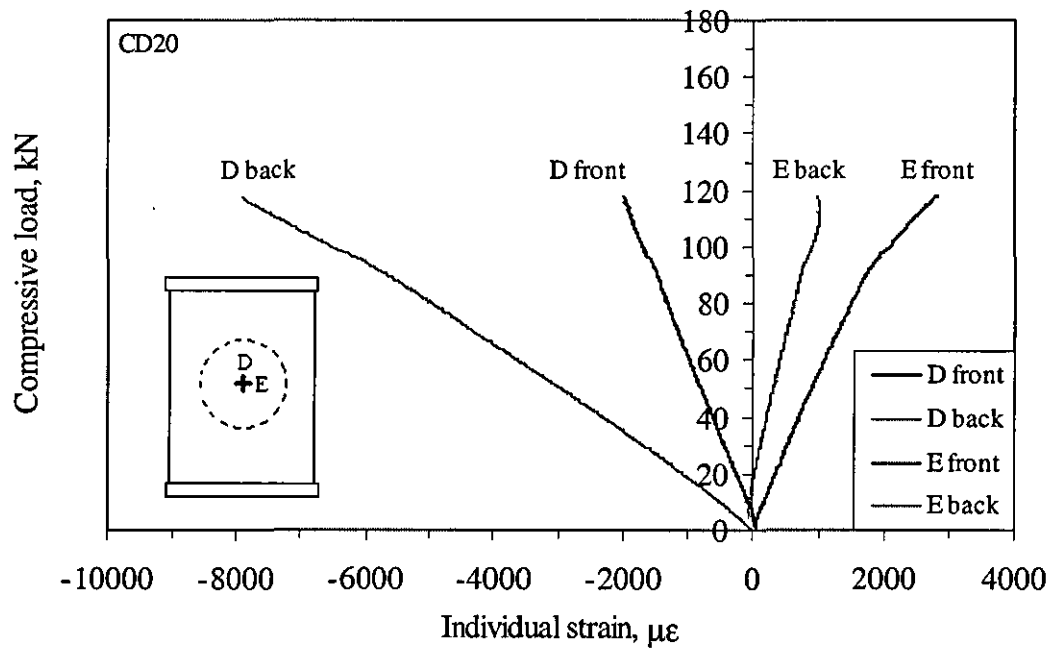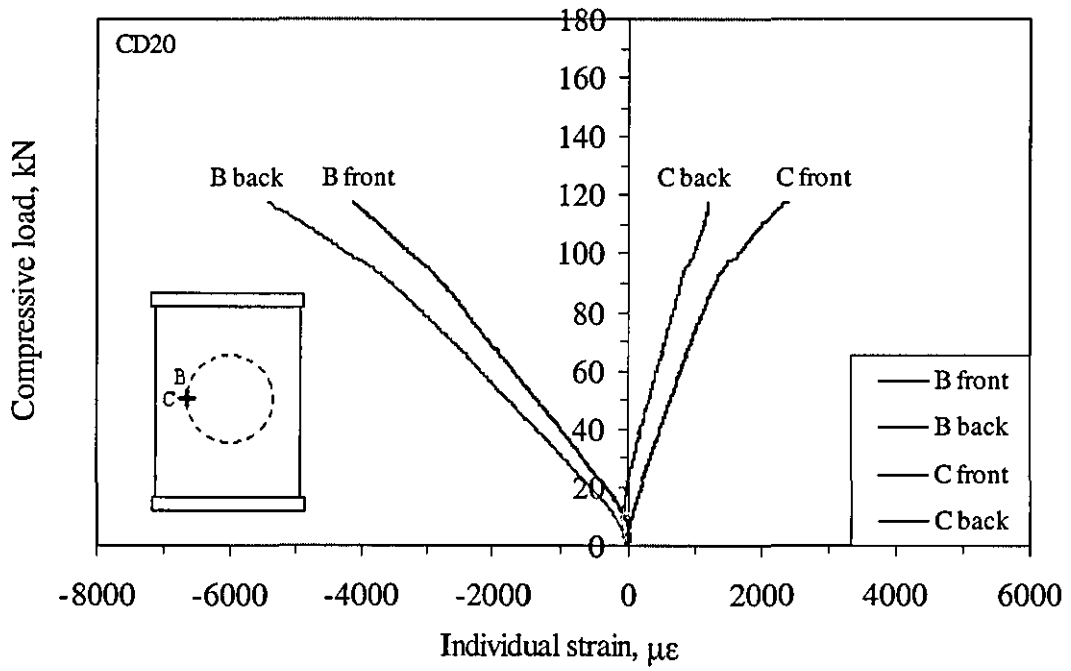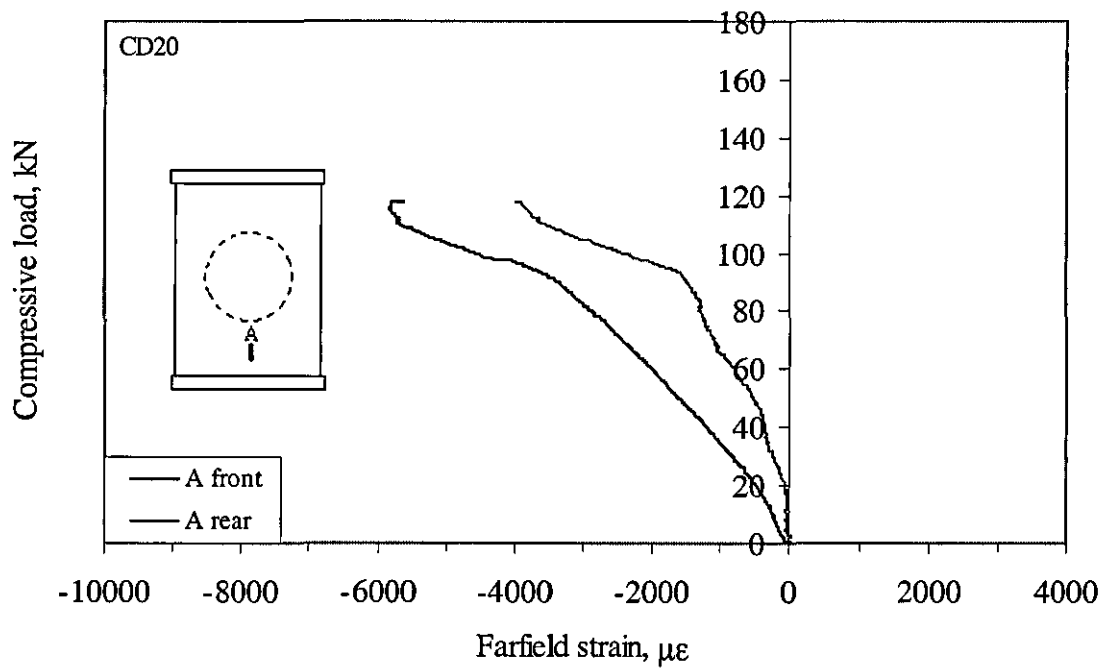
(c)

Figure 4.4.2 Individual strain response curves of (a) longitudinal and transverse central, (b) longitudinal and transverse side strain gauges and (c) far-field from a 4-mm thick panel with a 20-mm diameter circular dome
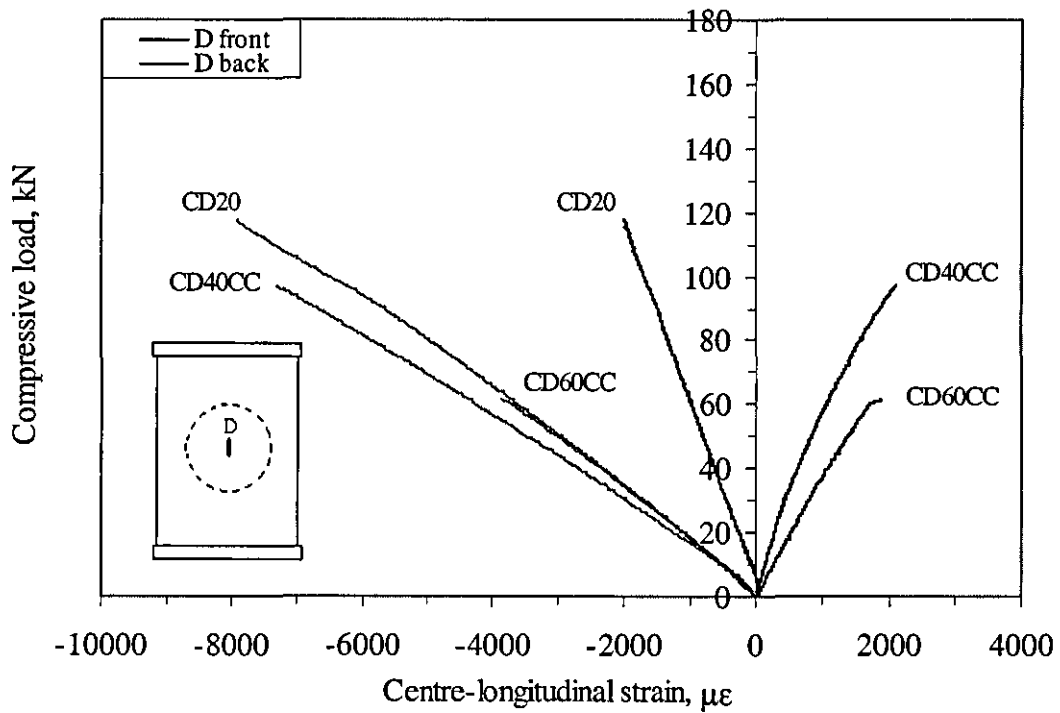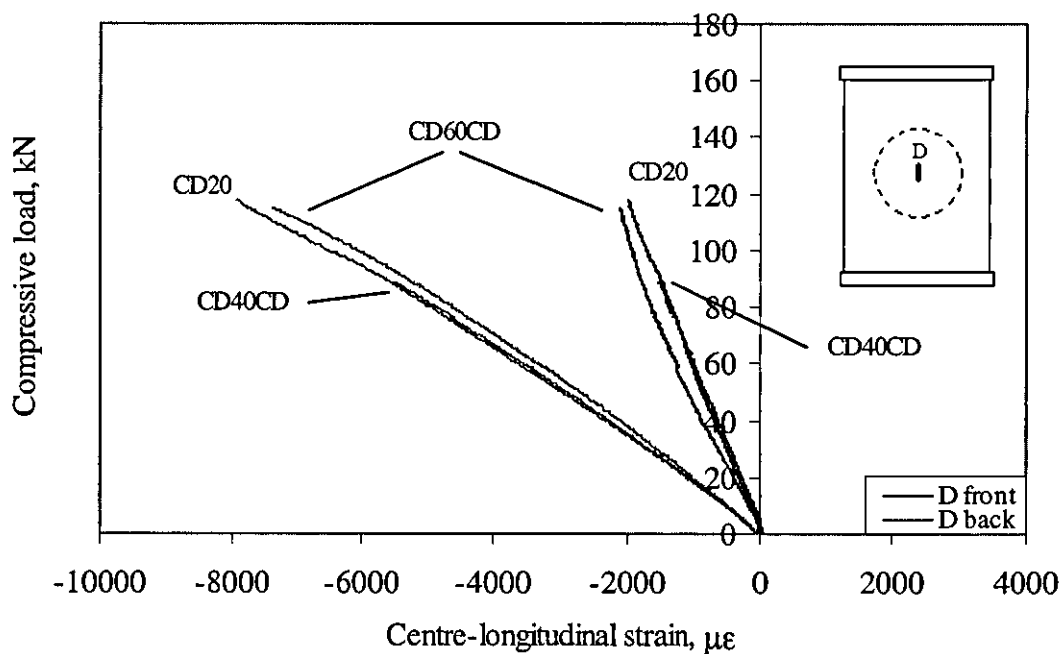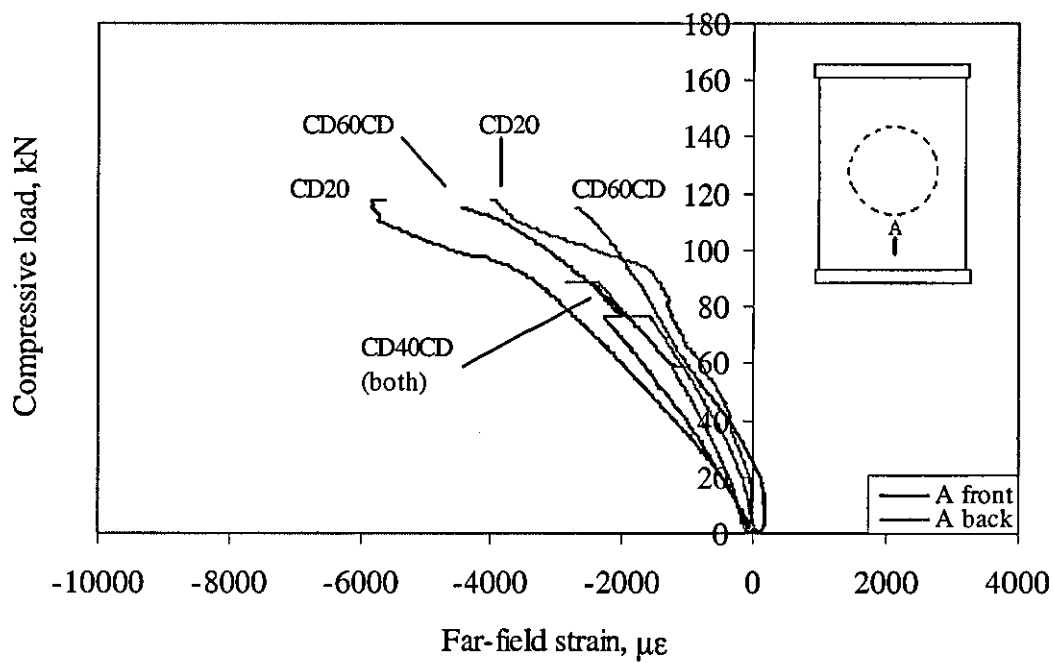

(a)
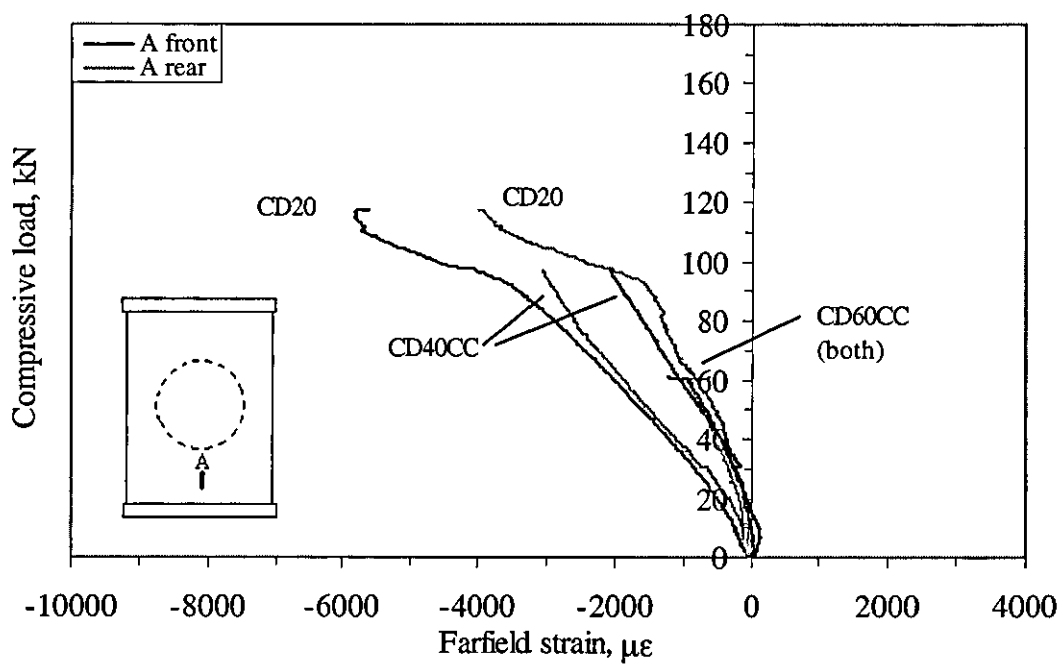
(b)

Figure 4.4.3 (a) Centre-longitudinal and (b) far-field strain gauge response from 4-mm thick panels with 20, 40 and 60-mm diameter circular dome with a constant curvature radius of 62.9-mm
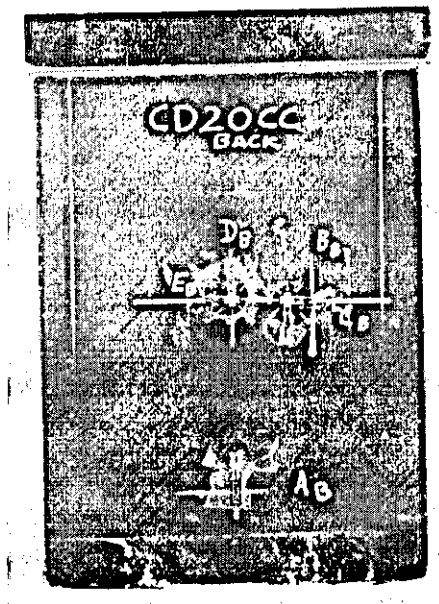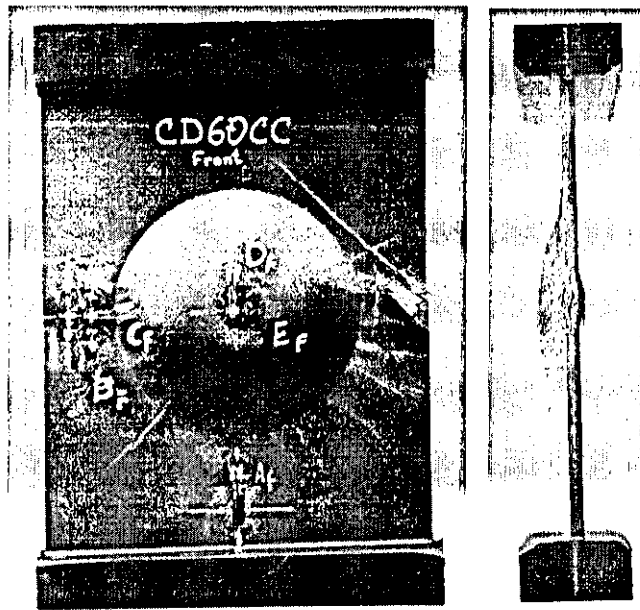

(a)

(b)

Figure 4.4.4 (a) Centre-longitudinal and (b) far-field strain gauge response from 4-mm thick panels with 20, 40 and 60-mm diameter circular dome with a constant depth of 0.8-mm

(a)

(b)

Figure 4.4.5 Photographs of failed specimens with a hemispherical-shaped dome of (a) 20-mm diameter (CD20) and (b) 60-mm diameter (CD60CC) with similar curvature radius of 62.9 mm
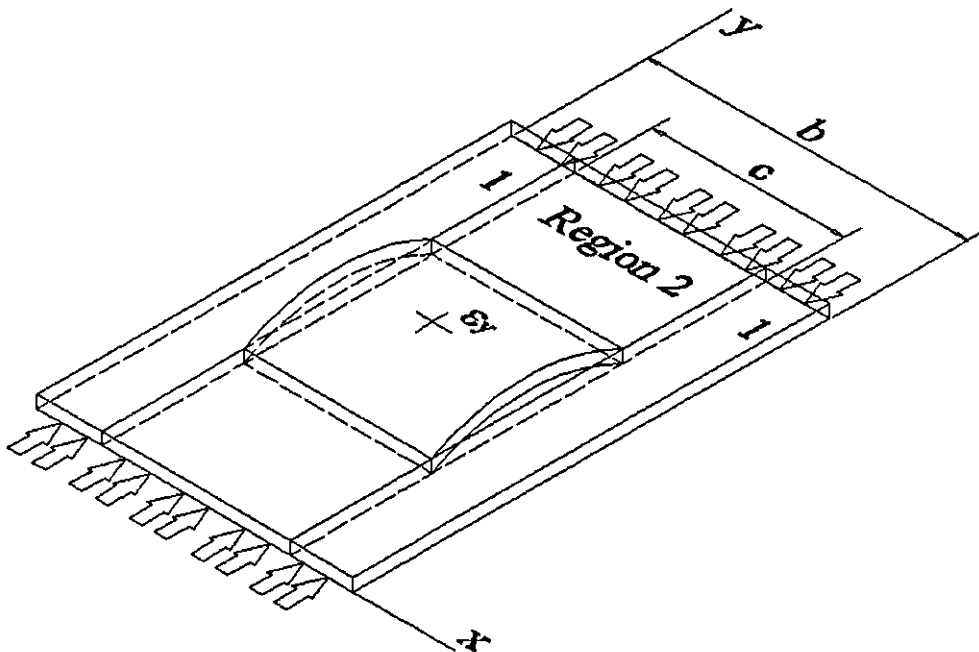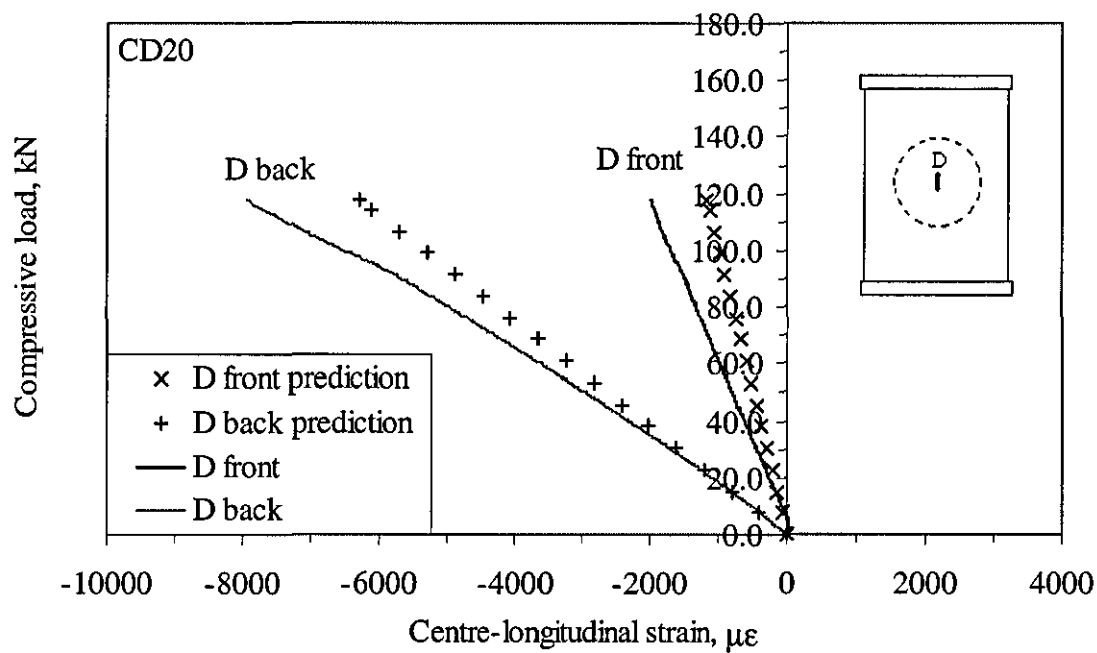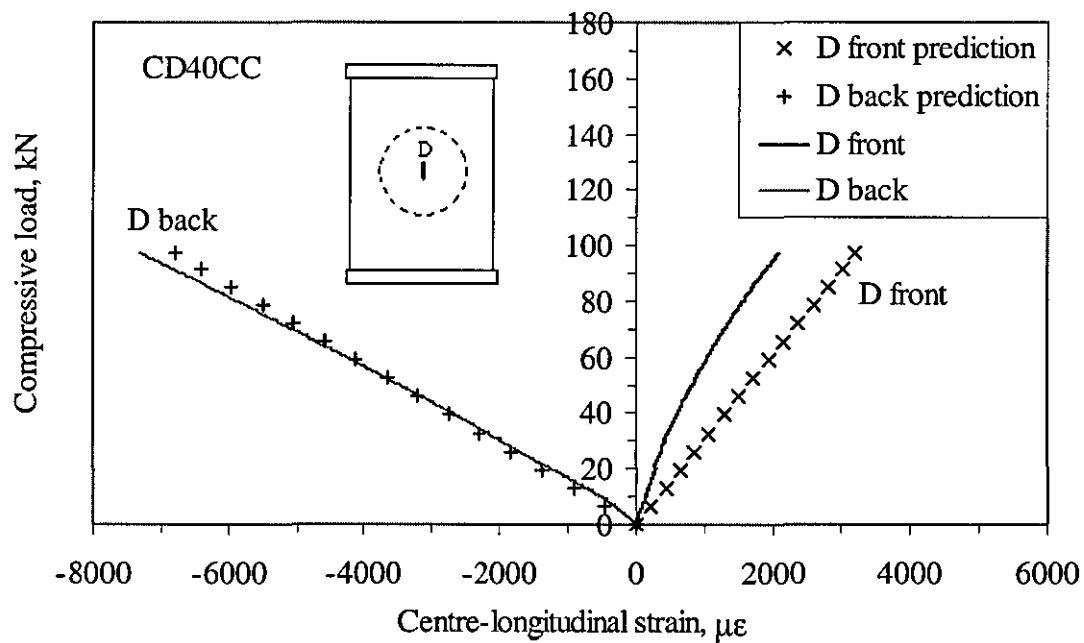

Figure 4.4.6 Model simplification for analytical prediction of central strain of panels with local change of geometry

(a)

(b)

195

(c)

(d)

196
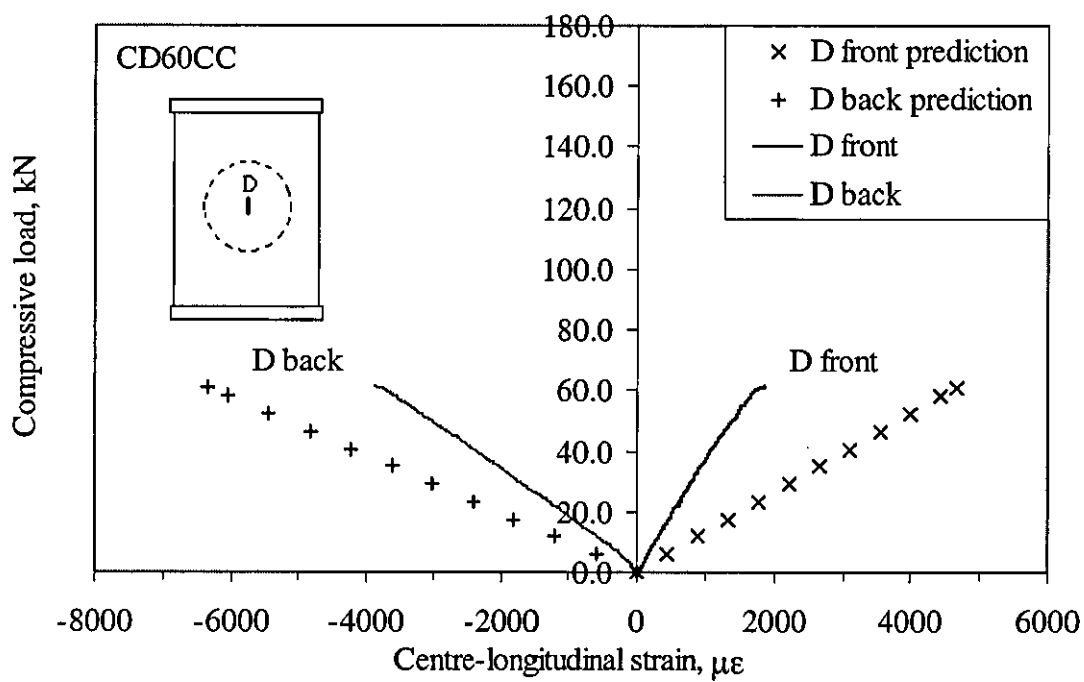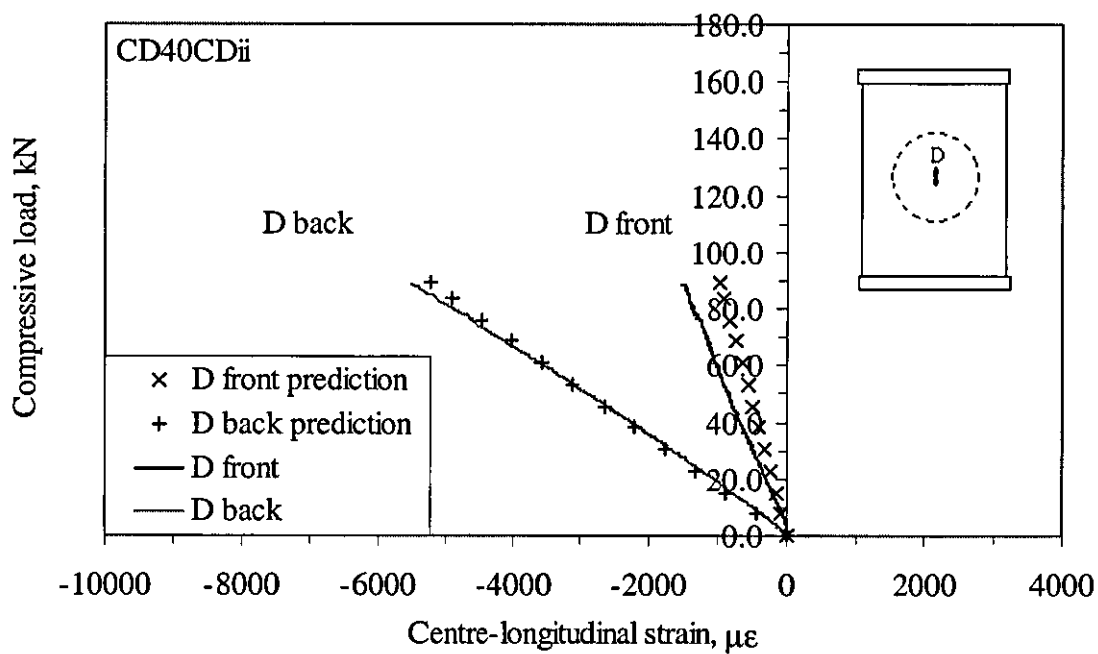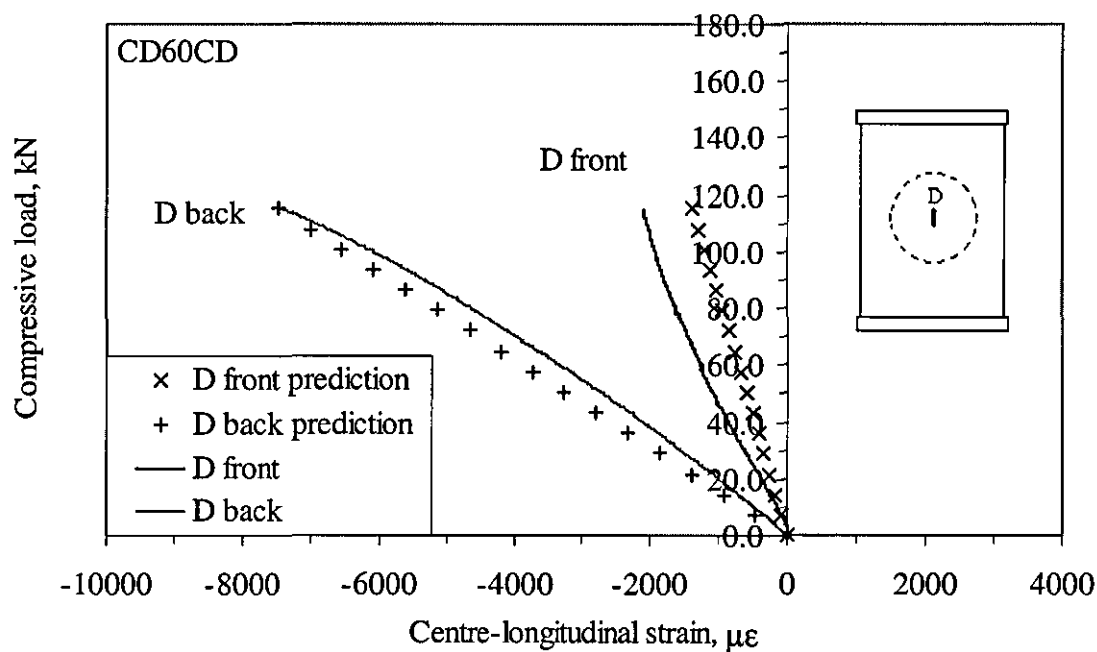
(e)

Figure 4.4.7 Centre-longitudinal strain prediction compared with the strain gauge response from 4-mm thick panels (a) CD20, (b) CD40CC, (c) CD60CC, (d) CD40CDii and (e) CD60CD
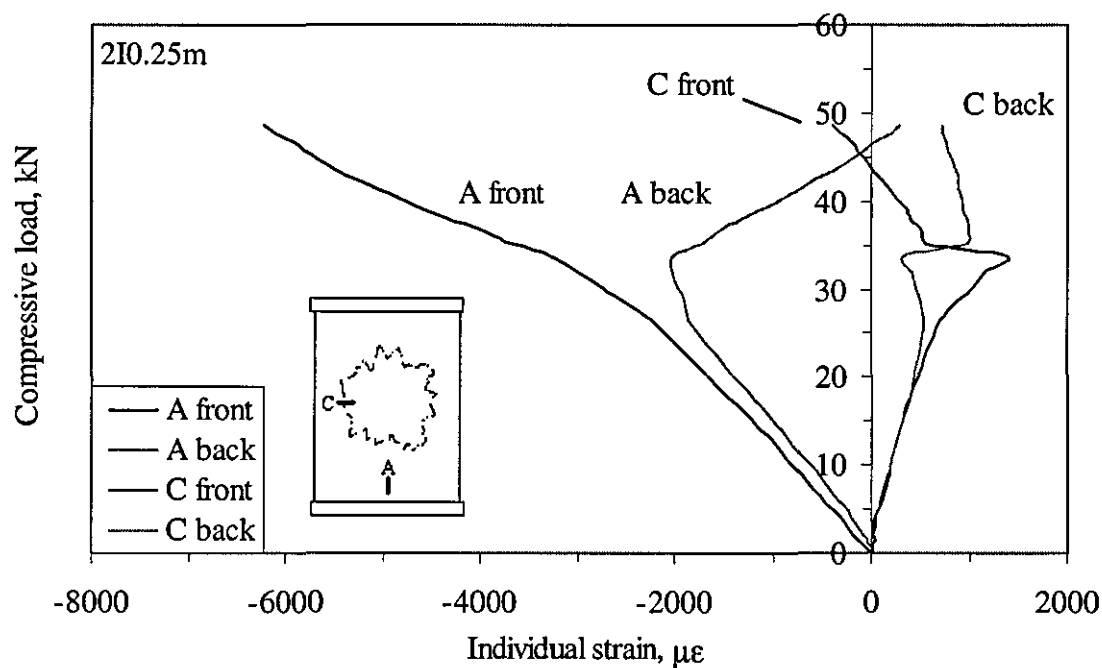
Figure 4.5.1 Load-strain response curves form far-field and transverse side strain gauges from a 2-mm thick panel impact-damaged at 3.7 J (2I0.250) [104]
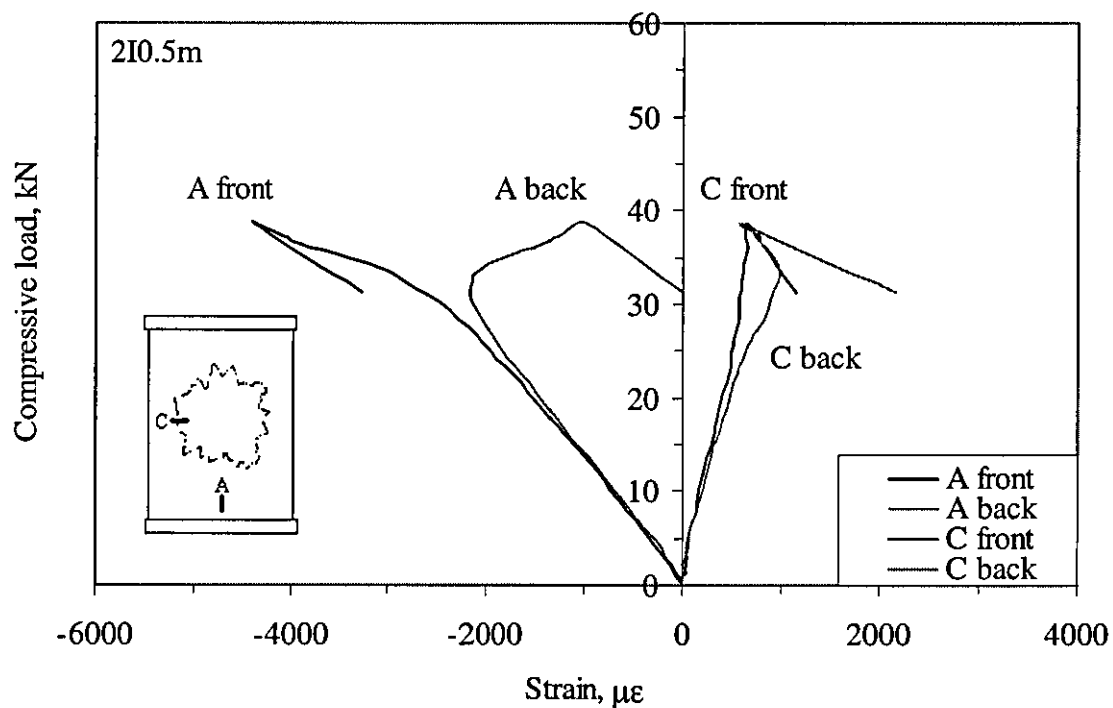
Figure 4.5.2 Load-strain response curves from far-field and transverse side strain gauges from a 2-mm thick panel impact-damaged at 7.8 J (2I0.500) [104]
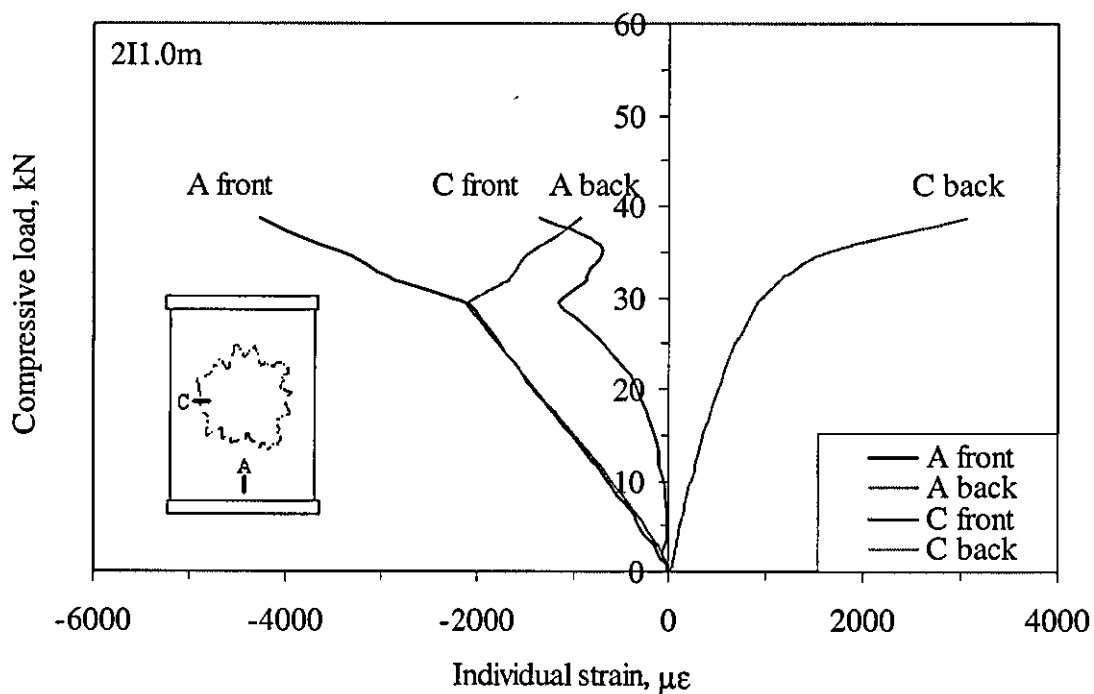
Figure 4.5.3 Load-far-field strain and transverse side strain response curves from a 2-mm thick panel impact-damaged at 15.8 J (2I1.000) [104]

198
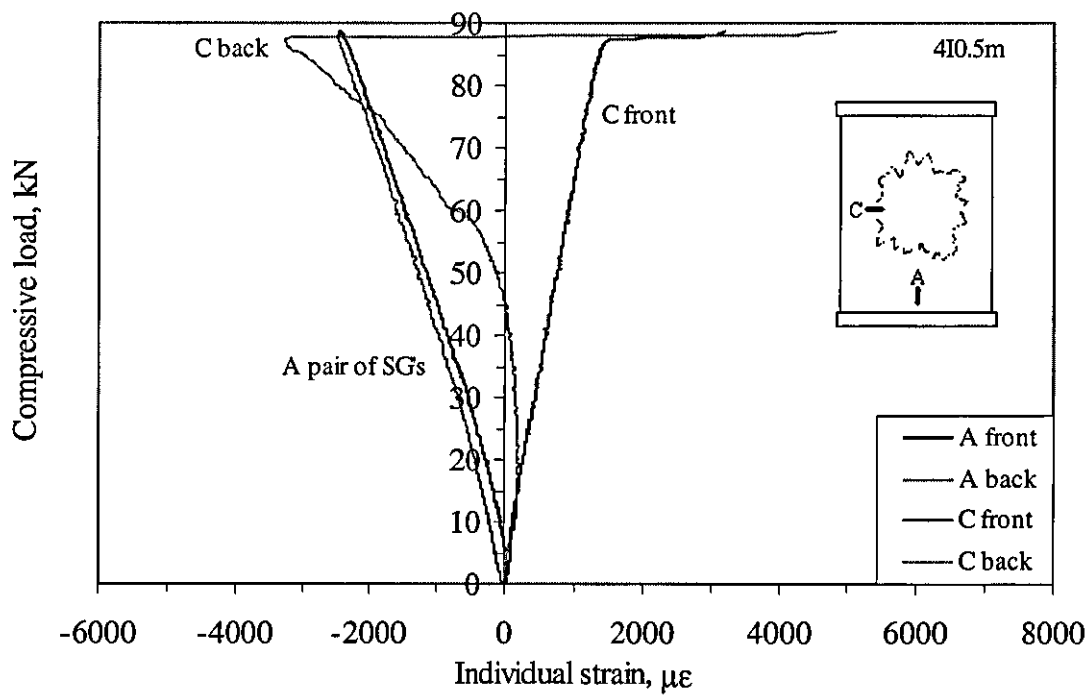
(a)
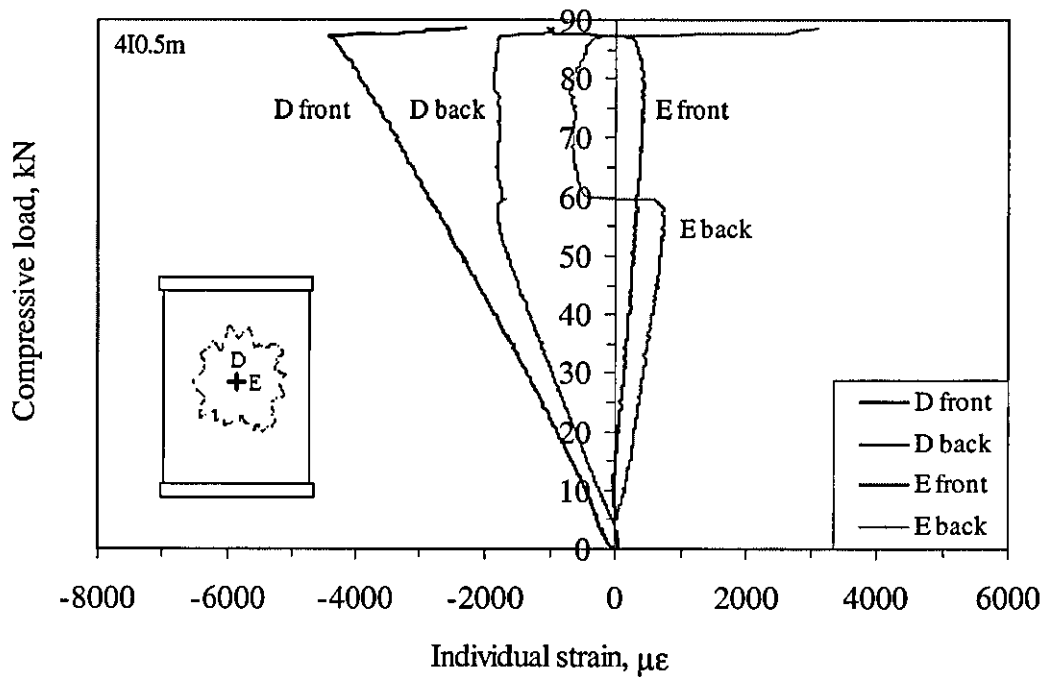
(b)

Figure 4.5.4 Individual strain response curves of (a) far-field and transverse side and (b) longitudinal and transverse central strain gauges from a 4-mm thick panel impacted at IKE of 6.9J (0.5 m height)
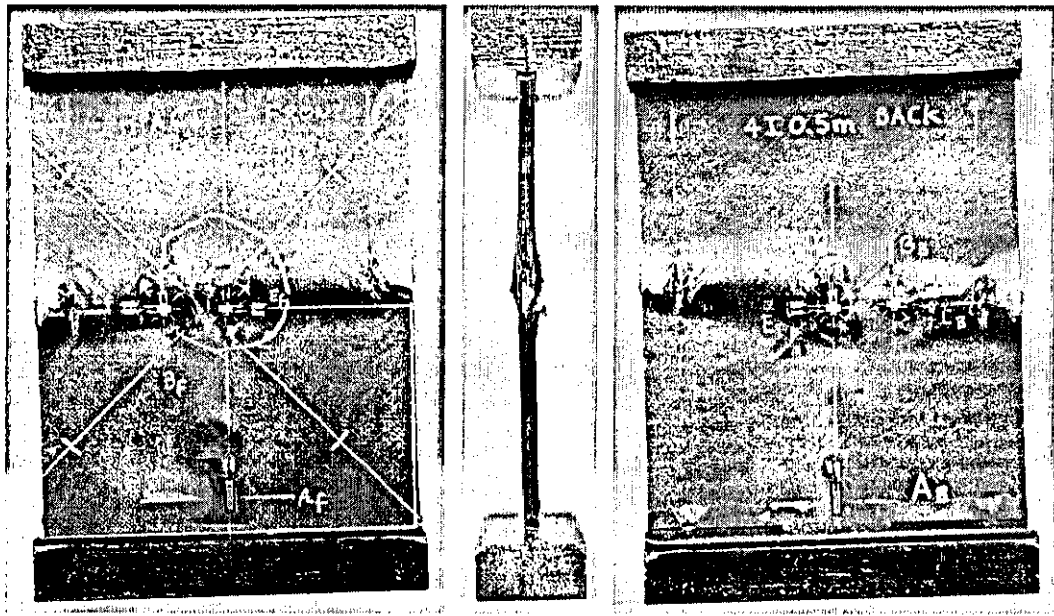
Figure 4.5.5 Photographs of a failed 4-mm thick panel (4I0.5m) containing impact damage (IKE 6.9J, 0.5 m height)

(a)

200

(b)
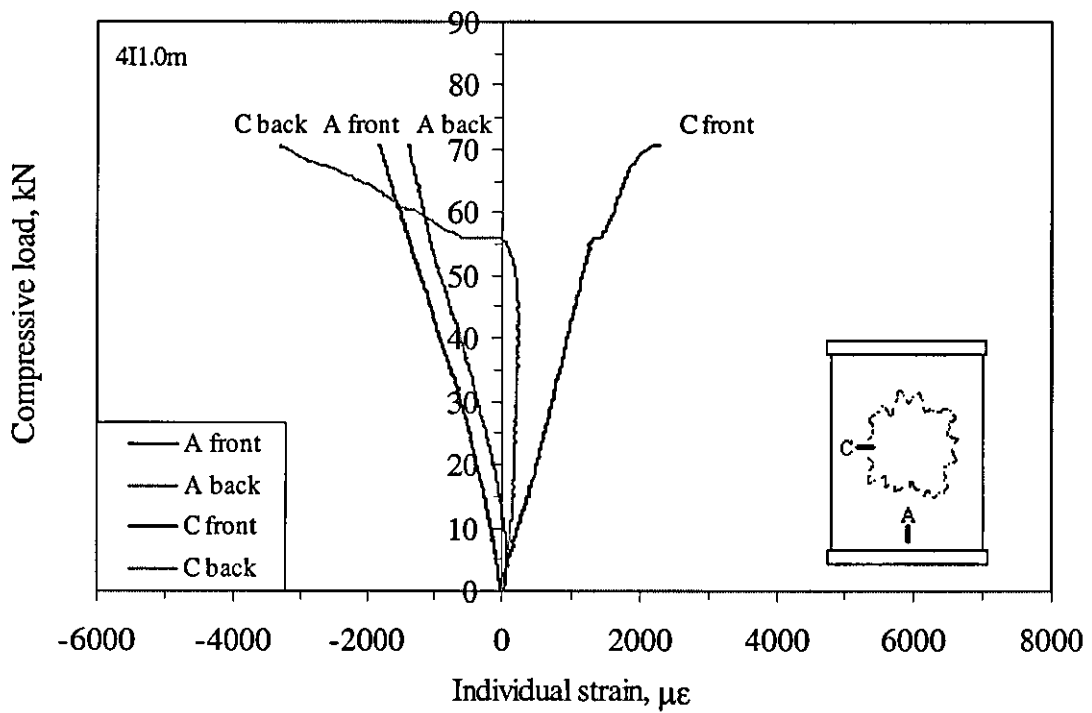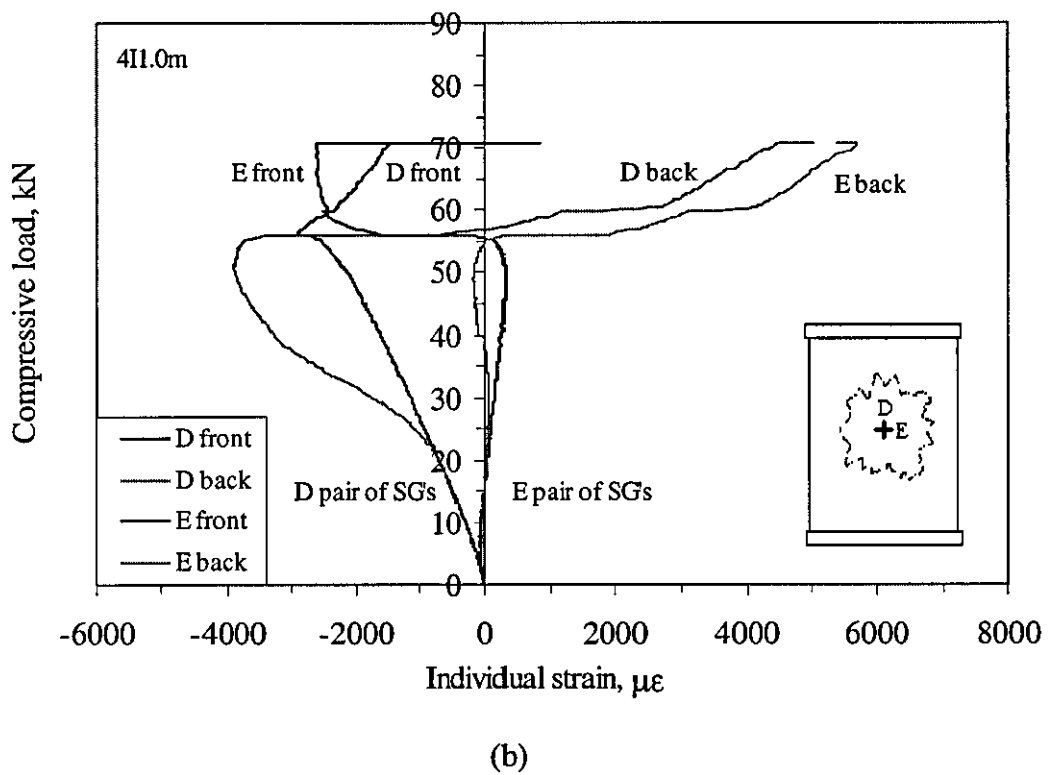
Figure 4.5.6 Individual strain response curves of (a) far-field and transverse side and (b) longitudinal and transverse central strain gauges from a 4-mm thick panel impacted at IKE of 13.7J (1.0 m height)

Figure 4.5.7 Photographs of a failed 4-mm thick panel (4I1.0m) containing impact damage (IKE 13.7J, 1.0 m height)

201
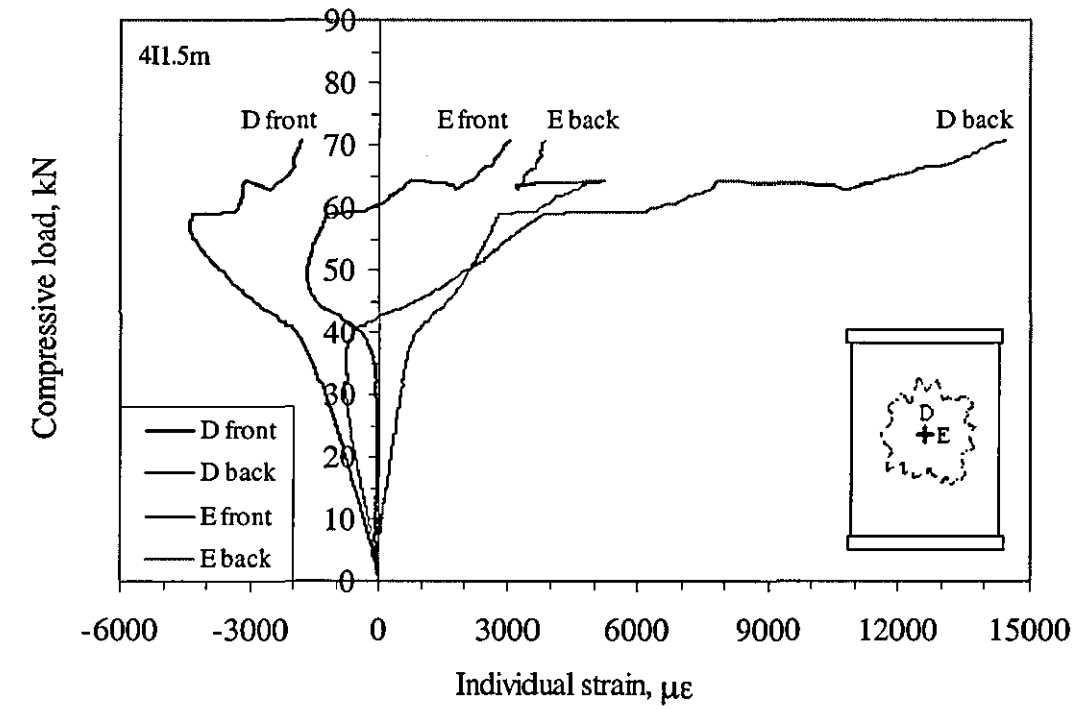
(a)
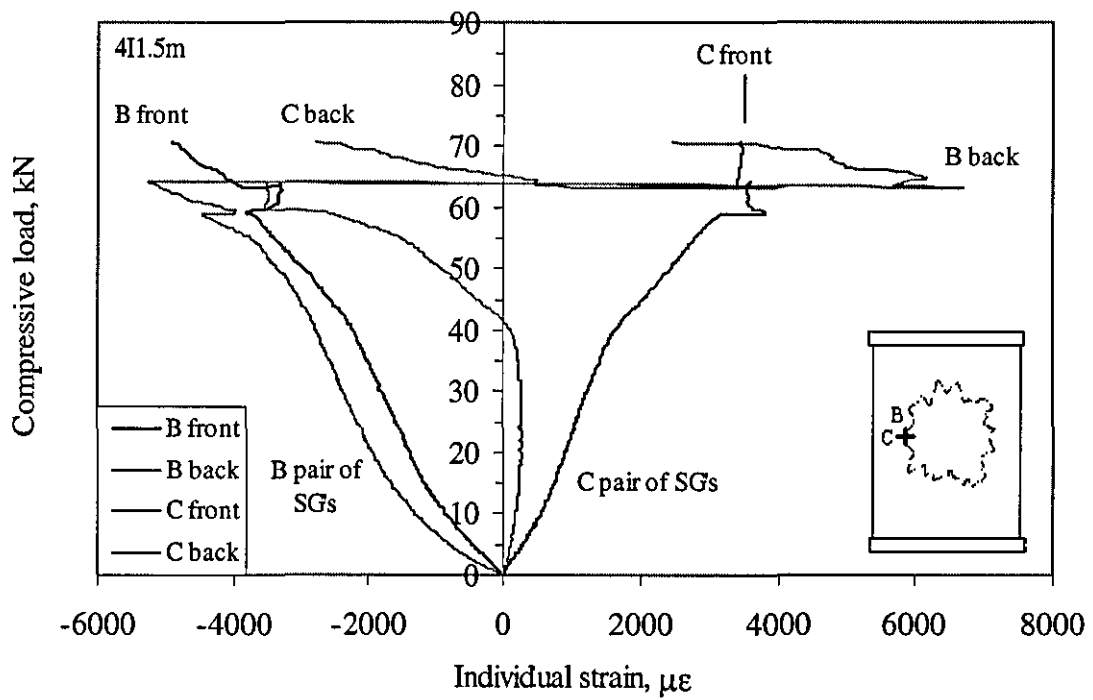
(b)

Figure 4.5.8 Individual strain response curves of (a) longitudinal and transverse central and (b) longitudinal and transverse side strain gauges from a 4-mm thick panel impacted at IKE of 21.1 J (1.5 m height)

Figure 4.5.9 Photographs of a failed 4-mm thick panel (4I1.5m) containing impact damage (IKE 21.1 J, 1.5 m height)

(a)

203
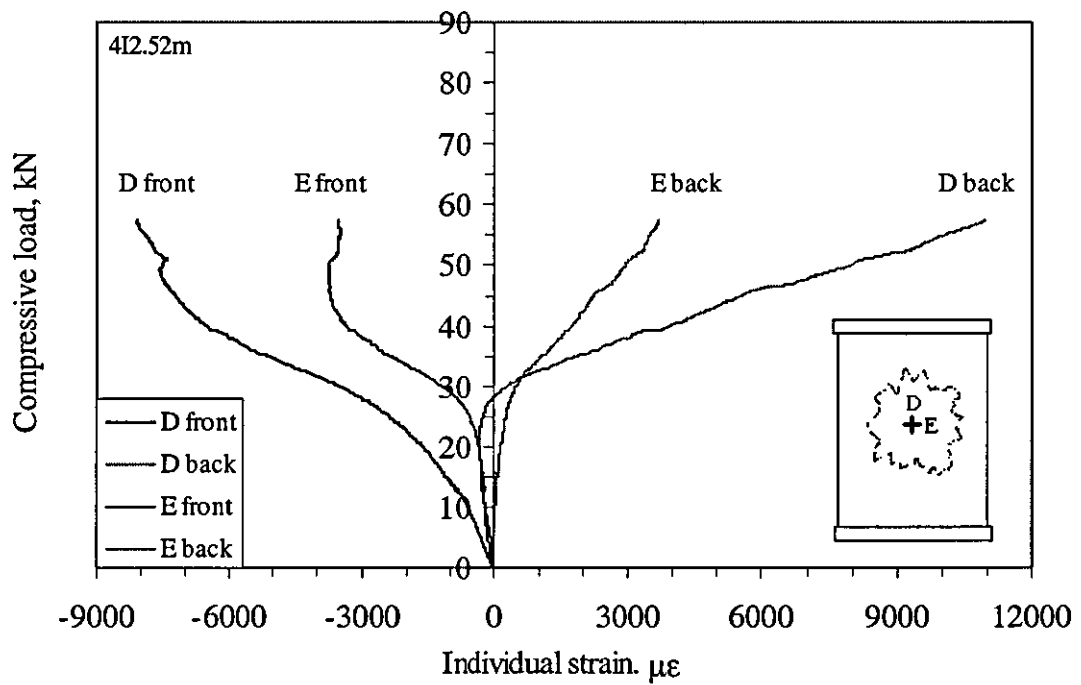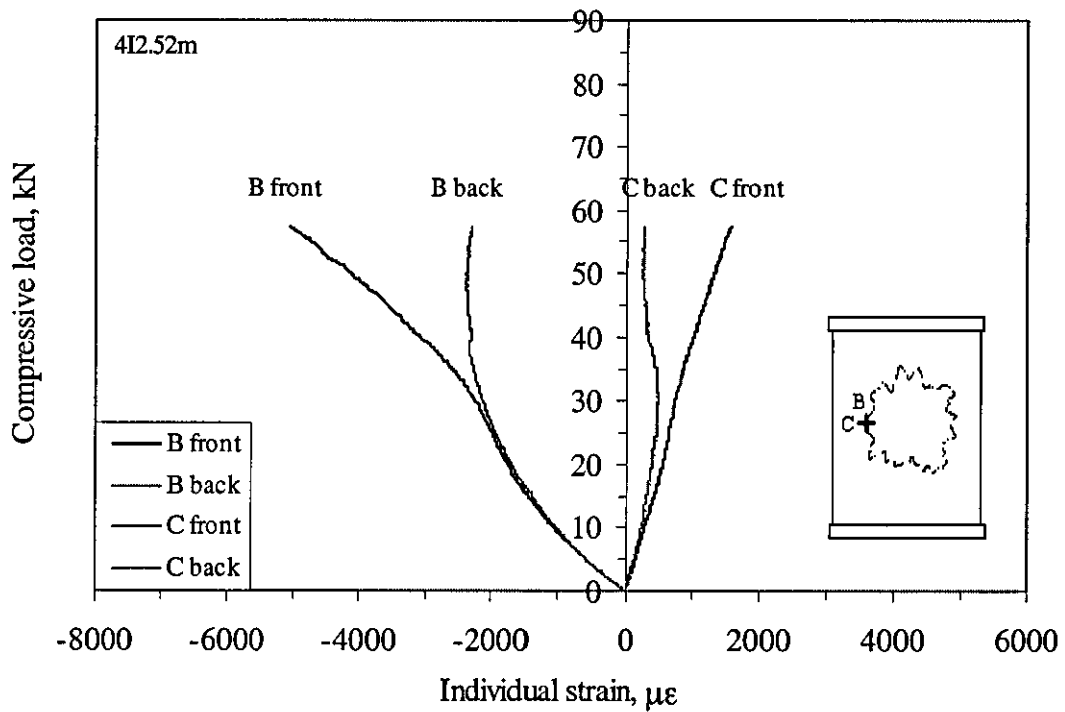
(b)

Figure 4.5.10 Individual strain response curves of (a) longitudinal and transverse central and (b) longitudinal and transverse side strain gauges from a 4-mm thick panel impacted at IKE of 41.7 J (2.52 m height)

Figure 4.5.11 Photograph of the cross section of a failed 4-mm thick panel (4I2.52m) containing impact damage (IKE 41.7 J). Interestingly, impact site could still be identified by the location of the shear cone.
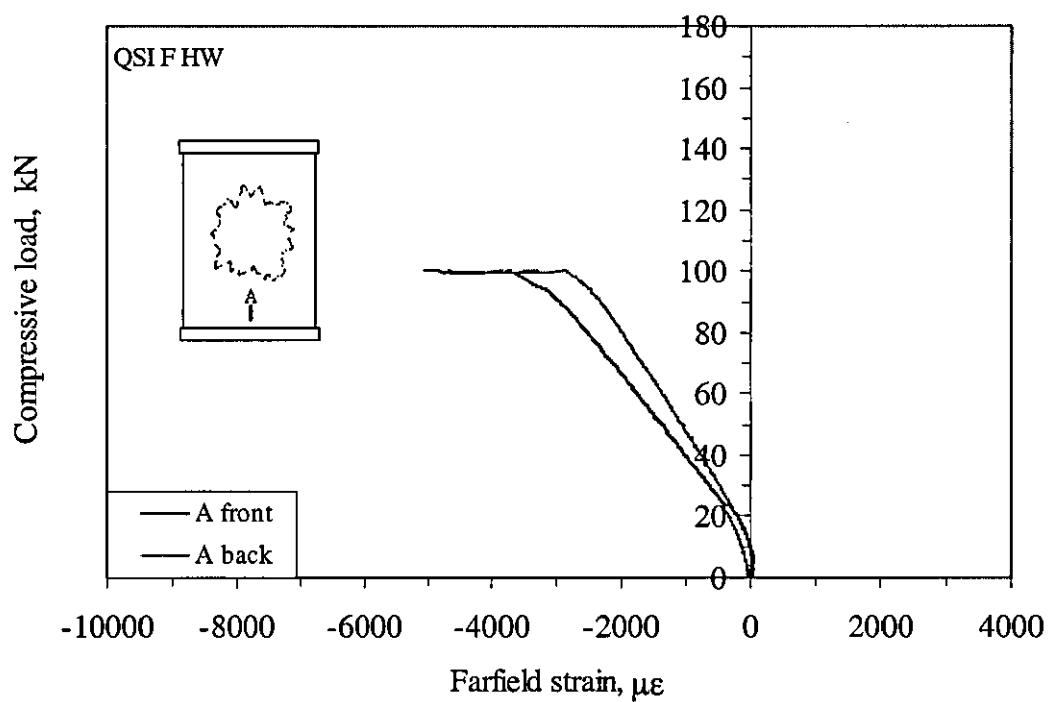
(a)
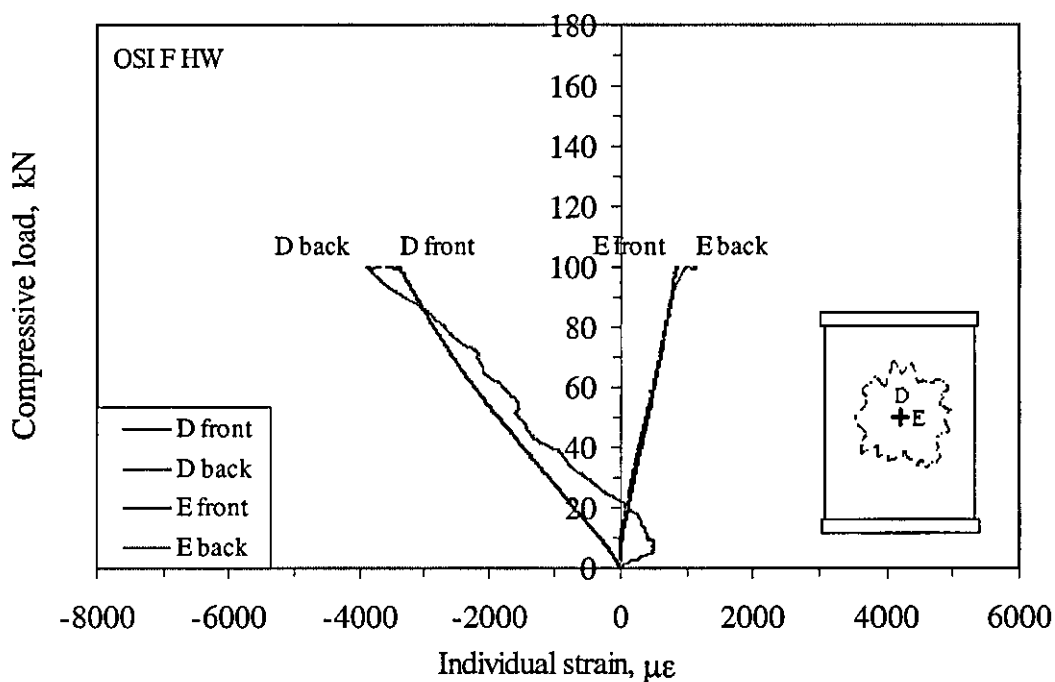
(b)

Figure 4.5.12 Individual strain response curves of (a) far-field and (b) longitudinal and transverse central strain gauges from a 4-mm thick quasi-statically-damaged panel (QSIFHW)

205
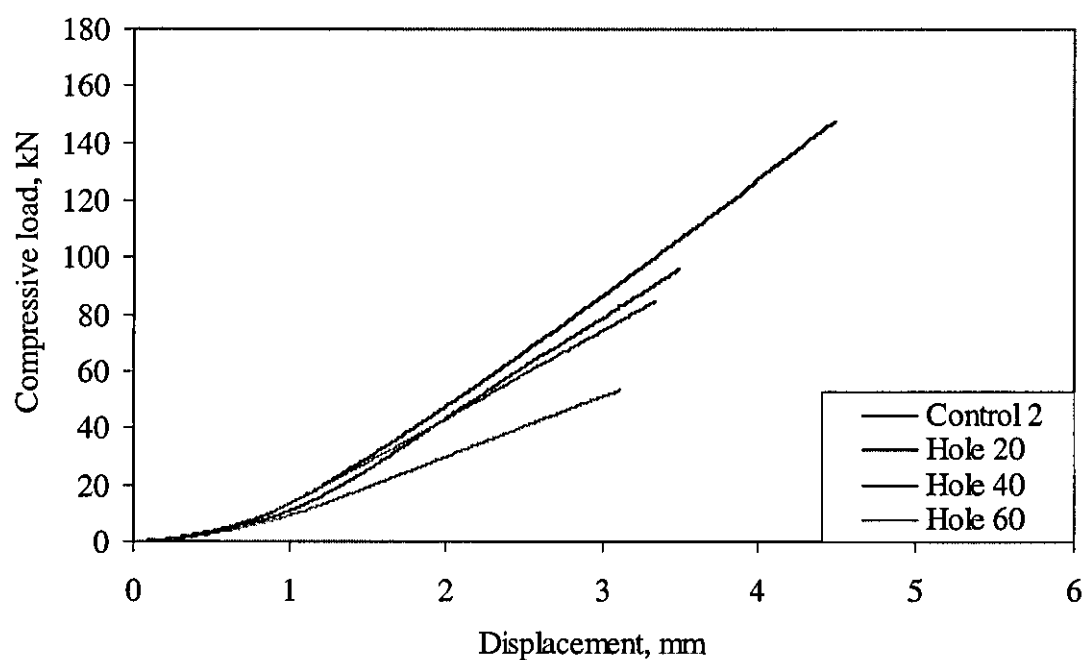
Figure 4.6.1 Load-displacement response curves from 4-mm thick panels with an open hole
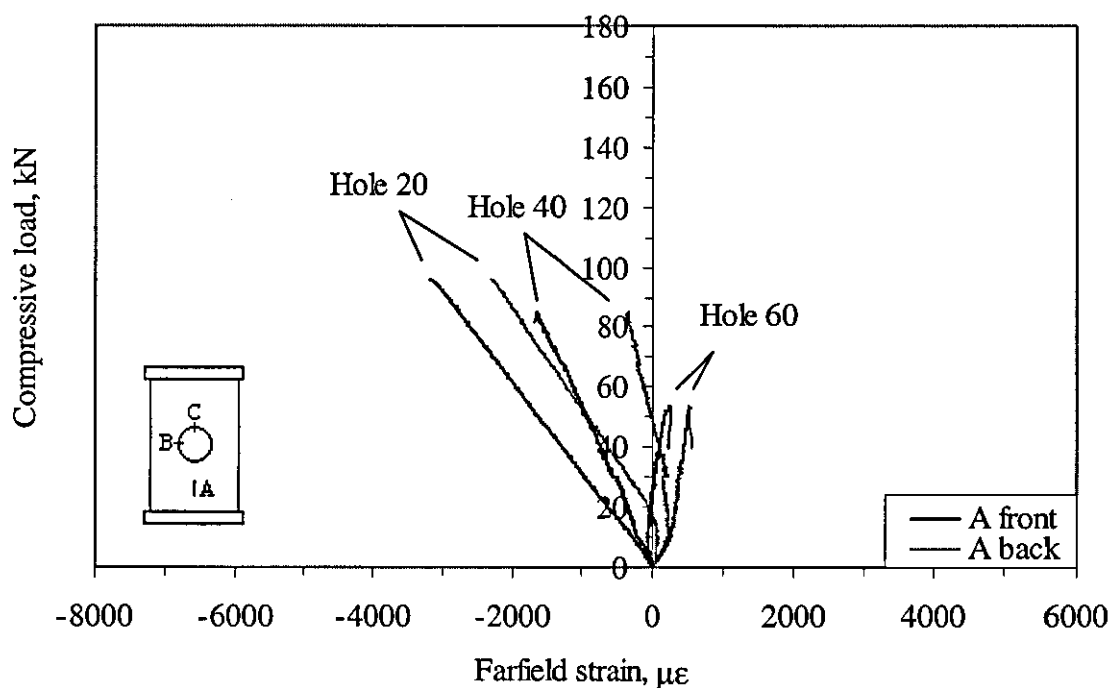
Figure 4.6.2 Load-far-field strain response curve from 4-mm thick panels with an open hole
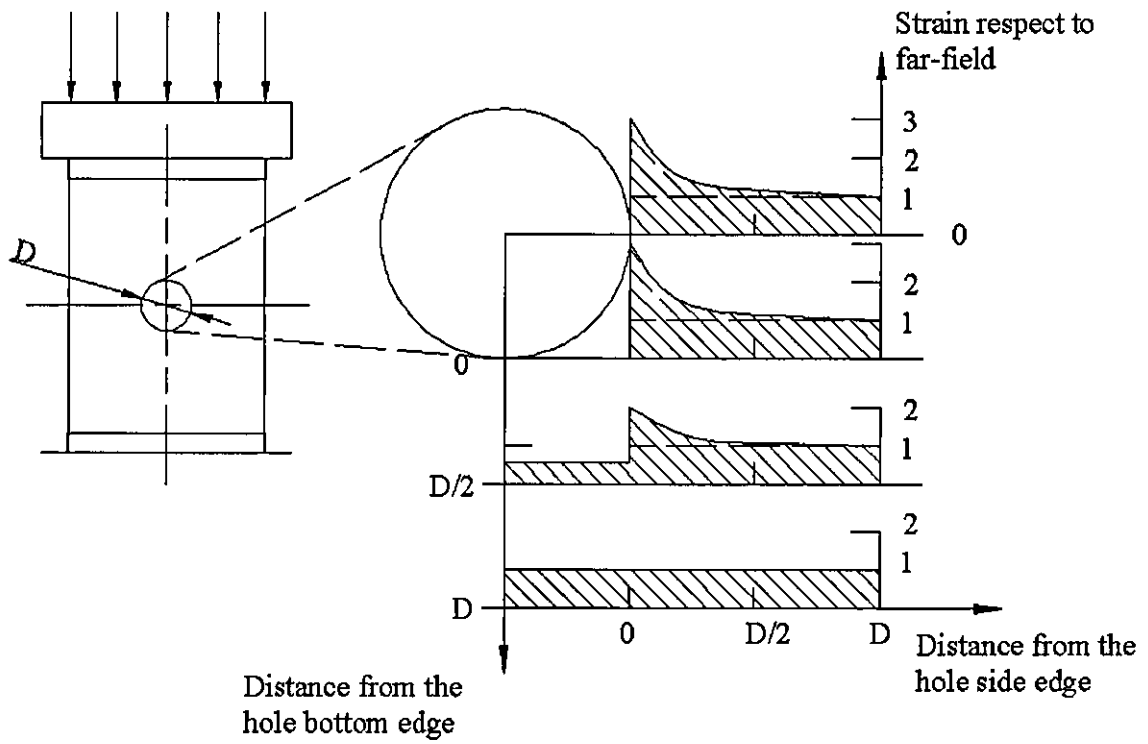
Figure 4.6.3 Schematic strain distribution along the load and width directions for panels with an open hole
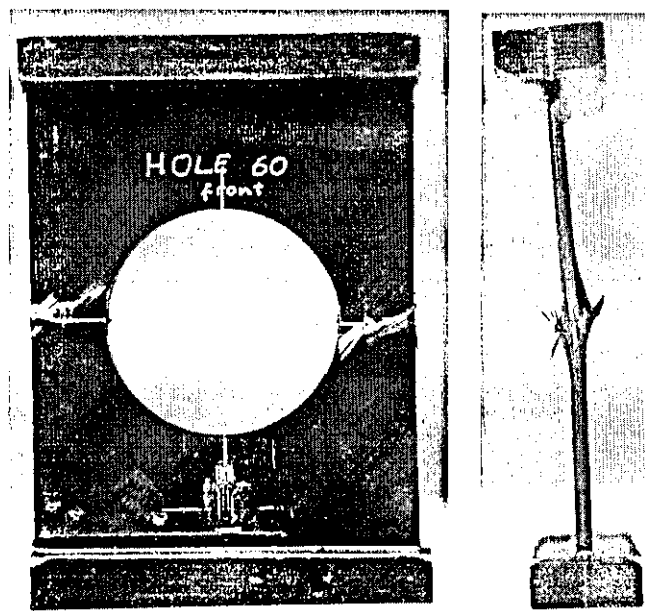
Figure 4.6.4 Photograph of a failed panel Hole 60
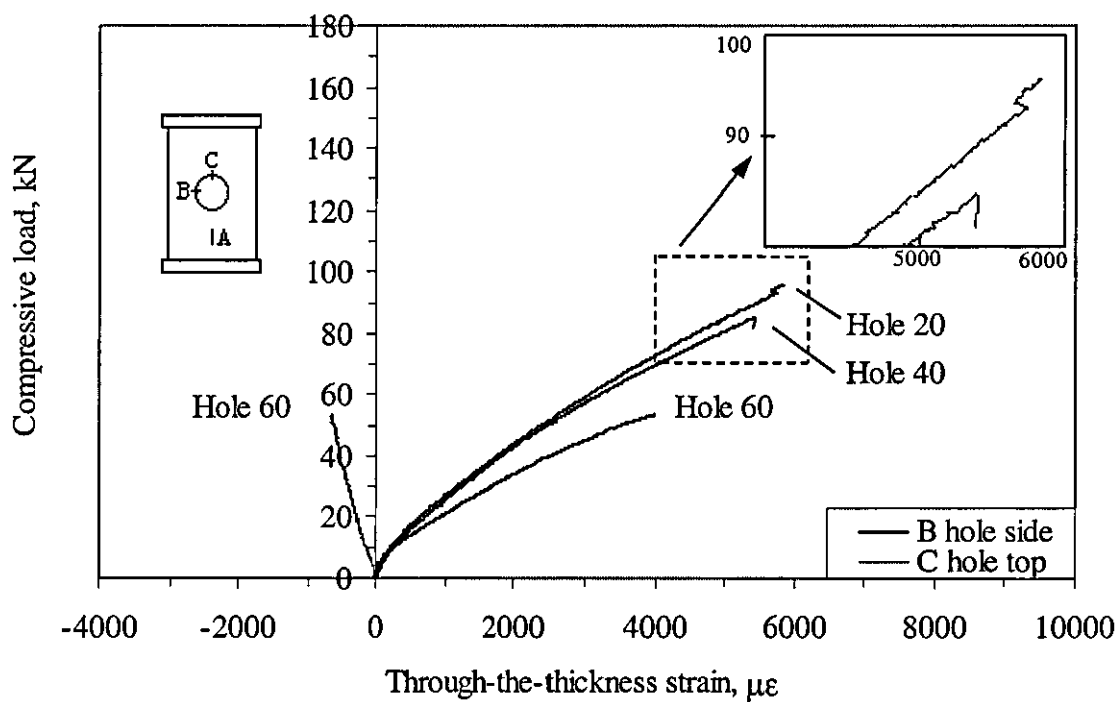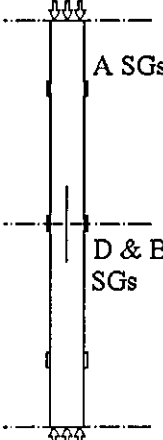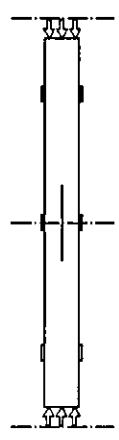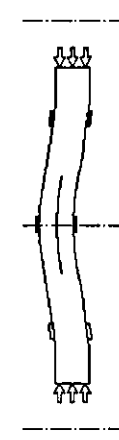
Figure 4.6.5 Load-strain response of gauges located at the edge of hole in the thickness direction in 4-mm thick panels with an open hole

208

I	II	III	III b	IV	V

Initial	Prebuckling	Local buckling	Frontal bulging	Global buckling I	Postbuckling (mode-II)
$\varepsilon_m^I = 0$	$\varepsilon_m^{II} > 0$	$\varepsilon_m^{III} > \varepsilon_m^{II}$	$\varepsilon_{front} \gg \varepsilon_{back}$	$\varepsilon_m^{IV} > \varepsilon_m^{III}$	$\varepsilon_m^V < \varepsilon_m^{IV}$
$\varepsilon_b^I = 0$	$\varepsilon_b^{II} = 0$	$\varepsilon_b^{III} > \varepsilon_b^{II}$		$\varepsilon_b^{IV} > \varepsilon_b^{III}$	$\varepsilon_b^V < \varepsilon_b^{IV}$ or $\varepsilon_b^V > \varepsilon_b^{IV}$
$P=0$	$0 < P$ and $P < P_{local}$	$P_{local} < P$ and $P < P_{global-I}$	$P_{local} < P$ and $P < P_{global-I}$	$P_{global-I} < P$ and $P < P_{global-II}$	$P_{global-II} < P$ and $P \le P_{failure}$

P_{local} — Local buckling (mode-I) load
$P_{global-I}$ — Incipient global buckling (mode-I) load
$P_{global-II}$ — Global buckling (mode I to mode II) load
$P_{failure}$ — Ultimate failure load
ε_b — Bending strain
ε_m — Mean strain

Figure 4.7.1 Deformation sequence of the compressive behaviour of preconditioned carbon/epoxy panels

209

SGs under unloaded conditions SGs under loaded conditions	Transverse strain
	Mean Bending

No propagation

Front

i)

Back

$$P_{local}>P>0$$

$$\varepsilon^{i}_{m\,centre} = \varepsilon^{i}_{m\,side} > 0 \quad \varepsilon^{i}_{b\,centre} = \varepsilon^{i}_{b\,side} = 0$$

Less probable propagation

ii)

$$P_{global-II} >P>P_{local} \quad \text{or} \quad P_{failure}>P>P_{global-II}$$

$$\varepsilon^{ii}_{m\,side} > \varepsilon^{i}_{m\,side} \qquad \varepsilon^{ii}_{b\,side} > \varepsilon^{i}_{b\,side}$$

$$\varepsilon^{ii}_{m\,centre} > \varepsilon^{i}_{m\,centre} \qquad \varepsilon^{ii}_{b\,centre} > \varepsilon^{i}_{b\,centre}$$

$$\varepsilon^{ii}_{m\,side} \doteq \varepsilon^{ii}_{m\,centre} \qquad \varepsilon^{ii}_{b\,side} \doteq \varepsilon^{ii}_{b\,centre}$$

Probable propagation

iiia)

$$P_{failure}>P>P_{global-II}$$

$$\varepsilon^{iiia}_{b\,side} > -\varepsilon^{iiia}_{b\,centre}$$

$$\varepsilon^{iiia}_{m\,side} \doteq \varepsilon^{iiia}_{m\,centre} \qquad \text{or}$$

$$\varepsilon^{iiia}_{b\,side} > \varepsilon^{iiia}_{b\,centre}$$

Definitive propagation

iiib)

$$P_{failure}>P>P_{global-II}$$

$$\varepsilon^{iiib}_{m\,side} < \varepsilon^{iiib}_{m\,centre} , \quad \varepsilon^{iiib}_{b\,side} < \varepsilon^{iiib}_{b\,centre}$$

$$\text{or}$$

$$\varepsilon^{iiib}_{m\,side} > \varepsilon^{iiib}_{m\,centre} , \quad \varepsilon^{iiib}_{b\,side} > \varepsilon^{iiib}_{b\,centre}$$

Figure 4.7.2 Illustration of transverse deformation sequence in the width direction
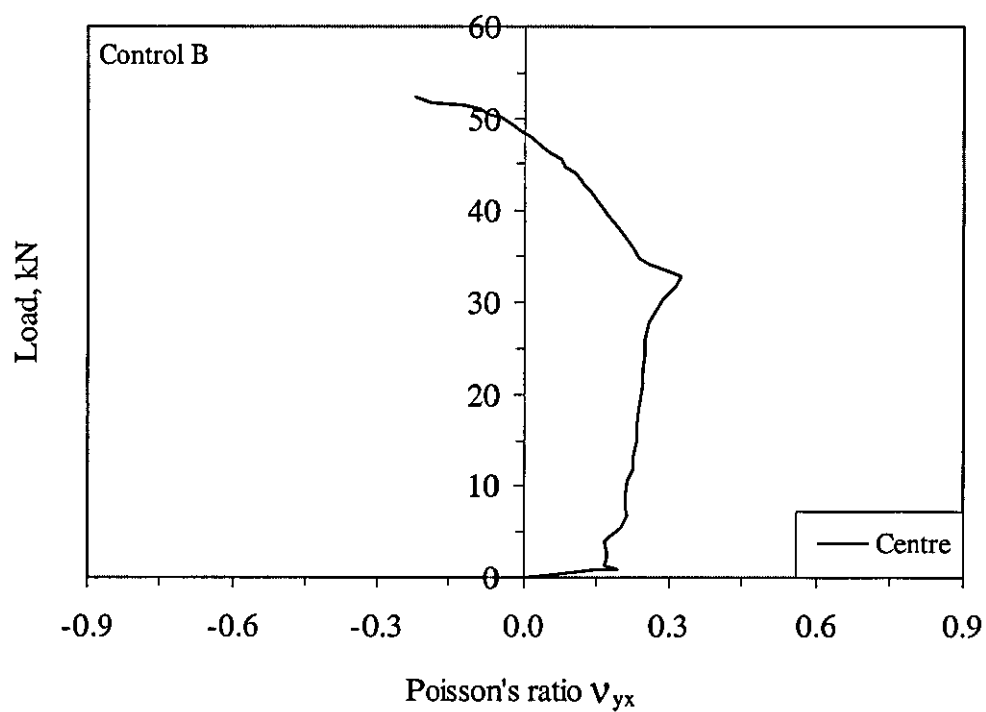
(a)
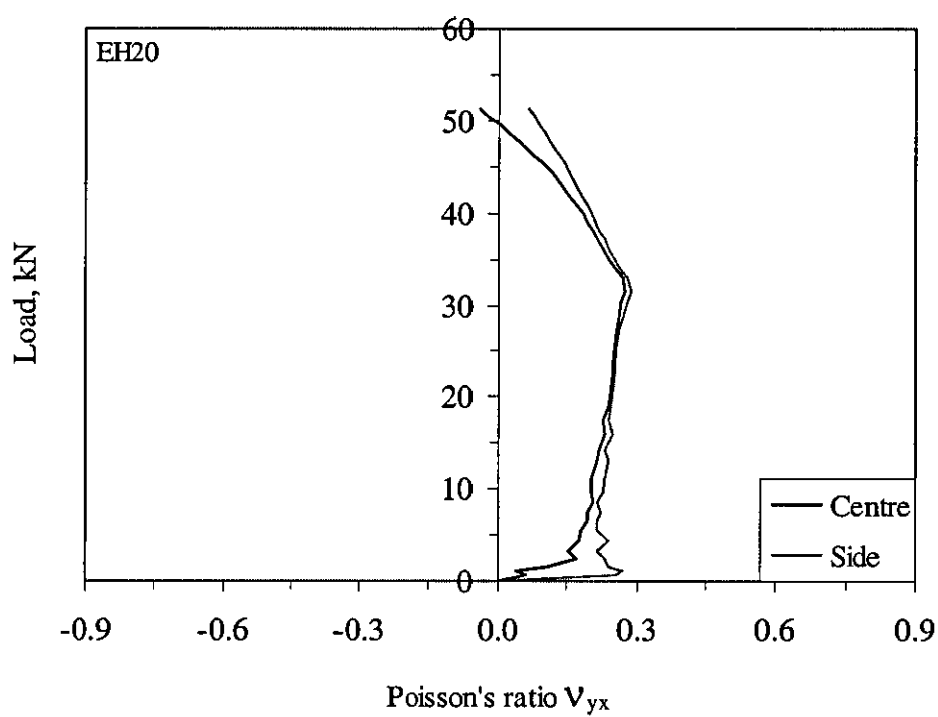
(b)
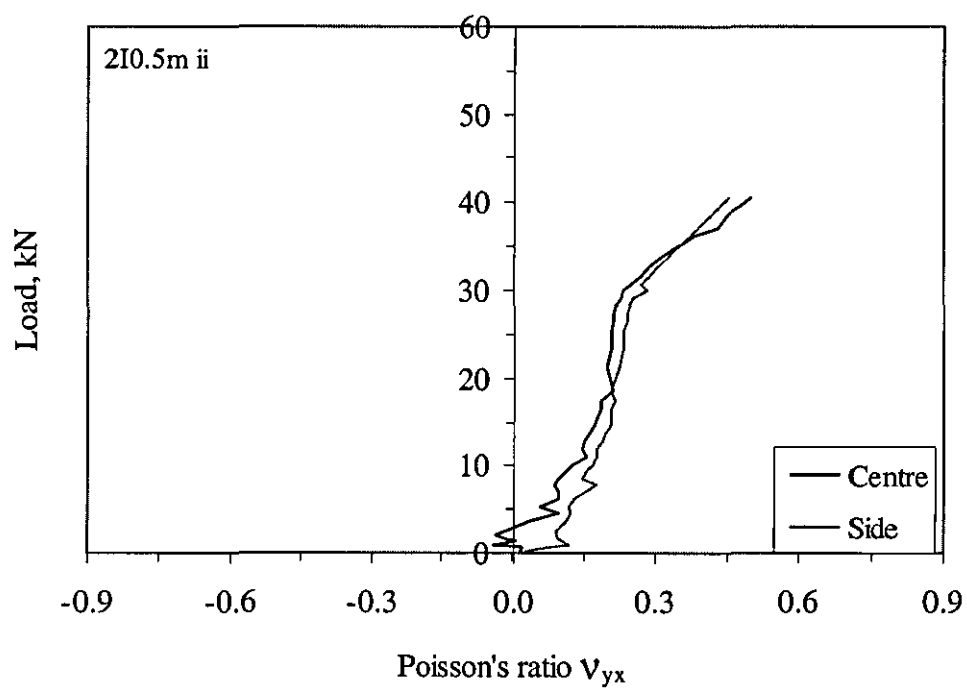
(c)
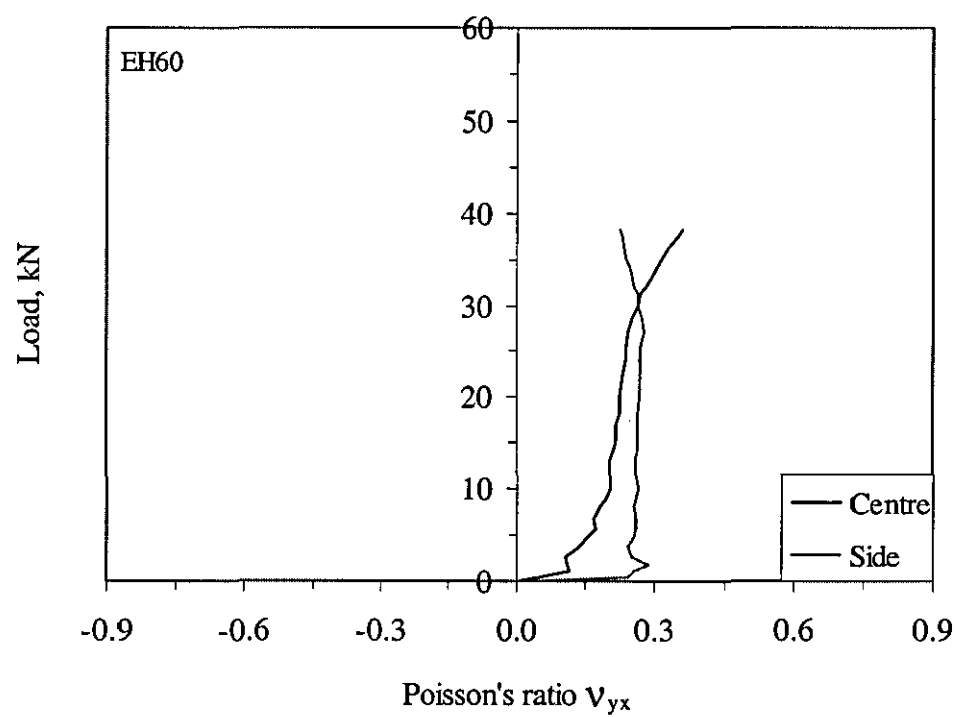
(d)
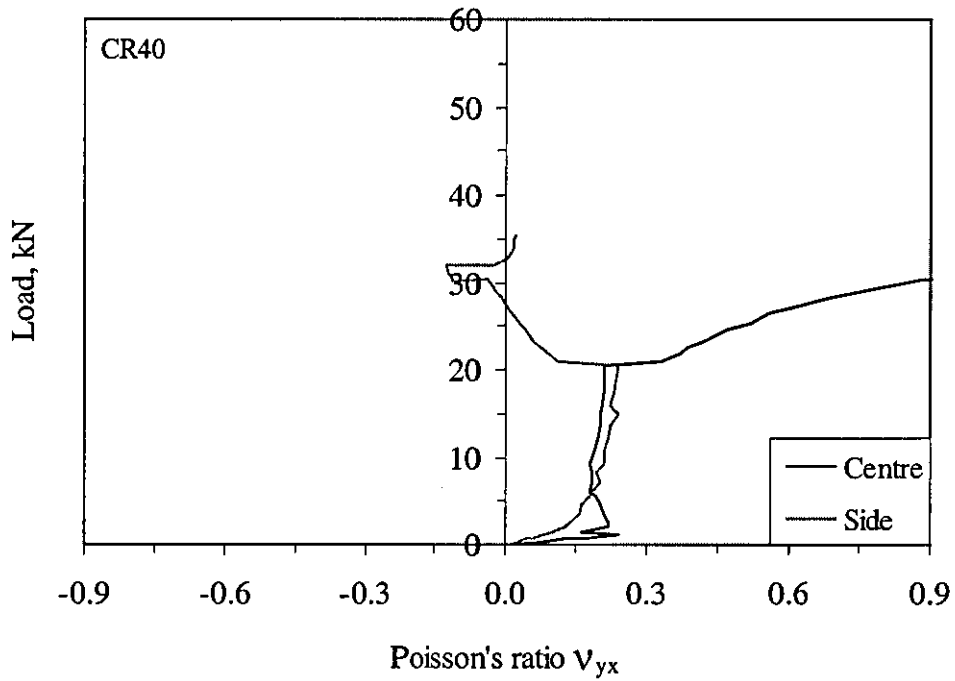
(e)

Figure 4.7.3 Load-Poisson's ratio relationships from 2-mm thick (a) intact panel, (b) panel with a 20-mm horizontal elliptical delamination, (c) panel with impact damage (IKE 7.9, height 0.5 m), (d) panel with a 60-mm horizontal elliptical delamination and (e) panel with a 40-mm circular delamination
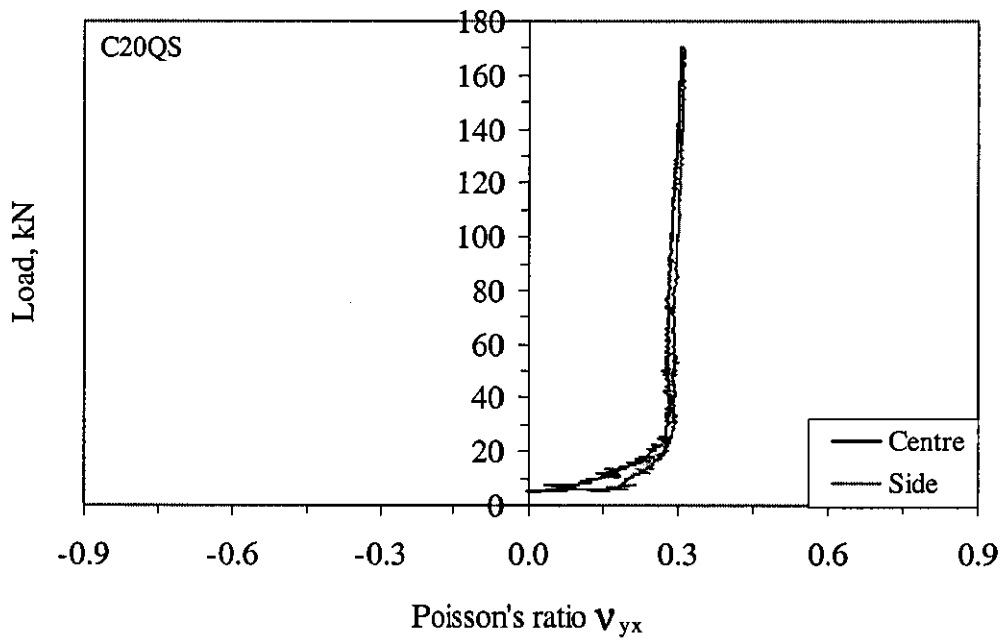
(a)
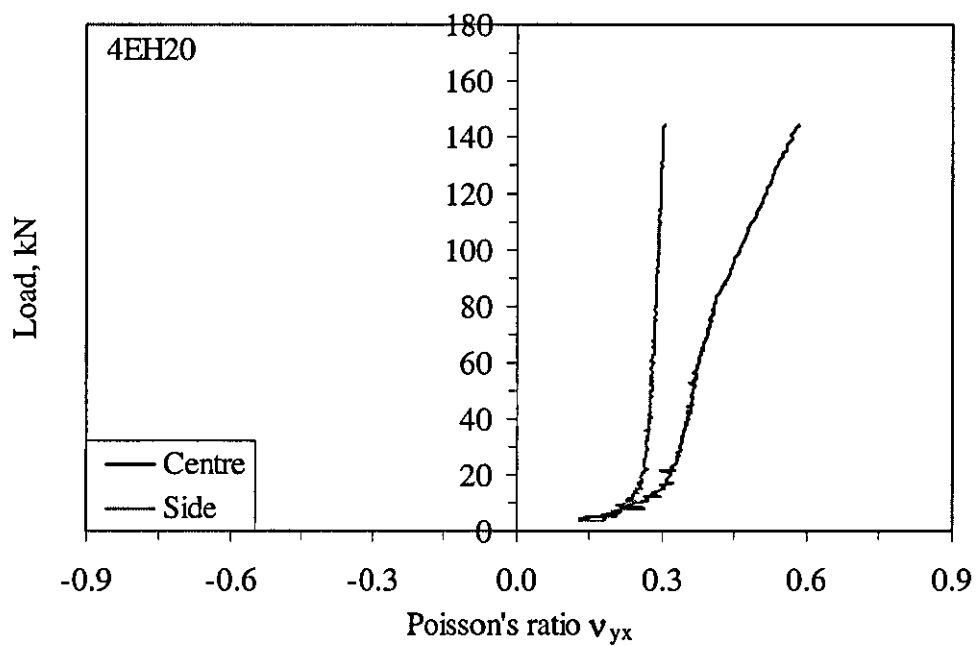
(b)
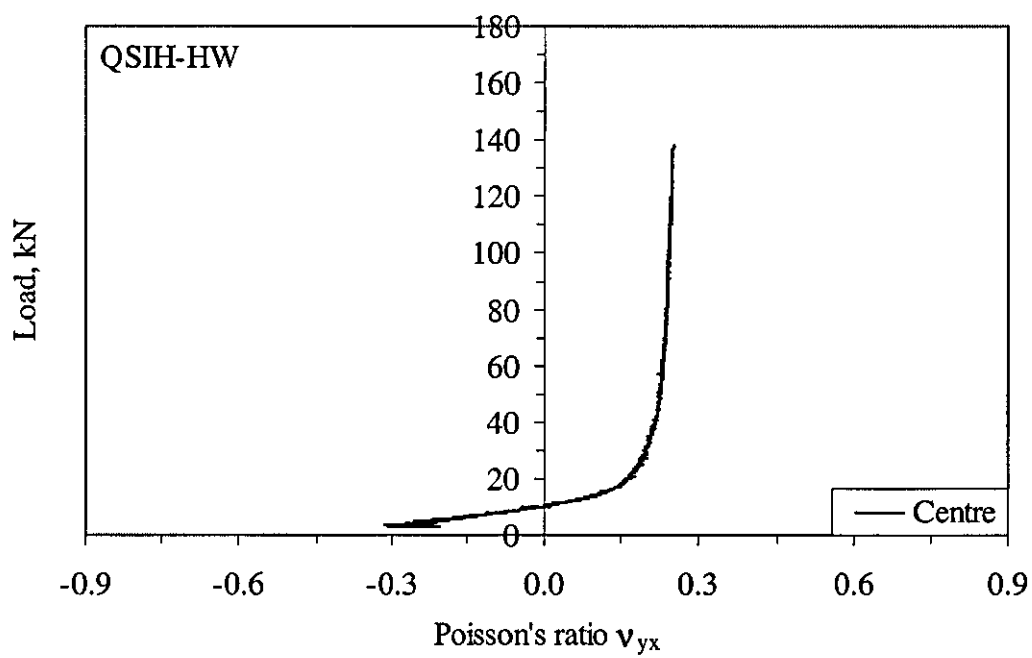
(c)
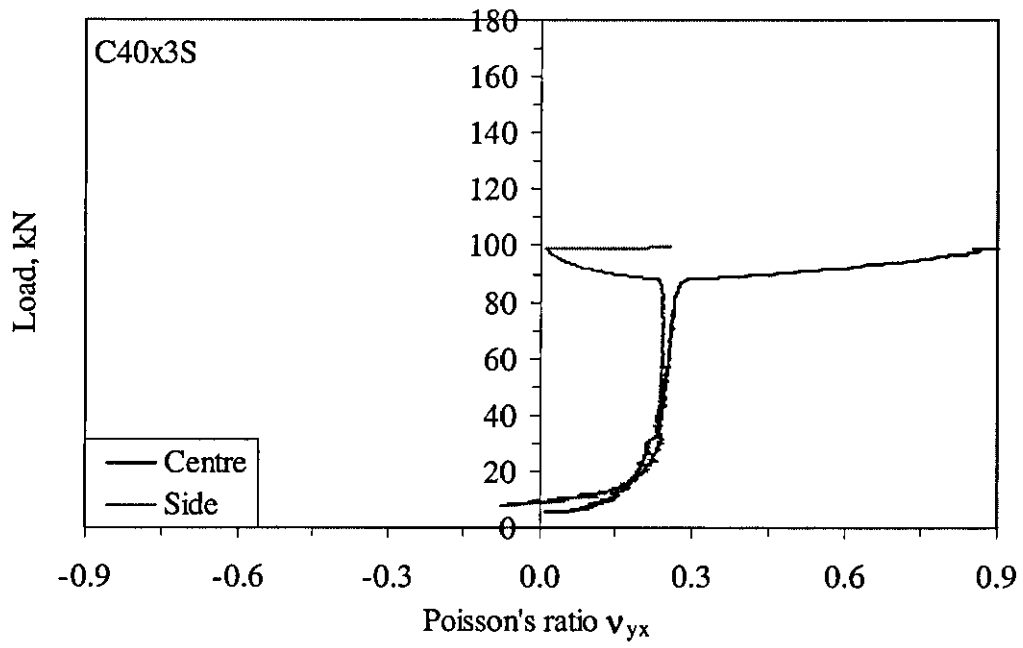
(d)
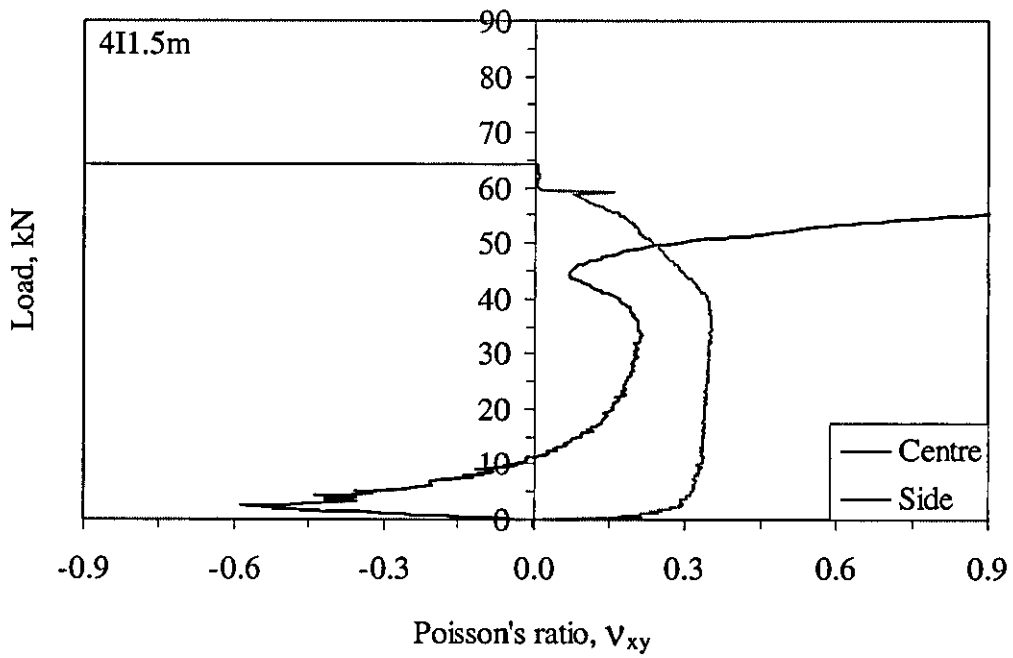
(e)

Figure 4.7.4 Load-Poisson's ratio relationships from 4-mm thick panel with (a) a 20-mm circular delamination at the quarter location, (b) a 20-mm horizontal elliptical delamination, (c) a quasi-statically damaged with a hemispherical indentor, (d) three 40-mm circular delaminations symmetrically distributed and (e) impact damage (IKE 21.1J height 1.5 m)

5 Damage Tolerance determination

Impact damage can significantly reduce the load bearing capabilities of a composite structure, in particular compressive properties such as strength, ultimate strain and stiffness. This reduction depends on parameters related to damage characteristics, specimen geometry and composite system. This chapter focuses on the effect of such parameters on the different metrics used for damage tolerance assessment, with special emphasis on the residual compressive strength (RCS).

5.1 Factors affecting residual compressive strength

The compressive behaviour of panels with preconditions has been studied in Chapter 4. In this section, the compressive strength retention factor (CSRF) of panels with embedded delamination, local change of geometry and open hole are compared with panels with impact and quasi-static damage. In this way, it is possible to ascertain the significance of individual preconditions on the ultimate compressive failure.

5.1.1 Effect of compressive response on RCS

Figures 5.1.1(a-b) summarises the results from Chapter 4 of local buckling (mode-I), global buckling (mode I to II) and failure loads of all the tested 2-mm thick panels in terms of transverse damage size and damage area. The overall trend of the local buckling (mode-I) loads is seen to be more or less constant, irrespective of shape, delamination size, or the other preconditions. The overall trend of the panel compression stiffness data in this stage shown in Figure 5.1.2 also show little degradation, though the variation of the data appears in a narrow band with an increase of damage size. Therefore the preconditions of whatever nature had little effect on the local buckling (mode-I) loads. Similar findings were observed in [91] where the strain field in the delaminated region prior to buckling was unaffected by the presence of delaminations. The global buckling (mode I to II) load data also appear in a narrow band and show the size-dependent degradation trend in Figures 5.1.1(a-b). When the transverse damage size is less than about 25% panel width or the damage area is less than about 455 mm^2, the global buckling (mode I to II) loads seem to be insensitive to

the preconditions and thus their reduction is small. However, beyond those respective thresholds, the degradation of the global buckling (mode I to II) loads and RCS values becomes noticeable but still in a slow trend. At the 60% panel width or the largest damage area, a 24% reduction was found for elliptical delaminations and 35% for circular delaminations in Figure 5.1.1(a-b). The greater reduction for the circular delaminations corresponds to the bigger delamination areas at the same transverse size. Three artificial delaminations of the same size for the present 16-ply laminates seem (symbols with an over-laid plus sign) to represent the worst conditions. Figure 5.1.1 (a-b) also includes the results of buckling (mode-I), global buckling (mode I to II) and failure loads, for 2-mm thick panels with impact-induced damage. Impacted panels had a constant trend of local buckling (mode-I), which is a little surprising, since the interior damage in these panels could degrade extensional stiffness. Panels with impact-induced damage had a decreasing trend of global buckling (mode I to II) and failure loads respect to the area of delamination. Such trend was not in a way different from that of the artificially preconditioned panels.

Figures 5.1.3(a-b) summarise the results of local buckling (mode-I), global buckling (mode I to II) and failure loads of all the tested 4-mm thick panels with artificial embedded delamination(s), in terms of transverse damage size and damage area. Figure 5.1.3(a) uses the delamination transverse width on the x-axis, mixing single and multiple delaminations with the same abscissa. To visualize the effect of delamination number, Figure 5.1.3(b) was plotted using the cumulative delamination area, which is the result of multiplying projected delamination area by the number of defects embedded. Failure location on the panel was taken in account to determine whether a panel had failed during the pre-buckling stage (failure at either the loading or far end) or postbuckling (mode-II) stage (failure at the mid-section).

On the one hand, the failure of panels that failed during the pre-buckling stage was similar to those of 4-mm thick intact panels. The failure occurred in end-crushing, as it was the case for panels with small delaminations, up to 1257 mm^2, which includes all elliptical delaminations and single circular delaminations up to 40-mm diameter. On the other hand, the failure of panels that failed during the postbuckling (mode-II) stage at the mid-section was markedly different than intact panel failure. The ultimate failure

was governed by the ILSS concentration at the mid-section, due to the panel global deformation. This was reflected in a more predictable trend, than the one exhibited by first set of panels. The failure patterns were similar to those of 2-mm thick panels. Buckling (mode-I) started locally at the delamination centre, remaining constant indistinctly of delamination size, a similar feature than 2-mm thick panels. Postbuckling (mode-II) was present in panels with large multiple delaminations, and just prior to the final failure. Both global buckling (mode I to II) and failure loads showed a steady decreasing trend with the increasing of delamination number and area. For the global buckling (mode I to II) load the critical area was 3770 mm^2, starting a steady reduction of 15% and 23% when increasing from 40 to 60-mm delamination size, for symmetrical and asymmetrical distributions respectively. The degrading trend for the ultimate failure started at 1257 mm^2, with a maximum reduction of CS of 39% and 33% for 60-mm multiple circular delamination, symmetrical and asymmetrical distributions respectively.

A particular local weakening of the frontal thin sublaminate was detected from the SG readings of 4-mm thick panels with asymmetric through-the-thickness (TTT) distribution of delaminations. This phenomenon was catalogued as *frontal bulging* and occurred between the local buckling (mode-I) and the global buckling (mode I to II) loads, as shown in Figure 5.1.4. The panels that presented it were the one with the largest single delamination (C60QS) and all the multiple delaminated panels (C20x3AS, C40x3AS, C60x3AS). Although it did not affect the overall failure of the panel, it evidenced both the presence of unbalanced sublaminates and asymmetric delamination TTT distribution. The trend of the frontal bulging respect to the delamination area is decreasing, as shown in Figure 5.1.4.

Figure 5.1.5 (a-b) summarises the results of local buckling (mode-I), global buckling (mode I to II) and failure loads of all tested 2-mm and 4-mm thick panels with impact damage in terms of IKE. The local buckling (mode-I) stress did not follow a constant trend, as a consequence of the buckling deformation right from the beginning of panels impacted at high energies. This was a difference respect to panels with embedded delamination (Figure 5.1.3) and to 2-mm thick panels with impact-induced damage (Figure 5.1.1). The bulging of delamination on the back side followed a decreasing

trend, similar to the one from panels with asymmetric distribution of delaminations (Figure 5.1.4). It was a phenomenon linked with the asymmetric distribution of damage inside the panel. The influence of this effect on panel behaviour can be related to the size of damage and with the level of eccentricity that this damage has inside the panel. Therefore panels impacted with higher IKE developed delamination bulging at lower compressive loads than panels with lower IKE. Also thick panels seemed prone to develop delamination bulging more than thin panels. In this study, 2-mm thick panels did not develop delamination bulging, whereas 4-mm thick panels with large damage did. Finally, global buckling (mode I to II) and failure loads followed a similar trend, which suggest that failure was closely related with the shifting of buckling mode, as it was also observed in panels with artificial delamination.

5.1.2 Effect of damage characteristics on RCS

Discussion in the previous section seems to suggest that the global buckling (mode I to II) stresses of 2-mm thick panels with large damage are close to, if not equal, the baseline compressive strength, as shown in Figure 5.1.1. This is also likely to be true for 4-mm thick panels with multiple delamination as shown in Figure 5.1.3, the RCSs from individual panels that failed in the mid-section region seem to correlate with respective global buckling (mode I to II) stresses. Therefore, the preconditions that affect global buckling (mode I to II) stress are likely to degrade RCS.

Delamination shape and orientation

In this section the effect of a single delamination on RCS is examined through the variation of delamination shape (circular and elliptical) and orientation of elliptical delamination for both 2-mm [104] and 4-mm thick panels.

It is clear from Figure 5.1.6(a) for 2-mm thick panels (open symbols) that delamination shape did not have a noticeable effect on CSRF when the transverse size of delaminations is small, say, less than 20 mm. However, when the transverse delamination size is large or greater than 40 mm, horizontal elliptical delaminations caused just fractionally less amount of degradation than circular ones, although their

respective areas for the same transverse size are three times less, as shown in Figure 5.1.6(b). However, when comparing the preconditioned panels using the damage area, the decreasing trend is much more clear, for 2-mm thick panels. The damage area threshold for 2-mm thick panels is around 314 mm^2. Beyond this figure, the damage area is significant enough to cause some reduction in the CS.

The variation of the major-axis orientation of elliptical delamination did not have a noticeable effect on CSRF, as shown in Figure 5.1.7(a). For elliptical delaminations oriented vertically, there was a steady reduction in CSRF for transverse damage sizes larger than 10-mm, whereas for the horizontal case, the reduction was present for sizes larger than 20-mm. At the transverse damage size of 20 mm, the delamination area (942 mm2) of the vertical ellipse is actually nine times greater than that of the horizontal one and is three times greater than the circular one. Thus its corresponding CSRF (open triangle symbol) shows moderate degradation as expected. However, the opposite seems true when the orientation of major axis of elliptical delaminations is examined in Figure 5.1.7(b). At the same delamination area, respective CSRFs of elliptical delaminations being either parallel (vertical) or perpendicular (horizontal) to the loading direction exhibit roughly the same amount of degradation, although the transverse size of horizontal elliptical delaminations is three times greater than that of vertical elliptical delaminations.

It was expected that elliptical delaminations with horizontal orientation would have greater stress concentrations at the two ends of major axis associated with greater curvature than the vertical orientation. The results are not conclusive in this respect. Examining Figure 5.1.7(b), no evidence is found about the orientation effect in CSRF reduction. Instead there was one decreasing trend in the reduction of CSRF and it was a function of the damage area only. Consequently, the size of the delamination in the width direction is not a good measure of the amount of damage, since it masks the real extent of the damage area. Additionally, the previously defined damage area threshold of 314 mm^2 for circular delamination (Figure 5.1.6(b)) is also valid for the CSRF reduction for elliptical delamination.

Examining Figure 5.1.6(a-b) for 4-mm thick panels (filled symbols), it can be seen that the shape of a single mid-plane delamination had no effect on the respective CSRFs at any transverse size, apart from the largest size (60-mm) in circular shape, with a 10% reduction. In the other cases, the damage area was not large enough to affect the CSRFs, this finding is supported by the fact that all these panels with single delamination (apart from the 60-mm circular shape) failed prematurely in end-crushing, as it is shown in Chapter 4. The threshold value for the damage area is determined as 1257 mm^2, for a single embedded delamination at the mid-plane in the TTT direction. Beyond this value the CSRF reduces if the damage area increases.

Delamination number and through-the-thickness (TTT) location

In this section the effect of a single and multiple circular delaminations on RCS are examined for 4-mm thick panels. In addition, the effect of the TTT distribution of delaminations on RCS is also studied.

The effect of delamination number is shown in Figures 5.1.8(a-b). It is observed that that the CSRF of panels with multiple delaminations (triangle symbol) is on average 28% less than the CSRF of panels with single delamination (circle symbol), irrespective of delamination size. Therefore, the projected delamination area cannot fully describe the extent of damage. If the internal damage state is known, the cumulative delamination area is a much reliable indicative of the damage extent, as shown in Figure 5.1.8(b). The cumulative area is defined as the sum of areas from individual delaminations. Examining data beyond the single delamination threshold previously found (1256 mm^2), it is clear that there is a decreasing trend in CSRF with respect to cumulative area. Such trend started with the panel with a 60-mm single delamination and continued with the panels with multiple delaminations. There was no damage threshold for panels with multiple delaminations; even delaminations of the smaller diameters (20-mm diameter) were enough to degrade the CSRF.

Shifting from symmetric to asymmetric distribution of delamination did not have any significant effect on the CSRF. For 4-mm thick panels in Figure 5.1.8(a-b), two different TTT distributions of three artificial delaminations were found to have no

anticipated effect on respective CSRFs. As a matter of fact, the panels with three symmetric delaminations seemed to have suffered fractionally more than the panels with three unsymmetric delaminations. This was expected as the thickest sublaminate consisted of 16 plies in the former and of only 10 plies in the latter. The additional contributing factor could be from the extension-shear and extension-bending couplings as all four sublaminates in the symmetric arrangement were asymmetric and unbalanced. All these results clearly confirm that it is the combined effect of projected damage size/area and intensity that dictates RCS.

Local change of geometry characteristics

Figure 5.1.9 summarises the compressive strength of all 4-mm tested panels with local change of geometry. Compressive failure strength of panels with constant dome curvature exhibited a steady decreasing trend with the increment in dome in-plane diameter. This may be attributed to the higher flexural stress at the centre for panels with larger eccentricity (i.e. dome depth). On the other hand, compressive failure strength of panels with constant dome depth had a minimum value for the intermediate dome diameter, while reaching a maximum in both the largest and the smallest defect. This behaviour is clearly due to the superposition of two different trends. The first one is inversely proportional to the dome diameter and it is related to the area of geometrical damage, the more the area of the geometrical damage is, the more reduced is the panel ultimate compressive strength. The second trend increases proportionally with the radius of curvature (i.e. diameter), the larger the radius of curvature is, the closer the panel is to the complete flatness, reducing the ILS along the dome boundary and increasing the load bearing capabilities of the panel.

Types of preconditions

CSRFs of 2-mm thick impact-damaged panels are examined along with that of panels with artificial delamination, both single and multiple, in Figure 5.1.10(a), as impact damages usually contain multiple delaminations. Again the CSRF data of the impact-damaged panels exhibit a very similar trend to that of the single delaminations with the same transverse size or damage area threshold. Moreover, the overall CSRF data band

seems slightly narrower, with the data of the impact-damaged panels appearing as the lower bound of the band. In particular, panels with three identical delaminations suffered slightly more than the impact-damaged ones at either the same transverse size or damage area. One (CR20X3S) was embedded with three 20-mm circular delaminations whereas the other (EH40X3S) had three 40-mm horizontal elliptical delaminations. As in both cases, the four sublaminates were non-balanced and asymmetric so that a Poisson's ratio mismatch of the sublaminates induced by the couplings may have contributed to the degradation, as also discussed in [86]. CSRFs of the impact-damaged panels were reduced by as much as 40%. The similar result of 16-ply laminates with seven circular artificial delaminations was reported in [90]. In addition, these results also show that the delamination number is as important as the delamination size when the CSRF of panel CR20X3S came out lower than that of panel CR60 with a single 60-mm delamination.

For 4-mm thick panels, the CSRFs of panels with impact-induced (or quasi-statically-induced) damage is examined along multiple artificial delaminations in an asymmetric TTT arrangement, local change of geometry in the means of a circular dome (constant curvature) and panels with open hole in Figure 5.1.10(b). Only these preconditions were considered because the damage produced by impact or quasi-static loading is characterised by multiple delaminations, asymmetrically distributed in the TTT direction, as seen in Chapter 3. Additionally in Chapter 4 it was observed that the compressive behaviour of thick impacted panels was a combination of characteristics from panels with multiple delaminations in an asymmetric TTT arrangement and panels with local change of geometry.

A reduction of the CSRFs in 4-mm thick panels with different preconditions is related to the compressive failure mode and the severity of the effect on the compressive response. Two trends in CSRF vs. damage area were observed from Figure 5.1.10(b). The first one offers a higher bound of CSRF and corresponds to panels with artificial delamination. The second trend exhibited a sharper initial reduction, offering a lower bound of CSRF and it corresponds to panels with open holes. These two trends can be explained based on the difference in compressive failure. On the one hand, panels with artificial delaminations large enough to cause a reduction of CS had a characteristic

compressive failure linked with the shifting in buckling mode-I to mode-II, that follows a similar decreasing trend as explained in Chapter 4. On the other hand, the compressive failure for open holes was linked with stress redistribution due to the reduction in cross sectional area.

The trends for panels with local change of geometry and impact damage were a combination of the two trends described above. On the one hand, small domes caused a reduction in the CS similar to multiple artificial delaminations. However for the larger sizes of domes (i.e. large eccentricity) the central region of the panels no longer carried a substantial amount of compressive load (as explained in Chapter 4), and the panels tended to behave more like a panel with open holes as shown in Figures 5.1.9 and 5.1.10(b). On the other hand, panels with impact-induced damage featured characteristics from artificially delaminated panels and panels with local change of geometry. At low IKEs, with small delamination area, the shifting in buckling mode-I to mode-II precipitated failure. However, the effect of geometric change due to the impact event became critical for the larger IKEs, thus the panel failure was increasingly triggered by stress concentration. This probably justifies why the panel impacted at the largest IKE did not fail at the mid-section but in end-crushing (panel 4I2.52).

5.1.3   Effect of panel thickness on RCS

In a qualitative sense, doubling the panel thickness seems to increase flexural rigidity and buckling stress by eight times. This contributed to a two major effects. One was that the difference in the mechanisms that govern damage generation during transverse loading. For thin panels, damage was dominated by membrane effects and it mainly consisted of a localised shear cone around the impact site. For thick panels, the damage was more dominated by ILSS, consisting of a main large delamination near the mid-section alongside a less dominant shear cone. The second effect was the significant difference in the compressive behaviour of individual panels, as seen in Chapter 4, to such an extent that the character of the response of 4-mm thick panels was no longer the same than 2-mm thick panels. That is, the 4-mm thick preconditioned panels simply failed with end crushing when contained either a single delamination of any size or shape, or three circular delaminations of 20-mm diameter in any TTT arrangement. In

addition, with the increase of panel thickness, the increased presence of transverse shear deformations could result in added flexibility, which may be substantial.

The thickness effect on the post-impact compressive response is summarised in Figure 5.1.5(b) by the local buckling (mode-I), global buckling (mode I to II) and failure loads. The stress was normalised using the compressive strength of the respective intact panel. Since delamination area was used to show the extent of damage, 2-mm thick panel data were grouped close to the y-axis, having smaller damage areas than 4-mm thick panels. The trends in local buckling (mode-I), global buckling (mode I to II) and failure stress of 4-mm thick panels are extrapolations of the trends from 2-mm thick panels. Additionally failure modes were similar for all the impacted panels, all of them failed at the mid-plane during the postbuckling stage.

Figure 5.1.11 shows the combined results of 2-mm and 4-mm thick panels, in which normalised data for each panel thickness are indicated by one symbol without distinguishing types of the preconditions. It is interesting to note that the 2-mm thick panel data seem to appear in a small cluster whereas the 4-mm thick panel data spread out quite a bit at a particular transverse damage size or damage area as expected. This is because the intensity of delaminations has a much greater effect on 4-mm thick panels than on 2-mm thick panels. The results in terms of damage area seem to be biased against 2-mm thick panels when damage area is relatively small. However, when a damage area is relatively large, both 2-mm and 4-mm thick panels suffered about 40% reduction in CSRF, providing that the damages were contained within respective panels. Findings in the literatures in [17, 49, 79, 80, 126] are not completely consistent but more CAI strength data seem to favour thicker panels. Nevertheless, it must be remembered that the baseline compressive strength of the thicker panels can be underestimated due to premature crushing failure at one of the loaded ends, as in the present investigation. Consequently, CSRF of the thicker panels may well be overestimated.

5.1.4 Effects of impact and quasi-static tests parameters on RCS

The main impact variables such as IKE, absorbed energy (AE), impactor-nose shape and maximum transverse force have a direct correlation with the extent of damage, resulting in a reduction of CS. This section studies this relationship for 2-mm and 4-mm thick panels.

Impact energy level

The top frame of Figure 5.1.12 shows the CSRF diagram in terms of delamination area for 2-mm and 4-mm thick panels. This figure shows that the behaviour of 2-mm and 4-mm thick panels with impact-induced damage may be considered as a single trend. However this diagram masks the difference in the AE vs. damage area trends between thick and thin panels, as observed in the central frame of Figure 5.1.12. Such difference lies on the fact that flexural stiffness determines the damage size along with the IKE level, as explained earlier. The relationship between damage area and absorbed energy is initially linear for both 2-mm and 4-mm thick panels, as discussed in Chapter 3. However, beyond 1.34 J/mm (correspondent to panel 2I0.625m, IKE 9.9J) the damage area does not seem to show the same increase rate with IKE for 2-mm thick panels, whereas for 4-mm thick panels the damage area carries on with the increasing trend. Beyond this energy level, 2-mm thick panels suffered fibre breakage (Chapter 3) and increased the proportion of IKE that was absorbed. This is reflected on the CSRF diagram when it is plotted in terms of the normalized absorbed energy, in the side frame of Figure 5.1.12. The initial reduction in CS for both sets of specimens, 2-mm and 4-mm thick panels, was similar, but beyond the mentioned energy level (1.34 J/mm) the CS did not reduce further than 35% for 2-mm thick panels. On the other hand, 4-mm thick panels carried on with the CS reducing trend up to 51% corresponding to an energy level of 2.75 J/mm (panel 4I1.5m, IKE 21.1J).

The relationship between IKE and AE is highly dependent on the panel flexural rigidity as shown in Chapter 3. For 2-mm thick panels, the initial linear trend of AE was only 21% of the IKE, whereas for 4-mm thick panels the proportion was 55%. Therefore, when IKE is used as a measure of damage extent, the thickness should be specified as

well as the proportion of IKE that goes into AE. Figure 5.1.13 shows the CSRF diagram in terms of the normalized IKE for both 2-mm and 4-mm thick panels. The top of the diagram is the same than in Figure 5.1.12. However, the central frame of Figure 5.1.13 uses the normalised IKE instead of the AE to show the linearity of IKE with the delamination area. The thicker panels contain larger delamination areas for the same normalised IKE level than the thinner panels, resulting in a lower CSRF as shown in the side frame of Figure 5.1.13.

Loading rate and impactor-nose shape

This section studies the effect of the applied transverse force and the effect of the impactor nose shape on CSRF using the CS results from panels with damage induced either by impact or by quasi-static transverse loading and using either hemispherical or flat-ended impactor nose shape.

Impact and quasi-static tests results could be considered as equivalent due to the similarity in damage mechanisms and in the deflection-load response from the panel, as shown in Chapter 3. Additionally the amount, location and type of damage that occurred in impact and quasi-static loading tests correlated well with applied force. When CSRF is plotted in terms of the transverse force, the difference between the two types of loading (impact and quasi-static) is negligible as shown in Figure 5.1.14(a), which presents the CSRF results in terms of maximum transverse force. The applied transverse force measured for impact panels has a decreasing trend that also covers the data of the quasi-static loading force when the hemispherical-ended indenter was used.

The impactor nose shape determines contact pressure distribution and the onset of damage, as discussed in Chapters 1 and 3. Thus the equivalence between impact and quasi-static load induced damage is valid providing that a similar indenter is used in both tests. If the hemispherical-ended indenter is replaced by a flat one, the force relates differently with the damage content and consequently with the CSRF. The CSRF trends for flat and hemispherical indenters are shown with dashed lines in Figure 5.1.14(a).

Figure 5.1.14(b) contains the CSRF for both quasi-static and impact damaged panels in terms of delamination area. The effect of the impactor-nose shape is evident; there are two different decreasing trends of CSRF when increasing the damage size. The first trend corresponds to the panels loaded with the flat-ended indenter and it has a less reduction with a 40% for the largest delamination. The second trend includes the damages induced by a hemispherical-ended indenter both in quasi-static and impact loadings. A larger reduction in CSRF of about 60% is exhibited by the largest delamination area. The change of local curvature of the panel around the hemispherical indenter seemed to have more dramatic effect on the CSRF than the flat indenter, at similar delamination areas.

5.2 Different metrics for damage tolerance assessment

The damage tolerance is determined by the degree of retention of mechanical properties, such as strength and ultimate strain. This section investigates the relationships between the different metrics used to express the damage tolerance, based on the compression of intact and preconditioned panels (Chapter 4) in terms of the extent of damage.

5.2.1 Damage measures

The extent of damage can be represented by the damage area, IKE and depth of surface dent. A state of damage represented by one of these parameters is related to a reduction of CS as discussed in the firs part of this chapter. The reason that all three seem necessary is that neither of the first two can accurately represent the damage state. In the case of the projected delamination area, it does not quantify the effect of number and TTT distribution of internal delaminations, neither individual shapes nor delamination orientation. Nevertheless it is costly and time consuming to get information about the internal delamination distribution, so the projected delamination size is often the only measure of damage available. The additional advantage of area is that other preconditions such as artificial embedded delamination and open hole can be easily represented in an accurate way.

In the case of IKE, different strength retention factors can be linked with the same energy level, depending on the mass/incident velocity combinations. Also the panel flexural rigidity determines the mechanism governing damage generation during transverse loading, affecting the proportion of IKE that is absorbed in addition to the damage area (Chapter 3). This is reflected on the variation of CS reduction for similar IKE levels on panels with different rigidities, i.e. different panel dimensions and composite systems (Chapter 4).

In the case of dent depth, it offers an immediate tool for damage assessment in particular for preventive maintenance purposes. However, the dent depth does not necessarily have a relationship with the delamination area, as shown in Chapter 1. Additionally, the CS reduction due to the effect of surface topology is the consequence of different mechanisms of compressive failure than in the case of internal delaminations (Chapter 4). Therefore the use of dent depth to measure impact damage is limited, in particular when the major damage is predominantly internal and invisible.

5.2.2 Tolerance assessment metrics

In conventional damage tolerance assessment, mainly RCS and residual compressive strain are assessed in terms of delamination area, IKE, AE or force. Other material properties such as in-plane stiffness could also be evaluated, but it is not always feasible to use it due to differences in compressive failure mode. This study includes the ratio of initial threshold force to maximum transverse force as an additional indicator of the panel post-impact load bearing capabilities [13, 127].

Compressive strength/strain retention factor

Figures 5.2.1 and 5.2.2 show the variation of strength and strain retention factors in terms of damage area for 2-mm and 4-mm thick panels, respectively. The strain was determined in two different ways. One used the mean strain reading from the gauge at the far-field location and the other used the strain derived from the axial displacement reading (measured by a LVDT) of the loading moving head. After comparing the strain with the strength data, it was observed that if damage does not affect the far-field

location (i.e. the gauge is truly in the far-field) then the strain reading is a precise measure of the strength reduction. On the other hand, axial strain retention factor is not always a good indicator of the damage tolerance, in particular when the compressive failure is in premature end-crushing. Such type of failure indicates that the damage did not interact with the compressive load.

Retention factors derived both from far-field and axial strains are shown in Figure 5.2.1(a) for 2-mm thick panels with embedded delamination. Far-field strain retention factor (filled symbols) followed the same trend of the strength retention factor (open symbols) for both types of delamination, circular and elliptical. Strain retention factor data are within 13% and 8% of the strength retention factor for circular and elliptical delaminations respectively. However if the axial strain from the displacement (partially filled symbols) is used instead of the far-field strain, the strength retention factor trend is either overestimated by up to 23% for circular delamination or underestimated by up to 14% (elliptical delamination). It seems that far-field strain is more precise than axial strain for estimating the retention factor.

In the case of 2-mm thick panels with impact damage in Figure 5.2.1(b), the trend of the residual far-field strain was much higher than the residual strength data, up to 41% overestimated. Although the material damage (internal delamination and fibre breakage) did not reach the far-field location, it suggests that the far-field stiffness was reduced by the damage. On the other hand, if the axial strain is used instead of the far-field strain, the retention factor is underestimated but by a closer value, up to 27% of the strength retention factor. The difference between the compressive strain retention factor and CSRF is due to the higher sensitivity of strain towards the presence of local change of geometry. This also explains the marked difference between axial and far-field strain retention factors. The effect of local change of curvature was reflected only on the axial strain because SGs at locations away from the impact site were unaffected, as it was the case for the far-field strain.

Figure 5.2.1(c) shows a comparison of all the preconditioned 2-mm thick panels in terms of the axial strain retention factor. There is a clear division between data of impact damage and artificial delamination. Impact damage in terms of strain retention

factor seems to be much more detrimental than single artificial delaminations when compared to CSRF. Thus impact-damage data provide a lower bound whereas single artificial-delamination data give an upper bound. Discussion of both compression tolerance metrics can be found in [128, 129]. The effects of damage characteristics on RCS can be presented by compressive strain retention factor in the case of 2-mm thick panels, because all the 2-mm thick panels failed in the mid-section region. For the same reasoning, axial strains are used for only few 4-mm thick panels as a large number of them failed in end crushing so that validity of axial strain measurements is deemed to be questionable. Similar difficulty associated with using far-field strains was reported in [17, 28], although no information on the tested panel failure modes was provided.

Figures 5.2.2(a-d) show the variation of strength and strain retention factors for 4-mm thick panels in terms of damage area. The majority of the panels failed at the mid-section. Retention factor of panels with multiple embedded delaminations in an asymmetric distribution is shown in Figure 5.2.2(a). Similar to 2-mm thick panels with circular delamination, comparing strength with strain data, the retention factor was underestimated by the far-field strain up to 28% and overestimated by the axial strain up to 16%.

Figure 5.2.2 (b-c) shows the retention factor derived from axial strain, far-field strain and strength for panels containing local change of curvature (constant curvature approach) and open hole. On the one hand, the axial strain retention factor followed the trend of the strength data remarkably well for the panel with local change of geometry and overestimated the strength data in the case of panels with open holes without any apparent reason found to explain such behaviour. On the other hand, the far-field strain retention factor was only close to the strength data for small damage areas. For the larger areas, the concept of retention factor was not applicable any longer since the location chosen for far-field was not truly far-field, being directly affected by the stress concentration around the region with damage. For panels with local change of geometry, the apparent far-field strain retention factor was 61% lower than the correspondent strength data. For panels with open hole, the effect of damage in the far-field location was so dramatic that the apparent strain retention factor changed sign for the largest hole diameter, being 119% lower than the strength data.

Strain retention factor of 4-mm thick panels with impact damage did not correlate well with strength data, as shown in Figure 5.2.2(d). On the one hand, the far-field strain retention factor underestimates the strength retention factor. The far-field strain was affected by two factors. One was that the influence of stress redistribution around damage, particularly significant for large delaminations with local change of curvature (i.e. high IKEs). The other factor was that global buckling (mode-II) developed as a result of the interaction between compressive loading and internal delaminations alongside topology change. Since this was not an issue for the far-field strain of the intact panels, the strain retention factor determined in this way was affected significantly. On the other hand, the axial strain and strength retention factors were close only for two panels (delamination area of 1697 and 7854 mm^2). In the other two cases (914 and 5468 mm^2) the difference between strength and axial strain retention factor was considerable, 18% and 29% for the smaller and the larger damage area respectively. No justification was found for such behaviour, apart from data scatter.

Initial threshold to maximum force ratio

In a recent study [13, 127], an observation of experimental results indicated that the RCS of a panel with damage induced by transverse loading is proportional to the amount in which the transverse peak load has exceeded the initial threshold force for the onset of delamination. Initially, the damage resistance of a transversely loaded is determined by the onset of delamination easily identifiable on a force-history or force-deflection plot. After this load level the amount of induced damage seemed to depend on the transverse peak load reached. Guided by the same idea, the ratio of peak transverse loads to the initial threshold force for delamination onset was obtained from force-history and force-deflection curves in Chapter 3 and compared with the CSRF in Figures 5.2.3(a-b) for 4-mm thick panels with impact and quasi-static indentation damage.

In the case of panels with impact damage, the trends of force ratio and CSRF in terms of damage area were remarkably close, as seen in Figure 5.2.3(a). The force ratios and the CSRFs were very close, in particular for damage areas larger than 913 mm^2. In the case

of quasi-static loading in Figure 5.2.3(b), the estimation of CSRF done by the force ratio was poor for partially loaded panels (until the onset of delamination) and slightly better for panels fully loaded (until transverse failure). For the former, the value of the force ratio at the onset of delamination was obviously unity, but the delamination area was 206 and 4734 mm^2 for hemispherical and flat-ended respectively. As a result, the RCS was reduced, but the effect was not picked up by the force ratio. For the latter, the force ratio underestimated the CSRF. This was attributed to an increase in peak load not reflected in the reduction of CS. The fact that the delamination area had reached the panel boundaries and the fact that the excessive friction forces induced at the stage of laminate perforation become significant at substantially large deflections support this assumption.

5.3 Concluding remarks

The preconditions that approximated better the CSRF of panels with impact damage were artificial delamination and hemispherical-shaped domes. 4-mm thick panels with multiple (×3) delaminations of large size had a reduction of CS of about 40%. Panels with localised curvature change had a reduction of CS of 55%. These two results can be compared to the final reduction in CS due to impact damage of about 50%.

The effect of damage area on the RCS is cumulative, particularly for 4-mm thick panels. The difference between single and multiple (×3) delaminations of the same projected area was around 30%. Therefore it is necessary to assess the TTT size distribution of internal delaminations when feasible. Similarly, this difference in 2-mm thick panels with single and multiple delaminations was around 25%.

The difference between CSRF and compressive strain retention factors was significant, due to the additional effect of local curvature. A difference of up to 60% between CSRF and compressive strain retention factors was present in 4-mm thick panels with impact damage. Similarly the difference in compressive strain retention factor between flat panels with artificial delaminations and panels with impact damage was around 40%.
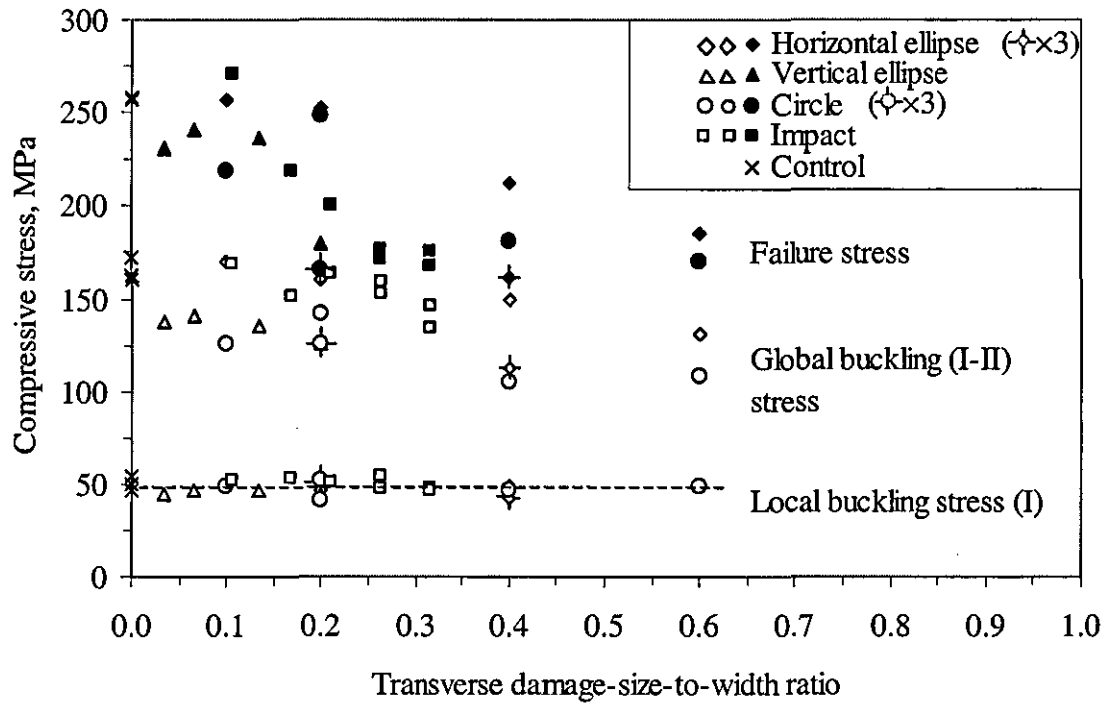
(a)
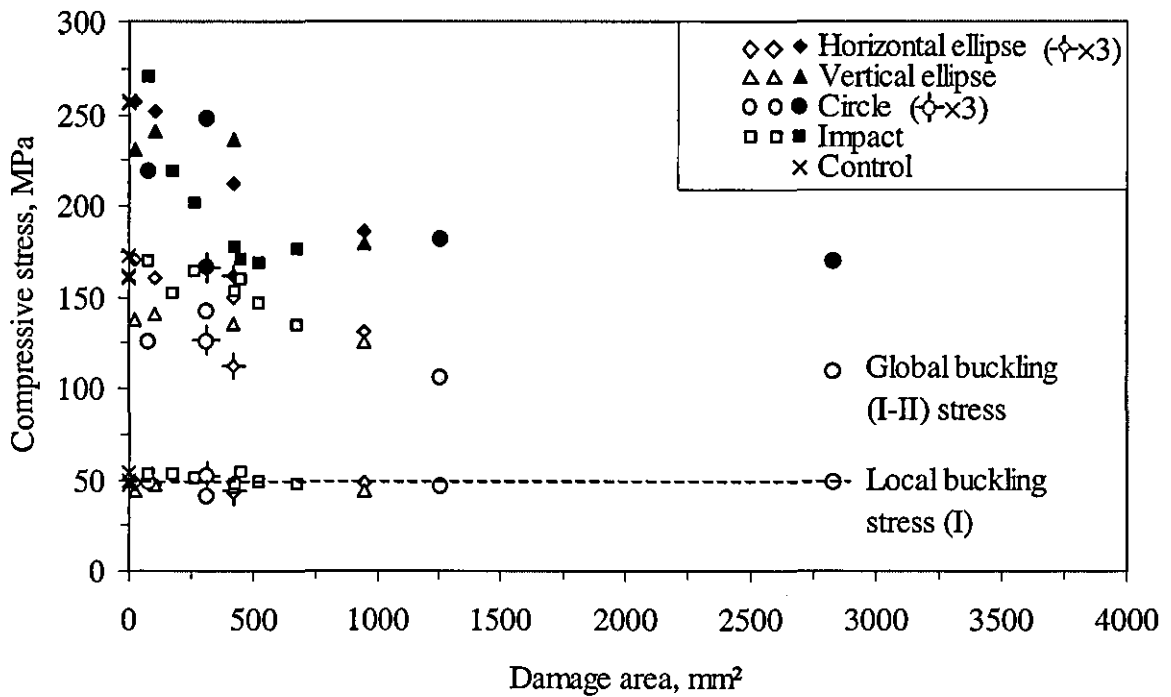
(b)

Figure 5.1.1 Local buckling (mode I), global buckling (mode I to II) and failure stresses in terms of (a) transverse damage-size-to-width ratio and (b) damage area for 2-mm thick carbon/epoxy panels [104]
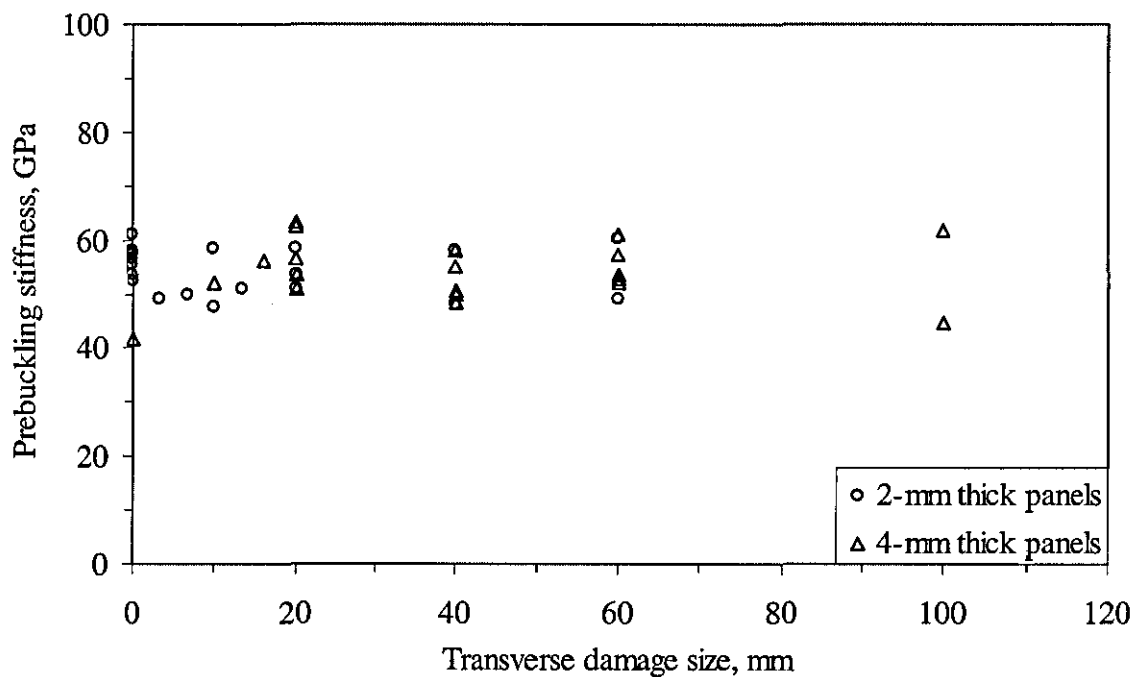
Figure 5.1.2 Variation of in-plane compression stiffness in terms of transverse damage size for 2-mm [104] and 4-mm thick carbon/epoxy panels

(a)

235

(b)
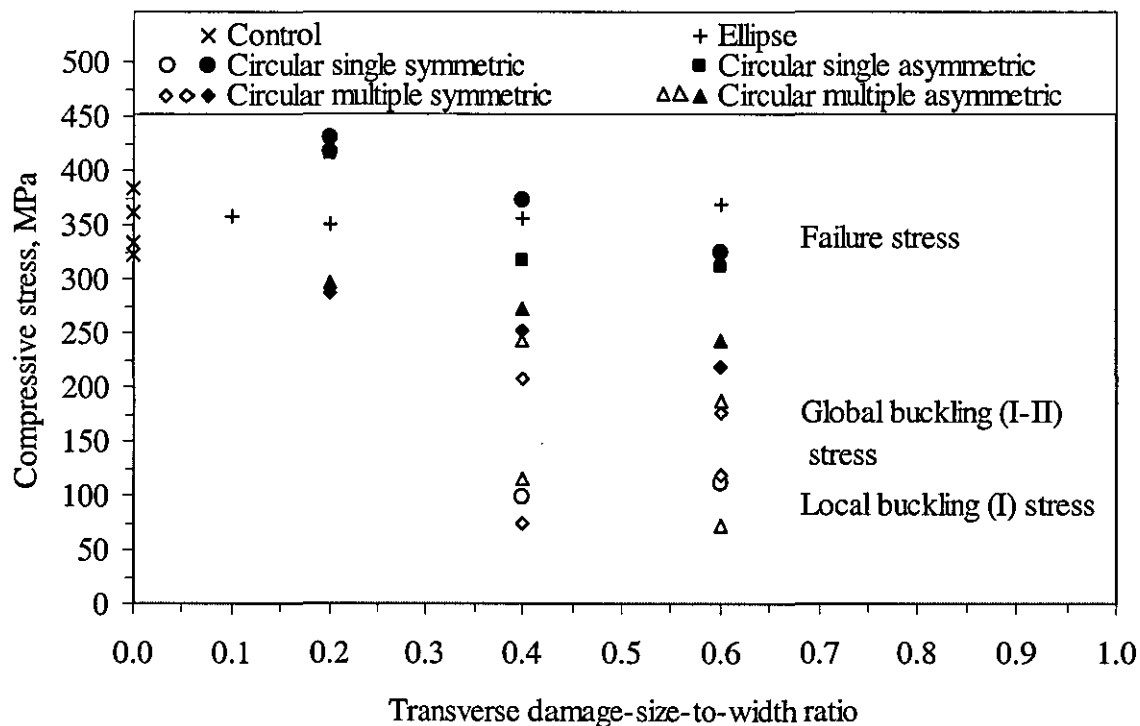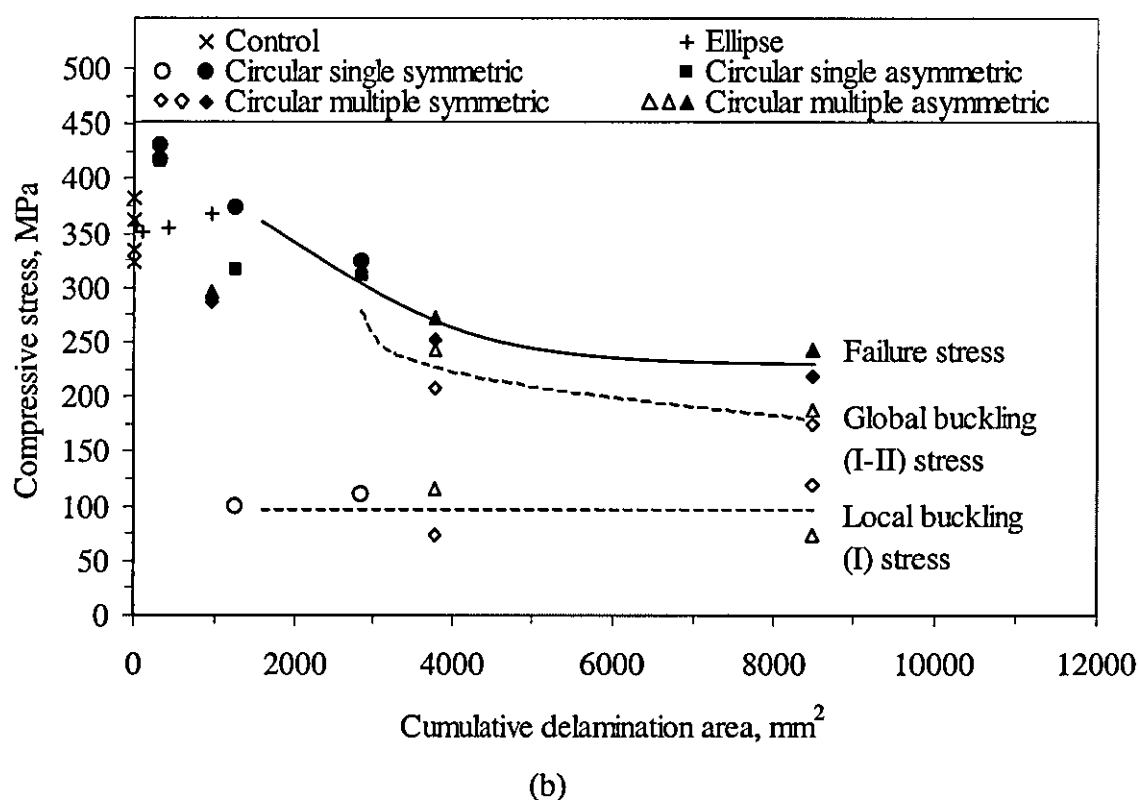
Figure 5.1.3 Local buckling (mode-I), global buckling (mode I to II) and failure stresses in terms of (a) transverse damage-size-to-width ratio and (b) cumulative delamination area for 4-mm thick carbon/epoxy panels with artificial embedded delamination
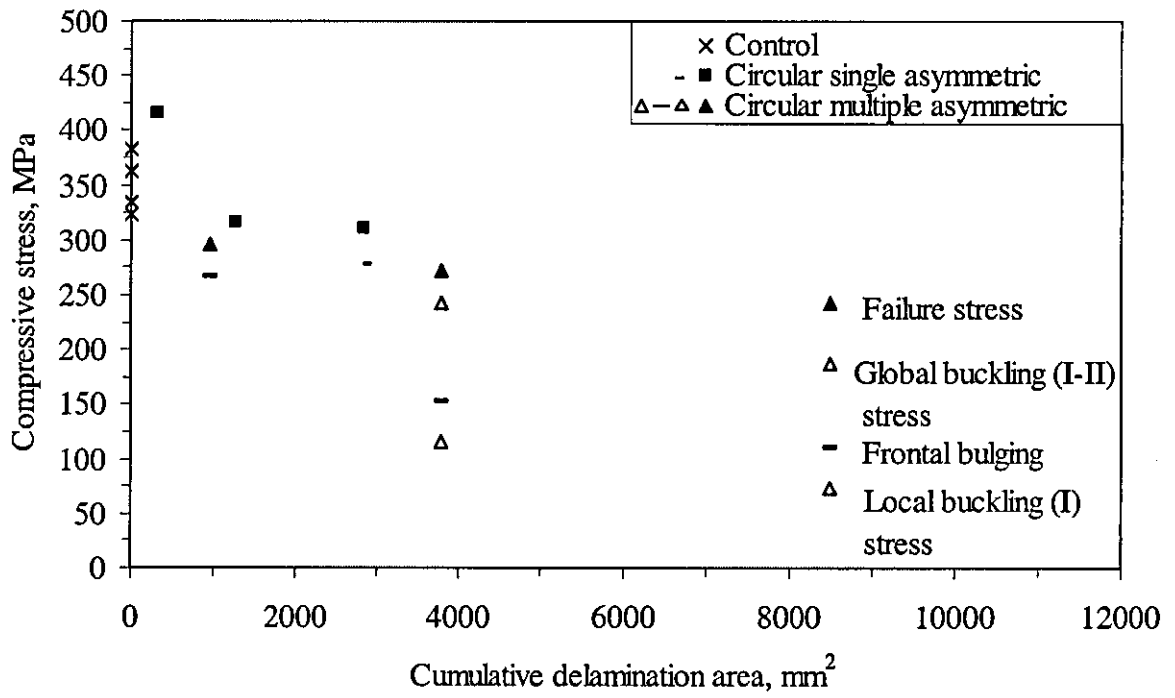
Figure 5.1.4 Local buckling (mode-I), frontal bulging, global buckling (mode I to II) and failure stresses in terms of cumulative delamination area for 4-mm thick panels with asymmetric delamination distribution through-the-thickness

(a)

237

(b)
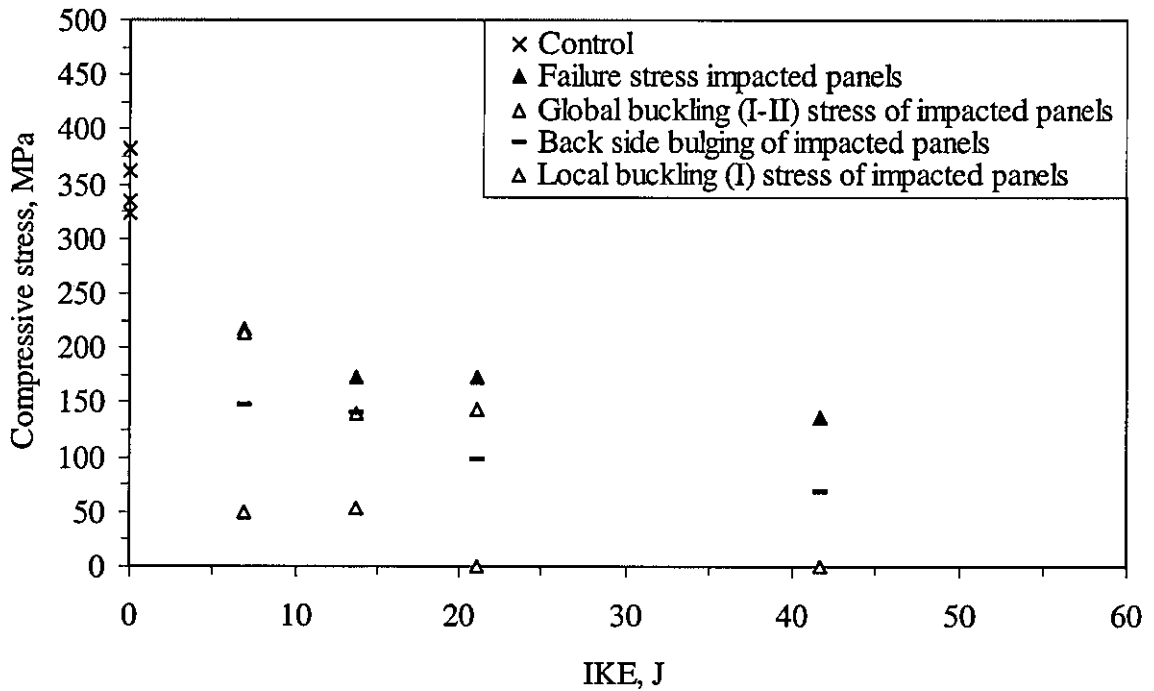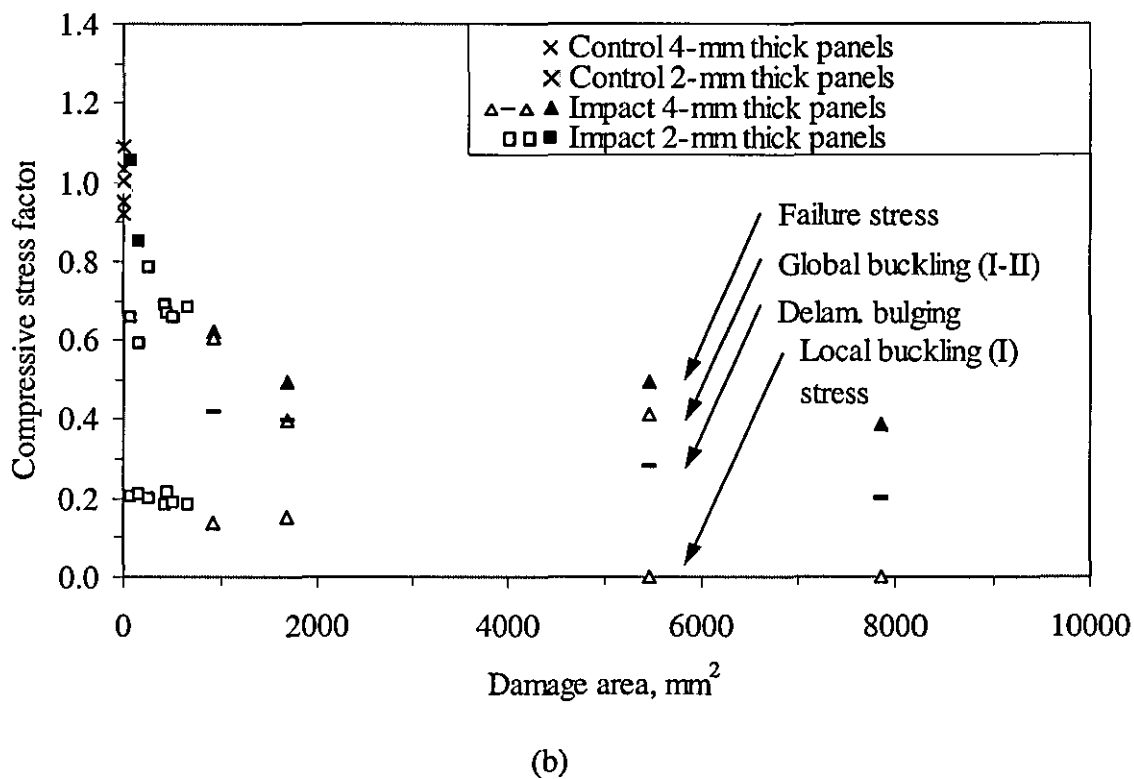
Figure 5.1.5 Local buckling (mode I), delamination bulging, global buckling (mode I to II) and failure stresses in terms of (a) IKE for 4-mm thick carbon/epoxy panels with damage from impact loading and (b) damage area for both 2-mm [104] and 4-mm thick panels

(a)

(b)
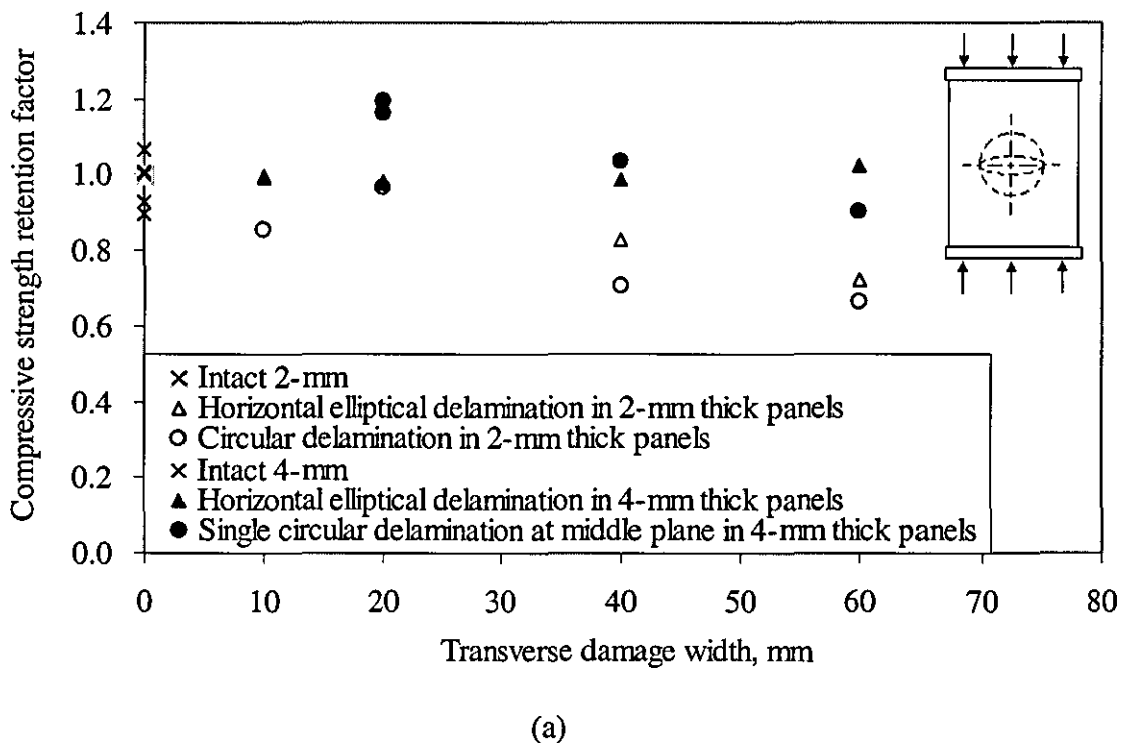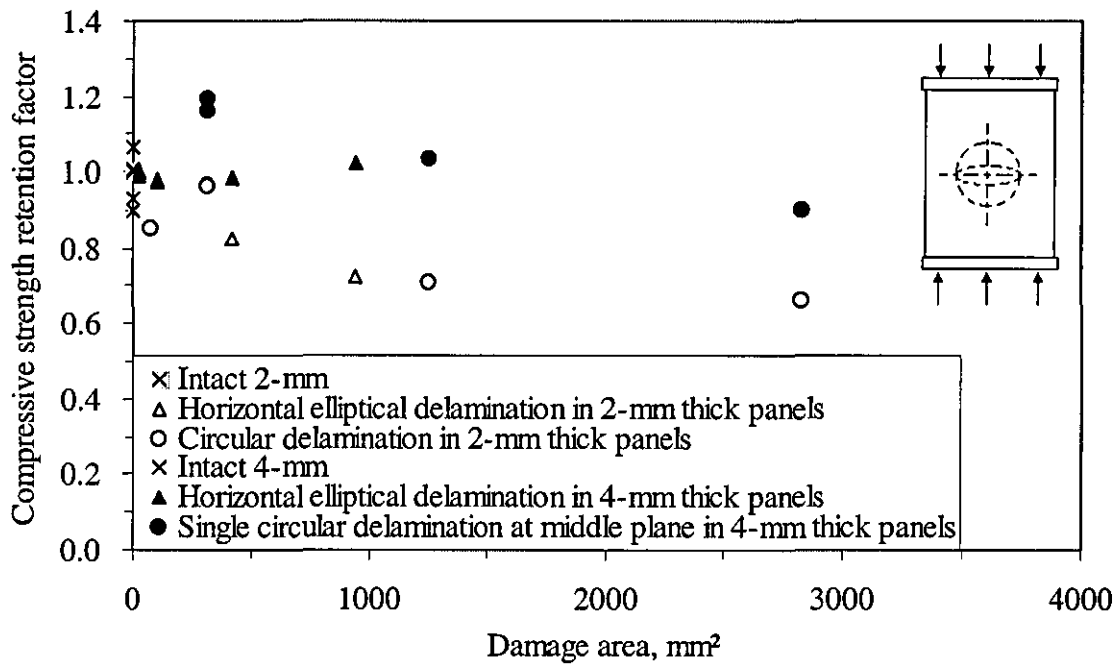
Figure 5.1.6 Variation of compressive strength retention factor with (a) transverse damage size and (b) damage area for 2-mm [104] and 4-mm thick carbon/epoxy panels containing a single embedded delamination

(a)
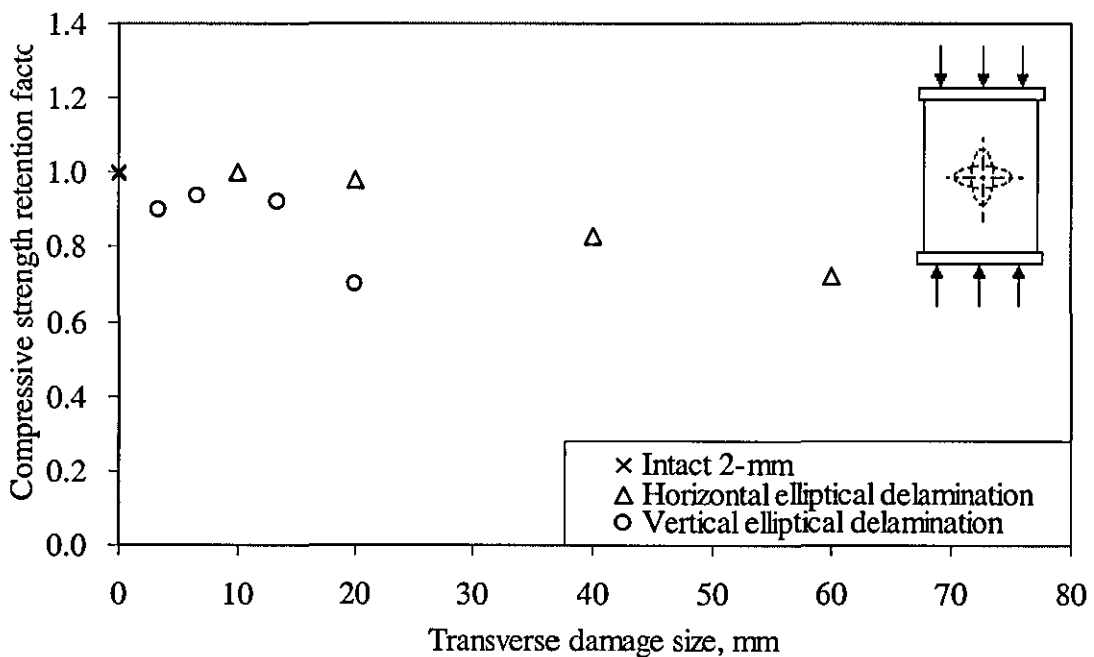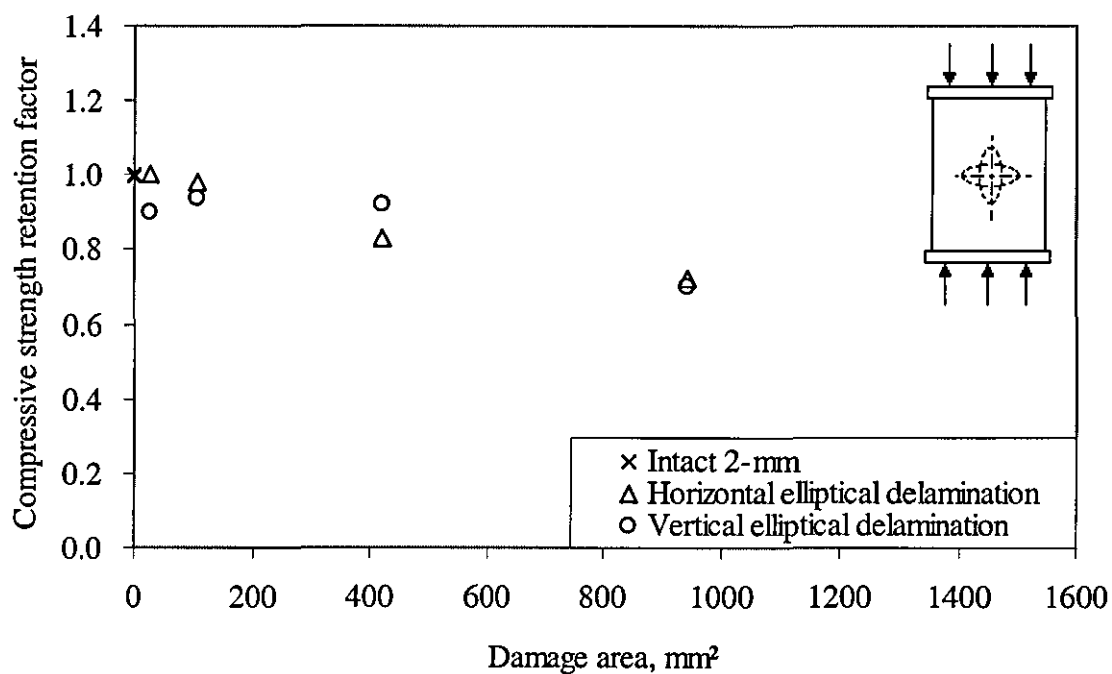
(b)

Figure 5.1.7 Variation of compressive strength retention factor with (a) transverse damage size and (b) damage area for 2-mm thick carbon/epoxy panels containing a single elliptical (aspect ratio 3:1) embedded delamination [104]
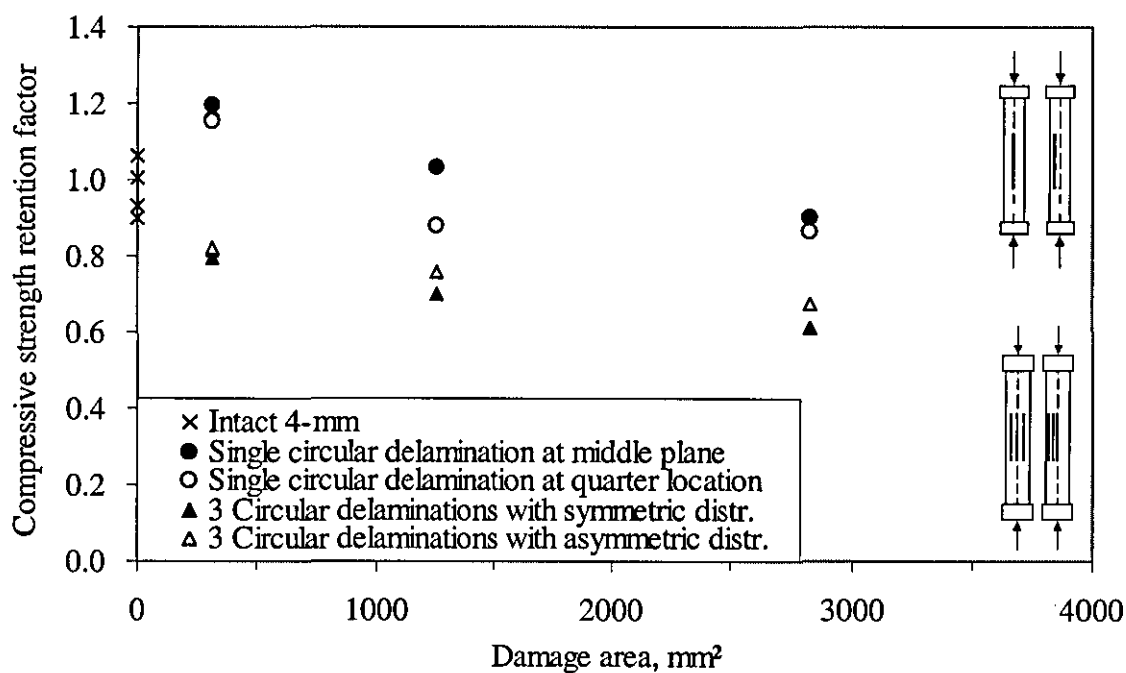
(a)
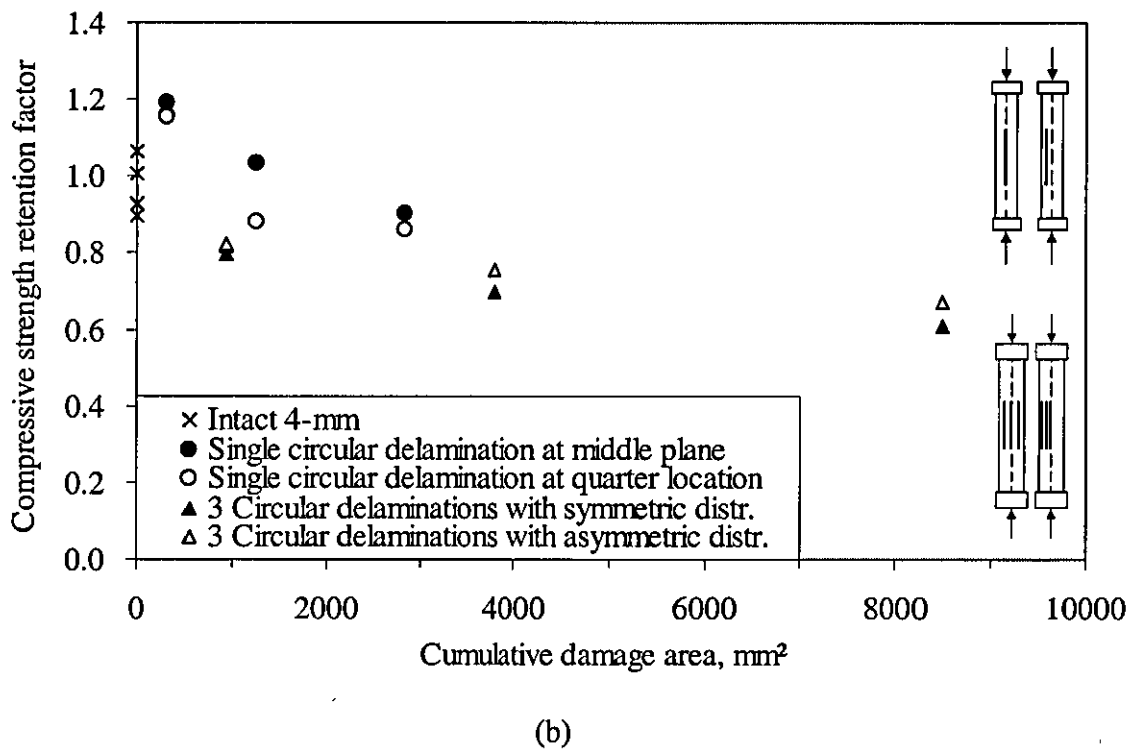
Figure 5.1.8 Variation of compressive strength retention factor with (a) damage area and (b) cumulative damage area for 4-mm thick carbon/epoxy panels containing a circular single or multiple (x3) embedded delamination
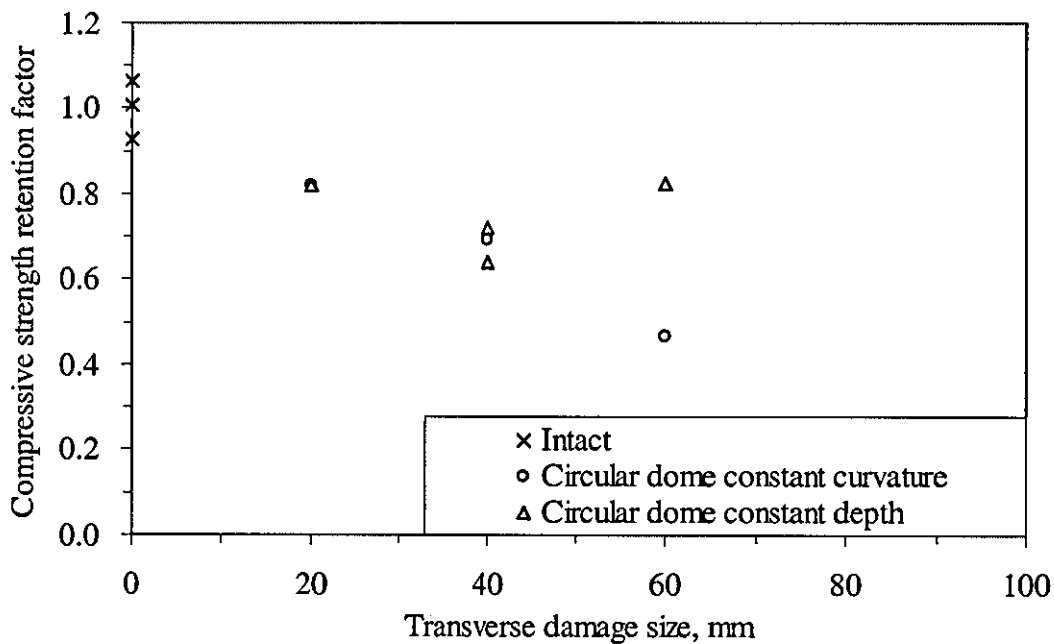
Figure 5.1.9 Compressive strength retention factor for 4-mm thick panels containing local change of geometry

241
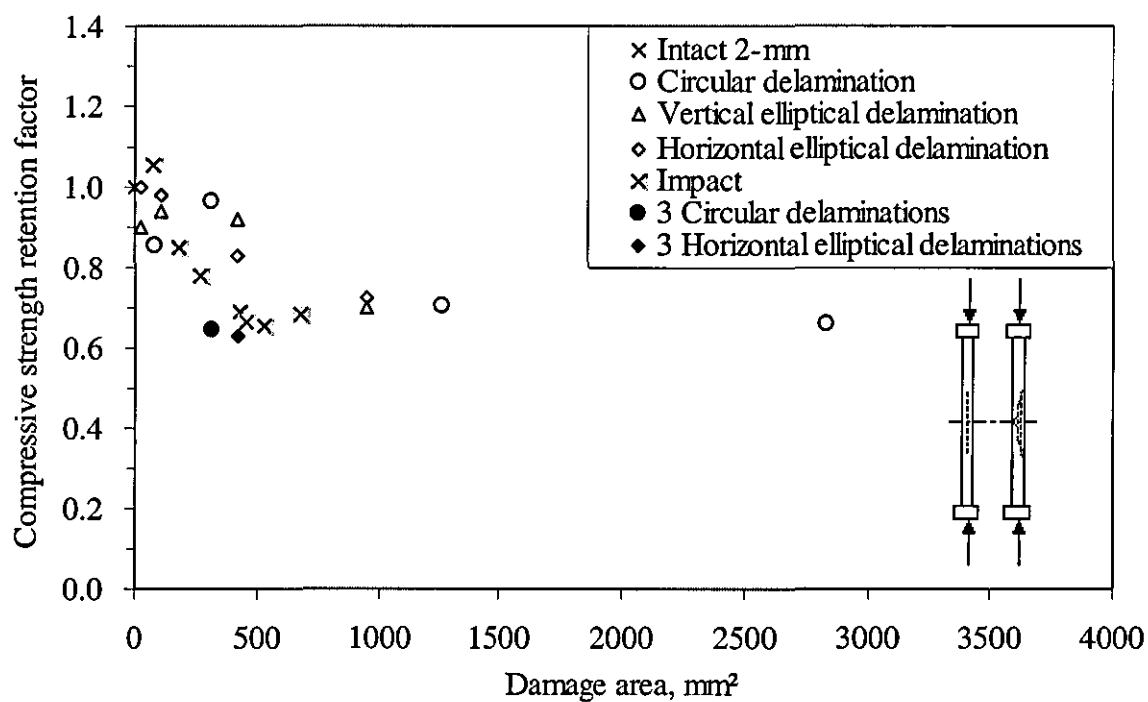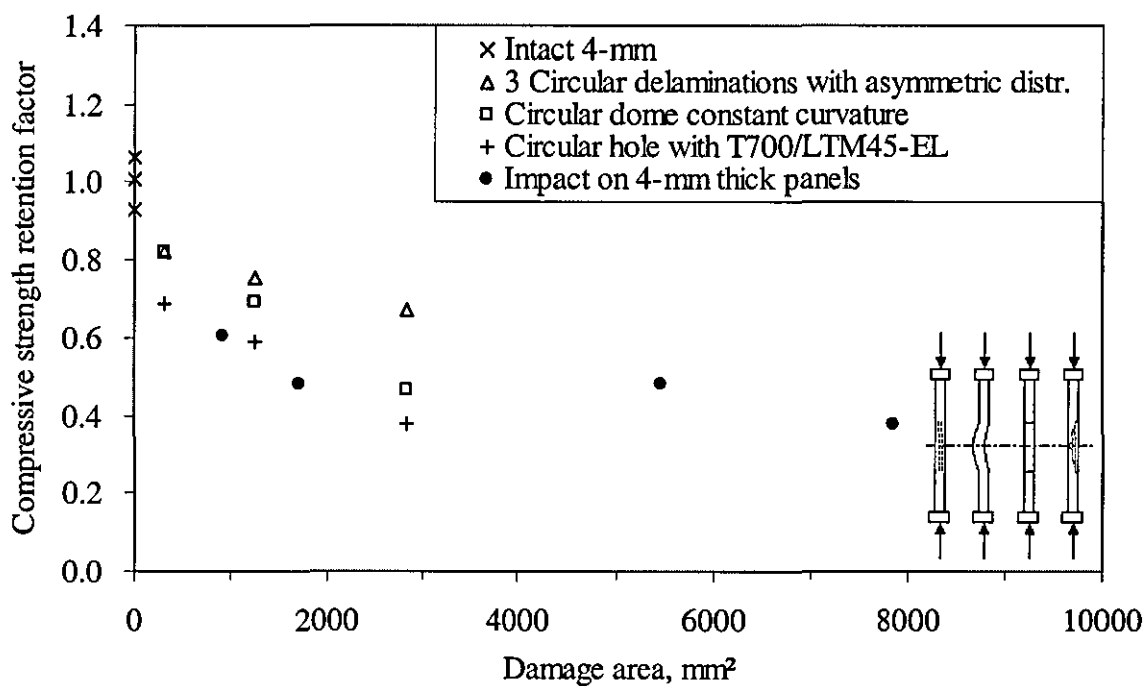
Figure 5.1.10 Variation of compressive strength retention factor with damage area for
(a) 2-mm thick panels [104] and (b) 4-mm thick carbon/epoxy panels containing
different types of damage
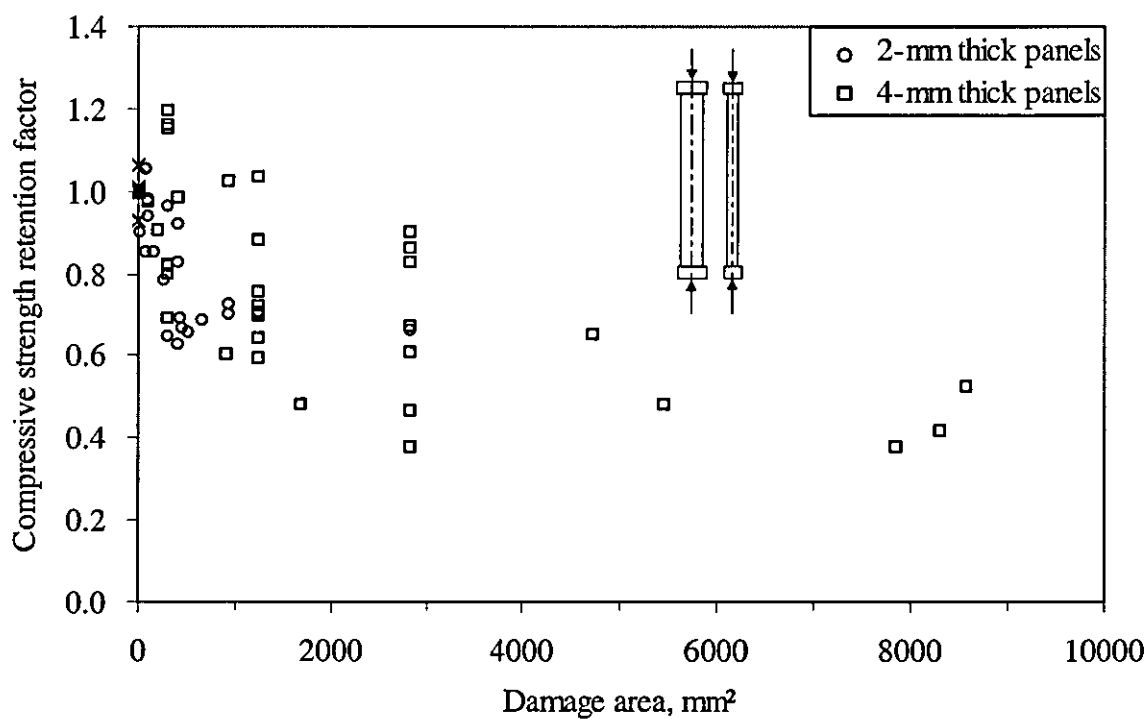
Figure 5.1.11 Variation of compressive strength retention factor with damage area for
2-mm thick panels [104] and 4-mm thick carbon/epoxy panels containing different
types of damage
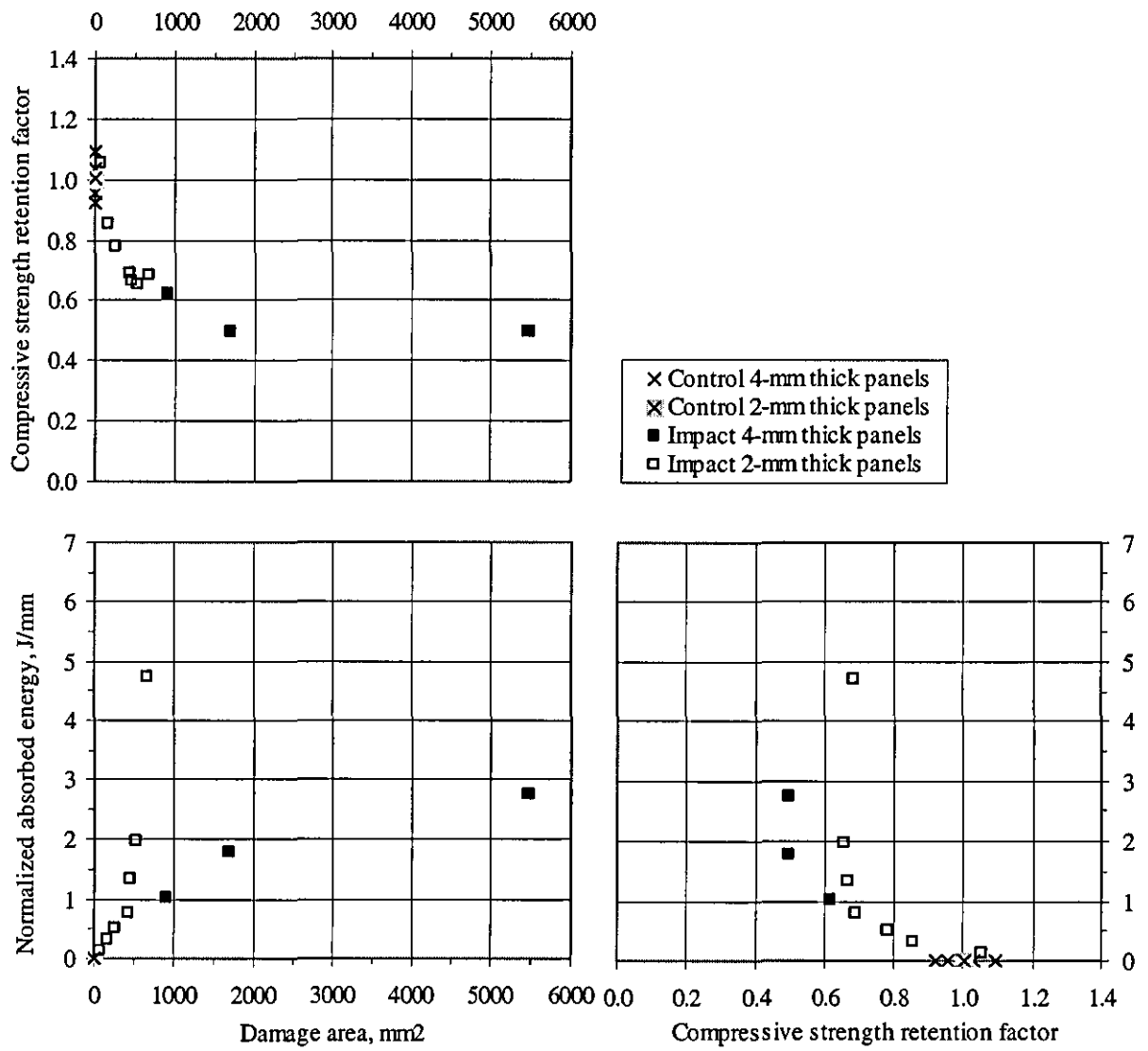
Figure 5.1.12 Variation of strength retention factor in terms of damage area and normalized absorbed energy (AE) for 2-mm [104] and 4-mm thick carbon/epoxy panels containing impact damage

Figure 5.1.13 Variation of strength retention factor in terms of damage area and normalized incident kinetic energy (IKE) for 2-mm [104] and 4-mm thick carbon/epoxy panels containing impact damage
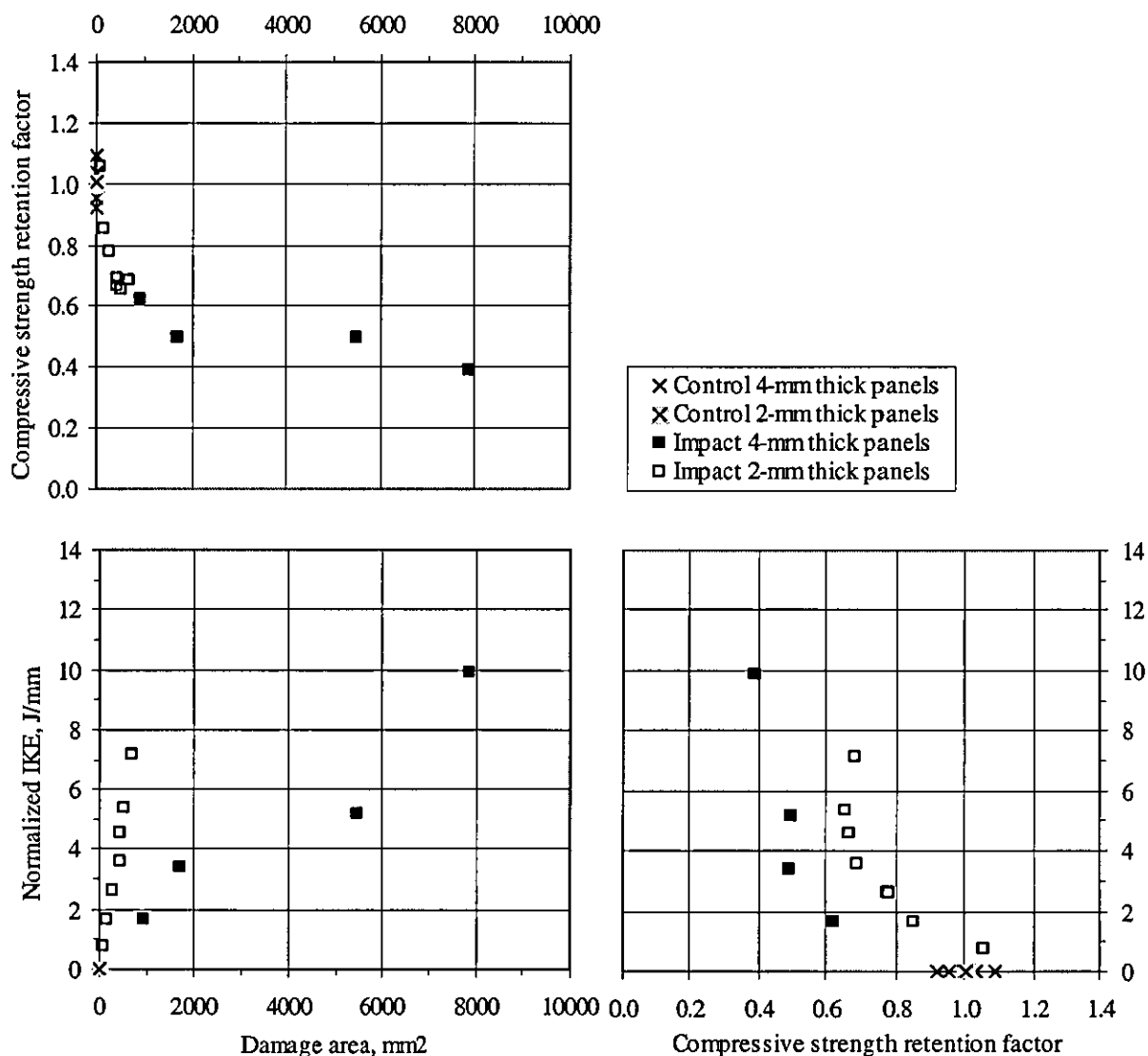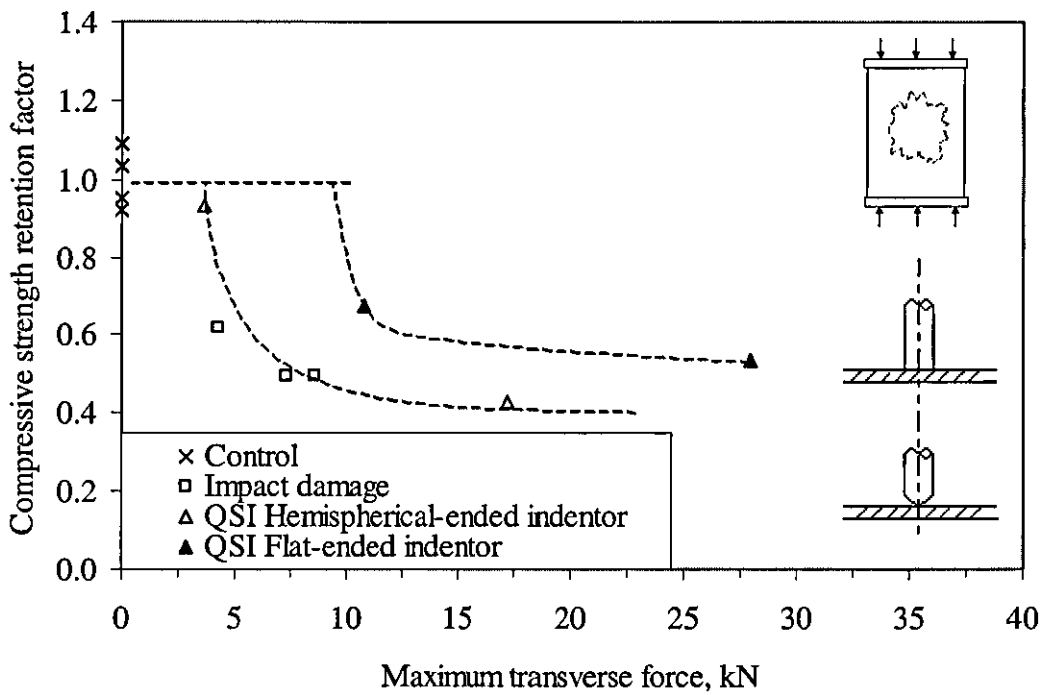
(a)
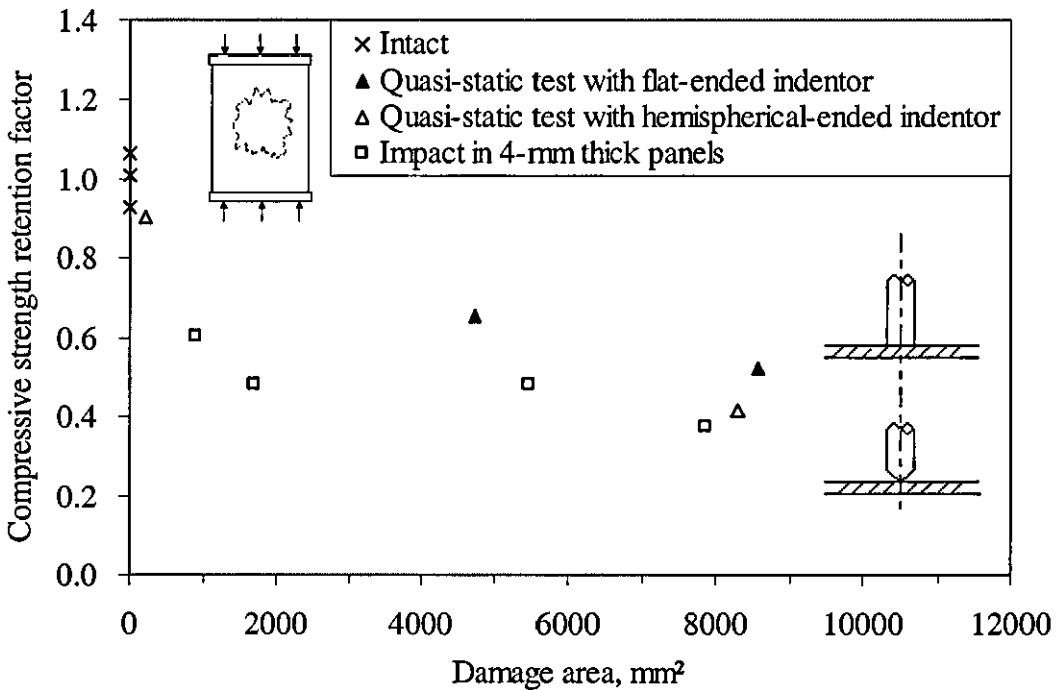
(b)

Figure 5.1.14 Variation of compressive strength retention factor with (a) maximum transverse force and (b) damage area for 4-mm thick carbon/epoxy panels containing damage induced by impact and quasi-static transverse indentation

246

(a)

(b)

247

(c)
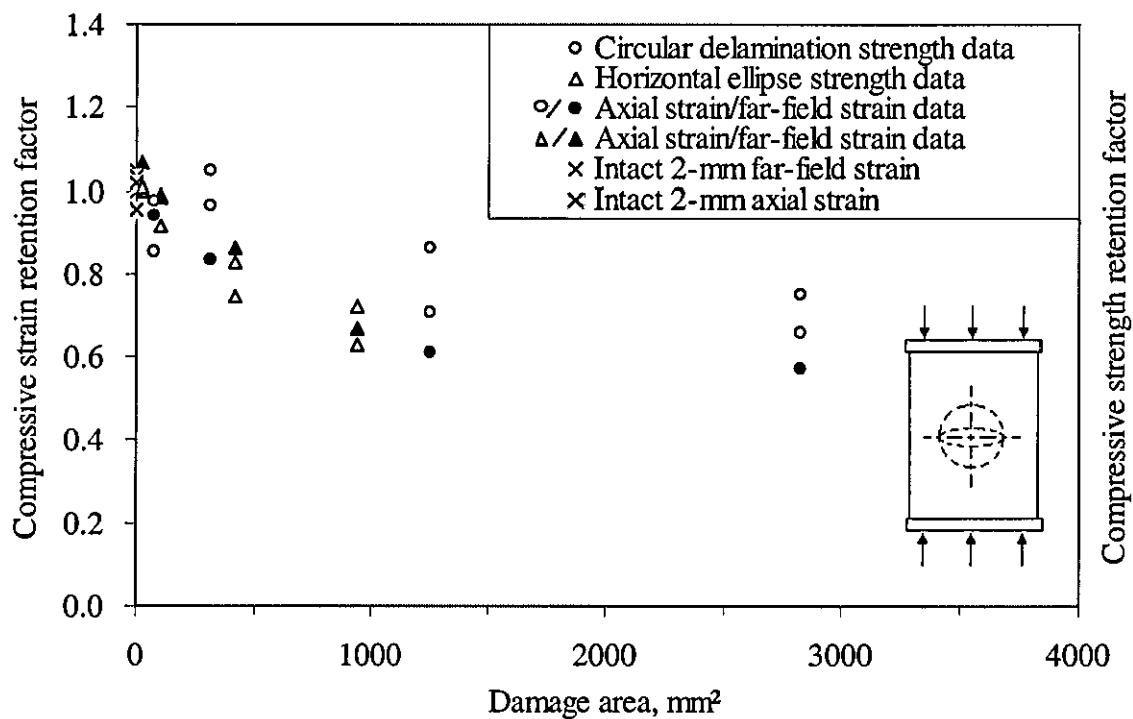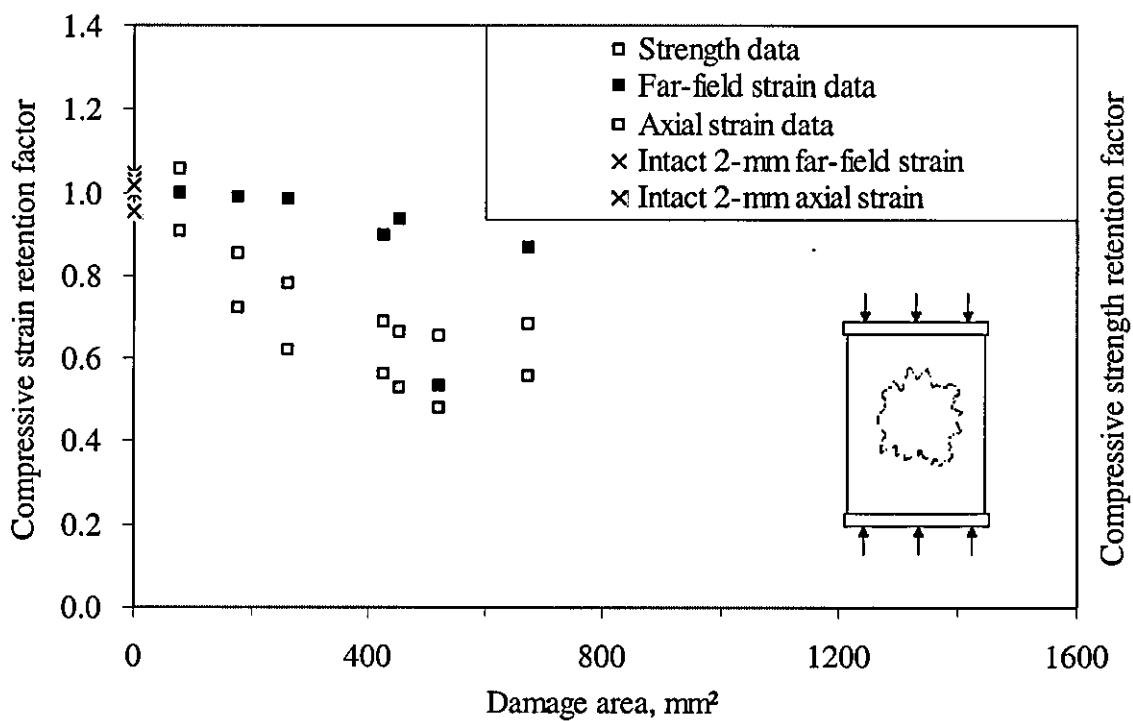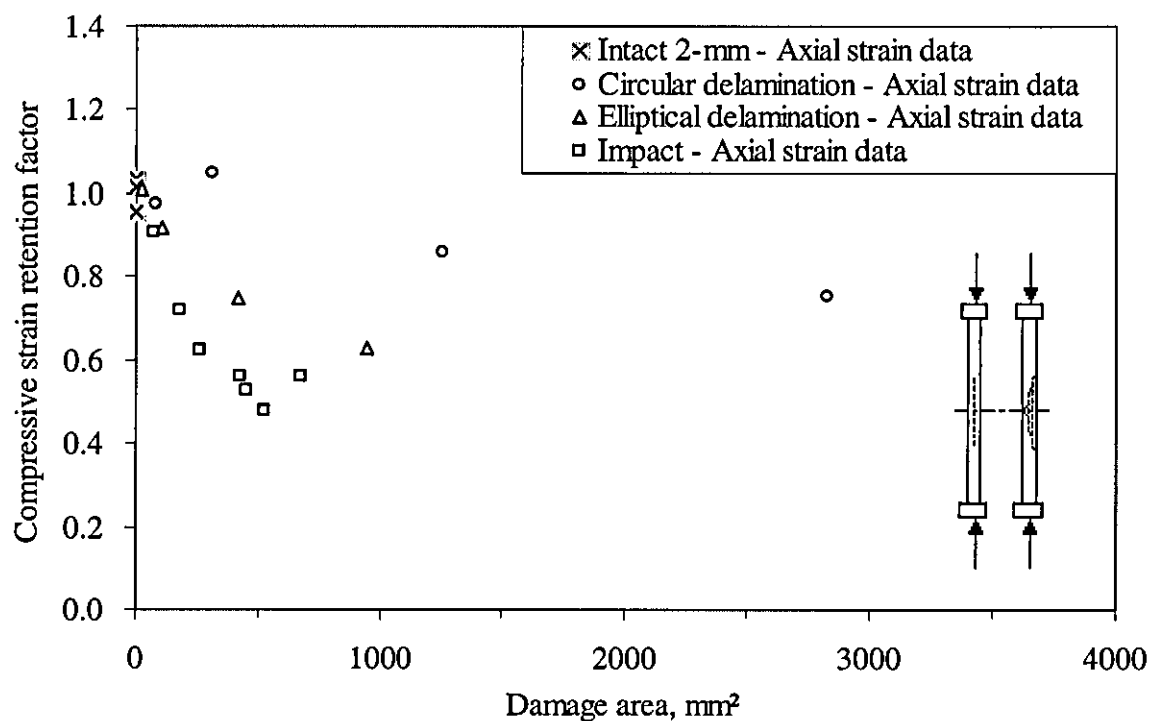
Figure 5.2.1 Comparison of strain and strength retention factor for 2-mm thick panels
with (a) artificial embedded delamination, (b) impact damage and (c) only axial strain
retention factor for all preconditions [104]

(a)

248

(b)

(c)

249

(d)
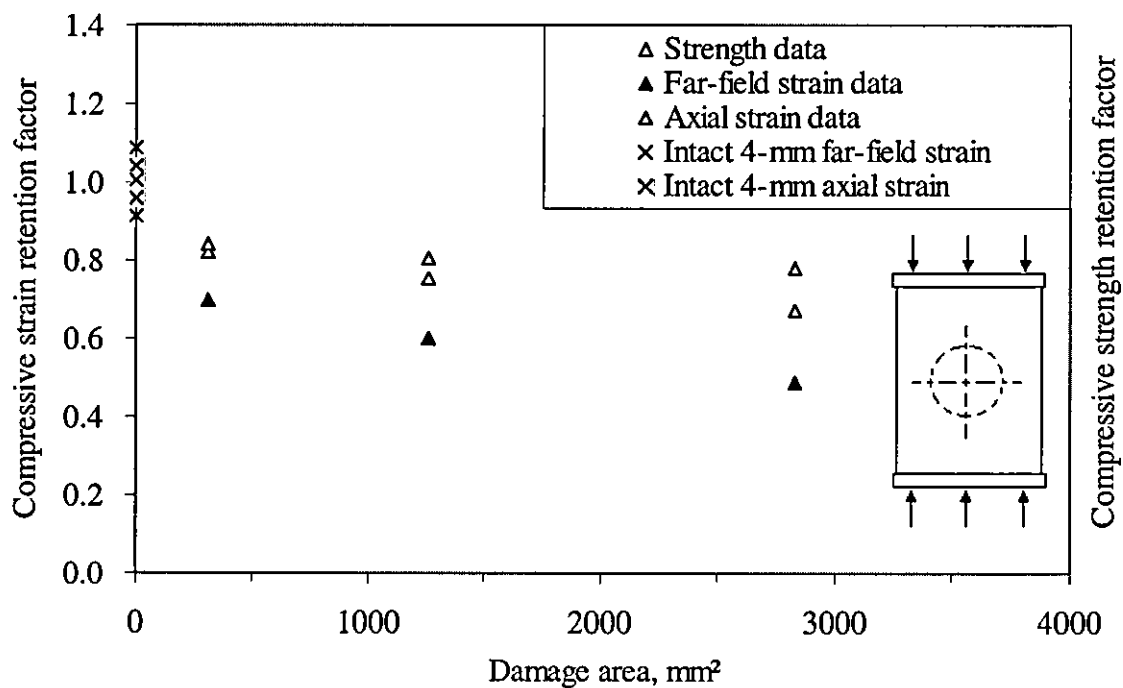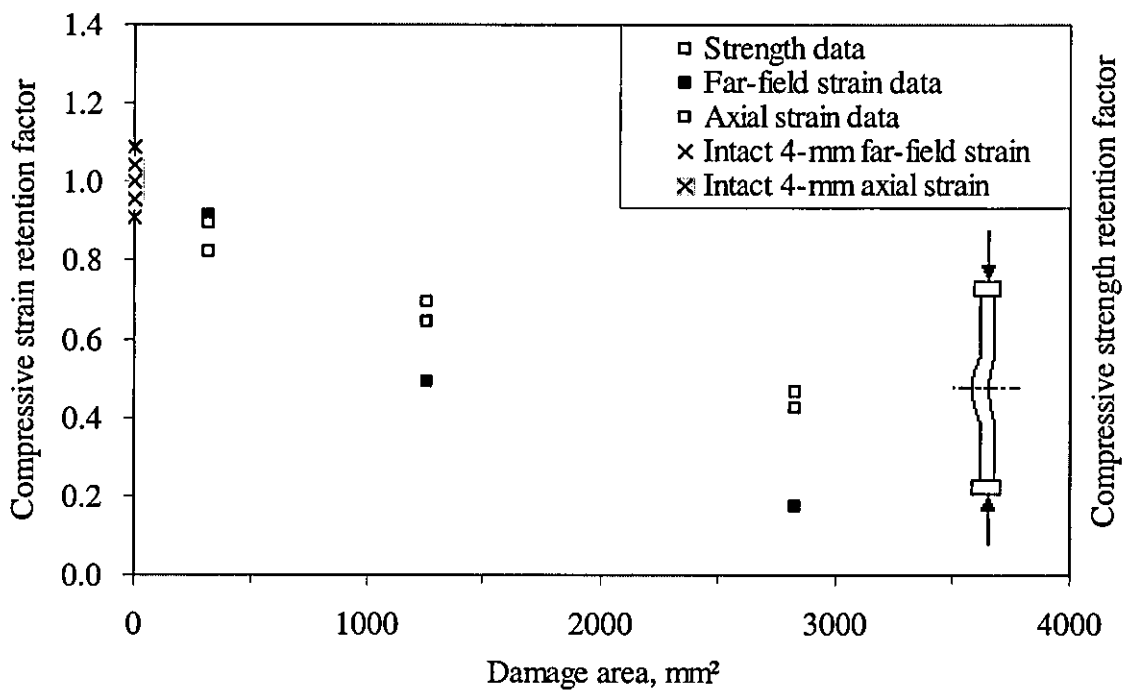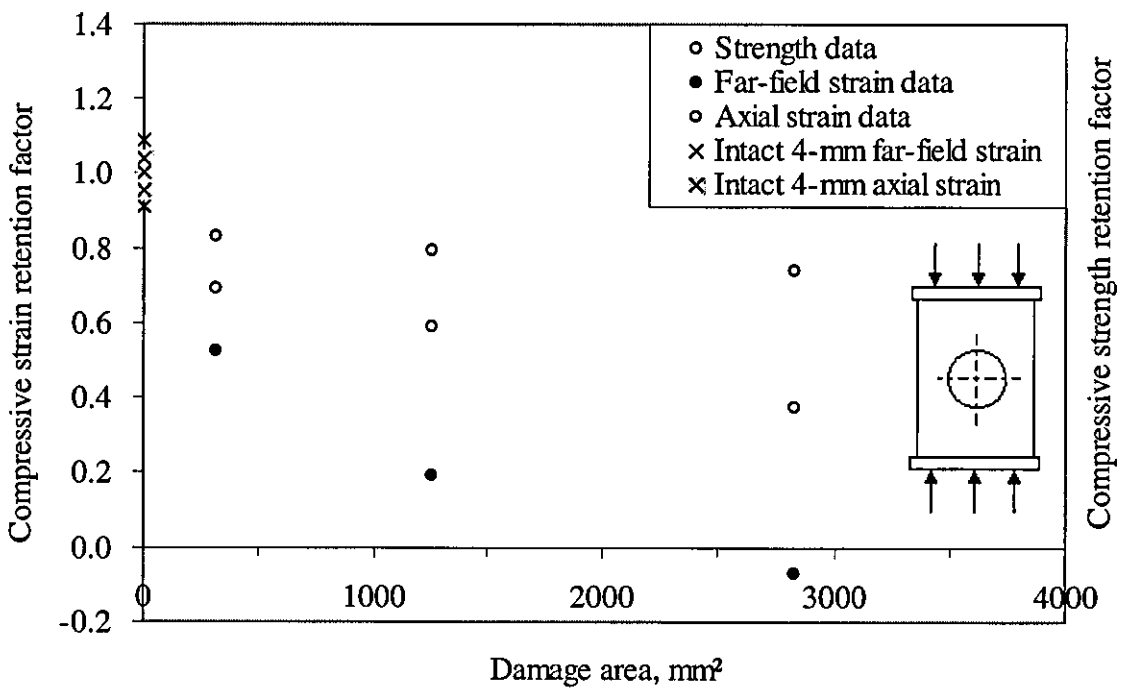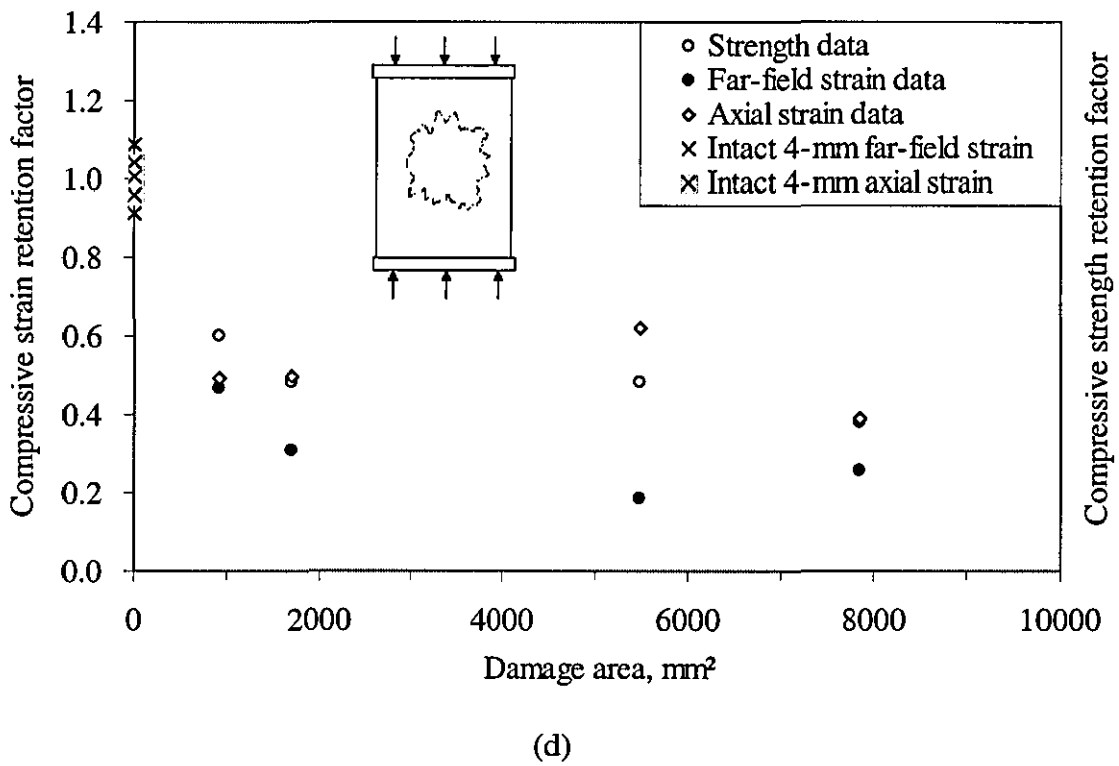
Figure 5.2.2 Comparison of strain and strength retention factor for 4-mm thick panels
with (a) artificial embedded delamination, (b) local change of geometry (constant
curvature approach), (c) open hole and (d) impact damage

(a)

250
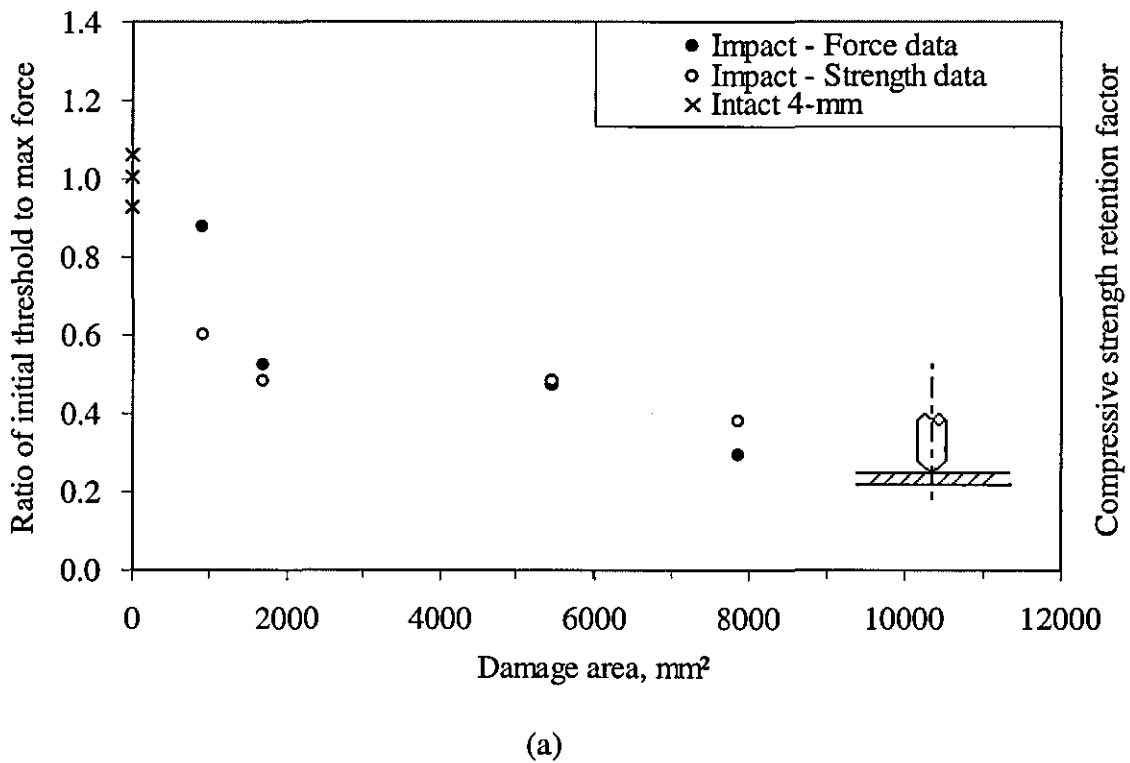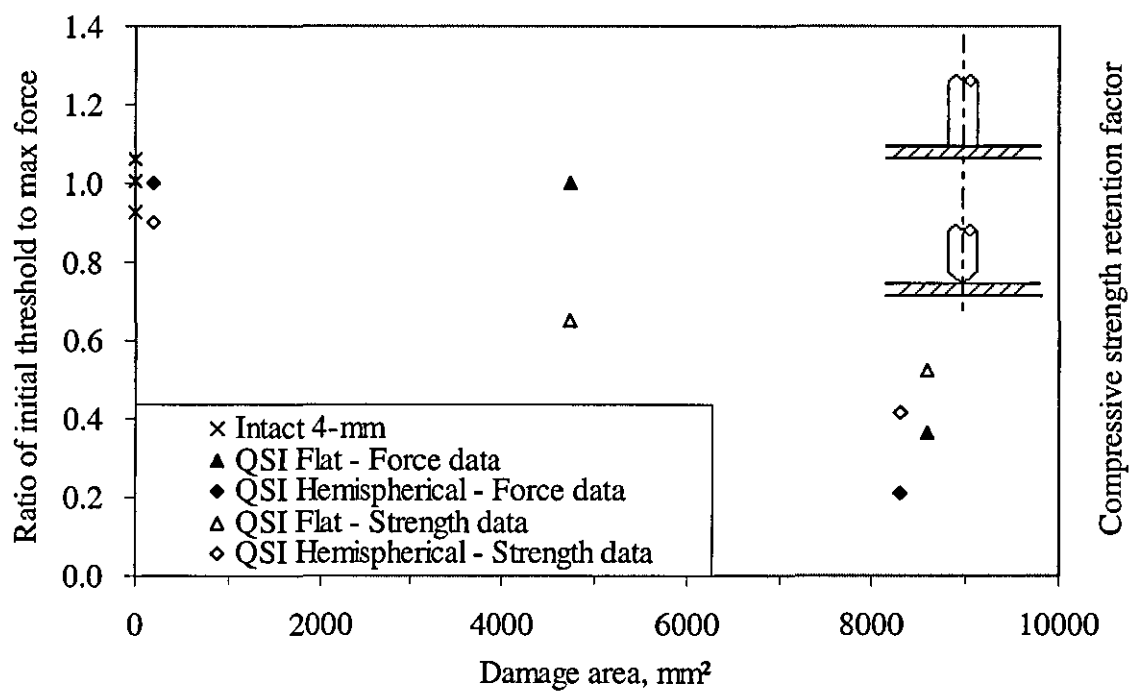
(b)

Figure 5.2.3 Comparison of force ratio and strength retention factor data for 4-mm thick panels with (a) impact damage and (b) quasi-static indentation induced damage

6 Analytical Models for Predicting Residual Compressive Strength

The effect of impact damage and its individual mechanisms on the compressive strength reduction has been experimentally studied in previous chapters. However a complete understanding of the damage tolerance on the basis of experimentation would be very expensive. Therefore development of an analytical model for predicting the residual compressive strength (RCS) becomes very desirable. The first section of this chapter presents an overview of previous work, concerning analytical and empirical predictions of the RCS. In the second section, an analytical model is developed on the basis of equating the compressive strength retention factor (CSRF) to the ratio of initial threshold force to maximum transverse force.

6.1 Overview of previous work

The theoretical prediction of the residual compressive strength (RCS) is still under development due to the complexity of impact-induced damage (Chapter 3), despite the large body of experimental observations and data regarding the post-impact compressive strength behaviour of composite panels. Theoretical investigations have been devoted to predicting the influence of low-velocity impact on the in-plane compressive strength of composite laminates. Four main approaches have been identified, namely blister model, model of ply strain mismatch, soft-inclusion model and empirical predictions.

6.1.1 One-dimension and two-dimensions blister models

The major damage mechanism induced by impact loading is delamination, as it was shown in Chapters 3 and 4. Consequently many authors have based their analytical models only on internal delaminations. The sublaminates created by internal delaminations can be studied separately in terms of compressive behaviour, stability and failure. For a single delamination a thinner sublaminate is called the blister whereas the other thicker sublaminate is called a solid substrate. Such thin blister is usually less stiff than the substrate and more prone to buckling. Depending on the blister's geometry, the analytical models can be divided into one-dimensional (1-D) and two-dimensional (2-

D). This type of blister models was originally developed by [130]. Other further developments could be found in [131, 132]. These models studied both a general case of the buckling of two sublaminates of equal thickness and a particular case of a thin sublaminate acting as a blister attached to a very thick substrate. Also the effect of the sublaminate thickness on the buckling load was studied and some specific results were tabulated, as shown in [131]. Additionally, a special postbuckling solution was derived for the panel displacements [132]. The results of these studies are compiled in [133]. Delamination propagation of the blister models was studied through the associated energy release rate. In [132, 134, 135] the compressive axial load of a delaminated beam was assessed using the energy release rate criteria. The critical fracture load becomes significant for certain delamination depths. The major limitation of all the 1-D blister models was the assumption of the longitudinal propagation of delamination. In contrast a realistic delamination in compression tends to propagate in the width direction as mentioned in [81, 87, 91-94, 136, 137].

Refinement was made by extending the 1-D models to the 2-D. However, the buckling of circular sublaminates was treated as a special case of the 1-D models in [138, 139]. The basic assumption was that the buckling deformation of the base plate was small compared to that of the delaminated layer as well as to the thickness of the plate, so the sublaminate behaved as a 2-D blister. It was found that the size and depth of the delamination significantly affected the critical buckling load. However the delamination growth was still aligned with the load direction, in opposition to the experimental observations. Consequently this model provided a good prediction only in the case of panels with a through-the-width delamination.

The limitation of exclusive longitudinal growth of delamination is removed by using 2-D blister models [140]. In this model the sublaminate buckled prior to propagation and the stress state at the tip of the crack drove the crack growth in both directions. However the determination of the buckling load of 2-D sublaminates was more complex than the 1-D case. The growth conditions and behaviour of the delamination were studied by breaking the overall problem into an elastic stability problem and a fracture problem. The sublaminate stability was determined using a solution based on the Rayleigh-Ritz (R-R) method. Then the fracture criterion was applied to the buckled

253

sublaminate, to determine whether or not the delamination had propagated. A similar model was presented in [141]. However, failure and delamination propagation are not necessarily linked, as observed experimentally in Chapter 4. Rather than triggering a catastrophic failure, the presence of a delamination reduces the global stability of the panel, reducing particularly the global buckling (mode I to II) load. The panel failure was linked to shifting in buckling mode-I to mode-II more than delamination propagation.

The determination of the sublaminate stability using the R-R method was studied in [142] for various shapes such as circular, strip, rectangle and elliptical blisters. An additional finite element analysis (FEA) was carried out to compare the results of both models. Generally, the R-R method uses a basic function for the transverse deflection of the sublaminate, and through minimization of the potential energy its coefficients are determined. It was found to be simple, inexpensive and accurate, except for highly anisotropic delaminated regions. The effects of delamination shape and orientation, material anisotropy and lay-up on buckling strains were examined.

Some of 2-D blister models were extended for the RCS prediction in [36, 143, 144]. That was carried out in five basic analytical steps. The first step was to simulate the characteristic damage state (CDS) as a sublaminate with ply stacking sequence and thickness representing an average of those appearing in the real CDS. Secondly, a sublaminate stability analysis was performed using damage diameter as an independent variable characterising the planar size of the CDS. This was done using a corrected version of the model presented in [142]. The correction took in account the asymmetry of sublaminates layup. Thirdly, the effective reduced stiffness of the impact damage zone was calculated using the results from the sublaminate stability analysis. Fourthly, the in-plane stress concentration associated with the reduced stiffness was determined, using FEA to account for size of damage/width interactions. Finally, the fifth step was the application of a maximum-strain failure criterion to predict CAI, based on the stress state determined in the fourth step. A similar methodology was presented in another model [145] with the difference that the damage/width interactions (4th step) were worked out using a closed form expression rather than FEA.

Failure is generally more sequential and less catastrophic, especially when there are more than two sublaminates. A sequential failure model was developed in [85] to find failure loads of individual sublaminates in an iterative manner until global failure was predicted. Three different calculations were done for every iteration, namely global buckling load, local buckling load [142] and compression failure load. These three values were then compared to determine which sublaminate has failed. The failed sublaminate was retired and the calculation was repeated, using a 'reduced' laminate with reduced stiffness. A similar sequential model was presented in [57] where each individual sublaminate was analysed for compressive failure through laminate theory and for stability through buckling analysis. Once a sublaminate buckled, it was assumed that it did not carry any load and the calculation was repeated for a reduced laminate, until a ultimate failure of the laminate was reached. This model showed remarkably good predictions. In [86] two issues were studied in addition to the analytical sequential model. One was the possible bending-stretching coupling behaviour of the delaminated region and the other one was the effect of Poisson's ratio mismatch between the delaminated and the base region. Both effects were observed experimentally in Chapter 4.

6.1.2 Soft inclusion and open hole models

The relationship between the damage state and the soft inclusion is, in the majority of the models, an empirical relationship that depends on the specimen configuration and on the laminate properties. To estimate the RCS of panels with impact damage with a soft inclusion model is necessary to link the IKE with the geometry of the inclusion by examining experimentally the damage characteristics. Nevertheless, the degree of precision that these models can provide is high, despite the simplifications and analogies that are assumed.

Impact loading creates a region of reduced stiffness. Some studies have focussed on the local change of mechanical properties to predict the RCS. The damage region has been modelled a 'soft inclusion', meaning a region with reduced stiffness [77, 146, 147]. It has also been modelled as an open hole of equivalent size to the damage region, as seen in [50, 99, 148]. The presence of a region with reduced stiffness creates a stress

rearrangement and concentration in the surroundings of the impact site during compression. This can eventually trigger failure, as shown experimentally in [147, 149]. The stress and displacement field around a soft inclusion can be analysed similarly to panels with open holes [150], defining a stress/strain concentration factor (SCF) that relates the intact far-field properties to the ones of the damaged region [123]. The SCF has been determined analytically [146, 151] and experimentally [149].

The stiffness reduction of the damaged area was represented by a semi-empirical expression [77]. The expression coefficients and the parameters of the soft inclusion were determined from experimental results and damage characterisation. Subsequently, the stress and displacement fields were obtained using the inhomogeneity model shown in [146]. The stresses along the inhomogeneity were compared with a critical value for compressive failure, so that the prediction of the RCS was based upon the concept of stress concentration.

The impact damage region can also be modelled as an equivalent open hole. Initially a model was developed [124] for predicting the compressive kinking failure of laminated coupon specimens containing an open hole. This model was later extended for impact damage in panels [50] to predict the RCS. Despite the difference in compressive failure and damage mechanisms between panels with impact damage and open hole (Chapters 3 and 4), the concept of the *equivalent hole diameter* was introduced to link impact-induced damage and open hole. In the model predictions the damage width used as equivalent hole diameter was mainly obtained from X-radiographs, by measuring the size of the darkest region and excluding the outer, lighter regions. The theoretical predictions agreed with the experimental results, with an error in most cases less than 10%. The concept of equivalent hole diameter was further elaborated in [99, 148]. Based on damage characterisation it was assumed that the entire fibres within the elliptic contour of the developed dent could no longer sustain any load, therefore the damage region was simplified as an elliptic hole, where the major and minor axes were equal to the damage width and the initial dent diameter respectively. Then the stress distribution was calculated using the complex potential method and the classical lamination theory. Finally a lay-up independent failure criterion was used to predict the RCS. The model predictions showed good agreement with a wide variety of materials.

6.1.3 Semi-empirical and empirical models

Generally, semi-empirical and empirical models have an expression for predicting the RCS of impacted panels. This expression have to be calibrated every time for a specific material and laminate configuration, therefore its precision relies on a strong experimental basis. The use of such models has to be carefully confined to the intended scope, in particular for fully empirical predictions.

A semi-empirical method was developed based on the assumption that the tensile/compressive strength degradation of a laminated plate containing multiple delaminations is proportional to the flexural stiffness degradation [152, 153]. This model used the concept of bending stiffness mismatch coefficient M developed in [21] (for two ply laminates) and its proportionality to the extent of delamination. The RCS was estimated as a function of the impact energy U and the bending mismatch coefficient M by using an extended formula that covered laminates with n-ply and multiple internal delaminations, all of them grouped in a new term m. The resulting expression had two unknown coefficients d and α that were determined experimentally. These predictions had good agreement with experimental results, showing a strong dependence on the lay-up configuration

$$\frac{\sigma_r}{\sigma_0} = m \frac{d}{U^\alpha} \tag{6.1.1}$$

In [76] a basic relationship was formulated in terms of the RCS, σ_R, the untouched CS, σ_U, the impact energy E, the critical energy for initiation of strength reduction, E_{ic} and the limiting energy beyond which RCS decreases only marginally, E_L. Two linear equations were used to describe this relationship over two energy ranges. The critical values and coefficients, m_1 and m_2, were obtained from the experimental data

$$\sigma_R = (E - E_{ic})m_1 + \sigma_U \quad \text{for } E_{ic} < E < E_L \tag{6.1.2}$$

$$\sigma_R = (E - E_L)m_2 + \sigma_{RL} \quad \text{for } E_L < E$$

An exponential relationship was formulated in [154] to relate the impact energy U with the reduction of CS. The coefficients of the model, U_0 and α, were calibrated using coupon specimens.

$$\frac{\sigma_r}{\sigma_0} = \left(\frac{U_0}{U}\right)^{\alpha} \tag{6.1.3}$$

The empirical model presented in [155] has the widest scope, due to the large amount of experimental work that is backing up the formulas. In this model, an empirical relationship between the CAI strength and the impact parameters was obtained from extensive data correlation. A total of six parameters were used, namely laminate layup, full-penetration stress, laminate thickness, material toughness, impact energy and impactor size parameter. The failure stress, σ_f, was expressed as

$$\sigma_f = \frac{\sigma_0}{1 + C_1 C_2 C_3 C_4 C_5 W_e} \tag{6.1.4}$$

6.1.4 Limitations of previous analytical models

It has been shown that the majority of the previous analytical (non-empirical) models are based on the compressive behaviour modelling of a damaged panel. They try to determine the stress state at critical locations and analyse the failure on each ply. However, the development of such stress-based models has some limitations. A first limitation is imposed by the simplification of impact damage as internal delaminations. It disregards other types of damage such as matrix cracks and local change of geometry that may have a significant effect on the RCS for high IKEs. A second limitation lays on the difficulty to include all the parameters involved in the complex relationships between IKE, AE and the damage state, such as the flexural rigidity of the panel and the governing damage mechanisms. A third limitation is dictated by the difficulty of modelling the compressive response of damaged panels after local buckling (mode-I). Since only some basic cases offer an analytical (closed form) solution, the majority of cases require numerical approximations, hence depending on model refinement to get

an acceptable degree of precision. Finally, there is a limitation on defining the compressive failure as the direct result of delamination propagation. As seen in Chapter 4, not always compressive failure can be linked to delamination propagation or global buckling. There are also particular factors such as delamination size, damage mechanisms and panel dimensions that determine the type of compressive failure.

6.2 Proposed model

The model proposed in this section is based on the experimental observation [13, 127] of the existing similarity between the ratio of initial threshold force to transverse peak load and the CSRF. This similarity was also observed Chapter 5 for 4-mm thick panels. The model does not analyse either the compressive response nor the compressive failure of panels containing damage.

6.2.1 Initial threshold force calculation

The threshold force for the onset of delamination has been obtained [30, 42] on the basis of an extension of a 1-D beam fracture model to a 2-D circular plate. The expression was

$$P_{thresh} = \left(\frac{8\pi^2 E h^2 G_{IIC}}{9\left(1 - \nu^2\right)} \right)^{1/2} \tag{6.2.1}$$

where E is the Young modulus, h is the plate thickness, G_{IIC} is the critical energy release rate in mode II and ν is the Poisson's ratio. However a more accurate expression can be obtained if the derivation is based on strain energy release rate of a 2-dimension circular plate. In general, an energy balance for a panel transversely loaded without fibre shear-out, is given by [156]

$$E_{QSE} = E_{IKE} \approx E_{AE} + E_{RE} = \left(E_{mc} + E_{od} + E_{pd}\right) + E_{RE} = \left(E_{mc} + G_{IIC} A\right) + E_{RE} \tag{6.2.2}$$

259

in which E_{QSE} denotes the external work performed by the transverse force, E_{IKE} = IKE is the incident kinetic energy, E_{AE} = AE is the absorbed energy, E_{RE} = RE is the rebound energy or stored elastic strain energy, E_{mc}, E_{od} and E_{pd} are the energies dissipated as matrix cracks, onset of delamination and propagation of delamination, respectively. The last two terms were grouped in the critical energy release rate term G_{IIc} multiplied by the delamination area A. Assuming that the energy dissipated by the creation and propagation of delamination is significantly higher than by matrix cracks, Eq. (6.2.2) can be rearranged as

$$G_{IIC} = \frac{E_{QSE} - E_{RE}}{A} \qquad (6.2.3)$$

If the delamination propagates an infinitesimal area dA, the energy balance can be rewritten as

$$G_{IIC} = \frac{dE_{QSE}}{dA} - \frac{dE_{RE}}{dA} \qquad (6.2.4)$$

Figure 6.2.1 shows the particular case of a thin circular plate of thickness h, containing a concentric delamination of radius a_1 at the middle plane. The delamination is growing from a radius a_1 to a radius $a_1 + da$, creating a new infinitesimal concentric area, shown by the shaded region in the figure. Consequently, Eq. (6.2.4) with the infinitesimal second order terms neglected becomes

$$G_{IIC} = \frac{dE_{QSE} - dE_{RE}}{\pi\left((a_1 + da)^2 - a_1^2\right)} = \frac{dE_{QSE} - dE_{RE}}{2\pi a_1 da} \qquad (6.2.5)$$

The energy terms in Eq. (6.2.5) are given by the force-displacement relationships before and after the propagation of delamination. If both stages are referred to as 1 and 2 in subscript respectively, a change in work performed by external forces is given by

$$dE_{QSE} = \left[\sum(P \times \delta)_i\right]_2 - \left[\sum(P \times \delta)_i\right]_1 \qquad (6.2.6)$$

And a change in elastic strain energy (i.e. rebound energy) is given by

$$dE_{RE} = \frac{1}{2}\left[\sum(P\times\delta)_i\right]_2 - \frac{1}{2}\left[\sum(P\times\delta)_i\right]_1$$

(6.2.7)

Substituting Eq. (6.2.6-7) into Eq. (6.2.5) leads to

$$G_{IIC} = \frac{\frac{1}{2}\left[\sum(P\times\delta)_i\right]_2 - \frac{1}{2}\left[\sum(P\times\delta)_i\right]_1}{2\pi a_1 da}$$

(6.2.8)

The critical load for delamination propagation can be obtained from Eq. (6.2.8) and the respective expressions for the central deflection in terms of applied force. From Appendix B, the central deflection δ of a clamped plate of radius a_2 with a concentric circular delamination of radius a_1 at the mid-plane is given by

$$\delta = \frac{P}{16\pi}\left[\frac{a_2^2 - a_1^2}{D'} + \frac{4a_1^2(3+v)}{D'(1+v)}\right]$$

(6.2.9)

in which D' is the flexural rigidity of the intact plate defined in Eq. (3.1.3). The expression for deflection in Eq. (6.2.9) can be used in the energy balance expression in Eq. (6.2.8) to predict the critical load value for delamination propagation. Before delamination propagation, the first term of Eq. (6.2.8) becomes

$$\left[\sum(P\times\delta)_i\right]_1 = \frac{P^2}{16\pi}\left[\frac{a_2^2 - a_1^2}{D'} + \frac{4a_1^2(3+v)}{D'(1+v)}\right]$$

(6.2.10)

After the infinitesimal propagation of delamination da, the second term in Eq. (6.2.8), after neglecting the high order terms, becomes

$$\left[\sum(P \times \delta)_i\right]_2 = \frac{P^2}{16\pi}\left[\frac{a_2^2 - (a_1 + da)^2}{D'} + \frac{4(a_1 + da)^2(3+v)}{D'(1+v)}\right]$$

$$\dots = \frac{P^2}{16\pi}\left[\frac{a_2^2 - (a_1^2 + 2a_1 da)}{D'} + \frac{4(a_1^2 + 2a_1 da)(3+v)}{D'(1+v)}\right]$$

(6.2.11)

Combining both Eq. (6.2.10) and (6.2.11) with Eq. (6.2.8) yields

$$G_{IIC} = \frac{\dfrac{P^2}{32\pi}\left\{\left[\dfrac{a_2^2 - (a_1^2 + 2a_1 da)}{D'} + \dfrac{4(a_1^2 + 2a_1 da)(3+v)}{D'(1+v)}\right] - \left[\dfrac{a_2^2 - a_1^2}{D'} + \dfrac{4a_1^2(3+v)}{D'(1+v)}\right]\right\}}{2\pi a_1 da}$$

(6.2.12)

Rearranging the above yields

$$G_{IIC} = \frac{P^2}{32\pi^2}\left[\frac{4(3+v)}{D'(1+v)} - \frac{1}{D'}\right]$$

(6.2.13)

thus the critical force for delamination growth is given by

$$P_{critical} = \sqrt{\frac{32 D' \pi^2 G_{IIC}}{\dfrac{4(3+v)}{(1+v)} - 1}} = 4\pi\sqrt{\frac{2(1+v)D' G_{IIC}}{11 + 3v}}$$

(6.2.14)

Table 6.2.1 Prediction for critical transverse load for crack onset in a circular plate

Property	Units	Equation	16 plies	32 plies
D'	GPa.mm^3	3.1.3	39.30	314.40
Plate thickness, h	mm	-	2.048	4.10
Engng. flexural modulus, E	GPa	3.1.16	53.12	52.92
Radial Poisson's ratio, v_{rz}	-	-	0.31	0.31
Critical energy release rate, G_{IIC}	J/m^2	-	940	940
Initial threshold force, P_{thresh}	kN	6.2.1	2.04	5.76
Initial threshold force, P_{thresh}	kN	6.2.14	1.13	3.20
Experimental impact avg.[a], P_{thresh}	kN	-	1.53	3.88
Experimental QSI avg.[b], P_{thresh}	kN	-	1.07	3.64

[a] The average result is derived from force history data of impact tests in Chapter 3.
[b] The average result is derived from load-displacement curves of quasi-static transverse loading using hemispherical-ended indenter in Chapter 3.

Table 6.2.1 shows predictions of critical loads for delamination propagation in 16- and 32-ply QI laminates, using both Eq.(6.2.1) and Eq. (6.2.14). The flexural modulus E and the flexural stiffness D' are shown in Table 3.1.5 in Chapter 3, whereas the critical strain energy release rate for mode II, G_{IIC}, is taken from [104]. The agreement between the experimental and predicted values is fortuitous, as two major assumptions were involved in the derivation for simplicity. One was that matrix cracking had a negligible contribution to the energy balance. The other one was that there was only one delamination located at the mid-plane.

6.2.2 Force-based model for predicting CSRF

This section shows an attempt to develop an analytical model on the basis of the ratio of the initial threshold force for delamination onset to the maximum transverse force. The link to RCS was an experimental observation in [13, 127] and Chapter 5. It postulated that the percentage by which the peak transverse loads exceeded the initial threshold forces is not only a good measure of the amount of damage but also a good indication of the residual strength of laminate plates. However, this relationship seemed to be valid only for relatively thick panels with thickness of 4 mm (Chapter 5) and 10 mm up to 25 mm in [127]. In the case of the thinner laminate, 16-plies, there was little resemblance between the CSRF values and the force ratio, probably due to the difference in the mechanisms governing the damage generation.

The basic assumption of the present model is that the CSRF and the ratio of initial threshold force to maximum force can be considered equivalent, for $P_{max} > P_{thresh}$

$$\frac{P_{thresh}}{P_{max}} \approx \frac{\sigma_{CAI}}{\sigma_0} = CSRF \qquad (6.2.15)$$

Where σ_{CAI} is the compressive strength of the panel after impact, and σ_0 is the compressive strength of an intact panel. In the case of $P_{max} < P_{thresh}$, there is not internal damage in the panel and the CSRF value is equal to 1. On the one hand, the initial threshold force, P_{thresh}, is worked out using Eq. (6.2.14). On the other hand, the

maximum force, P_{max}, can be obtained based on the AE of the plate during transverse loading.

Figure 6.2.2 shows a schematic load-displacement transverse response both in loading and unloading, with the enclosed area hatched representing the AE by the panel (Chapter 3 and [41]). On the one hand the area under the loading path A-B-C represents the energy transfer from the impactor to the laminate, either elastic or dissipation in internal damage and local indentation. This energy can be measured using the area under the curve A-C. Initially, the panel response (A-B) is elastic up to the delaminating onset. After this load level (B-C) the force-displacement curve reflects damage growth, with drops in flexural strength due to the appearance of thinner sublaminates. On the other hand the unloading path C-D represents all the elastic energy that the damaged laminate is passing back to the impactor, as rebound energy (RE). The unloading response of the panel is determined by the membrane and flexural stiffness of the damaged laminate. The IKE, AE and RE are related by the energy balance in Eq. (6.2.2).

The peak load (P_{max}) can be estimated using the elastic transverse response of the damaged laminate and the RE, provided that the peak load and the load for maximum displacement are relatively close. The transverse elastic response of a panel with multiple delaminations is mainly membrane governed, as a result of the low flexural stiffness of individual sublaminates. Thus, the elastic response can be approximated by the membrane response only, without considering negligible flexural contributions. For a damaged panel the transverse force-displacement response (Eq. (3.1.19b)) can be approximated by

$$k_m w_0^3 = P \tag{6.2.16}$$

in which k_m is given by Eq. (3.1.13b) in Chapter 3. The RE is the area under the curve determined by the path C-D in Figure 6.2.3, so that it can be expressed in terms of Eq. (6.2.16) as

$$RE = \int_0^x P\,dw = \int_0^x k_m w_0^3\,dw \qquad (6.2.17)$$

The unknown in Eq. (6.2.17) is the maximum displacement x corresponding to the maximum force. Solving the Eq. (6.2.17) for x it yields

$$x = \left(\frac{4RE}{k_m}\right)^{1/4} \qquad (6.2.18)$$

Therefore, the maximum load is given in Eq. (6.2.16) by replacing $w_0 = x$ as

$$k_m \left(\frac{4RE}{k_m}\right)^{3/4} = P_{max} \qquad (6.2.19)$$

Finally, the prediction of CSRF in Eq. (6.2.15) can be expressed now in terms of the initial threshold force and the maximum force in Eqs. (6.2.14) and (6.2.19) respectively

$$CSRF = 1 \qquad ; \text{for } P_{max} < P_{thresh}$$

$$\frac{P_{thresh}}{P_{max}} = \frac{4\pi\sqrt{\dfrac{2(1+v)D'G_{IIC}}{11+3v}}}{k_m\left(\dfrac{4RE}{k_m}\right)^{3/4}} \approx CSRF \qquad ; \text{for } P_{max} > P_{thresh} \qquad (6.2.20)$$

The predicted values are plotted in Figure 6.2.3(a-b) as function of the IKE and of the RE. In the case of IKE, the prediction was based on the assumption that the proportion of AE energy was 55% so the RE was 45% of the total IKE, as found experimentally in Chapter 3 for 4-mm thick panels. Figure 6.2.3(a-b) also includes the experimental results of 4-mm thick panels with impact-induced damage for CSRF and the ratio of initial threshold to maximum force. The model estimates the ratio of initial threshold to maximum force well and it is expected to predict the CSRF with reasonable precision if there is a resemblance between CSRF and the force ratio.

The initial threshold, maximum force and CSRF values are listed in Table 6.2.2 for analytically estimated and experimental results. Both set of results for 4-mm thick panels show good correlation. Contrastingly, experimental results for the 2-mm thick panel were significantly different from the analytical estimation, as a result of the difference between the experimental force ratio and the experimental CSRF.

Table 6.2.2 Experimental and analytical prediction results for initial threshold and maximum force ratio and CSRF

Panel	Energy			Experimental results				Analytical prediction		
	IKE	AE	RE	Initial thres.	Max. force	Force ratio	CSRF	Initial thres.	Max. force	Force ratio / CSRF
	J	J	J	KN	kN	%	%	kN	kN	%
4I 0.5m	6.9	4.2	2.7	3.73	4.27	87.3	60.2	3.20	3.56	90.0
4I 1.0m	13.7	7.3	6.4	3.83	7.35	52.1	48.0	3.20	5.95	53.8
4I 1.5m	21.1	11.2	9.9	4.07	8.57	47.5	48.1	3.20	8.22	38.9
4I2.52m	41.7	22.9[a]	18.8[a]	3.88	13.41	28.9	41.7	3.20	13.71	23.4
2I 0.5ii	7.9	2.1	5.8	1.53	4.73	32.3	80.8	1.13	5.05	22.4

[a] AE for the panel 4I 2.52m was determined using the average absorption ratio of 55% of the IKE, since the experimental result was missing

The expression in Eq. (6.2.20) allows the calculation of the critical energy level for damage onset. If the CSRF is set to 1, the equation can be solved in terms of the RE

$$RE_{critical} = \frac{\left(\dfrac{32\pi^2(1+v)D'G_{IIC}}{11+3v}\right)^{2/3}}{4k_m^{1/3}}$$

(6.2.21)

The critical level of RE for damage onset for 4-mm thick panels is 2.70 J, given by Eq. (6.2.21). If the absorbed energy is 55% of the total IKE, then the critical IKE for damage onset is 6.00 J. Fortuitously, this value correlates well with the experimental of 6.14 J, found in Chapter 3.

Figure 6.2.4 shows the effect of indenter size on the CSRF prediction trend. Increasing the indenter size is reflected in a reduction of the membrane stiffness via the loading area factor *LAF* (Eq. (3.1.13b)). Thus, the CSRF and the critical energy for damage onset are also lowered when the indenter size is increased. The indenter size was varied only from 0% to 50% of the total plate radius. The model estimation of the CSRF has

reasonable precision within this range. A significant error is introduced for larger indenters, for two main reasons. The first one is that the derivation of the membrane stiffness for deflection in Chapter 3 only accounts the elastic energy stored in the outer part of the plate surrounding the indenter. When the indenter covers a significant area of the panel, the model underestimates an important amount of elastic energy stored under the indenter. In order to account this contribution, the membrane effect has to be worked out in a different way that is not covered in this study. The second source of error is that the initial threshold force value is determined assuming that the applied transverse load is concentrated at the panel centre for the simplicity in the derivation.
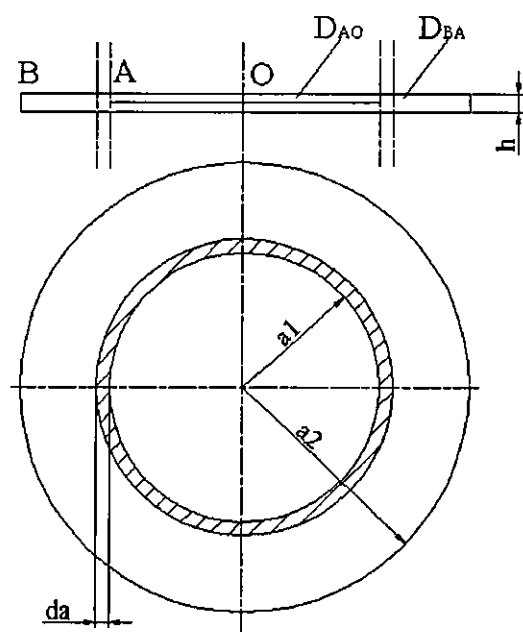
Figure 6.2.1 Circular plate of radius a_2 with a concentric growing crack of radius a_1
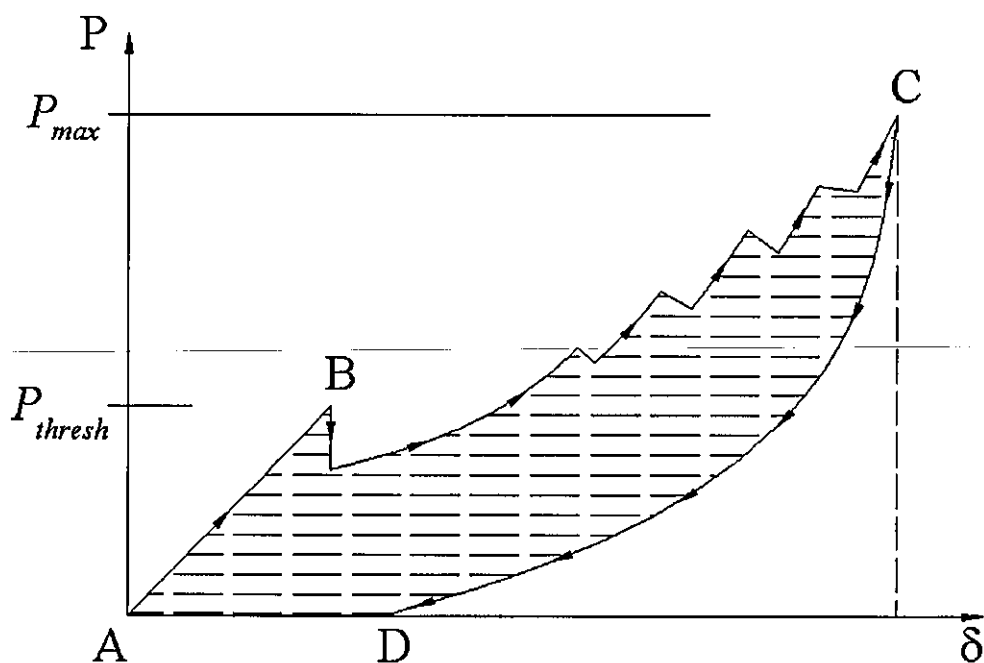
Figure 6.2.2 Schematic force-displacement diagram indicating the loading path A-B-C and the unloading path C-D. The absorbed energy (AE) is the hatched area enclosed by the hysteretical loop. The rebound energy (RE) is the area under C-D
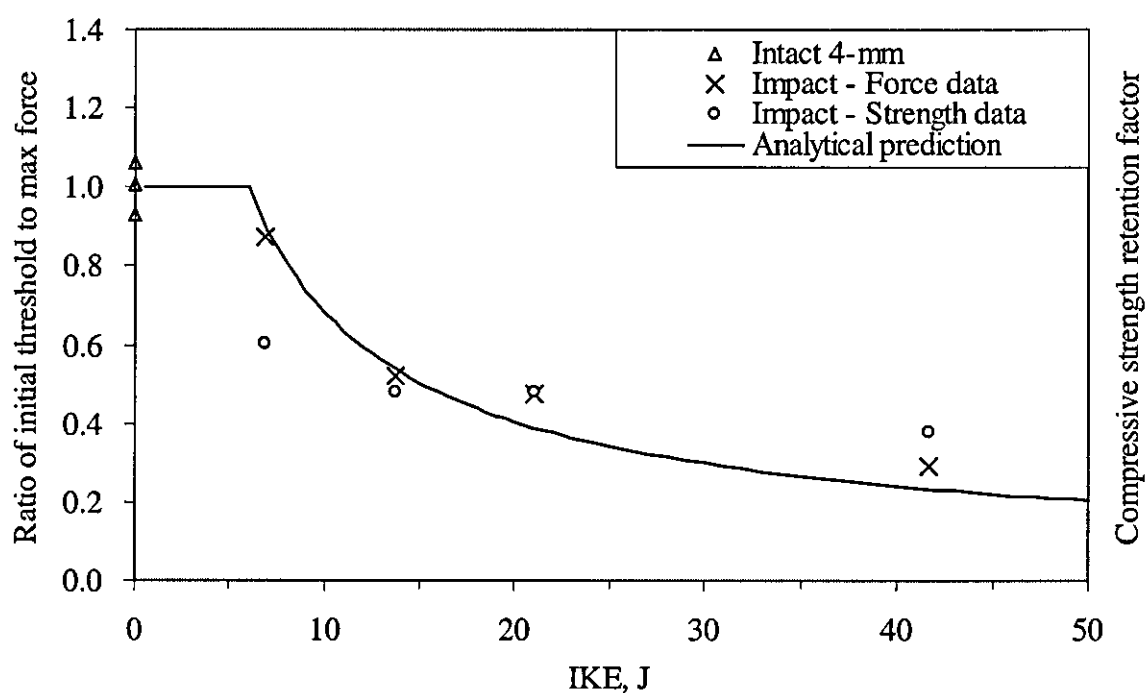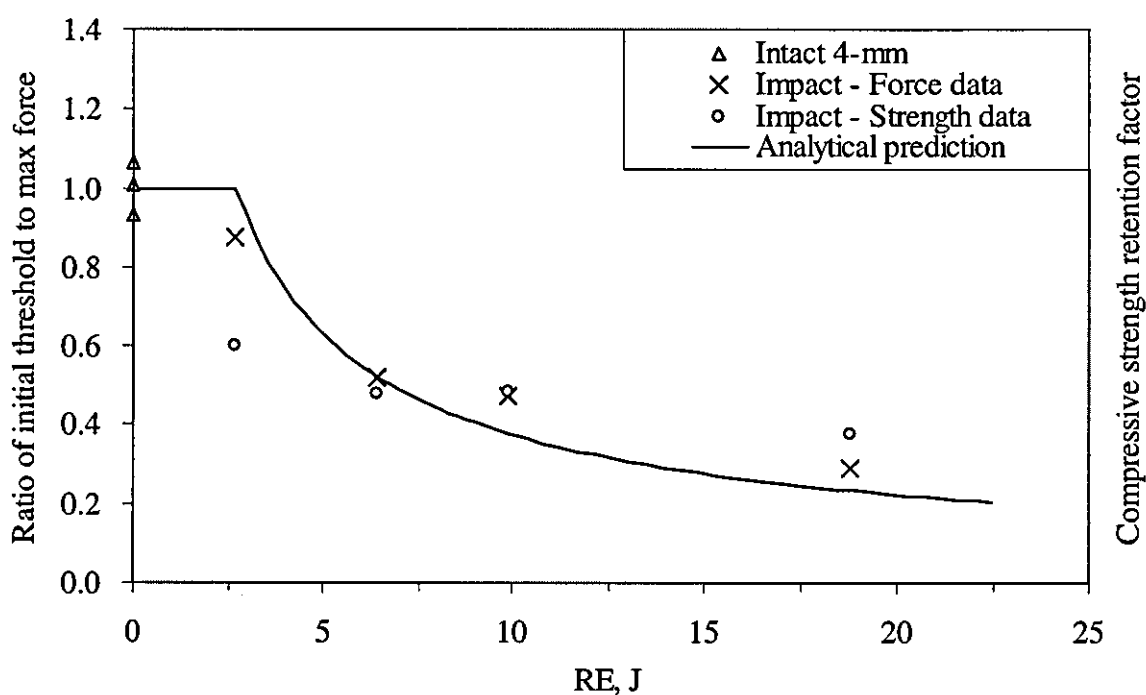
Figure 6.2.3 Analytical prediction for CSRF compared with the experimental initial threshold to maximum force ratio and experimental CSRF of 4-mm impacted panels in terms of (a) IKE and (b) rebound energy, RE
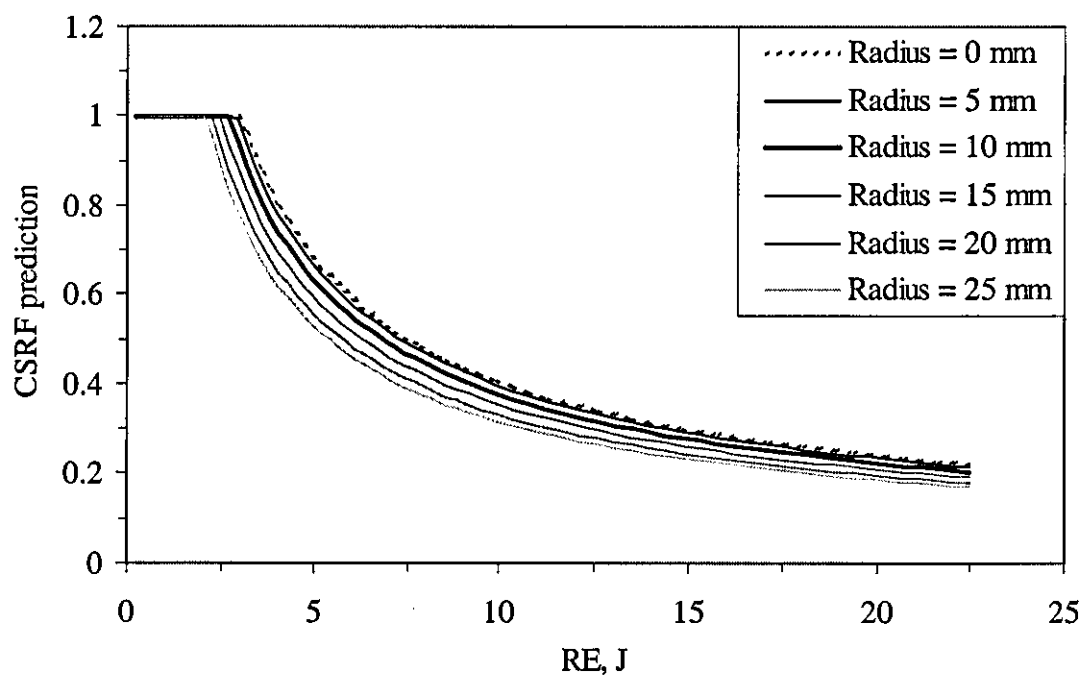
Figure 6.2.4 Indenter size effect on the analytical prediction of CSRF in terms of the rebound energy (RE)

Conclusions and Recommendations

The use and design of composite structures has to consider the effect of impact damage on the residual compressive strength. Due to the complexity of impact damage, a clear understanding of the mechanisms leading to this reduction requires an alternative study of all the types of damage involved. In this thesis a three 'bounding' approach was taken to simulate impact damage, using simplified well-defined damages. The first one used open holes as the representation of ultimate material damages. The second one used embedment of artificial delaminations to experimentally simulate as many elements of impact damage characteristics as possible, including size, shape, number (of the same size), TTT distribution and TTT location. The third one considered the effect of local curvature change by introducing hemispherical-shaped domes of different curvatures and depths into panels. The effect of impact damage was expected to fall among these three bounds. Panels with the three preconditions described above plus panels with impact- and quasi-static transverse loading-induced damage were tested in compression. The respective compressive behaviour and failure were obtained experimentally by in-plane compressing 4-mm thick quasi-isotropic T700/LTM45-EL carbon/epoxy preconditioned of 150×100 mm in a universal testing machine. The panel was fitted into a specially designed anti-buckling jig that provided simply supported boundary conditions on the unloaded edges. Epoxy potted ends were added to the loading ends to increase the contact area and prevent hinge-like rotation. In this way the loaded ends were effectively close to clamped condition but without clamping surface pressure. Load, displacement and local surface strains were monitored during the compressive test for subsequent analysis and cross-examination. Data of 2-mm thick panels with impact damage and artificial delaminations were available mostly from a previous study [104] and were also included in the analysis.

The following conclusions could be drawn:

(A) The approximation of impact damage through artificial delamination proved to be extremely useful. The validity of this approach was examined by comparing compressive strain responses of impacted and preconditioned panels in Chapter 4. In the case of 2-mm thick panels, impact damage was well represented by a single

271

delamination of equivalent projected area. Both types of preconditioned panels followed the sequential behaviour of in-plane compression (or pre-buckling), local buckling (mode-I), global buckling (mode-I), global post-buckling (mode-II) and ultimate failure in the mid-section region. The validity of the approach was reinforced by the existence of a common damage threshold, at the 25% panel width or 455-mm^2 damage area, irrespective of shape, orientation or nature of damages.

(B) The validity of simulating impact damage with artificial delamination had some noticeable limitations for thicker 4-mm thick panels. Panels with a single delamination had a completely different response from impacted panels with equivalent damage area. Moreover, these panels tended to behave like the intact panels, as they were crushed at one end. A reduction in CS was observed only when damage area became greater than 1257 mm^2, or when multiple delaminations of medium and large sizes were embedded. In addition, the compressive response and failure of artificially delaminated panels resembled those of panels with impact damage of the same area. Moreover, for these panels, the compressive behaviour characteristics were similar to that of 2-mm thick panels.

(C) The compressive failure of panels with internal delaminations is not necessarily linked to delamination propagation. After the damage threshold for CS reduction, the compressive failure seemed to be related to the mode shifting (mode I to II) at the global buckling load. As observed in Chapter 5 both RCS and global buckling (mode I to II) followed a similar trend. However, global buckling (mode I to II) was not necessarily a synonym of delamination propagation. The delamination propagation was estimated in Chapter 4 on the basis of panel deformation sequences in the longitudinal and width directions. Depending on the size of delamination, the delamination propagation may be influenced by the ILSS concentration at the edge of delamination due to the transverse deformation in conjunction with the longitudinal buckled shape. An observation of the Poisson's ratio data provided a good indicator of delamination propagation.

(D) The area of delamination tends to follow a linear relationship with the IKE for low and intermediate energy levels. Within this IKE range the simulation of impact

damage through artificial delamination was accurate. However at higher IKEs, other types of damage became more dominant (as shown in Chapter 3) such as local curvature change and fibre breakage. In particular local curvature change had a significant effect on the compressive response of impacted panels at high IKEs, as shown in Chapter 4. The effect of local curvature change was also reflected on the lower residual compressive strain of impacted panels at high IKEs (Chapter 5) compared to the residual compressive strength. Residual strain tends to be more sensitive to local change of geometry than strength. Panels with artificial delaminations alone cannot completely simulate the features unless local curvature change is included.

(E) Impact damage induced at high IKEs was represented by material damage and local change of curvature. Panels with hemispherical-shaped domes (Chapter 4) provided basic information on the interaction between local curvature change and compressive load. Their compressive response and failure was governed by flexural stresses and ILSS concentration at the centre and along the boundary of the dome, respectively. The flexural stress was induced by the inherent eccentricity introduced with the hemispherical-shaped dome. The ILSS concentration was induced by the abrupt change of fibre direction that acted as a softer region in the panel, similarly to panels with open holes.

(F) The damage initiation and propagation as well as the energy absorption characteristics during transverse loading (Chapter 3) were dependent on panel thickness. Relatively flexible 2-mm thick panels had small projected areas of delamination with a dominant and localised shear cone induced by membrane effects. The energy absorbed by delamination was around 20% of the given IKE. On the contrary, damage of stiffer 4-mm thick panels was dominated by a large delamination near the mid-plane induced by high ILSS alongside a small shear cone. The energy dissipated by delamination was around 50% of the given IKE.

(G) Alongside the experimental observations, two analytical models were developed for the prediction of panel deflection and CSRF. The comparison between predictions and experimental results of panel deflection showed the importance of

the membrane stretching effect, particularly in thin panels. The influence of boundary conditions on the membrane response was not considered in the model. The comparison also showed that the effect of local indentation effect could be significant for thick panels.

(H) The predictions of CSRF from the analytical model developed in Chapter 6 were in good agreement with CSRF of 4-mm thick panels. This may seem fortuitous, since major assumptions were made during the derivation. The model was based on an experimental observation of the correlation between the degree of reduction in CS and the ratio of maximum transverse load to initial threshold for damage initiation. In addition, the model provides a method to estimate the initial threshold force for damage initiation and the energy threshold for the reduction in CS.

The main recommendations can be made for future research work in this area:

(I) In the experimental aspect, the method to simulate impact damage with artificial delaminations can be further refined. The refinement should focus on multiple delaminations (more than 3) and their TTT distribution of different delamination sizes, simulating both damage states of thin and thick panels. Therefore not only the shear cone should be simulated but also a small shear cone alongside a large delamination near the mid-plane. The largest delamination could be located at various TTT locations to observe the effect on the compressive response and failure.

(II) The method of simulating impact damage can also incorporate the effect of local curvature change by embedding artificial delaminations and introducing hemispherical-shaped domes in the same panel. The resulting panel could resemble more panels impacted at high IKEs. However this will imply technical problems in the panel manufacturing that needs to be solved in advance.

(III) The analytical model for predicting CSRF is still in embryonic state. There is a large potential to further develop the concept proposed in this thesis. A major issue would be to establish an analytical basis so that the force ratio (initial

274

threshold force to maximum transverse force ratio) can be linked to the reduction in CS.

(IV) The relationship between panel transverse deformation (skewing), delamination size and propagation can be further studied, to find experimental and analytical relationships for a given composite system and panel geometry. This would entail the use of additional SGs in the transverse direction or Moire interferometry. An analytical relationship could be obtained through the combination of deformation simulation of a damaged panel, ILSS distribution and critical energy release rate for fracture.

References

1   Abrate, S, Impact on laminated composite materials, *ASME Appl. Mech. Rev*, 44 (4), 155-190, 1991.

2   Abrate, S, Impact on laminated composites: recent advances, *ASME Appl. Mech. Rev.*, 47 (11), 517-544, 1994.

3   Cantwell, W.J. and J. Morton, The impact resistance of composite materials - a review, *Composites*, 22 (5), 347-362, 1991.

4   Potter, D.S., V. Gupta and S. Hauert, Effects of specimen size and sample aspect ratio on the compressive strength of graphite/epoxy laminates, *Composites Sci. Tech.*, 60 (12-13), 2525-2538, 2000.

5   Potter, D.S., V. Gupta and S. Hauert, Effects of specimen size and sample aspect ratio on the elastic stiffness of graphite/epoxy laminates, *Composites Sci. Tech.*, 60 (12-13), 2517-2524, 2000.

6   Chen, Y., A.K. Srivastava and M.S. Madhukar, Mechanical responses from scale models of carbon fiber reinforced composites, *Design and Manufacturing of Advanced Composites, Conf. Proc. 5th annual ASM/ESD Advanced Composites Conf.*, 89-95, 1989.

7   Gower, M.R.L. and G.D. Sims, Damage tolerance testing of composites: a standard procedure for the introduction of impact damage, *NPL Report CMMT(C) 39*, 1998.

8   Prichard, J.C. and P.J. Hogg, Role of impact damage in post-impact compression testing, *Composites*, 21 (6), 503-511, 1990.

9   Kelkar, A.D., C. Grace and J. Sankar, Threshold damage criteria for thin and thick laminates subjected to low velocity impact loads, *ICCM 12, Paris, France*, No. 355, 1999.

10   Hull, D. and Y.B. Shi, Damage mechanism characterisation in composite damage tolerance investigations, *Composite Structures*, 23, 99-120, 1993.

11   Davies, G.A.O. and X. Zhang, Impact damage prediction in carbon composite structures, *Int. J. Impact Engng.*, 16 (1), 149-170, 1995.

12   Cantwell, W.J. and J. Morton, Geometrical effects in the low velocity impact response of CFRP, *Composite Structures*, 12 (39-59), 1989.

13   Zhou, G. and L.J. Greaves, Damage resistance and tolerance of thick laminated woven roving GFRP plates subjected to low-velocity impact, *Impact Behaviour of Fibre Reinforced Composite Materials and Structures, Ed. By S.R. Reid & G. Zhou*, 133-185, 2000.

14   Clark, G., Modelling of impact damage in composite laminates, *Composites*, 20 (3), 209-214, 1989.

15   Horton, R.E. and J.E. McCarty, Damage tolerance of composites, *Engng. Materials Handbook*, 1, 259-267, 1987.

16   Lesser, A.J. and A.G. Filippov, Mechanisms governing the damage resistance of laminated composites subjected to low-velocity impacts, *Int. J. of Damage Mechanics*, 3, 408-432, 1994.

17   Guynn, E.G. and T.K. O'Brien, The influence of lay-up and thickness on composite impact damage and compression strength, *26th AIAA/ASME/ASCE/AHS Struc., Struc. Dyn. & Mater. Conf.*, AIAA-85-0646, 187-196, 1985.

18   Guan, Z. and C. Yang, Low-velocity impact and damage of composite laminates, *J. Composite Materials*, 36 (7), 851-871, 2002.

19   Cantwell, W.J. and J. Morton, The significance of damage and defects and their detection in composite materials: a review, *J. of Strain Analysis*, 27 (1), 29-42, 1992.

20   Lagace, P.A., J.E. Williamson, P.H.W. Tsang, E. Wolf and S. Thomas, The use of force as a (impact) damage resistance parameter, *7th Tech. Conf. Amer. Soc. of Composites*, 991-1000, 1992.

21   Liu, D., Impact -induced delamination- A view of bending stiffness mismatching, *J. Composite Materials*, 22 (July), 674-692, 1988.

22   Wardle, B.L. and P.A. Lagace, On the use of dent depth as an impact damage metric for thin composites structures, *J. of Reinforced Plastics and Composites*, 16 (12), 1093-1110, 1997.

23   Demuts, E. and R.S. Sandhu, Barely visible damage threshold in a BMI, *AGARD Conf. Proc. 530 Debonding/Delamination of Composites*, 18.1-18.6, 1992.

24   Nettles, A.T. and M.J. Douglas, A comparison of quasi-static indentation testing to low velocity impact testing, *ASTM STP 1416, Composite Materials: Testing,*

Design and Acceptance Criteria, Ed. by A. Zureick and A.T. Nettles, 116-130, 2002.

25   Lin, K.Y. and E.L. Poole, Degradation of the compressive after impact strength of IM7/K3B laminates due to isothermal ageing, *Collection of Tech. Papers - AIAA/ASME/ASCE/AHS/ASC Structures, Structural Dynamics and Materials Conf.*, 3, 2058-2066, 1999.

26   Found, M.S., G.J. Holden and R.N. Swamy, Static indentation and impact behaviour of GRP pultrued sections, *Proc. 1st Int. Conf. on Composite Sci. and Tech. Durban, South Africa*, 131-136, 1996.

27   Hong, S. and D. Liu, On the relationship between impact energy and delamination area, *Experimental Mechanics*, 29 (2), 115-120, 1989.

28   Liu, D., B.B. Raju and X. Dang, Size effects on impact response of composite laminates, *Int. J. Impact Engng.*, 21 (10), 837-854, 1998.

29   Raju, B.B., D. Liu and X. Dang, Thickness effects on impact response of composite laminates, *Proc. 13th Annual Tech. Conf. on Composite Materials, Baltimore, USA*, 1810-1820, 1998.

30   Robinson, P. and G.A.O. Davies, Impactor mass and specimen geometry effects in low velocity impact of laminated composites, *Int. J. Impact Engng.*, 12 (2), 189-207, 1992.

31   Kwon, Y.S. and B.V. Sankar, Indentation-flexure and low velocity impact damage in graphite epoxy laminates, *J. of Composites Tech. And Research*, 15 (2), 101-111, 1993.

32   Zhou, G. and J.C. Lloyd, Effects of indenter nose shape and size on the mechanical behaviour of carbon/epoxy plates, *5th Int. Conf. Deformation and Fracture of Composites, IOM Communications*, 149-157, 1999.

33   Siow, Y.P. and V.P.W. Shim, An experimental study on low velocity impact damage in woven fiber composites, *J. Composite Materials*, 32 (12), 1178-1202, 1998.

34   Delfosse, D. and A. Poursartip, Experimental parameter study of static and dynamic out-of-plane loading of CFRP laminates, *ICCM 10, Vancouver, Canada*, V583-V590, 1995.

35   Dost, E.F., L.B. Ilcewicz, W.B. Avery and B.R. Coxon, Effects of stacking sequence on impact damage resistance and residual strength for quasi-isotropic

laminates, *ASTM STP 1110, Composite Materials: Fatigue and Fracture, Ed. by T.K. O'Brien*, 476-500, 1991.

36 Dost, E.F., W.B. Avery, L.B. Ilcewicz, B.R. Coxon and D.H. Grande, Impact damage resistance of composite fuselage structure, part I, *9th DoD/NASA/FAA Conf. on Fibrous compsites in Structures, Atlantic City*, 1037-1069, 1991.

37 Cartie, D.D.R. and P.E. Irving, Effect of resin and fibre properties on impact and compression after impact of CFRP, *Composites Part A*, 33, 483-493, 2002.

38 Sun, C.T. and S.R. Kelly, Failure in composite angle structures, part I: Initial failure, *J. of Reinforced Plastics and Composites*, 7 (May), 220-232, 1988.

39 Mahfuz, H., M. Saha, R. Biggs and S. Jeelani, Damage Tolerance of Resin Infiltrated Composites Under Low Velocity Impact - Experimental and Numerical Studies, *Key Engng. Materials*, 141-143 (Pt 1), 209-234, 1998.

40 Winkel, J.D. and D.F. Adams, Instrumental drop weight impact testing of cross-ply and fabric composites, *Composites*, 16 (4), 268-278, 1985.

41 Delfosse, D. and A. Poursartip, Energy-based approach to impact damage in CFRP laminates, *Composites Part A*, 28A, 647-655, 1997.

42 Davies, G.A.O., D. Hitchings and J. Wang, Prediction of threshold impact energy for onset of delamination in quasi-isotropic carbon/epoxy composite laminates under low-velocity impact, *Composites Sci. Tech.*, 60 (1), 1-7, 2000.

43 Griffin, C.F., Damage tolerance of toughened resin graphite composites, *ASTM STP 937, Toughened Composites*, 23-33, 1987.

44 Srinivasan, K., W.C. Jackson and J.A. Hinkley, Response of composite materials to low velocity impact, *NASA CR 187624*, 1991.

45 Ambur, D.R. and H.L. Kemmerly, Influence of impactor mass on the damage characteristics and failure strength of laminated composite plates, *Proc. 39th AIAA/ASME/ASCE/AHS/ASC Structures, Structural Dynamics, and Material Conf.*, AIAA Paper 98-1784, 1-9, 1998.

46 Belingardi, G. and R. Vadori, Influence of the laminate thickness in low velocity impact behavior of composite material plate, *Composite Structures*, 61, 27-38, 2003.

47 Bucinell, R.B., R.J. Nuismer and J.L. Koury, Response of composite plates to quasi-static impact events, *ASTM STP 1110, Composite Materials: Fatigue and Fracture, Ed. by T.K. O'Brien*, 3, 528-549, 1991.

48 Prandy, J., J. Boyd, H. Recker and V. Altstaedt, Effect of absorbed energy on the compression after impact (CAI) performance for composite materials, *36th Int. SAMPE Symp.*, 36 (1), 901-911, 1991.

49 Manders, P.W. and W.C. Harris, A parametric study of composite performance in compression-after-impact testing, *SAMPE, J.*, Nov/Dec, 47-51, 1986.

50 Soutis, C. and P.T. Curtis, Prediction of the post-impact compressive strength of CFRP laminated composites, *Composites Sci. Tech.*, 56 (6), 677-684, 1996.

51 Paulisch, D., Damage-growth investigations on modern carbon-fibre reinforced composites, *6th Int. Conf. Deformation and Fracture of Composites, IOM Communications*, 325-334, 2001.

52 Demuts, E., R.S. Sandhu and J.A. Daniels, Post impact compressive strength in composites, *9th DoD/NASA/EAA Conf. on Fibrous compsites in Structures, Atlantic City*, 2, 1097-1104, 1992.

53 Recker, H.G., V. Altstadt, W. Eberle, T. Folda, D. Gerth, W. Heckmann, P. Ittemann, H. Tesch and T. Weber, Toughened thermosets for damage tolerant carbon fibre reinforced composites, *21st Int. SAMPE Tech. Conf.*, 264-274, 1989.

54 Stuart, M. and V. Altstad, Carbon fibre surface treatment and effect on composite damage tolerance performance, *21st Int. SAMPE Tech. Conf.*, 264-274, 1989.

55 Henderson, B. and P. Myler, The influence of diaminodipherylsulphone upon damage tolerance after a barely vissible impact damage (BVID), *6th Int. Conf. Deformation and Fracture of Composites, IOM Communications*, 295-304, 2001.

56 Ying, L., L. Chang, C.C. Xian, Z.Y. Ning and Y. Xu, Investigation of impact residual strength of woven and non-woven composites, *ICCM 13, Beijing, China*, ID-1171, 2001.

57 Gottesman, T., S. Girshovich, E. Drukker, N. Sela and J. Loy, Residual strength of impacted composites: analysis and tests, *J. of Composites Technology & Research*, 16 (3), 244-255, 1994.

58 Kohndker, O.A., I. Herszberg and H. Hamada, Measurements and prediction of the compression-after-impact strength of glass knitted textile composites, *Composites Part A*, 35, 145-157, 2004.

59 Greenhalgh, E. and M. Hiley, The assessment of novel materials and processes for the impact tolerant design of stiffened composite aerospace structures, *Composites Part A*, 34, 151-161, 2003.

60   Yang, G., C.T. Lim and S. Ramakrishna, Low-velocity impact damage of knitted carbon fabric/epoxy composites, *ICCM 13, Beijing, China*, ID-1058, 2001.

61   Shahid, I., F.-K. Chang and B.M. Shah, Impact damage resistance and damage tolerance of composite with progressive damage, *37th AIAA/ASME/ASCE/AHS SDM Conf, Salt Lake City*, 2, 766-775, 1996.

62   Gong, J.C. and B.V. Sankar, Impact properties of three-dimensional braided graphite/epoxy composites, *J. Composite Materials*, 25, 715-731, 1991.

63   Steeves, C.A. and N.A. Fleck, Z-pinned composite laminates: knockdown in compressive strength, *5th Int. Conf. Deformation and Fracture of Composites, ImechE*, 53-59, 1999.

64   Cartie, D.D.R. and I.K. Partridge, Z-pinned composite laminates: improvements in delamination resistance, *5th Int. Conf. Deformation and Fracture of Composites, ImechE*, 53-59, 1999.

65   Cartie, D.D.R. and I.K. Partridge, Delamination behaviour of Z-pinned laminates, *Fracture of polymers, composites and adhesives, ESIS publ. 27, Ed. by J.G. Williams and A. Pavan*, 27-36, 2000.

66   Larsson, F., Damage tolerance of a stitched carbon/epoxy laminate, *Composites Part A*, 28 (11), 923-934, 1997.

67   Farley, G.L. and L.C. Dickinson, Removal of surface loop from stitched composites can improve compression and compression-after-impact strengths, *J. Reinforced Plastics and Composites*, 11, 633-642, 1992.

68   Farley, G.L., B.T. Smith and J. Maiden, Compression response of thick layer composite laminates with through-the-thickness reinforcement, *J. Reinforced Plastics and Composites*, 11, 787-810, 1992.

69   Hosur, M.V., M. Ayda, U.K. Vaidya, A. Mayer and S. Jeelani, Characterization of affordable stitched plain wave carbon/epoxy composites under impact loading, *ICCM 13, Beijing, China*, ID-1520, 2001.

70   Duarte, A., I. Herszberg and R. Paton, Impact resistance and tolerance of interleaved tape laminates, *Composite Structures*, 47 (1-4), 753-758, 1999.

71   Duarte, A., I. Herszberg and R. Paton, Impact resistance and tolerance of interleaved RTM laminates, *ICCM 12, Paris, France*, No. 1032, 1999.

72 Park, R. and J. Jang, Effect of stacking sequence on the compressive performance of impacted aramid fiber/glass fiber hybrid composite, *Polymer Composites*, 21 (2), 231-237, 2000.

73 Hitchen, S.A. and R.M.J. Kemp, Development of novel cost effective hybrid ply carbon-fibre composites, *Composites Sci. Tech.*, 56 (9), 1047-1054, 1996.

74 Krober, I., Effect of impacts on CFRP structures, results of a comprehensive test program for practical use, *AGARD Conf. Proc. 530 Debonding/Delamination of Composites*, 29.1-29.6, 1992.

75 Nyman, T., A. Bredberg, and J. Schon, Equivalent damage and residual strength for impact damage composite structures, *Proc. 13th Annual Tech. Conf. on Composite Materials, Baltimore, USA*, 1759-1775, 1998.

76 Hosur, M.V., C.R.L. Murthy and T.S. Ramamurthy, Residual compressive strength of quasi-isotropic CFRP laminates subjected to low-velocity impact, *Proc. 13th Annual Tech. Conf. on Composite Materials, Baltimore, USA*, 842-853, 1998.

77 Wang, J, Prediction of post-impact compressive strength of composite laminates using an inhomogeneity model, *J. Composite Materials*, 33 (24), 2226-2247, 1999.

78 Davies, G.A.O., D. Hitchings and G. Zhou, Impact damage and residual strengths of woven fabric glass/polyester laminates, *Composites Part A*, 27A (7), 1147-1156, 1996.

79 Zhou, G., Effect of impact damage on residual compressive strength of glass-fibre reinforced polyester laminates, *Composite Structures*, 35, 171-181, 1996.

80 Avva, V.S., Effect of specimen size on the buckling behavior of laminated composites subjected to low-velocity impact, *ASTM STP 808, Compression Testing of Homogeneous Materials and Composites*, 140-154, 1983.

81 Tratt, M.D., Analysis of delamination growth in compressively loaded composite laminates, *ASTM STP 1110, Composite Materials: Fatigue and Fracture, Ed. by T.K. O'Brien*, 3, 359-372, 1991.

82 Yeh, M and C. Tan, Buckling of elliptically delaminated composite plates, *J. Composite Materials*, 28 (1), 36-52, 1994.

83   Cairns, D.S., P.J. Minguet and M.G. Abdallah, Theoretical and experimental response of composite laminates with delamination loaded in compression, *Composite Structures*, 27 (4), 431-437, 1994.

84   Suemasu, H., T. Kumagai and K. Gozu, Compressive behaviour of rectangular composite laminates with multiple circular delaminations, *Proc. 37th AIAA/ASME/ASCE/AHS Structures, Structural Dynamics & Materials Conf.*, 2552-2559, 1996.

85   Davidson, B.D., On modelling the residual strength of impact damaged compression loaded laminates, *21st Int. SAMPE Tech. Conf.*, 109-119, 1989.

86   Davidson, B.D., Delamination buckling: theory and experiment, *J. Composite Materials*, 25 (10), 1351-1378, 1991.

87   Suemasu, H. and H. Wakabayashi, Failure mechanism of composite laminates with different size multiple delaminations subjected to compressive load, *Collection of Tech. Papers - 41st AIAA/ASME/ASCE/AHS/ASC Structures, Structural Dynamics and Materials Conference*, 1 (1), 529-538, 2000.

88   Suemasu, H., Y. Osada and H. Wakabayashi, Compressive behavior of composite laminates with different size multiple delaminations, *ICCM 13, Beijing, China*, ID1654, 2001.

89   Ishikawa, T., S. Sugimoto, M. Matsushima and Y. Y. Hayashi, Some experimental findings in compression-after-impact (CAI) tests of CF/PEEK (APC-2) and conventional CF/Epoxy flat plates, *Composites Sci. Tech.*, 55, 349-363, 1995.

90   Laman, S.A., M.R. Groleau and M. Vedula, Use of controlled interply delaminations to study the damage tolerance of composites, *24th International SAMPE Tech. Conf.*, 821-833, 1992.

91   Davidson, B.D., Experimental investigation of delamination buckling and growth, *31st AIAA/ASME/ASCE/AHS/ASC Structures, Structural Dynamics and Materials Conf.*, 2, 1218-1226, 1990.

92   Nilsson, K.-F., L.E. Asp, J.E. Alpman and L. Nystedt, Delamination buckling and growth for delaminations at different depths in a slender composite panel, *Int. J. Solids Struct.*, 38, 3039-3071, 2001.

93   Asp, L.E., S. Nilsson and S. Singh, An experimental investigation of the influence of delamination growth on the residual strength of impacted laminates, *Composites Part A*, 32, 1229-1235, 2001.

94   Chai, H., W.G. Knauss and C.D. Babcock, Observation of damage growth in compressively loaded laminates, *Experimental Mechanics*, 23, 329-337, 1983.

95   Guedra-Degeorges, D., S. Maison, D. Trallero and J.L. Peitiniot, Buckling and post-buckling behaviour of a delamination in a carbon-epoxy laminated structure: experiments and modelling, *AGARD Conf. Proc. 530 Debonding/Delamination of Composites*, 7.1-7.11, 1992.

96   Reeder, J.R, P.B Chanchu, K. Song and D.R. Ambur, Postbuckling and growth of delaminations in composite plates subjected to axial compression, *AIAA Paper No. 2002-1746*, 1-10, 2002.

97   Short, G.J., F.J. Guild and M.J. Pavier, The effect of delamination geometry on the buckling and failure of GFRP plates, *ICCM 12, Paris, France*, No. 991, 1999.

98   Short, G.J., F.J. Guild and M.J. Pavier, The effect of delamination geometry on the compressive failure of composite laminates, *Composites Sci. Tech.*, 61 (14), 2075-2086, 2001.

99   Puhui, C., S. Zhen and W.J. Yang, A new method for compression after impact strength prediciton of composite laminates, *J. Composite Materials*, 36 (5), 589-610, 2002.

100   Bibo, G.A., P.J. Hogg and M. Kemp, High-temperature damage tolerance of carbon fibre-reinforced plastics: 2. Post-impact compression characteristics, *Composites Part A*, 26 (2), 91-102, 1995.

101   Bibo, G.A., D. Leicy, P.J. Hogg and M. Kemp, High-temperature damage tolerance of carbon fibre-reinforced plastics, part 1: impact characteristics, *Composites*, 25 (6), 414-424, 1994.

102   Brandt, J. and J. Warnecke, Influence of material parameters on the impact performance of carbon-fibre-reinforced polymers, *7th Int. Conf. on High Tech - The Way into the Nineties, Ed. by K. Brunsch, H.O. Golden and C.M. Herket*, 35, 251-260, 1986.

103   Qi, B. and I. Herszberg, An engineering approach for predicting residual strength of carbon/epoxy laminates after impact and hygrothermal cycling, *Composite Structures*, 47 (1-4), 483-490, 1999.

104 Lloyd, J.C., Impact damage and damage tolerance of fibre reinforced advanced composite laminate structures, *PhD thesis, Loughborough University*, 2002.

105 Incropera, F. P. and D. P. DeWitt, Fundamentals of heat and mass transfer, 5th ed.,, 239-324, 2002.

106 Scott, R.F., S. Lee, C. Poon and P.C. Gaudert, Impact and compression response of composite materials containing fortifiers, *Polym. Engng. and Sci.*, 31 (18), 1310-1315, 1991.

107 Ruhala, L.A. and R.S. Engel, An investigation of the effects of fiber volume fractionon the impact properties of fiber reinforced composite laminated plates, *Proc. 13th Annual Tech. Conf. on Composite Materials, Baltimore, USA*, 116-127, 1998.

108 Sim, L.M., Smart composite aeronautical structures with embedded optical fibres for damage detection - Fourth six month report, *Internal communication*, 65-71, 2001.

109 Timoshenko, S. and S. Woinowsky-Krieger, Theory of plates and shells, *2nd Edition, McGraw Hill Publishing Company, New York, USA*, 1959.

110 Shivakumar, K.N., W. Elber and W. Illg, Prediction of impact force and duration due to low-velocity impact on circular composite laminates, *J. Appl. Mech.*, 52, 674-680, 1985.

111 Caprino, G., A. Langella and V. Lopresto, Elastic behaviour of circular composite plates transversely loaded at the centre, *Composites Part A*, 33, 1191-1197, 2002.

112 Caprino, G., A. Langella and V. Lopresto, Prediciton of the first failure energy of circular carbon fibre reinforced plastic plates loaded at the centre, *Composites Part A*, 34, 349-357, 2003.

113 Caprino, G., A. Langella and V. Lopresto, Indentation and penetration of carbon fibre reinforced plastic laminates, *Composites Part B*, 34, 319-325, 2003.

114 Zhou, G., Static behaviour and damage of thick composite laminates, *Composite Structures*, 36 (1-2), 13-22, 1996.

115 Fitcher, W.B., Some solutions for the large delfections of uniformly loaded circular membranes, *NASA technical Paper 3658*, 1-20, 1997.

116 Zhang, Y., S. Wang and B. Petersson, Large deflection analysis of composite laminates, *J. Materials Processing Tech.*, 138, 34-40, 2003.

117 Lekhnitskii, S.G., S.W. Tsai and T. Cheron, Bending of homogeneous elliptic circular plates clamped along the edge, *Anisotropic Plates, Gordon and Breach Sci. Publ., New York, USA*, 365-369, 1968.

118 Lukasiewicz, S.A., Introduction of concentrated loads in plates and shells, *Progress in Aerospace Science*, 17 (2), 109-146, 1976.

119 Gao, S.-L and J.-K. Kim, Cooling rate influences in carbon fibre/PEEK composites. Part III: impact damage performance, *Composites Part A*, 32, 775-785, 2001.

120 Timoshenko, S. and J.N. Goodier, Theory of Elasticity, *3rd Edition, McGraw Hill Publishing Company, New York, USA*, 1970.

121 Stone, M.A. and H.D. Chandler, Errors in double sine series solutions for simply supported symmetrically laminated plates, *Int. J. Mech. Sci.*, 38 (5), 517-526, 1996.

122 Dost, E.F., S.R. Finn, J.J. Stevens, K.Y. Lin and C.E. Fitch, Experimental investigations into composite fuselage impact damage resistance and post-impact compression behavior, *37th Int. SAMPE Symp.*, 1199-1212, 1992.

123 Starnes, J.H., M.D. Rhodes and J.G. Williams, Effect of impact damage and holes on the compressive strength of a graphite/epoxy laminate, *ASTM STP 696, Non-destructive Evaluation and Flaw Critically for Composite Materials*, 145-171, 1979.

124 Soutis, C., N.A. Fleck and P.A. Smith, Failure prediction technique for compression loaded carbon fibre-epoxy laminate with open holes, *J. Composite Materials*, 25, 1476-1498, 1991.

125 Heslehurst, R.B., J.P. Baird and H.M. Williamson, Location and direction of the propagation of an existing delamination in composite panels, *J. Advanced Materials*, 30 (3), 38-43, 1998.

126 Vedula, M., W.M. Lee, E.E. Benedetto and M.R. Groleau, Screening test for compression after impact strength evaluation of composites, *Proc. 7th Conf. Amer. Soc. Comp.*, 804-814, 1992.

127 Zhou, G., The use of experimentally-determined impact force as a damage measure in impact damage resistance and tolerance of composite structures, *Composite Structures*, 42 (4), 375-382, 1998.

128 Reid, S.R. and G. Zhou, Impact behaviour of fibre-reinforced composite materials and structures, *Impact behaviour of fibre-reinforced composite materials and structures, Woodhead Publishing Ltd, Cambridge, UK & CRC Press, Florida, USA*, 2000.

129 Guy, T.A. and P.A. Lagace, Compressive residual strength of graphite/epoxy laminates after impact, *9th DoD/NASA/FAA Conf. on Fibrous Composites in Structures, Atlantic City*, 1, 253-274, 1992.

130 Chai, H., C.D. Babcock and W.G. Knauss, One dimensional modelling of failure in laminated plates by delamination opening, *Int. J. Solids Struct.*, 17 (11), 1069-1083, 1981.

131 Simitses, G.J., S. Sallam and W.L. Yin, Effect of delamination of axially loaded homogeneous laminated plates, *AIAA J.*, 23 (9), 1437-1444, 1985.

132 Yin, W.L., S. Sallam and G.J. Simitses, Ultimate axial load capacity of a delaminated beam plate, *AIAA J.*, 24 (1), 123-128, 1986.

133 Simitses, G.J., Delamination buckling of flat composites, *Buckling and Postbuckling of Composites plates, ed. by G.J. Turvey and I.H. Mashall*, 299-328, 1995.

134 Sallam, S. and G.J. Simitses, Delamination buckling and growth of flat, cross-ply laminates, *Composite Structures*, 4, 361-381, 1985.

135 Williams, J.G., On the calculation of energy release rates for cracked laminates, *Int. J. of Fracture*, 36, 101-119, 1988.

136 Zhou, G. and J.C. Lloyd, Investigation of the compressive behaviour of thin carbon/epoxy panels conatining artificial delaminations, *Proc. 6th Int. Conf. Deformation and Fracture of Composites, IOM Communications*, 463-472, 2001.

137 Zhou, G., Compressive behaviour of large undamaged and damaged thick laminated panels, *Composite Structures*, 38 (1-4), 589-597, 1997.

138 Yin, W.-L. and Z. Fei, Buckling load of a circular plate with a concentric delamination, *Mechanics Research Communications*, 11, 337-344, 1984.

139 Yin, W.-L. and Z. Fei, Delamination buckling and growth in a clamped circular plate, *AIAA J.*, 26 (4), 438-445, 1988.

140 Chai, H. and C.D. Babcock, Two-dimensional modelling of compressive failure in delaminated laminates, *J. Composite Materials*, 19, 67-98, 1985.

141 Webster, J.D., Flow criticality of circular disbond defects in compressive laminates-1980-81 Interim. Report, *NASA CR 164830*, 1981.

142 Shivakumar, K.N. and J.D. Whitcomb, Buckling of a sublaminate in a quasi-isotropic composite laminate, *J. Composite Materials*, 19, 2-18, 1985.

143 Ilcewicz, L., E. Dost, and R. Coggeshall, A model for compression after impact strength evaluation, *21st Int. SAMPE Tech. Conf.*, 264-274, 1989.

144 Dost, E.F., W.B. Avery, G.D. Swanson and K.Y. Lin, Developments in impact damage modeling for laminated composite structures, *1st Nasa Conf. on Advanced Composites Tech.*, 721-736, 1991.

145 Xiong, Y., C. Poon, P.V. Straznicky and H. Vietinghoff, A prediction method for the compressive strength of impact damaged composite laminates, *Composite Structures*, 30 (4), 357-367, 1995.

146 Wang, J., J.H. Andreasen and B.L. Karihaloo, The solution of an inhomogeneity in a finite plane region and its application to comopsite materials, *Composites Sci. Tech.*, 60, 75-82, 2000.

147 Sjogren, A., A. Krasnikovs and J. Varna, Experimental determination of elastic properties of impact damage in carbon fibre/epoxy laminates, *Composites Part A*, 32, 1237-1242, 2001.

148 Shen, Z., P. Chen, X. Tang, Y. Chan, S. Yang, F. Liu, New progress on prediction methodology for residual strength of damaged composite laminates in ASRI, *ICCM 13, Beijing, China*, ID-1085, 2001.

149 Kassapoglou, C., Compression strength of composite sandwich structures after barely visible impact damage, *J. Composite Technol. Res.*, 18 (4), 274-284, 1996.

150 Long, Z.Z., C. Xiaoquan and Y. Xiaosu, An investigation on the impact resistance and residual compressive strength of composite materials, *ICCM 13, Beijing, China*, ID-1115f, 2001.

151 Kassapoglou, C., Buckling, post-buckling and failure of elliptical delaminations in laminates under compression, *Composite Structures*, 9, 139-159, 1988.

152 Papanicolaou, G.C., A.M. Blanas, A.V. Pournaras and C.D. Stavropoulos, Impact Damage and Residual Strength of FRP Composites, *Key Engng. Materials*, 141-143 (Pt 1), 127-148, 1998.

153 Stravopoulos, C. and G.C. Papanicolaou, Prediction of the residual compressive strength in laminated composites after impact induced damage, *2nd Int. Conf. Deformation and Fracture of Composites, Conf. Proc.*, 21.1-21.10, 1993.

154 Caprino, G., Residual strength prediction of impacted CFRP laminates, *J. Composite Materials*, 18 (6), 508-518, 1984.

155 Kan, H.P., Enhanced reliability prediction methodology for impact damaged composite structures, *FAA report No. DOT/FAA/AR-97/79*, 1-42, 1998.

156 Zhou, G., Characteristics of impact energy absorption during damage development in laminated composites, *Proc. 4th Int. Conf. on Deformation and Fracture of Composites, Manchester, UK*, 55-67, 1997.

157 Lee, S.W.R. and C.T. Sun, On the apparent bending isotropy in clamped elliptic composite laminates, *J. Composite Materials*, 29 (12), 1601-1620, 1995.

158 Young, W.C., Roark's formulas for stress and strain, 6th edition, 1989.

159 Liu, D. and X. Dang, Testing and simulation of laminated composites subjected to impact loading, *ASTM STP 1330. Composite Materials: Fatigue and Fracutre, 7th Vol.*, 273-284, 1998.

160 Qian, Y., S.R. Swanson, R.J. Nuismer and R.B. Bucinell, An experimental study of scaling rules for impact damage in fiber composites, *J. Composite Materials*, 24, 559-570, 1990.

161 Soutis, C., F.C. Smith and F.L. Matthews, Predicting the compressive engineering performance of carbon fibre-reinforced plastics, *Composites Part A*, 31 (6), 531-536, 2000.

162 Zhang, X., G.A.O. Davies and D. Hitchings, Impact damage with compressive pre-load and post-impact compression of carbon composite plates, *Int. J. of Impact Engng.*, 22 (5), 485-509, 1999.

163 Ishai, O. and A. Shragai, Effect of impact loading on damage and residual compressive strength of CFRP laminated beams, *Composite Structures*, 14 (4), 319-337, 1990.

164 Aramah, S.E. and P.J. Hogg, Compression testing of glass epoxy non-crimp fabrics containing elastic inserts, *ICCM 13, Beijing, China,*, ID-1608, 2001.

165 Ashton, H.R., Damage tolerance and durability testing for F/A-18 E/F composite materials structures, *37th Structures, Structural Dynamics Materials Conf., AIAA, Part I*, 1, 1-13, 1996.

166 Zhang, B., X. Chen and P. Li, Discussion of Compression strength after impact (CAI) of BMI/carbon fiber composites, *J. of Advanced Materials*, 33 (1), 13-16, 2001.

167 Shuart, M.J. and J.G. Williams, Compression failure characteristics of +/-45 dominated laminates with a circular hole or impact damage, *AIAA Paper No. 84-0848*, 399-409, 1984.

168 Baker, D, Mechanical property characterisation and impact resistance of selected graphite/PEEK composite materials, *J. of the American Helicopter Soc.*, 39 (1), 24-30, 1994.

169 Dow, M.B. and D.L. Smith, Damage-tolerant composite materials produced by stitching carbon fabrics, *21st Int. SAMPE Tech. Conf.*, 595-605, 1989.

170 Ishikawa, T., E. Hara, M. Matsushima and G. G. Ben, Examination of compression after impact (CAI) test methods and relationships with open hole compression (OHC), *ICCM 13, Beijing, China*, ID-1421, 2001.

171 Reddy, A.D., L.W. Rehfield and R.S. Haag, Influence of prescribed delaminations on stiffness-controlled behavior of composite laminates, *ASTM STP 836, Symp. on Effects of Defects on Composite Materials*, 71-83, 1984.

Appendix A

Panel dimensions were measured by using a digital calliper at several locations on panels.

A.1 Control panels

Coordinates		Thickness in mm					
X	Y	Control 0	Control 3	Control 2	Control holes 1 [a]	Control holes 2 [a]	Control holes 3 [a]
0	25	4.07	3.94	4.44	3.97	3.94	3.98
0	50	4.07	3.88	4.44	3.97	3.99	4.03
0	75	4.04	3.87	4.41	3.98	4.00	4.00
0	100	4.05	3.87	4.41	3.98	3.99	3.96
0	125	4.00	3.83	4.47	3.97	3.98	3.92
100	25	4.10	3.94	4.43	4.00	3.94	3.98
100	50	4.10	3.86	4.44	4.02	3.99	4.00
100	75	4.09	3.88	4.45	4.01	3.99	4.00
100	100	4.08	3.92	4.45	4.01	4.00	4.00
100	125	4.06	3.89	4.47	3.97	3.98	3.91
Average		4.07	3.89	4.44	3.99	3.98	3.98
Standard dev		0.03	0.04	0.02	0.02	0.02	0.04

Coordinates		Length in mm					
X	Y	Control 0	Control 3	Control 2	Control holes 1 [a]	Control holes 2 [a]	Control holes 3 [a]
0	-	146.73	148.89	NA	149.64	151.83	151.36
25	-	146.76	148.92	NA	149.64	151.81	151.26
50	-	146.76	148.87	NA	149.66	151.80	151.16
75	-	146.77	148.87	NA	149.63	151.81	151.11
100	-	146.80	148.94	NA	149.65	151.78	151.04
Average		146.76	148.90	NA	149.64	151.81	151.19
Standard dev		0.03	0.03	NA	0.01	0.02	0.13

Coordinates		Width in mm					
X	Y	Control 0	Control 3	Control 2	Control holes 1 [a]	Control holes 2 [a]	Control holes 3 [a]
-	25	99.92	100.44	99.55	98.80	98.76	99.12
-	50	99.93	100.27	99.66	98.76	98.80	99.15
-	75	99.94	100.29	99.65	98.63	98.75	98.98
-	100	99.95	100.23	99.67	98.47	98.60	98.94
-	125	99.95	100.21	99.70	98.50	98.61	98.96
Average		99.94	100.29	99.65	98.63	98.70	99.03
Standard dev		0.01	0.09	0.06	0.15	0.09	0.10

[a] Panels were made of T300/epoxy composite system rather than the usual T700/epoxy

A.2 Panels with single delamination

Coordinates		Thickness in mm					
X	Y	C20 MS	C40 MS	C60 MS	C20 QS	C40 QS	C60 QS
0	25	3.79	4.10	4.09	4.05	4.23	4.30
0	50	3.79	4.09	4.06	4.08	4.16	4.21
0	75	3.78	4.12	4.08	4.17	4.20	4.20
0	100	3.78	4.14	4.08	4.16	4.21	4.19
0	125	3.78	4.17	4.09	4.20	4.19	4.18
100	25	3.84	4.07	4.10	4.08	4.22	4.13
100	50	3.86	4.08	4.13	4.10	4.23	4.15
100	75	3.86	4.10	4.15	4.15	4.20	4.14
100	100	3.84	4.12	4.14	4.18	4.21	4.12
100	125	3.83	4.13	4.14	4.22	4.20	4.09
Average		3.82	4.11	4.11	4.14	4.21	4.17
Standard dev		0.03	0.03	0.03	0.06	0.02	0.06

Coordinates		Length in mm					
X	Y	C20 MS	C40 MS	C60 MS	C20 QS	C40 QS	C60 QS
0	-	145.16	147.54	147.57	147.64	149.14	147.42
25	-	145.18	147.58	147.61	147.63	149.14	147.44
50	-	145.18	147.56	147.60	147.64	149.13	147.43
75	-	145.17	147.57	147.57	147.63	149.15	147.44
100	-	145.14	147.55	147.56	147.63	149.15	147.43
Average		145.17	147.56	147.58	147.63	149.14	147.43
Standard dev		0.02	0.02	0.02	0.01	0.01	0.01

Coordinates		Width in mm					
X	Y	C20 MS	C40 MS	C60 MS	C20 QS	C40 QS	C60 QS
-	25	94.44	98.74	99.41	99.20	99.39	99.56
-	50	94.43	98.64	99.42	99.18	99.35	99.55
-	75	94.43	98.57	99.41	99.19	99.35	99.57
-	100	94.38	98.59	99.42	99.20	99.33	99.52
-	125	94.37	98.61	99.41	99.18	99.34	99.47
Average		94.41	98.63	99.41	99.19	99.35	99.53
Standard dev		0.03	0.07	0.01	0.01	0.02	0.04

A.3 Panels with multiple (×3) delaminations

Coordinates		Thickness in mm					
X	Y	C20x3S	C40x3S	C60x3S	C20x3AS	C40x3AS	C60x3AS
0	25	3.93	3.87	3.96	3.83	3.92	3.80
0	50	3.90	3.88	3.99	3.84	3.94	3.80
0	75	3.90	3.90	3.99	3.85	3.92	3.80
0	100	3.91	3.90	3.99	3.84	3.91	3.83
0	125	3.94	3.91	3.94	3.86	3.91	3.88
100	25	3.95	3.95	3.88	3.82	3.92	3.82
100	50	3.95	3.97	3.89	3.84	3.90	3.82
100	75	3.95	3.97	3.88	3.85	3.94	3.83
100	100	3.95	3.99	3.88	3.85	3.91	3.84
100	125	3.95	3.98	3.88	3.86	3.91	3.84
Average		3.93	3.93	3.93	3.84	3.92	3.83
Standard dev		0.02	0.04	0.05	0.01	0.01	0.02

Coordinates		Length in mm					
X	Y	C20x3S	C40x3S	C60x3S	C20x3AS	C40x3AS	C60x3AS
0	-	149.00	148.75	148.57	148.18	148.84	147.62
25	-	148.98	148.74	148.57	148.20	148.86	147.67
50	-	148.96	148.75	148.58	148.20	148.86	147.65
75	-	148.97	148.75	148.58	148.21	148.87	147.67
100	-	148.96	148.75	148.60	148.22	148.87	147.68
Average		148.97	148.75	148.58	148.20	148.86	147.66
Standard dev		0.02	0.00	0.01	0.01	0.01	0.02

Coordinates		Width in mm					
X	Y	C20x3S	C40x3S	C60x3S	C20x3AS	C40x3AS	C60x3AS
-	0	-	-	-	-	-	-
-	25	98.52	100.67	100.42	100.23	99.92	100.27
-	50	98.48	100.70	100.26	100.13	99.93	100.22
-	75	98.43	100.69	100.23	100.20	99.96	100.22
-	100	98.44	100.66	100.15	100.21	99.99	100.18
-	125	98.81	100.62	100.25	100.31	100.01	100.15
-	150	-	-	-	-	-	-
Average		98.54	100.67	100.26	100.22	99.96	100.21
Standard dev		0.16	0.03	0.10	0.06	0.04	0.05

A.4 Panels with local change of geometry

Coordinates		Thickness in mm				
X	Y	CD20 CC	CD40 CC	CD60 CC	CD40 DC	CD60 DC
0	25	3.96	3.88	3.66	3.83	3.80
0	50	3.95	3.99	3.75	3.91	3.86
0	75	4.02	4.03	3.77	3.97	3.87
0	100	3.99	4.00	3.74	3.92	3.85
0	125	3.87	3.93	3.66	3.86	3.73
100	25	3.95	3.82	3.61	3.82	3.84
100	50	4.04	3.93	3.76	3.89	3.99
100	75	4.10	3.98	3.81	3.90	4.00
100	100	4.08	3.89	3.84	3.88	3.96
100	125	3.97	3.71	3.87	3.80	3.84
Average		3.99	3.92	3.75	3.88	3.87
Standard dev		0.07	0.10	0.08	0.05	0.09

Coordinates		Length in mm				
X	Y	CD20 CC	CD40 CC	CD60 CC	CD40 DC	CD60 DC
0	-	149.12	149.18	149.30	149.24	149.99
25	-	149.10	149.11	149.13	149.25	150.01
50	-	149.09	149.04	149.01	149.23	150.01
75	-	149.06	149.00	148.93	149.16	150.07
100	-	149.05	149.04	148.80	149.17	150.15
Average		149.08	149.07	149.03	149.21	150.05
Standard dev		0.03	0.07	0.19	0.04	0.07

Coordinates		Width in mm				
X	Y	CD20 CC	CD40 CC	CD60 CC	CD40 DC	CD60 DC
-	25	99.72	99.53	99.84	99.80	100.07
-	50	99.87	99.54	99.85	99.80	100.02
-	75	99.88	99.47	99.88	99.75	99.72
-	100	99.88	99.42	99.92	99.89	100.01
-	125	99.60	99.50	99.93	100.09	100.07
Average		99.79	99.49	99.88	99.87	99.98
Standard dev		0.13	0.05	0.04	0.14	0.15

A.5 Panels with impact-induced damage

Coordinates		Thickness in mm			
X	Y	4I0.5m	4I1.0m	4I1.5m	4I 2.52m
0	25	4.09	4.09	3.95	4.27
0	50	4.13	4.11	4.00	4.30
0	75	4.15	4.16	4.05	4.34
0	100	4.18	4.19	4.07	4.32
0	125	4.19	4.18	4.07	4.32
100	25	4.00	3.93	4.08	4.07
100	50	4.03	4.02	4.12	4.13
100	75	4.03	4.02	4.14	4.14
100	100	4.06	4.05	4.17	4.14
100	125	4.07	4.07	4.18	4.16
Average		4.09	4.08	4.08	4.22
Standard dev		0.07	0.08	0.07	0.10

Coordinates		Length in mm			
X	Y	4I0.5m	4I1.0m	4I1.5m	4I 2.52m
0	-	149.32	146.21	147.93	149.26
25	-	149.35	146.21	147.92	149.23
50	-	149.33	146.21	147.92	149.24
75	-	149.30	146.21	147.90	149.27
100	-	149.30	146.20	147.90	149.28
Average		149.32	146.21	147.91	149.26
Standard dev		0.02	0.00	0.01	0.02

Coordinates		Width in mm			
X	Y	4I0.5m	4I1.0m	4I1.5m	4I 2.52m
-	25	100.00	100.50	100.13	99.99
-	50	100.02	100.49	100.07	99.69
-	75	100.90	100.47	100.30	100.02
-	100	99.92	100.49	100.26	100.05
-	125	100.08	100.50	100.14	100.04
Average		100.18	100.49	100.18	99.96
Standard dev		0.40	0.01	0.10	0.15

A.6 Panels with quasi-static transverse loading damage

Coordinates		Thickness in mm			
X	Y	QSIF	QSIFHWii	QSIH	QSIHHW
0	25	4.28	4.14	4.12	4.16
0	50	4.32	4.19	4.16	4.14
0	75	4.36	4.25	4.22	4.12
0	100	4.35	4.31	4.19	4.11
0	125	4.36	4.33	4.18	4.10
100	25	4.14	4.17	4.33	4.33
100	50	4.20	4.17	4.30	4.30
100	75	4.34	4.20	4.34	4.26
100	100	4.33	4.23	4.31	4.24
100	125	4.28	4.23	4.35	4.21
Average		4.30	4.22	4.25	4.20
Standard dev		0.07	0.06	0.08	0.08

Coordinates		Length in mm			
X	Y	QSIF	QSIFHWii	QSIH	QSIHHW
0	-	148.24	149.19	148.68	147.42
25	-	148.16	149.19	148.69	147.46
50	-	148.19	149.20	148.67	147.45
75	-	148.16	149.22	148.68	147.47
100	-	148.18	149.21	148.67	147.46
Average		148.19	149.20	148.68	147.45
Standard dev		0.03	0.01	0.01	0.02

Coordinates		Width in mm			
X	Y	QSIF	QSIFHWii	QSIH	QSIHHW
-	25	100.68	101.12	100.79	100.69
-	50	100.31	100.81	100.51	100.59
-	75	100.50	100.97	100.47	101.02
-	100	100.46	100.62	100.19	100.83
-	125	100.74	100.86	100.29	101.20
Average		100.54	100.88	100.45	100.87
Standard dev		0.17	0.19	0.23	0.25

A.7 Panels with open holes

Coordinates		Thickness in mm		
X	Y	HOLE 20	HOLE 40	HOLE 60
0	25	3.84	3.97	3.91
0	50	3.85	3.95	3.78
0	75	3.83	3.94	3.80
0	100	3.82	3.93	3.80
0	125	3.76	3.92	3.82
100	25	3.97	3.99	4.05
100	50	3.97	4.00	4.06
100	75	3.96	3.99	4.01
100	100	3.94	3.97	3.97
100	125	3.92	3.95	4.00
Average		3.89	3.96	3.92
Standard dev		0.07	0.03	0.11

Coordinates		Length in mm		
X	Y	HOLE 20	HOLE 40	HOLE 60
0	-	149.70	149.36	149.48
25	-	149.68	149.37	149.45
50	-	149.77	149.33	149.45
75	-	149.88	149.35	149.46
100	-	149.94	149.40	149.46
Average		149.79	149.36	149.46
Standard dev		0.11	0.03	0.01

Coordinates		Width in mm		
X	Y	HOLE 20	HOLE 40	HOLE 60
-	25	99.42	100.58	100.22
-	50	99.49	100.62	100.25
-	75	99.41	100.61	100.31
-	100	99.48	100.64	100.42
-	125	99.52	100.60	100.71
Average		99.46	100.61	100.38
Standard dev		0.05	0.02	0.20

A.8 Repeated tests

Coordinates		Thickness in mm			
X	Y	C20MSii	C20x3Sii	CD60CCii	CD40CDii
0	25	3.97	4.00	3.69	3.78
0	50	3.92	3.96	3.70	3.88
0	75	3.95	3.98	3.74	3.88
0	100	3.93	4.03	3.80	3.88
0	125	3.94	4.05	3.75	3.84
100	25	3.91	3.90	3.48	3.81
100	50	3.93	3.91	3.65	3.89
100	75	3.92	3.91	3.64	3.90
100	100	3.95	3.94	3.61	3.89
100	125	3.95	3.96	3.57	3.82
Average		3.94	3.96	3.66	3.86
Standard dev		0.02	0.05	0.09	0.04

Coordinates		Length in mm			
X	Y	C20MSii	C20x3Sii	CD60CCii	CD40CDii
0	-	149.72	149.73	149.21	149.09
25	-	149.73	149.72	149.20	149.10
50	-	149.71	149.72	149.21	149.09
75	-	149.72	149.71	149.21	149.10
100	-	149.73	149.71	149.26	149.12
Average		149.72	149.72	149.22	149.10
Standard dev		0.01	0.01	0.02	0.01

Coordinates		Width in mm			
X	Y	C20MSii	C20x3Sii	CD60CCii	CD40CDii
-	25	99.66	100.30	100.03	100.35
-	50	99.64	100.26	100.06	100.36
-	75	99.64	100.18	100.16	100.36
-	100	99.40	100.21	99.82	100.28
-	125	99.41	100.22	100.14	100.32
Average		99.55	100.23	100.04	100.33
Standard dev		0.13	0.05	0.14	0.03

A.9 Two-mm thick panels

Coordinates		Thickness in mm			
X	Y	2I0.5 ii	2QSIHHW	2EH40x3S	2C20x3S
0	25	1.90	1.96	1.86	1.86
0	50	1.96	2.00	1.84	1.88
0	75	2.00	2.02	1.86	1.88
0	100	2.02	2.02	1.86	1.88
0	125	2.02	2.02	1.90	1.88
100	25	1.87	1.86	1.95	1.82
100	50	1.91	1.89	2.00	1.85
100	75	1.94	1.91	1.99	1.88
100	100	1.95	2.08	1.96	1.85
100	125	1.98	1.95	1.91	1.87
Average		1.96	1.97	1.91	1.87
Standard dev		0.05	0.07	0.06	0.02

Coordinates		Length in mm			
X	Y	2I0.5 ii	2QSIHHW	2EH40x3S	2C20x3S
0	-	147.09	149.50	149.72	149.89
25	-	147.10	149.56	149.42	149.50
50	-	147.11	149.56	149.27	149.34
75	-	147.10	149.50	149.40	149.46
100	-	147.10	149.47	149.53	149.50
Average		147.10	149.52	149.47	149.54
Standard dev		0.01	0.04	0.17	0.21

Coordinates		Width in mm			
X	Y	2I0.5 ii	2QSIHHW	2EH40x3S	2C20x3S
-	25	99.60	100.49	100.26	100.22
-	50	99.79	100.37	100.23	100.07
-	75	100.06	100.30	100.20	100.06
-	100	99.89	100.25	100.27	100.05
-	125	100.02	100.24	100.29	100.03
Average		99.87	100.33	100.25	100.09
Standard dev		0.19	0.10	0.04	0.08

Appendix B

B.1 Deflection of a clamped intact plate with a distributed load over a concentric area

B.1.1 Small deflection analysis

Timoshenko [109] obtained the central deflection of a simply supported plate under a distributed load on a concentric area. In the following the same method is followed to obtain an analogous expression for a clamped composite plate. The governing equation of a symmetric orthotropic thin laminated plate in bending is expressed by [109]

$$D_{11} w_{,xxxx} + 2(D_{12} + 2D_{66}) w_{,xxyy} + D_{22} w_{,yyyy} = -q \tag{B.1.1}$$

A proven solution for circular anisotropic panels with uniformly distributed load is

$$w(r) = \frac{q(a^2 - r^2)^2}{64 D'} \tag{B.1.2}$$

Radius r is related to the Cartesian coordinates by $r^2 = x^2 + y^2$. To satisfy Eq. (B.1.1), the equivalent flexural stiffness [109, 117] is given by

$$D' = \frac{1}{8}[3D_{11} + 2(D_{12} + 2D_{66}) + 2D_{22}] \tag{B.1.3}$$

For different loading cases, the deflection expression might not have an exact solution, when composite anisotropic materials are analysed instead of isotropic materials. In reality composite materials undergoing non-uniform loading deflect in a non-axisymmetric way [157]. Nevertheless in the quasi-isotropic lay-up case, an expression using the equivalent flexural stiffness with isotropic analysis can be adopted with reasonable accuracy, as demonstrated by [157]. Consequently, the analysis carries on using D' as the equivalent flexural modulus.

Plate deflection under any axisymmetric distributed load is found by the superposition of the concentric ring load case, repeated for different values of radius b, as shown in Figure B.1.1. The deflection of the outer unloaded region $b<r<a$ of a clamped plate loaded by a distributed force P along a concentric ring of radius b, is given by

$$w(r) = \frac{P}{8\pi D'}\left[\left(b^2 + r^2\right)\log(r/a) + \frac{\left(a^2 - r^2\right)\left(a^2 + b^2\right)}{2a^2}\right] \qquad (B.1.4)$$

For the inner loaded region of the plate $0<r<b$, a deflection is given by

$$w(r) = \frac{P}{8\pi D'}\left[\left(b^2 + r^2\right)\log(b/a) + \frac{\left(a^2 + r^2\right)\left(a^2 - b^2\right)}{2a^2}\right] \qquad (B.1.5)$$

Superimposition of the above deflections for different values of radius b can be obtained through the integration over the load application area, as shown in Figure B.1.1. The deflection can be worked out for two regions in an independent way, on the one hand the unloaded region of the plate and on the other hand the central and loaded region of the plate. For the integration, the force P distributed over an infinitesimal area, so that the distributed load is $q=P/(2\pi b \times db)$.

Deflection expression for the outer unloaded region of the plate

Superimposing the outer deflections produced by all the ring loads within the loading area, we obtain a valid expression valid over the outer unloaded part of the plate from Eq. (B.1.4) for $c<r<a$ as

$$w(r) = \frac{1}{4D'}\int_0^c\left\{\left(b^2 + r^2\right)\log(r/a) + \frac{\left(a^2 - r^2\right)\left(a^2 + b^2\right)}{2a^2}\right\}q(r)b\,db \qquad (B.1.6)$$

If the load function for the external distributed load $q(r)$ is considered constant (i.e. there is no influence of the nose-shape), the integration gives, for $c<r<a$

$$w(r) = \frac{q}{4D'}\left[\left(\frac{b^4}{4}+\frac{b^2 r^2}{2}\right)\log(r/a)+\frac{(a^2-r^2)}{2a^2}\left(\frac{b^2 a^2}{2}+\frac{b^4}{4}\right)\right]_{b=0}^{b=c}$$ (B.1.7a)

After evaluating Eq. (B.1.7a) within the integration range and replacing the distributed load by $q=P/(\pi c^2)$ for $c<r<a$, it yields

$$w(r) = \frac{P}{4\pi D'}\left[\left(\frac{c^4}{4}+\frac{c^2 r^2}{2}\right)\log(r/a)+\frac{(a^2-r^2)}{2a^2}\left(\frac{c^2 a^2}{2}+\frac{c^4}{4}\right)\right]$$ (B.1.7b)

This equation can be rearranged in terms of the Loading Area Factor (LAF) defined in Chapter 3, as

$$w(r) = \frac{w_0}{LAF}\left[2\left(1-\left(\frac{r}{a}\right)^2\right)\left(1+\left(\frac{c}{a}\right)^2\right)+\log(r/a)\left(\left(\frac{c}{a}\right)^2+2\left(\frac{r}{a}\right)^2\right)\right]$$ (B.1.7c)

Deflection expression for the central loaded region of the plate

Obtaining an expression for the deflection over the loaded sector of the plate, $0<r<c$, is more complicated; because both inner and outer deflections have to be considered on the integration. The disturbing term is related to Eq. (B.1.4), since it tends to infinite when the radius of application tends to zero. Therefore, for simplicity, only the central deflection is obtained. The central deflection $w_{max}(0)$ at the centre of the panel is obtained by setting r to 0 in Eq. (B.1.5) and superimposing the central deflection by integrating

$$w(0) = \frac{1}{4D'}\int_0^c [b^2 \log(b/a)+1/2(a^2-b^2)]q(r)bdb$$ (B.1.8a)

Multiplying by b and considering the load function $q(r)$ as constant, it yields

$$w(0) = \frac{q}{4D'}\int_0^c [b^3 \log(b/a)+1/2(a^2 b)-1/3(b^3)]db$$ (B.1.8b)

302

After integrating Eq. (B.1.8b) and using $q=P/(\pi c^2)$ we have

$$w(0) = \frac{q}{4D'}\left[\frac{b^4}{4}\log(b/a) - \frac{b^4}{16} + \frac{a^2 b^2}{4} - \frac{b^4}{8}\right]_{b=0}^{b=c} = \frac{P}{4\pi D'}\left[\frac{c^2}{4}\log(c/a) - \frac{3c^2}{16} + \frac{a^2}{4}\right] \quad \text{(B.1.9)}$$

This expression can be rearranged as

$$w(0) = \frac{Pa^2}{16\pi D'}\left\{1 + \left[(c/a)^2\left(\log(c/a) - \frac{3}{4}\right)\right]\right\} = \frac{Pa^2}{16\pi D'} \times LAF \quad \text{(B.1.10)}$$

Eq. (B.1.10) expresses the central deflection of a plate uniformly loaded over a concentric area, as shown in Figure 3.1.17. The term in curly brackets was defined in Chapter 3 as the Loading Area Factor, LAF.

B.1.2 Large deflection analysis

The deflection equation is defined using the method of virtual displacements [109], in terms of strain energy due to bending and strain energy due to membrane stretching as

$$\frac{d(V + V_1)}{dw_0}\delta w_0 = \frac{dV + dV_1}{dw_0}\delta w_0 = 2\pi\int_0^a q\delta w r dr \quad \text{(B.1.11)}$$

In the following part of the analysis expressions are derived for each individual term in Eq. (B.1.11), focusing on the membrane stretching effect term. First, the strain energy due to bending is defined from

$$dV = -\frac{1}{2}\left(M_x w_{,xx} + M_y w_{,yy}\right)dxdy \quad \text{(B.1.12a)}$$

If the classical laminate theory is used, together with a change of the coordinate systems, Eq. (B.1.12) can be rewritten as

$$dV = \frac{1}{2}\left\{\left(D_{11}w_{,rr} + D_{12}\frac{1}{r}w_{,r}\right)w_{,rr} + \left(D_{12}w_{,rr} + D_{22}\frac{1}{r}w_{,r}\right)\frac{1}{r}w_{,r}\right\}drd\theta \quad \text{(B.1.12b)}$$

Integration over all the plate area gives the strain energy due to bending for circular plates

$$V = \frac{1}{2}\int_0^{2\pi}\int_0^a\left\{\left(D_{11}w_{,rr} + D_{12}\frac{1}{r}w_{,r}\right)w_{,rr} + \left(D_{12}w_{,rr} + D_{22}\frac{1}{r}w_{,r}\right)\frac{1}{r}w_{,r}\right\}drd\theta \quad \text{(B.1.13)}$$

The second term V_1 in Eq. (B.1.11) is for the strain energy due to membrane stretching as

$$V_1 = 2\pi\int_0^a 1/2\left(N_r\varepsilon_r + N_t\varepsilon_t\right)rdr \quad \text{(B.1.14)}$$

Using the classical laminate theory for a quasi-isotropic laminate with $A_{11} = A_{22}$, we have

$$V_1 = \pi\int_0^a\left((A_{11}\varepsilon_r + A_{12}\varepsilon_t)\varepsilon_r + (A_{12}\varepsilon_r + A_{11}\varepsilon_t)\varepsilon_t\right)rdr \quad \text{(B.1.15)}$$

The relationship between strain-displacement relationships is given by [109]

$$\varepsilon_r = \frac{du}{dr} + \frac{1}{2}\left(\frac{dw}{dr}\right)^2$$
$$\varepsilon_t = \frac{u}{r} \quad \text{(B.1.16a,b)}$$

Definition of the displacement field u is approximated by a series and neglecting the high order terms

$$u = r(a-r)(C_1 + C_2 r + C_3 r^2 + ...) = r(a-r)(C_1 + C_2 r) \qquad (B.1.17)$$

Combining Eqs. (B.1.16a,b&B.1.17) with Eq. (B.1.15) yields

$$V_1 = \pi A_{11} \int_0^a \left((u_{,r} + 1/2 w_{,r}^2)^2 + (u/r)^2 \right) r dr + 2\pi A_{12} \int_0^a (u_{,r} + 1/2 w_{,r}^2)(u/r) r dr \qquad (B.1.18)$$

For the outer part of the plate the deflection $w(r)$ can be approximated by the small deflection analysis for the entire plate, as in Eq. (B.1.7c). This approximation regards the energy contribution of the region under the applied load as small quantity compared with the outer part of the plate, especially for a small indenter.

Adding Eq. (B.1.13) and (B.1.18)

$$V + V_1 = \frac{1}{2} \int_0^{2\pi} \int_0^a \left\{ \left(D_{11} w_{,rr} + D_{12} \frac{1}{r} w_{,r} \right) w_{,rr} + \left(D_{12} w_{,rr} + D_{22} \frac{1}{r} w_{,r} \right) \frac{1}{r} w_{,r} \right\} dr d\theta + ...$$

$$... \pi A_{11} \int_0^a \left((u_{,r} + 1/2 w_{,r}^2)^2 + (u/r)^2 \right) r dr + 2\pi A_{12} \int_0^a (u_{,r} + 1/2 w_{,r}^2)(u/r) r dr$$

$$(B.1.19a)$$

Using Eq. (B.1.7c) and its derivatives, we get a 4th degree polynomial expression for w_0 as given by

$$V + V_1 = T_1 w_0^2 + T_2 w_0^4 \qquad (B.1.19b)$$

where T_1 and T_2 are polynomial coefficients. Due to their length they are not fully expanded. After replacing distributed load q by $P/(\pi c^2)$ and using the results from Eq. (B.1.19b), Eq. (B.1.11) yields

$$T_1 w_0 + T_2 w_0^3 = T_3 P \qquad (B.1.20)$$

305

The term T_1 can be considered similar to the counterpart small deflection analysis given by Eq. (3.1.2) as

$$T_1 = \frac{16\pi D'}{LAF} \tag{B.1.21}$$

Terms T_2 and T_3 are obtained after a lengthy derivation. In the case of T_3, it is equal to the square of plate radius a^2. The other term, T_2 accounts the membrane stretching effect. It can be obtained by combining Eq. (B.1.11) and Eq. (B.1.19a) and grouping the coefficients for w_0^3

$$T_2 w_0^3 = \frac{d}{dw_0} \left(\pi A_{11} \int_0^a 1/4\, w_{,r}^4 r dr \right) \tag{B.1.22}$$

The term inside the integral is defined in terms of the first derivative of the deflection w. Differentiating Eq. (B.1.7c) respect to r yields

$$w_{,r}(r) = \frac{w_0}{LAF} \left[\frac{4r}{a^2} \left(\log(r/a) - 1/2 - (c/a)^2 \right) + \frac{1}{r}(c/a)^2 \right] \tag{B.1.23}$$

and replacing Eq. (B.1.23) into Eq. (B.1.23) we obtain

$$T_2 w_0^3 = \frac{d}{dw_0} \left(\pi A_{11}\, 1/4\, \frac{w_0^4}{LAF^4} \int_0^a \left[\frac{4r}{a^2} \left(\log(r/a) - 1/2 - (c/a)^2 \right) + \frac{1}{r}(c/a)^2 \right]^4 r dr \right) \tag{B.1.24}$$

Differentiating respect the central deflection w_0, we have

$$T_2 w_0^3 = \pi A_{11}\, \frac{w_0^3}{LAF^4} \int_0^a \left[\frac{4r}{a^2} \left(\log(r/a) - 1/2 - (c/a)^2 \right) + \frac{1}{r}(c/a)^2 \right]^4 r dr \tag{B.1.25}$$

Therefore T_2 is given by

$$T_2 = \pi A_{11} \frac{1}{LAF^4} \int_0^a \left[\frac{4r}{a^2} \left(\log(r/a) - 1/2 - (c/a)^2 \right) + \frac{1}{r}(c/a)^2 \right]^4 rdr \qquad \text{(B.1.26)}$$

The solution of the integral is

$$T_2 = \pi A_{11} \frac{1}{LAF^4} \left\{ \begin{array}{l} 0.217 + (c/a)^2[-0.465] + (c/a)^4[-0.140] + \\[2mm] (c/a)^6 \left[0.466 - 2.259\log(c/a) - 1.240\log^2(c/a) + \frac{7}{36}\log^3(c/a) + \frac{1}{6}\log^4(c/a) \right] + \\[2mm] (c/a)^8 \left[0.183 - 1.139\log(c/a) - \frac{1}{12}\log^2(c/a) + \log^3(c/a) \right] + \\[2mm] (c/a)^{10} \left[0.029 - \frac{5}{48}\log(c/a) - \frac{1}{16}\log^2(c/a) \right] + \\[2mm] (c/a)^{12} \left[0.003 + \frac{1}{96}\log(c/a) \right] + \\[2mm] (c/a)^{14} \left[-\frac{1}{1536} \right] \end{array} \right\}$$

$$\text{(B.1.27a)}$$

The contribution from the high order terms to the final solution is small. If only the first two terms are taken in to account, T_2 can be approximated by

$$T_2 = \pi A_{11} \frac{1}{LAF^4} \left\{ 0.217 - 0.465 \left(\frac{c}{a} \right)^2 \right\} \qquad \text{(B.1.27b)}$$

The central deflection can be expressed in terms of T_1, T_2 and T_3 as

$$\frac{16\pi D'}{a^2} \frac{1}{LAF} w_0 + \frac{\pi A_{11}}{a^2} \frac{1}{LAF^4} \left\{ 0.217 + (c/a)^2[-0.465] \right\} w_0^3 = P \qquad \text{(B.1.28)}$$

307

B.2 Deflection of a clamped plate with a circular delamination at the mid-plane centrally loaded

The plate loading conditions are shown in Figure B.2.1. For simplicity, the plate is assumed to be transversely loaded at the centre by a concentrated force. The deflection of a panel containing a single delamination at the mid-plane can be obtained by adding the correspondent deflections of the outer intact region and the delaminated region, indicated as BA and AO regions respectively in Figure B.2.1. Thus, the total deflection is given by

$$\delta_{total} = \delta_{BA} + \delta_{AO} \tag{B.2.1}$$

The deflection of an intact plate due to a central load is (Eq. 92 in [109])

$$w(r) = \frac{P}{16\pi D}\left[a_2^2 - r^2\left(1 + 2\ln\left(\frac{a_2}{r}\right)\right)\right] \tag{B.2.2}$$

The contribution of the region BA to the central deflection is obtained by evaluating Eq. (B.2.2) at $r = a_1$

$$\delta_{BA} = w(a_1) = \frac{P}{16\pi D_{BA}}\left[a_2^2 - a_1^2\left(1 + 2\ln\left(\frac{a_2}{a_1}\right)\right)\right] \tag{B.2.3}$$

where the flexural rigidity D' of the plate is defined in Eq. (B.1.3). On the other hand, the flexural rigidity D_{AO} of one of the sublaminates of the region AO can be approximated by using the proportionality between the plate thickness and the cubic root of the flexural rigidity (rigorously speaking this proportionality is only true for isotropic materials). Assuming that the delamination is located at the mid-plane, then the flexural rigidity D_{AO} can be approximated by

$$\frac{D'}{D_{AO}} \approx \frac{h^3}{(h/2)^3} = 8$$

$$D_{AO} \approx \frac{1}{8}D'$$

(B.2.4a,b)

The deflection analysis for the delaminated region AO is similar to that shown in Chapter 3 of [109] for a clamped plate loaded at the centre by a concentrated force. The total deflection of the plate AO, $w_{AO,total}$, is the superimposition of the deflection of a simply supported plate centrally loaded, $w_{AO,SS}$, and the deflection produced by an applied moment M at the panel boundary, $w_{AO,M}$. Thus. the deflection of the region AO is given by

$$w_{AO,total}(0) = w_{AO,M}(0) + w_{AO,SS}(0)$$

(B.2.5)

where the subscripts M and SS stand for the applied moment and simply supported, respectively. The applied moment, M, can be obtained based on the slope continuity at radius a_1 between regions BA and AO. The slope θ is obtained by differentiating Eq. (B.2.2) respect to the radius

$$\frac{dw}{dr} = \theta(r) = \frac{-P}{4\pi D'} r \ln\left(\frac{a_2}{r}\right)$$

(B.2.6a)

substituting $r = a_1$, Eq. (B.2.6a) becomes

$$\theta(a_1) = \frac{-P}{4\pi D'} a_1 \ln\left(\frac{a_2}{a_1}\right)$$

(B.2.6b)

The correspondent moment M applied at the boundary of the plate AO that produces the slope given in Eq. (B.2.6b) is obtained using the Eq. (46) in [109]

$$\theta(a_1) = \frac{1}{r_x} a_1 = \frac{M}{D_{AO}(1+v)} a_1$$

(B.2.7)

Combining Eq. (B.2.6b) and Eq. (B.2.7) it yields

$$\frac{-P}{4\pi D'} a_1 \ln\left(\frac{a_2}{a_1}\right) + \frac{Ma_1}{D_{AO}(1+\nu)} a_1 = 0$$

(B.2.8)

And solving for the applied moment M

$$M = \frac{P}{4\pi} \frac{D_{AO}(1+\nu)}{D'} \ln\left(\frac{a_2}{a_1}\right) = P \frac{(1+\nu)}{32\pi} \ln\left(\frac{a_2}{a_1}\right)$$

(B.2.9)

The central deflection induced by M can be obtained through the expression derived in [158] (table 24, case 13)

$$w_{AO,M}(0) = \frac{M_0 r_0^2}{2D}\left(\frac{1}{1+\nu} + \ln\left(\frac{a}{r_0}\right)\right)$$

(B.2.10)

Where D, M_0, r_0, and a are the flexural rigidity, applied moment, radius at which moment is applied and plate radius respectively. Replacing by the corresponding values of moment M and radius a_1, for the circular plate AO, Eq. (B.2.10) becomes

$$w_{AO,M}(0) = \frac{Pa_1^2}{8\pi D'} \ln\left(\frac{a_2}{a_1}\right)$$

(B.2.11)

The second term in Eq. (B.2.5) corresponds to the central deflection of a simply supported plate loaded at the centre, $w_{AO,SS}(0)$. It can be obtained through Eq. (88) in [109]. However, the load used in this expression should be only half of the total applied load P, since two identical laminates are loaded simultaneously in the delaminated region BA. Deflection $w_{AO,SS}(0)$ is given by

$$w_{AO,SS}(0) = \left(\frac{P}{2}\right)\frac{a^2}{16\pi D}\frac{3+\nu}{1+\nu}$$

(B.2.12a)

310

Replacing with the values for plate AO at the centre $r=0$

$$w_{AO,SS}(0) = \frac{Pa_1^2}{4\pi D'} \frac{3+v}{1+v}$$

(B.2.12b)

The total deflection of the delaminated region AO in Eq. (B.2.5) becomes

$$\delta_{AO} = w_{AO,total}(0) = w_{AO,SS}(0) + w_{AO,M}(0) = \frac{Pa_1^2}{4\pi D'} \frac{3+v}{1+v} + \frac{Pa_1^2}{8\pi D'} \ln\left(\frac{a_2}{a_1}\right)$$

(B.2.13)

The total deflection of the complete plate, including regions BA and AO, is given by Eq. (B.2.1). Replacing with the deflection expressions (B.2.3) and (B.2.13) it yields

$$\delta_{total} = \frac{Pa_1^2}{4\pi D'} \frac{3+v}{1+v} + \frac{Pa_1^2}{8\pi D'} \ln\left(\frac{a_2}{a_1}\right) + \frac{P}{16\pi D'}\left[a_2^2 - a_1^2\left(1+2\ln\left(\frac{a_2}{a_1}\right)\right)\right]$$

(B.2.14a)

Rearranging Eq. (B.2.14a) yields

$$\delta_{total} = \frac{P}{16\pi}\left[\frac{a_2^2 - a_1^2}{D'} + \frac{4a_1^2(3+v)}{D'(1+v)}\right]$$
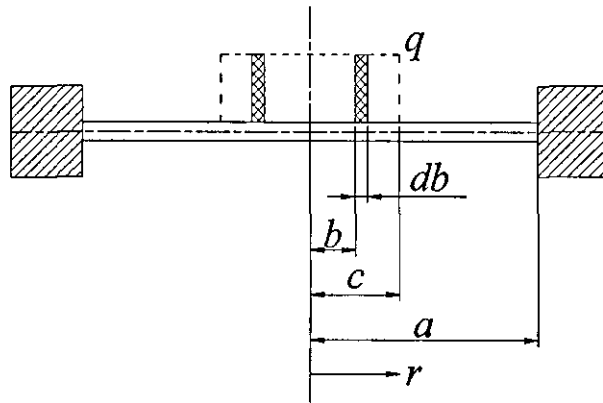
(B.2.14b)

Figure B.1.1 Concentrically loaded plate: superposition of deflections
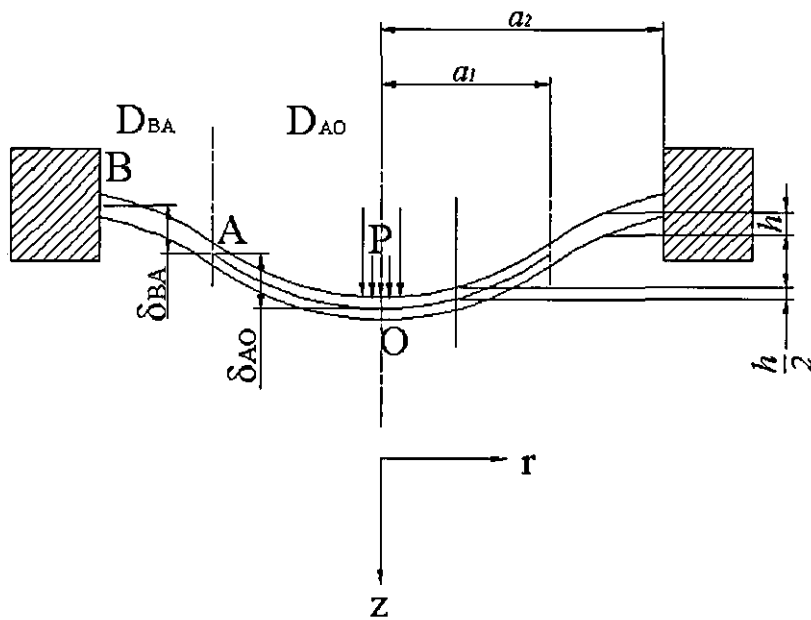

Figure B.2.1 Circular plate transversely loaded with a concentric crack at the mid-plane

312

Appendix C

C.1 Matlab script for analytical model of transverse deflection with indentation effect in Chapter 3

C.1.1 First function: data post-processing

```
function[]=dispforce()


%INPUT DATA
%MATERIAL PROPERTIES for Graphite Epoxy system

% km      membrane stiffness GPa.mm^-1
km=0.17202;

% ki      contact stiffness GPa.mm^(1/n)
ki=47.2;

% kbs     bending and shear stiffness GPa.mm
%Flat indentor kbs=5.2411;
%Hemispherical indentor kbs=4.5592;
kbs=5.2411;

% n       exponential constant
n=1.83;

% p       applied force kN, initial value
p=10;

%Algorithm to plot the force-displacement graph
dispforce=zeros(200,2);
for index=1:200
    % disp       displacement of the indentor mm
    disp=0+0.05*index;
    p=10;
    %Calling the main algorithm
    [force]=ecusolv(km,ki,kbs,n,disp,p);
    dispforce(index,:)=[disp force];
end
dispforce=[0 0; dispforce]
plot(dispforce(:,1),dispforce(:,2))
axis([0 10 0 60])
xlabel('Displacement  mm','FontName','Times New Roman','FontSize',18);
ylabel('Load  kN','FontName','Times New Roman','FontSize',18);
set(gca,'Fontname','Times New Roman');
set(gca,'Fontsize',18);
set(gcf,'color',[1,1,1]);

grid on;
```

C.1.2 Second function: main algorithm

```
function[pop]=ecusolv(km,ki,kbs,n,disp,p)

%  p   initial value for x
%  exit conditions for the iterations
tol = 0.001;
Itera= 100;

%
%    Newton-Raphson
%
ite=0;
D=0;
F=0;

while ite<Itera,
    [D]=deriv(km,ki,kbs,n,disp,p);
    [F]=gzmodel(km,ki,kbs,n,disp,p);
    pn=p-F/D;
    if abs(p-pn)<tol
        ite=Itera;
    else
        ite=ite+1;
    end
    p=pn;
end

pop=p;
```

C.1.3 Third function: calculation of first derivative

```
function[D]=deriv(km,ki,kbs,n,disp,p)

% derivative of function F
%
%
delta=1e-3;
[F]=gzmodel(km,ki,kbs,n,disp,p);

pd=p;
    if  p<=1e-30
        pd=p+0.001;
    else
        pd=(1+delta)*p;
    end
    [Fd]=gzmodel(km,ki,kbs,n,disp,pd);

    if p<=1e-30
        D=(Fd-F)/0.001;
      else
        D=(Fd-F)/(p*delta);
        end

    pd=p;
```

314

C.1.4 Fourth function: main equation based on analytical model:

```
function[F]=gzmodel(km,ki,kbs,n,disp,p)

% function[F]=gzmodel(km,ki,kbs,n,disp,p)
% Relationship between force and displacement, taking account of
% indentation, membrane, shear and flexural response from the laminate
% km      membrane stiffness GPa.mm^-1
% ki      contact stiffness GPa.mm^(1/n)
% kbs     bending and shear stiffness GPa.mm
% disp       displacement of the indentor mm
% p       applied force kN

F=-km*p^(3/n)/ki^(3/n);
F=F+3*disp*km*p^(2/n)/ki^(2/n);
F=F-(km*3*disp^2+kbs)*p^(1/n)/ki^(1/n);
F=F+km*disp^3+kbs*disp-p;
```

C.2 Matlab script for in-plane compressive failure prediction in Chapter 4

```
function[P_applied,factor_m45,factor_0,factor_45,factor_90]=admatrices
(plies)

%function[]= admatrices(plies)
%If plies = 32 then is a normal QI laminate of 32 plies with layup: (-
45,0,+45,90)4s
%If plies = 16 then is a normal QI laminate of 16 plies with layup: (-
45,0,+45,90)2s

%Extensional stiffness matrix A in GPa-mm
switch plies
case 32
   A=[224.88 67.42 0;67.42 224.88 0;0 0 78.73];
case 16
   A=[112.44 33.71 0;33.71 112.44 0; 0 0 39.36];
end
%Inverting the matrix A in (kN/mm)^-1
ainv=A^-1;

%Transformed reduced stiffness matrix Q bar in GPa
Qm45=[41.28 30.08 -29.68; 30.08 41.28 -29.68; -29.68 -29.68 32.84];
Q0=[127.88 2.84 0; 2.84 9.16 0; 0 0 5.60];
Q45=[41.28 30.08 29.68; 30.08 41.28 29.68; 29.68 29.68 32.84];
Q90=[9.16 2.84 0; 2.84 127.88 0; 0 0 5.60];

%Generating the mean strains
%Force vector in kN
if plies==16
   Py=-[0:1:100]./100;
elseif plies==32
   Py=-[0:2:200]./100;
end
Px=zeros(size(Py));
Pz=zeros(size(Py));
P=[Px; Py; Pz];
```

```matlab
%Strain vector
strain=zeros(size(P));
for i=1:length(Py)
    strain(:,i)=ainv*P(:,i);
end

%Stress for each ply in global panel coordinates, in MPa
stress_global_m45=zeros(size(strain));
stress_global_0=zeros(size(strain));
stress_global_45=zeros(size(strain));
stress_global_90=zeros(size(strain));
for i=1:length(Py)
    stress_global_m45(:,i)=Qm45*strain(:,i)*1000;
    stress_global_0(:,i)=Q0*strain(:,i)*1000;
    stress_global_45(:,i)=Q45*strain(:,i)*1000;
    stress_global_90(:,i)=Q90*strain(:,i)*1000;
end

%Stress in local ply coordinates, in MPa
%Angles in rad
am45=-45*pi/180;
a0=0*pi/180;
a45=45*pi/180;
a90=90*pi/180;
%Matrix T for angle transformation
Tm45=[cos(am45)^2 sin(am45)^2 2*cos(am45)*sin(am45); sin(am45)^2
cos(am45)^2 -2*cos(am45)*sin(am45); -sin(am45)*cos(am45)
sin(am45)*cos(am45) cos(am45)^2-sin(am45)^2];
T0=[cos(a0)^2 sin(a0)^2 2*cos(a0)*sin(a0); sin(a0)^2 cos(a0)^2 -
2*cos(a0)*sin(a0); -sin(a0)*cos(a0) sin(a0)*cos(a0) cos(a0)^2-
sin(a0)^2];
T45=[cos(a45)^2 sin(a45)^2 2*cos(a45)*sin(a45); sin(a45)^2 cos(a45)^2
-2*cos(a45)*sin(a45); -sin(a45)*cos(a45) sin(a45)*cos(a45) cos(a45)^2-
sin(a45)^2];
T90=[cos(a90)^2 sin(a90)^2 2*cos(a90)*sin(a90); sin(a90)^2 cos(a90)^2
-2*cos(a90)*sin(a90); -sin(a90)*cos(a90) sin(a90)*cos(a90) cos(a90)^2-
sin(a90)^2];
%Local stress arrays
stress_local_m45=zeros(size(strain));
stress_local_0=zeros(size(strain));
stress_local_45=zeros(size(strain));
stress_local_90=zeros(size(strain));
for i=1:length(Py)
    stress_local_m45(:,i)=Tm45*stress_global_m45(:,i);
    stress_local_0(:,i)=T0*stress_global_0(:,i);
    stress_local_45(:,i)=T45*stress_global_45(:,i);
    stress_local_90(:,i)=T90*stress_global_90(:,i);
end

%Tsai-Hill criteria for each ply
%Critical compressive strength values in MPa
stress_1c=1032;
stress_2c=130;
stress_12c=66.30;
%Calculation of the failure factor
factor_m45=zeros(size(Py));
factor_0=zeros(size(Py));
factor_45=zeros(size(Py));
factor_90=zeros(size(Py));
for i=1:length(Py)
```

316

```
    factor_m45(i)=stress_local_m45(1,i)^2/(stress_1c^2)-
    stress_local_m45(1,i)*stress_local_m45(2,i)/(stress_1c^2)+
    stress_local_m45(2,i)^2/(stress_2c^2)+stress_local_m45(3,i)^2/
    (stress_12c^2);

    factor_0(i)=stress_local_0(1,i)^2/(stress_1c^2)-
    stress_local_0(1,i)*stress_local_0(2,i)/(stress_1c^2)+
    stress_local_0(2,i)^2/(stress_2c^2)+stress_local_0(3,i)^2/
    (stress_12c^2);

    factor_45(i)=stress_local_45(1,i)^2/(stress_1c^2)-
    stress_local_45(1,i)*stress_local_45(2,i)/(stress_1c^2)+
    stress_local_45(2,i)^2/(stress_2c^2)+stress_local_45(3,i)^2/
    (stress_12c^2);

    factor_90(i)=stress_local_90(1,i)^2/(stress_1c^2)-
    stress_local_90(1,i)*stress_local_90(2,i)/(stress_1c^2)+
    stress_local_90(2,i)^2/(stress_2c^2)+stress_local_90(3,i)^2/
    (stress_12c^2);

end
P_applied=Py*100;

%Postprocessing the outputs
P_applied=P_applied';
stress_local_m45=stress_local_m45';
stress_local_0=stress_local_0';
stress_local_45=stress_local_45';
stress_local_90=stress_local_90';
factor_m45=factor_m45';
factor_0=factor_0';
factor_45=factor_45';
factor_90=factor_90';

%Saving the stress in local ply coordinates in text files
stress_out=[P_applied stress_local_m45 stress_local_0 stress_local_45
 stress_local_90];

if plies==16
    save stress_16.txt stress_out -ASCII
elseif plies==32
    save stress_32.txt stress_out -ASCII
end

%Saving the tsai hill factors in text files
output=[P_applied factor_m45 factor_0 factor_45 factor_90];
if plies==16
    save tsai_hill_16.txt output -ASCII
elseif plies==32
    save tsai_hill_32.txt output -ASCII
end
```

Appendix D

D.1 Determination of extensional stiffness matrix A

The reduced stiffness matrix is given by

$$[Q] = \begin{bmatrix} \dfrac{E_1}{1-\nu_{12}\nu_{21}} & \dfrac{\nu_{12}E_2}{1-\nu_{12}\nu_{21}} & 0 \\ \dfrac{\nu_{12}E_2}{1-\nu_{12}\nu_{21}} & \dfrac{E_2}{1-\nu_{12}\nu_{21}} & 0 \\ 0 & 0 & G_{12} \end{bmatrix}$$

(D.1.1)

Substituting by the material properties given in Table 2.1.1, the reduced stiffness matrix becomes

$$[Q] = \begin{bmatrix} 127.88 & 2.84 & 0 \\ 2.84 & 9.16 & 0 \\ 0 & 0 & 5.60 \end{bmatrix}$$

(D.1.2)

The transformed reduced stiffness matrix could be given by using Eq. (4.3.8) as

$$\begin{aligned}
[\overline{Q_{11}}] &= Q_{11}\cos^4\theta + 2(Q_{12}+2Q_{66})\sin^2\theta\cos^2\theta + Q_{22}\sin^4\theta \\
[\overline{Q_{12}}] &= (Q_{11}+Q_{22}-4Q_{66})\sin^2\theta\cos^2\theta + Q_{12}(\sin^4\theta+\cos^4\theta) \\
[\overline{Q_{22}}] &= Q_{11}\sin^4\theta + 2(Q_{12}+2Q_{66})\sin^2\theta\cos^2\theta + Q_{22}\cos^4\theta \\
[\overline{Q_{16}}] &= (Q_{11}-Q_{12}-2Q_{66})\sin\theta\cos^3\theta + (Q_{12}-Q_{22}+2Q_{66})\sin^3\theta\cos\theta \\
[\overline{Q_{26}}] &= (Q_{11}-Q_{12}-2Q_{66})\sin^3\theta\cos\theta + (Q_{12}-Q_{22}+2Q_{66})\sin\theta\cos^3\theta \\
[\overline{Q_{66}}] &= (Q_{11}+Q_{22}-2Q_{12}-2Q_{66})\sin^2\theta\cos^2\theta + Q_{66}(\sin^4\theta+\cos^4\theta)
\end{aligned}$$

(D.1.3)

As lay-ups were (-45°/0°/+45°/90°)$_{2S}$ for 16-ply laminates and (-45°/0°/+45°/90°)$_{4S}$ for 32-ply laminates, the transformed reduced stiffness matrix are given by

$$[Q]_{-45} = \begin{bmatrix} 41.28 & 30.08 & -29.68 \\ 30.08 & 41.28 & -29.68 \\ -29.68 & -29.68 & 32.84 \end{bmatrix} \text{GPa} \quad \text{for -45}^\circ \text{ plies} \qquad (D.1.3a)$$

$$[Q]_0 = \begin{bmatrix} 127.88 & 2.84 & 0 \\ 2.84 & 9.16 & 0 \\ 0 & 0 & 5.60 \end{bmatrix} \text{GPa} \quad \text{for 0}^\circ \text{ plies} \qquad (D.1.3b)$$

$$[Q]_{45} = \begin{bmatrix} 41.28 & 30.08 & 29.68 \\ 30.08 & 41.28 & 29.68 \\ 29.68 & 29.68 & 32.84 \end{bmatrix} \text{GPa} \quad \text{for 45}^\circ \text{ plies} \qquad (D.1.3c)$$

$$[Q]_{90} = \begin{bmatrix} 9.16 & 2.84 & 0 \\ 2.84 & 127.88 & 0 \\ 0 & 0 & 5.60 \end{bmatrix} \text{GPa} \quad \text{for 90}^\circ \text{ plies} \qquad (D.1.3d)$$

The extensional stiffness matrix A is given by

$$A_{ij} = \sum_{k=1}^{n} [\overline{Q}_{ij}]_k (z_k - z_{k-1}) \qquad (D.1.4a)$$

where z_k and z_{k-1} are the distances measured from the mid-plane to the bottom and top surfaces of the k-ply. For laminates with constant ply thickness, Eq. (D.1.4a) can be rearranged by taking advantage of ply thickness t_k for the convenience of computation as follows

$$A_{ij} = \sum_{k=1}^{n} [\overline{Q}_{ij}]_k t_k \qquad (D.1.4b)$$

in which the ply thickness t_k is 0.128 mm, as indicated in Chapter 2. Combining Eqs. (D1.3a-d) with Eq. (D.1.4b) yields

$$[A] = \begin{bmatrix} 112.44 & 33.71 & 0 \\ 33.71 & 112.44 & 0 \\ 0 & 0 & 39.36 \end{bmatrix} \text{ GPa-mm} \qquad \text{for 16-ply laminate} \qquad \text{(D.1.5a)}$$

$$[A] = \begin{bmatrix} 224.88 & 67.42 & 0 \\ 67.42 & 224.88 & 0 \\ 0 & 0 & 78.73 \end{bmatrix} \text{ GPa-mm} \qquad \text{for 32-ply laminate} \qquad \text{(D.1.5b)}$$

The corresponding inverted matrices (i.e. compliance matrices) are

$$[A]^{-1} = [A'] = \begin{bmatrix} 0.0098 & -0.0029 & 0 \\ -0.0029 & 0.0098 & 0 \\ 0 & 0 & 0.0254 \end{bmatrix} \text{(GPa-mm)}^{-1} \text{ for 16-ply laminate} \quad \text{(D.1.6a)}$$

$$[A]^{-1} = [A'] = \begin{bmatrix} 0.0049 & -0.0015 & 0 \\ -0.0015 & 0.0049 & 0 \\ 0 & 0 & 0.0127 \end{bmatrix} \text{(GPa-mm)}^{-1} \text{ for 32-ply laminate} \quad \text{(D.1.6b)}$$

D.2 Determination of bending stiffness matrix D

The bending stiffness matrix is defined by

$$D_{ij} = \frac{1}{3} \sum_{k=1}^{n} [\overline{Q}_{ij}]_k \left(z_k^3 - z_{k-1}^3 \right) \qquad \text{(D.2.1a)}$$

Similarly to the extensional matrix $[A]$, Eq (D.2.1a) can be rearranged by taking advantage of ply thickness as follows

$$D_{ij} = \frac{1}{3} \sum_{k=1}^{n} [\overline{Q}_{ij}]_k t_k \left(t_k^2 + 3 z_k z_{k-1} \right) \qquad \text{(D.2.1b)}$$

After carrying out all the calculations, the bending stiffness matrices are

$$[D] = \begin{bmatrix} 44.44 & 13.61 & -4.48 \\ 13.61 & 30.50 & -4.48 \\ -4.48 & -4.48 & 15.59 \end{bmatrix} \text{GPa-mm}^3 \quad \text{for 16-ply laminates} \qquad \text{(D.2.2a)}$$

$$[D] = \begin{bmatrix} 336.96 & 101.58 & -16.93 \\ 101.58 & 277.21 & -16.93 \\ -16.93 & -16.93 & 117.38 \end{bmatrix} \text{GPa-mm}^3 \quad \text{for 32-ply laminates} \qquad \text{(D.2.2b)}$$

The corresponding inverted matrices (i.e. compliance matrices) are

$$[D]^{-1} = [D'] = \begin{bmatrix} 0.0263 & -0.0111 & 0.0044 \\ -0.0111 & 0.0389 & 0.0080 \\ 0.0044 & 0.0080 & 0.0677 \end{bmatrix} \text{(GPa-mm}^3)^{-1}, \text{ for 16-ply laminate} \quad \text{(D.2.3a)}$$

$$[D]^{-1} = [D'] = \begin{bmatrix} 0.0033 & -0.0012 & 0.0002 \\ -0.0012 & 0.0041 & 0.0003 \\ 0.0002 & 0.0003 & 0.0057 \end{bmatrix} \text{(GPa-mm}^3)^{-1}, \text{ for 32-ply laminate} \quad \text{(D.2.3b)}$$